OCEAN ISLAND VOLCANOES: GENESIS, EVOLUTION AND IMPACT

EDITED BY: Adriano Pimentel, Ricardo S. Ramalho, Laura Becerril, Patricia Larrea and Richard J. Brown

PUBLISHED IN: Frontiers in Earth Science

frontiers Research Topics

Frontiers eBook Copyright Statement

The copyright in the text of individual articles in this eBook is the property of their respective authors or their respective institutions or funders. The copyright in graphics and images within each article may be subject to copyright of other parties. In both cases this is subject to a license granted to Frontiers.

The compilation of articles constituting this eBook is the property of Frontiers.

Each article within this eBook, and the eBook itself, are published under the most recent version of the Creative Commons CC-BY licence. The version current at the date of publication of this eBook is CC-BY 4.0. If the CC-BY licence is updated, the licence granted by Frontiers is automatically updated to the new version.

When exercising any right under the CC-BY licence, Frontiers must be attributed as the original publisher of the article or eBook, as applicable.

Authors have the responsibility of ensuring that any graphics or other materials which are the property of others may be included in the CC-BY licence, but this should be checked before relying on the CC-BY licence to reproduce those materials. Any copyright notices relating to those materials must be complied with.

Copyright and source acknowledgement notices may not be removed and must be displayed in any copy, derivative work or partial copy which includes the elements in question.

All copyright, and all rights therein, are protected by national and international copyright laws. The above represents a summary only. For further information please read Frontiers' Conditions for Website Use and Copyright Statement, and the applicable CC-BY licence.

ISSN 1664-8714
ISBN 978-2-88963-728-7
DOI 10.3389/978-2-88963-728-7

About Frontiers

Frontiers is more than just an open-access publisher of scholarly articles: it is a pioneering approach to the world of academia, radically improving the way scholarly research is managed. The grand vision of Frontiers is a world where all people have an equal opportunity to seek, share and generate knowledge. Frontiers provides immediate and permanent online open access to all its publications, but this alone is not enough to realize our grand goals.

Frontiers Journal Series

The Frontiers Journal Series is a multi-tier and interdisciplinary set of open-access, online journals, promising a paradigm shift from the current review, selection and dissemination processes in academic publishing. All Frontiers journals are driven by researchers for researchers; therefore, they constitute a service to the scholarly community. At the same time, the Frontiers Journal Series operates on a revolutionary invention, the tiered publishing system, initially addressing specific communities of scholars, and gradually climbing up to broader public understanding, thus serving the interests of the lay society, too.

Dedication to Quality

Each Frontiers article is a landmark of the highest quality, thanks to genuinely collaborative interactions between authors and review editors, who include some of the world's best academicians. Research must be certified by peers before entering a stream of knowledge that may eventually reach the public - and shape society; therefore, Frontiers only applies the most rigorous and unbiased reviews.
Frontiers revolutionizes research publishing by freely delivering the most outstanding research, evaluated with no bias from both the academic and social point of view. By applying the most advanced information technologies, Frontiers is catapulting scholarly publishing into a new generation.

What are Frontiers Research Topics?

Frontiers Research Topics are very popular trademarks of the Frontiers Journals Series: they are collections of at least ten articles, all centered on a particular subject. With their unique mix of varied contributions from Original Research to Review Articles, Frontiers Research Topics unify the most influential researchers, the latest key findings and historical advances in a hot research area! Find out more on how to host your own Frontiers Research Topic or contribute to one as an author by contacting the Frontiers Editorial Office: researchtopics@frontiersin.org

OCEAN ISLAND VOLCANOES: GENESIS, EVOLUTION AND IMPACT

Topic Editors:
Adriano Pimentel, Centro de Informação e Vigilância Sismovulcânica dos Açores (CIVISA), Portugal
Ricardo S. Ramalho, Instituto Dom Luiz (IDL), Universidade de Lisboa
Laura Becerril, Servicio Nacional de Geología y Minería (SERNAGEOMIN), Chile
Patricia Larrea, Universidad de Chile
Richard J. Brown, Durham University, United Kingdom

Ocean island volcanoes constitute some of the most prominent and rapidly-formed features on Earth, and yet they cannot be explained by conventional plate tectonics. Although typically associated with intraplate settings (hotspots), these volcanoes also occur in different geodynamic settings (near mid-ocean ridges). The nature of ocean island magmatism is still the subject of intense debate within the geological community. Traditionally it has been linked to the presence of mantle plumes at depth (e.g. Hawaii), although the interaction with plate tectonics is also recognized to play a significant role (e.g. Azores, Galápagos). Magma compositions may range from basaltic to more differentiated, which consequently is accompanied by striking changes in the eruption style from effusive-dominated to highly explosive volcanism. Understanding how these magmas evolve and how volcanic processes act at ocean island volcanoes are key issues of modern volcanology. Moreover, the growth of ocean island volcanoes from their rise on the seafloor as seamounts, to island emergence and subsequent formation of shield volcanoes (and in some cases large caldera volcanoes) is governed by multiple interrelated changes. It is well known that competing processes model ocean island volcanoes during alternating and/or coeval periods of construction and destruction. The geological evolution of these volcanoes results from the balance among volcanism, intrusions, tectonics, subsidence/uplift, mass wasting, sedimentation, and subaerial and wave erosion. A better knowledge of the interplay between these processes is crucial to obtain a more comprehensive understanding of the evolution of such volcanoes, and to the eventual formulation of a unified model for ocean island evolution. Ocean islands are especially vulnerable to volcanic eruptions and other geological hazards on account of their typical small size, rough topography and isolation, which make risk management and evacuation difficult. Volcanic eruptions, in particular, may have a significant impact on local populations, infrastructures, economy and even on the global climate. It is therefore fundamental to monitor these volcanoes with complementary geophysical, geodetic and geochemical techniques in order to forecast future eruptions and their impacts. However, the assessment of volcanic hazards on ocean islands is challenging due to the large variety of phenomena involved (e.g. lava flows, tephra fallout, pyroclastic density currents, lahars, gas emissions). Different approaches are used to assess volcanic hazards, either based on empirical methods or sophisticated numerical models, focusing on a single phenomenon or the combination of different hazards. This Frontiers Research Topic aims to promote discussion within the scientific community, representing an important step forward in our knowledge of ocean island volcanoes in order to serve as a reference for future research.

Citation: Pimentel, A., Ramalho, R. S., Becerril, L., Larrea, P., Brown, R. J., eds. (2020). Ocean Island Volcanoes: Genesis, Evolution and Impact. Lausanne: Frontiers Media SA. doi: 10.3389/978-2-88963-728-7

Table of Contents

frontiers in Earth Science

EDITORIAL
published: 31 March 2020
doi: 10.3389/feart.2020.00082

Editorial: Ocean Island Volcanoes: Genesis, Evolution and Impact

Adriano Pimentel[1,2,3]*, *Ricardo S. Ramalho*[4,5,6,7], *Laura Becerril*[8], *Patricia Larrea*[9] and *Richard J. Brown*[10]

[1] Centro de Informação e Vigilância Sismovulcânica dos Açores (CIVISA), Ponta Delgada, Portugal, [2] Instituto de Investigação em Vulcanologia e Avaliação de Riscos (IVAR), Universidade dos Açores, Ponta Delgada, Portugal, [3] Centro de Investigação em Biodiversidade e Recursos Genéticos (CIBIO), InBIO Laboratório Associado, Pólo dos Açores, Ponta Delgada, Portugal, [4] Instituto Dom Luiz (IDL), Faculdade de Ciências, Universidade de Lisboa, Lisbon, Portugal, [5] Departamento de Geologia, Faculdade de Ciências, Universidade de Lisboa, Lisbon, Portugal, [6] School of Earth Sciences, University of Bristol, Bristol, United Kingdom, [7] Lamont-Doherty Earth Observatory at Columbia University, Palisades, NY, United States, [8] Servicio Nacional de Geología y Minería (SERNAGEOMIN), Santiago, Chile, [9] Department of Geology and Andean Geothermal Center of Excellence, Facultad de Ciencias Físicas y Matemáticas, Universidad de Chile, Santiago, Chile, [10] Department of Earth Sciences, Durham University, Durham, United Kingdom

Keywords: hotspots, magmatic processes, seamounts, geochronology, tectonic control, flexure models, volcanic hazard

Editorial on the Research Topic

Ocean Island Volcanoes: Genesis, Evolution and Impact

Ocean island volcanoes are exceptional geological features that rise from the seafloor. They are small windows in the vast oceans that allow an indirect look into the otherwise inaccessible Earth's interior. The genesis of ocean island volcanoes is intrinsically related to their geodynamic setting and magma-supply rate over time (Menard and Ladd, 1963). However, ocean island magmatism cannot be explained within the framework of plate tectonics without the presence of mantle melting anomalies. How ocean island magmas are generated, evolve, and erupt are key questions for petrology and volcanology. The geological evolution of ocean island volcanoes is governed by multiple internal and external factors. A better knowledge of the interplay between growth and decay processes is crucial for a comprehensive understanding of the evolution of such volcanoes (Ramalho et al., 2013). On account of their typically isolated location and small area, ocean islands are especially vulnerable to geological hazards. Volcanic eruptions, in particular, may have devastating consequences on local communities, but also impact global economy and climate (Wilson et al., 2014). It is therefore crucial to increase our knowledge on these volcanoes to respond to the challenge of forecasting future eruptions and their short- to long-term impacts. This Research Topic covers different subjects related to ocean island volcanoes within the Pacific and Atlantic Oceans.

Haase et al. address the process of melting by mantle plumes, through a comparison of intraplate volcanoes in the Pacific Ocean. The authors compare published compositional and geochronological data from Hawaii, Society, Marquesas and Samoa, finding systematic variations of magma composition with similar-sized melting anomalies, notwithstanding the different temperatures. They show that shield stages last ∼1 Ma and there is an overlap of shield and post-shield volcanism for up to 200 ky. The study suggests that the evolution of these volcanoes does not strictly follow the Hawaiian model.

Harpp and Geist offer a comparative study of geological, geochemical, and geophysical data to investigate the evolution of the western and eastern Galápagos, concluding that it is conditioned by a change in tectonic setting ∼1 Ma ago. The authors suggest that the eastern volcanoes are not an evolved stage of the young western volcanoes, but conversely were emplaced in a near-ridge environment with a lower magma-supply rate. They also suggest western volcanoes were formed by a different constructional mechanism controlled

OPEN ACCESS

Approved by:
Valerio Acocella,
Roma Tre University, Italy

***Correspondence:**
Adriano Pimentel
adriano.hg.pimentel@azores.gov.pt

Specialty section:
This article was submitted to Volcanology, a section of the journal Frontiers in Earth Science

Received: *29 February 2020*
Accepted: *10 March 2020*
Published: *31 March 2020*

Citation:
Pimentel A, Ramalho RS, Becerril L, Larrea P and Brown RJ (2020) Editorial: Ocean Island Volcanoes: Genesis, Evolution and Impact. Front. Earth Sci. 8:82. doi: 10.3389/feart.2020.00082

by the proximity of the Galápagos Spreading Center 1 to 3 Ma ago.

Continuing in the Galápagos, Schwartz et al. look at the shallow seamounts near the western Galápagos to identify erosional or volcanic terrace-like morphologic features using direct seafloor observations and bathymetrical information. This study confirms that the western archipelago experienced significant subsidence at rates of 0.2–0.4 m/ka over the past 1 Ma, concluding that all islands in the central archipelago were intermittently connected between 435 and 900 ka.

Thordarson and Garcia discuss the origins of the rejuvenated volcanism at Kīlauea Point, Kaua'i (Hawai'i) by looking at the products of three well-dated rejuvenated stage eruptions. The authors conclude that the timing of volcanism and the elevation of Kīlauea Point relative to sea level are inconsistent with the predictions of the flexural melting model, indicating that decompression melting related to plate flexure cannot be the sole driver for the rejuvenated volcanism.

Lara et al. provide new dating along the Juan Fernández Ridge to test the hypothesis that this volcanic chain constitutes a hotspot track. Newly obtained $^{40}Ar/^{39}Ar$ ages range from 8.4 to 0.62 Ma and show an east-west gradation. These results indicate a clear age progression with a mean Nazca plate velocity of ∼81 mm/yr, which is consistent with a hotspot track resulting from the impingement of a mantle plume beneath the Juan Fernández Ridge.

Le Corvec and McGovern investigate how loading of ocean water affects the internal stress of basaltic island volcanoes. Specifically, they run two finite element models, one considering an instantaneous volcanic edifice growth, and a second one with an edifice incrementally built over time. Their results show that eruptions are more likely to occur within incrementally-built edifices, irrespective of the load of a water body, but where the stress signatures of lithospheric flexure are reduced.

Moving to the Atlantic Ocean, Romer et al. investigate the relationship between magmatic and tectonic processes in Faial volcanic system (Azores), through a combined bathymetric, geophysical, geochemical, and isotopic approach. They show that the stress field under Faial has not changed in the last 1 Ma, despite a progressive decrease in melt productivity over time. This suggests that the distribution of compositionally similar lavas is tectonically controlled. The youngest mafic and intermediate melts were erupted along rift zones from a more enriched source, whilst the older, and more widespread volcanism was originated from a more depleted one.

Jeffery and Gertisser review the occurrence of peralkaline felsic magmatism in Atlantic volcanoes through a review of published geochemical, thermobarometric, and geochronological datasets to identify the primary controls of formation of such magmas. The authors suggest that peralkaline magmas in these islands are generated primarily by extended (up to 95%), open system fractional crystallization of mantle-derived mafic magmas. They also suggest that the magma generation is likely controlled by the system magma-flux rate.

Finally, Kueppers et al. address the problem of potentially biased volcanic hazard assessments due to incomplete eruption records at ocean island volcanoes. Using a recently discovered mid-distal pumice lapilli fall deposit in the central part of São Miguel (Azores), the authors constrained the eruptive source parameters and wind conditions during the last paroxysmal explosive eruption of Sete Cidades volcano. Critically, the newly obtained parameters allow a more realistic assessment of the potential impact that a future sub-Plinian eruption would have on the island.

This collection of articles offers probe of some of the critical questions and possible answers in our stepwise understanding of ocean island volcanoes, and they highlight the uniqueness and complexity of these geological features. We anticipate this Research Topic to be a valuable reference for future research on ocean island volcanoes and will stimulate thinking on some key problems related to their genesis, growth and hazards.

AUTHOR CONTRIBUTIONS

All authors listed have made a substantial, direct and intellectual contribution to the work, and approved it for publication.

FUNDING

RR acknowledges his IF/01641/2015 Investigador FCT contract. PL was supported by Fondos de Instalación Académica - FCFM, Universidad de Chile.

ACKNOWLEDGMENTS

We thank the chief editor Valerio Acocella for the kind invitation to organize this Research Topic.

REFERENCES

Menard, H., and Ladd, H. (1963). "Oceanic islands, seamounts, guyots and atolls," in *The Sea*, Vol. 3, ed M. N. Hill (New York, NY: Wiley Interscience), 365–385.

Ramalho, R. S., Quartau, R., Trenhaile, A. S., Mitchell, N. C., Woodroffe, C. D., and Ávila, S. P. (2013). Coastal evolution on volcanic oceanic islands: a complex interplay between volcanism, erosion, sedimentation, sea-level change and biogenic production. *Earth Sci. Rev.* 127, 140–170. doi: 10.1016/j.earscirev.2013.10.007

Wilson, G., Wilson, T. M., Deligne, N. I., and Cole, J. W. (2014). Volcanic hazard impacts to critical infrastructure: a review. *J. Volcanol. Geotherm. Res.* 286, 148–182. doi: 10.1016/j.jvolgeores.2014.08.030

Conflict of Interest: The authors declare that the research was conducted in the absence of any commercial or financial relationships that could be construed as a potential conflict of interest.

Copyright © 2020 Pimentel, Ramalho, Becerril, Larrea and Brown. This is an open-access article distributed under the terms of the Creative Commons Attribution License (CC BY). The use, distribution or reproduction in other forums is permitted, provided the original author(s) and the copyright owner(s) are credited and that the original publication in this journal is cited, in accordance with accepted academic practice. No use, distribution or reproduction is permitted which does not comply with these terms.

frontiers in Earth Science

HYPOTHESIS AND THEORY
published: 04 January 2019
doi: 10.3389/feart.2018.00242

A Comparison of the Magmatic Evolution of Pacific Intraplate Volcanoes: Constraints on Melting in Mantle Plumes

Karsten M. Haase, Christoph Beier and Fabian Kemner*

GeoZentrum Nordbayern, Friedrich-Alexander-Universität Erlangen-Nürnberg (FAU), Erlangen, Germany

The interaction of deep mantle plumes with lithospheric plates is one fundamental concept of plate tectonics. Based on observations mainly made on the Hawaiian volcanoes the compositional evolution of hotspot volcanoes is believed to reflect the variation of partial melting and source composition as the plate moves across the different melting zones of the mantle plume. The model predicts the formation of several magmatic stages that differ in composition. In order to test this model, we compare published compositional and age data from the intraplate volcanoes of the Hawaii, Society, Marquesas and Samoa hotspots on the older part of the Pacific Plate. The compiled data indicate that most volcanoes display variations within and between several magmatic series, and in most cases the more evolved lavas are associated with the voluminous shield stage. The Hawaiian volcanoes show up to four different series ranging from tholeiites to nephelinites/melilitites, whereas the other hotspots mainly erupt two magmatic series consisting of transitional basalts and basanites. Submarine preshield stages at the Society and Marquesas hotspots resemble those observed at Hawaii. The large variation of primitive magmas in the Hawaiian plume as opposed to the other Pacific intraplate systems may reflect the higher temperatures, higher buoyancy flux, and extreme chemical heterogeneity at Hawaii. The shield stage activity at all four hotspots lasts for 1 million years indicating similar widths of the melting zone, although the temperatures of the distinct mantle plumes vary considerably. The relatively depleted shield stage magmatism typically overlaps by ∼200 kyrs with the formation of the more enriched postshield magmas indicating that the two melting and magma ascent systems exist contemporaneously.

Keywords: hawaii, samoa, society, marquesas, geochemistry, mantle melting, hotspots

OPEN ACCESS

Edited by:
Adriano Pimentel, Centro de Informação e Vigilância Sismovulcânica dos Açores (CIVISA), Portugal

Reviewed by:
J. Gregory Shellnutt, National Taiwan Normal University, Taiwan
Ian Ernest Masterman Smith, The University of Auckland, New Zealand
Dennis Geist, National Science Foundation (NSF), United States

****Correspondence:***
Christoph Beier
christoph.beier@fau.de

Specialty section:
This article was submitted to Petrology, a section of the journal Frontiers in Earth Science

Received: *15 June 2018*
Accepted: *14 December 2018*
Published: *04 January 2019*

Citation:
Haase KM, Beier C and Kemner F (2019) A Comparison of the Magmatic Evolution of Pacific Intraplate Volcanoes: Constraints on Melting in Mantle Plumes. Front. Earth Sci. 6:242. doi: 10.3389/feart.2018.00242

INTRODUCTION

One of the fundamental features of the plate tectonic model is the interaction of lithospheric plates with so-called hotspots or melting anomalies that are likely caused by deep mantle plumes (Wilson, 1963; Morgan, 1971). Recent models suggest that there are different source regions from which deep mantle plumes ascend. They may either rise directly from the core-mantle boundary or from

large low-velocity regions in the lower mantle (e.g., Courtillot et al., 2003; Jellinek and Manga, 2004; French and Romanowicz, 2015). The underlying assumption is that, during the period of most voluminous eruptions of the so-called shield stage, the active volcanic system is situated above the center of the melting anomaly providing the required excess heat, anomalously fertile (pyroxenite) rich mantle, and/or volatiles causing melting (e.g., Liu and Chase, 1991; Putirka et al., 2007; Herzberg and Asimov, 2008; Hofmann and Farnetani, 2013). As the plate moves across the mantle plume the degree and source of partial melting vary, leading to chemical and isotopic variations in the magmas feeding the volcanoes (Frey et al., 1990; Woodhead, 1992). Thus, age-progressive volcanic chains are formed with life-times of up to 80 million years (Duncan and Richards, 1991; Clouard and Bonneville, 2005) and, in some cases even exceeding 90 million years, e.g., at the Louisville seamount chain (Koppers et al., 2011). Within many of these chains the volcanoes seem to show a systematic compositional evolution ranging from tholeiitic to alkaline basalts with decreasing age (McDougall and Duncan, 1980; Woodhead, 1992). This magma evolution model is largely based on the Hawaiian volcanic chain because the Hawaii-Emperor Chain represents the best-studied plume track globally both from the subaerial and submarine edifices. According to the observations on the Hawaiian volcanoes four different magmatic stages were postulated to exist in intraplate volcanoes; (1) a preshield stage. (2) a shield stage. (3) a postshield stage, and (4) a rejuvenated stage (Clague and Dalrymple, 1987; Frey et al., 1990). The eruptive volumes increase through the preshield stage and reach a maximum during the shield stage when 80 to 95% of the entire volume of the volcano is produced. After the shield stage the erupted volumes decrease leading, in some cases, to several million years of volcanic quiescence before small volumes of lavas may erupt during the rejuvenated (or posterosional) stage (Clague and Dalrymple, 1987; Frey et al., 1990). The distinct Hawaiian eruption stages have been recently questioned because they are mainly based on subaerial sampling and volcanic evolution, and do not reflect gradual changes in magma compositions (Clague and Sherrod, 2014). According to the model, the magma composition of the hotspot volcanoes varies from highly SiO_2-undersaturated preshield alkaline basalts to tholeiitic shield basalts and then again to alkaline SiO_2-undersaturated postshield lavas. The mantle plume model suggests that the different stages reflect the different parts of the mantle plume. Little is known about the preshield stage because these lavas are probably covered by the later voluminous shield lavas, but this early stage indicates the arrival of the lithospheric plate at the edge of the melting anomaly. Increasing degrees of partial melting occur as the lithosphere moves across the mantle plume with the shield stage representing the largest degrees of melting in the plume center and the most voluminous volcanism. As the plate continues to move over the plume the degree of melting decreases during the postshield stage. The generation of the highly SiO_2-undersaturated posterosional or rejuvenated stage magmas is not well-understood because many of these magmas form several million years after the plate passed the mantle plume (Garcia et al., 2010; Konter and Jackson, 2012). The duration of the shield stage and the composition of the magmas yield important insights into the composition, temperature and structure of the mantle plume and the melting processes. Additionally, the determination of the absolute plate velocities relative to mantle plumes depends on the understanding of the composition and duration of the shield stage (McDougall and Duncan, 1980). However, so far there has been little effort to compare the shield stages of volcanoes from different hotspots in order to define potential similarities and differences (Woodhead, 1992). Most recent studies have concentrated on the definition of mantle sources using radiogenic isotope compositions (e.g., Hofmann, 2003; Jackson and Dasgupta, 2008; White, 2010) but did not take into account the evolution of major and incompatible element compositions of the lavas on the scale of a single volcanic system.

Here, we compile and use the ages and compositions of lavas from the Hawaii, Society, Samoa, and Marquesas volcanic chains on the older portions of the Pacific Plate, where lithosphere thickness and motion should be comparable and thus similarities in magma genesis and duration of volcanism are expected. We selected these four hotspots because they are comparable in their setting and because many of their volcanoes are reasonably well-studied (see **Supplementary Material**). Indeed, we find very similar patterns of volcanic activity in all of these hotspots but we also note several features that are difficult to explain within the framework of the plume model. The Hawaiian plume is believed to represent the hottest mantle plume with the highest buoyancy flux on Earth (Davies, 1988; Sleep, 1990), yet the duration of shield volcanism in the other Pacific hotspots is similar (∼1 million years) suggesting similar widths of the melting zones. Additionally, the Hawaiian hotspot volcanoes erupt lavas indicating both higher and lower degrees of partial melting than the other three hotspots investigated in this study which may indicate either a very heterogeneous nature of the mantle plume (including more pyroxenitic and carbonatitic sources), or more extreme melting conditions due to the higher temperature and a stronger buoyancy flux of the plume.

GEOLOGICAL SETTING OF THE PACIFIC HOTSPOTS

The Hawaii-Emperor chain of age-progressive volcanoes represents the type example of hotspot volcanism caused by a deep mantle plume (Wilson, 1963; Morgan, 1972). The Hawaiian intraplate volcanoes vary in size from the largest volcanic edifices on Earth with a height of some 10 km to much smaller volcanoes and accordingly, the volume estimates of the Hawaiian volcanoes range from 9,000 to 74,000 km^3 (Clague and Sherrod, 2014). The Hawaiian Islands are the best-studied intraplate volcanoes on Earth and the Hawaii volcanic chain consists of 21 islands and several islets that show an age progression from SSE to NNW (e.g., Clague and Dalrymple, 1987; Sharp and Clague, 2006; O'Connor et al., 2013). The Hawaiian intraplate volcanoes lie on oceanic crust of Cretaceous age ranging from 87 to 94 million years (Detrick et al., 1981; Müller et al., 2008). The age progression of shield volcanism of the Hawaiian Islands implies an average velocity

of the Pacific Plate of 10 cm/yr across the plume (Clague and Sherrod, 2014). However, the exact rate of age progression may differ as a result of the plume moving south (Tarduno et al., 2003). Additionally, several volcanoes show volumetrically small stages of rejuvenated volcanism occurring up to 5.5 million years after initiation of the volcanism (Clague and Sherrod, 2014; Thordarson and Garcia, 2018). A strong buoyancy flux of Hawaii is reflected by large magma volumes as indicated by the size of the volcanic islands (Sleep, 1990). The present-day position of the front of the plume melting zone is beneath Loihi seamount ∼35 km SE of the coast of Big Island (e.g., Moore et al., 1982; Watson and McKenzie, 1991). The detailed sampling of many Hawaiian volcanoes led to the model of four stages of magmatic evolution although much of this variation is based on subaerial lavas whereas submarine data have only recently been included into the existing model (Clague and Sherrod, 2014). The youngest Hawaiian volcanoes are in their shield or postshield stages and rejuvenated lavas are only known from Lanai, Molokai, Koolau, Kauai, and Niihau (Sinton et al., 2017; Thordarson and Garcia, 2018). The decreasing postshield magma production also leads to the establishment of magma reservoirs at the base of the crust, so that postshield lavas frequently are hawaiitic and mugearitic rather than basaltic in composition (e.g., Clague, 1987; Frey et al., 1990).

The Society Islands are part of French Polynesia, a region of an anomalously high rate of intraplate volcanism (Adam et al., 2010). Several aligned and age-progressive volcanoes form the ∼800 km long Society Island chain (Dymond, 1975; Guillou et al., 2005). The islands formed on late Cretaceous oceanic crust increasing in age from 66 million years at Mehetia in the southeast to 84 million years at Maupiti in the northwest of the island chain (Müller et al., 2008). The ages of the volcanism decrease from 4.5 million years at Maupiti to less than 0.3 million years at Mehetia yielding a velocity of 11.3 cm/yr for the Pacific Plate (Duncan et al., 1994; Uto et al., 2007). The best-studied island is Tahiti consisting of two volcanoes with stratigraphically defined and chemically distinct shield and postshield stages (Duncan et al., 1994; Hildenbrand et al., 2004). Other older volcanoes like Moorea and Huahine also consist of shield volcanoes with a caldera forming toward the end of the volcanism and later postshield lavas and intrusions (Guillou et al., 2005). The position of the present-day melting anomaly of the Society hotspot is located southeast of Tahiti evident from volcano-seismic activity at the submarine flanks of Mehetia and numerous submarine active volcanoes (Talandier and Okal, 1984; Devey et al., 1990; Binard et al., 1992).

The Marquesas volcanic chain consists of eight large islands between the about 5.0 to 5.5 million year-old Eiao in the NW, and the 1.0 to 1.5 million year-old Fatu Hiva in the southeast (Guillou et al., 2014). The youngest volcanism with ages <0.5 million years occurs at a seamount SE of Fatu Hiva (Desonie et al., 1993) and at the Marquesas Fracture Zone some 100 km south of Fatu Hiva (Révillon et al., 2017). The Pacific Plate moves with a velocity of ∼10.5 cm/yr across the Marquesas mantle plume (McDougall and Duncan, 1980; Révillon et al., 2017) and lithospheric ages are on the order of 50 million years (Müller et al., 2008). The Marquesas islands consist of large shield volcanoes like, for example, the Tekao volcano on Nuku Hiva that have been suggested to mainly consist of olivine tholeiites (Guillou et al., 2014). These shield volcanoes frequently collapsed and the shield lavas were then covered by more incompatible element-enriched alkaline lavas, like the Taiohae formation on Nuku Hiva (Guillou et al., 2014). Similar patterns of volcanic evolution are observed at Ua Huka with the Hikitau shield volcano followed by the alkaline Hane lavas.

The Samoa volcanic chain is an ∼1,300 km long complex structure consisting of numerous seamounts and seven islands with the oldest ages of 13.2 million years occurring on the westernmost seamount and the youngest ages in the east, indicating a hotspot origin (Koppers et al., 2008, 2011). The age progression appears to be restricted to the shield volcanism of the Samoan chain whereas rejuvenated volcanism without systematic age progression occurs on many of the eastern islands (Natland, 1980; Koppers et al., 2011). The easternmost and youngest portion of the Samoan chain apparently consists of two parallel seamount chains with the youngest activity at the Vailulu'u submarine volcano in the north (Hart et al., 2000) and the Malu Malu volcano in the south (Koppers et al., 2011). The age variation along the chain suggest that the ∼100 million year-old lithospheric plate moves at a velocity of ∼7.2 cm/yr across the Samoa mantle plume (Koppers et al., 2008; McDougall, 2010). The volcanism of the Samoa Islands has been suggested to evolve from tholeiitic to mildly alkaline basalts to highly alkaline post-erosional basalts, for example, on Upolu and Savai'i (Natland, 1980; McDougall, 2010) but the large volume of the late highly alkaline eruptions is notable (Konter and Jackson, 2012). The complex and abundant rejuvenated volcanism of the eastern Samoan chain is attributed to the geodynamic situation close to the Tonga subduction zone that may cause fracturing or flexuring of the lithosphere as well as additional mantle upwelling (e.g., Natland, 1980; Konter and Jackson, 2012; Strak and Schellart, 2018).

RESULTS

The Comparison of the Compositional Variation of the Hotspot Lavas

We compiled data on the age and chemical composition of lavas from volcanoes of the hotspots of Hawaii, Society, Marquesas, and Samoa (data sources can be found in the **Supplementary Material**), all situated on the older portion of the Pacific Plate (**Figure 1**). The total alkali-silica (TAS) classification of the lavas combined with the division line for tholeiitic and alkaline lavas from Hawaii (Macdonald and Katsura, 1964) reveals that only the Hawaiian volcanoes show a pronounced tholeiitic stage whereas the other three hotspots erupt mainly alkaline and transitional basalts and rare tholeiites (**Figure 2**). Many of the Hawaiian volcanoes like Kaua'i and Koolau show highly variable lava compositions ranging from tholeiitic basalts to basanites and nephelinites and melilitites (**Figure 2a**). Field observations combined with geochemistry suggest that all Hawaiian volcanoes evolve through a voluminous stage of tholeiitic eruptions followed by increasingly alkaline

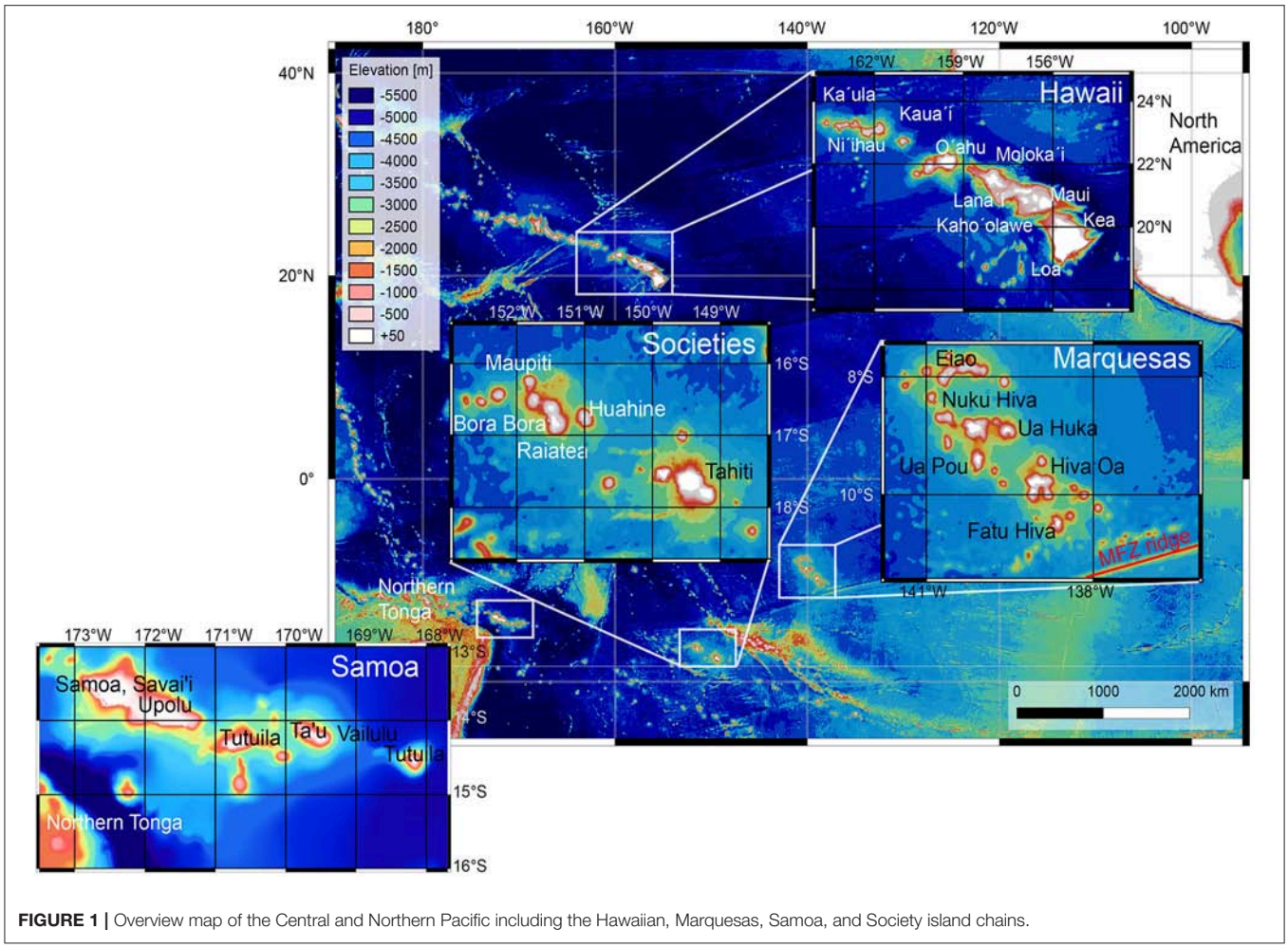

FIGURE 1 | Overview map of the Central and Northern Pacific including the Hawaiian, Marquesas, Samoa, and Society island chains.

lavas with alkali basalts, basanites, and nephelinites (Clague and Dalrymple, 1987). Additionally, Molokai and West Maui volcanoes erupted lavas that are significantly more evolved than the alkali basalts. The other hotspot volcanoes typically show variations between alkali basalts and basanites and most more evolved lavas are also related to the alkali basalts (**Figure 2**). The young volcanic edifices of the Society hotspot with the island Mehetia and the seamounts Teahitia and Rocard apparently consist of basanite and more evolved lavas like trachytes and phonolites. In contrast, alkali basalts and few tholeiites occur on Tahiti and older volcanoes like Maupiti, Moorea, and Huahine (**Figure 2b**).

The Nb/Zr ratio has been widely used to distinguish the different magma series because these incompatible elements are not fractionated during crystallization processes (**Figure 3**) and are sensitive to source composition because Nb/Zr correlates, for example, with Sr isotope ratios (Clague and Dalrymple, 1988). There is a broad negative correlation between the SiO_2 content of the magmas and Nb/Zr, for example, in the Hawaiian lavas, where the tholeiites have the lowest Nb/Zr and the alkaline magmas increasingly higher Nb/Zr (**Figure 3**). Thus, although there are also differences in Nb/Zr among the Hawaiian shield stage lavas (Frey et al., 1994), the Hawaiian tholeiites in general have Nb/Zr ratios of 0.05 to 0.11 (**Figure 3a**). The lavas with the lowest Nb/Zr at the Society hotspot range from 0.09 to 0.16, at the Marquesas islands between 0.08 to 0.14, and at Samoa between 0.12 and 0.18 (**Figure 3**). The mafic lavas with lower SiO_2 typically have higher Nb/Zr and the most extreme Nb/Zr of 0.38 are found in nephelinites and melilitites at Kaua'i volcano (**Figure 3a**). Basanites of the young Mehetia volcano in the Society hotspot have similar Nb/Zr to the alkali basalts from the older volcanoes like Maupiti and Huahine (**Figure 3b**). On the other hand, the alkali basalts from the young Vailulu volcano in Samoa are much higher in Nb/Zr than alkali basalts from the older volcanoes Ta'u and Tutuila (**Figure 3d**).

The range of SiO_2 for primitive magmas with 12 to 15 wt.% MgO varies considerably between the different hotspots (**Figure 4**). The control lines for addition of olivine with forsterite (Fo) contents of 88 are also shown because most lavas with MgO contents >10 wt.% probably formed by addition, lavas with MgO < 10 wt.% by fractionation of olivine (±clinopyroxene and plagioclase). Primitive lavas (MgO > 5 wt.%) of the Hawaiian volcanoes show a range from 36 to 52 wt.% SiO_2, whereas those of the Societies, Marquesas and Samoa all range from 41 to 48 wt.%

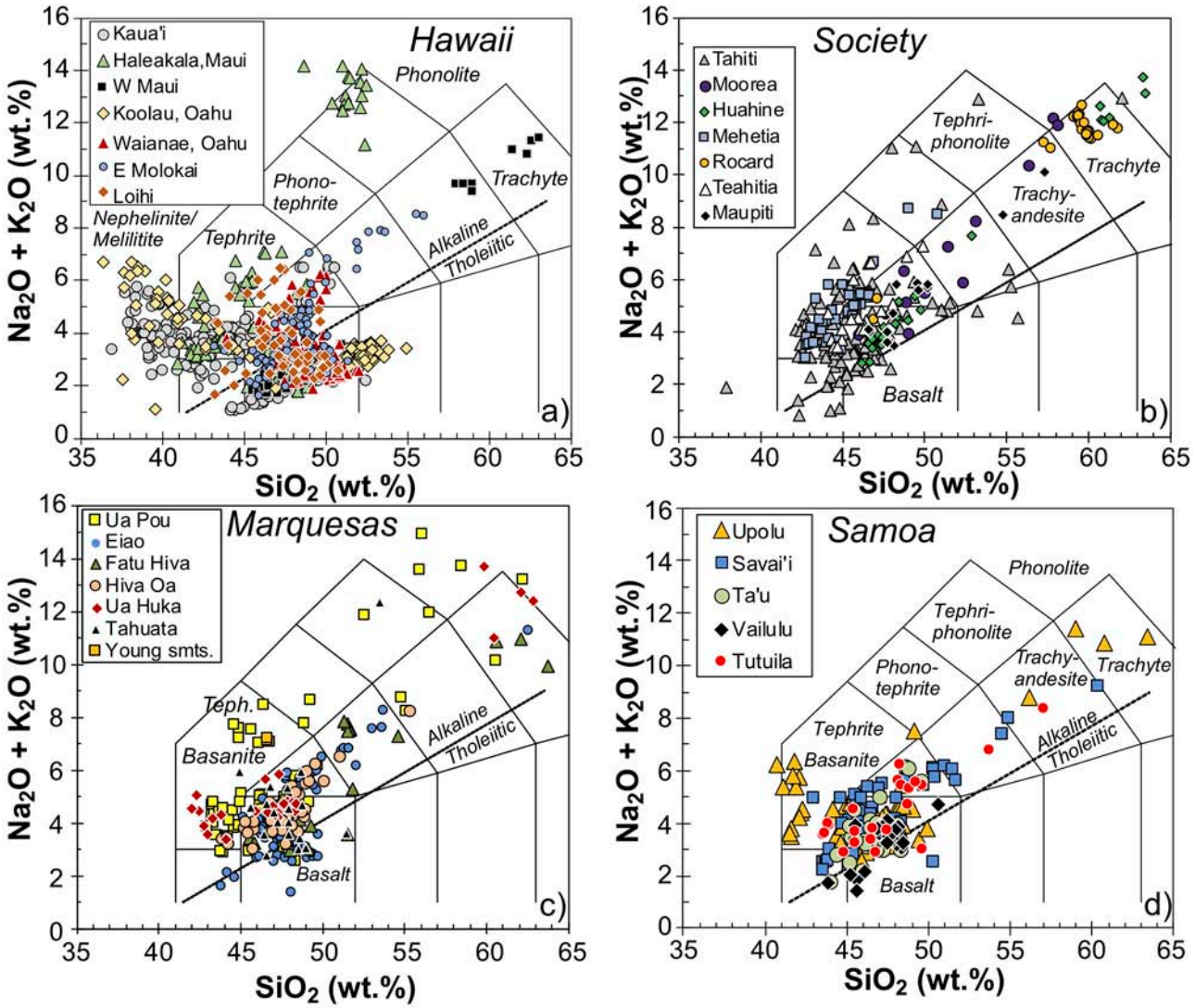

FIGURE 2 | The total alkalies-silica (TAS) diagram (Le Bas et al., 1986) for lavas from different volcanoes of the **(a)** Hawaiian, **(b)** Society, **(c)** Marquesas, and **(d)** Samoa hotspots. The dashed line shows the distinction between alkaline and tholeiitic lavas after Macdonald and Katsura (1964). Data sources can be found in the **Supplementary Material**.

SiO_2 (**Figure 4**), i.e., they cover a much smaller range compared to Hawaii. Most volcanoes show well-defined increasing different trends of SiO_2 with decreasing MgO implying parental magmas with different SiO_2 contents.

The variation of incompatible element ratios with SiO_2 is most pronounced in the chondrite-normalized Ce/Yb ratios [= $(Ce/Yb)_N$]. The $(Ce/Yb)_N$ of the lavas from all hotspots display a negative correlation toward the lowest SiO_2 contents of each volcano (**Figure 5**). This trend can be defined for the primitive Hawaiian lavas of Koolau volcano on Oahu and Kaua'i as $(Ce/Yb)_N = -2.5xSiO_2 + 115$. The correlation trend is plotted into the diagrams of the lavas from the other hotspot volcanoes for comparison. Whereas, many of the most primitive lavas of the Marquesas hotspot lie close to this trend, the Society and Samoa hotspot lavas have higher $(Ce/Yb)_N$ for a given SiO_2 content (**Figure 5**) and lack an obvious correlation for the Society lavas.

The Variation of the Chemical Composition With the Age

The Nb/Zr ratios plotted against the age of the volcanism (**Figure 6**) reveal significant changes of lava composition with time in the Hawaii, Society and Marquesas hotspot volcanoes. Unfortunately, there are few samples with both geochemical and age data available from the Samoan hotspot so that we cannot show the variation with age for this hotspot. The earliest age-dated stages of the different volcanoes typically have the lowest Nb/Zr whereas later erupted lavas have higher Nb/Zr ratios (**Figure 6**). We interpret this to represent the transition from the

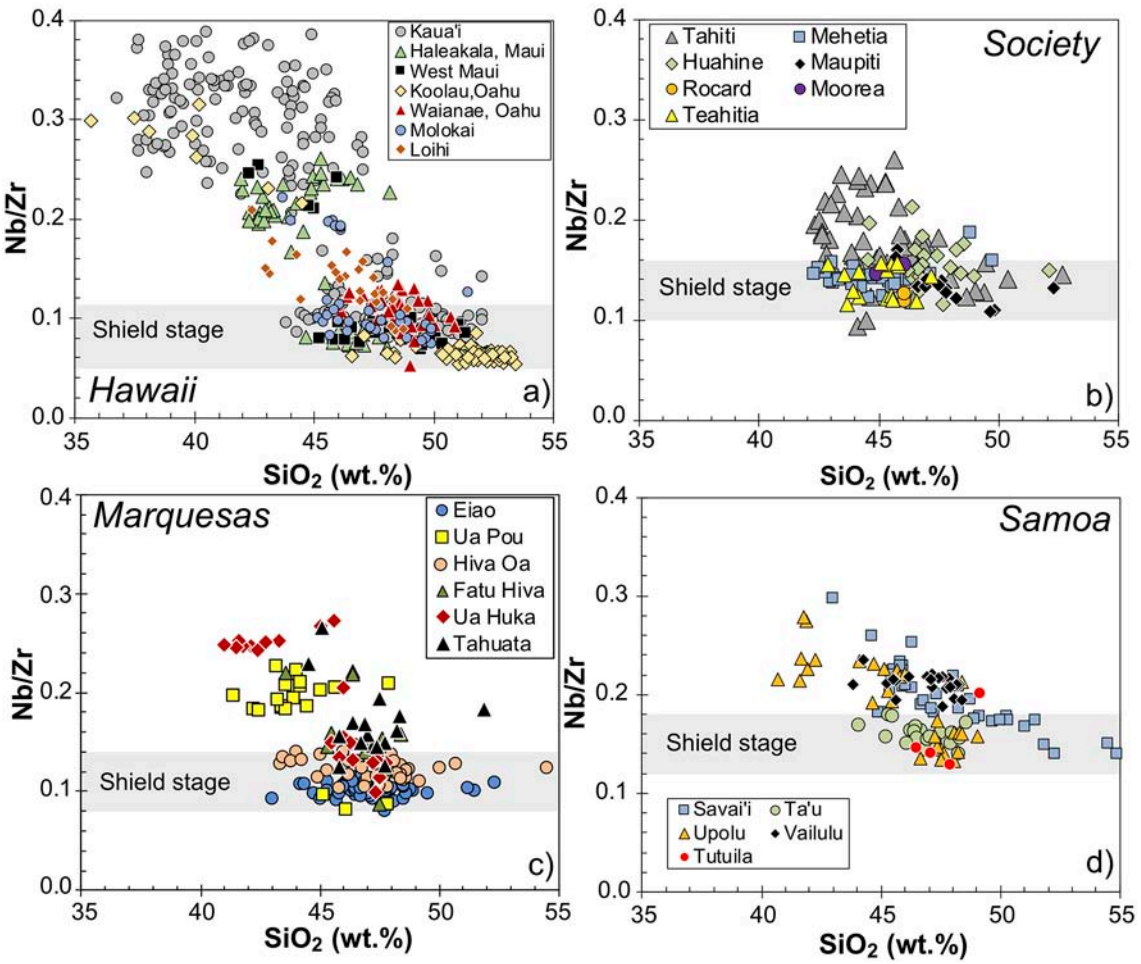

FIGURE 3 | The variation of Nb/Zr ratios with SiO_2 contents for the lavas from the **(a)** Hawaiian, **(b)** Society, **(c)** Marquesas, and **(d)** Samoa hotspots. The Nb/Zr ratio remains constant during much of the magma evolution and is generally not affected by fractional crystallization. The differences of Nb/Zr ratios in lavas from the same volcanoes reflect different magma series of volcanic stages. The lavas with the lowest Nb/Zr typically represent the shield stage as outlined by the gray bars. Data sources can be found in the **Supplementary Material**.

shield to the postshield stage that often appears to be gradual, for example, at West Maui, Tahiti, and Tahuata (**Figure 6**). We cannot define the timing at which the preshield stages changed to shield volcanism because of a lack of coexisting preshield lavas for the shield and postshield stages shown here. However, the duration of the shield stage as indicated by the occurrence of lavas with low Nb/Zr can be defined to be on the order of 1 million years in the case of West Maui, Koolau, and Kaua'i in the Hawaiian hotspot (**Figure 6a**). The shield stage appears to last for similar periods of time at the well-studied volcanoes of Tahiti in the Societies, and Tahuata and Ua Huka in the Marquesas. Toward the end of the shield stage defined by the low Nb/Zr ratios, volcanoes at all three hotspots show a coeval eruption of more enriched lavas with an overlap of several 100 kyrs (**Figure 6**). In the case of Hawaiian volcanoes and the Tahiti and Huahine volcanoes in the Societies the change to more enriched postshield lavas is relatively small. The Hawaii data display the large age and compositional difference of the rejuvenated lavas compared to the shield and postshield lavas (**Figure 6a**). The relatively well-studied volcanoes in the Marquesas show a similar pattern with much higher Nb/Zr lavas erupting after a 1 million year-long break at Ua Huka whereas the rejuvenated lavas at Fatu Hiva and Tahuata erupt subsequent to the shield and postshield stage (**Figure 6c**).

DISCUSSION

The Compositional Variation of the Submarine Preshield Volcanic Stage

Because the preshield stage of the oceanic intraplate volcanism at hotspots occurs at great water depths and are covered by the younger stages, little is known about these eruptions and the composition of the lavas. Basanitic to tholeiitic basalts were recovered from Loihi seamount SE of the island of Hawaii (**Figure 2a**) and these lavas were interpreted to reflect initiation of melting at the plume edge beneath the lithosphere (Moore

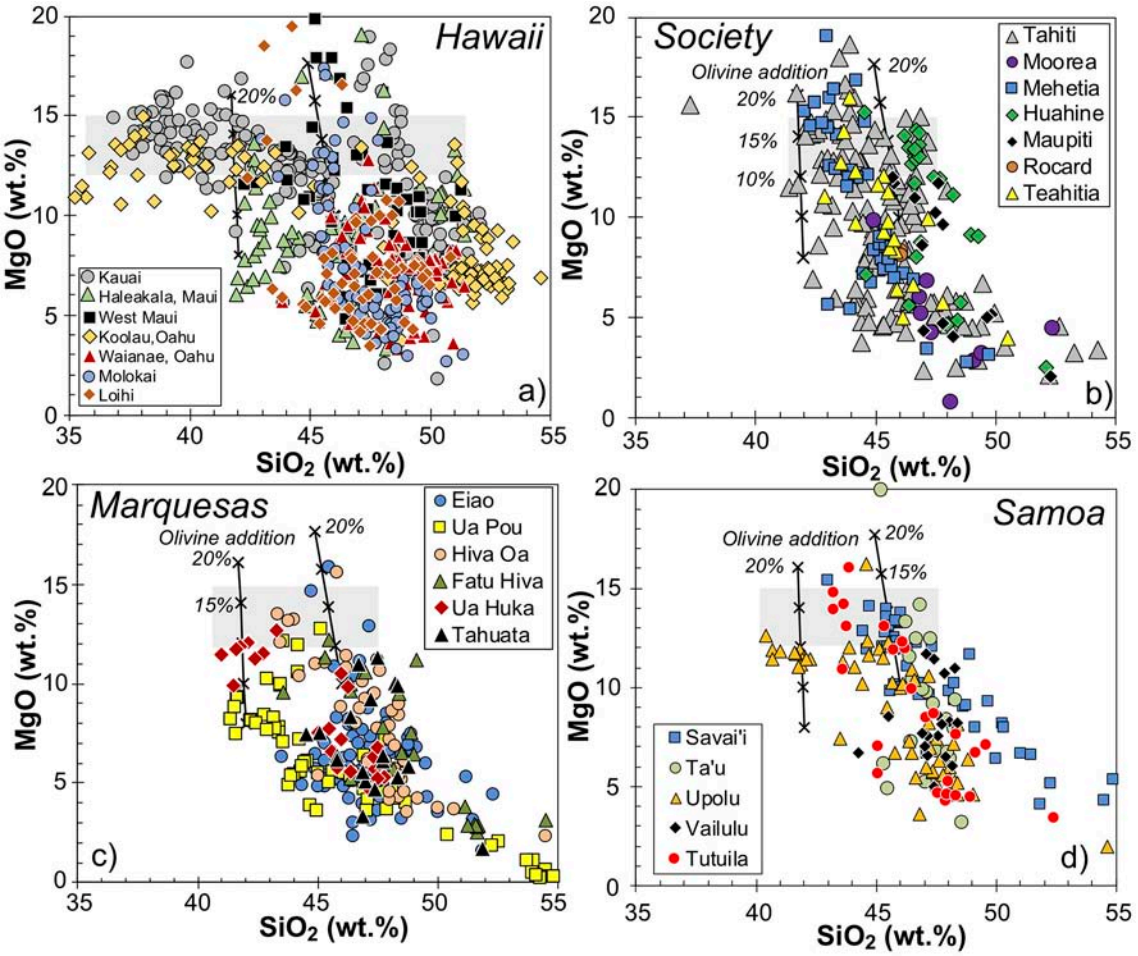

FIGURE 4 | The variation of SiO_2 vs. MgO contents in the lavas from the **(a)** Hawaiian, **(b)** Society, **(c)** Marquesas, and **(d)** Samoa hotspots. The SiO_2 contents typically increase with decreasing MgO due to crystal fractionation processes. Lavas with 12–15 wt.% MgO represent near-primary compositions of magmas from the mantle and their range is indicated by the gray box. Note that the Hawaiian volcanoes show a much larger range of SiO_2 contents (36–52 wt.%) for these primary magmas than the other hotspots (41–48 wt.%). The two black lines show the addition of olivine with forsterite (Fo) contents of 88 in 5% increments indicated by the crosses. Data sources can be found in the **Supplementary Material**.

et al., 1982). Clague and Sherrod (2014) suggest that preshield lavas can be observed at the four Hawaiian volcanoes Loihi, Kilauea, Kohala, and perhaps Hualalai, whereas lavas of this stage are buried at most other volcanoes. The submarine young volcanoes at the other three studied hotspots also differ from the subaerial lavas. At the Society hotspot, lavas at the young Mehetia and Teahitia volcanoes are more SiO_2-undersaturated basanites than the subaerial alkali basalts of Tahiti, Huahine, or Moorea (**Figure 2b**) although the Nb/Zr ratios are similar (**Figure 3b**). Both the submarine and subaerial lavas recovered from the youngest island Mehetia are basanites (**Figure 2b**) indicating that the volcano may still be in the preshield stage of volcanism of the Society hotspot. Thus, similarly to the case in Hawaii, the young preshield alkaline melts may have formed by lower degrees of melting than the transitional basalts of the later subaerial shield stage. Devey et al. (2003) suggested that the preshield stage at the Society hotspot formed by melting of the most incompatible element-enriched source which could explain the high Nb/Zr ratios. Additionally, the small preshield volcanoes at the Society hotspot like Rocard erupted relatively evolved lavas with trachytic composition (**Figure 2b**) indicating longer times of stagnation in the lithosphere before a stable magma system with larger volumes of magma is established (Devey et al., 2003). Little is known about the youngest volcanism of the Marquesas hotspot because this volcanism occurs at the submarine Marquesas Fracture Zone but the lavas recovered from two small young seamounts are tephritic (Révillon et al., 2017), i.e., more alkaline than the alkali basalts of the Marquesas shield stage lavas (**Figure 2c**). In contrast, the lavas from the young submarine Vailulu volcano at the eastern end of the Samoan chain have similar transitional basaltic compositions to those from the older subaerial volcanoes (**Figure 2d**) but higher Nb/Zr (**Figure 3d**). Thus, with the exception of Samoa the preshield submarine volcanism at the three hotspots of Hawaii, Society and Marquesas appears to be more alkaline

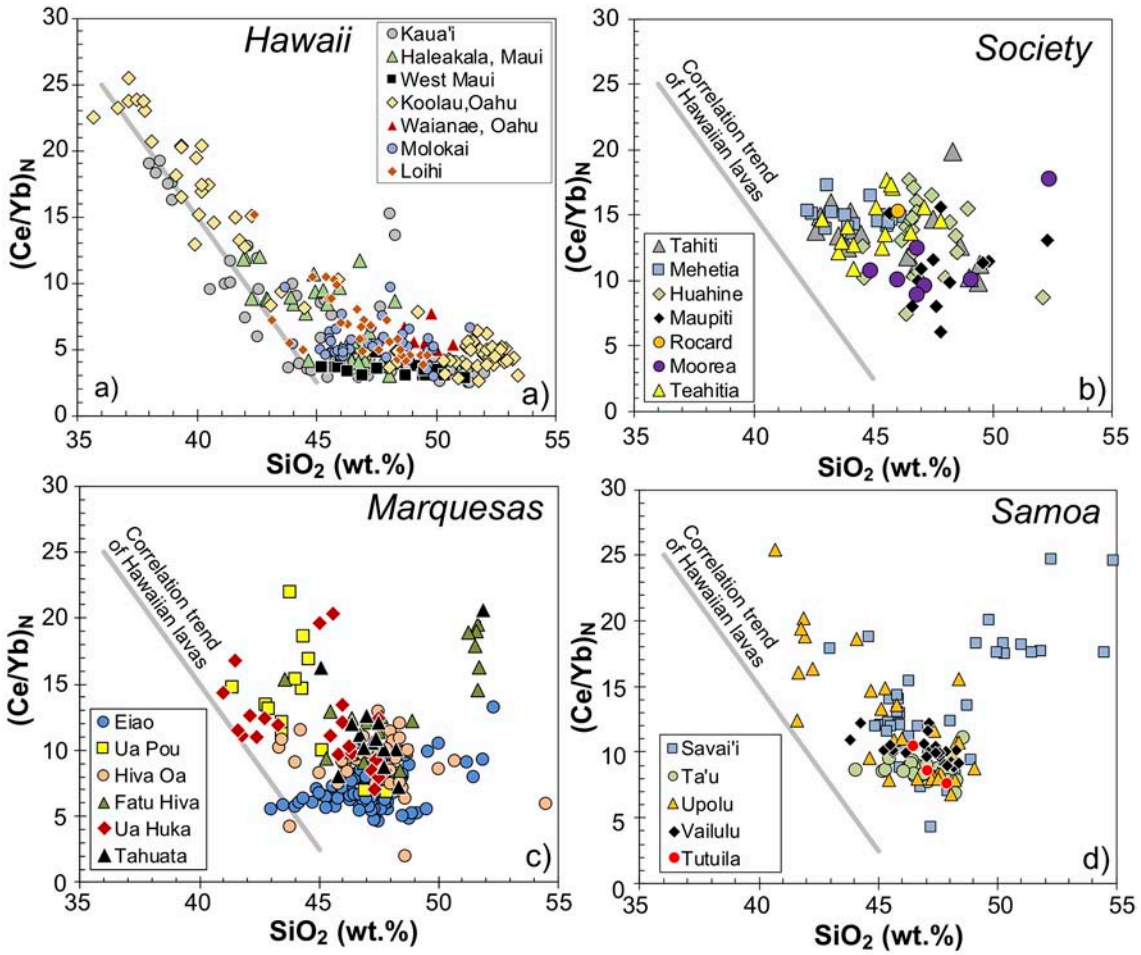

FIGURE 5 | The variation of chondrite-normalized Ce/Yb ratios with SiO_2 contents of the lavas from the **(a)** Hawaiian, **(b)** Society, **(c)** Marquesas, and **(d)** Samoa hotspots. Note that there is a negative correlation between the $(Ce/Yb)_N$ and the lowest SiO_2 content. Different magma series have relatively constant $(Ce/Yb)_N$ but crystal fractionation leads to increasing SiO_2 contents. The average trend of the variation observed at Koolau and Kaua'i is shown in all diagrams for comparison. Data sources can be found in the **Supplementary Material**.

than the later subaerial shield stages which probably indicates lower degrees of partial melting during the earliest volcanic stage.

Variation of Shield Stage Lava Compositions

The shield stage of a volcano is generally defined by structural and stratigraphic observations of the most voluminous eruptive stage yielding 85 to 90% of a volcano (Clague and Sherrod, 2014). The observations at the subaerial parts of the volcanoes indicate that tholeiitic basalts erupt during the shield stage but that there is a chemical transition to the alkaline postshield stage (e.g., Chen et al., 1991; Sinton et al., 2017). The tholeiitic basalts of the Hawaiian shield stage have the lowest Nb/Zr ratios of all Hawaiian lavas (**Figure 3a**) which was pointed out previously (Clague and Dalrymple, 1988; Frey et al., 1994). The well-studied shield lavas in the Hawaiian volcanoes are tholeiitic basalts but in the other hotspots the shield lavas are tholeiitic to alkali basaltic (**Figure 2**). The shield lavas of Tahiti are relatively well-defined based on field observations and a well-dated ∼1 million year-long stage with eruption of transitional basaltic lavas with relatively low Nb/Zr (**Figure 6**). Similarly, Moorea and Huahine volcanoes in the Society hotspot largely consist of transitional basalts that lie on the division line in **Figure 2** and are interpreted as shield stage lavas. We suggest that all shield stage lavas of the studied Pacific hotspot volcanoes are typically the least incompatible element-enriched samples, i.e., those with the lowest alkali content, Nb/Zr and $(Ce/Yb)_N$ but they also display relatively high SiO_2 contents (**Figures 2–4**, **6**). Whereas, the variable SiO_2 content largely reflects differences in degree and mean pressure of melting (Green et al., 2001), the incompatible element ratios mainly reflect differences in composition of the mantle source composition (Frey et al., 1978). Thus, we conclude in agreement with previous studies (e.g., Frey et al., 1991; Duncan et al., 1994; Farnetani and Hofmann, 2010) that the shield stage of the different hotspot volcanoes represents the highest degrees

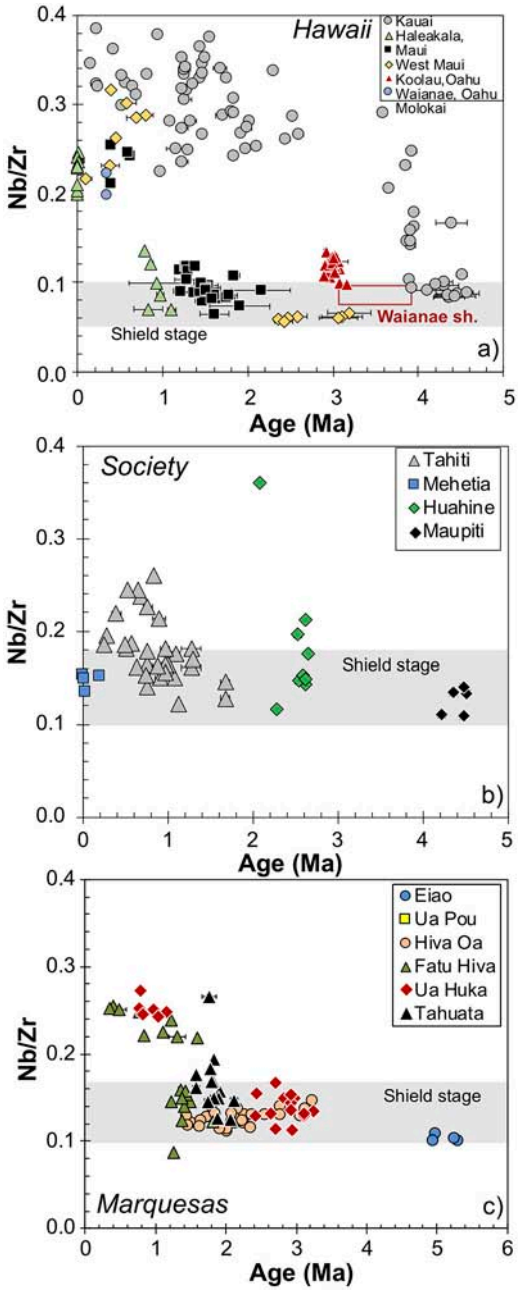

FIGURE 6 | Variation of the Nb/Zr ratios in the lavas with age for the best-studied volcanoes of the **(a)** Hawaii, **(b)** Society, and **(c)** Marquesas hotspots. Note that error bars are shown for most ages but are typically smaller than the symbols. The chemical variation of the lavas with age implies changes in the magma formation and mantle source. The red box in **(a)** indicates the range of eruption ages and compositions of the shield lavas at Waianae volcano. Note also that there is considerable overlap between shield stage volcanism and later more enriched postshield or rejuvenated volcanism in Kaua'i, Tahiti, Huahine, Tahuata, and Fatu Hiva. Data sources can be found in the **Supplementary Material**.

of partial melting although only the Hawaiian hotspot shows voluminous tholeiitic shield stage basalts. The recurrent relatively high degrees of partial melting beneath thick lithospheric plates support the formation in a long-lived melting anomaly probably caused by thermal or chemical mantle plumes. The covariation of SiO_2 and incompatible element ratios (**Figures 3**, **5**) indicates that the degree of partial melting varies with source composition in agreement with melting of variably enriched mantle sources.

The different volcanoes of most hotspots show very similar compositions in their shield stages (**Figures 2**, **3**) implying that the variation in major and incompatible element source compositions and melting process with time is relatively small although there are significant differences in terms of radiogenic isotope compositions (e.g., Abouchami et al., 2005; Payne et al., 2013). This can best be explained by thermally and compositionally homogenous melting zones in the different hotspots over time periods of several million years. Such a systematic homogeneity is especially observed at the Hawaiian shield volcanoes but the estimated volumes of the youngest volcanoes vary from ∼9,000 km^3 for West Maui to ∼74,000 km^3 for Mauna Loa (Clague and Sherrod, 2014). Even if a significant variation of degree of eutectic melting may produce tholeiitic magmas, the incompatible element ratios would be variably diluted which is not observed. Thus, while the recurrent geochemical composition of shield tholeiites implies a constant degree of melting during the shield stage the magma production varies by a factor of 8. This may imply that the erupted magma volume above mantle plumes may not be simply related to the degrees of partial melting.

The lavas from the Hawaiian hotspot indicate a larger variation in primitive magma compositions than those from the other Pacific hotspots (**Figure 4**). Experiments suggest that the large variation of SiO_2 contents in Hawaiian primary magmas between 36 and 52 wt.% requires low-degree melting of CO_2-rich mantle (e.g., Brey and Green, 1975; Clague and Frey, 1982; Cousens and Clague, 2015) on the one hand, and melting of pyroxenite-rich mantle on the other hand (e.g., Hauri, 1996). In contrast, the other three hotspot magmas range from basanites, alkali basalts, to rare tholeiitic basalts (**Figure 2**) most of which have been produced experimentally by variable degrees of partial melting of peridotite bearing some CO_2 (Takahashi and Kushiro, 1983; Hirose, 1997; Green et al., 2001; Dasgupta et al., 2007). This relatively restricted compositional variation of the mantle sources in the other three hotspots may indicate that CO_2-rich components and pyroxenite are absent and the source probably mainly consists of garnet peridotite.

Age Variation of Shield Stages

The plume model predicts that the shield stage of the volcanoes should reflect the plate velocity and the width of the central plume melting zone. In the case of the hotspots beneath the old and thick Pacific Plate the width of the plume should be the most important parameter directly related to both composition and age of the erupted melts. The definition of the period of time for the shield stage of each volcano is difficult to establish because the beginning cannot be established due to volcano growth and rare samples from the preshield stages. Preshield lavas were sampled and age-dated at the Loihi, Kilauea, and Kohala volcanoes of the Hawaiian hotspot and are typically basanites and alkali basalts (Clague and Sherrod, 2014). As

discussed above the preshield stages are poorly defined at the other hotspots and we suggest that early submarine stages of intraplate volcanism may have a different magmatic evolution compared to the Hawaiian volcanoes. Because of the unknown initiation of shield volcanism the age range observed in the compiled ages for shield stage lavas are minimum ages. The compiled data for the well-studied Hawaiian volcanoes Koolau, West Maui, and Kauai show relatively low Nb/Zr ratios for ∼1 million years (**Figure 6**) indicating that the shield stage of Hawaiian volcanoes may typically last ∼1 million years, whereas earlier studies suggested relatively short shield stages <0.5 million years (Frey et al., 1990). The well-studied lavas from Tahiti and those from Hiva Oa, Tahuata, and Ua Huka in the Marquesas suggest that the shield stage of these volcanoes also lasted ∼1 million years (**Figure 6**). The Pacific Plate moves with the same velocity of ∼10 cm/yr across the Hawaii, Society and Marquesas plumes (Gripp and Gordon, 2002). Thus, the apparent similarity of the duration of the shield stage in the different hotspots indicates similar widths of ∼100 km for the central melting anomalies. This observation is surprising considering that the buoyancy fluxes and likely the temperatures are distinct between the different plumes (Davies, 1988; Sleep, 1990). The variation of magma compositions indicates that the degree of melting varies and, for example, the alkaline shield lavas of the Marquesas formed at lower degrees of melting than the tholeiites of Hawaii implying that the Hawaii plume has a higher temperature than the other plumes (Herzberg and Asimov, 2008). We thus conclude that the widths of the melting anomalies are not linked to the temperature of the plumes but may be rather be affected by the velocity of the plate and the resulting plume shear. The similarity in melting zone width may be due to the horizontal spreading of the ascending plume by the relatively fast Pacific Plate (Farnetani and Hofmann, 2010) that may affect plumes with lower buoyancy more than the strong Hawaiian plume. This also implies that there will be no simple correlation between duration of the respective volcanic stages and the physical properties of the plume. The occurrence of more enriched signatures in the Samoa, Marquesas and Society islands may largely reflect mantle heterogeneity due to the smaller buoyancy flux as compared to the Hawaiian mantle plume in which much of this heterogeneity may be overprinted by the extensive melting regime.

The Transition From the Shield to the Postshield and Rejuvenated Stages

Large geochemical differences between shield lavas occur at Samoa but some volcanoes of this hotspot appear to erupt very large volumes of postshield and rejuvenated lavas, too, probably reflecting the tectonic influence of the Tonga subduction zone on mantle melting (Natland, 1980; Konter and Jackson, 2012). Thus, the Samoan intraplate volcanism deviates from the more regular pattern of volcano evolution of the other Pacific hotspots. Hence, the Hawaiian model may not be easily applicable to other intraplate volcanoes. Toward the end of the shield stage, more enriched lavas with higher Nb/Zr ratios are observed at West Maui and Kaua'i but also at Tahiti, Tahuata, and Fatu Hiva (**Figure 6**) implying that the formation of postshield magmas overlaps with that of the shield stage by up to 200 kyrs. This evolution has been described previously for Hawaiian volcanoes (Clague and Sherrod, 2014; Sinton et al., 2017), but seems to be a typical feature also observed in lavas from other Pacific hotspots. Interestingly, a few samples at Kauai, Tahuata, and Fatu Hiva suggest that the volcanoes erupt the most enriched lavas contemporaneously to the final shield and the postshield lavas (**Figure 6**). The variation of age and Nb/Zr ratios displays a significant overlap of the lavas formed during the different stages and there appears to be a period toward the end of the shield stage when relatively SiO_2-rich and less incompatible element-enriched lavas erupt parallel to more alkaline and enriched postshield stage lavas (**Figure 6**). This overlap requires at least two separate magma systems in the mantle feeding the eruptions at the top with limited mixing occurring in between the different ascent systems. The postshield magmas are typically more alkaline than the shield magmas and probably formed by lower degrees of partial melting. A numerical dynamic model of the Hawaiian plume (Farnetani and Hofmann, 2010) suggests that the postshield magmas represent deeper melts than the shield magmas which is in agreement with the lower SiO_2 contents and higher $(Ce/Yb)_N$ of the melts (**Figure 5**). We conclude that the melting zone of many mantle plumes produces different melts for about 200 kyrs and that these magmas rise in separate systems to the surface. At a plate velocity of 10 cm/yr this period of time suggests an ∼20 km wide zone of overlap in the melting region feeding the different magmas which will be on the scale of a single volcanic system.

Putting the Hawaiian Model to a Test

The compilation of the chemical and age data for the four Pacific hotspot lavas indicates that Hawaii is unusual in the chemical variation of the lavas (**Figure 4**), but that there are similar patterns of magma evolution from alkaline submarine preshield eruptions to relatively SiO_2-rich shield lavas and then more alkaline postshield and rejuvenated lavas. Only Samoa seems to show a different evolution where the youngest submarine stage at Vailulu resembles that of subaerial shield stages at older volcanoes and where rejuvenated lavas appear to be extremely abundant. However, more data with better age resolution are required to test the applicability of the Hawaiian model at the Samoan volcanoes. In the well-studied Marquesas and Society hotspot volcanoes the change from shield to postshield and rejuvenated volcanism is comparable to that observed at Hawaiian volcanoes (**Figure 6**). The interpretation of the preshield volcanism is similarly complicated for Hawaii, Society, and Marquesas because this stage is mainly known from few samples from single submarine volcanoes without a clear relation to shield volcanism. We suggest that the Hawaiian model explains the observed systematic variation of magma composition with time as a reflection of variable degrees of partial melting due to movement of the plate across a plume.

Some inter-shield variability within the Marquesas, Society, and the Hawaiian island chain (**Figure 3**) can be observed between the islands of the northern- and islands of the southern groups (Abouchami et al., 2005; Payne et al., 2013). The physically different source components contribute to

the formation of the shield volcanoes over small spatial distances of less than few km's (Pietruszka and Garcia, 1999) strongly supporting the complex and heterogeneous nature of plumes and their surrounding mantle material. The presence of tholeiitic, large degree melts during the shield stages may be restricted to large, stationary plume systems that preferentially have larger buoyancy fluxes leading to larger degrees of partial melting. On the other hand, the extremely enriched and SiO_2-undersaturated melts of the Hawaiian rejuvenated magmas may indicate either more variable mantle sources or remelting of enriched sources by the extremely hot Hawaiian plume. We conclude that the evolution of ocean island volcanoes through distinct volcanological, petrological, and geochemical stages does not strictly follow the Hawaiian model and chemical variation is smaller but that the compositional changes between the different stages are clearly discernable.

CONCLUSIONS AND OUTLOOK

The limited age and compositional data of lavas from the Pacific hotspots reveal systematic variations of magma composition with age in most volcanoes where the late lavas are typically more enriched in incompatible elements and more alkaline than those of the shield stage. The Society and Marquesas hotspots show basanitic submarine volcanism apparently preceding the shield stage with alkali basaltic magmas. This variation most likely reflects the movement of the lithospheric plate across a thermal mantle plume forming a zoned melting anomaly with variable degrees of partial melting. However, more data with combined chemical and age constraints are required to better define the evolution of the intraplate magmatic systems. Existing data indicate that the shield stages of the well-studied volcanoes last about 1 million years and seem to similar for both strong and weak plumes. Because the velocity of the Pacific Plate is similar at the studied hotspots this implies similar sizes of the melting anomalies although the temperatures in the mantle plumes differ. The overlap of shield and postshield stage volcanism for up to 200 kyrs is also typical at different hotspots and indicates about 20 km wide transitional melting zone at the flank of the plume during which there are contemporaneous eruptions of both shield stage and postshield stage melts through distinctively different channels of ascent. More age and geochemical data of stratigraphically controlled samples are required from different volcanoes in order to understand the trends of magma evolution, melting processes, and mantle dynamics.

AUTHOR CONTRIBUTIONS

CB and KH compiled data, wrote the manuscript, and prepared the figures. FK worked on the initial data compilation and filtering and contributed ideas.

ACKNOWLEDGMENTS

We thank the editor Adriano Pimentel for inviting this contribution and for his patience during the completion of this manuscript. We acknowledge the helpful and constructive reviews by J. G. Shellnutt, I. E. M. Smith, and D. Geist that have considerably improved the quality of this work. CB acknowledges support by I. MacLeod. We acknowledge funding by the Deutsche Forschungsgemeinschaft (DFG) through grant BE4459/7-1.

SUPPLEMENTARY MATERIAL

The Supplementary Material for this article can be found online at: https://www.frontiersin.org/articles/10.3389/feart.2018.00242/full#supplementary-material

REFERENCES

Abouchami, W., Hofmann, A. W., Galer, S. J. G., Frey, F. A., Eisele, J., and Feigenson, M. (2005). Lead isotopes reveal bilateral asymmetry and vertical continuity in the Hawaiian mantle plume. *Nature* 434, 851–856. doi: 10.1038/nature03402

Adam, C., Yoshida, M., Isse, T., Suetsugu, D., Fukao, Y., and Barruol, G. (2010). South Pacific hotspot swells dynamically supported by mantle flows. *Geophys. Res. Lett.* 37:L08302. doi: 10.1029/2010GL042534

Binard, N., Hékinian, R., Cheminée, J. L., and Stoffers, P. (1992). Styles of eruptive activity on intraplate volcanoes in the Society and Austral hot spot regions: bathymetry, petrology, and submersible observations. *J. Geophys. Res.* 97, 13999–14015. doi: 10.1029/92JB00692

Brey, G., and Green, D. R. (1975). The role of CO_2 in the genesis of olivine melilitite. *Contrib. Mineral. Petrol.* 49, 93–103. doi: 10.1007/BF00373853

Chen, C.-Y., Frey, F. A., Garcia, M. O., Dalrymple, G. B., and Hart, S. R. (1991). The tholeiite to alkalic basalt transition at Haleakala Volcano, Maui, Hawaii. *Contrib. Mineral. Petrol.* 106, 183–200. doi: 10.1007/BF00306433

Clague, D.A., and Sherrod, D.R. (2014). "Growth and degradation of Hawaiian volcanoes," in *Characteristics of Hawaiian Volcanoes,* eds M. P. Poland, T. J. Takahashi, and C. M. Landowski (Washington, DC: U.S Geological Survey Professional Paper), 97–146.

Clague, D. A. (1987). Hawaiian xenolith populations, magma supply rates, and development of magma chambers. *Bull. Volcanol.* 49, 577–587. doi: 10.1007/BF01079963

Clague, D. A., and Dalrymple, G. B. (1987). The Hawaiian-emperor volcanic chain Part I. geologic evolution. *U.S. Geol. Surv. Prof. Paper.* 1350, 5–54.

Clague, D. A., and Dalrymple, G. B. (1988). Age and petrology of alkalic postshield and rejuvenated-stage lava from Kauai, Hawaii. *Contrib. Mineral. Petrol.* 99, 202–218. doi: 10.1007/BF00371461

Clague, D. A., and Frey, F. A. (1982). Petrology and trace element geochemistry of the Honolulu Volcanics, Oahu: implications for the oceanic mantle below Hawaii. *J. Petrol.* 23, 447–504. doi: 10.1093/petrology/23.3.447

Clouard, V., and Bonneville, A. (2005). "Ages of seamounts, islands, and plateaus on the Pacific plate," in *Plates, Plumes, and Paradigms*, eds G. R. Foulger, J. H. Natland, D. C. Presnall, and D. L. Anderson (Boulder, CO: Geological Society of America Special Paper), 71–90.

Courtillot, V., Davaille, A., Besse, J., and Stock, J. (2003). Three distinct types of hotspots in the Earth's mantle. *Earth Planet. Sci. Lett.* 205, 295–308. doi: 10.1016/S0012-821X(02)01048-8

Cousens, B. L., and Clague, D. A. (2015). Shield to rejuvenated stage volcanism on Kauai and Niihau, Hawaiian Islands. *J. Petrol.* 56, 1547–1584. doi: 10.1093/petrology/egv045

Dasgupta, R., Hirschmann, M. M., and Smith, N. D. (2007). Partial melting experiments of peridotite + CO_2 at 3 GPa and genesis of alkalic ocean island basalts. *J. Petrol.* 48, 2093–2124. doi: 10.1093/petrology/egm053

Davies, G. F. (1988). Ocean bathymetry and mantle convection 1. Large-scale flow and hotspots. *J. Geophys. Res.* 93, 10467–10480. doi: 10.1029/JB093iB09p10467

Desonie, D. L., Duncan, R. A., and Natland, J. H. (1993). Temporal and geochemical variability of volcanic products of the Marquesas Hotspot. *J. Geophys. Res.* 98, 17649–17666. doi: 10.1029/93JB01562

Detrick, R. S., von Herzen, R. P., Crough, S. T., Epp, D., and Fehn, U. (1981). Heat flow on the Hawaiian Swell and lithospheric reheating. *Nature* 292, 142–143. doi: 10.1038/292142a0

Devey, C. W., Albarède, F., Cheminée, J.-L., Michard, A., Mühe, R., and Stoffers, P. (1990). Active submarine volcanism on the Society Hotspot Swell (west Pacific): a geochemical study. *J. Geophys. Res.* 95, 5049–5066. doi: 10.1029/JB095iB04p05049

Devey, C. W., Lackschewitz, K. S., Mertz, D. F., Bourdon, B., Cheminée, J.-L., Dubois, J., et al. (2003). Giving birth to hotspot volcanoes: distribution and composition of young seamounts from the seafloor near Tahiti and Pitcairn islands. *Geology* 31, 395–398. doi: 10.1130/0091-7613(2003)031andlt;0395:GBTHVDandgt;2.0.CO;2

Duncan, R. A., Fisk, M. R., White, W. M., and Nielsen, R. L. (1994). Tahiti: geochemical evolution of a French Polynesian volcano. *J. Geophys. Res.* 99, 24341–24357. doi: 10.1029/94JB00991

Duncan, R. A., and Richards, M. A. (1991). Hotspots, mantle plumes, flood basalts, and true polar wander. *Rev. Geophys.* 29, 31–50. doi: 10.1029/90RG02372

Dymond, J. (1975). K-Ar ages of Tahiti and Moorea, society Islands, and implications for the hot-spot model. *Geology* 3, 236–240. doi: 10.1130/0091-7613(1975)3andlt;236:KAOTAMandgt;2.0.CO;2

Farnetani, C. G., and Hofmann, A. W. (2010). Dynamics and internal structure of the Hawaiian plume. *Earth Planet. Sci. Lett.* 295, 231–240. doi: 10.1016/j.epsl.2010.04.005

French, S. W., and Romanowicz, B. (2015). Broad plumes rooted at the base of the Earth's mantle beneath major hotspots. *Nature* 525, 95–99. doi: 10.1038/nature14876

Frey, F. A., Garcia, M. O., and Roden, M. F. (1994). Geochemical characteristics of Koolau Volcano: implications of intershield geochemical differences among Hawaiian volcanoes. *Geochim. Cosmochim. Acta* 58, 1441–1462. doi: 10.1016/0016-7037(94)90548-7

Frey, F. A., Garcia, M. O., Wise, W. S., Kennedy, A., Gurriet, P., and Albarède, F. (1991). The evolution of Mauna Kea volcano, Hawaii: petrogenesis of tholeiitic and alkalic basalts. *J. Geophys. Res.* 96, 14347–14375. doi: 10.1029/91JB00940

Frey, F. A., Green, D. H., and Roy, S. D. (1978). Integrated models of basalt petrogenesis: a study of quartz tholeiites to olivine melilitites from south eastern Australia utilizing geochemical and experimental petrological data. *J. Petrol.* 19, 463–513. doi: 10.1093/petrology/19.3.463

Frey, F. A., Wise, W. S., Garcia, M. O., West, H., Kwon, S.-T., and Kennedy, A. (1990). Evolution of Mauna Kea volcano, Hawaii: petrologic and geochemical constraints on postshield volcanism. *J. Geophys. Res.* 95, 1271–1300. doi: 10.1029/JB095iB02p01271

Garcia, M. O., Swinnard, L., Weis, D., Greene, A. R., Tagami, T., Sano, H., et al. (2010). Petrology, geochemistry and geochronology of Kaua'i lavas over 4·5 Myr: implications for the origin of rejuvenated volcanism and the evolution of the Hawaiian Plume. *J. Petrol.* 51, 1507–1540. doi: 10.1093/petrology/egq027

Green, D. H., Falloon, T. J., Eggins, S. M., and Yaxley, G. M. (2001). Primary magmas and mantle temperatures. *Eur. J. Mineral.* 13, 437–451. doi: 10.1127/0935-1221/2001/0013-0437

Gripp, A. E., and Gordon, R. G. (2002). Young tracks of hotspots and current plate velocities. *Geophys. J. Int.* 150, 321–361. doi: 10.1046/j.1365-246X.2002.01627.x

Guillou, H., Maury, R. C., Blais, S., Cotten, J., Legendre, C., Guille, G., et al. (2005). Age progression along the Society hotspot chain (French Polynesia) based on new unspiked K-Ar ages. *Bull. Soc. Geol. Fr.* 176, 135–150. doi: 10.2113/176.2.135

Guillou, H., Maury, R. C., Guille, G., Chauvel, C., Rossi, P., Pallares, C., et al. (2014). Volcanic successions in Marquesas eruptive centers: a departure from the Hawaiian model. *J. Volcanol. Geotherm. Res.* 276, 173–188. doi: 10.1016/j.jvolgeores.2013.12.003

Hart, S. R., Staudigel, H., Koppers, A. A. P., Blusztajn, J., Baker, E. T., Workman, R., et al. (2000). Vailulu'u undersea volcano: the new Samoa. *Geochem. Geophys. Geosyst.* 1:1056. doi: 10.1029/2000GC000108

Hauri, E. H. (1996). Major-element variability in the Hawaiian mantle plume. *Nature* 382, 415–419. doi: 10.1038/382415a0

Herzberg, C., and Asimov, P. D. (2008). Petrology of some oceanic island basalts: PRIMELT2.XLS software for primary magma calculation. *Geochem. Geophys. Geosyst.* 9:Q09001. doi: 10.1029/2008GC002057

Hildenbrand, A., Gillot, P.-Y., and LeRoy, I. (2004). Volcano-tectonic and geochemical evolution of an oceanic intra-plate volcano: Tahiti-Nui (French Polynesia). *Earth Planet. Sci. Lett.* 217, 349–365. doi: 10.1016/S0012-821X(03)00599-5

Hirose, K. (1997). Partial melt compositions of carbonated peridotite at 3 GPa and role of CO_2 in alkali-basalt magma generation. *Geophys. Res. Lett.* 24, 2837–2840. doi: 10.1029/97GL02956

Hofmann, A. W. (2003). *Sampling Mantle Heterogeneity Through Oceanic Basalts: Isotopes and Trace Elements, Treatise on Geochemistry*. Amsterdam: Elsevier. doi: 10.1016/B0-08-043751-6/02123-X

Hofmann, A. W., and Farnetani, C. G. (2013). Two views of Hawaiian plume structure. *Geochem. Geophys. Geosyst.* 14, 5308–5322. doi: 10.1002/2013GC004942

Jackson, M. G., and Dasgupta, R. (2008). Compositions of HIMU, EM1, and EM2 from global trends between radiogenic isotopes and major elements in ocean island basalts. *Earth Planet. Sci. Lett.* 276, 175–186. doi: 10.1016/j.epsl.2008.09.023

Jellinek, A. M., and Manga, M. (2004). Links between long-lived hot spots, mantle plumes, D", and plate tectonics. *Rev. Geophys.* 42:RG3002. doi: 10.1029/2003RG000144

Konter, J. G., and Jackson, M. G. (2012). Large volumes of rejuvenated volcanism in Samoa: evidence supporting a tectonic influence on late-stage volcanism. *Geochem. Geophys. Geosyst.* 13:Q0AM04. doi: 10.1029/2011GC003974

Koppers, A. A. P., Russell, J. A., Jackson, M. G., Konter, J. G., Staudigel, H., and Hart, S. R. (2008). Samoa reinstated as a primary hotspot trail. *Geology* 36, 435–438. doi: 10.1130/G24630A.1

Koppers, A. A. P., Russell, J. A., Roberts, J., Jackson, M. G., Konter, J. G., Wright, D. J., et al. (2011). Age systematics of two young en echelon Samoan volcanic trails. *Geochem. Geophys. Geosyst.* 12:Q07025. doi: 10.1029/2010GC003438

Le Bas, M. J., Le Maitre, R. W., Streckeisen, A., and Zanettin, B. (1986). A chemical classification of volcanic rocks based on the total alkali-silica diagram. *J. Petrol.* 27, 745–750. doi: 10.1093/petrology/27.3.745

Liu, M., and Chase, C. G. (1991). Evolution of Hawaiian basalts: a hotspot melting model. *Earth Planet. Sci. Lett.* 104, 151–165. doi: 10.1016/0012-821X(91)90201-R

Macdonald, G. A., and Katsura, T. (1964). Chemical composition of Hawaiian lavas. *J. Petrol.* 5, 82–133. doi: 10.1093/petrology/5.1.82

McDougall, I. (2010). Age of volcanism and its migration in the Samoa Islands. *Geol. Mag.* 147, 705–717. doi: 10.1017/S0016756810000038

McDougall, I., and Duncan, R. A. (1980). Linear volcanic chains-recording plate motions? *Tectonophys* 63, 275–295. doi: 10.1016/0040-1951(80)90117-1

Moore, J. G., Clague, D. A., and Normark, W. R. (1982). Diverse basalt types from Loihi seamount, Hawaii. *Geology* 10, 88–92. doi: 10.1130/0091-7613(1982)10<88:DBTFLS>2.0.CO;2

Morgan, W. J. (1971). Convection plumes in the lower mantle. *Nature* 230, 42–43. doi: 10.1038/230042a0

Morgan, W. J. (1972). Deep mantle convection plumes and plate motions. *Am. Ass. Petrol. Geol. Mem.* 56, 203–213.

Müller, R. D., Sdrolias, M., Gaina, C., and Roest, W. R. (2008). Age, spreading rates, and spreading asymmetry of the world's ocean crust. *Geochem. Geophys. Geosys.* 9:Q04006. doi: 10.1029/2007GC001743

Natland, J. (1980). The progression of volcanism in the Samoan linear volcanic chain. *Am. J. Sci.* 280, 709–735.

O'Connor, J., Steinberger, B., Regelous, M., Koppers, A., Wijbrans, J., Haase, K., et al. (2013). Constraints on past plate and mantle motion from new ages for the Hawaiian-Emperor seamount chain. *Geochem. Geophys. Geosyst.*14, 4564–4584. doi: 10.1002/ggge.20267

Payne, J. A., Jackson, M. G., and Hall, P. S. (2013). Parallel volcano trends and geochemical asymmetry of the society Islands hotspot track. *Geology* 41, 19–22. doi: 10.1130/G33273.1

Pietruszka, A. J., and Garcia, M. O. (1999). A rapid fluctuation in the mantle source and melting history of Kilauea volcano inferred from the geochemistry of its historical summit lavas (1790-1982). *J. Petrol.* 40, 1321–1342. doi: 10.1093/petroj/40.8.1321

Putirka, K. D., Perfit, M., Ryerson, F. J., and Jackson, M. G. (2007). Ambient and excess mantle temperatures, olivine thermometry, and active vs. passive upwelling. *Chem. Geol.* 241, 177–206. doi: 10.1016/j.chemgeo.2007.01.014

Révillon, S., Guillou, H., Maury, R. C., Chauvel, C., Aslanian, D., Pelleter, E., et al. (2017). Young marquesas volcanism finally located. *Lithos* 294–295, 356–361. doi: 10.1016/j.lithos.2017.10.013

Sharp, W. D., and Clague, D. A. (2006). 50-Ma initiation of Hawaiian-Emperor bend records major change in Pacific Plate motion. *Science* 313, 1281–1284. doi: 10.1126/science.1128489

Sinton, J. M., Eason, D. E., and Duncan, R. A. (2017). Volcanic evolution of Moloka'i, Hawai'i: implications for the shield to postshield transition in Hawaiian volcanoes. *J. Volcanol. Geotherm. Res.* 340, 30–51. doi: 10.1016/j.jvolgeores.2017.04.011

Sleep, N. H. (1990). Hotspots and mantle plumes: some phenomenology. *J. Geophys. Res.* 95, 6715–6736. doi: 10.1029/JB095iB05p06715

Strak, V., and Schellart, W. P. (2018). A subduction and mantle plume origin for Samoan volcanism. *Sci. Rep.* 8:10424. doi: 10.1038/s41598-018-28267-3

Takahashi, E., and Kushiro, I. (1983). Melting of a dry peridotite at high pressures and basalt magma genesis. *Am. Mineral.* 68, 859–879.

Talandier, J., and Okal, E. A. (1984). New survey of Macdonald Seamount, south Central Pacific, following volcanoseismic acitivity, 1977-1983. *Geophys. Res. Lett.* 11, 813–816. doi: 10.1029/GL011i009p00813

Tarduno, J. A., Duncan, R. A., Scholl, D. W., Cottrell, R. D., Steinberger, B., Thordarson, T., et al. (2003). The Emperor Seamounts: southward motion of the Hawaiian hotspot plume in Earth's mantle. *Science* 301, 1064–1069. doi: 10.1126/science.1086442

Thordarson, T., and Garcia, M. O. (2018). Variance of the flexure model predictions with rejuvenated volcanism at Kilauea Point, Kaua'i, Hawai'i. *Front. Earth Sci.* 6:121. doi: 10.3389/feart.2018.00121

Uto, K., Yamamoto, Y., Sudo, M., Uchiumi, S., Ishizuka, O., Kogiso, T., et al. (2007). New K-Ar ages of the Society Islands, French Polynesia, and implications for the Society hotspot feature. *Earth Planets Space* 59, 879–885. doi: 10.1186/BF03352750

Watson, S., and McKenzie, D. (1991). Melt generation by plumes: a study of Hawaiian volcanism. *J. Petrol.* 32, 501–537. doi: 10.1093/petrology/32.3.501

White, W. M. (2010). Oceanic island basalts and mantle plumes: the geochemical perspective. *Ann. Rev. Earth Planet. Sci.* 38, 133–160. doi: 10.1146/annurev-earth-040809-152450

Wilson, J. T. (1963). A possible origin of the Hawaiian Islands. *Can. J. Earth Sci.* 41, 863–870. doi: 10.1139/p63-094

Woodhead, J. D. (1992). Temporal geochemical evolution in oceanic intraplate volcanics: a case study from the Marquesas (French Polynesia) and comparison with other hotspots. *Contrib. Mineral. Petrol.* 111, 458–467. doi: 10.1007/BF00320901

Conflict of Interest Statement: The authors declare that the research was conducted in the absence of any commercial or financial relationships that could be construed as a potential conflict of interest.

Copyright © 2019 Haase, Beier and Kemner. This is an open-access article distributed under the terms of the Creative Commons Attribution License (CC BY). The use, distribution or reproduction in other forums is permitted, provided the original author(s) and the copyright owner(s) are credited and that the original publication in this journal is cited, in accordance with accepted academic practice. No use, distribution or reproduction is permitted which does not comply with these terms.

frontiers in Earth Science

HYPOTHESIS AND THEORY
published: 08 May 2018
doi: 10.3389/feart.2018.00050

The Evolution of Galápagos Volcanoes: An Alternative Perspective

Karen S. Harpp[1]* *and Dennis J. Geist*[1,2]

[1] Department of Geology, Colgate University, Hamilton, NY, United States, [2] Division of Earth Sciences, U.S. National Science Foundation, Alexandria, VA, United States

The older eastern Galápagos are different in almost every way from the historically active western Galápagos volcanoes. Geochemical, geologic, and geophysical data support the hypothesis that the differences are not evolutionary, but rather the eastern volcanoes grew in a different tectonic environment than the younger volcanoes. The western Galápagos volcanoes have steep upper slopes and are topped by large calderas, whereas none of the older islands has a caldera, an observation that is supported by recent gravity measurements. Most of the western volcanoes erupt evolved basalts with an exceedingly small range of Mg#, La_n/Sm_n, and Sm_n/Yb_n. This is attributed to homogenization in a crustal-scale magmatic mush column, which is maintained in a thermochemical steady state, owing to high magma supply directly over the Galápagos mantle plume. In contrast, the eastern volcanoes erupt relatively primitive magmas, with a large range in Mg#, La_n/Sm_n, and Sm_n/Yb_n. These differences are attributed to isolated, ephemeral magmatic plumbing systems supplied by smaller magmatic fluxes throughout their histories. Consequently, each batch of magma follows an independent course of evolution, owing to the low volume of supersolidus material beneath these volcanoes. The magmatic flux to Galápagos volcanoes negatively correlates to the distance to the Galápagos Spreading Center (GSC). When the ridge was close to the plume, most of the plume-derived magma was directed to the ridge. Currently, the active volcanoes are much farther from the GSC, thus most of the plume-derived magma erupts on the Nazca Plate and can be focused beneath the large young shields. We define an intermediate sub-province comprising Rabida, Santiago, and Pinzon volcanoes, which were most active about 1 Ma. They have all erupted dacites, rhyolites, and trachytes, similar to the dying stage of the western volcanoes, indicating that there was a relatively large volume of mush beneath them. The paradigm established by the evolution of Hawaiian volcanoes as they are carried away from the hotspot does not apply to most archipelagos.

Keywords: ocean islands, hotspot, Galápagos Islands, caldera, petrology, igneous geochemistry, magma supply

OPEN ACCESS

Edited by:
Ricardo S. Ramalho,
Universidade de Lisboa, Portugal

Reviewed by:
Alessandro Tibaldi,
Università degli Studi di Milano Bicocca, Italy
Timothy Druitt,
Université Clermont Auvergne, France
Cornelia Class,
Lamont Doherty Earth Observatory (LDEO), United States
Andreas Klügel,
University of Bremen, Germany

***Correspondence:**
Karen S. Harpp
kharpp@colgate.edu

Specialty section:
This article was submitted to Volcanology, a section of the journal Frontiers in Earth Science

Received: *14 January 2018*
Accepted: *18 April 2018*
Published: *08 May 2018*

Citation:
Harpp KS and Geist DJ (2018) The Evolution of Galápagos Volcanoes: An Alternative Perspective. Front. Earth Sci. 6:50. doi: 10.3389/feart.2018.00050

INTRODUCTION

Volcanoes of the Galápagos Islands exhibit remarkable diversity in morphology, eruptive behavior, and magmatic composition. Existing models for the evolution of ocean island volcanoes such as those of Hawaii (e.g., Macdonald et al., 1983; Clague and Dalrymple, 1987, 1988; Walker, 1990) and the Galápagos (e.g., McBirney and Williams, 1969; White et al., 1993; Geist et al., 2014) attribute

differences in lava composition and eruptive behavior along the island chain to the location of each volcano relative to the mantle plume. In Hawaii, for example, tholeiitic basalts are effusively erupted during the high-flux, shield-building phase, and alkalic magma is produced in the post-shield phase, when magma supply is waning (e.g., Walker, 1990). Such models assume a progressive evolution in a volcano's eruptive products, directly correlated to the distance between the volcano and the plume, and therefore the volcano's age.

In the Galápagos Archipelago, there is a dichotomy between the younger, western volcanic province and the older, eastern province, with distinct differences in structural features, lithospheric fractionation conditions, and melt generation processes (**Table 1**). Among the most striking variations is the prevalence of large calderas up to several kilometers across and several hundred meters deep on the young western shield volcanoes, contrasting with the older eastern volcanoes, which lack calderas or any morphological evidence of them (**Figures 1**, **2**). On the basis of a synthesis of published geochemical, geologic, and geophysical data, we propose that the Galápagos volcanoes do not follow a consistent evolutionary trend but instead require an alternative to the progressive Hawaiian evolutionary model. We hypothesize that the eastern volcanoes are not an evolved stage of the young western volcanoes but instead formed by a different constructional mechanism controlled by the proximity of the Galápagos Spreading Center (GSC) 1–3 Ma.

TECTONIC SETTING OF THE GALÁPAGOS

The Galápagos Islands are the manifestation of a mantle plume located ∼1,000 km off the west coast of Ecuador, on the Nazca Plate, which is moving eastward at 51 km/my relative to the hotspot (Argus et al., 2011). The east-west striking GSC is 250 km north of Fernandina Island, and is offset at ∼90°50′W by a ∼100 km transform fault (the Galápagos Transform Fault, GTF; **Figure 1**). The GSC is currently migrating away from the archipelago at 47 km/my to the northeast (55°, the difference between the GSC half-spreading velocity and absolute motion of the Nazca plate), progressively increasing plume-ridge distance. On the basis of magnetic data collected across the northern Galápagos seafloor, Mittelstaedt et al. (2012) determined that the GSC has jumped southward at least twice, once ∼2.5–3.5 Ma and again ∼1 Ma, resulting in a current plume-ridge separation of 145–215 km.

COMPARISON OF THE WESTERN AND EASTERN GALÁPAGOS VOLCANOES

Geology and Ages of the Volcanoes

The western Galápagos volcanoes are the youngest in the archipelago (**Figure 1**), owing to the eastward motion of the Nazca plate. Fernandina is the westernmost and youngest island, hosting a single shield. Cosmogenic helium exposure ages led Kurz et al. (2014) to estimate that Fernandina emerged ∼32 ka and has been entirely resurfaced in the last 4.3 ka. Isabela Island consists of 6 separate shield volcanoes, Cerro Azul, Sierra Negra, Alcedo, Darwin, Wolf, and Ecuador, which are connected by land bridges formed from lava flows. Most lavas from the western Galápagos are too young for age determinations using radiogenic argon; all are normally polarized, and Geist et al. (2014) estimate that the oldest ones emerged <500 ka.

The major islands of the eastern Galápagos Archipelago are Santiago, Pinzón, Rábida, Santa Cruz, Floreana, San Cristóbal, Santa Fe, and Española (**Figure 1**). The oldest are San Cristóbal (oldest recorded ages to date are 2.33 ± 0.04 and 2.35 ± 0.03 Ma; White et al., 1993), and Española (2.61 ± 0.11 and 2.71 ± 0.36 Ma; White et al., 1993). Santa Cruz has lavas that span the range from 1.6 Ma to 30 ka (White et al., 1993; Schwartz, 2014). Similarly, Floreana Island lava ages vary from 1.63 Ma to 26 ka (Bow and Geist, 1992; White et al., 1993; Harpp et al., 2014). The limited age data from Santa Fe Island vary from 0.72 ± 0.09 to 2.76 ± 0.06 Ma (White et al., 1993). Rábida's lavas range from 1.03 ± 0.05 to 0.92 ± 0.09 Ma, similar to those from Pinzón, which have ages between 1.4 ± 0.08 and 0.93 ± 0.14 Ma (Swanson et al., 1974; White et al., 1993). Santiago is the youngest of the

TABLE 1 | Compilation of geologic, geophysical, and geochemical differences between the western, eastern, and intermediate volcanoes.

Attribute	Parameter	Western volcanoes	Intermediate volcanoes	Eastern volcanoes
Profile	Morphology	Steep flanks	Shallow slopes	Shallow slopes
Caldera	Morphology	Yes	Perhaps buried	Never
Gravity signal	Gravity	∼30 mg high	unknown	No detectable Bouguer Anomaly
Hydrovolcanism	Tuff cones and rings	Caldera and shorelines	Low elevations only	Low elevations only
Fissure systems	Morphology	Circumferential and radial	Linear; tectonic control	Linear; tectonic control
Faults	Geology	Related to calderas	Rare or absent	Tectonic and abundant
Ages	Geochronology	<0.5 Ma	Most 0.5–1 Ma	Most 1–3 Ma
Eruptive style	Deposits	Mostly lava	Silicic pyroclastic deposits and dome	Intense Strombolian + lavas
Crustal evolution	Mg# variation	Fractionated and buffered	Extensive fractionation	Widely variable cooling histories
Depth of melting	Sm/Yb	D_{top} = 56–58 km	51–57 km	51–53 km
Extent of melting	$\Delta La_n/Sm_n$	Consistent	Consistent	Widely variable
Homogenization	Mg#, Sm/Yb, and $\Delta La_n/Sm_n$	Well-mixed	Poorly mixed	Independent magma batches

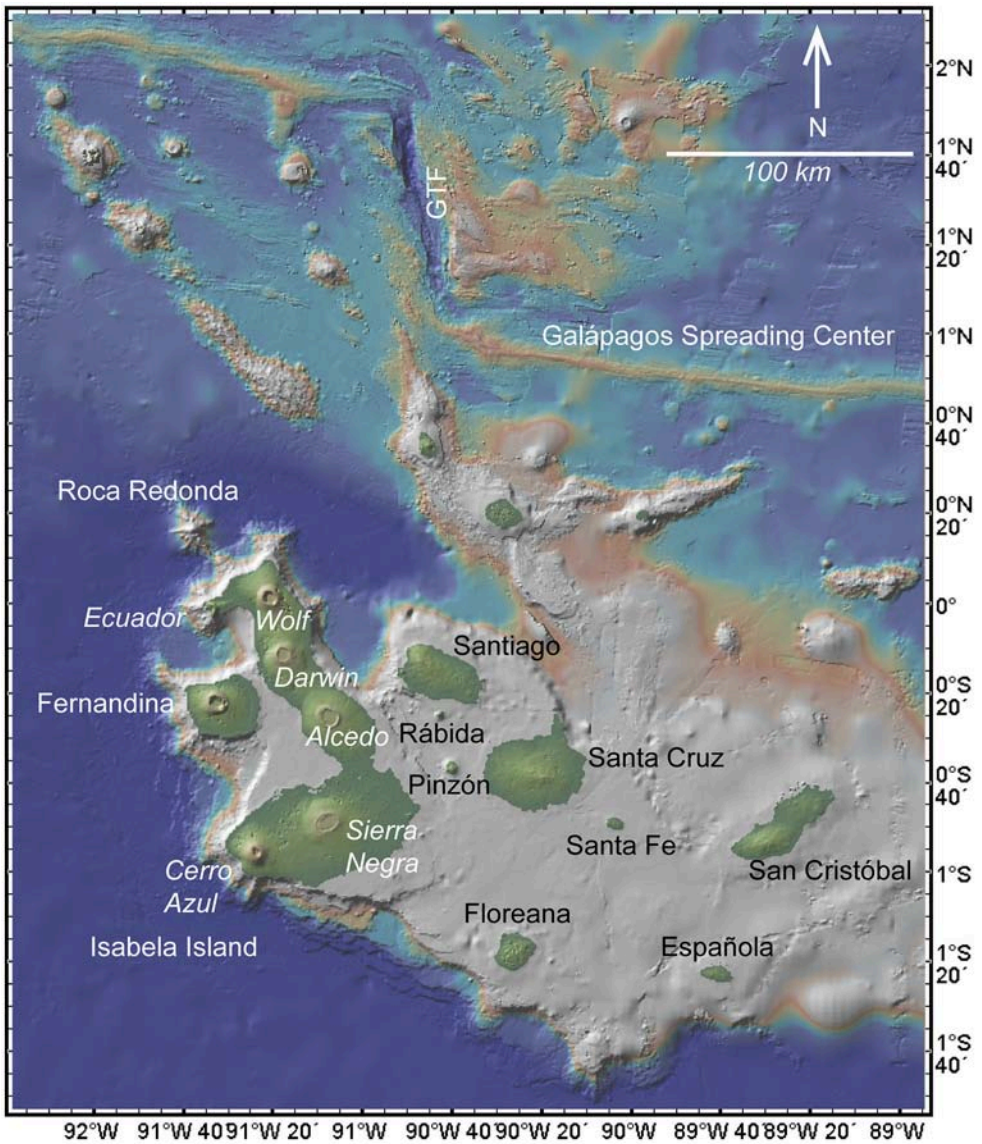

FIGURE 1 | Map of the Galápagos Islands and surrounding bathymetry. Plate motion is almost directly east (51 km/my; Argus et al., 2011). Bathymetric data are from Geomapapp (Ryan et al., 2009). The western volcanoes are labeled in white, those of the intermediate and eastern province in black. GTF, Galápagos Transform Fault.

eastern volcanoes, with only normally polarized lavas and an oldest recorded age of 770 ± 12 ka (Swanson et al., 1974), as well as historical activity, including an eruption in 1906 (Siebert et al., 2011).

Volcano Morphology and Eruptive Fissure Pattern

Western volcanoes

McBirney and Williams (1969) originally described the shapes of the western Galápagos shields as having "overturned soup bowl" profiles (**Figure 2A**). The lower and uppermost flanks are shallow, but mid-flank slopes are significantly steeper, a shape that has been attributed to the distinctive eruptive fissure pattern of the volcanoes (e.g., Rowland, 1996). The western Galápagos volcanoes have circumferentially oriented eruptive fissures around their summits, which shift to radial down the flanks (**Figure 2C**; McBirney and Williams, 1969; Chadwick and Howard, 1991). On the basis of numerical modeling results, Chadwick and Dieterich (1995) attributed this pattern to stresses generated by construction of the edifice plus the influence of a pressurized diapir-shaped magma reservoir; finite element models show that caldera decompression also contributes to the state of stress and fissure orientation (Corbi et al., 2015). A cycle develops, in which the formation of radial dikes establishes conditions for subsequent generation of circumferential dikes, the formation of which encourages initiation of radial dikes, an alternating pattern exhibited by Fernandina's eruptive activity over the past few decades (e.g., Chadwick et al., 2011; Bagnardi and Amelung, 2012; Bagnardi

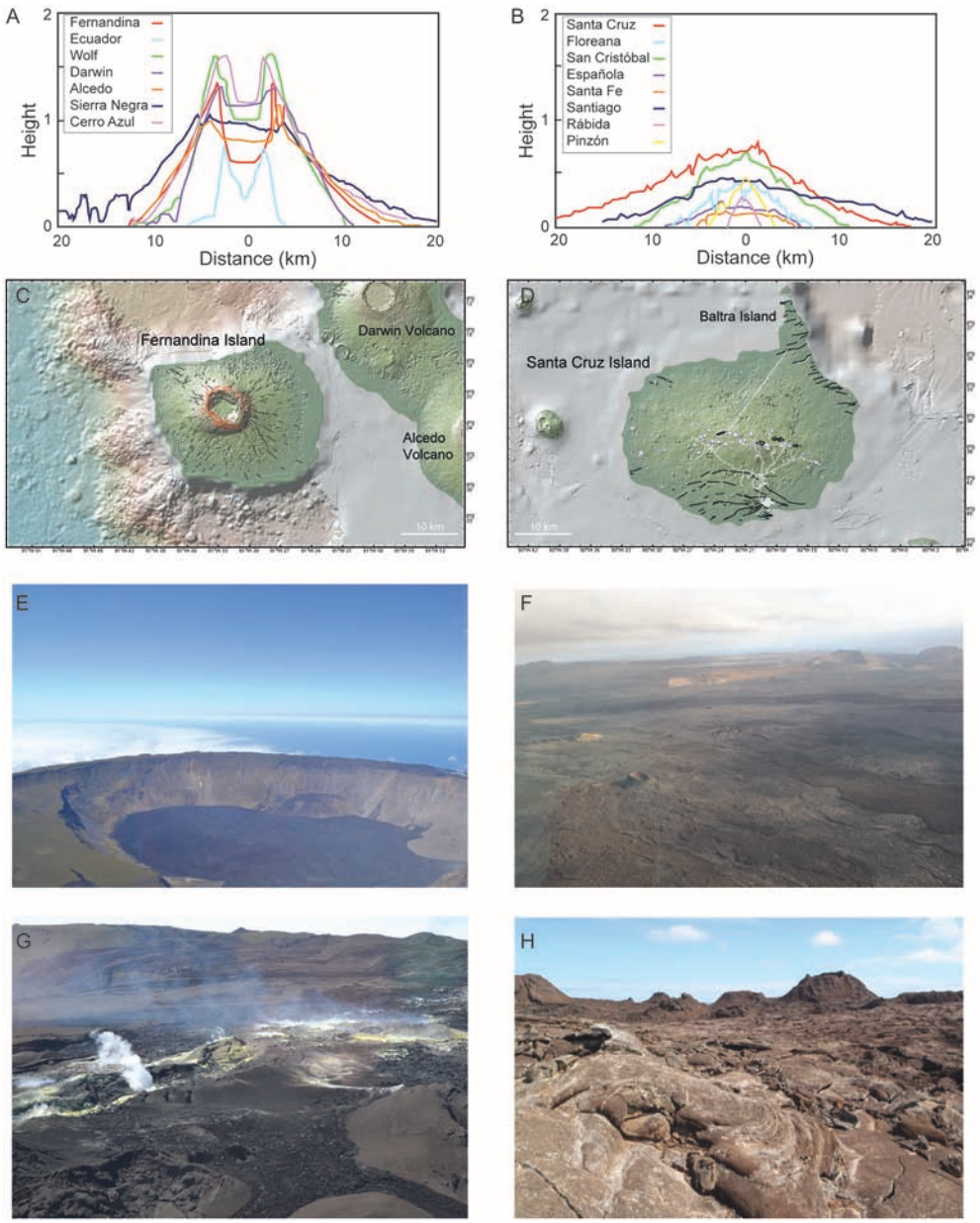

FIGURE 2 | Geomorphic comparison of western and eastern Galápagos volcanoes. **(A)** Profiles of western volcanoes (data from Google Earth). Note prevalence of calderas on all the volcanoes. **(B)** Profiles of eastern volcanoes (data from Google Earth). Note lack of calderas. **(C)** Map of Fernandina Island showing radial (black) and circumferential (red) faults after Chadwick and Howard (1991). Base map from Geomapapp (Ryan et al., 2009). **(D)** Map of Santa Cruz Island showing faults (black) and cinder cones (gray circles) (structural features mapped by Schwartz, 2014). Roads are also shown (gray). Base map from Geomapapp (Ryan et al., 2009). **(E)** Aerial view of the Wolf Volcano caldera. **(F)** Aerial view of NE Santiago Island. **(G)** Aerial view of site of 2015 eruption of Wolf Volcano along circumferential fault at summit. Caldera is to the left in the image. **(H)** Ground-level view of fissures in young volcanic province of San Cristóbal Island. Photo credits: K. Harpp.

et al., 2013). As initially observed by Simkin et al. (1973), short lava flows are erupted from the circumferential fissures that ring the volcano summits, constructing the steep upper slopes of the western shields (Chadwick and Howard, 1991). The transition from circumferential to radial fissures occurs at the break in slope down the flanks, from which longer flows emanate to build the shallower lower flanks (Chadwick and Howard, 1991). Recent geodetic evidence suggests that individual dikes actually twist 90° as they intrude from the summit platform to the lower flanks (Bagnardi et al., 2013).

The submarine environment in the western Galápagos is dominated by flat lying sheet flows and focused rifts that emanate from the subaerial structures (**Figures 1**, **2C**) but relatively few small seamounts, and there is no submarine Loihi-like edifice

growing at the leading edge of the hotspot track. The sheet flows are stacked in terraces that define the western edge of the Galápagos Platform (Geist D. et al., 2008). The submarine rift zones are well-developed on the flanks of Fernandina, Cerro Azul, Ecuador, Wolf, and Darwin Volcanoes (**Figure 2C**; Geist D. J. et al., 2006).

Eastern volcanoes

The older, eastern Galápagos Islands have strikingly different morphologies from the western shields, with greater variability in size and shape (**Figures 1**, **2B**). For example, Santa Cruz is 40 km across (larger than Fernandina at ∼30 km), whereas Santa Fe is only 7 km in diameter. Santiago, San Cristóbal, Santa Fe, and Española are notably elongate, compared to the more circular shapes of Floreana and Santa Cruz. The eastern islands also have lower summits and more consistently shallow slopes than the western shields (**Figure 2B**).

Several eastern islands, particularly those with more elongate shapes, exhibit structural alignments of eruptive cones, pit craters, fissures, and faults; there is no evidence of the circumferential or radial fissure structures that are observed on the western shields (e.g., Chadwick and Howard, 1991). On Santa Cruz, a WNW-trending alignment of scoria cones and pit craters stretches across the island, as well as two sets of E-W/ENE oriented faults that formed in distinct episodes, one no later than ∼1.16 Ma, and the second between 40 and 270 ka (Schwartz, 2014; **Figure 2D**). Eruptive activity along the cross-island fissure system coincided with the initiation of the E-W oriented faults on the southern flank of Santa Cruz (**Figure 2D**; Schwartz, 2014). San Cristóbal, which consists of two smaller shield volcanoes, has a set of ENE-striking faults that are parallel to eruptive cone alignments, particularly in the youngest lava province (Geist et al., 1986; Mahr et al., 2016). Floreana's abundant cinder cones are also arranged in an ENE-striking swath that crosses the island (Harpp et al., 2014). Many fissures on Santiago are parallel to the elongation of that island (Swanson et al., 1974). The E-W faults that cross-cut Santa Fe and Española Islands have resulted in the formation of a series of horst and graben structures across the islands (Hall, 1983; Geist et al., 1985).

The submarine environment in the eastern Galápagos is not as extensively mapped as that in the west, but recent research expeditions (e.g., Schwartz et al., 2017) have identified clusters of monogenetic seamounts off the coasts of Santiago, Santa Cruz, and Floreana Islands. Despite limited high resolution bathymetric surveys, neither structures comparable to the western terraces (Geist D. et al., 2008) nor large submarine rift zones (e.g., Geist D. J. et al., 2006) exist in the eastern archipelago.

Eruptive Style

Western volcanoes

The eruptive style of the western shields is predominantly effusive, generally beginning with Hawaiian-style lava fountaining either along circumferential fissures near the caldera rim or radial fissures on the flanks (e.g., Teasdale et al., 2005; Geist D. J. et al., 2008; **Figures 2C,E,G**). A Strombolian phase can follow the lava fountaining once the eruption has focused to a few active vents (e.g., Geist D. J. et al., 2008). Eruptions that have been observed (including Fernandina in 2017, 2009, 2005, 1995; Wolf in 2015; Sierra Negra in 2005, 1979; Cerro Azul in 2008) have been relatively short in duration, ranging from days (Fernandina, 6 days in 2017) to weeks (Cerro Azul, 5 weeks in 1998, Teasdale et al., 2005; Sierra Negra, 8 weeks in 1979, Reynolds et al., 1995).

Hydrovolcanic activity occurs within the calderas of the western volcanoes, owing to interaction of magma with caldera lakes and caldera-bound aquifers (e.g., Cerro Azul, Naumann and Geist, 2000; Sierra Negra, Reynolds et al., 1995; Fernandina, Simkin and Howard, 1970; Howard et al., in press). Abundant large tuff cones also occur along the shorelines (e.g., Tagus Cove on the western coast of Volcan Darwin) or just offshore (Islas Tortuga and Cowley), as well as a rootless cone fields (e.g., on the flanks of Cerro Azul). The 1968 eruption of Fernandina resulted in a major caldera floor collapse event that was accompanied by explosive phreatomagmatic activity owing to the presence of a lake on the caldera floor (Simkin and Howard, 1970; Howard et al., in press).

Alcedo is the only western shield that has documented Plinian-style activity, having erupted ∼1 km^3 of rhyolitic tephra and lava (dense rock equivalent) ∼100,000 years ago (Geist et al., 1994, 1995). Geist et al. (1995) attribute the explosive behavior and evolved compositions to extensive crystallization of magma reservoirs in systems that are cooling (Geist et al., 2014).

Eastern volcanoes

The largest of the eastern islands have young lavas and protracted periods (>1 million years) of eruptive activity. The smaller volcanoes of Pinzón and Rábida are exceptional, because they went extinct shortly after their peak activity at ∼1 Ma (Swanson et al., 1974). On Santiago, historical activity has been identified on both the eastern and western ends of the island (**Figure 2F**; 1906 C.E. at Sulivan Bay in the east and ∼1754 C.E. at James Bay in the west; Siebert et al., 2011). Floreana's Alayeri cone and associated lavas have a cosmogenic surface exposure age of 26 ± 7 ka (Kurz and Geist, 1999; Harpp et al., 2014). Available age data suggest that although activity at Santiago and Floreana has been waning, it has been continual (Gibson et al., 2012; Harpp et al., 2014), as opposed to rejuvenescent (e.g., Chen and Frey, 1983). To date, no lavas younger than ∼2.5 Ma have been identified on Española, nor does the island host a morphologically young lava field (White et al., 1993; McGuire et al., 2015). Even though there is no obvious morphologically young province on Santa Fe, White et al. (1993) publish a 0.72 Ma age, nearly 2 million years younger than the oldest dated lava from this small island, suggesting a span of activity comparable to that of the larger eastern islands.

Santa Cruz has experienced several eruptive phases. There have been at least two periods of activity, one between 1,620 and 1,160 ka and another lasting from about 700 to 20 ka (Schwartz, 2014), although lavas from the intervening episode may exist beneath the younger cover. San Cristóbal hosts a young lava province, located near the junction between the two shield volcanoes (Geist et al., 1986; **Figure 2H**). These large lava fields were emplaced between 5 and 174 ka, according to cosmogenic

helium surface dating (Mahr et al., 2016). The sharp boundary between the young lava province and the rest of the island's more heavily vegetated surfaces suggests that there may have been a hiatus in eruptive activity (Mahr et al., 2016), but there are currently too few age determinations from the main shield volcanoes to be certain. Moreover, older lavas are certainly buried beneath the southwest shield (Geist et al., 1986; White et al., 1993).

Much of the late-stage activity on Santiago, Floreana, Santa Cruz, and San Cristóbal was more explosive than is observed in the western shields. All of the eastern islands are notable for their numerous monogenetic scoria and tuff cones. Effusive eruptions during the late-stage activity are largely from tectonically directed fissures (Geist et al., 1986; Bow and Geist, 1992; Gibson et al., 2012; Wilson, 2013; Harpp et al., 2014; Schwartz, 2014; McGuire et al., 2015; Mahr et al., 2016; Pimentel et al., 2016). For instance, the youngest San Cristóbal lavas emanate from sets of aligned cones that parallel the ENE-trending faults along the north coast and elongation of the island (**Figure 2H**; Geist et al., 1986; Mahr et al., 2016). Similarly, the most recent eruptive activity on Santa Cruz was localized along an E-W trending summit vent system of cinder cones (Bow, 1979; Schwartz, 2014; **Figure 2D**).

Floreana, Santiago, San Cristóbal, Pinzón, and Rábida volcanoes have erupted with sufficient energy that they have transported mafic and ultramafic xenoliths to the surface (McBirney and Williams, 1969; Baitis and Lindstrom, 1980; Geist et al., 1986; Lyons et al., 2007; Bercovici et al., 2016). In most cases, xenoliths tend to be found at tuff-cones and scoria-rich vents (especially the older vents on Floreana, Bow and Geist, 1992; Lyons et al., 2007; Harpp et al., 2014; Rábida, Bercovici et al., 2015, 2016). A rhyodacitic ignimbrite deposit is exposed on the northeast coast of Rábida Island, the only evidence of explosive silicic volcanism found to date in the eastern Galápagos.

Despite being small compared to the major eastern Galápagos volcanoes, Española embodies many of the characteristics common to those volcanoes, including E-W trending faults and abundant scoria and tuff cones. Most of the monogenetic vents are located along the northern coast of the island, whereas the southern coast consists of steep cliffs that expose nearly horizontally stacked, 1–5 m thick lava flows (McGuire et al., 2015), some of which bury a single scoria cone (Hall, 1983). Given the volcano's small area and these observations, Española may be the remnant of a larger structure that experienced sector collapse or extensive wave erosion of its southern half.

Calderas (and Lack Thereof)

Western-volcanoes

The most striking geomorphic feature of the western shields is the large caldera at the summit of each volcano (**Figures 1**, **2A,C,E**). All of the young western shield volcanoes (with the exception of Roca Redonda, which does not lie on the Galápagos Platform; Standish et al., 1998; **Figure 1**) are endowed with major calderas, which can be classified in two morphological groups. Sierra Negra, Alcedo, and Darwin volcanoes on Isabela Island have shallow, wide calderas, similar to those of Mauna Loa and Kilauea, Hawaii (Poland, 2014). For example, the Sierra Negra caldera has a diameter of about 9 km and is about 100 m deep. In contrast, the calderas of Wolf (**Figure 2E**), Cerro Azul, and Fernandina volcanoes are narrower and deeper, typically ∼5 km in diameter and 600–1,000 m deep (e.g., Munro and Rowland, 1996). All of the calderas have complex structural histories of multiple collapses and refilling events (e.g., Reynolds et al., 1995; Poland, 2014), making it difficult to correlate caldera to with magma supply in a straightforward manner. For example, Sierra Negra, which erupted most recently in 2005 (Geist D. J. et al., 2008), is shown to cyclically inflate, fault, and subside in less than a decade (Chadwick et al., 2006).

Gravity surveys conducted at Fernandina and Sierra Negra volcanoes detect well-defined, localized Bouguer gravity highs reaching ∼30 mGal over the centers of the calderas (Ryland, 1971; Case et al., 1973; Geist D. et al., 2006; Vigouroux et al., 2008). As is the case for similar signals observed over Hawaiian volcanoes (50–100 mGal; Kinoshita, 1965; Flinders et al., 2013), the elevated gravity anomalies have been attributed to dense (predicted sub-surface densities higher by ∼600 kg/m^3), residual cumulate bodies beneath the calderas.

Eastern volcanoes

The major eastern islands lack large calderas (**Figures 2B,D,F**). Pinzón has a small (∼1,500 m diameter) caldera near the summit (Baitis and Lindstrom, 1980), and a sequence of arcuate faults may be remnants of a filled caldera at Rábida (Bercovici et al., 2015, 2016).

In contrast to the ∼30 mGal Bouguer Anomaly (BA) highs detected at Fernandina and Sierra Negra calderas (Case et al., 1973; Vigouroux et al., 2008), recent gravity surveys reveal variations of only ± ∼6 mGal on Santa Cruz and ± ∼3 mGal on San Cristóbal's southern edifice (Cleary et al., in review), indicating that there are no dense cumulate bodies underlying either island.

Compositional Observations

It has been long recognized that the eastern and western Galápagos Archipelago define fundamentally different volcanic and petrologic provinces (McBirney and Williams, 1969). The compositional variation is summarized here by examining parameters governed by extent of lithospheric fractionation, depth of melt generation, and extent of melting.

Shallow Fractionation

Western volcanoes

Geist et al. (2014) used magnesium number (Mg# = molar [MgO/(MgO + FeO)]*100) as a metric to document the thermal conditions of the magma reservoirs supplying each of the young western shield volcanoes. Mg# is a strong function of the extent of olivine and pyroxene crystallization but is not affected by plagioclase accumulation, thereby providing an estimate of magmatic temperature; Geist et al. (2014) calculated that for every 3.6°C of cooling, Mg# decreases by 1. To characterize the extent of fractionation at each volcano, we use the methods of Geist et al. (2014), who produced Gaussian kernel density distributions (Rudge, 2008; Wessa, 2015) of Mg#. We interpret the maximum density (MD) for each volcano as an indicator of average extent of fractionation and the inter-quartile range (IR) as

a measure of temperature variation (**Figures 3**, **4A**). The western Galápagos shield volcanoes have Mg# MD values from a high of 56.3 ($n = 60$) at Cerro Azul to a low of 39.9 ($n = 22$) at Alcedo volcano, which has produced the most evolved magmas in the archipelago.

Geist et al. (2014) divided the western shields into two categories on the basis of their inter-quartile ranges (**Figures 3**, **4A**). "Monotonous" volcanoes include Fernandina, Wolf, and Darwin volcanoes. "Diverse" volcanoes, in contrast, erupt lavas with a greater range of temperatures and in the Geist et al. (2014) classification, included Cerro Azul, Alcedo, Sierra Negra, and Ecuador. On the basis of our analysis, which includes all published data from the western shields (**Figure 3**), Fernandina and Darwin volcanoes exhibit the least variation in Mg#, with an IR of 3.4. Wolf, Ecuador, and Sierra Negra volcanoes are close, extending to an IR of 5.1 for Sierra Negra. The real distinction comes for Cerro Azul and Alcedo, which exhibit considerably more variation than the other western shields, with IRs of 10.3 and 30.7. Thus, we suggest a minor adjustment to the Geist et al. (2014) classification; "Monotonous" volcanoes are Fernandina, Darwin, Wolf, Ecuador, and Sierra Negra, whereas only Cerro Azul and Alcedo are considered "Diverse," but of course there is likely a spectrum of compositional variation.

Eastern volcanoes

The average composition of every major eastern Galápagos volcano is significantly more primitive than any of the western shields (**Figures 3**, **4A**). Floreana, San Cristóbal, Española, and Santa Cruz all erupt lavas with relatively high Mg#s, with MDs from 63.2 ($n = 120$; Santa Cruz) to 70.0 ($n = 181$; Floreana). Santiago lavas yield an MD of 59.4 ($n = 60$) and Santa Fe's MD is 50.1 ($n = 10$), intermediate between typical eastern and western volcanic extents of fractionation. Rábida and Pinzón, both of which have produced silicic lavas comparable to those erupted by Alcedo volcano, have correspondingly low MD values of 35.0 ($n = 44$) and 38.0 ($n = 42$).

Furthermore, all the eastern volcanoes exhibit considerably greater variability in their major element compositions than is observed for the "monotonous" volcanoes of the western archipelago (**Figures 3**, **4A**). Floreana (5.9; $n = 181$), San Cristóbal (6.2; $n = 79$), and Española (6.2; $n = 57$) have the least variable Mg# signatures, but their IRs still exceed those of Sierra Negra (5.1; $n = 42$). Santiago has the greatest Mg# variability, with an IR of 21.4 ($n = 60$), between those of Cerro Azul and Alcedo.

Depth of Melt Generation

Western volcanoes

Variations in depth of melting can be examined using the Sm_n/Yb_n (the ratio of chondrite-normalized concentrations) of erupted basalts, owing to fractionation of the heavy rare-earth elements by garnet in an ascending melt column (e.g., Gibson and Geist, 2010). The depth of the garnet-spinel reaction depends on temperature and composition, but is between ~70 and 90 km for peridotite (Klemme and O'Neill, 2000). In their study of

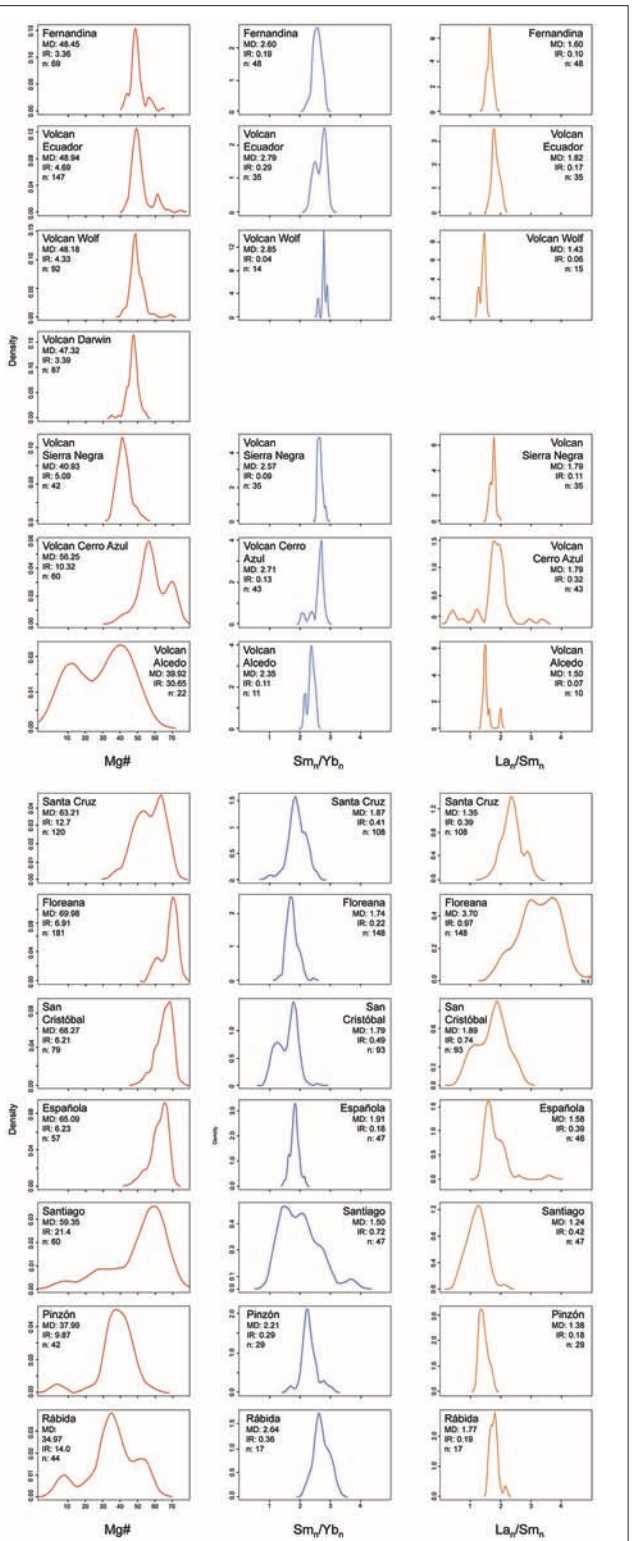

FIGURE 3 | Distributions of Mg#, Sm_n/Yb_n, and La_n/Sm_n variations across the western and eastern Galápagos volcanoes, displayed as probability density functions (generated using Gaussian kernel density estimations; MD, Maximum Density and IR, Interquartile Range). For the Sm_n/Yb_n, and La_n/Sm_n analyses, only samples within MgO > 4 wt.% were included;

(Continued)

FIGURE 3 | all available data were used for the Mg# analyses. Data sources are compilations of downloaded data from PetDB, representing only subaerial samples from the volcanoes, plus unpublished data (unpublished sources: Darwin Volcano data from T. Naumann, pers. comm., 2017; Española data from McGuire et al., 2015; Santa Cruz data from Wilson, 2013; San Cristóbal data from Mahr et al., 2016, and Pimentel et al., 2016). Smoothing bandwidths for Gaussian kernel density estimations were selected automatically using the Sheather and Jones (1991) method. For Mg#s, they range between 0.92 and 7.59 for the western volcanoes, and 0.94 and 2.75 for the eastern volcanoes. For Sm_n/Yb_n, smoothing bandwidths vary between 0.01 and 0.14 for the western volcanoes, and 0.04 and 0.22 for the eastern volcanoes. For La_n/Sm_n, western bandwidths are 0.02–0.10, and eastern values are 0.06–0.32. Slight disagreements between the IR and MD of the western shields from the Geist et al. (2014) calculations are the result of minor differences in the datasets that were used in the two studies. Rare earth element ratios are normalized to chondrite (McDonough and Sun, 1995).

lithospheric thickness beneath the Galápagos, Gibson and Geist (2010) showed that lithospheric thickness (H) can be predicted by the equation:

$$H = 46.57 * (\frac{Sm}{Yb})_n^{0.216}$$

and it ranges from 58 km at Fernandina to 46 km at San Cristobal.

Our synthesis (which includes more analyses from the eastern islands than that of Gibson and Geist, 2010) with MgO > 4% from the western shield volcanoes exhibit higher Sm_n/Yb_n than in the rest of the archipelago, with the lowest values occurring at Alcedo (2.35; $n = 11$) and the highest at Wolf Volcano (2.85; $n = 14$; **Figures 3**, **4B**). Inter-quartile ranges for Sm_n/Yb_n are quite low, indicating relatively little variability in melt generation conditions at each volcano (**Figures 3**, **4B**).

Eastern volcanoes

Most eastern Galápagos magmas have lower Sm_n/Yb_n values than is observed in the western archipelago, indicating shallower average depths of melt generation in the east. Only Rábida has an MD for Sm_n/Yb_n that falls within the range of the western shields (2.64; $n = 17$), and Pinzón's is close with an MD of 2.21 ($n = 29$). Otherwise, in the east, Santiago has the lowest MD of Sm_n/Yb_n (1.50; $n = 47$), whereas Santa Fe has the highest (1.98; $n = 3$; **Figures 3**, **4B**). Individual eastern volcanoes exhibit significantly more variation (IR) in Sm_n/Yb_n and consequently depth to the top of the melt column than is the case for the western shields, particularly the larger islands of Santa Cruz, San Cristóbal, Santa Fe, and Santiago (**Figures 3**, **4B**).

Extent of Melting

Any attempt to use simple incompatible trace element ratios (e.g., La_n/Sm_n) to document extent of melt generation in the archipelago must take into account the complexities imposed by the compositionally distinct mantle reservoirs that contribute to Galápagos magmas. When plotted on an archipelago-wide scale, ε_{Nd} correlates inversely with the lowest La_n/Sm_n from individual volcanoes (**Figure 5**; e.g., White et al., 1993). We attribute this correlation to mixing between mantle sources with different compositions, specifically a depleted mantle source (with low La_n/Sm_n and high ε_{Nd}) and 3 plume components (all with high La_n/Sm_n and low ε_{Nd}); mantle endmember variations in the Galápagos have been documented in numerous regional studies (e.g., White and Hofmann, 1978; Geist et al., 1988; Geist, 1992; White et al., 1993; Harpp and White, 2001). Magmas with higher La_n/Sm_n (those that lie to the higher La_n/Sm_n side of the ε_{Nd}-lowest La_n/Sm_n correlation line on **Figure 5**) then must therefore be the result of lower extents of melting of the mixed source. We define the parameter $\Delta La_n/Sm_n$ as the difference between a rock's measured La_n/Sm_n and the La_n/Sm_n value along the correlation line (**Figure 5**). The $\Delta La_n/Sm_n$ parameter, discussed below, reflects variations in degree of melting, taking into account different source compositions.

Western volcanoes

The average $\Delta La_n/Sm_n$ for western volcano basalts (MgO > 4.0 wt.%) varies from a high of 0.72 ($1\sigma = 0.12$) at Volcan Ecuador to 0.38 ($1\sigma = 0.08$) at Fernandina (**Figure 5**). The two compositionally "diverse" volcanoes, Cerro Azul and Alcedo (e.g., Geist et al., 2014), exhibit the greatest variability in $\Delta La_n/Sm_n$.

Eastern volcanoes

Values of $\Delta La_n/Sm_n$ at San Cristobal, Santa Cruz, Espanola, and Santa Fe are similar to those of the western shields, but Floreana lavas have a dramatically elevated average $\Delta La_n/Sm_n$ compared to the rest of the Galápagos volcanoes (**Figure 5**). Clearly, the $\Delta La_n/Sm_n$ metric may not completely compensate for the extreme incompatible trace element compositions at Floreana, which are attributed to an infusion of ancient recycled ocean crust (e.g., Harpp et al., 2014). Floreana volcano aside, the extent of melting as reflected in $\Delta La_n/Sm_n$ does not vary significantly between the western and eastern Galápagos provinces. In contrast, the *variability* in extent of melt generation is greater in the eastern Galápagos, with standard deviations that mostly exceed those at western volcanoes (**Figure 5**).

DISCUSSION

There is a striking dichotomy between eastern and western Galápagos volcanoes in terms of their age, eruptive flux, volcano morphology, and magma compositions. Two possibilities may explain this systematic difference: either the young lavas of the eastern archipelago overlie western-type volcanoes and are in a later stage of evolution, or the eastern volcanoes have always been different in most fundamental respects.

Three of the eastern volcanoes that have been studied in detail, Santa Cruz, Floreana, and San Cristóbal, have exposed lavas that erupted over 1 million years apart, and in the case of San Cristóbal, the duration of volcanism exceeds 2 million years (Bow, 1979; Geist et al., 1986; Bow and Geist, 1992; Harpp et al., 2014; Schwartz, 2014). Although the geochronological data are insufficient to document the eruptive flux (e.g., Kurz and Geist, 1999), the magmatic flux at all of the eastern islands has been many times smaller than that of the western volcanoes. At all three of the large eastern islands islands, no relationship has been found between the age of eruption and composition. None of these volcanoes is significantly incised by erosion in the arid Galápagos, thus older lavas with different compositions

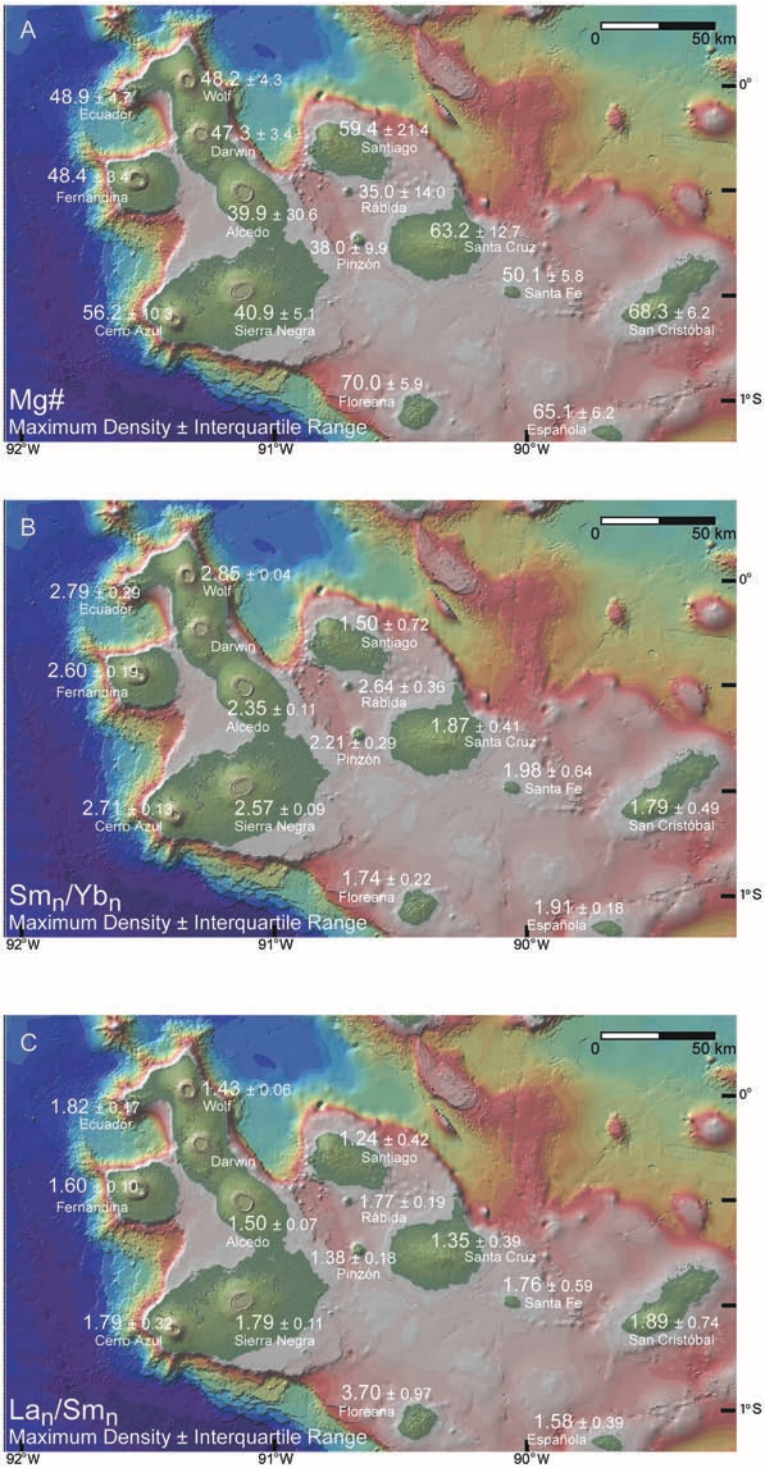

FIGURE 4 | Map views of geochemical and petrologic variations in Galápagos volcanoes (map courtesy of E. Mittelstaedt and Z. Cleary, pers. comm., 2017). MD, Maximum density; IR, Interquartile range; n, number of datapoints used in density calculations (see text for details). Data sources the same as in **Figure 3**. **(A)** Distribution of Mg# in Galápagos volcanoes. Mg# is used as a measure of magmatic temperature and extent of shallow fractionation. **(B)** Distribution of Sm_n/Yb_n variations in Galápagos volcanoes. Sm_n/Yb_n is used as a measure of depth of melting. **(C)** Distribution of La_n/Sm_n variations in Galápagos volcanoes. La_n/Sm_n is used as a measure of extent of melting (see text for details). Rare earth element ratios are normalized to chondrite (McDonough and Sun, 1995).

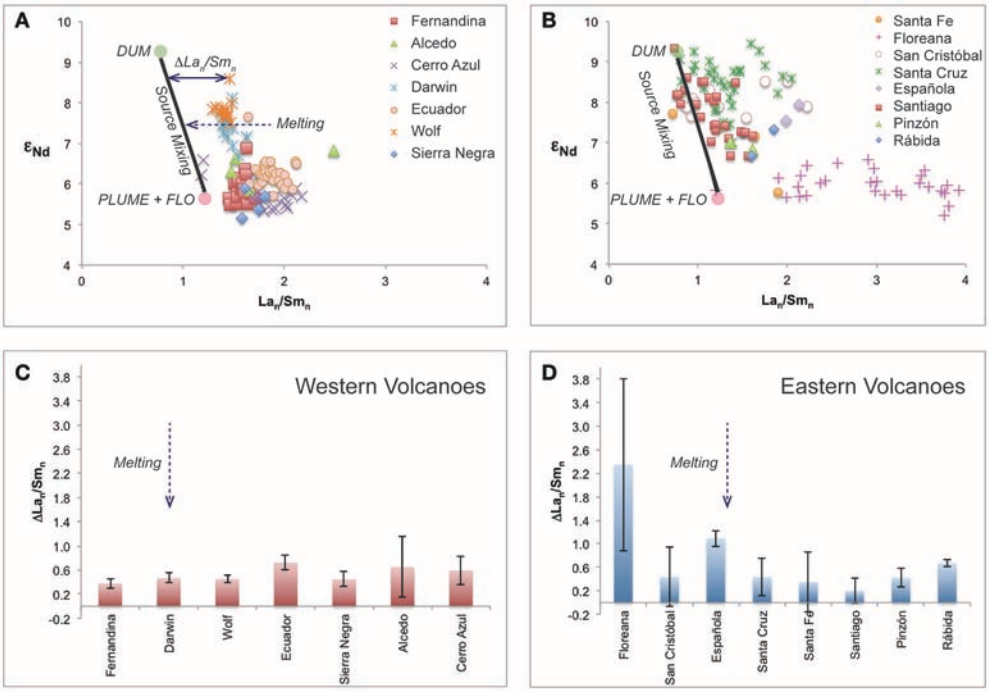

FIGURE 5 | (A) Distribution of ε_{Nd} and La_n/Sm_n in western Galápagos volcanoes. The solid line indicates the relationship between ε_{Nd} and the lowest La_n/Sm_n value across the archipelago. *DUM* is the composition of derived from the depleted upper mantle. PLUME and FLO are the compositions of magmas derived from mantle sources in the Galápagos plume, from Harpp and White (2001). **(B)** Distribution of ε_{Nd} and La_n/Sm_n in eastern Galápagos volcanoes; solid line as in **(A)**. **(C)** $\Delta La_n/Sm_n$ for western Galápagos volcanoes; a graphical representation of the calculation is shown as the double-headed arrow. $\Delta La_n/Sm_n$ is defined as the difference between a rock's measured La_n/Sm_n and the La_n/Sm_n value predicted by the line for the island's average ε_{Nd} shown in **(A)** and **(B)**. The $\Delta La_n/Sm_n$ parameter is interpreted as a measure of variation in extent of melting (as indicated by the dashed arrows), having taken into account different mantle source compositions. Error bars are $\pm 1\sigma$. **(D)** $\Delta La_n/Sm_n$ for eastern Galápagos volcanoes. Error bars are $\pm 1\sigma$. Numbers of samples used for each volcano are: Fernandina (20); Darwin (10); Wolf (13); Ecuador (29); Sierra Negra (4); Alcedo (4); Cerro Azul (19); Floreana (36); San Cristóbal (10); Española (2); Santa Cruz (33); Santiago (25); Pinzón (2); Rábida (2). Only lavas with both ε_{Nd} and La_n/Sm_n data were used in this analysis, from data sources listed in **Figure 3**.

could exist beneath the oldest sampled lavas. Nevertheless, the existing evidence is that the exposed lavas reflect the entire composition spectrum of each volcano. Also, as described below, geophysical observations indicate that the eastern volcanoes do not cap subsided western Galápagos edifices.

Implications of Physical Differences

Physical Structures

The expansive calderas topping the western shields are directly related to large, shallow magma reservoirs, which have been identified by both deformation and seismic studies (Amelung et al., 2000; Geist D. et al., 2006; Tepp et al., 2014). The calderas are multi-cyclical, owing to many episodes of collapse and partial refilling. The exact mechanism between magma evacuation and caldera formation is poorly understood; the only documented caldera collapse was related to a small but explosive eruption at Fernandina in 1969 (Simkin and Howard, 1970; Howard et al., in press). The existence of the calderas is also tied to the active historical record of eruptions at these volcanoes, indicating a strong magma flux.

Further support for robust, long-lived magma reservoirs beneath the western volcanoes comes from gravity studies. The ∼30 mGal Bouguer Anomaly gravity highs detected at Fernandina (Case et al., 1973) and Sierra Negra (Vigouroux et al., 2008) have been attributed to large bodies of dense cumulate bodies. These dense rocks are complements to the relatively evolved eruptive rocks, and development of crustal-wide cumulate bodies has been attributed to steady state magmatic reservoirs with high magma supplies, in order to achieve the conditions necessary to regulate crystallization prior to eruption (e.g., Geist et al., 2014).

Large magma flux, calderas, shallow magma chambers, and the lack of strong tectonic deviatoric stresses contribute to the characteristic morphology of the western Galápagos shields. Stresses imparted by the calderas and the steep slopes overwhelm tectonic influences, leading to nearly symmetrical shapes and the pattern of circumferential fissures near the summit and radial fissures on the lower and submarine flanks (**Figures 2A,C,E**; Chadwick and Howard, 1991; Chadwick and Dieterich, 1995; Geist et al., 2005; Chadwick et al., 2011; Bagnardi et al., 2013).

In marked contrast, the eastern volcanoes lack calderas (**Figures 2B,D**). According to modeling carried out on gravity data from San Cristóbal and Santa Cruz, the small Bouguer Anomaly gravity signals beneath the islands (±∼ 3 mGal on

San Cristóbal, ±∼ 6 mGal on Santa Cruz; Cleary et al., in review) eliminate the possibility of a significant cumulate body underlying the volcanoes. These signals cannot be explained by infilling of older calderas by lava flows (Cleary et al., in review). The authors conclude that neither San Cristóbal nor Santa Cruz ever hosted the long-lived shallow magma reservoir requisite for producing a caldera.

Furthermore, most of the eastern Galápagos volcanoes are elongate, dominated by linear fissures and faults, or have linear rift zones, in contrast to the more symmetrical structures of the western volcanoes. These observations suggest that the eastern volcanoes were supplied by a less robust magma flux. The consistently ∼E-W trending structures across the eastern archipelago also reflect formation in an environment of relatively strong, regional tectonic stress (e.g., Harpp and Geist, 2002; Harpp et al., 2003).

Petrologic Implications

Shallow Fractionation

Most of the western Galápagos volcanoes erupt monotonous suites of lava, with Mg# varying by only a few percent (**Figure 3**), indicating that the magmas erupted within a range of $<30^{\circ}$C over the history of the volcano; these are referred to as being in a "steady state" phase (Geist et al., 2014). Moreover, the eruptive lavas tend to be relatively strongly evolved, with Mg# <50. The evolved compositions and their limited variation are the result of thermochemical buffering by a crustal-wide mush column (Geist et al., 2014). The mush column is maintained in a steady state owing to a relatively high magma supply rate, which in turn is reflected by the high eruption rate. The magmas typically equilibrate with their phenocryst assemblage at shallow levels (Geist et al., 1998), consistent with the geophysical evidence of shallow subcaldera magma bodies.

Cerro Azul and Alcedo volcanoes are not in a steady state. Cerro Azul has both the most primitive and most diverse basalt compositions of any volcano in the west (**Figures 3**, **4**). This has been attributed to Cerro Azul being in a juvenile transient phase of magmatism at the leading edge of the hotspot; a crustal-scale mush column has yet to be assembled there. This interpretation is consistent with petrologic (Geist et al., 1998) and geophysical (Amelung et al., 2000) studies, which indicate that Cerro Azul's magma body is deeper than the others in the western Galápagos.

Alcedo is unique among the active western volcanoes because of its rhyolitic eruptions (Geist et al., 1994). Petrologic studies show that the rhyolites result from fractional crystallization within the mush column, which occurs because the volcano has been carried away from the hotspot (Geist et al., 1995). We note that Sierra Negra's magmas are also more evolved than the other western volcanoes (Reynolds and Geist, 1995); it is possible that its mush column is also cooling as it is being carried away from the hotspot, as Cerro Azul receives a progressively more robust magma supply with time.

In almost every compositional parameter, the eastern islands contrast with the western ones (**Figures 3**, **4**). The eastern lavas on the whole are much more primitive, and they have undergone a greater range of cooling and crystallization, as measured by the interquartile range of the Mg# (**Figures 3**, **4A**). This suggests that different batches of magma undergo independent ascent and cooling histories, and the extent of fractionation is more or less random. This idea is supported by the wide range in La_n/Sm_n and Sm_n/Yb_n, which precludes homogenization of distinct magma batches in a long-lived magma body (**Figures 3**, **4B,C**). Previous estimates of the depth of crystallization indicate that magmas supplying the eastern volcanoes undergo crystallization in the middle and deep crust, and only a few cool and crystallize in the shallow crust (Geist et al., 1998).

On the basis of their age (∼1 Ma), proximity, and the occurrence of rhyolites, trachytes, and dacites, we separate Santiago, Pinzón, and Rábida from the eastern province and define a new "intermediate" province. These three volcanoes have very large interquartile ranges of Mg# (**Figures 3**, **4A**), as one would expect from the existence of strongly evolved lavas. In many respects, their petrologic suites resemble that of Alcedo volcano, although the intermediate volcanoes are morphologically quite different from Alcedo. These observations indicate that although at 1 Ma the intermediate volcanoes erupted in a tectonic environment different than that of the present-day western Galápagos, and that the magma flux was likely different at the time, these volcanoes each had dying mush columns, from which evolved magmas were produced by extensive fractional crystallization (e.g., Geist et al., 2014).

Depth of Melt Generation

The western volcanoes have systematically higher Sm_n/Yb_n ratios than the eastern volcanoes, and the intermediate volcanoes have transitional values of Sm_n/Yb_n. This suggests a greater role for garnet beneath the western volcanoes, an idea that has been suggested previously in studies of both individual volcanoes (Geist et al., 1986, 2005; Harpp et al., 2014) and regional studies (White et al., 1993; Gibson and Geist, 2010). In turn, the garnet signature is equated to deeper melting, both due to hotter upwelling mantle and a thicker lithospheric lid (Villagómez et al., 2007, 2011; Gibson and Geist, 2010).

The parameterization of Gibson and Geist (2010) permits the conversion of Sm_n/Yb_n (**Figures 3**, **4B**) into an estimation of the depth to the top of the melting column (D_{top}); the deeper the top of the melting column, the greater the influence of garnet and the higher the Sm_n/Yb_n. The greatest D_{top} is 58 km at Volcan Wolf, despite being the western volcano closest to the GSC. The estimated top of the melting column then decreases in depth to the south and east, reaching 56–57 km at Alcedo and Sierra Negra volcanoes. The intermediate volcanoes do not show a southward gradient in D_{top}, but they have transitional values ranging from 51 km at Santiago to 57 km at Rábida. In contrast, the D_{top} estimates for the eastern islands are all shallower than the western volcanoes, from 51 km at San Cristóbal to 53 km at Santa Cruz.

The primary conclusion from the D_{top} comparison is that the melting regime has changed systematically over the past 3 million years in the Galápagos. Between 1 and 3 million years ago, the volcanoes that were most active were derived from relatively shallow melting, owing to a thinner lithospheric lid. The average depth of melting then deepened by 1.0–0.7 Ma, when the Intermediate volcanoes were most active, and it is deepest

with the currently active volcanoes in the western Galápagos (**Figure 4B**).

Extent of Melting

Average $\Delta La_n/Sm_n$, which we use as a measure of' the average extent of melting, does not correlate well with any other parameter considered in this paper, with a single exception. These parameters include island age, the estimated top of the melting column (D_{top}), and the morphology of the volcano. The exceptions are the southern volcanoes of the eastern province, Floreana, Española, and San Cristóbal, which all have substantially higher $\Delta La_n/Sm_n$ than the other volcanoes (**Figure 5**), indicating that they are constructed of magmas generated from lower extents of melting that is observed in the rest of the Galápagos. These volcanoes are all south of the central axis of the archipelago, furthest from the GSC. Notably, the southern volcanoes of the currently active western Galápagos (Cerro Azul and Sierra Negra) do not share this characteristic.

The variability in La_n/Sm_n (and $\Delta La_n/Sm_n$), as measured by the interquartile range (and standard deviation), differs between the eastern and western volcanoes. The western volcanoes vary relatively little (except Cerro Azul; **Figures 3**, **4C**, **5**), in contrast to the eastern volcanoes, which exhibit considerable ranges in La_n/Sm_n and $\Delta La_n/Sm_n$. As with most other parameters, the intermediate volcanoes are transitional in La_n/Sm_n. We attribute the widely different variations in extent of melting to be due to two factors. First, the variable compositions in the east may be due to melts being extracted from different parts of the melt column; basalts with high La_n/Sm_n originate from the deeper segments, where upwelling mantle is just beginning to melt, and basalts with lower La_n/Sm_n come from the more extensively melted upper parts of the melt column. Second, the compositionally diverse melts from the eastern volcanoes must never have been homogenized in a long-lived magmatic plumbing system.

To interpret melt generation systematics in the Galápagos, we must also consider the homogeneity of basalts from the western volcanoes. Do these melts all originate from the same part of a variably melted zone in the mantle, or are heterogeneous melts from different parts of the column homogenized in the lithospheric plumbing system prior to eruption? Melt inclusion data from Fernanandina suggest that heterogeneous melts are hybridized, because although the bulk-rocks have little compositional diversity, olivine-hosted melt inclusions exhibit a range of major element (Hedfield and Geist, 2003), trace element (Koleszar et al., 2009), and isotopic heterogeneity (Peterson et al., 2014).

Cerro Azul is the exceptional western volcano, with relatively large variation in La_n/Sm_n (**Figures 3**, **4C**, **5**). This observation is consistent with the relatively large variation in Mg# (**Figures 3**, **4A**) at Cerro Azul and the geophysical observation that it lacks a shallow subcaldera magma reservoir (e.g., Amelung et al., 2000; Geist et al., 2014). Because it is still in a juvenile, developing phase, and because it lacks a well-connected crustal-scale mush column, heterogeneity is preserved as the melts ascend (e.g., Geist et al., 2014).

A Non-evolutionary Model for Galápagos Volcanism

On the basis of major element systematics and petrologic observations exclusively from the western Galápagos shields (see Geist et al., 2014, and references therein), Geist et al. (2014) constructed a three-stage evolutionary model for Galápagos volcanoes:

1. The Juvenile Transient Phase: As volcanoes begin to grow at the leading edge of the hotspot, batches of hot, relatively primitive magma undergo cooling and crystallization throughout the crust. On average, magma reservoirs are relatively small, hot, isolated, and deep, as the volcano's plumbing system begins to be established by a waxing magma supply. Geist et al. (2014) place Cerro Azul (Naumann and Geist, 2000) and Ecuador Volcanoes (Geist et al., 2002) in this stage (in this work, it is clear however that Ecuador belongs in the Mature Steady State Phase, below, owing to its lack of petrologic and geochemical variability). The crust thickens from ∼8 to ∼15 km in this phase (Feighner and Richards, 1994).
2. The Mature Steady State Phase: As magma supply increases, individual reservoirs coalesce into a several kilometer-thick mush zone, permitting a compositional and thermal steady state to be established. Within the plumbing system, magmas experience partial crystallization, maintaining a sill 1–3 km beneath the caldera surface with a temperature of ∼1,150°C. Consequently, erupted lavas are moderately evolved and relatively homogeneous compared to other constructional phases. Fernandina (Allan and Simkin, 2000), Wolf (Geist et al., 2005), and Darwin Volcanoes (Naumann, pers. comm., 2017) are currently in this stage, according to Geist et al. (2014). This stage thickens the crust to ∼18 km (Feighner and Richards, 1994).
3. The Dying Cooling Phase: Once carried away from the plume center, a volcano's magma supply wanes, causing the reservoir to cool below 1050°C, crystallize further, and erupt cooler lavas. Variable but significant amounts of crystallization result in a wide range of erupted compositions, extending in some cases (i.e., Alcedo) all the way to rhyolite (Geist et al., 1995). Geist et al. (2014) put Alcedo and Sierra Negra in this waning stage.

The Geist et al. (2014) evolutionary model for the Galápagos is primarily a function of the available magma flux, with the extent of shallow fractionation increasing with the age of the volcano. This evolutionary model bears broad resemblance to mechanisms proposed to explain geochemical and petrologic variations in the Hawaiian Islands. Lavas erupted during the shield-building phases are tholeiitic and exhibit little compositional variation, whereas post-shield lavas are the result of significant differentiation as the magma supply wanes (Macdonald et al., 1983; Clague and Dalrymple, 1987, 1988; Walker, 1990; Stolper et al., 2004). Increased extents of differentiation during the youngest waning phase of volcanism is a common theme at other ocean island volcanoes as well, including La Palma in the Canary Islands (Klügel et al., 2017).

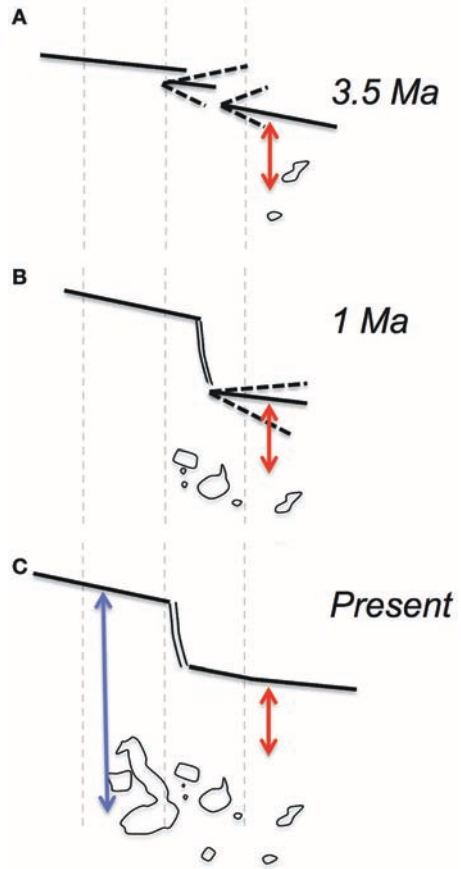

FIGURE 6 | Evolution of the Galápagos hotspot-GSC system since 3.5 Ma, after Mittelstaedt et al. (2012). Note that the coastlines of the volcanoes are drawn as they appear today and do not reflect older shapes of the islands. **(A)** At the time of the formation of San Cristóbal and Espanola, the distance between the plume and the GSC was <100 km, indicated by the red arrow, which is included for each of the time intervals for reference. **(B)** By 1 Ma, the GSC had drifted more than 100 km north, away from the Galápagos plume, but the eastern segment jumped south, creating the incipient transform at 90.5° W. Thus, at the time that Santiago, Rábida, and Pinzón were directly over the plume, the eastern segment of the GSC was close, but the western segment was >200 km away. **(C)** The blue arrow indicates the current distance from the seismically imaged plume and the GSC.

We hypothesize that the eastern volcanoes have undergone little evolution since they emerged on pre-existing oceanic lithosphere above the hotspot; they have always erupted more primitive and compositionally heterogeneous basalts from tectonically controlled edifices. This implies a discrete shift in the fundamental set of conditions responsible for volcano formation between 1 Ma and the present (**Figure 6**). The most obvious differences were that the GSC was closer to the plume at 3 Ma than it is today, and the long transform fault at 90.5°W was opening due to northward motion of the GSC relative to the plume and 2 discrete southward jumps of the GSC (Wilson and Hey, 1995; Mittelstaedt et al., 2012).

The proximity of the GSC to the plume from 1 to 3 Ma is consistent with the strong tectonic controls during constructional volcanism in the eastern Galápagos. In fact, the elongation of the volcanoes and the volcanic lineaments and fault orientations in the eastern Galápagos are in many ways comparable to similar structures in the present near-ridge Northern Galápagos Province (Harpp et al., 2014). For example, the structure of San Cristóbal is subparallel to Genovesa Ridge (the submarine fissure system that extends to the east of the island), which has been attributed to the stresses around the outside corner of a ridge-transform intersection (Harpp and Geist, 2002; Harpp et al., 2003). The E-W to WNW structures that control the morphologies of Santiago, Santa Cruz, Santa Fe, and Española islands are comparable to ridge-parallel fault patterns in the Northern Galápagos Province (Mittelstaedt et al., 2012).

Our interpretation is that the eastern volcanoes result from low magma fluxes relative to their western counterparts. Lower magma productivity accounts for the absence of a crustal mush column, which buffers the compositions of the magmas and produces a compositionally homogeneous product in the western volcanoes. It also accounts for the absence of hidden calderas in the eastern archipelago. The lower magma productivity, however, is at odds with the interpretation that the top of the melting column was shallower beneath the eastern and intermediate volcanoes from 1 to 3 Ma than it is beneath the western volcanoes (**Figure 4B**). This explanation is paradoxical; most models of near-ridge volcanism predict greater productivity with a shallower lithospheric lid (e.g., Regelous et al., 2003). One possible resolution is that the Galápagos plume has become more robust over the past million years, developing a greater magma flux despite the thicker lithospheric lid. This is a challenging hypothesis to test, although it may be reasonable given both long- and short-term evidence for large variations in the flux of the Hawaiian plume (e.g., Wessel, 2015). Another possibility is that the proximal GSC siphons magma from the hotspot province, for example through melt-rich channels between the plume and ridge (Mittal and Richards, 2017).

CONCLUSIONS

The Galápagos Archipelago underwent a distinct change in volcano morphology and magma compositions ∼1 Ma, which resulted from an evolving tectonic regime, emplacement onto thicker lithosphere, and waxing magmatic flux. The eastern volcanoes were emplaced in a near-ridge environment with a lower magma supply rate. The eastern volcanoes never had large calderas like the present-day western islands and had relatively magma-starved, ephemeral magmatic plumbing systems, leading to the eruption of more primitive magmas with large differences in incompatible trace-element compositions. Regional-scale tectonic stresses caused magma to be directed along strongly oriented fissures, and the volcanoes underwent faulting.

At about 1 Ma, when the intermediate islands of Pinzón, Rábida, and Santiago were forming over the hotspot, the tectonic setting was changing. The principal difference is that the separation between the plume and the GSC increased, owing

to the northward motion of the GSC (Wilson and Hey, 1995; Mittelstaedt et al., 2012). Notably, the distance between the ridge and the still-active eastern volcanoes did not increase appreciably (**Figure 6**), owing to southward jumps of the eastern GSC and the formation of the large transform at 90.5°W. The lithosphere is thicker beneath the central islands, and the erupted magmas had largely been homogenized in the magmatic plumbing systems. Santiago, which was closer to the ridge during its peak activity, had strong tectonic controls on its morphology. Bodies of mush were of consequential size, so when the volcanoes were carried off the hotspot and the mush columns cooled and crystallized, and dacites, trachytes, and rhyolites formed.

For the past 0.5 Ma, the western Galápagos volcanoes have been forming farther from the GSC than any other active volcano in the province for at least the past 5 million years. Thus, they are being built on relatively thick lithosphere, and a greater fraction of the melt being created by the Galápagos plume is being fed to the Galápagos Archipelago and less to the GSC. Consequently, after an initial phase of volcano growth, the magmatic plumbing systems are dominated by a crustal scale mush column, which homogenizes and thermally and chemically buffers the magma composition. The robust magma supply and relatively small influence of regional tectonic stresses lead to nearly radially symmetric volcanoes topped by large calderas, owing to the presence of a well-developed shallow magma chamber. As these volcanoes are carried off the hotspot, the mush column cools and solidifies, producing highly evolved melts.

This view of the development of Galápagos volcanoes is very different than that at Hawaii, where the prevailing theory is that there is a consistent evolutionary trend. This results in similar stratigraphy from island to island, which in turn is dictated by common changes in eruption style and magma compositions. Because of the constantly changing tectonic environment, Galápagos volcanoes have followed disparate lineages from different precursors, analogous to phylogenic lineages from separate nodes. The eastern volcanoes form one evolutionary lineage, driven by proximity of the GSC and relatively low magmatic supply rates. The intermediate volcanoes formed at a time when the GSC was transitioning from a proximal to a distal setting relative to the plume. The currently most active western shield volcanoes are forming farthest from the GSC and have a magma supply that has been unprecedented in the past 5 million years.

AUTHOR CONTRIBUTIONS

KH conceived of the idea of this paper, designed some of the analysis, performed the calculations, and organized its structure; DG wrote several of the sections, designed some of the analysis, and contributed to the discussion section.

ACKNOWLEDGMENTS

KH would like to acknowledge support from National Science Foundation grant EAR 1347731. DG's effort is based upon work while serving at the National Science Foundation and funded by NSF grant EAR-1145271. Special thanks to important contributions from University of Idaho graduate students Darin Schwartz and Emily Wilson, and Colgate undergraduates Rita Van Kirk, Maggie McGuire, Kevin Varga, Jake Mahr, Regina Pimentel, Hannah Bercovici. We also thank Marco Córdova Aguilar and Marco Almeida, volcanology students from the Instituto Geofisico de Quito for their efforts in the field. We extend our gratitude for the generous assistance and permission from the Galápagos National Park and the Charles Darwin Research Station. Captain Lenin Cruz and the R/V Pirata provided invaluable support in the field. We would like to thank the reviewers, Tim Druitt, Connie Class, Andreas Klugel, and Alessandro Tibaldi, for their thoughtful comments on an earlier draft, and Ricardo Ramalho for inviting us to contribute to this research topic and his editorial prowess.

REFERENCES

Allan, J. F., and Simkin, T. (2000). Fernandina volcano's evolved, well-mixed basalts: Mineralogical and petrological constraints on the nature of the Galápagos plume. *J. Geophys. Res. Solid Earth* 105, 6017–6041. doi: 10.1029/1999JB900417

Amelung, F., Jónsson, S., Zebker, H., and Segall, P. (2000). Widespread uplift and 'trapdoor' faulting on Galápagos volcanoes observed with radar interferometry. *Nature* 407, 993–996. doi: 10.1038/35039604

Argus, D. F., Gordon, R. G., and DeMets, C. (2011). Geologically current motion of 56 plates relative to the no-net-rotation reference frame. *Geochem. Geophys. Geosyst.* 12:Q11001. doi: 10.1029/2011GC003751

Bagnardi, M., and Amelung, F. (2012). Space-geodetic evidence for multiple magma reservoirs and subvolcanic lateral intrusions at Fernandina volcano, Galápagos Islands. *J. Geophys. Res. Solid Earth* 117:B10406. doi: 10.1029/2012JB009465

Bagnardi, M., Amelung, F., and Poland, M. P. (2013). A new model for the growth of basaltic shields based on deformation of Fernandina volcano, Galápagos Islands. *Earth Planet. Sci. Lett.* 377, 358–366. doi: 10.1016/j.epsl.2013.07.016

Baitis, H. W., and Lindstrom, M. M. (1980). Geology, petrography, and petrology of Pinzón Island, Galápagos archipelago. *Contr. Mineral. Petrol.* 72, 367–386. doi: 10.1007/BF00371345

Bercovici, H., Geist, D., Harpp, K. S., and Almeida, M. (2015). "Evidence for a dying magma chamber at Rábida Island," in *AGU Fall Meeting Abstracts*.

Bercovici, H., Geist, D., Harpp, K. S., Almeida, M., Mahr, J., Pimentel, R., et al. (2016). "A little island with a big secret: Isla Rábida, Galápagos," in *AGU Fall Meeting Abstracts*.

Bow, C. S. (1979). *Geology and Petrogeneses of the Lavas of Floreana and Santa Cruz Islands: Galápagos Archipelago*. Eugene, OR: Oregon University.

Bow, C. S., and Geist, D. J. (1992). Geology and petrology of Floreana island, Galápagos archipelago, Ecuador. *J. Volcanol. Geother. Res.* 52, 83–105. doi: 10.1016/0377-0273(92)90134-Y

Case, J. E., Ryland, S. L., Simkin, T., and Howard, K. A. (1973). Gravitational evidence for a low-density mass beneath the Galápagos Islands. *Science* 181, 1040–1042. doi: 10.1126/science.181.4104.1040

Chadwick, W. W., and Dieterich, J. H. (1995). Mechanical modeling of circumferential and radial dike intrusion on Galápagos volcanoes. *J. Volcanol. Geother. Res.* 66, 37–52. doi: 10.1016/0377-0273(94)00060-T

Chadwick, W. W., Geist, D. J., Jónsson, S., Poland, M., Johnson, D. J., and Meertens, C. M. (2006). A volcano bursting at the seams: inflation, faulting,

and eruption at Sierra Negra Volcano, Galápagos. *Geology* 34, 1025–1028. doi: 10.1130/G22826A.1

Chadwick, W. W., and Howard, K. A. (1991). The pattern of circumferential and radial eruptive fissures on the volcanoes of Fernandina and Isabela islands, Galápagos. *Bull. Volcanol.* 53, 259–275. doi: 10.1007/BF00414523

Chadwick, W. W., Jónsson, S., Geist, D. J., Poland, M., Johnson, D. J., Batt, S., et al. (2011). The May 2005 eruption of Fernandina volcano, Galápagos: the first circumferential dike intrusion observed by GPS and InSAR. *Bull. Volcanol.* 73, 679–697. doi: 10.1007/s00445-010-0433-0

Chen, C. Y., and Frey, F. A. (1983). Origin of Hawaiian tholeiite and alkalic basalt. *Nature* 302, 785–789. doi: 10.1038/302785a0

Clague, D. A., and Dalrymple, G. B. (1987). The Hawaiian-Emperor volcanic chain. part I. Geologic evolution. *Volcanism Hawaii* 1, 5–54.

Clague, D. A., and Dalrymple, G. B. (1988). Age and petrology of alkalic postshield and rejuvenated-stage lava from Kauai, Hawaii. *Contr. Mineral. Petrol.* 99, 202–218. doi: 10.1007/BF00371461

Corbi, F., Rivalta, E., Pinel, V., Maccaferri, F., Bagnardi, M., and Acocella, V. (2015). How caldera collapse shapes the shallow emplacement and transfer of magma in active volcanoes. *Earth Planet. Sci. Lett.* 431, 287–293. doi: 10.1016/j.epsl.2015.09.028

Feighner, M. A., and Richards, M. A. (1994). Lithospheric structure and compensation mechanisms of the Galápagos Archipelago. *J. Geophys. Res.* 99, 6711–6729. doi: 10.1029/93JB03360

Flinders, A. F., Ito, G., Garcia, M. O., Sinton, J. M., Kauahikaua, J., and Taylor, B. (2013). Intrusive dike complexes, cumulate cores, and the extrusive growth of Hawaiian volcanoes. *Geophys. Res. Lett.* 40, 3367–3373. doi: 10.1002/grl.50633

Geist, D. J. (1992). An appraisal of melting processes and the Galápagos hotspot: major-and trace-element evidence. *J. Volcanol. Geotherm. Res.* 52, 65–82. doi: 10.1016/0377-0273(92)90133-X

Geist, D., Chadwick, W., and Johnson, D. (2006). Results from new GPS and gravity monitoring networks at Fernandina and Sierra Negra Volcanoes, Galápagos, 2000–2002. *J. Volcanol. Geother. Res.* 150, 79–97. doi: 10.1016/j.jvolgeores.2005.07.003

Geist, D., Diefenbach, B. A., Fornari, D. J., Kurz, M. D., Harpp, K., and Blusztajn, J. (2008). Construction of the Galápagos platform by large submarine volcanic terraces. *Geochem. Geophys. Geosyst.* 9:Q03015. doi: 10.1029/2007GC001795

Geist, D., Howard, K. A., Jellinek, A. M., and Rayder, S. (1994). The volcanic history of Volcán Alcedo, Galápagos Archipelago: a case study of rhyolitic oceanic volcanism. *Bull. Volcanol.* 56, 243–260. doi: 10.1007/BF00302078

Geist, D., Howard, K. A., and Larson, P. (1995). The generation of oceanic rhyolites by crystal fractionation: the basalt-rhyolite association at Volcan Alcedo, Galápagos Archipelago. *J. Petrol.* 36, 965–982. doi: 10.1093/petrology/36.4.965

Geist, D. J., McBirney, A. R., and Duncan, R. A. (1986). Geology and petrogenesis of lavas from San Cristóbal Island, Galápagos archipelago. *Geol. Soc. Am. Bull.* 97, 555–566. doi: 10.1130/0016-7606(1986)97<555:GAPOLF>2.0.CO;2

Geist, D. J., Bergantz, G., and Chadwick, W. W. (2014), "Galapagos magma chambers," in *The Galápagos: A Natural Laboratory for the Earth Sciences*, Vol. 204, eds K. S. Harpp, E. Mittelstaedt, N. d'Ozouville, and D. W. Graham (Hoboken, NJ: John Wiley & Sons, Inc.), 55. doi: 10.1002/9781118852538.ch5

Geist, D. J., Fornari, D. J., Kurz, M. D., Harpp, K. S., Adam Soule, S., Perfit, M. R., et al. (2006). Submarine Fernandina: magmatism at the leading edge of the Galápagos hot spot. *Geochem. Geophys. Geosyst.* 7:Q12007. doi: 10.1029/2006GC001290

Geist, D. J., Harpp, K. S., Naumann, T. R., Poland, M., Chadwick, W. W., Hall, M., et al. (2008). The 2005 eruption of Sierra Negra volcano, Galápagos, Ecuador. *Bull. Volcanol.* 70, 655–673. doi: 10.1007/s00445-007-0160-3

Geist, D. J., McBirney, A. R., and Duncan, R. A. (1985). Geology of Santa Fe island: the oldest Galápagos volcano. *J. Volcanol. Geother. Res.* 26, 203–212. doi: 10.1016/0377-0273(85)90056-3

Geist, D. J., Naumann, T. R., Standish, J. J., Kurz, M. D., Harpp, K. S., White, W. M., et al. (2005). Wolf volcano, Galápagos archipelago: melting and magmatic evolution at the margins of a mantle plume. *J. Petrol.* 46, 2197–2224. doi: 10.1093/petrology/egi052

Geist, D. J., White, W. M., and McBirney, A. R. (1988). Plume-asthenosphere mixing beneath the Galápagos Archipelago. *Nature* 333, 657–660. doi: 10.1038/333657a0

Geist, D., Naumann, T., and Larson, P. (1998). Evolution of Galápagos magmas: Mantle and crustal fractionation without assimilation. *J. Petrol.* 39, 953–971. doi: 10.1093/petroj/39.5.953

Geist, D., White, W. M., Albarede, F., Harpp, K., Reynolds, R., Blichert-Toft, J., et al. (2002). Volcanic evolution in the Galápagos: the dissected shield of Volcan Ecuador. *Geochem. Geophys. Geosyst.* 3:1061. doi: 10.1029/2002GC000355

Gibson, S. A., and Geist, D. (2010). Geochemical and geophysical estimates of lithospheric thickness variation beneath Galápagos. *Earth Planet. Sci. Lett.* 300, 275–286. doi: 10.1016/j.epsl.2010.10.002

Gibson, S. A., Geist, D. G., Day, J. A., and Dale, C. W. (2012). Short wavelength heterogeneity in the Galápagos plume: evidence from compositionally diverse basalts on Isla Santiago. *Geochem. Geophys. Geosyst.* 13:Q09007. doi: 10.1029/2012GC004244

Hall, M. L. (1983). Origin of espanola island and the age of terrestrial life on the Galápagos islands. *Science* 221, 545–547. doi: 10.1126/science.221.4610.545

Harpp, K., and Geist, D. (2002). Wolf–Darwin lineament and plume–ridge interaction in northern Galápagos. *Geochem. Geophys. Geosyst.* 3, 1–19. doi: 10.1029/2002GC000370

Harpp, K. S., Fornari, D. J., Geist, D. J., and Kurz, M. D. (2003). Genovesa submarine ridge: a manifestation of plume-ridge interaction in the Northern Galápagos Islands. *Geochem. Geophys. Geosyst.* 4:8511. doi: 10.1029/2003GC000531

Harpp, K., Geist, D., Koleszar, A. M., Christensen, B., Lyons, J., Sabga, M., et al. (2014). "The geology and geochemistry of Isla Floreana, Galápagos: a different type of late-stage ocean island volcanism," in *The Galápagos: A Natural Laboratory for the Earth Sciences*, Geophysical Monograph 204, eds K. S. Harpp, E. Mittelstaedt, N. d'Ozouville, and D. W. Graham (Washington, DC: American Geophysical Union), 71–117.

Harpp, K. S., and White, W. M. (2001). Tracing a mantle plume: isotopic and trace element variations of Galápagos seamounts. *Geochem. Geophys. Geosyst.* 2:2000GC000137. doi: 10.1029/2000GC000137

Hedfield, E. J., and Geist, D. J. (2003). "Insight into the magmatic evolution of Fernandina Volcano, Galápagos, from olivine-and plagioclase-hosted melt inclusions," in *AGU Fall Meeting Abstracts* (San Francisco, CA).

Howard, K., Simkin, T., Geist, D., Merlen, G., and Nolf, B. (in press). Large hydromagmatic eruption related to Fernandina Volcano's 1968 caldera collapse–deposits, landforms, and ecosystem recovery. *Geol. Soc. Am. Spec. Pap.*

Kinoshita, W. T. (1965). A gravity survey of the island of Hawai'i. *Pac. Sci.* 19, 339–340.

Klemme, S., and O'Neill, H. S. (2000). The near-solidus transition from garnet lherzolite to spinel lherzolite. *Contr. Mineral. Petrol.* 138, 237–248. doi: 10.1007/s004100050560

Klügel, A., Galipp, K., Hoernle, K., Hauff, F., and Groom, S. (2017). Geochemical and volcanological evolution of La Palma, Canary Islands. *J. Petrol.* 58, 1227–1248. doi: 10.1093/petrology/egx052

Koleszar, A. M., Saal, A. E., Hauri, E. H., Nagle, A. N., Liang, Y., and Kurz, M. D. (2009). The volatile contents of the Galápagos plume; evidence for H 2 O and F open system behavior in melt inclusions. *Earth Planet. Sci. Lett.* 287, 442–452. doi: 10.1016/j.epsl.2009.08.029

Kurz, M. D., and Geist, D. (1999). Dynamics of the Galápagos hotspot from helium isotope geochemistry. *Geochim. Cosmochim. Acta* 63, 4139–4156. doi: 10.1016/S0016-7037(99)00314-2

Kurz, M. D., Rowland, S., Curtice, J., Saal, A., and Naumann, T. (2014). "Eruption rates for Fernandina volcano: a new chronology at the Galápagos hotspot center," in *The Galaápagos: A Natural Laboratory for the Earth Sciences*, Geophysical Monograph 204, eds K. S. Harpp, E. Mittelstaedt, N. dâ'Ozouville, and D. W. Graham (Washington, DC: American Geophysical Union), 41–54.

Lyons, J., Geist, D., Harpp, K., Diefenbach, B., Olin, P., and Vervoort, J. (2007). Crustal growth by magmatic overplating in the Galápagos. *Geology* 35, 511–514. doi: 10.1130/G23044A.1

Macdonald, G. A., Abbott, A. T., and Peterson, F. L. (1983). *Volcanoes in the Sea: The Geology of Hawaii*. Honolulu, HI: University of Hawaii Press.

Mahr, J., Harpp, K. S., Kurz, M. D., Geist, D., Bercovici, H., Pimentel, R., et al. (2016). "Rejuvenescent volcanism on San Cristóbal island, Galápagos: a late "plumer"," in *AGU Fall Meeting Abstracts* (San Francisco, CA).

McBirney, A. R., and Williams, H. (1969). Geology and petrology of the Galápagos Islands. *Geol. Soc. Am. Memoirs* 118, 1–197. doi: 10.1130/MEM118-p1

McDonough, W. F., and Sun, S. S. (1995). The composition of the Earth. *Chem. Geol.* 120, 223–253. doi: 10.1016/0009-2541(94)00140-4

McGuire, M., Varga, K. C., Harpp, K. S., Geist, D., and Hall, M. L. (2015). "Volcanic evolution in the Galápagos: the geochemistry and petrology of Espanola island," in *AGU Fall Meeting Abstracts* (San Francisco, CA).

Mittal, T., and Richards, M. A. (2017). Plume-ridge interaction via melt channelization at Galápagos and other near-ridge hotspot provinces. *Geochem. Geophys. Geosyst.* 18, 1711–1738. doi: 10.1002/2016GC006454

Mittelstaedt, E., Soule, S., Harpp, K., Fornari, D., McKee, C., Tivey, M., et al. (2012). Multiple expressions of plume-ridge interaction in the Galápagos: volcanic lineaments and ridge jumps. *Geochem. Geophys. Geosyst.* 13:Q05018. doi: 10.1029/2012GC004093

Munro, D. C., and Rowland, S. K. (1996). Caldera morphology in the western Galápagos and implications for volcano eruptive behavior and mechanisms of caldera formation. *J. Volcanol. Geother. Res.* 72, 85–100. doi: 10.1016/0377-0273(95)00076-3

Naumann, T., and Geist, D. (2000). Physical volcanology and structural development of Cerro Azul Volcano, Isabela Island, Galápagos: implications for the development of Galápagos-type shield volcanoes. *Bull. Volcanol.* 61, 497–514. doi: 10.1007/s004450050001

Peterson, M. E., Saal, A. E., Nakamura, E., Kitagawa, H., Kurz, M. D., and Koleszar, A. M. (2014). Origin of the 'ghost plagioclase'signature in Galápagos melt inclusions: new evidence from Pb Isotopes. *J. Petrol.* 55, 2193–2216. doi: 10.1093/petrology/egu054

Pimentel, R., Harpp, K. S., Geist, D., Bercovici, H., Mahr, J., Cleary, Z., et al. (2016). "Are you there plume? It's me, San Cristóbal: geochemical evolution of a Galápagos Island," in *AGU Fall Meeting Abstracts* (San Francisco, CA).

Poland, M., (2014). "Contrasting volcanism in Hawai'i and the Galápagos," in *The Galápagos: A Natural Laboratory for the Earth Sciences*, Geophysical Monograph 204, eds K. S. Harpp, E. Mittelstaedt, N. d'Ozouville, and D. W. Graham (Washington, DC: American Geophysical Union), 5–26.

Regelous, M., Hofmann, A. W., Abouchami, W., and Galer, S. J. G. (2003). Geochemistry of lavas from the Emperor Seamounts, and the geochemical evolution of Hawaiian magmatism from 85 to 42 Ma. *J. Petrol.* 44, 113–140. doi: 10.1093/petrology/44.1.113

Reynolds, R. W., and Geist, D. J. (1995). Petrology of lavas from sierra negra volcano, isabela island, Galápagos archipelago. *J. Geophys. Res. Solid Earth* 100, 24537–24553. doi: 10.1029/95JB02809

Reynolds, R. W., Geist, D., and Kurz, M. D. (1995). Physical volcanology and structural development of Sierra Negra volcano, Isabela island, Galápagos archipelago. *Geol. Soc. Am. Bull.* 107, 1398–1410. doi: 10.1130/0016-7606(1995)107<1398:PVASDO>2.3.CO;2

Rowland, S. K. (1996). Slopes, lava flow volumes, and vent distributions on Volcan Fernandina, Galápagos Islands. *J. Geophys. Res. Solid Earth* 101, 27657–27672. doi: 10.1029/96JB02649

Rudge, J. F. (2008). Finding peaks in geochemical distributions: a re-examination of the helium-continental crust correlation. *Earth Planet. Sci. Lett.* 274, 179–188. doi: 10.1016/j.epsl.2008.07.021

Ryan, W. B., Carbotte, S. M., Coplan, J. O., O'Hara, S., Melkonian, A., Arko, R., et al. (2009). Global multi-resolution topography synthesis. *Geochem. Geophys. Geosyst.* 10:Q03014. doi: 10.1029/2008GC002332

Ryland, S. L. (1971). *A Gravity and Magnetic Study of the Galápagos Islands.* Doctoral dissertation, University of Missouri–Columbia.

Schwartz, D. (2014). *Volcanic, Structural, and Morphological History of Santa Cruz Island, Galápagos Archipelago*. Master's thesis, Moscow, University of Idaho.

Schwartz, D. M., Wanless, V. D., Berg, R., Jones, M., Fornari, D. J., Soule, S. A., et al. (2017). Petrogenesis of alkalic seamounts on the Galápagos Platform. *Deep Sea Res. Part II Topical Stud. Oceanogr.* doi: 10.1016/j.dsr2.2017.09.019

Sheather, S. J., and Jones, M. C. (1991). A reliable data-based bandwidth selection method for kernel density estimation. *J. R. Statist. Soc. B*, 53, 683–690.

Siebert, L., Simkin, P., and Kimberly, P. (2011). *Volcanoes of the World, 3rd Edn*. Berkeley, CA: University of California Press.

Simkin, T., Shagam, R., Hargraves, R. B., Morgan, W. J., Van Houton, F. B., Burk, C. A., et al. (1973). Origin of some flat-topped volcanoes and guyots. *Geol. Soc. America Mem.* 132, 183–194.

Simkin, T., and Howard, K. A. (1970). Caldera collapse in the Galápagos Islands, 1968. *Science* 169, 429–437.

Standish, J., Geist, D., Harpp, K., and Kurz, M. D. (1998). The emergence of a Galápagos shield volcano, Roca Redonda. *Contr. Mineral. Petrol.* 133, 136–148. doi: 10.1007/s004100050443

Stolper, E., Sherman, S., Garcia, M., Baker, M., and Seaman, C. (2004). Glass in the submarine section of the HSDP2 drill core, Hilo, Hawaii. *Geochem. Geophys. Geosyst.* 5:Q07G15. doi: 10.1029/2003GC000553

Swanson, F. J., Baitis, H. W., Lexa, J., and Dymond, J. (1974). Geology of Santiago, Rábida, and Pinzón Islands, Galápagos. *Geol. Soc. Am. Bull.* 85, 1803–1810. doi: 10.1130/0016-7606(1974)85<1803:GOSRAP>2.0.CO;2

Teasdale, R., Geist, D., Kurz, M., and Harpp, K. (2005). 1998 Eruption at Volcán Cerro Azul, Galápagos islands: I. Syn-Eruptive petrogenesis. *Bull. Volcanol.* 67, 170–185. doi: 10.1007/s00445-004-0371-9

Tepp, G., Ebinger, C. J., Ruiz, M., and Belachew, M. (2014). Imaging rapidly deforming ocean island volcanoes in the western Galápagos archipelago, Ecuador. *J. Geophys. Res. Solid Earth* 119, 442–463. doi: 10.1002/2013JB010227

Vigouroux, N., Williams-Jones, G., Chadwick, W., Geist, D., Ruiz, A., and Johnson, D. (2008). 4D gravity changes associated with the 2005 eruption of Sierra Negra volcano, Galápagos. *Geophysics* 73, WA29–WA35. doi: 10.1190/1.2987399

Villagómez, D. R., Toomey, D. R., Hooft, E. E. E., and Solomon, S. C. (2007). Upper mantle structure beneath the Galápagos archipelago from surface wave tomography. *J. geophys. Res.* 112:B07303. doi: 10.1029/2006JB004672

Villagómez, D. R., Toomey, D. R., Hooft, E. E., and Solomon, S. C. (2011). Crustal structure beneath the Galápagos Archipelago from ambient noise tomography and its implications for plume-lithosphere interactions. *J. Geophys. Res. Solid Earth* 116:B04310. doi:10.1029/2010JB007764

Walker, G. P. L. (1990). Geology and volcanology of the Hawaiian Islands. *Pacific Sci.* 44, 315–347.

Wessa, P. (2015), *Kernel Density Estimation (v1.0.12) in Free Statistics Software (v1.2.1), Office for Research Development and Education.* Avaiable online at: http://www.wessa.net/rwasp_density.wasp/

Wessel, P. (2015). Regional–residual separation of bathymetry and revised estimates of Hawaii plume flux. *Geophys. J. Int.* 204, 932–947. doi: 10.1093/gji/ggv472

White, W. M., and Hofmann, A. W. (1978). *Geochemistry of the Galápagos Islands: implications for mantle dynamics and evolution. Year Book* Carnegie Inst. *Washington*, 77, 596–606.

White, W. M., McBirney, A. R., and Duncan, R. A. (1993). Petrology and geochemistry of the Galápagos Islands: Portrait of a pathological mantle plume. *J. Geophys. Res. Solid Earth* 98, 19533–19563.

Wilson, D. S., and Hey, R. N. (1995). History of rift propagation and magnetization intensity for the Cocos-Nazca sspreading center. *J. Geophys. Res. Solid Earth* 100, 10041–10056. doi: 10.1029/95JB00762

Wilson, E. (2013). *The Geochemical evolution of Santa Cruz Island, Galápagos Archipelago*. Master's thesis, University of Idaho, Moscow.

Conflict of Interest Statement: The authors declare that the research was conducted in the absence of any commercial or financial relationships that could be construed as a potential conflict of interest.

Copyright © 2018 Harpp and Geist. This is an open-access article distributed under the terms of the Creative Commons Attribution License (CC BY). The use, distribution or reproduction in other forums is permitted, provided the original author(s) and the copyright owner are credited and that the original publication in this journal is cited, in accordance with accepted academic practice. No use, distribution or reproduction is permitted which does not comply with these terms.

frontiers in Earth Science

ORIGINAL RESEARCH
published: 03 July 2018
doi: 10.3389/feart.2018.00088

Identification of Erosional Terraces on Seamounts: Implications for Interisland Connectivity and Subsidence in the Galápagos Archipelago

Darin M. Schwartz[1]*, *S. Adam Soule*[2], *V. Dorsey Wanless*[1] and *Meghan R. Jones*[2]

[1] Department of Geosciences, Boise State University, Boise, ID, United States, [2] Geology and Geophysics Department, Woods Hole Oceanographic Institution, Woods Hole, MA, United States

Shallow seamounts at ocean island hotspots and in other settings may record emergence histories in the form of submarine erosional terraces. Exposure histories are valuable for constraining paleo-elevations and sea levels in the absence of more traditional markers, such as drowned coral reefs. However, similar features can also be produced through primary volcanic processes, which complicate the use of terraced seamounts as an indicator of paleo-shorelines. In the western Galápagos Archipelago, we utilize newly collected bathymetry along with seafloor observations from human-occupied submersibles to document the location and depth of erosional terraces on seamounts near the islands of Santiago, Santa Cruz, Floreana, Isabela, and Fernandina. We directly observed erosional features on 22 seamounts with terraces. We use these observations and bathymetric analysis to develop a framework to identify terrace-like morphologic features and classify them as either erosional or volcanic in origin. From this framework we identify 79 erosional terraces on 30 seamounts that are presently found at depths of 30 to 300 m. Although intermittent subaerial connectivity between the islands has been hypothesized, the depths of these erosional terraces in the Santiago region are the first direct evidence of paleo-connectivity in the modern archipelago. Collectively, the terraces have non-randomly distributed depths. We suggest that peaks in the distribution of terrace depths likely represent long durations of exposure (i.e., sea-level still or lowstands). By comparing these peaks to those of subsidence adjusted sea-level curves, we identify the average subsidence rate that best reproduces the observed terrace distributions. These rates are 0.2–0.4 m/ka for this portion of the central Galápagos, since the formation of the seamounts, consistent with previous independent estimates. Using these subsidence rates and evidence for erosional terraces at depths up to 300 m, we conclude that all islands in the central archipelago have been intermittently connected starting between 435 and 900 ka. Individual island pairs have likely been repeatedly subaerially connected for short intervals since that time.

Keywords: erosional terraces, paleogeography, hotspot, ocean island, multibeam bathymetry, wave erosion

OPEN ACCESS

Edited by:
Ricardo S. Ramalho, Universidade de Lisboa, Portugal

Reviewed by:
Neil Mitchell, University of Manchester, United Kingdom
Daneiele Casalbore, Sapienza Università di Roma, Italy
Rui Quartau, Instituto Hidrográfico, Portugal

***Correspondence:**
Darin M. Schwartz
darinschwartz@boisestate.edu

Specialty section:
This article was submitted to Volcanology, a section of the journal Frontiers in Earth Science

Received: *03 February 2018*
Accepted: *12 June 2018*
Published: *03 July 2018*

Citation:
Schwartz DM, Soule SA, Wanless VD and Jones MR (2018) Identification of Erosional Terraces on Seamounts: Implications for Interisland Connectivity and Subsidence in the Galápagos Archipelago. Front. Earth Sci. 6:88. doi: 10.3389/feart.2018.00088

INTRODUCTION

Volcanic seamounts generated at oceanic hotspots grow over short durations, compared to the subaerial islands that they typically surround (Clague et al., 2000). These volcanic landforms help to resolve the spatial and temporal variability of magmatism, which is largely obscured by superimposed lava flows exposed on polygenetic islands (e.g., Moore et al., 1982). Furthermore, the morphology and lithology of the seamounts record information about the conditions during and after their formation (e.g., Ramalho et al., 2013; Huppert et al., 2015; Casalbore, 2018). In other words, if individual seamounts are active for only short durations, but seamounts are generated throughout the volcanic life of the hotspot, they provide a semi-continuous record of magmatic and environmental conditions above a mantle plume. The scarcity of detailed bathymetric mapping and difficulty in making direct observations at these submarine features has previously limited their utility for this purpose. In this study, we utilize new multi-beam bathymetric data and observations of seamounts in the western Galápagos Archipelago to constrain models for ocean island evolution and theories related to natural selection, which are both a function of paleogeography. Although there is strong evidence for past subaerial connectivity between the islands via genetics (e.g., Ali and Aitchison, 2014), landforms that can explain these connections mostly sit at depths greater than would be exposed during glacial maxima over the past 1 Ma. Our investigation of the seamounts is used to corroborate claims that combined sea level changes and subsidence have resulted in subaerial connectivity between the islands in the archipelago's past.

We report on new bathymetric mapping in the Galápagos that has revealed > 100 seamounts with summit depths from near sea level to 1,000 m, many of which were not previously known (**Figure 1**). The new mapping reveals complex morphological characteristics of the seamounts that were previously unresolvable, including terraced summits and flanks (**Figures 2**, **3A**). Preserved terraces and beach cobble deposits in ocean island systems and on continental margins are commonly interpreted to be the result of wave abrasion at the coastline during sea level still-stands (Trenhaile, 2000; Ramalho et al., 2013 and references therein; Zecchin et al., 2015; Casalbore et al., 2017). Wave action at the coastlines of volcanic islands creates shore platforms by quarrying and dislodgement of joint blocks and abrasion (Ramalho et al., 2013; Quartau et al., 2014, 2016). The effectiveness of these processes is thought to decrease rapidly at water depths of a few meters for bedrock and up to 50 m for clastic deposits (e.g., Menard and Ladd, 1963; Kokelaar and Durant, 1983; Romagnoli and Jakobsson, 2015). Seamounts large enough to reach the sea surface should, in theory, record the same coastal erosion processes, and provide useful constraints on ocean island paleogeographies and vertical motions in the absence of more traditional markers, such as drowned coral reefs (Campbell, 1984; Moore and Fornari, 1984; Rubin et al., 2000; Huppert et al., 2015). However, volcanic processes that are independent of depth can result in features that mimic erosional terraces, including submarine lava ponding (e.g., Clague et al., 2000), lava flows with primarily concave-out morphologies (Geist et al., 2006, 2008) and laminar spreading and deposition of near-surface pyroclastic deposits, which should be relatively smooth features with gentle upper flank slopes (Mitchell et al., 2012; Casalbore et al., 2015). Despite work toward characterizing morphologies associated with these processes (e.g., Chaytor et al., 2007), there is no systematic way to delineate seamount terraces as primary (volcanic) or secondary (erosional) features. From our observations, we develop a binary framework for determining the origins of terraces based on their morphology, which may be applicable to other seamount systems.

BACKGROUND AND METHODS

Direct observations of paleo-elevations at some ocean islands are made possible through the dating of drowned coral reefs (e.g., Hawaii; Moore and Fornari, 1984; Ludwig et al., 1991) as well as transitions from subaerial to submarine lavas in boreholes (e.g., Ascension; Minshull et al., 2010). These measurements, along with sea level reconstructions, are used to constrain island vertical motions through time (e.g., Huppert et al., 2015). These vertical motions are primarily the combined result of topographic loading and flexure (e.g., Moore, 1970; Watts and Ten Brink, 1989), cooling and deepening of the lithosphere as it ages (e.g., Marty and Cazenave, 1989) and/or transport over and away from the hotspot swell (e.g., Detrick and Crough, 1978). However, a large number of ocean islands are devoid of large carbonate platforms despite supporting reefs, likely due to low average annual water temperatures (Kleypas et al., 1999; Couce et al., 2012), and lack borehole data, thus vertical motions cannot be constrained using these approaches.

The Galápagos Archipelago is a hotspot sourced volcanic island chain located in the equatorial Pacific ∼1,000 km west of South America. The Galápagos consists of 13 major volcanic islands, numerous smaller islands, and volcanic seamounts (**Figure 1**; McBirney and Williams, 1969; Christie et al., 1992; Sinton et al., 2014; Schwartz et al., 2018). The central and eastern islands rise from a shallow volcanic platform that stands ∼3,000 m above the surrounding seafloor (Geist et al., 2008) and comprises the majority of the archipelago's erupted volume. The hotspot center lies southwest of Fernandina volcano (Kurz and Geist, 1999; Villagómez et al., 2014), which is the westernmost and most active volcanic island in the Galápagos (Allan and Simkin, 2000). There is a general age progression and corresponding decrease in eruption rate from west to east across the archipelago (White et al., 1993). The youngest island in the archipelago is Fernandina, which emerged at ∼70 ka (Kurz et al., 2014). Volcanoes get progressively older to the east, where the emergence of Santiago is ∼1 Ma, Santa Cruz and Floreana ∼2.3 Ma and San Cristobal ∼6 Ma (Geist et al., 2014). There are numerous "drowned" islands, which lie to the southeast (Christie et al., 1992) and east (Sinton et al., 2014) of the present archipelago extending the age of emergence for the archipelago to at least 9 Ma.

Vertical motions in the Galápagos have been estimated based upon measurements of the maximum height of islands and large seamounts, as well as platform depth, as a function of distance

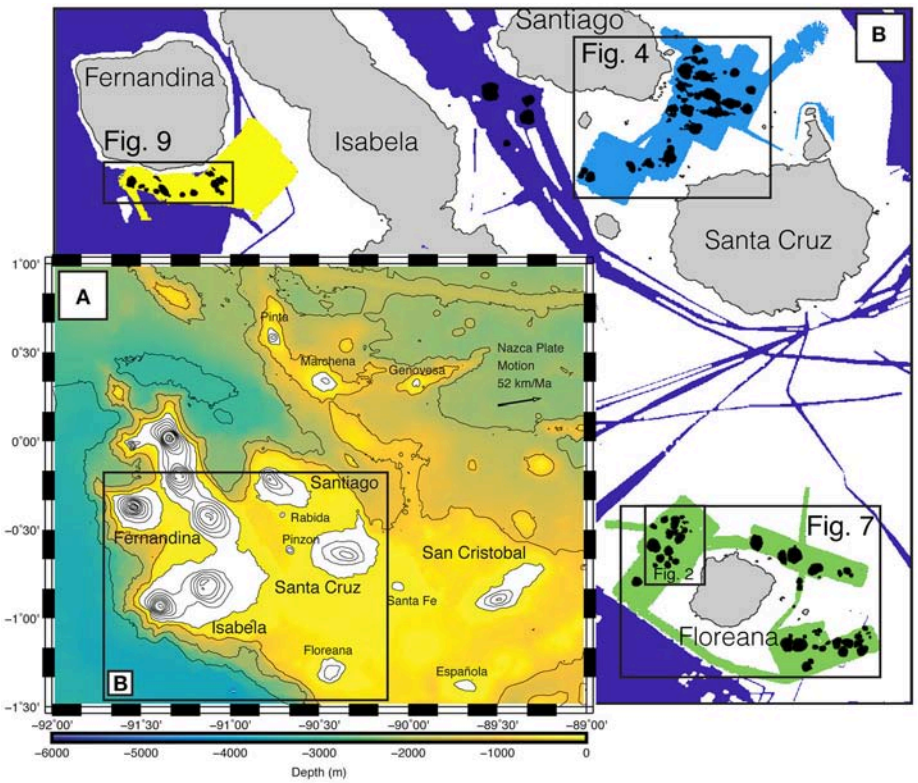

FIGURE 1 | (A) Map of the Galápagos Archipelago. Subaerial contours show elevations at 200 m intervals (Weatherall et al., 2015). Submarine contours show bathymetry at 500 m intervals. Solid black box indicates location of **(B)** in this figure. **(B)** Mapped regions and seamounts. Gray polygons show island locations. Dark violet polygon shows previously collected bathymetry, other colored polygons (light blue, yellow, green) show mapping locations from this study and are shown in more detail in **Figures 4**, **7**, **9**. Solid black polygons show footprints of newly located seamounts.

from the plume center (Geist, 1984; Geist et al., 2014). Trends in subsidence rate derived from these measurements follow an exponential decrease, that peaks at 2 m/ka at Fernandina and rates asymptotically approach 0.4–0.5 m/ka at the distance of Santiago, Floreana, and Santa Cruz (Equation 8.6; Geist et al., 2014). These rates are comparable to those of the Hawaiian Islands for islands of similar ages (0–4 m/ka for islands younger than 1 Ma; Huppert et al., 2015). The estimate of Galápagos rates relies upon the assumption that the Galápagos plume flux has contributed uniformly to archipelago formation for the past several million years. This is uncertain due to clear evidence for variable plume-ridge interaction in the archipelago's past (e.g., Harpp and Geist, 2002; Harpp et al., 2003; Sinton et al., 2014). Moreover, the relative contribution of the plume to volcanism on the Nazca and Cocos plates has fluctuated through time due to variations in the relative position of the mantle plume to the ridge and position beneath respective plates (e.g., Werner et al., 2003) and continued ridge jumps (Mittelstaedt et al., 2012).

In 2015 we conducted a research cruise in the western Galápagos Archipelago aboard the M/V *Alucia*. During the cruise we conducted seafloor mapping with a ship-mounted Reson multibeam sonar (yellow, light-blue and green areas in **Figure 1**). In addition, we collected seafloor observations and samples with two 1,000-m rated human occupied vehicles (HOVs), Deep Rover 2 and Nadir (gold lines in **Figures 4**–**9**). Through a combination of morphology from seafloor mapping and direct seafloor observations we develop a framework to distinguish between morphological features resulting from coastal (i.e., erosional) processes and those resulting from primary volcanic (i.e., constructional) processes within the mapped region. With this framework we are able to identify erosional terraces across the study area to (1) provide the first direct observations of interisland connections via erosional features in the modern archipelago, and (2) document how the combination of sea-level change and island subsidence contribute to the paleogeography of the archipelago through the use of comparative statistics.

Mapping the Galápagos Platform and Seamounts

Bathymetric mapping focused on three regions on the Galápagos platform, east and south of Santiago Island, surrounding Floreana Island and south of Fernandina Island (between 20 and 2,000 m water depth; **Figure 1**). Surveys were conducted on M/V *Alucia* using a Reson 7160 44 kHz multibeam sonar with Reson SeaBat acquisition software and PDS2000 for real time viewing and adjustment of sonar settings to optimize data quality, including frequency, depth range, beam steering, and gain. Swath

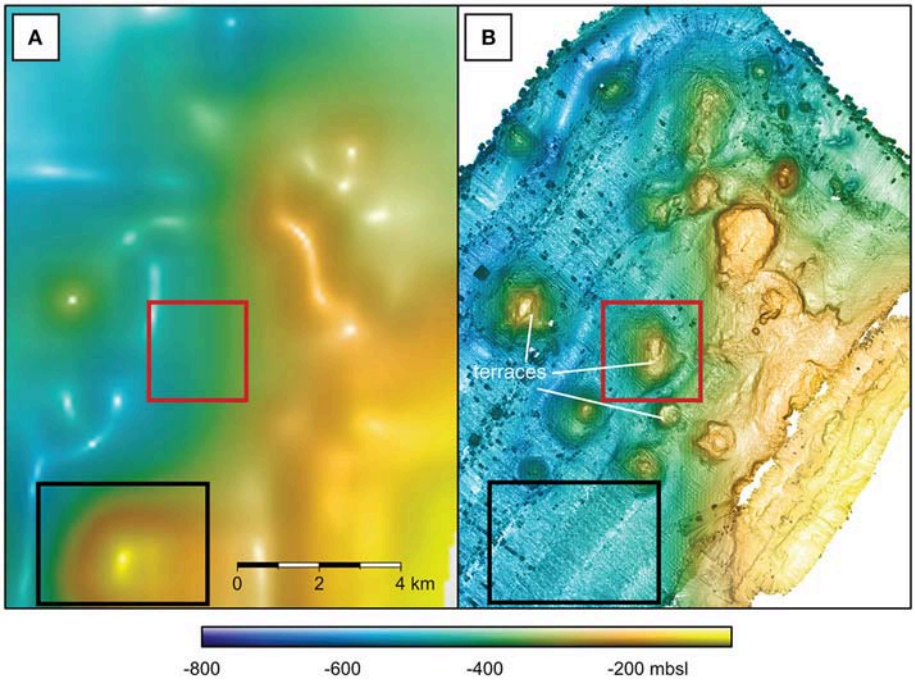

FIGURE 2 | Comparison of global bathymetry to M/V *Alucia* multibeam NW of Floreana, location of figure is indicated in **Figure 1**. **(A)** Bathymetry derived from sparse sounding data and gravity anomalies calculated from satellite altimetry, gridded at ~900 m (Smith and Sandwell, 1997; Weatherall et al., 2015). **(B)** Mulitbeam bathymetry encompassing the identical area as in **(A)**, data are gridded at 10 m. Note large anomaly in **(A)** (apparent seamount indicated by the black box) does not appear in **(B)**. Numerous smaller features not visible in the altimetry-based data appear in the multibeam data, including seamounts (indicated by the red box) and terraces are identified in the multibeam data.

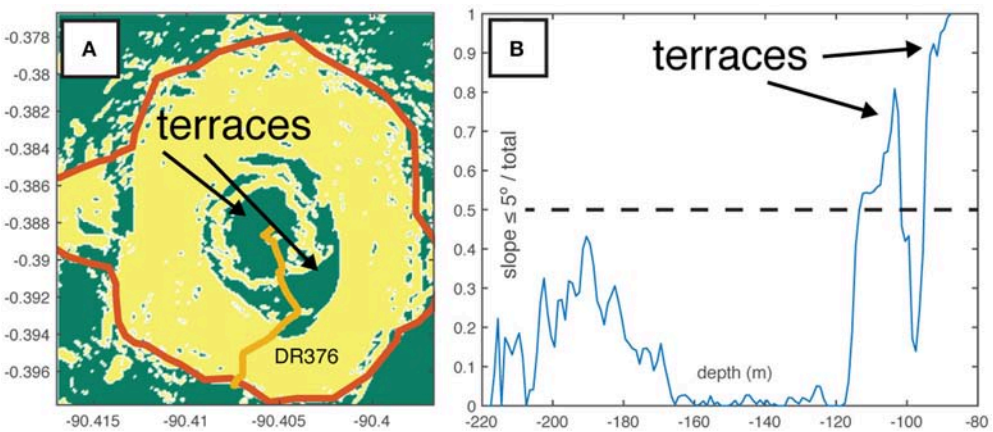

FIGURE 3 | Example of terrace identification. **(A)** Slope map of a seamount where two terraces have been identified. Areas where slopes are $\leq 5°$ (terraces) are shown in green and slopes $> 5°$ are shown in yellow. Seamount footprint is shown as a thick red line and was manually digitized as the break in slope $\geq 5°$. Gold line shows the dive track for seamount DR376. **(B)** ratio of pixels with slope $\leq 5°$ to all pixels at that depth within the seamount footprint. Peaks in the distribution where ratio is $> 50\%$ are identified as terraces.

widths were typically 5x water depth, but decreased at depths greater than 1,500 m.

Data processing was conducted with Caris™ HIPS and SIPS. Navigation and attitude data were verified and a tide correction was applied based on observed tides from the Instituto Oceanográfico de la Armada (INOCAR) station at Baltra Island. Sound velocity corrections were applied based on XBT data, which were collected at least once every 12 h of multibeam operations. Sonar data was automatically filtered at beam angles $> 65°$, manually edited to remove outliers, and gridded at 10 m for analysis. Remarkably little of the Galápagos volcanic platform has been mapped prior to this study, thus

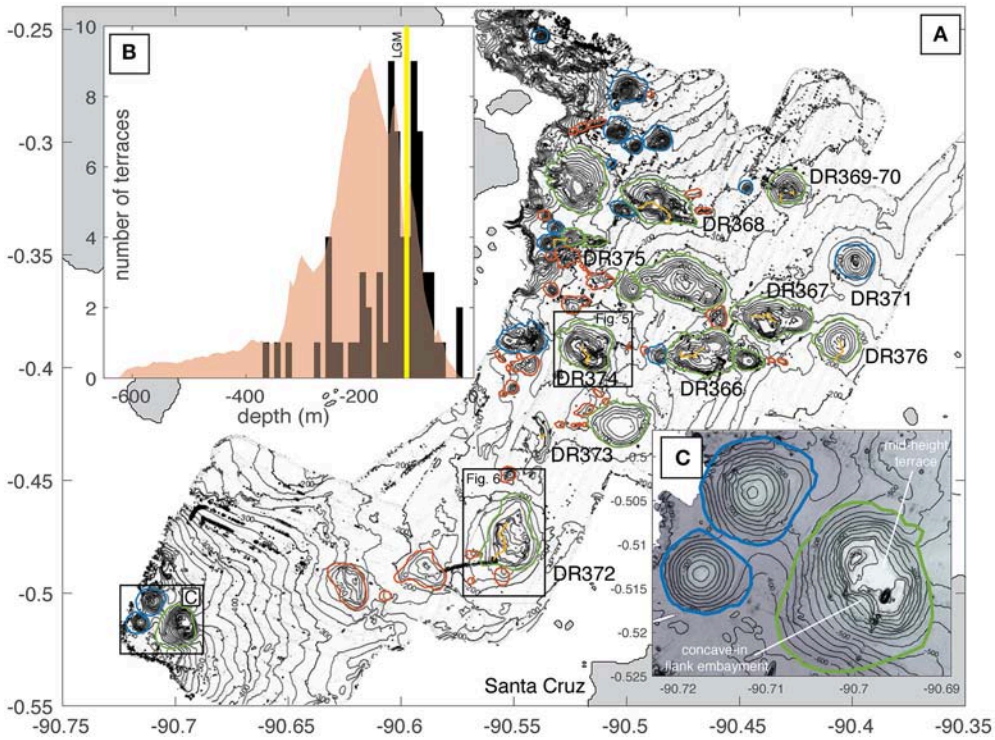

FIGURE 4 | (A) Bathymetric map of the Santiago seamounts. Gray polygons locate islands. Bathymetric contour interval is 20 m. Green lines locate seamounts > 100 m of relief that have identified terraces. Blue lines locate other mapped seamounts > 100 m. Red lines locate mapped seamounts, which are < 100 m in relief. Gold lines indicate dive tracks. Locations of inset **(C)** and **Figures 4**, **5** are indicated by black boxes. **(B)** Black/gray bars are histogram of depths of all identified terraces. Semi-transparent red polygon shows the probability distribution of all depths within the mapped seamount footprints. Yellow bar indicates the depth of the last glacial maximum sea-level lowstand (Bintanja et al., 2005) **(C)** Seamount with summit depth ~300 m with identified terrace and summit embayment and irregular shaped summit features.

the best available bathymetric data was from global data sets derived from sparse echo-soundings and global gravity anomalies derived from satellite altimetry (e.g., Smith and Sandwell, 1997). The new mulibeam bathymetry is 90x higher resolution than the existing global data (**Figure 2**; Geist et al., 2006; Weatherall et al., 2015) for the study area. As a result, the new bathymetry allows identification of seamounts with relief greater than 10 m, most of which were previously undetectable (**Figure 2**). Although correspondence of larger seamounts between satellite-derived bathymetry and the new multibeam data is good, we find numerous examples of both undetected and spurious seamounts in satellite-derived bathymetry when compared to the new multibeam data (**Figure 2**).

Using criteria of Bohnenstiehl et al. (2012), seamount extents were defined by the break in slope from the seafloor > 5° and their footprints were manually digitized using QGIS software. For seamounts with >100 m of relief, spatial statistics including summit and base depth, relief, and diameter were collected using MATLAB software and are summarized in **Table 1** for seamounts visited by HOV. Seamount slopes were binned into two categories of ≤ 5°(terraces) and >5°(seamount flanks) and integrated as a function of depth. The ratio of pixels ≤ 5° and > 5° was then calculated for these depth distributions (e.g., Passaro et al., 2011). Terraces were identified as peaks in those final distributions where ≥ 50% of pixels at a given depth have slopes of ≤ 5° (**Figure 3**). Once identified, seamounts with terraces were manually evaluated for concave-in flank embayments, which have been interpreted as erosion-induced collapse in other volcanic seamounts (e.g., Chaytor et al., 2007) (**Table 1**). These and constructional features, such as summit craters (Clague et al., 2000; Chaytor et al., 2007), convex out lobes formed at lava flow boundaries (Geist et al., 2006) are corroborated with seafloor observations (e.g., **Figures 5**, **6**, **8**, **9**). Although terraces were also identified on seamounts < 100 m in relief and seamounts in the older coarser resolution bathymetry, including one seamount visited by HOV (DR375; **Figure 4A**), we do not include these seamounts because sonar sounding density is insufficient to confidently discriminate between erosional and primary volcanic features. From our observations, we suggest that features should have relief of at least 10x the spatial resolution of the bathymetric data in order to confidently identify terraces.

Seafloor Observations and Sample Collection

HOV dives were conducted on 25 seamounts in the three study regions (**Table 1**). Each dive consisted of tandem launches of the Nadir and Deep Rover 2 submersibles. Typically, dives started

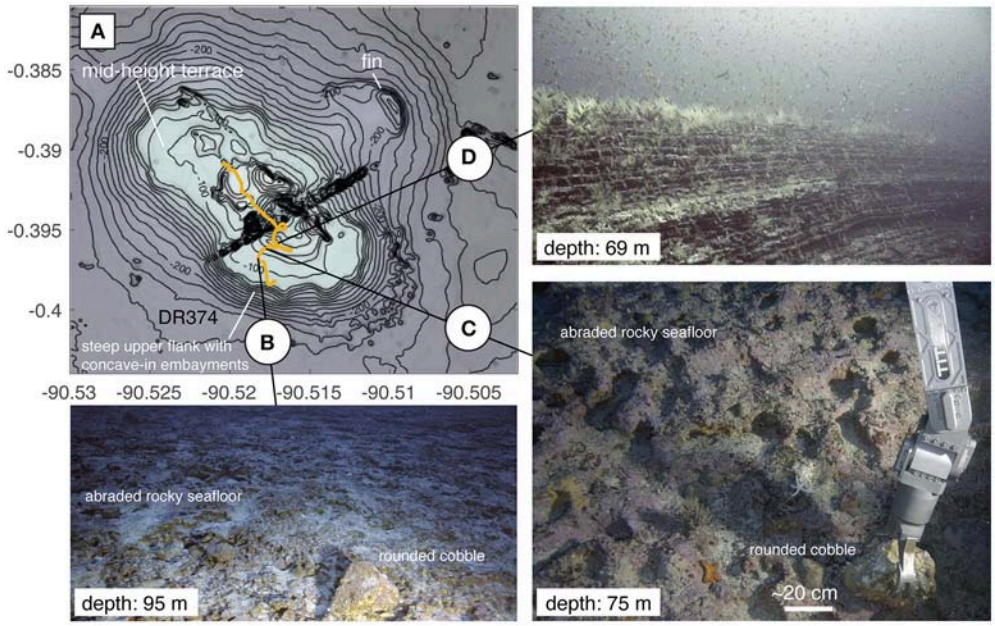

FIGURE 5 | Map and images of DR374 seamount. **(A)** Bathymetric contour interval is 10 m. Gold line shows dive track for seamount DR374. The seamount has steep upper flanks and a broad mid-height terrace that is concentric about the seamount's summit (i.e., encircles the entire seamount). The contour of the terrace edge is irregular and includes flank embayments giving it a scalloped shape. There are multiple irregular spines and fins protruding from the seamount's flank and summit. NE-SW striking linear feature near the summit of the seamount is a data artifact. **(B)** Rounded boulder on smoothed bedrock material constituting the seamount's terrace. **(C)** Collection of rounded cobbles and detailed view of smoothed bedrock constituting the seamount's terrace. **(D)** Truncated outcrop of thinly bedded volcaniclastic material near the seamount's summit. Depths in photos indicate the depth of the seafloor at the point of image capture.

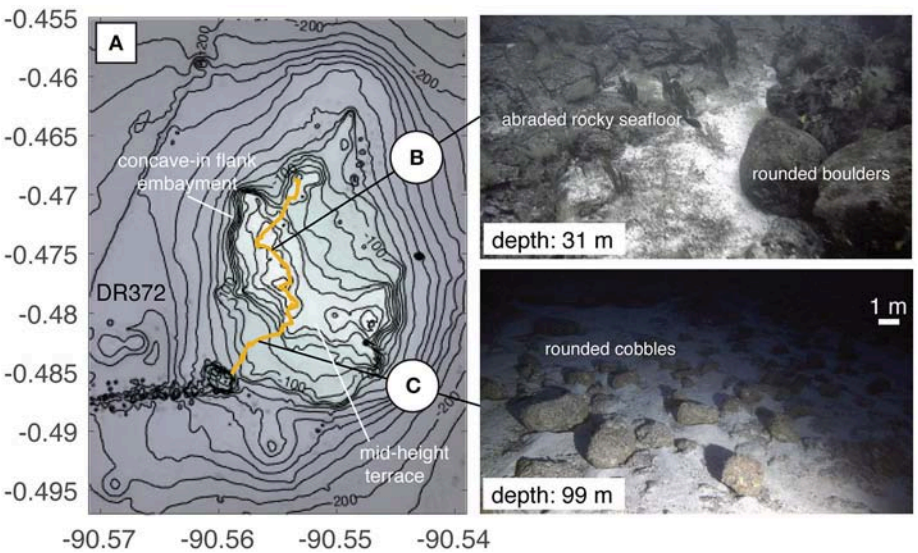

FIGURE 6 | Map of DR372 seamount. **(A)** Bathymetric contour interval is 10 m. Gold line shows dive track for seamount DR372. This seamount is highly irregular in shape, with a N-S trending elongation at it's base and NW-SE elongation near it's summit. The seamount has steep upper flanks and is adorned by multiple irregular summit features. There are multiple terraces on this seamount, which are flanked by steep sides with flank embayments. ENE-WSW striking linear feature SW of the seamount is a data artifact. **(B)** Rounded boulder on smoothed bedrock material constituting the seamount's terrB The left portion of the image shows bulbous/rounded basaltic lava flow bedrock and the right side shows rounded basaltic boulders of a similar size and roundness. **(C)** Field of rounded cobble-boulder sized clasts on flat lying bedrock, which is mostly obscured by fine sediment. Depths in photos indicate the depth of the seafloor at the point of image capture.

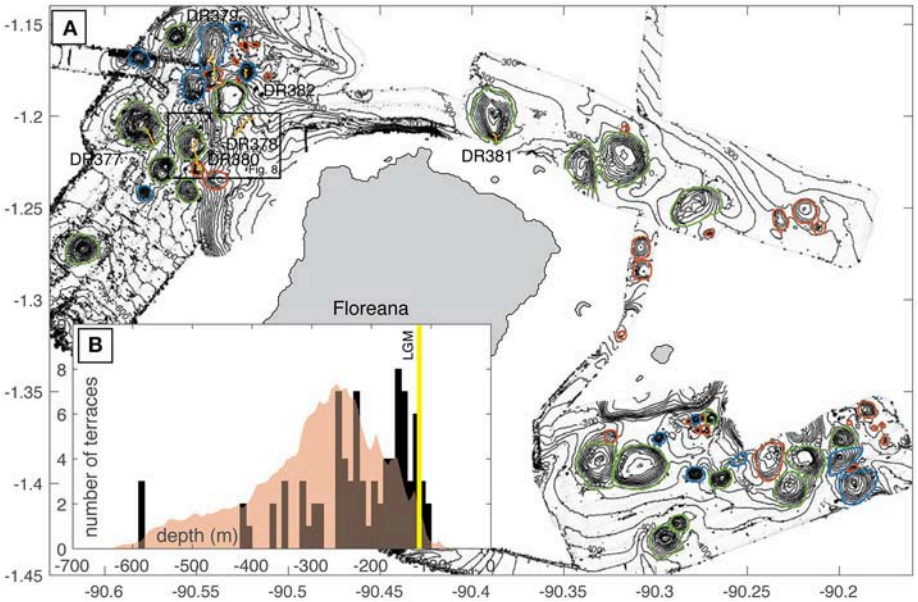

FIGURE 7 | (A) Bathymetric map of the Floreana seamounts. Gray polygons locate islands. Bathymetric contour interval is 20 m. Green lines indicate footprints for seamounts > 100 m of relief that have identified terraces. Blue lines indicate other mapped seamounts > 100 m. Red lines indicate mapped seamounts, which are <100 m in relief. Gold lines indicate dive tracks. Location of **Figure 8** is indicated by a black box. **(B)** Black/gray bars are histogram of depths of all identified terraces. Semi-transparent red polygon shows the probability distribution of all depths within the mapped seamount footprints. Yellow bar indicates the depth of the last glacial maximum sea-level lowstand.

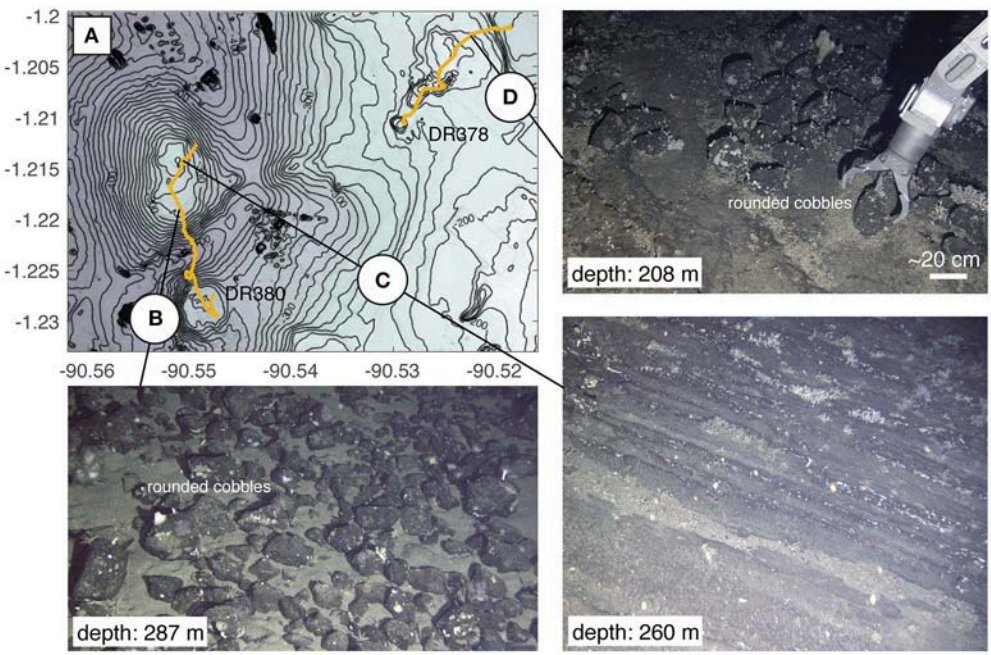

FIGURE 8 | Map of DR378 and DR380 seamounts. **(A)** Bathymetric contour interval is 10 m. Gold lines shows dive tracks for seamounts DR378 and DR380. The two seamounts visited on seamount DR380 have terraced/flat summits. The northernmost of the two is irregular in plan view, with small embayments on the western flank and has a small summit spire. The southernmost is round with no irregular summit features, except for its flat top, and resembles seamounts found in the Fernandina region (**Figure 9**) **(B)** Field of rounded cobble-boulder sized clasts setting on a flat surface obscured by fine sediment. **(C)** Near vertical outcrop of sub-horizontally bedded volcaniclastic material. **(D)** Collection of rounded cobble from top of terrace. Depths in photos indicate the depth of the seafloor at the point of image capture.

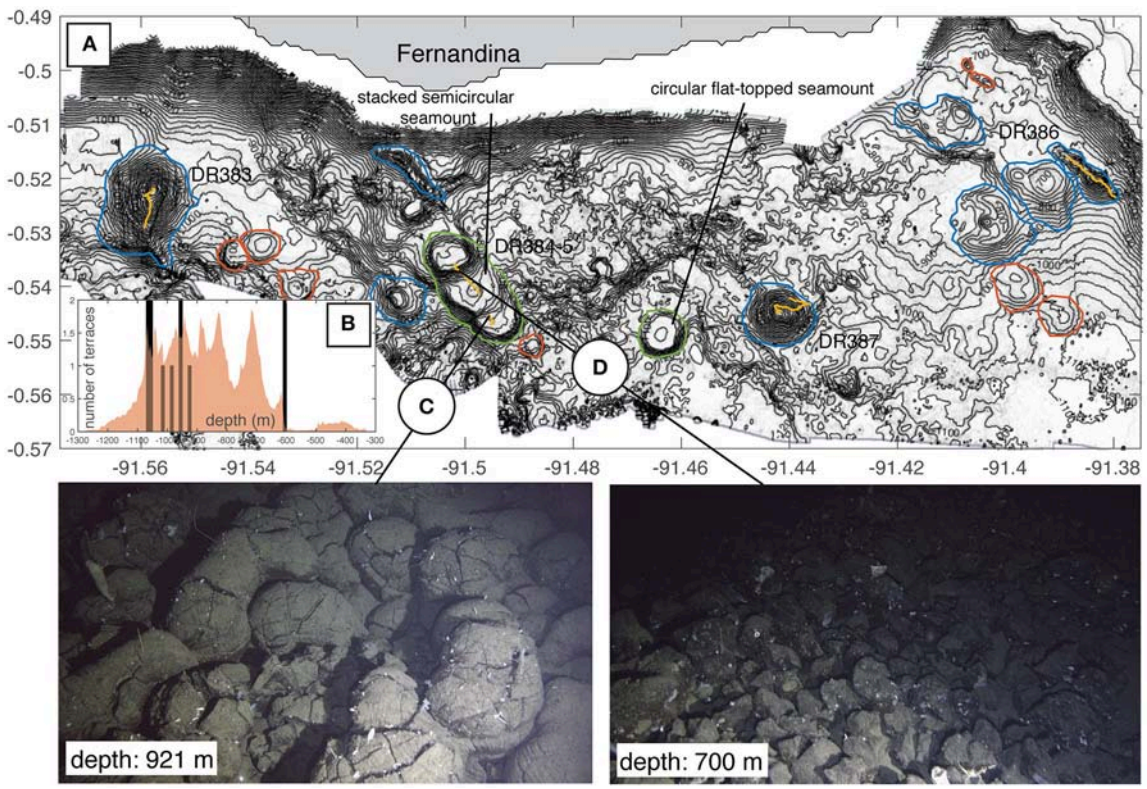

FIGURE 9 | (A) Bathymetric map of the Fernandina seamounts. Gray polygon indicates island location. Bathymetric contour interval is 20 m. Green lines indicate footprints for seamounts > 100 m of relief that have identified terraces. Blue lines indicate other mapped seamounts > 100 m. Red lines indicate mapped seamounts, which are <100 m in relief. Gold lines indicate dive tracks. **(B)** Histogram of depths of identified terraces. Semi-transparent red polygon shows the probability distribution of all depths within the mapped seamount footprints. **(C)** Pillow lavas, which serve as the bedrock for the lowermost terrace on this seamount. **(D)** Steep talus pile on the seamount's flank. Talus is comprised of pillow fragments retaining some of the curved sides of the original pillows and more blocky/polygonal interiors.

at or near the base of a target seamount and proceeded up to the seamount summit. Continuous HD video was collected throughout the dive and samples were collected where obvious changes in lithology were observed (**Table 1**; Supplementary Data). Following the cruise, the video data was classified based on the observed morphology and inferred lithology using the collected samples. Two additional seamounts were visited on a previous cruise and are included in our evaluation (Carey et al., 2016).

RESULTS

Observational Results

From the 150 seamounts that were digitized from the new and existing multibeam bathymetry, 76 are > 100 m in relief, and 34 of these seamounts have terraces. Most terraces occur between the seamount base and summit (mid-height terraces; $N = 24$), the rest are found at or near (within 10 m) the summit (summit terraces; $N = 10$). Terraces are identified in all three mapping regions and range in depth from 15 to 1,100 m (**Figures 4–9**).

We recovered 147 rock samples from 22 dives on 25 seamounts. Of the samples collected, 127 are basaltic lavas and the remaining 20 are of lithified volcaniclastic deposits. The samples are correlated with seafloor morphology using continuous dive video (**Table 1**). We categorized seafloor morphology into primary volcanic features/textures formed during emplacement or secondary features/textures formed during exposure. Primary volcanic features include pillow lavas (e.g., **Figure 9C**) and rough aa-like lava flow textures (Supplementary Data; Image DR372-1655). Secondary features include rounded beach cobble deposits (**Figures 5B,C**, **6B,C**, **8B,D**), smoothed abrasional rocky surfaces (**Figures 5B,C**), erosional cliffs (**Figure 5D**), terraces (**Figures 5B,C**), and spires (Supplementary Data, Image 375–1558; e.g., Trenhaile, 1987). We use the presence of rounded cobbles on terraces to definitively identify exposure to abrasional processes at or near the sea surface (e.g., Ramalho et al., 2013; **Table 1**). Further, we equate variations in observed morphologic features from smooth to more bulbous rocky surfaces to be the result of abrasion by water-borne particles on various volcanic lithologies ranging from basalts to hyaloclastities and/or pyroclastic deposits (e.g., Ramalho et al., 2013). Bedded pyroclastic deposits were commonly observed (**Figures 5D**, **8C**) and although we do not necessarily ascribe them to primary or secondary volcanic features, they are evidence of shallow eruption processes (e.g., Cas, 1992) or

TABLE 1 | Table of seamounts visited by HOV relating direct seafloor observations to bathymetric features.

ID	Lat	Long	Dive	Summit depth (m)	Relief (m)	Terrace	Mid-terrace	Concentric	Concave-in flank embayment	Rounded clasts/ abrasional textures
SANTIAGO REGION										
114	−0.3948	−90.4700	DR366	24.486	189	Yes	Yes	Yes	Yes	Yes
119	−0.3776	−90.4360	DR367	27.848	191	Yes	Yes	Yes	Yes	Yes
127	−0.3265	−90.4890	DR368	98.436	219	Yes	No	–	No	No
117	−0.3209	−90.4300	DR369–70	91.221	179	Yes	yes	Yes	No	Yes
116	−0.3530	−90.3990	DR371	45.556	165	No	–	–	No	Yes
104	−0.4773	−90.5550	DR372	22.929	145	Yes	Yes	Yes	Yes	Yes
111	−0.3917	−90.5180	DR374	18.994	230	Yes	Yes	Yes	Yes	Yes
24	−0.3462	−90.5350	DR375	54.123	153	No	–	–	No	Yes
25	−0.3429	−90.5260	DR375	162.51	121	Yes	Yes	Yes	No	Yes
3	−0.3884	−90.4060	DR376	86.999	107	Yes	Yes	Yes	No	Yes
FLOREANA REGION										
130	−1.2040	−90.5790	DR377	253.17	292	Yes	Yes	Yes	Yes	Yes
40	−1.1598	−90.5410	DR379	299.59	140	No	–	–	Yes	Yes
49	−1.1795	−90.5410	DR379	252.29	90	Yes	No	–	Yes	Yes
35	−1.2283	−90.5490	DR380	302.85	82	Yes	No	–	No	No
36	−1.2141	−90.5510	DR380	257.92	159	Yes	No	–	Yes	Yes
131	−1.1994	−90.3870	DR381	23.317	242	Yes	Yes	Yes	Yes	Yes
46	−1.1773	−90.5240	DR382	183.98	175	No	–	–	Yes	Yes
FERNANDINA REGION										
12	−0.5222	−91.5580	DR383	577.69	487	No	–	–	No	No
29	−0.5349	−91.5020	DR384–5	607.22	301	Yes	Yes	No	No	No
100	−0.5165	−91.3870	DR386	623.39	147	No	–	–	No	No
129	−0.5447	−91.4420	DR387	692.7	320	No	–	–	No	No

reworking of material at or near the sea surface (Ramalho et al., 2013).

Santiago Seamounts

In the Santiago region, terraces are present at water depths from 20 to 375 m and have principle modes at depths of 110 and 130 m (**Figure 4B**), with minor modes at greater depths. Typically, terraces in this region occur as mid-height features whose outer edges are concentric with contours on the seamount slope and about the seamount's midpoint (**Figures 4A**, **5A**). Seamounts with terraces are irregular in plan view (**Figures 5A**, **6A**) and are adorned by steep cliffs (**Figure 5A**) and vertical fins or spires, which are visible in the maps (e.g., **Figure 5**) and on smaller scales in photos collected from the submersibles (e.g., Supplemental Data; Image DR375-1558). On nine of the 10 seamounts visited in this region we observed rounded cobbles and smoothed and bulbous surfaces, indicative of exposure to waves at or near sea surface (**Figures 5**, **6**). Of these nine seamounts, all but two have mid-height terraces and/or summit terraces. Only one seamount had a morphologically identified terrace (at its summit) but no obvious evidence for erosional features from direct seafloor observations (DR368). Intact pillow lavas were observed from the submersibles on this seamount's flanks, the only observation of pillows in the Santiago region (Supplementary Data; Images DR368-1502, 1520, 1524).

Floreana Seamounts

Similar features to those observed in the Santiago region were observed surrounding Floreana (**Figure 7A**). Terraces are present at water depths of 100–600 m and have a shallow mode at 150 m and a secondary mode at 250 m (**Figure 7B**), with minor modes at greater depths. Thinly bedded laminar deposits are observed at depths between 100 and 400 m (e.g., **Figure 8C**). Rounded cobbles are present at water depths up to 300 m (**Figures 8B,D**). These deep cobbles are similar in size and roundness to those observed at shallower depths and in the Santiago region (**Figures 6B**, **8D**). Of note, the cobbles at 287 m water depth shown in **Figure 8B** were observed on a terrace at the seamount summit, excluding the possibility of downslope transport. Similar bathymetric features to those observed in the Santiago region are also observed in the Floreana region, including steep cliffs with scalloped and complex contour patterns (**Figures 7**, **8**). Of the seven seamounts visited by HOV, all but one showed evidence of exposure to wave abrasion in the form of rounded cobbles or other abrasional surfaces. Of these six seamounts, five have summit terraces, and two of those five had mid-height terraces. Similar to the Santiago region, the only seamount with a morphologically-identified terrace that showed no obvious evidence for erosional features from direct seafloor observations (DR380 southern seamount), only had a summit terrace and had what appeared to be intact pillow lavas at its summit (Supplementary Data; Images DR380-1500).

Fernandina Seamounts

Terraces in the Fernandina region are observed at depths from 600 to 1,100 m, with no obvious depth modes. Terraces occur as circular and stepped semicircular features. As opposed to the terraces visited in the Santiago and Floreana regions, deep terraces in the Fernandina region were associated with pillow lavas (**Figures 9A,B**). Pillows were typically observed as intact, flat deposits (**Figure 9C**) and mounds as well as incised cliffs and associated talus slopes (**Figure 9D**). Talus slopes originating from these constructions contain sub-meter sized clasts with remnant outer pillow surfaces. These clasts are easily identified as pillow fragments, as opposed to reworked cobbles, due to their presence as steep deposits at the base of intact pillow cliffs and their polygonal and blocky sides. Other lava features are observed including columnar jointed flow interiors. No observations of laminar pyroclastic deposits, wave base erosional surfaces, or rounded clasts were observed in the Fernandina region.

Framework for Identifying Erosional Terraces

From our combined bathymetric analyses and direct seafloor observations we have developed a binary framework to delineate erosional terraces from those created from other processes (**Figure 10**). The seafloor observations and their relationships to terraces and flank embayments serve as the training dataset for the binary framework. The 21 visited seamounts (**Table 1**) are ultimately used to evaluate our interpretations (e.g., identify false positives and negatives). Visited seamounts with terraces constituting the training datasets ($N = 14$; **Table 1**) represent nearly half of all seamounts with terraces ($N = 34$), which we deem adequate for confidently assessing the accuracy of our classification scheme.

We take a conservative approach in our classification relying primarily on terrace characteristics (e.g., summit vs. mid-height terrace) in order to reduce false positives and the effect of human interpretation biases. We note that only 11 of the 14 seamounts visited by HOV with direct observations indicating erosion at or near the sea surface (e.g., beach cobbles), have identified terraces. This leads to an initial false negative rate of 21%. However, without direct seafloor observations the absence of bathymetrically identifiable terraces (e.g., **Figure 3**) for the remaining unvisited seamounts is an impasse that excludes further identification ($N = 42$; **Figure 10A**). Thus, all seamounts without bathymetrically identified terraces are excluded from analysis of island subsidence and paleogeography. Interestingly, seamounts with no terraces identified, but show direct seafloor evidence for erosion ($N = 3$; false negatives), are of comparable size and depth to the seamounts that are positively identified by both metrics. This may suggest that some seamounts are too young to have experienced the same lowstands as nearby seamounts, or that variations in lithology between seamounts may be a primary control on the formation and preservation of terraces.

When present, seamount terraces occur on summits ($N = 10$), or at mid-level on the seamount in the presence or absence of a summit terrace ($N = 24$; **Figure 10B**). If the seamount only has a summit terrace and the seamount does not possess any obvious erosional features such as concave-in scalloped flanks, then it cannot be positively identified as erosional (**Figure 10D**). Three seamounts with only summit terraces and lacking erosional features are observed and are found in all three mapping regions (**Table 1**) and include DR368 (**Figure 4**) and DR380 (southern seamount; **Figure 8**). Flat-topped seamounts are commonly observed seafloor features (e.g., Chaytor et al., 2007). These features are thought to form from the ponding of lavas at seamount summits, similar to subaerial volcanoes in the Galápagos (Clague et al., 2000; Naumann and Geist, 2000), or due to spreading of pyroclastic material due to shallow eruption

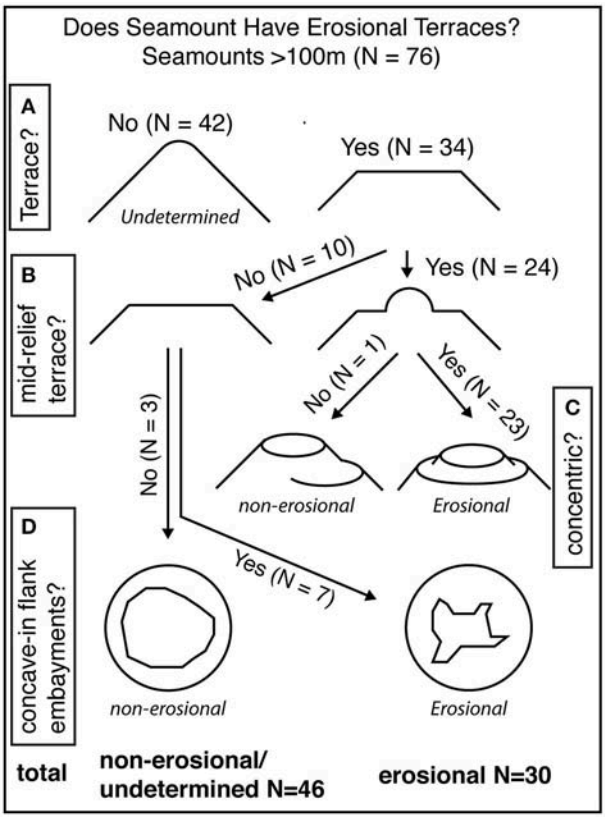

FIGURE 10 | Flow chart for extrapolating mapped terraces as erosional terraces indicating observations leading to, and the number of seamounts within, each classification step. See section Framework for Identifying Erosional Terraces for more detailed description of each classification step and discussion of false positives and negatives. **(A)** Initially seamounts are discriminated by the presence of bathymetrically identified terraces. Seamounts without bathymetrically identified terraces (left) cannot be positively identified as erosional. **(B)** Seamounts terraces occur on summits (left) or at mid-level on the seamount +/− a summit terrace (right). **(C)** Of seamounts with mid-level terraces, terraces can either occur non-concentrically (left) or concentrically (right) about the seamount's summit. Seamounts with non-concentric terraces are classified as non-erosional, whereas seamounts with concentric terraces are classified as erosional. **(D)** For seamounts with summit terraces only seamounts are manually discriminated by the absence (left) or presence (right) of concave-in flank embayments. The former are classified as non-erosional and the later as erosional.

processes without direct interaction with waves (Mitchell et al., 2012; Casalbore et al., 2015). Both of these mechanisms should result in circular seamounts with relatively gentle summit slopes (Clague et al., 2000; Mitchell et al., 2012). Both DR368 and DR380 only have summit terraces and do not show morphological or seafloor evidence for erosion. In fact, irregularities in extent of the summit of DR380 are convex-out, which more likely indicate volcanic constructional processes (e.g., Geist et al., 2006). There are no false positives or negatives identified in our training dataset for this classification step.

By contrast, we assert that summit terraces, on seamounts with concave-in, scalloped flanks, or steep upper slopes are most likely created by coastal erosional processes ($N = 7$; **Figure 10D**). Seven seamounts, which have only summit terraces, are accompanied by complex summit shapes as well as steep and scalloped flanks that lead up to terraces (**Figure 10D**). The seamounts that we mapped are all < 1 km in relief and thus should not be gravitationally unstable and therefore not have been significantly modified by large scale mass wasting (Mitchell, 2001). Similarly, these features would not be expected to result from lateral spreading of pyroclastic material or submarine lava ponding for volcanoes of this size (Clague et al., 2000; Mitchell et al., 2002, 2012). Direct seafloor observations of all seamounts in this group ($N = 3$; **Table 1**) indicate exposure at the sea surface, leading to no false positives or negatives.

Twenty-four seamounts have mid-level terraces (**Figure 10B**). These mid-level terraces occur either concentrically about the same mid-point (e.g., **Figure 3**) or non-concentrically (e.g., DR384-5; **Figure 9A**). If the seamount has a mid-level terrace, but the terraces do not occur concentrically ($N = 1$; **Figure 10C**) then the terrace may not be erosional. The most obvious example of non-concentric terracing is in the Fernandina region, where multiple overlapping flat-topped seamounts are built on a slope producing series of steps (e.g., DR384-5; **Figure 9A**). Seamounts with this morphology have been observed on the flanks of Hawaii at depths where there is no evidence for exposure (e.g., Clague et al., 2000). In addition, prevalent intact pillow lavas are observed on the Fernandina seamounts (e.g., **Figure 9C**), which are deeper than 600 m. These observations, as opposed to observations indicating coastal exposure, make sense, as it would be unreasonable to infer more than 500 m of subsidence for these seamounts, given their close proximity to the hotspot center.

If the mid-level terraces are predominately concentric about the summit of the seamount, then this provides evidence that the seamount has likely been affected by coastal erosional processes, such as the formation of insular shelves ($N = 23$; Quartau et al., 2010, 2014, 2015, 2016; Ramalho et al., 2013). This claim is supported unanimously by our training data set, where all seamounts with multiple, concentric terraces show direct seafloor evidence for modification by erosion near to the sea surface (**Table 1**). Based on the lack of false positives, we conclude that the presence of multiple concentric terraces alone is enough to positively identify a seamount as being modified by coastal processes. Of note however, all seamounts but one that we observed with mid-level terraces are also accompanied by concave-in scalloped flanks and irregular summit shapes (e.g., **Figures 4C**, **5**, **6**, **8**). These observations could be used in tandem to strengthen the identification of erosional seamounts. However, we choose to end classification of these erosional seamounts at this stage because this further classification would require additional manual discrimination (e.g., summit shape), which may result in errors (**Figure 10C**).

After applying our classification to all of the newly mapped seamounts, and including those that we directly observed by HOV, we are able to positively identify 30 of the 74 as having erosional characteristics. This constitutes ∼90% of all terraced seamounts ($N = 34$) in the study region. It would be expected that terraces formed from constructional processes should be randomly distributed about the depths within the seamount footprints, and correlated only with the summit heights of the seamounts. Although the data is sparse, this is what is observed at Fernandina (**Figure 9B**). In this region, there are no preferential depths of terraces, which support the interpretation that they are formed by constructional processes. By contrast, terraces formed through erosional processes should be clustered at similar water depths (i.e., paleo-sea level) and independent of seamount depths. This is observed in terrace depth distributions in both the Santiago and Floreana regions, which show prominent peaks in terrace depth and are skewed toward much shallower depths compared to seamount depth distributions (**Figures 4B**, **7B**).

DISCUSSION

Seamount Exposures and Terrace Formation During the Last Glacial Maximum

Early observations of features created by island vertical motions combined with sea-level fluctuations were identified in echosounder profiles of guyots and seamounts and coupled with observations of beach cobbles and gravels at the summits of these features (e.g., Carsola and Dietz, 1952; Schwartz, 1972; Lambeck, 1984). Similar terraces have been mapped on the upper 200 m of continental shelves in echosounder profiles, with the prevalence of terraces at a given depth taken to reflect the relative duration of stillstands at that level (e.g., Pratt and Dill, 1974; Wagle et al., 1994). However, uncertainty in sea level fluctuations at the time of these studies limited the appeal of using submarine terraces for reconstructing subsidence rates and/or sea level given the known instability of the oceanic lithosphere, foundering due to thermal contraction with time, and ambiguities arising from primary volcanic terraces (e.g., Chaytor et al., 2007). With established paleo-sea level reconstructions for the past 1,000 ka (e.g., Bintanja et al., 2005) along with improved dating methods and models of subsidence, this approach has been revisited (e.g., Kim et al., 2013; Romagnoli et al., 2018).

Sea-level curves for the past 500 ka have been well established from multiple methods and in various ocean basins (e.g., Shackleton, 1987; Siddall et al., 2003). This record has recently been extended to 1,000 ka by coupling sediment core and ice volume models (Bintanja et al., 2005). Over this interval there have been at least eight glacial and interglacial cycles, which have resulted in sea level lowstands comparable to that of the last glacial maximum (>100 m; **Figure 11**). Depth of shelf edge

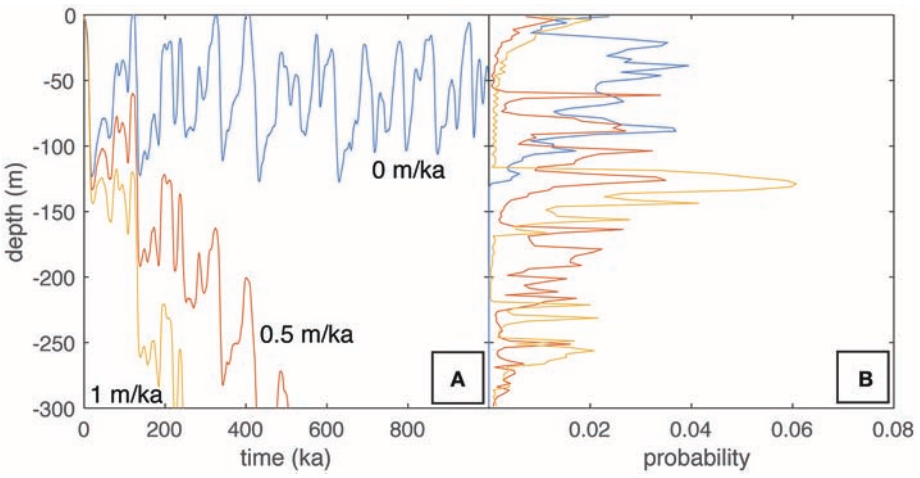

FIGURE 11 | Examples of subsidence normalized sea level depth integrations. **(A)** Sea level as a function of time for the past 1,000 ka. Blue curve shows sea level assuming no subsidence (Bintanja et al., 2005). Red curve shows the same sea level data adjusted for a subsidence rate of 0.5 m/ka, representing relative sea level change at this rate. Orange curve shows the same sea level data adjusted for a subsidence rate of 1 m/ka, representing relative sea level change at this rate. **(B)** Probability distributions representing the time integrated durations of sea level at all depths for each subsidence rate. Colors shown as defined in **(A)**.

below −130 m has also been used by Quartau et al. (2014, 2015, 2016) to infer subsidence rates assuming that insular shelves formed immediately after the end of the volcanic phase and subsided afterwards. For ocean island systems that have not experienced uplift, we hypothesize that terraces formed during these lowstands and were preserved on seamounts by removal from wave action due to subsidence. We visited 10 seamounts with summit depths < 130 m and all show evidence for exposure at the sea surface. Further, five seamounts with summit depths of 130–300 m show evidence for exposure. These features include rounded beach cobbles that range in size from decimeter to meter scale. Thinly bedded deposits, which appear to be primarily pyroclastic in origin (**Figures 5D**, **8C**), are observed at depths up to but no deeper than 300 m. Bedrock textures on summit terraces include smoothed lava flow surfaces (**Figure 6B**) and shorter wavelength undulating surfaces and cavities (**Figures 5B,C**). These are likely secondary textures due to abrasion at or within tens of meters of the sea surface (e.g., Santos et al., 2010; Romagnoli and Jakobsson, 2015). However, we assert that erosive conditions tend to be most vigorous at the sea surface (Quartau et al., 2010; Ramalho et al., 2013), and decrease significantly at depths greater than 20 m for rocky surfaces. These combined observations confirm that these terrace surfaces now 20–300 m deep must have once been at or near the sea surface.

The intersection of a seamount and the sea surface produces erosional terraces, the depth of these terraces is dependent on the vertical motions of the seamount (e.g., uplift, subsidence) and sea level changes since formation. In the absence of major vertical movements and on islands that have experienced at least one glacial/interglacial eustatic cycle, terrace depths should range from present sea level up to 120 m water depth (Quartau et al., 2010), assuming that similar eustatic conditions existed in the Galápagos. Thus, seamounts with terraces at these depths were present during the LGM at ∼20 ka and have likely only experienced minor subsidence or uplift since that time. There is a prevalent peak in the number of terraces at both Santiago (**Figure 4B**) and Floreana (**Figure 7B**) around the depth of sea level during the LGM. These LGM terraces are nearly all associated with directly observed erosional features.

For terraces and erosional features at depths > 130 m, seamounts must be older than 20 ka and must have subsided since their exposure at the sea surface (Quartau et al., 2014, 2015, 2016). From the lack of terraces above 120 m water depth, despite the presence of numerous seamounts within that depth range, the formation of a terrace during a non-lowstand is much less prevalent (**Figures 4B**, **7B**). This is most likely due to greater rates of sea level change (i.e., lack of stillstands) during non-lowstand periods. Nevertheless, it is reasonable to assume that erosional terraces occurring at depths > 130 m have either been exposed during earlier sea level still or lowstands and have been subsequently transported to their present depths. Evaluating the mechanism and timing of terrace formation for terraces deeper than 130 m will be discussed in the following section.

Evaluating Subsidence Rates and Paleogeography

Since Darwin's visit to the Galápagos in 1835, the archipelago has played a pivotal role in forming and testing the theory of evolution by natural selection (e.g., Darwin, 1859; Ali and Aitchison, 2014). The archipelago is in a geographical nexus ∼1,000 km west of South America, which effectively isolates it from most biologic communication with the continental landmass, but is close enough to enable colonization by non-aquatic, non-volant vertebrates (e.g., Wyles and Sarich, 1983; Rassmann, 1997; Caccone et al., 2002). The Galápagos Islands are also far enough apart to isolate species and promote endemism (e.g., Ricklefs and Bermingham, 2007). Recent evolutionary models have been proposed that link speciation

events with glacial maxima where, at extreme sea level lowstands, the islands have presumably been connected, allowing cross-colonization (e.g., Ali and Aitchison, 2014). However, sea level oscillations over the past 1,000 ka alone (<130 m; Bintanja et al., 2005) cannot explain speciation trends between all of the major islands in the Galápagos that are separated by submarine bridges, which are presently > 300 m below sea level (**Figure 1A**).

We have confirmed the presence of erosional terraces at depths of 290 m through direct observations of beach cobbles and secondary bedrock morphologies, indicative of abrasion driven erosion by wave action (**Figure 8B**; e.g., Ramalho et al., 2013). We have expanded the observation of these terraces beyond those visited by HOV to include all terraces with similar morphologies (**Figures 4C**, **10**). From this dataset it is clear that there are several depth ranges with significant terrace abundances that are deeper than sea level has reached in the past 1,000 ka. It is hypothesized that terrace width should be proportional to the duration of wave base erosion at a given depth (e.g., Pratt and Dill, 1974; Menard, 1983; Quartau et al., 2010). For any subsiding archipelago this duration is a function of the sea-level curve as well as the subsidence rate. Thus, with terraces present at the appropriate depths, within the range of predicted sea level variations, the distribution of the terraces provides an independent means by which to test proposed subsidence rates in the Galápagos. The appropriate depth range will be different for all archipelagos, and requires the formation and transport of seamounts for some duration of time appropriate for the subsidence rate. In summary, to relate the terrace distribution on seamounts to subsidence, seamounts must be produced somewhat continuously at the appropriate depth range in order to have a record of these processes.

Based on the emergence ages of Santiago (1 Ma), Santa Cruz and Floreana (2.3 Ma) and the range of ages of lavas on those islands we predict that the seamounts are also on the order of 1 Ma (Geist et al., 2014). Further, we assume that individual seamounts were produced over a relatively short time period, and thus have not been "repaved" and represent unobscured records of exposure since their formation (Schwartz et al., 2018). Assuming an average subsidence rate of 0.4 m/ka, which is the inferred value for the Galápagos in the vicinity of the seamounts (Geist et al., 2014) we predict that the oldest (∼1 Ma) and thus deepest possible terraced seamounts, which may have formed during sea level lowstands of ∼100 m could now have terraces at depths of ∼600 m. Terraces that we positively identify as erosional range in depth from 0 to 300 m. This depth range is half that of the maximum expected depth range for terraces and thus should provide sufficient information on subsidence rates over at least the past 500 ka. Since we do not have independent age control on any of the erosional terraces we suggest that by using the combined seamount terrace depth distribution we should be able to assess subsidence rates.

In order to assess subsidence rates we have combined all bathymetric data within the seamount footprints, which have been positively identified as erosional (**Figure 10**) and determined the relative proportion of data with slopes < 5° at all depths as a proxy for the terrace distribution (**Figure 3**). Although the subsidence rates vary spatially over the archipelago, we assert that the study areas are aligned almost perpendicular to plate motion and have correspondingly similar emergence ages (Geist et al., 2014), so have similar loading histories. Moreover, the submarine platform that underlies Santiago and Floreana makes up a majority of the erupted volume of the archipelago is likely the largest contribution to the gravitational load and was presumably constructed simultaneously for both regions (Geist et al., 2008). We evaluate the subsidence modified sea-level curve that best reproduces the observed terrace distributions (**Figure 11**). This is done by comparing the terrace depth distribution to sea level depth distributions, which are first offset at a constant rate between 0 and 1 m/ka, which is reasonable for the archipelago of 1–2 Ma in age (**Figure 12**; Geist et al., 2014). These depth distributions are then time integrated to represent the probability that sea level has reached a given depth over the past 1 Ma. Similarity between the actual terrace depth distribution and that predicted from sea level history with an imposed subsidence rate are assessed using the Kullback-Leibler Divergence (D_{KL}), which is a metric for assessing the amount of information that is lost by substituting the terrace distribution for the subsidence adjusted sea-level curve at each subsidence rate (**Figures 12A,B**). The lowest D_{KL} is attained when the substituted distribution most closely matches that of the original distribution. The D_{KL} is calculated from the following equation:

$$D_{KL}(p||q) = \sum_{x} p(x) \cdot \log \frac{p(x)}{q(x)} \quad (1)$$

where x is depth in 1 m intervals, $p(x)$ is the terrace depth distribution and $q(x)$ is the distribution produced by the integration of the sea-level curve. We discretize depth in 1 m intervals. The summation is an approximation of the integral definition of the D_{KL} (see MacKay (2003) for more details). In addition to the D_{KL} we compare the cumulative density functions for the subsidence-corrected sea level distributions and terrace distributions using a Kilinogorov-Smirnov (k-s test), using the MATLAB function *kstest2* to assess the similarity of the curves. The k-s test provides a p-value, which indicates the similarity of the curves; a p-value > 0.05 indicates that the curves are indistinguishable at the 95% confidence interval (**Figures 12A,C**). From the D_{KL} for each subsidence rate there is a clear trend and minima at 0.2 m/ka. Similarly, the results from the k-s test indicate that the two cumulative probability density curves are indistinguishable between 0.2 and 0.4 m/ka. These subsidence rates are slightly lower than, but on the same order as estimates by other researchers (0.4–0.5 m/ka; Geist et al., 2014).

Our calculated rate of subsidence of 0.2 m/ka is an order of magnitude faster than what is predicted for transport beyond a hotspot swell similar to that of Hawaii for young lithosphere (0.04 m/ka; Detrick and Crough, 1978), thus is more likely due to loading or aging of the underlying lithosphere. The subsidence rates are nearly identical to those determined for Ascension Island near the Mid-Atlantic Ridge (0.3 m/ka; Minshull et al., 2010), which is on similarly aged lithosphere (∼6–10 Ma; Minshull and Brozena, 1997; Villagómez et al., 2007), and of approximately the same age (2–3 Ma; Minshull et al., 2010) as the islands of Floreana and Santiago. Minshull et al. (2010) invoke

viscoelastic relaxation in response to loading of the volcanic edifice as the only mechanism able to produce the observed subsidence rates. Given that we only observe 200 m of subsidence in our dataset, it is possible that elastic loading (110 m; Minshull et al., 2010), and/or cooling of the lithosphere away from the Galápagos spreading center over the past 2 Ma (e.g., Marty and Cazenave, 1989) could together produce the observed subsidence (∼150 m; Kane and Hayes, 1994). It is out of the scope of this study to determine the mechanisms of subsidence, but it seems likely that volcanic loading is important in the evolution of the Galápagos Archipelago.

We have mapped the area that would be exposed at two time intervals based on the sea-level curves of Bintanja et al. (2005) modified using our derived subsidence rates. Land between Isabela and Santa Cruz could be connected as early as the LGM (**Figure 13A**), but additional mapping is needed to prove this given that significant changes may have occurred in island volume due to volcanic activity over the past 20 ka. Further,

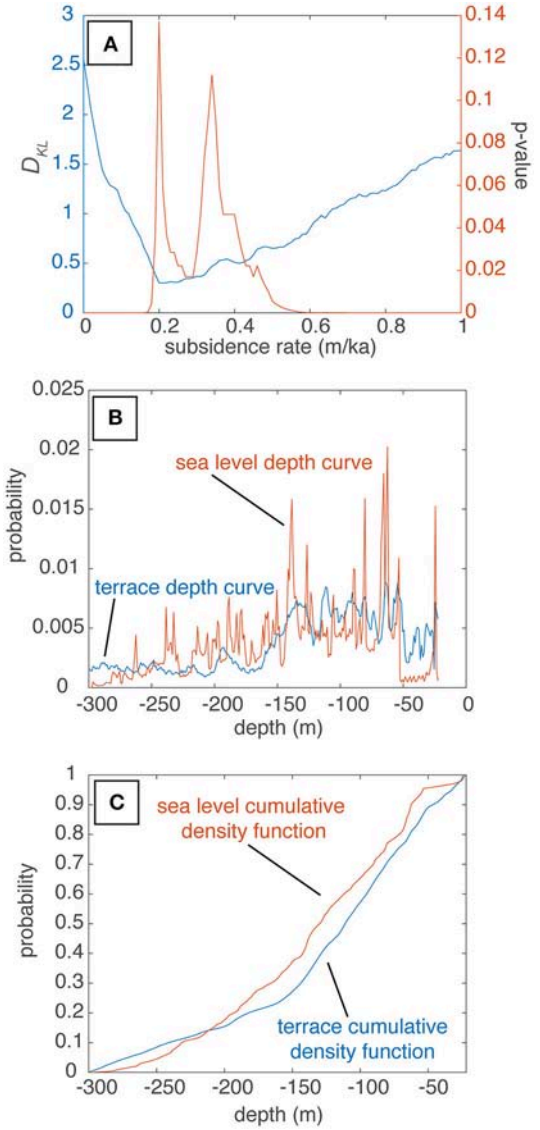

FIGURE 12 | Comparison of sea level data with terrace depths at various subsidence rates. **(A)** Kullback-Leibler Divergence (D_{KL}; blue line) and k-s test (red line) results comparing terrace to sea level distributions adjusted by subsidence rates between 0 and 1 m/ka. The minimum D_{KL} between the two distributions is 0.2 m/ka, and the cumulative distribution function of the curves are indistinguishable at the 2-sigma confidence interval between about 0.2 and 0.4 m/ka. **(B)** Comparison of probability density functions for terrace distribution (blue line) and time integrated sea level distribution adjusted for a subsidence rate of 0.2 m/ka (red line) used for calculating the D_{KL}. **(C)** Comparison of cumulative density functions for terrace distribution (blue line) and time integrated sea level distribution adjusted for a subsidence rate of 0.2 m/ka (red line) used for performing the k-s test.

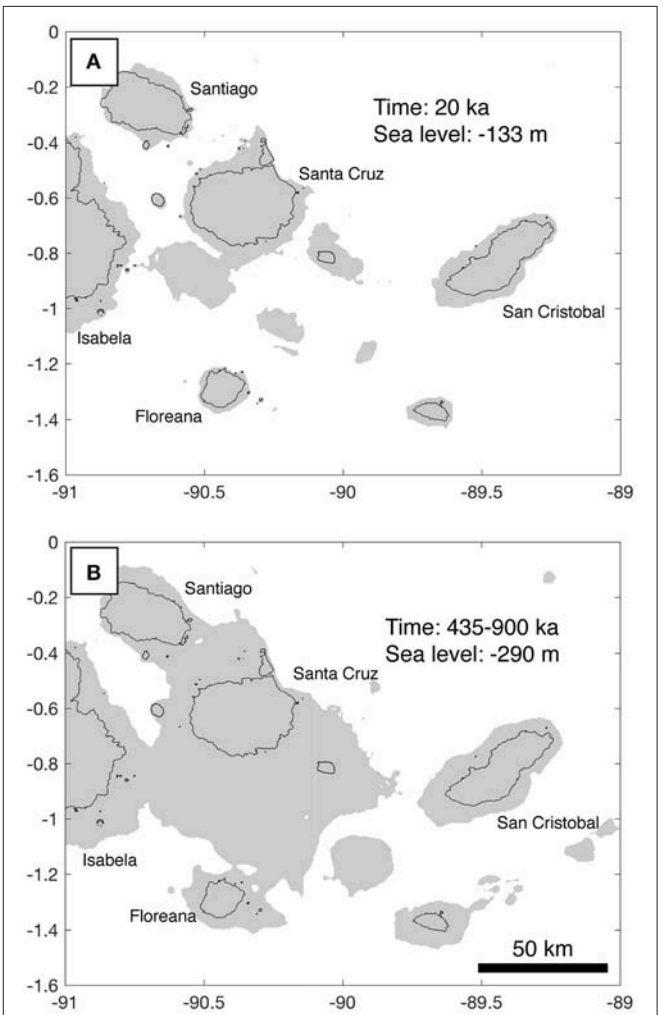

FIGURE 13 | (A) Map of the central Galápagos Archipelago during the last glacial maximum assuming a subsidence rate of 0.2 m/ka. Black lines show modern shorelines. Gray area shows exposed areas adjusted for the combined sea level change and subsidence. **(B)** Map of the central Galápagos Archipelago that was emerged based on the max depth that rounded cobbles on erosional terraces were observed (290 m; **Figure 8B**). Black lines show modern shorelines. Gray area shows exposed areas adjusted for the combined sea level change and subsidence. Based on our best-fit subsidence rates of 0.2 to 0.4 m/ka this paleo-topography was first possible between 435 and 900 ka.

given the current data, we have provided evidence that the central Galápagos Archipelago areas that are now at 290 m water depth were in the past at <130 m water depth. This evidence includes rounded cobbles atop a terrace at that depth in the Floreana region (**Figure 8**) and seamounts with scalloped upper flanks and terraces resembling those exposed during the last glacial maximum in the Santiago region (**Figure 4C**). We estimate based on the range of subsidence rates that we determined (0.2–0.4 m/ka) that at 435–900 ka, these surfaces were at sea level during the lowstands (**Figure 13B**). Using the previously accepted value of 0.5 m/ka (Geist et al., 2014), these terraces were at lowstand sea levels of ∼130 m water depth at 350 ka. During sea level lowstands in this time period it is conceivable that all islands in the central archipelago could be connected by present day bathymetric highs. This prediction hinges on limited modification of the potential bridges due to sedimentation, which at this point cannot be determined due to the lack of seismic data in the Galápagos. Future work should be targeted toward these drowned land bridges in search of evidence for their exposure history to confirm this speculation and search for evidence of deeper features that show evidence for exposure at the sea surface. These observations would provide a means to more rigorously assess the spatial and temporal variations in subsidence rate across the archipelago. Further, direct dating of terraces through micropaleontology or dating of sparse carbonates buried by beach cobbles on the deepest terraces may provide further age-depth relationships.

CONCLUSION

Through direct seafloor observations of seamounts and correlation with bathymetric data we have confirmed that the modern archipelago has experienced significant subsidence over the past ∼1 Ma. We observed rounded cobbles and boulders in addition to other bedrock features, which we interpret to represent exposure of many seamounts at the sea surface. Bathymetric features, including submarine terraces, are correlated with direct seafloor observations of erosional features, which we use to create a framework to identify seamounts, which have experienced exposure at the sea surface. Seamounts with rounded cobble deposits and with similar morphologic features are observed to depths of 300 m in both the Santiago and Floreana regions. These are the first direct observations that indicate all islands in the central archipelago have subsided around ∼200 m and could have been at least intermittently connected in the past. Without independent age data on the seamount terraces we are able to use their distribution and established sea-level curves to assess subsidence rates, and thus obtain approximate timing of potential inter-island connections. The comparison of these distributions leads us to conclude that since the formation of the seamounts the archipelago has been subsiding between 0.2 and 0.4 m/ka. We infer from these subsidence rates that the deepest observed terraces were formed between 435 and 900 ka during or within close proximity to lowstands. Extending this record to greater depths (and ages), will impact the interpretation of inter-island migration and speciation in the Galápagos. Combined seafloor observation and use of seamount terrace depth distributions have the potential to provide a more complete and robust understanding of paleogeography in ocean island systems. As the resolution of the timing and nature of sea level fluctuations increases, the interpretations resulting from terrace depth distributions on seamounts will only improve.

AUTHOR CONTRIBUTIONS

All authors aided in the collection of shipboard data including submersible observations, video, rock samples and bathymetric mapping. DS conducted the primary data analysis and prepared the manuscript. SS contributed to the design of the study, facilitated shipboard and on-land data processing for bathymetric data, and aided in the preparation of the manuscript. VW contributed to the design of the study and aided in the preparation of the manuscript. MJ processed a majority of the shipboard bathymetric data and aided in the preparation of the manuscript.

FUNDING

This project was carried out with financial support from the NSF (OCE-1634685 to SS and OCE-1634952 to VW) and the Dalio Explore Fund.

ACKNOWLEDGMENTS

We would first like to thank the captain and crew of the M/V *Alucia* for their hard work during the cruise upon which the data for this project were acquired. Further, we would like to acknowledge the skilled HOV pilots for their dedication to the safety and success of the dive operations over the course of the cruise. We acknowledge the Galápagos National Park directorate for permission to map and collect submarine rock samples (PC-44-15), and our colleagues at the Charles Darwin Foundation for facilitating scientific collaboration in the Galápagos. We are grateful to the Government of Ecuador and INOCAR for permission to operate in their territorial waters and marine protected areas. We thank Dan Fornari, Mark Richards, Pelayo Salinas de León for their assistance in data acquisition and scientific input on the cruise, as well as Hannah Bercovici for assistance with rock sample preparation and data processing. We appreciate Neil Mitchell, Rui Quartau and Daneiele Casalbore for their detailed and thoughtful reviews, which greatly improved the manuscript.

SUPPLEMENTARY MATERIAL

The Supplementary Material for this article can be found online at: https://www.frontiersin.org/articles/10.3389/feart.2018.00088/full#supplementary-material

REFERENCES

Ali, J. R., and Aitchison, J. C. (2014). Exploring the combined role of eustasy and oceanic island thermal subsidence in shaping biodiversity on the Galápagos. *J. Biogeogr.* 41, 1227–1241. doi: 10.1111/jbi.12313

Allan, J. F., and Simkin, T. (2000). Fernandina volcano's evolved, well-mixed basalts: Mineralogical and petrological constraints on the nature of the Galápagos plume. *J. Geophys. Res.* 105, 6017–6041. doi: 10.1029/1999JB900417

Bintanja, R., van de Wal, R. S. W., and Oerlemans, J. (2005). Modelled atmospheric temperatures and global sea levels over the past million years. *Nature* 437, 125–128. doi: 10.1038/nature03975

Bohnenstiehl, D. R., Howell, J. K., White, S. M., and Hey, R. N. (2012). A modified basal outlining algorithm for identifying topographic highs from gridded elevation data, Part 1: motivation and methods. *Comput. Geosci.* 49, 308–314. doi: 10.1016/j.cageo.2012.04.023

Caccone, A., Gentile, G., Gibbs, J. P., Fritts, T. H., Snell, H. L., Betts, J., et al. (2002). Phylogeography and History of Giant Galapagos Tortoises. *Evolution* 56, 2052–2066. Available online at: http://www.jstor.org/stable/3094648

Campbell, J. F. (1984). Rapid subsidence of Kohala Volcano and its effect on coral reef growth. *Geo Mar. Lett.* 4, 31–36. doi: 10.1007/BF02237971

Carey, S., Fisher, C. R., de Leon, P. S., Roman, C., Raineault, N. A., Suarez, J., et al. (2016). Exploring the undersea world of the Galápagos Islands. *Ocean. Mag.* 29, 32–34.

Carsola, A. J., and Dietz, R. S. (1952). Submarine geology of two flat-topped northeast Pacific seamounts. *Am. J. Sci.* 250, 481–497. doi: 10.2475/ajs.250.7.481

Cas, R. A. F. (1992). Submarine volcanism: eruption styles, products, and relevance to understanding the host-rock successions to volcanic-hosted massive sulfide deposits. *Econ. Geol.* 87, 511–541. doi: 10.2113/gsecongeo.87.3.511

Casalbore, D. (2018). *Volcanic Islands and Seamounts. Submarine Geomorphology Springer Geology*. Cham: Springer, 333–347.

Casalbore, D., Falese, F., Martorelli, E., Romagnoli, C., and Chiocci, F. L. (2017). Submarine depositional terraces in the Tyrrhenian Sea as a proxy for paleo-sea level reconstruction: problems and perspective. *Quat. Int.* 439, 169–180. doi: 10.1016/j.quaint.2016.02.027

Casalbore, D., Romagnoli, C., Pimentel, A., Quartau, R., Casas, D., Ercilla, G., et al. (2015). Volcanic, tectonic and mass-wasting processes offshore Terceira Island (Azores) revealed by high-resolution seafloor mapping. *Bull. Volcanol.* 77:24. doi: 10.1007/s00445-015-0905-3

Chaytor, J. D., Keller, R. A., Duncan, R. A., and Dziak, R. P. (2007). Seamount morphology in the Bowie and Cobb hot spot trails, Gulf of Alaska. *Geochem. Geophys. Geosyst.* 8, 1–26. doi: 10.1029/2007GC001712

Christie, D. M., Duncan, R. A., McBirney, A. R., Richards, M. A., White, W. M., Harpp, K. S., et al. (1992). Drowned islands downstream from the Galápagos hotspot imply extended speciation times. *Nature* 355, 246–248. doi: 10.1038/355246a0

Clague, D. A., Moore, J. G., and Reynolds, J. R. (2000). Formation of submarine flat-topped volcanic cones in Hawai'i. *Bull. Volcanol.* 62, 214–233. doi: 10.1007/s004450000088

Couce, E., Ridgwell, A., and Hendy, E. J. (2012). Environmental controls on the global distribution of shallow-water coral reefs. *J. Biogeogr.* 39, 1508–1523. doi: 10.1111/j.1365-2699.2012.02706.x

Darwin, C. (1859). *The Origin of Species by Means of Natural Selection*. London.

Detrick, R. S., and Crough, S. T. (1978). Island subsidence, hot spots, and lithospheric thinning. *J. Geophys. Res. Solid Earth* 83, 1236–1244.

Geist, D. (1984). On the emergence and submergence of the Galápagos islands. *Not. Galápagos* 56, 5–9.

Geist, D., Diefenbach, B. A., Fornari, D. J., Kurz, M. D., Harpp, K., and Blusztajn, J. (2008). Construction of the Galápagos platform by large submarine volcanic terraces. *Geochem. Geophys. Geosyst.* 9, 1–27. doi: 10.1029/2007GC001795

Geist, D. J., Fornari, D. J., Kurz, M. D., Harpp, K. S., Adam Soule, S., Perfit, M. R., et al. (2006). Submarine Fernandina: Magmatism at the leading edge of the Galápagos hot spot. *Geochem. Geophys. Geosyst.* 7, 1–27. doi: 10.1029/2006GC001290

Geist, D., Snell, H., Snell, H., Goddard, C., and Kurz, M. D. (2014). *A Paleogeographic Model of the Galápagos Islands and Biogeographical and Evolutionary Implications*. Galápagos Nat. Lab. Earth Sci. Am. Geophys. Union, Washington DC, 145–166.

Harpp, K., and Geist, D. (2002). Wolf-Darwin lineament and plume-ridge interaction in northern Galápagos. *Geochem. Geophys. Geosyst.* 3, 1–19. doi: 10.1029/2002GC000370

Harpp, K. S., Fornari, D. J., Geist, D. J., and Kurz, M. D. (2003). Genovesa Submarine Ridge: A manifestation of plume-ridge interaction in the northern Galápagos Islands. *Geochem. Geophys. Geosyst.* 4, 1–27. doi: 10.1029/2003GC000531

Huppert, K. L., Royden, L. H., and Perron, J. T. (2015). Dominant influence of volcanic loading on vertical motions of the Hawaiian Islands. *Earth Planet. Sci. Lett.* 418, 149–171. doi: 10.1016/j.epsl.2015.02.027

Kane, K. A., and Hayes, D. E. (1994). A new relationship between subsidence rate and zero-age depth. *J. Geophys. Res. Earth* 99, 21759–21777. doi: 10.1029/94JB01747

Kim, G. B., Yoon, S. H., Sohn, Y. K., and Kwon, Y. K. (2013). Wave-planation surfaces in the mid-western East Sea (Sea of Japan): indicators of subsidence history and paleogeographic evolution of back-arc basin. *Mar. Geol.* 344, 65–81. doi: 10.1016/j.margeo.2013.07.008

Kleypas, J. A., Mcmanus, J. W., and Menez, L. A. B. (1999). Environmental limits to coral reef development : where do we draw the line? *Am. Zoo.* 39 , 146–159. doi: 10.1093/icb/39.1.146

Kokelaar, B. P., and Durant, G. P. (1983). The submarine eruption and erosion of Surtla (Surtsey), Iceland. *J. Volcanol. Geotherm. Res.* 19, 239–246. doi: 10.1016/0377-0273(83)90112-9

Kurz, M. D., and Geist, D. (1999). Dynamics of the Galápagos hotspot from helium isotope geochemistry. *Geochim. Cosmochim. Acta* 63, 4139–4156. doi: 10.1016/S0016-7037(99)00314-2

Kurz, M. D., Rowland, S. K., Curtice, J., Saal, A. E., and Naumann, T. (2014). "Eruption rates for fernandina volcano: a new chronology at the galápagos hotspot center," in *The Galápagos: A Natural Laboratory for the Earth Sciences*, eds K. S. Harpp, E. Mittelstaedt, N. d'Ozouville, and D. W. Graham (Washington, DC), 41–54. doi: 10.1002/9781118852538.ch4

Lambeck, K. (1984). Subsidence of a guyot west of Flores, Azores. *Can. J. Earth Sci.* 21, 960–963. doi: 10.1139/e84-100

Ludwig, K. R., Szabo, B. J., Moore, J. G., and Simmons, K. R. (1991). Crustal subsidence rates off Hawaii determined from 234U/238 ages of drowned coral reefs. *Geology* 19, 171–174. doi: 10.1130/0091-7613(1991)019<0171:CSROHD>2.3.CO;2

MacKay, D. J. C. (2003). *Information Theory, Inference and Learning Algorithms*. Cambridge: Cambridge University Press.

Marty, J. C., and Cazenave, A. (1989). Regional variations in subsidence rate of oceanic plates: a global analysis. *Earth Planet. Sci. Lett.* 94, 301–315. doi: 10.1016/0012-821X(89)90148-9

McBirney, A. R., and Williams, H. (1969). Geology and petrology of the Galápagos Islands. *Geol. Soc. Am. Mem.* 118, 1–197. doi: 10.1130/MEM118-p1

Menard, H. W. (1983). Insular erosion, isostasy, and subsidence. *Science* 220, 913–918. doi: 10.1126/science.220.4600.913

Menard, H. W., and Ladd, H. S. (1963). Oceanic islands, seamounts, guyots and atolls. *Sea* 3, 365–385.

Minshull, T. A., and Brozena, J. M. (1997). Gravity anomalies and flexure of the lithosphere at Ascension Island. *Geophys. J. Int.* 131, 347–360. doi: 10.1111/j.1365-246X.1997.tb01227.x

Minshull, T. A., Ishizuka, O., and Garcia-Castellanos, D. (2010). Long-term growth and subsidence of Ascension Island: constraints on the rheology of young oceanic lithosphere. *Geophys. Res. Lett.* 37, 3–7. doi: 10.1029/2010GL045112

Mitchell, N. C. (2001). Transition from circular to stellate forms of submarine volcanoes. *J. Geophys. Res. Solid Earth* 106, 1987–2003. doi: 10.1029/2000JB900263

Mitchell, N. C., Masson, D. G., Watts, A. B., Gee, M. J. R., and Urgeles, R. (2002). The morphology of the submarine flanks of volcanic ocean islands: a comparative study of the Canary and Hawaiian hotspot islands. *J. Volcanol. Geotherm. Res.* 115, 83–107. doi: 10.1016/S0377-0273(01)00310-9

Mitchell, N. C., Stretch, R., Oppenheimer, C., Kay, D., and Beier, C. (2012). Cone morphologies associated with shallow marine eruptions: east Pico Island, Azores. *Bull. Volcanol.* 74, 2289–2301. doi: 10.1007/s00445-012-0662-5

Mittelstaedt, E., Soule, S., Harpp, K., Fornari, D., McKee, C., Tivey, M., et al. (2012). Multiple expressions of plume-ridge interaction in the Galápagos: volcanic lineaments and ridge jumps. *Geochem. Geophys. Geosyst.* 13:Q05018. doi: 10.1029/2012GC004093

Moore, J. G. (1970). Relationship between subsidence and volcanic load, Hawaii. *Bull. Volcanol.* 34, 562–576. doi: 10.1007/BF02596771

Moore, J. G., Clague, D. A., and Normark, W. R. (1982). Diverse basalt types from Loihi seamount, Hawaii. *Geology* 10, 88–92. doi: 10.1130/0091-7613(1982)10<88:DBTFLS>2.0.CO;2

Moore, J. G., and Fornari, D. J. (1984). Drowned reefs as indicators of the rate of subsidence of the island of Hawaii. *J. Geol.* 92, 752–759. doi: 10.1086/628910

Naumann, T., and Geist, D. J. (2000). Volcano, Isabela Island, Galµpagos : implications for the development. *Bull. Volcanol.* 61, 497–514. doi: 10.1007/s004450050001

Passaro, S., Ferranti, L., and de Alteriis, G. (2011). The use of high-resolution elevation histograms for mapping submerged terraces: tests from the Eastern Tyrrhenian Sea and the Eastern Atlantic Ocean. *Quat. Int.* 232, 238–249. doi: 10.1016/j.quaint.2010.04.030

Pratt, R. M., and Dill, R. F. (1974). Deep eustatic terrace levels: Further speculations. *Geology* 2, 155–156. doi: 10.1130/0091-7613(1974)2<155:DETLFS>2.0.CO;2

Quartau, R., Hipólito, A., Romagnoli, C., Casalbore, D., Madeira, J., Tempera, F., et al. (2014). The morphology of insular shelves as a key for understanding the geological evolution of volcanic islands: insights from Terceira Island (Azores). *Geochem. Geophys. Geosyst.* 15, 1801–1826. doi: 10.1002/2014GC005248

Quartau, R., Madeira, J., Mitchell, N. C., Tempera, F., Silva, P. F., and Brandão, F. (2015). The insular shelves of the Faial-Pico Ridge: a morphological record of its geologic evolution (Azores archipelago). *Geochem. Geophys. Geosyst.* 16, 1401–1420. doi: 10.1002/2015GC005733

Quartau, R., Madeira, J., Mitchell, N. C., Tempera, F., Silva, P. F., and Brandão, F. (2016). Reply to comment by Marques et al. on "The insular shelves of the Faial-Pico Ridge (*Azores archipelago*): A morphological record of its evolution." *Geochem Geophys Geosyst.* 17, 633–641. doi: 10.1002/2015GC006180

Quartau, R., Trenhaile, A. S., Mitchell, N. C., and Tempera, F. (2010). Development of volcanic insular shelves: insights from observations and modelling of Faial Island in the Azores Archipelago. *Mar. Geol.* 275, 66–83. doi: 10.1016/j.margeo.2010.04.008

Ramalho, R. S., Quartau, R., Trenhaile, A. S., Mitchell, N. C., Woodroffe, C. D., and Ávila, S. P. (2013). Coastal evolution on volcanic oceanic islands: a complex interplay between volcanism, erosion, sedimentation, sea-level change and biogenic production. *Earth Sci. Rev.* 127, 140–170. doi: 10.1016/j.earscirev.2013.10.007

Rassmann, K. (1997). Evolutionary age of the Galápagos iguanas predates the age of the present Galápagos Islands. *Mol. Phylogenet. Evol.* 7, 158–172. doi: 10.1006/mpev.1996.0386

Ricklefs, R. E., and Bermingham, E. (2007). The causes of evolutionary radiations in archipelagoes: passerine birds in the lesser antilles. *Am. Nat.* 169, 285–297. doi: 10.1086/510730

Romagnoli, C., Casalbore, D., Ricchi, A., Lucchi, F., Quartau, R., Bosman, A., et al. (2018). Morpho-bathymetric and seismo-stratigraphic analysis of the insular shelf of Salina (*Aeolian archipelago*) to unveil its Late-Quaternary geological evolution. *Mar. Geol.* 395, 133–151. doi: 10.1016/j.margeo.2017.10.003

Romagnoli, C., and Jakobsson, S. P. (2015). Post-eruptive morphological evolution of island volcanoes: surtsey as a modern case study. *Geomorphology* 250, 384–396. doi: 10.1016/j.geomorph.2015.09.016

Rubin, K. H., Fletcher, C. H., and Sherman, C. (2000). Fossiliferous Lana'i deposits formed by multiple events rather than a single giant tsunami. *Nature* 408, 675–681. doi: 10.1038/35047008

Santos, R. S., Tempera, F., Colaço, A., Cardigos, F., and Morato, T. (2010). Spotlight 11: Dom João de Castro Seamount. *Oceanography* 23, 200–201. doi: 10.5670/oceanog.2010.83

Schwartz, D. M., Wanless, V. D., Berg, R., Jones, M., Fornari, D. J., Soule, S. A., et al. (2018). Petrogenesis of alkalic seamounts on the Galápagos Platform. *Deep Sea Res. Part II Top. Stud. Oceanogr.* 150, 170–180. doi: 10.1016/j.dsr2.2017.09.019

Schwartz, M. (1972). Seamounts as sea-level indicators. *Geol. Soc. Am. Bull.* 83, 2975–2979. doi: 10.1130/0016-7606(1972)83[2975:SASI]2.0.CO;2

Shackleton, N. J. (1987). Oxygen isotopes, ice volume and sea level. *Quat. Sci. Rev.* 6, 183–190. doi: 10.1016/0277-3791(87)90003-5

Siddall, M., Rohling, E., Almogi-Labin, A., Hemleben, C., Meischner, D., Schmelzer, I., et al. (2003). Sea-level fluctuations during the last glacial cycle. *Nature* 423, 853–858. doi: 10.1038/nature01690

Sinton, C. W., Harpp, K. S., and Christie, D. M. (2014). A preliminary survey of the northeast seamounts, galápagos platform. *Galápagos A Nat. Lab. Earth Sci.* 335–362. doi: 10.1002/9781118852538.ch16

Smith, W. H. F., and Sandwell, D. T. (1997). Global sea floor topography from satellite altimetry and ship depth soundings. *Science* 277, 1956–1962. doi: 10.1126/science.277.5334.1956

Trenhaile, A. S. (1987). *The Geomorphology of Rock Coasts*. Oxford: Oxford University Press.

Trenhaile, A. S. (2000). Modeling the development of wave-cut shore platforms. *Mar. Geol.* 166, 163–178. doi: 10.1016/S0025-3227(00)00013-X

Villagómez, D. R., Toomey, D. R., Geist, D. J., Hooft, E. E. E., and Solomon, S. C. (2014). Mantle flow and multistage melting beneath the Galápagos hotspot revealed by seismic imaging. *Nat. Geosci.* 7, 151–156. doi: 10.1038/ngeo2062

Villagómez, D. R., Toomey, D. R., Hooft, E. E. E., and Solomon, S. C. (2007). Upper mantle structure beneath the Galápagos Archipelago from surface wave tomography. *J. Geophys. Res.* 112:B07303. doi: 10.1029/2006JB004672

Wagle, B. G., Vora, K. H., Karisiddaiah, S. M., Veerayya, M., and Almeida, F. (1994). Holocene submarine terraces on the western continental shelf of India; Implications for sea-level changes. *Mar. Geol.* 117, 207–225. doi: 10.1016/0025-3227(94)90016-7

Watts, A. B., and Ten Brink, U. S. (1989). Crustal structure, flexure, and subsidence history of the Hawaiian Islands. *J. Geophys. Res. Solid Earth* 94, 10473–10500. doi: 10.1029/JB094iB08p10473

Weatherall, P., Marks, K. M., Jakobsson, M., Schmitt, T., Tani, S., Arndt, J. E., et al. (2015). A new digital bathymetric map of the world's oceans. *Earth Space Sci.* 2, 331–345. doi: 10.1002/2015EA000107

Werner, R., Hoernle, K., Barckhausen, U., and Hauff, F. (2003). Geodynamic evolution of the Galápagos hot spot system (Central East Pacific) over the past 20 m.y.: Constraints from morphology, geochemistry, and magnetic anomalies. *Geochem. Geophys. Geosyst.* 4. doi: 10.1029/2003GC000576

White, W. M., McBirney, A. R., and Duncan, R. A. (1993). Petrology and geochemistry of the Galápagos Islands: Portrait of a pathological mantle plume. *J. Geophys. Res. Solid Earth* 98, 19533–19563. doi: 10.1029/93JB02018

Wyles, J. S., and Sarich, V. M. (1983). "Are the Galápagos iguanas older than the Galápagos? Molecular evolution and colonization models for the archipelago," in *Patterns of Evolution in Galapagos Organisms*, eds R. I. Bowman, M. Berson, and A. E. Levinton (San Francisco, CA: American Association for the Advancement of Science, Pacific Division), 177–185.

Zecchin, M., Ceramicola, S., Lodolo, E., Casalbore, D., and Chiocci, F. L. (2015). Episodic, rapid sea-level rises on the central Mediterranean shelves after the Last Glacial Maximum: a review. *Mar. Geol.* 369, 212–223. doi: 10.1016/j.margeo.2015.09.002

Conflict of Interest Statement: The authors declare that the research was conducted in the absence of any commercial or financial relationships that could be construed as a potential conflict of interest.

Copyright © 2018 Schwartz, Soule, Wanless and Jones. This is an open-access article distributed under the terms of the Creative Commons Attribution License (CC BY). The use, distribution or reproduction in other forums is permitted, provided the original author(s) and the copyright owner(s) are credited and that the original publication in this journal is cited, in accordance with accepted academic practice. No use, distribution or reproduction is permitted which does not comply with these terms.

frontiers in Earth Science

ORIGINAL RESEARCH
published: 04 September 2018
doi: 10.3389/feart.2018.00121

Variance of the Flexure Model Predictions With Rejuvenated Volcanism at Kīlauea Point, Kaua'i, Hawai'i

Thor Thordarson[1]* *and Michael O. Garcia*[2]

[1] Faculty and Institute of Earth Sciences, University of Iceland, Reykjavik, Iceland, [2] Department of Geology and Geophysics, University of Hawai'i at Mānoa, Honolulu, HI, United States

The origin of rejuvenated volcanism on mantle plume related oceanic islands remains controversial. One commonly cited model is decompressional melting related to plate flexure from the rapid loading of the lithosphere by the formation of a shield volcano above the plume stem. This model provides testable predictions about the timing and subsidence history of the island. Here we evaluate the flexure model by examining the products of three well dated rejuvenation stage eruptions at Kīlauea Point, Kaua'i, (Hawaii); the 2.65 ± 0.35 Ma Mōkōlea Point lava, 1.67 ± 0.11 Ma for Crater Hill tuff cone and 0.69 ± 0.03 Ma for Kīlauea Point lava events. These eruptions record the flexure of the island over a 2 Ma period, the longest sequence of rejuvenated volcanism within the Hawaiian Islands. These three eruptions, including two subaerial flows (the Mōkōlea Point and Kīlauea Point lavas) and the only phreatomagmatic vent structure on Kaua'i (the Crater Hill tuff cone), document the progressive sinking and uplift of the island related to sea level as the island drifted away from the Hawaiian hot spot at ∼10 cm/year. The timing of volcanism and the elevation of Kīlauea Point relative to sea level are inconsistent with the predictions of the flexural melting model. These new results indicate that decompression melting cannot be the sole driver for rejuvenated volcanism on Kaua'i. Additional explanations are needed to account for the timing and volume of rejuvenated volcanism in Hawai'i.

Keywords: Hawai'i, Kaua'i, Kīlauea Point, rejuvenated volcanism, volcanic succession, geochronology, phreatomagmatic, effusive

OPEN ACCESS

Edited by:
Richard James Brown, Durham University, United Kingdom

Reviewed by:
J. Gregory Shellnutt, National Taiwan Normal University, Taiwan
Jörn-Frederik Wotzlaw, ETH Zürich, Switzerland

***Correspondence:**
Thor Thordarson
torvth@hi.is

Specialty section:
This article was submitted to Volcanology, a section of the journal Frontiers in Earth Science

Received: *06 March 2018*
Accepted: *10 August 2018*
Published: *04 September 2018*

Citation:
Thordarson T and Garcia MO (2018) Variance of the Flexure Model Predictions With Rejuvenated Volcanism at Kīlauea Point, Kaua'i, Hawai'i. Front. Earth Sci. 6:121. doi: 10.3389/feart.2018.00121

INTRODUCTION

Rejuvenated magmatism on Hawaiian and other ocean islands occurs hundreds of kilometers downstream from the stem of the ascending mantle plume following a hiatus of ∼0·5–2 millions of years (Myrs) in volcanism (e.g., Macdonald et al., 1983; Garcia et al., 2010). The six oldest of nine main Hawaiian Islands (spanning the age range of ∼6 to 1.5 Myrs; Garcia et al., 2010) feature rejuvenated volcanism. Although, products of rejuvenated volcanism represent a small fraction of the total volume of individual islands or ≤0.1 vol. % (e.g., Walker, 1990; Garcia et al., 2010), it poses significant risk on the more densely populated islands (i.e., Kaua'i, O'ahu, Moloka'i, and Maui). The rejuvenated volcanic products are commonly highly alkalic in nature and geochemically distinct from the underlying shield lavas (e.g., Clague and Frey, 1982; Cousens and Clague, 2015).

The indication of a depleted source for the rejuvenated magmatism in Hawaii, inferred to be either in the ocean lithosphere or as a component of the deflected mantle plume (e.g., Maaløe et al., 1992; Lassiter et al., 2000; Yang et al., 2003; Fekiacova et al., 2007), has resulted in three conceptual models for its origin: (i) melting of the oceanic lithosphere (e.g., Gurriet, 1987), (ii) decompressional melting of the plume following lateral spreading beneath the lithosphere (e.g., Ribe and Christensen, 1999), and (iii) decompressional melting caused by flexural uplift as a consequence of lithospheric loading above the plume stem (e.g., Jackson and Wright, 1970). Accordingly, as each volcano drifts off the plume, the subsidence is followed by uplift as it rides the fore-bulge of the Hawaiian flexural arch and subsides after passing its crest (e.g., Wessel, 1993). It has been proposed that the distance (i.e., the temporal gap) between the loading islands and the flexural arch is on par with the distance between contemporaneous shield and rejuvenation volcanism, implying that these features are intrinsically linked (e.g., Bianco et al., 2005).

These models provide predictions on the age range of the rejuvenated volcanic constructs as well as the range in erupted magma volumes and compositions. The lithospheric melting and decompressional melting models fail to account for the South and North Arch Volcanic Fields (e.g., Lipman et al., 1989; Clague et al., 1990) that formed on the flexural arch ∼250 km off the of the island-chain axis (e.g., Bianco et al., 2005). However, the predictableness of the flexural uplift model implies that it could be evaluated, or even validated, via examination of age-constrained sequences of rejuvenated volcanic units. Such an opportunity is provided at Kīlauea Point on Kaua'i (**Figure 1**), where three pulses of rejuvenated volcanism span ∼2 Myrs, covering the main pulse of rejuvenated volcanism (e.g., Garcia et al., 2010). This site also records two oscillations of the island relative to sea level. Here we present a new map and analysis of the rejuvenated volcanic succession at Kīlauea Point. The results and interpretations are used to evaluate the timing of subsidence and flexural uplift, and its impact on rejuvenated volcanism on Kaua'i.

GEOLOGIC BACKGROUND

The island of Kaua'i features the second oldest and the most voluminous record of rejuvenated volcanism among the Hawaiian Islands, covering the eastern half of the island (**Figure 1**). The rejuvenated lavas rest unconformably on shield-building Wameia Canyon tholeiite lavas (∼3.9–5.1 million years ago) and post-shield lava (3.6–3.9 million years ago; Macdonald et al., 1960; Sherrod et al., 2007; Garcia et al., 2010; Cousens and Clague, 2015; Sherrod et al., 2015). The rapid loading of Cretaceous lithosphere under the Hawaiian Islands has caused several km of subsidence for the older shield volcanoes (Moore,

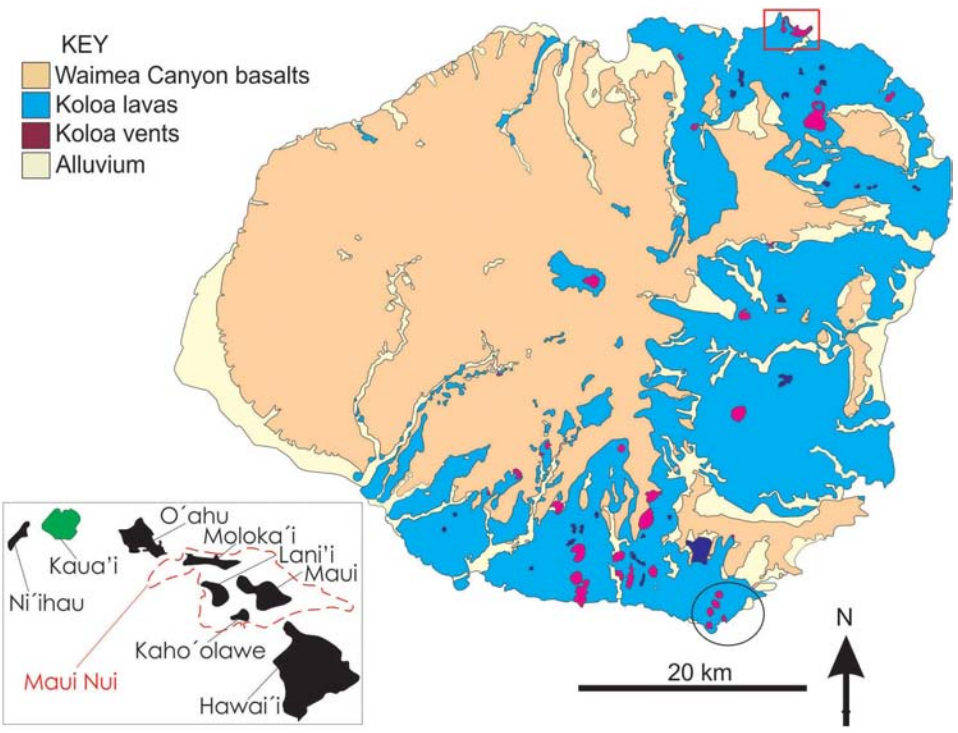

FIGURE 1 | Geological map of island of Kaua'i showing the distribution of the main rock units including vents (purple areas) for the rejuvenated Kōloa Volcanic Series. The location of the study area, Kīlauea Point, is indicated by the red box. The dark blue areas are lakes and the black circles outlines the study area of Hearty et al. (2005), see text for further details. (Inset: map of the chain of Hawaiian Islands showing the approximate outlines of Maui Nui (Greater Maui). This volcanic complex was forming over the Hawaiian hotspot when the Kōloa Volcanic Series was erupted. Redrafted using information from Sherrod et al. (2007) and Garcia et al. (2010).

1987). The shield stage shoreline of the island until ∼4 million years ago is currently at least 6 km offshore from Kīlauea Point and ∼0.85 to 1 km below sea level (Flinders et al., 2010). Rejuvenated volcanism on Kaua'i (Kōloa Volcanic Series) formed ∼58 km^3 (dense rock equivalent) of alkali basalt tephra cones and lava flow fields between 0.15 and ∼2.6 million years ago (Garcia et al., 2010). Recent $^{40}Ar/^{39}Ar$ dating of chips of basanite and nephelinite from drilling in Lihue Basin reveal ages in the range of ∼3.1 to ∼3.4 million years ago (e.g., Sherrod et al., 2015), suggesting that Kōloa-like magmatism may have followed the post-shield stage without a significant break in volcanic activity (e.g., Cousens and Clague, 2015). About 40 widely dispersed Kōloa vent structures have been identified (Macdonald et al., 1960). Most of the vent structures consist of scoria or spatter cones and their associated 'a'a and pāhoehoe lava flow fields cover the lowlands the eastern side of the island and also filled many of the deep valleys on the island to depths of hundreds of meters (Macdonald et al., 1960; Garcia et al., 2010). Volcanic units within the Kōloa Volcanic Series are either separated by sedimentary deposits (mostly conglomerates) or soil horizons. The northernmost subaerial Kōloa vents are found at Kīlauea Point on the northeast shore of the island (**Figure 1**). Here the volcanic succession is unique in the Hawaiian Islands in recording at a single location three eruptive events spanning the bulk of the main period of rejuvenation stage volcanism on Kaua'i as well as preserving the only phreatomagmatic vent structures of the Kōloa Volcanic Series (Macdonald et al., 1960).

VOLCANIC SUCCESSION AT KĪLAUEA POINT: LITHOLOGY, ARCHITECTURE AND HISTORY

Our new geological map of the Kīlauea Point area highlights the superbly exposed Kōloa volcanic sequence (**Figure 2**). Here a nephelinite lava outcrops at the nearby Mōkōlea Point. It is overlain by a ∼90-m-thick cone sequence of phreatomagmatic tephra, which is cut by ∼1-m-thick olivine-bearing basanitoid dike that produced a ∼100-m-thick fountain-fed basanite spatter and lava that cap the succession (**Figures 2**, **3a**). These three eruptive units are referred to here, from the oldest to the youngest, as the Mōkōlea Point lava, Crater Hill tuff cone, and Kīlauea Point lava.

Mōkōlea Point Lava (2.65 Ma)

The Mōkōlea Point lava is exposed along the base of the Mōkōlea Point (**Figures 2**, **3**). The Mōkōlea Point lava is ≥8 m thick at the northern tip of the point as its lower contact is submerged (**Figure 3**). The upper part of this exposure consists of decimeter to meter thick pāhoehoe sheet lobes and spongy pāhoehoe (i.e., equivalent to P- and S-type pāhoehoe of Wilmoth and Walker, 1993). **Figure 4** illustrates the typical three-fold vertical division of the Mōkōlea Point lava lobes into vesicular upper crust, lava core and basal crust, which is indicative of emplacement by insulated transport and flow inflation (e.g., Self et al., 1998; Thordarson and Self, 1998). On the northern tip of the Mōkōlea Point and at the very top of the lobe sequence, a 0.5–2 m-thick sheet lobe is separated from the rest of the Mōkōlea Point lava by 5–20 cm-thick normally graded, ash to fine lapilli tephra bed (**Figure 3d**). The tephra contains abundant sub-mm size olivine macrocrysts, similar to those observed in the Mōkōlea Point lava. Also, morphologically and petrographically the top lobe is identical to the lobes beneath the tephra. This indicates that a distinct explosive phase with associated tephra fallout that took place toward the end of the Mōkōlea Point eruption. Consequently, the top lobe represents a late-stage lava emplacement in that event.

The pāhoehoe nature of the Mōkōlea Point lava confirms that it was formed by a subaerial eruption. The surface of the lava slopes inland (i.e., to the west-southwest, **Figures 2**, **3b**) at a shallow angle of ∼1°. It drops 8 m over a distance of 620 m disappearing below sea level to the west along the shoreline of the bay (**Figure 2**). It is noteworthy that upper surface of the Mōkōlea Point lava is partly eroded, providing evidence of subaerial erosion. The distinctive slope of the flow surface strongly indicates that the lava advanced from the east-northeast, implying that the source vent was located ocean ward of the present-day shoreline (**Figure 5**). Hence, when the Mōkōlea Point lava formed at ∼2.6 Ma, the island of Kaua'i stood significantly higher relative to sea level than it does at present.

Sample KR-5 (**Table 1**) was collected from a quarry on the east side of the point from a weakly vesicular (<0.5 vol. %) pāhoehoe sheet lobe (X on MP-lava in **Figure 2**). It is an olivine and melilite phyric nephelinite (foidite; **Figure 6A**) with 10–15 vol. % olivine (>0.5 mm) and 15–25 vol. % melilite microphenocrysts (0.1–0.5 mm) along with rare cm-size dunite fragments (**Figure 3c**) in a fine-grained (<0.1 mm) holocrystalline matrix dominated by clinopyroxene with lesser nepheline and magnetite plus minor melilite. No secondary minerals were observed. An unspiked K-Ar age determination on the groundmass from this sample gave an eruption age of 2.65 ± 0.35 Ma (**Table 1**), making it the oldest verified Kōloa event on Kaua'i. It is also one of the most alkalic lavas on Kaua'i, probably produced by very low degree of partial melting (**Figure 6B**).

Crater Hill Tuff Cone (1.67 Ma)

The Crater Hill tuff cone is the only known Kōloa phreatomagmatic vent (e.g., Macdonald et al., 1960). The 2-km-long coastal cliff exposure from Mōkōlea Point to Kīlauea Point (**Figure 2**) is comprised of >90 m-thick, bedded phreatomagmatic tephra sequence (**Figure 7**). This sequence is a remnant of ∼2-km wide tuff cone, which is twice the size of the famous Honolulu landmark Diamond Head and larger than any other Hawaiian tuff cone. It is comprised of a well-bedded sequence with a radial dip of 11–21° (**Figure 2**). The intercepts of dip-directions (**Figure 5**) indicate a probable vent location about 750 m off the shore. The base of the tuff cone is exposed at Mōkōlea Point, where the tephra sequence rests on the Mōkōlea Point lava.

The lowest part of the tuff cone consists of three meters-thick, very poorly sorted, massive lapilli-tuff breccia (LTB) units featuring decimeter to a meter-size ballistic blocks and juvenile bombs often forming similarly large bomb-sags. The LTB units are intercalated with decimeter-thick units of cross-bedded and

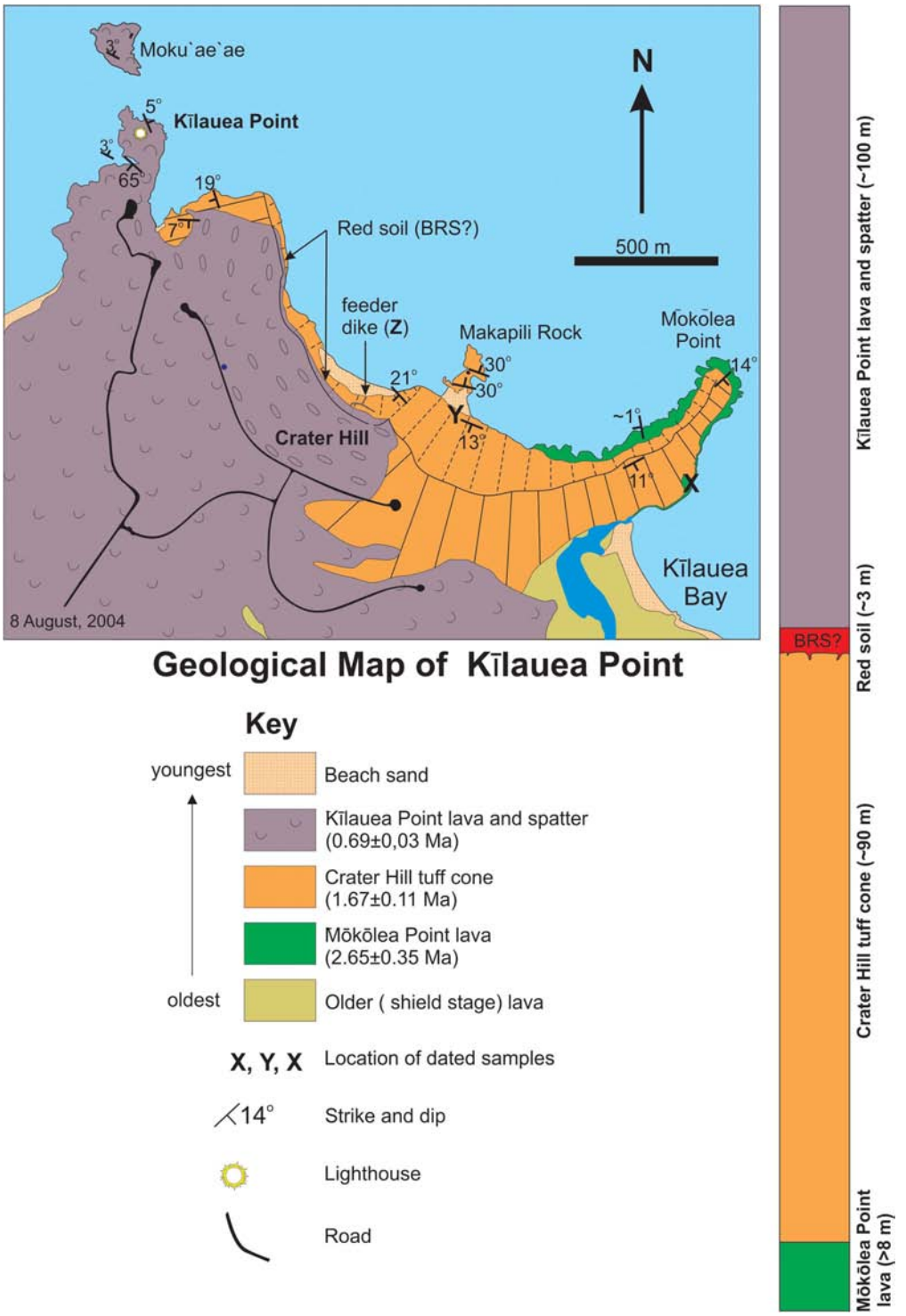

FIGURE 2 | Geological map and simplified stratigraphic column (right) of the Kōloa Volcanic Series at Kīlauea Point, Kaua'i based on new mapping. The red soil horizon is not visible on the map, but its position is indicated as shown on the stratigraphic column. BRS stands for the Big Red Soil. See text for further details.

ash-rich lapilli tuff (LT1 on **Figure 7**). The upper part of the sequence of the tuff cone consists of alternating decimeter to a few meters thick lapilli tuff (LT2) and tuff (T) units (**Figure 7**). The LT units are diffuse-bedded, poorly sorted lapilli tuffs with multiple meters-long, clast-supported pumice lapilli lenses (**Figure 7**). The bedding is frequently deformed by decimeter-size ballistic blocks

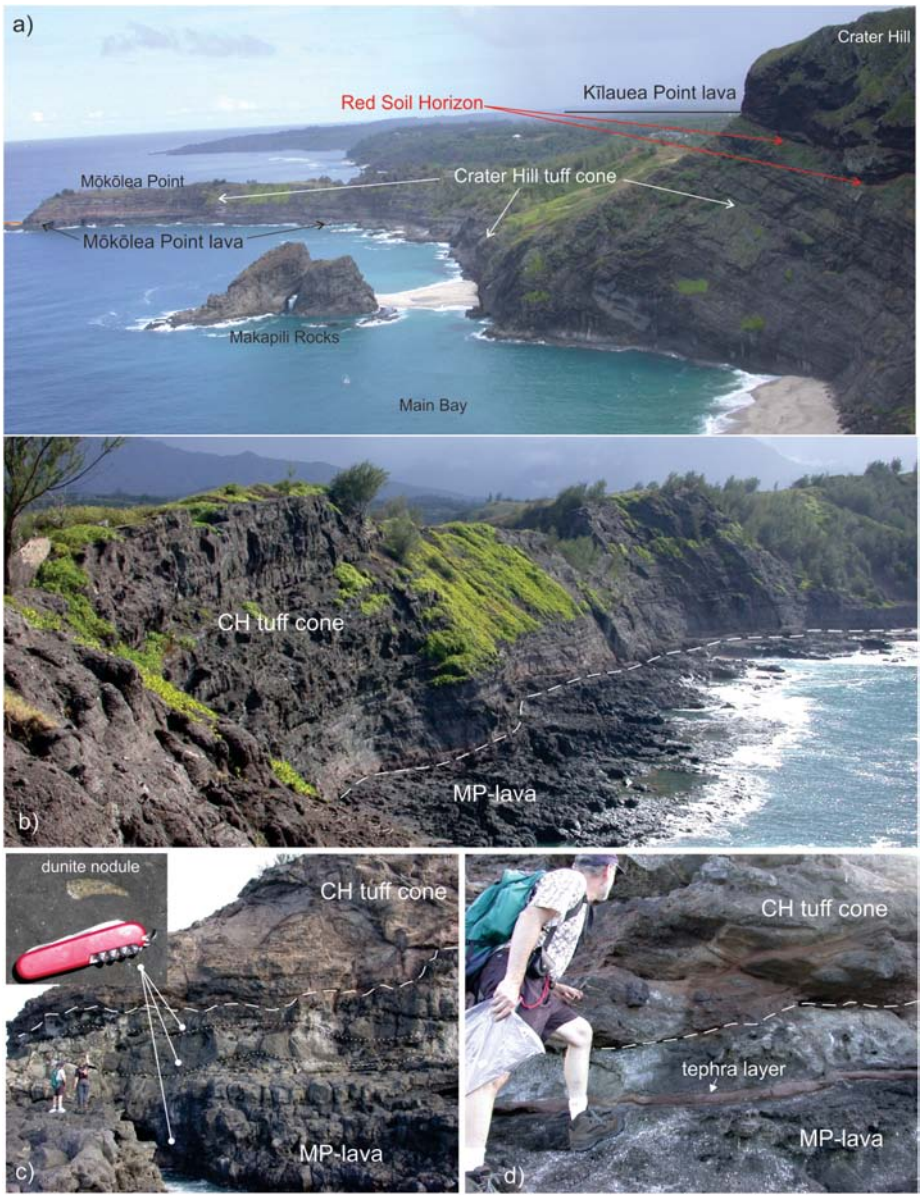

FIGURE 3 | Photographs of the Kīlauea Point area. **(a)** Oblique view looking east along the coast from Kīlauea Point. **(b)** The Mōkōlea Point (MP) lava and lowest part of the Crater Hill (CH) tuff cone sequence at Mōkōlea Point. View looking south from the north end of the point illustrating the slight southward dip of the MP lava surface (indicated by white broken line). **(c)** A stack of three, decimeters to meters thick, pahoehoe sheet lobes overlain by the CH tuff cone deposits (white broken line) at the northern tip of the point. View is to the east. The thickest sheet lobe is at the base and the thinnest at the top (the white dotted lines indicate lobe boundaries). Each lobes contains dunite nodules (inset) in its lava core, as indicated by the circle-ended bars. The boundary between the top two lobes is demarcated by a cm-thick alkali basalt tephra fall deposit (see d for close up). The overlying CH tuff cone deposits consist of massive lapilli-tuff breccia (LTB) units. People (lower left) for scale. **(d)** Close up of the contact (white broken line) between the MP-lava and the CH tuff cone. The white arrow points to the tephra layer that separates the top two lobes of the MP-lava. View is to the east.

and bombs. The T units are either comprised of cross-bedded, moderately sorted medium to coarse ash (T1 on **Figure 7**) or diffuse cross- or planar-bedded, very poorly sorted ash with dispersed armored and accretionary lapilli (T2 on **Figure 7**).

We interpret the LBT units to have been formed by discrete tephra jets fed by rooster-tail explosions at the onset of the eruption. The diffuse-bedded and poorly sorted LT units are taken to represent aggradational deposition from simultaneous fall and flow sustained but pulsating activity lasting for several hours. Such activity has also been described as continuous uprush (Thorarinsson, 1967). The lapilli fraction corresponds to the tephra fall, while the ash-grade portion is deposited by dilute pyroclastic density currents (i.e., base surges). The cross- and planar-bedded bedded tuffs are interpreted to have been

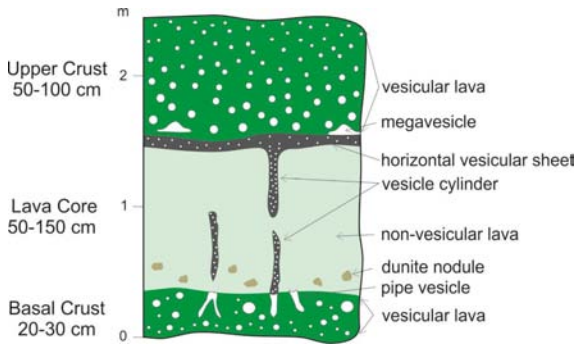

FIGURE 4 | A vertical section through a representative pahoehoe sheet lobe within the Mōkōlea Point (MP) lava, showing the three-fold division of upper lava crust, lava core and basal crust, along with segregation features such as pipe vesicles at the top of the basal crust and vesicle cylinders and associated horizontal vesicle sheets in the lava core. When present, the dunite fragments are confined to the lower part of the lava core, which corresponds to the liquid lava portion of the lobe during emplacement. These internal structures typify pāhoehoe formed by endogenous growth and inflation (e.g., Self et al., 1998). The total thickness of the lobe is about 2.25 m.

emplaced by dry (T1) and wet (T2) dilute pyroclastic density currents (**Figure 7**). Their occurrence as distinct horizons in-between the LT units indicates that they were formed after a brief lull in the activity. By analog to the 1963–1967 Surtsey eruption in Iceland, the early stage rooster tail explosions were formed when the crater was inundated by sea water, while the periods of continuous up-rush took place when the crater alternates from being almost free of and partly filled with sea water (Thorarinsson, 1967). These evidence, along with the presence of reef-limestone fragments in Crater Hill deposits, are consistent with the interpretation that the eruption site was in shallow coastal waters. Thus, when the Crater Hill tuff cone was formed at ∼1.7 Ma sea level relative to the island was almost the same as today.

A juvenile bomb (KR-2 in **Table 1**) collected from the tuff cone (labeled Y on **Figure 2**) is a weakly vesicular (<5 vol. %) olivine nephelinite (foidite **Figure 6A**) with 5–8 vol. % olivine and minor (1–2 vol. %) of 0.1–0.5 mm clinopyroxene microphenocrysts sitting in a holocrystalline matrix of clinopyroxene, nepheline and magnetite. Some olivine have thin (<0.01 mm thick) rims of iddingsite but no other secondary minerals are present. An unspiked K-Ar age determination on the groundmass of this bomb gave an eruption age of 1.67 ± 0.11 Ma (**Table 1**).

The Red Paleosol Horizon

The Crater Hill tuff cone sequence and Kīlauea Point lava are separated by a 2–3 m thick red paleosol (i.e., saprolite) horizon formed by weathering of the tuff cone tephra during sustained surface exposure (**Figures 3a**, **7**). It signifies that a substantial weathering period between eruptions consistent with the ∼1 Myr age difference between the Crater Hill tuff cone and the Kīlauea Point lava (i.e., **Table 1**). This paleosol horizon is probably

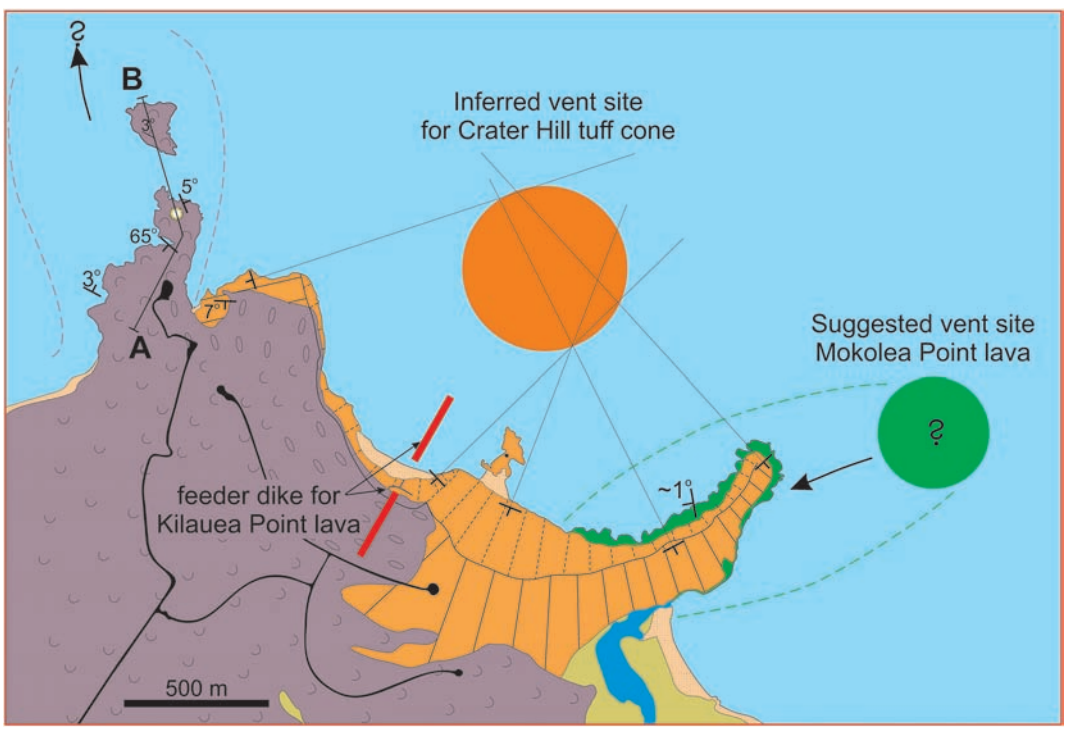

FIGURE 5 | Proposed vent positions for the Kīlauea Point eruptions. The circles show the inferred vent positions of Mōkōlea Point lava (green) and Crater Hill tuff cone (orange). The broken red line marks the inferred position of the Kīlauea Point lava feeder dyke. The Line A-B indicates the location of the cross section in **Figure 7**. The strike and dip symbols for bedding in the tuff come are shown without dip values for sake of clarity (see **Figure 2** for values).

TABLE 1 | The rock type, chemical composition and unspiked K-Ar ages for the three Kōloa Volcanic Series units making up the succession at Kīlauea Point on the island of Kaua'i.

Sample	Mōkōlea Point lava (KR-5)	Crater Hill tuff cone (KR-2)	Kīlauea Point lava (KR-3)
Rock type	**Olivine-melilite nephelinite**	**Olivine nephelinite**	**Basanite**
Major elements (wt.%)			
SiO_2	37.75	39.90	43.53
TiO_2	3.46	3.31	2.81
Al_2O_3	9.25	10.14	13.55
Fe_2O_3*	15.39	14.44	13.40
MnO	0.23	0.21	0.19
MgO	14.42	13.67	6.88
CaO	13.29	12.75	14.39
Na_2O	3.32	3.61	2.67
K_2O	0.98	0.49	1.30
P_2O_5	0.93	0.70	0.49
Total	99.01	99.21	99.20
Trace elements (ppm)			
V	323	270	310
Cr	493	528	336
Ni	329	331	111
Rb	27	10	30
Sr	1085	802	699
Y	25	22	21
Zr	292	203	151
Nb	88	69	51
Ba	991	763	708
La	59	46	30
Ce	127	98	59
Age (Ma)	2.65	1.67	0.69
1 sigma	0.35	0.11	0.03

*For further information on samples and analytical procedures see Garcia et al. (2010). The labels given in the parenthesis are sample numbers. *Total iron as Fe_2O_3.*

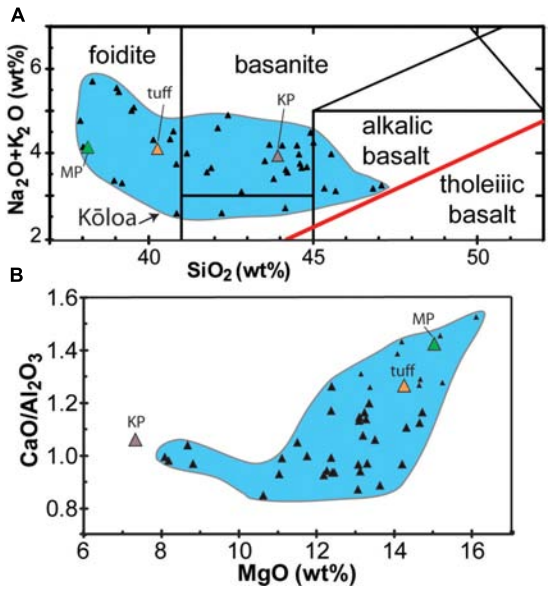

FIGURE 6 | Plots of XRF major element abundance and ratio for the rejuvenated eruption units at Kīlauea Point (large colored symbols) and other the Kōloa Volcanic Series lavas (black triangles; from Garcia et al., 2010). **(A)** Total alkalis vs. SiO_2. Kīlauea Point units are nephelinite (i.e., fodite) and basanite, typical of the Kaua'i rejuvenated lava compositions. The tholeiitic-alkalic dividing line (red) is from Macdonald and Katsura (1964). **(B)** CaO/Al_2O_3 vs. MgO. Kōloa Volcanics. The higher CaO/Al_2O_3 value is indicative of larger degree of partial melting and the horizontal offshoot removal of olivine by fractional crystallization. MP: Mōkōlea Point lava, tuff: Crater HIll tuff cone, KP: Kīlauea Point lava.

the time equivalent of the Big Red Soil (BRS) of Hearty et al. (2005) on the south coast of Kaua'i. The BRS is 0.5–1.5 m thick and present within a raised carbonate platform formation. It is thought to have formed during a prolonged surface exposure of the platform between 0.5 and 1.0 Ma (Hearty et al., 2005).

Kīlauea Point Lava (0.69 Ma)

The Kīlauea Point lava is the youngest eruptive unit at Kīlauea Point. The north to south trending dike connects to the Kīlauea Point lava near the center of coastal outcrop (**Figures 2**, **6**). The near-vent deposits are ∼100-m-thick accumulation of spatter and scoria, representing a crater rampart that rests directly on the red paleosol horizon at the top of Crater Hill tuff cone sequence (**Figure 7**). Down slope, this succession grades into >60-m-thick fountain-fed lava flow that was flowed south and northwest from the erupting fissure (**Figure 2**). The lava features a massive columnar jointed core that is flanked by compound pāhoehoe lobes (**Figure 8**). The massive facies may represent the fill of lava channel and the compound facies probably were levees and overbank flows. The northwest branch of the Kīlauea Point lava extends seaward at least to the islet of Moku'ae'ae (>300 m beyond the present coastline; **Figure 2**). A 3° dip of lobe contacts and laterally continuous internal planes indicate that the flow may extend >20–30 m below sea level at Moku'ae'ae (**Figure 8**). Therefore, the Kīlauea Point lava must have been emplaced when sea level relative to the island stood was 10's of meters lower than today.

Sample KR-3 is from Kīlauea Point lava feeder dyke which yields an unspiked K-Ar eruption age of 0.69 ± 0.03 Ma (**Table 1**). It is comprised of nearly aphyric basanite (**Figure 4a**) with <1 vol. % olivine phenocrysts and microphenocrysts of clinopyroxene (3–5 vol. %) in a holocrystalline matrix of clinopyroxene, nepheline and magnetite (no plagioclase). It is massive and moderately vesicular (15–25 vol. %) with calcite partially filling some vesicles.

DISCUSSION

Vertical Movement of the Island of Kaua'i Revealed by the Kōloa Succession at Kīlauea Point

The rapidly loading of the ∼90 million year old Pacific Ocean lithosphere by a growing Hawaiian volcano causes the crust to

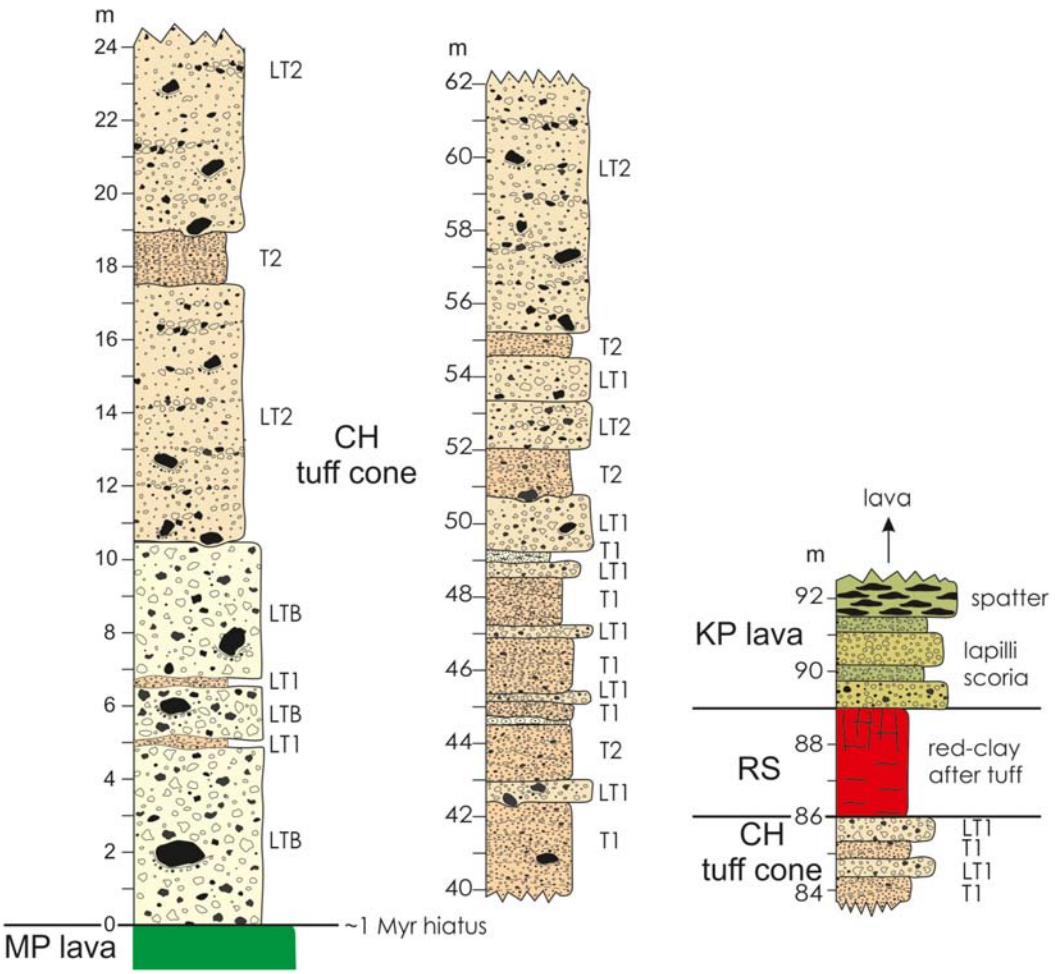

FIGURE 7 | Stratigraphic log of the CH tuff cone tephra sequence and its contacts with underlying MP lava and overlying KP lava units. Lower tephra consists of massive lapilli-tuff breccia (LTB) intercalated cross-bedded lapilli tuff (LT1) units. The overlying section consists of alternating lapilli tuff (LT1/LT2) and cross bedded tuff (T1/T2) units. The LT2 units are diffuse-bedded lapilli tuffs with multiple clast-supported pumice lapilli lenses. The tuff units are either cross-bedded medium to coarse ash (T1) or diffuse cross- or planar-bedded fine to medium ash (T2), usually containing accretionary lapilli. Throughout the sequence the bedding is commonly deformed by decimeter- to meter-size ballistic blocks and bombs. The lower contact with the MP lava represents a 1 Myr-long hiatus, while the contact between the CH tuff cone and the KP lava is demarcated by thick red soil horizon (RS) formed by weathering of the very top of the tuff cone sequence in the time between the two events.

subside at rate of ∼2.6 mm/year (Moore, 1987; Ludwig et al., 1991). As each volcano drifts off the plume, the subsidence is followed by uplift as it rides up the Hawaiian flexural arch and subsides again after passing its crest (e.g., Wessel, 1993). The island Kaua'i has been exposed to this type of "subsidence-rise-subsidence," with a vertical extent of ∼500 m or more, during the 5 Myr passage from its formation above the Hawaiian mantle plume to its current position. It has been hypothesized that the distance (=the temporal gap) between the loading islands and the flexural arch is similar to the distance between contemporaneous shield and rejuvenation volcanism, underpinning the proposal that these features are intrinsically linked (e.g., Bianco et al., 2005).

The succession of Kōloa volcanics at Kīlauea Point is unique in the Hawaiian Islands in that it provides, at one location, three rejuvenated eruptive units spanning ∼2 Myrs all recording formation at different sea level stands (**Figure 9**). Furthermore, it is evident, that at the time of the Crater Hill eruption (∼1.7 Ma) the relative sea level was similar to the present, while the overlying ∼0.7 Ma Kīlauea Point lava and underlying ∼2.7 Ma Mōkōlea Point lava were formed when the relative sea level was substantially lower than today (**Figure 9**). Thus, the volcanic succession at Kīlauea Point records a subsidence of the island of Kaua'i in the ∼1-Myr-long hiatus between the formation of Mōkōlea Point lava and the Crater Hill tuff cone and a rise at least up until formation of the Kīlauea Point lava, again followed subsidence (**Figures 9**, **10**).

Kīlauea Point is situated about 1000 m above paleoshoreline of Kaua'i near the end of its shield-building stage (Flinders et al., 2010). It follows for Crater Hill tuff cone eruption to have taken place at sea level at ∼1.7 Ma, the island of the Kaua'i subsided ∼1000 m in the time between drifting off the hot spot at ∼3.9 Ma

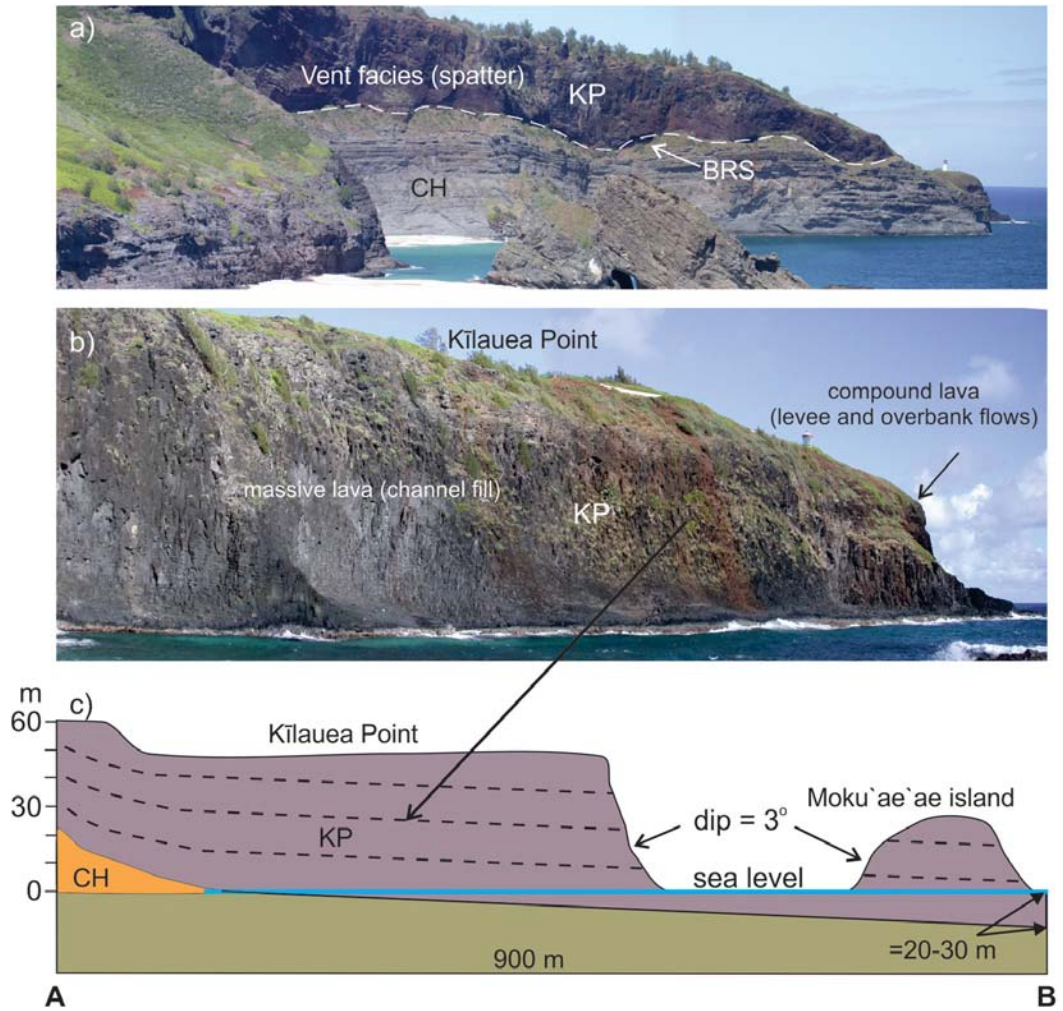

FIGURE 8 | (a) The vent facies of the Kīlauea Point (KP) lava on top of the Crater Hill (CH) tuff cone at the main bay. The view is to the west. The white broken line delineates he contact between the two eruptive units. Directly below the contact is a 2–3 m –thick red soil horizon (BRS). **(b)** The massive KP lava (channel fill) facies at Kīlauea Point flanked by the compound lava. View is to the northwest. **(c)** Schematic cross section of the KP lava from Kīlauea Point to Moku'ae'ae island (see **Figure 2** for position) illustrating the seaward dip of the strata and the minimum degree of subsidence since formation (lower right).

and the Crater Hill eruption. This indicates a mean subsidence rate of 0.45 mm/year for this period. This rate is about factor six lower than the current subsidence rate of the Big Island of Hawaii, which is ∼2.6 mm/year over the last 0.46 Myrs (Ludwig et al., 1991). However, the estimated average subsidence rate of O'ahu since its shield volcanoes became inactive at ∼2.2 Ma (Yamasaki et al., 2011) was also slow (∼0.3 mm/year, equal to 600 m of subsidence; Walker, 1990), because it has been counterbalanced by an uplift rate in the range of 0.015–0.06 mm/year (equal to 7.5–30 m of uplift) over the last 0.5 Myrs (Hearty, 2002; McMurtry et al., 2010). Moore (1987) indicated the subsidence rate of the Hawaiian Islands is highest during the first million years. Volcano subsidence rate decreases from 2.6 mm/year to <0.3 mm/year as it migrates away from the mantle plume. Using the mean subsidence rate of 0.45 mm/year for Kaua'i in the period ∼3.9 to ∼1.7 Ma implies that the Kīlauea Point area would have been situated 500–600 m above sea level at the time of the Mōkōlea Point lava eruption at ∼2.7 Ma. These vertical movements on the scales of 100's of meters make it unlikely that the cyclic changes in the relative sea level described above are recording the rise and fall of the global sea level during the latter stages of the Plio-Pleistocene period, because in none-glaciated areas those changes have amplitudes of meters to 10's of meters (e.g., Hearty et al., 2005; Hansen et al., 2013). Our data do not allow assessment of the islands' rise rate during the period between the ∼1.7 million year old Crater Hill tuff cone and the ∼0.7 million year old Kīlauea Point lava eruption. The rise rate of Kaua'i as it ascended the Hawaiian flexural arch was probably similar to the rate estimated for nearby O'ahu, or ≥ 0.015–0.06 mm/year (Hearty, 2002; McMurtry et al., 2010). This implies a rise of 15–60 m for the island in the period leading to the Kīlauea Point lava eruption. Hearty et al. (2005) describe three older couplets (I-III) that are separated from the younger ones by the Big Red Soil (BRS) that was developed during the period

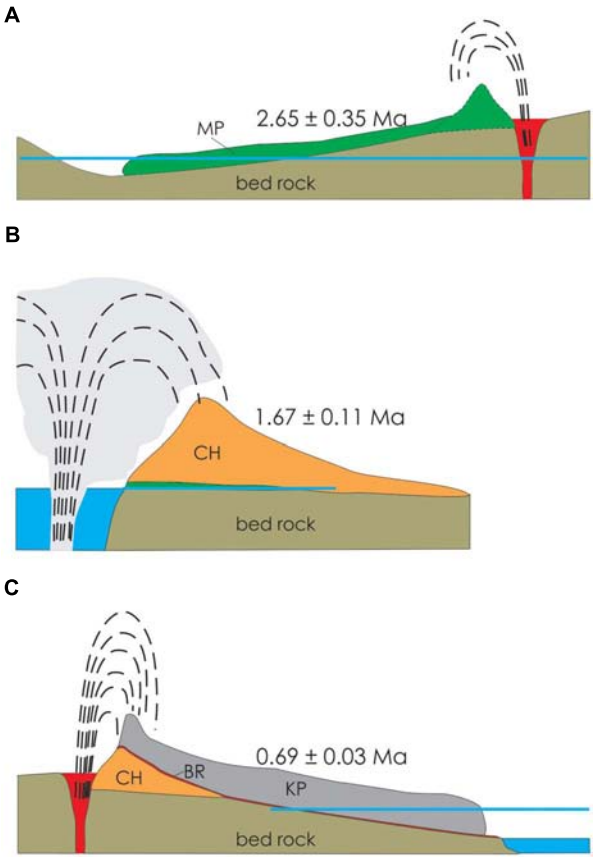

FIGURE 9 | Schematic illustrations of the three eruption scenarios from a viewpoint looking west: **(A)** Mōkōlea Point lava (MP), **(B)** Crater Hill (CH) and **(C)** Kīlauea Point lava (KP) events. BR indicates the red soil horizon (see text for details). Age of each event is indicated and the blue horizontal line indicates current sea level. Sea level at the time of the eruptions is shown by the blue pattern. Note the illustrations are not drawn to scale and the presence of a cone in **(A)** is inferred.

from ∼1.0 to ∼0.5 Ma by sustained upward tectonic motion of the island of Kaua'i as it crossed the fore-bulge of the Hawaiian flexural arch, a passage expected to have taken about 0.9 Myrs. The red paleosol horizon at top of the Crater Hill tuff cone sequence developed during approximately the same time interval, i.e., from ∼1.7 and ∼0.7 Ma, underpinning the inferences made by Hearty et al. (2005). Hence, we conclude that the volcanic succession at Kīlauea Point records the key vertical tectonic movements (i.e., "subsidence-rise-subsequence") during the last ∼3 Myrs when the island of Kaua'i traveled from the hot spot over and down the Hawaiian flexural arch to its current location (**Figure 10**).

The Kīlauea Point Succession and the Rejuvenated Volcanism-Flexural Decompression Model

Here we evaluate how the scenario outlined above conforms to the rejuvenated volcanism-flexural decompression model of Bianco et al. (2005). In addition to the observations on Kaua'i presented above, it is useful to consider these additional observations:

(i) The paleo-island Maui Nui (**Figure 1**, inset), which consisted of seven shield volcanoes, provided the crustal loading when Kaua'i was passing over the flexural moat and arch. Kaua'i is situated about 350 km west-northwest of the weighted center of Maui Nui (represented by West Maui), about 250 km from western Maui Nui (=West Moloka'i) and 370 km from eastern Maui Nui (=Haleakalā). The Maui Nui volcanoes featured its major shield-building phases in the period from > 2.1 to 0.95 Ma (e.g., Sinton et al., 2017).

(ii) Current distance from the volcanoes producing the crustal loading (i.e., the Island of Hawai'i volcanoes) to the flexural moat is in the range of 110–140 km and about 250 km to the crest of the flexural arch. For the purpose of this discussion, similar distance values are assumed for the times of Maui Nui.

(iii) Assuming a plate spreading rate of 10 cm per year (e.g., Garcia et al., 1987), the island of Kaua'i had been displaced from the anticipated loading shield volcanoes at the time of the ∼2.7 Ma Mōkōlea Point lava, the ∼1.7 Ma Crater Hill tuff cone and the ∼0.7 Ma Kīlauea Point lava eruptions as indicated in **Figure 10**.

(iv) Rejuvenated volcanism on Kaua'i spans at least 2.45 Myrs (2.65–0.15 Ma; Garcia et al., 2010) and possibly 3.25 Myrs (3.4–0.15 Ma; e.g., Cousens and Clague, 2015).

(v) About 58 km^3 magma was erupted during Kaua'i's rejuvenation stage (Garcia et al., 2010). The reconstructed magma production rate indicates steady increase in magma production from onset of rejuvenated activity at ∼2.65 to ∼1.3 Ma, followed by a sharp decline until ∼0.8 Ma and stops at 0.15 Ma (**Figure 10**).

The data presented in this paper along with the evidence collated above on the Kōloa Volcanic Series highlight significant inconsistencies between the flexural decompression model as outlined by Bianco et al. (2005) and data obtained for the Kīlauea Point sequence (**Figure 10**). Firstly, the model does not predict uplift during the early onset of rejuvenated volcanism on Kaua'i. This volcanism precedes the predicted model onset by at least ∼0.7 Myrs, as exemplified by the Mōkōlea Point lava event on **Figure 10**. Secondly, observed magma production rates (24 km^3/Myrs; Garcia et al., 2010) are almost a factor two higher than predicted by the flexural decompression model (13 km^3/Myrs; Bianco et al., 2005). Thirdly, data presented here do not match well with the model predicted rate of flexural uplift induced by loading of the Maui Nui complex (weighted loading center = West Maui) onto a Pacific plate with effective elastic plate thickness (Te) of 25 and 35 km, respectively (**Figure 10a**). However, if the weighted loading center is shifted east toward Haleakalā, then the model predicted rate of flexural uplift for the case of Te = 25 km exhibits a good match to observations of the last 1.5 Myrs, especially the peak in magma production centered on ∼1.3 Ma (**Figure 10**). This is also consistent with the prediction that flexure-driven asthenosphere decompression, as Kaua'i passed over the Arch,

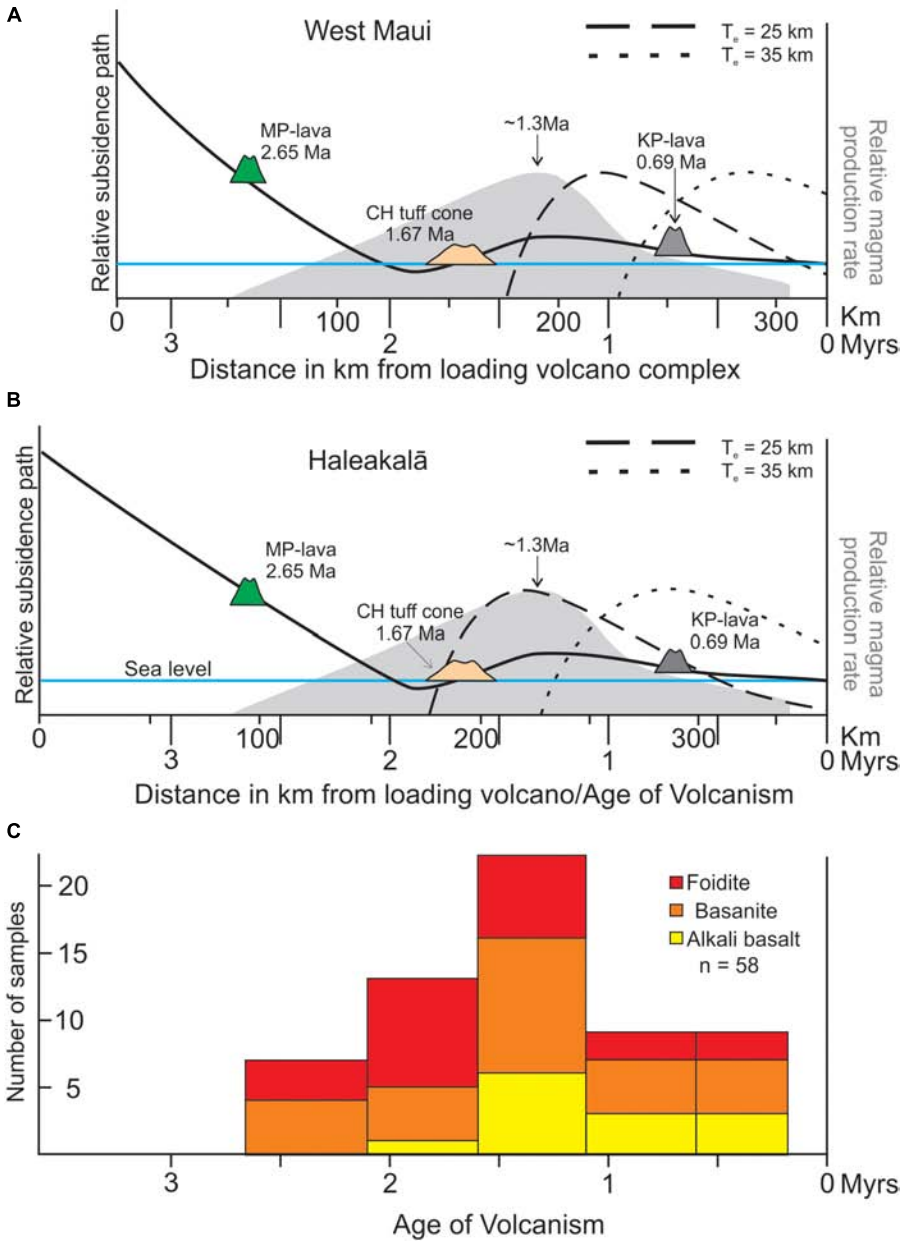

FIGURE 10 | Schematic representation of the subsidence history as depicted by the volcanic succession at Kīlauea Point, with the weighted center of the load focus as **(A)** West Maui and **(B)** Haleakalā. Solid black curve represents the reconstructed subsidence path of the Kīlauea Point area striding across the flexural arch between ~3.9 and ~0.7 Ma. The elevations of the Mōkōlea Point (MP) and Kīlauea Point (KP) lavas is inferred to be 500 and ≤60 m, respectively (see text for details). Temporal variation in predicted rate of flexural uplift (= magma flux rate) from the loading of the Pacific plate by Maui Nui volcanism (Bianco et al., 2005) is illustrated with broken lines for effective elastic plate thickness (T_e) of 25 and 35 km, respectively (see key). The *y*-axis on the right indicates also the relative observed magma production rate (gray shaded area) as constructed by Garcia et al. (2010). The Pacific plate is assumed to have moved WNW at a rate of ~100 km/Myr. It is noteworthy that rejuvenated volcanism began, at least, ~0.7 Myr (T_e = 25 km; Haleakalā) to about 1.8 Myrs (T_e = 35 km; West Maui) earlier than predicted by the model. The observations on magmatism in the last 1.5 Ma only exhibits a reasonable fit with the model prediction for an effective elastic plate thickness T_e = 25 km and Haleakalā volcano as the weighted loading center. **(C)** Histogram of rock types vs. age in ~0.5 million-year bins. Oldest rocks are strongly alkalic, foidites and basanites and no alkali basalts. At the peak in rejuvenated volcanism on Kaua'i about 1.3 Ma, the rejuvenated magmatism is producing all three rock types and maintains that feature thereafter. Drafted based on information from Bianco et al. (2005) and Garcia et al. (2010).

increases degree of melting and magma production (Bianco et al., 2005). The change from foidite/basanite dominated magmatism to production of significant amounts of alkali basalt magma at ~1.3 Ma adds credence to this perception. Even so, the observations demonstrate that the flexural decompression model does not on its own capture all aspects of the rejuvenated

magmatism on Kaua'i. The inconsistencies listed above indicate that flexural uplift (e.g., Bianco et al., 2005) or buoyancy-driven melting (Ribe and Christensen, 1999) do not fully explain the onset of rejuvenated magmatism (e.g., Garcia et al., 2010; Cousens and Clague, 2015). However, as suggested by Garcia et al. (2010), it may be possible to overcome these discrepancies by combining these two plume source models. In this context, it is noteworthy that the aerial extent of Maui Nui is estimated to have been 40% larger than that of the Big Island of Hawaii, while its mass is estimated to be 14% less (Robinson and Eakins, 2006). Also, the mass distribution is different between the two, where the main mass loading on the Big Island (i.e., Mauna Loa and Mauna Kea) is close to the islands center, but on Maui Nui it is situated at the far east end the center island (i.e., Haleakalā). Is it possible that these differences in aerial extent and mass distribution played a role in generating the observed pattern of age, rock type and geochemistry that typifies the rejuvenated magmatism on Kaua'i.

CONCLUSION

In general, the observations and data presented here do not provide support for the flexural decompression model of by Bianco et al. (2005) as the sole driver for rejuvenated volcanism on Kaua'i, especially during the early stages of volcanism (2.6–2.0 Ma; **Figure 10**). However, as current models can only explain part of the key features of rejuvenated volcanism on Kaua'i and other Hawaiian islands (see Garcia et al., 2010 for further discussion), the quest for the all-inclusive model is still on. In this context, it might be fruitful to look at the possible role of the loading-island-mass as a variable.

The following deductions on the volcanism at Kīlauea Point may also be of interest. The eruptions that formed the Crater Hill tuff cone and Kīlauea Point lava appear to have had conduits that followed effectively the same lineament toward the surface, despite having taken place about 1 Myrs apart. This strongly suggests that the magma that fed these eruptions, and possibly the Mōkōlea Point lava eruption as well, followed the same, preexisting structural weakness to reach the surface as implied by Macdonald et al. (1960), rather than creating their own pathway. Hence, it may be practical to explore other rejuvenated volcanic vent constructs on Kaua'i and other islands, such as O'ahu, in this context and assess if they exhibit similar relationships with preexisting structural lineaments. Such knowledge would be of value for volcanic risk assessment and mitigation plans regarding future rejuvenation stage eruptions on the Hawaiian Islands.

AUTHOR CONTRIBUTIONS

TT and MG contributed equally to all aspects of the research and manuscript preparation.

ACKNOWLEDGMENTS

We thank the Kīlauea Point Wildlife Refuge, Kaua'i for access to their land and financial support for this project. We also thank Darcy Wanless for assistance with field work, the reviewers JS and J-FW for constructive and helpful reviews. The editor RB for handling of the manuscript and chief editor Valerio Acocella for suggestions to improve the text.

REFERENCES

Bianco, T. A., Ito, G., Becker, J. M., and Garcia, M. O. (2005). Secondary Hawaiian volcanism formed by flexural arch decompression. *Geochem. Geophys. Geosyst.* 6:Q08009, doi: 10.1029/2005GC000945

Clague, D. A., and Frey, F. A. (1982). Petrology and trace element geochemistry of the Honolulu volcanics, Oahu: implications for the oceanic mantle below Hawaii. *J. Petrol.* 23, 447–504. doi: 10.1093/petrology/23.3.447

Clague, D. A., Holcomb, R. T., Sinton, J. M., Detrick, R. S., and Torresan, M. E. (1990), Pliocene and Pleistocene alkalic flood basalts on the seafloor north of the Hawaiian islands. *Earth Planet Sci. Lett.* 98, 175–191. doi: 10.1016/0012-821X(90)90058-6

Cousens, B. L., and Clague, D. A. (2015). Shield to rejuvenated stage volcanism on Kauai and Niihau, Hawaiian Islands. *J. Petrol.* 56, 1547–1584. doi: 10.1093/petrology/egv045

Fekiacova, Z., Abouchami, W., Galer, S. J. G., Garcia, M. O., and Hofmann, A. W. (2007). Temporal evolution of Koʻolau volcano: inferences from isotope results on the Koʻolau scientific drilling project (KSDP) and Honolulu volcanics. *Earth Planet. Sci. Lett.* 261, 65–83. doi: 10.1016/j.epsl.2007.06.005

Flinders, A., Ito, I., and Garcia, M. O. (2010). Gravity anomalies of the Northern Hawaiian Islands: implications on the shield evolution of Kauai and Niihau. *J. Geophys. Res.* 115:B08412. doi: 10.1029/2009JB006877

Garcia, M. O., Grooms, D., and Naughton, J. (1987). Petrology and geochronology of volcanic rocks from seamounts along and near the Hawaiian Ridge. *Lithos* 20, 323–336. doi: 10.1016/S0024-4937(87)80005-1

Garcia, M. O., Swinnard, L., Weis, D., Greene, A. R., Tagami, T., Sano, H., and Gandy, C. E. (2010). Petrology, geochemistry and geochronology of Kauai lavas over 4.5 Myr: implications for the origin of rejuvenated volcanism and the evolution of the Hawaiian plume. *J. Petrol.* 51, 1507–1540. doi: 10.1093/petrology/egq027

Gurriet, P. (1987). A thermal model for the origin of post-erosional alkalic lava, Hawaii. *Earth Planet. Sci. Lett.* 82, 153–158. doi: 10.1016/0012-821X(87)90115-4

Hansen, J., Sato, M., Russell, G., and Kharecha, P. (2013). Climate sensitivity, sea level and atmospheric carbon dioxide. *Philos. Trans. R. Soc. A* 371:20120294. doi: 10.1098/rsta.2012.0294

Hearty, P. J. (2002). The Ka'ena highstand of O'ahu, Hawai'i: further evidence of Antarctic ice collapse during the middle pleistocene. *Pac. Sci.* 56, 65–81. doi: 10.1353/psc.2002.0004

Hearty, P. J., Karner, D. B., Renne, P. R., Olson, S. L., and Fletcher, S. (2005). 40Ar/39Ar age of a young rejuvenation basalt flow: implications for the duration of volcanism and the timing of carbonate platform development during the quaternary on Kaua'i, Hawaiian Islands. *N. Z. J. Geol. Geophys.* 48, 199–211. doi: 10.1080/00288306.2005.9515110

Jackson, E. D., and Wright, T. L. (1970). Xenoliths in the Honolulu volcanic series, Hawaii. *J. Petrol.* 11, 405–430. doi: 10.1093/petrology/11.2.405

Lassiter, J. C., Hauri, E. H., Reiners, P. W., and Garcia, M. O. (2000). Generation of Hawaiian post-erosional lavas by melting of mixed lherzolite/pyroxenite source. *Earth Planet. Sci. Lett.* 178, 269–284. doi: 10.1016/S0012-821X(00)00084-4

Lipman, P. W., Clague, A., Moore, J. G., and Holcomb R. T. (1989). South Arch volcanic field–Newly identified young lava flows on the sea floor south of the Hawaiian Ridge. *Geology* 17, 611–614. doi: 10.1130/0091-7613(1989)017<0611:SAVFNI>2.3.CO;2

Ludwig, K. R., Szabo, B. L., Moore, J. G., and Simmons, K. R. (1991). Crustal subsidence rate off Hawaii determined from 234U/238U ages of drowned coral

reefs. *Geology* 19, 171–174. doi: 10.1130/0091-7613(1991)019<0171:CSROHD>2.3.CO;2

Maaløe, S., James, D., Smedley, P., Petersen, S., and Garmann, L. B. (1992). The Kōloa volcanics suite of Kaua'i, Hawaii. *J. Petrol.* 33, 761–784. doi: 10.1093/petrology/33.4.761

Macdonald, G. A., Abbott, A. T., and Peterson, F. L. (1983). *Volcanoes in the Sea: The Geology of Hawaii*. Honolulu: University of Hawaii Press.

Macdonald, G. A., Davis, D. A., and Cox, D. C. (1960). Geology and groundwater resources of the Island of Kauai, Hawaii. *Hawaii Div. Hydrogr. Bull.* 13:212.

Macdonald, G. A., and Katsura, T. (1964). Chemical composition of the Hawaiian lavas. *J. Petrol.* 5, 82–133. doi: 10.1093/petrology/5.1.82

McMurtry, G. M., Campbell, J. F., Fryer, G. J., and Fietzke, J. (2010). Uplift of O'ahu, Hawaii, during the past 500 k.y. as recorded by elevated reef deposits. *Geology* 38, 27–30, doi: 10.1130/G30378.1

Moore, J. G. (1987). "Subsidence of the Hawaiian ridge," in *Volcanism in Hawaii: U.S. Geological Survey Professional Paper 1350*, Vol. 1, eds R. W. Decker, T. L. Wright, and P. H. Stauffer, 85-100. Available at: https://pubs.usgs.gov/pp/1987/1350/.

Ribe, N. M., and Christensen, U. R. (1999). The dynamical origin of Hawaiian volcanism. *Earth Planet. Sci. Lett.* 171, 517–531. doi: 10.1016/S0012-821X(99)00179-X

Robinson, J. E., and Eakins, B. W. (2006). Calculated volumes of individual shield volcanoes at the young end of the Hawaiian ridge. *J. Volcanol. Geothermal Res.* 151, 309–317. doi: 10.1016/j.jvolgeores.2005.07.033

Self, S., Keszthelyi, L., and Thordarson, T. (1998). The importance of pahoehoe. *Annu. Rev. Earth Planet. Sci.* 26, 81–110. doi: 10.1146/annurev.earth.26.1.81

Sherrod, D. R., Izuka, S. K., and Cousens, B. (2015). "Onset of rejuvenated-stage volcanism and the formation of līhue basin: Kaua'i, events that occurred 3–4 million years ago" in *Hawaiian volcanoes: from Source to Surface. American Geophysical Union Monograph*, Vol. 208. eds R. Carey, V. Cayol, M. Poland, and D. Weis, 105–124.

Sherrod, D. R., Sinton, J. M., Watkins, S. E., and Brunt, K. M. (2007). *Geologic Map of the State of Hawaii*. US Geological Survey Open-File Report, 2007–1089. Available at: https://pubs.usgs.gov/of/2007/1089/

Sinton, J. M., Eason, D. E., and Duncan R. A. (2017). Volcanic evolution of Moloka'i, Hawai'i: implications for the shield to postshield transition in Hawaiian volcanoes. *J. Volcanol. Geothermal Res.* doi: 10.1016/j.jvolgeores.2017.04.011

Thorarinsson, S. (1967). *Surtsey - The New Island in the North Atlantic*. New York, NY: Viking Press, 105.

Thordarson, T., and Self, S. (1998). The Roza Member, Columbia River Basalt Group – a gigantic pahoehoe lava flow field formed by endogenous processes. *J. Geophys. Res.* 103, 27411–27445. doi: 10.1029/98JB01355

Walker, G. P. L. (1990). Geology and volcanology of the Hawaiian islands. *Pac. Sci.* 44, 315–347.

Wessel, P. (1993). A reexamination of the flexural deformation beneath the Hawaiian Islands, *J. Geophys. Res.* 98, 12177–12190. doi: 10.1029/93JB00523

Wilmoth, R. A., and Walker, G. P. L. (1993). P-type and S-type pahoehoe: a study of vesicle distribution patterns in Hawaiian lava flows. *J. Volcanol. Geothermal Res.* 55, 129–142. doi: 10.1016/0377-0273(93)90094-8

Yamasaki, S., Sawada, R., Ozawa, A., Tagami, T., Watanabe, Y., and Takahasi, E. (2011). Unspiked K–Ar dating of Koolau lavas, Hawaii: evaluation of the influence of weathering/alteration on age determinations. *Chem. Geol.* 287, 41-53. doi: 10.1016/j.chemgeo.2011.05.003

Yang, H. J., Frey, F. A., and Clague, D. A. (2003). Constraints on the source components of lavas forming the Hawaiian North Arch and Honolulu Volcanics. *J. Petrol.* 44, 603–627. doi: 10.1093/petrology/44.4.603

Conflict of Interest Statement: The authors declare that the research was conducted in the absence of any commercial or financial relationships that could be construed as a potential conflict of interest.

Copyright © 2018 Thordarson and Garcia. This is an open-access article distributed under the terms of the Creative Commons Attribution License (CC BY). The use, distribution or reproduction in other forums is permitted, provided the original author(s) and the copyright owner(s) are credited and that the original publication in this journal is cited, in accordance with accepted academic practice. No use, distribution or reproduction is permitted which does not comply with these terms.

frontiers in Earth Science

ORIGINAL RESEARCH
published: 09 November 2018
doi: 10.3389/feart.2018.00194

$^{40}Ar/^{39}Ar$ Geochronological Constraints on the Age Progression Along the Juan Fernández Ridge, SE Pacific

Luis E. Lara[1], Javier Reyes[2,3], Brian R. Jicha[4] and Juan Díaz-Naveas[5]*

[1] Servicio Nacional de Geología y Minería, Santiago, Chile, [2] Departamento de Geología, Facultad de Ciencias Físicas y Matemáticas, Universidad de Chile, Santiago, Chile, [3] Centro de Excelencia en Geotermia de los Andes, Santiago, Chile, [4] University of Wisconsin–Madison, Madison, WI, United States, [5] Escuela de Ciencias del Mar, Pontificia Universidad Católica de Valparaíso, Valparaíso, Chile

Juan Fernández Ridge (JFR) is a *ca*. 800 km long volcanic chain composed by seamounts, guyots and oceanic islands in the SE Pacific. JFR is thought to be related to a deep mantle plume and usually scores high in the hotspots catalogs (e.g., Anderson, 2005; Jackson et al., 2017). High $^{3}He/^{4}He$ in Robinson Crusoe is probably the most undoubted feature of lower mantle involvement. However, one of the most convincing pieces of evidence for a source rooted deep in the mantle is the age progression along a volcanic chain, which is poorly constrained for JFR. In fact, some scarce K-Ar dates in Alejandro Selkirk and Robinson Crusoe islands, and a total fusion age for O'Higgins Guyot published more than 20 years ago, is the only evidence available for such a hypothesis in previous works. Here we integrate recently published $^{40}Ar/^{39}Ar$ ages and 17 new results on groundmass step heating experiments from rocks corresponding to the late shield stage (O'Higgins Guyot: 8.4 Ma; Alpha Guyot: 4.6 Ma; Robinson Crusoe Island: 3.7 Ma; Alejandro Selkirk Island: 0.83 Ma; Friday Seamount: 0.62 Ma) to document a solid age progression which yields a long-term absolute velocity of *ca*. 81 mm/year^{-} for the Nazca Plate. This value is much higher than the velocity prescribed by plate tectonic models that assume fixed hotspots, and still somewhat higher than models that take into account hotspot drift, indicating that the Juan Fernández hotspot is moving *ca*. 20 mm/year toward East Pacific Rise. Present hotspot would be *ca*. 20 km west of Domingo Seamount. Merging geochronological data with our current understanding of the mantle sources and magmatic evolution, we provide a case for a hotspot possibly rooted in a weak primary plume, and discuss some causes and consequences of that.

Keywords: seamounts, guyots, mantle plumes, Juan Fernández Ridge, SE Pacific

OPEN ACCESS

Edited by:
Adriano Pimentel, Centro de Informação e Vigilância Sismovulcânica dos Açores (CIVISA), Portugal

Reviewed by:
Bernhard Maximilian Steinberger, Helmholtz-Zentrum Potsdam Deutsches Geoforschungszentrum (HZ), Germany
Marcel Regelous, Friedrich-Alexander-Universität Erlangen-Nürnberg, Germany
Marco Brenna, University of Otago, New Zealand

****Correspondence:***
Luis E. Lara
luis.lara@sernageomin.cl

Specialty section:
This article was submitted to Petrology, a section of the journal Frontiers in Earth Science

Received: *15 May 2018*
Accepted: *19 October 2018*
Published: *09 November 2018*

Citation:
Lara LE, Reyes J, Jicha BR and Díaz-Naveas J (2018) $^{40}Ar/^{39}Ar$ Geochronological Constraints on the Age Progression Along the Juan Fernández Ridge, SE Pacific. Front. Earth Sci. 6:194. doi: 10.3389/feart.2018.00194

INTRODUCTION

Seamounts are conspicuous features of the deep seafloor, and together with oceanic islands, form a widespread expression of intraplate volcanism. Linear arrays of seamounts, some of them forming age progressive trails of intraplate volcanoes were early described from the Hawaiian chain by McDougall (1964, 1971) based on K-Ar geochronology. From that

finding emerged the fixed hotspot concept (e.g., Wilson, 1963; Morgan, 1971, 1972) with a remarkable and long-lasting influence on plate tectonics and modern geodynamics. However, in the last decades more detailed global bathymetry has revealed more seamounts in a wide range of size and geometry, many of them isolated and others forming chains with no clear age progression. The latter became evident for the Pacific basin (Clouard and Bonneville, 2001) and thus new ideas were raised to question the fixed hotspot model, and the mantle plumes theory. Bonatti et al. (1977) early proposed the "hot lines" as a kind of leaky fractures controlling linear arrays. Lithosphere cracking was proposed by Sandwell and Fialko (2004) whereas Ballmer et al. (2007) proposed the small-scale sublithospheric convection as a way to form long chains that violate the age progression expected for fixed hotspots. A milestone in testing age progressions is geochronology, and the advent of $^{40}Ar/^{39}Ar$ geochronology with modern spectrometers opened avenues to study these features with growing accuracy.

A suitable target for this kind of study is the Juan Fernández Ridge (JFR) in the SE Pacific, close to the south-eastern corner of the so-called Pacific Large-Low Shear Velocity Province (Steinberger and Torsvik, 2012). JFR is thought to be related to a deep mantle plume and usually scores high in the hotspots catalogs (e.g., Anderson, 2005; Jackson et al., 2017), mostly because of high $^{3}He/^{4}He$ ratios in Robinson Crusoe Island, but firm geochronology is still lacking. In fact, some scarce K-Ar dates for Alejandro Selkirk and Robinson Crusoe islands (Booker et al., 1967; Stuessy et al., 1984) and a total fusion $^{40}Ar/^{39}Ar$ age for O'Higgins Guyot published more than 20 years ago (von Huene et al., 1997) is the only evidence available for such a hypothesis. In addition, JFR seems to be also important for the evolution of the South American continental margin. In fact, the intersection of the JFR with the continental margin coincides with the southern limit of the Pampean flat slab (Ramos et al., 2002; Ramos and Folguera, 2009) and is the starting point for high sedimentation rates at the trench (von Huene et al., 1997) and hence is thought to be playing a role on the segmentation of the margin and to control processes in the overriding plate (Kay et al., 1991; Reich et al., 2003; Le Roux et al., 2005; Rosenbaum and Mo, 2011; Arriagada et al., 2013). Therefore, a better understanding of the nature and specially timing of the JFR collision would shed light on some of those relevant margin-scale processes.

Here we use $^{40}Ar/^{39}Ar$ geochronology on groundmass, whole rock and plagioclase separates to date shield stage lavas along the JFR, and by comparison with other age-progressive seamount chains on the Nazca Plate (e.g., Easter Seamount Chain, ESC), we discuss their origin in the context of mantle plumes and plate tectonics.

REGIONAL TECTONIC SETTING

The JFR intersects the continental margin at ∼33.4°S and its eastern component (O'Higgins seamounts group) is located ∼120 km west of the Chile-Peru Trench (**Figure 1**), where the Nazca Plate sinks beneath South America with an azimuth of 78.4° at a high convergence rate of 74 mm/year according to the MORVEL model (DeMets et al., 2010) or 70.5 mm/year according to the GEODVEL 2010 model (Argus et al., 2010). The age of the Nazca Plate underneath the JFR ranges from 27 to 37 Ma (Müller et al., 2008) and is segmented by the Challenger Fracture Zone, which defines a conspicuous magnetic domain that disrupts the normal pattern of the oceanic plate and cuts the JFR near Robinson Crusoe Island (Rodrigo and Lara, 2014). South of the Challenger Fracture Zone, the oceanic crust of the Nazca Plate forms at the Chile Ridge whereas its northern domain is originated at the fast spreading East Pacific Rise (Cande and Haxby, 1991). The Challenger Fracture Zone is EW-trending at the Chile Ridge but changes to a more oblique ENE strike near the Selkirk trough, south of the JFR (**Figure 1**). Close to the JFR, the Challenger Fracture Zone is poorly defined but appears as a sharp discontinuity of the magnetic fabric (Rodrigo and Lara, 2014). 3D modeling of the magnetization suggests that the fracture zone would also have channelized intrusions in a trend that departs from the JFR (Rodrigo and Lara, 2014).

Global bathymetry based on satellite altimetry (Weatherall et al., 2015; GEBCO 2014 at www.GeoMapApp.org) shows the JFR to be a *ca.* 800 km long EW-trending chain that extends eastward from the Friday and Domingo seamounts (at 97.5°W/34°S, close to where the present hotspot would be located; e.g., von Huene et al., 1997) nearly parallel to the convergence vector. The JFR has a roughly continuous morphology west of 76.5°W (Gamma Seamount), where a free air gravity response can be observed (Yáñez et al., 2002; Tassara et al., 2006). Negative anomalies along the flanks define a moat structure as expected by flexural loading of the oceanic crust. Beyond a bathymetric gap, this signature is not evident further east where the gravimetric anomaly is centered at the O'Higgins seamounts cluster without a resolved moat structure (Flueh et al., 2002; Kopp et al., 2004). The latter has been interpreted as the absence of a crustal root, although a broader feature could be masked by the Nazca Plate bending at the outer-rise (Kopp et al., 2004).

Long-term effects of the collision of JFR against the continental margin have been extensively proposed in terms of tectonics (e.g., Yáñez et al., 2002; Le Roux et al., 2005; Arriagada et al., 2013), magmatism (Kay et al., 1991) and even mineral resources (e.g., Reich et al., 2003), although based on the existing poor geochronology and an arguable geometry of the subducted portion of the ridge (Yáñez et al., 2001). In fact, the NE- bending of the trail at *ca.* 25–26 Ma proposed by Yáñez et al. (2001) implies a rapid southward migration of the ridge collision point for ∼1400 km since 22 Ma to a more orthogonal encounter at 10 Ma, when the EW segment started to subduct.

MATERIALS AND METHODS

$^{40}Ar/^{39}Ar$ Geochronology

Eleven $^{40}Ar/^{39}Ar$ laser incremental heating experiments were conducted at the WiscAr Geochronology Laboratory using both MAP 215-50 and Noblesse 5-collector mass spectrometers. Groundmass separates were prepared by crushing, sieving to 250–355 μm, magnetic sorting, and density separation

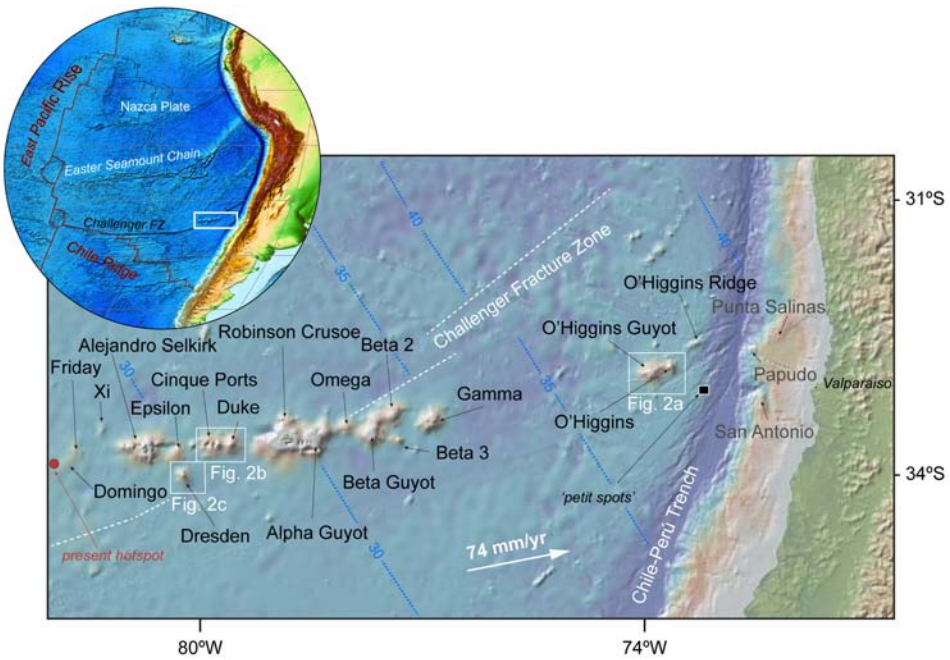

FIGURE 1 | Juan Fernández Ridge (JFR), SE Pacific (bathymetry from GEBCO, downloaded from www.GeoMapApp.org). White boxes show O'Higgins seamounts cluster, Dresden and Cinque Ports seamounts (close up view in **Figure 2**). Inferred location of the hotspot is based on the age progression defined by new $^{40}Ar/^{39}Ar$ data (see text for details). Location of the subducted Papudo Seamount is from Yáñez et al. (2001). Black box shows the area of the "petit spots" identified by Hirano et al. (2013). The Easter Seamount Chain is also pointed out, along with the Challenger Fracture Zone. Present day displacement is shown with a white arrow for the Nazca Plate relative to South America, according to the MORVEL 2010 model (DeMets et al., 2010), with an azimuth of ∼80°. Selected index contours for the seafloor age are shown in light blue (after Müller et al., 2008). Inset on the left is modified from ETOPO1 Global Relief (Amante and Eakins, 2009) and shows the area of the Juan Fernández Ridge in a white rectangle.

using methylene iodide. The separates were then ultrasonically leached as needed in a 5–10% HCl, rinsed ultrasonically with deionized water, and then hand-picked under a binocular microscope to remove altered domains. Groundmass separates, along with the 28.201 Ma Fish Canyon sanidine standard (Kuiper et al., 2008) or the 1.18 Ma Alder Creek rhyolite sanidine (Jicha et al., 2016), were irradiated at the Oregon State University TRIGA reactor in the Cadmium-Lined In-Core Irradiation Tube (CLICIT). Groundmass separates of ∼20 mg were incrementally heated with a 25 W CO_2 laser following the procedures in Jicha and Brown (2014) and analyzed using the MAP 215-50 single collector mass spectrometer. Youngest sample 'FRIDAY' was incrementally heated with a 60 W CO_2 laser and analyzed using a Noblesse 5-collector mass spectrometer following the procedures in Jicha et al. (2016). Reported ages in **Table 2** were calculated using the decay constants of Min et al. (2000) and analytical uncertainties, including J contributions (neutron fluence monitor during irradiation), are reported at the 95% confidence level ($\pm$ 2σ).

Nine samples (**Table 2**) were analyzed by $^{40}Ar/^{39}Ar$ laser incremental heating at the SERNAGEOMIN Geochronology Laboratory using a MAP 215-50 mass spectrometer. Fresh rock fragments were crushed to 250–180 μm grain sizes and hand-picked to extract major phenocrysts or weathered surfaces. Single aliquots were placed in a disk of high purity aluminum together with a monitor grain of Fish Canyon sanidine (28.03 $\pm$ 0.1 Ma; Renne et al., 1994). Sealed disk was sent for irradiation to La Reina nuclear reactor (Chile), operated by the Comisión Chilena de Energía Nuclear. Samples were irradiated for 20 h. Once the samples were received from the reactor, individual total fusion analyses were performed for all the monitors from the disk, and J factors were calculated for each grain. The distribution of J in 2 dimensions across the disk is modeled by a 2-dimensional quadratic fit to the data, resulting in a J surface for the disk (e.g., Lara et al., 2006 and references therein). Individual J factors for each sample are thus calculated depending upon the coordinates of the sample. Following each three heating steps a line blank was analyzed. Then, the noble gases were separated by means of a cold trap at ≈133°C and a ST101 getter operated at 2.2 A. Once purified, the noble gases were introduced into a high resolution MAP 215-50 mass spectrometer in electron multiplier mode. The isotopes ^{36}Ar, ^{37}Ar, ^{38}Ar, ^{39}Ar, and ^{40}Ar were analyzed in 10 cycles, and the $^{36}Ar/^{40}Ar$, $^{37}Ar/^{40}Ar$, $^{38}Ar/^{40}Ar$, and $^{39}Ar/^{40}Ar$ ratios were calculated for time zero to eliminate the effects of isotope fractionation during the analysis. The baseline was analyzed at the beginning and the end of the analysis, for each step, and subtracted from the peak heights. Spectrometer bias was corrected using periodic analyses of air samples, from which a correction factor was calculated. A reproducible result was considered when a plateau age was defined using the approach

TABLE 1 | Morphological features and inferred ages along the JFR.

Seamount/Island	Lat (°S)	Long (°W)	Vol (km^3) (eroded)	Age (Ma)* ± 2σ		Crust age ± 0.5 (Ma) Muller et al. (2008)	Δage ± 1 (Ma)	Comments	Relevant references
Punta Salinas Ridge	32 25.00′	72°05.00′	-	10.74	0.50	39.4	28.7	Subducted, no reliable volume estimation	Yáñez et al., 2001
San Antonio Seamount	33 05.00′	72°05.00′	-	10.59	0.50	38.8	28.2	Subducted, no reliable volume estimation	Laursen and Normark, 2002
Papudo seamount	32°36.00′	72°30.00′	380	10.23	0.50	38.8	28.6	Subducted; volume from magnetic anomaly	Yáñez et al., 2001
O′Hiigins ridge	32°34.71′	73°18.24′	345	*9.42*	*0.50*	37.6	28.2	Age inferred from age progression	von Huene et al., 1997
O′Higgins seamount	32°53.80′	73°50.10′	380	*9.02*	*0.50*	36.9	27.9	Age inferred from age progression	von Huene et al., 1997
O′Higgins (Guyot)	32°54.16′	73°54.17′	1305	8.64	0.28	36.5	27.9	$^{40}Ar/^{39}Ar$ geochronology	Lara et al., 2018
Gamma	33 27.28′	76°51.91′	2400	*5.59*	*0.50*	32.2	26.6	Age inferred from age progression	
Beta 3	33 41.05′	77°20.10′	400	*5.07*	*0.50*	31.4	26.3	Age inferred from age progression	
Beta 2	33 23.14′	77°27.08′	1100	*5.00*	*0.50*	31.5	26.5	Age inferred from age progression	
Beta (Guyot)	33 37.54′	77°43.56′	3000	*4.68*	*0.50*	31.1	26.4	Age inferred from age progression	
Omega	33 31.93′	78°02.55′	700	*4.37*	*0.50*	30.8	26.4	Age inferred from age progression	
Alfa (Guyot)	33 40.50′	78°28.59′	4300	3.91	0.06	30.3	26.4	$^{40}Ar/^{39}Ar$ geochronology	
Robinson Crusoe	33 38.26′	78°51.48′	7600	3.52	0.11	30,0	26.5	$^{40}Ar/^{39}Ar$ geochronology	Booker et al., 1967; Stuessy et al., 1984; Baker et al., 1987; Reyes et al., 2017
Duke	33 43.68′	79°36.94′	1600	*2.73*	*0.50*	29.7	27.0	Age inferred from age progression	Rodrigo and Lara, 2014
Cinque Ports	33 44.89′	79°52.28	1600	*2.47*	*0.50*	29.5	27.0	Age inferred from age progression	Rodrigo and Lara, 2014
Dresden	34 04.91′	80°15.70′	600	*2.06*	*0.50*	28.9	26.8	Age inferred from age progression	Rodrigo and Lara, 2014
Epsilon	33 49.61′	80°20,94′	750	*1.96*	*0.50*	29.2	27.2	Age inferred from age progression	
Alejandro Selkirk	33 45.66′	80°47.22′	4800	*1.54*	*0.10*	28.7	27.2	$^{40}Ar/^{39}Ar$ geochronology	
Xi	33 34.57′	81°22.41′	150	*1.09*	*0.50*	28.6	27.5	Age inferred from age progression	
Friday	33 47,40′	81°43.50′	600	*0.66*	*0.50*	28.4	27.7	$^{40}Ar/^{39}Ar$ geochronology	Farley et al., 1993
Domingo	33 56.80′	81°50.70′	320	*0.42*	*0.50*	28.2	27.8	Age inferred from age progression	Devey et al., 2000

**Ages reported in italics are from the regression line (see text for details). Age of the seafloor taken from Muller et al. (2008) in GeoMapApp, with a nominal maximum uncertainty of 0.5 Ma. Δage is the difference between Age and Crust age with 1 Ma of nominal uncertainty. Volumes estimated from the best bathymetry available, mostly from GRMT in GeoMapApp, or published sources, with nominal uncertainty of 10%. Higher discrepancy is expected for guyots.*

of Fleck et al. (1977) and Sharp and Renne (2005). Reported ages were calculated with the decay constants published by Steiger and Jagger (1977).

In order to obtain comparable values, we recalculated the age and uncertainties following the procedures by Mercer and Hodges (2016) using ArAR software tool[1], with the age published by Kuiper et al. (2008) for the Fish Canyon sanidine (28.201 Ma) and the decay constants of Min et al. (2000). **Table 2** contains

[1]http://group18software.asu.edu

TABLE 2 | Summary of $^{40}Ar/^{39}Ar$ incremental heating results of volcanic rocks from JFR shield stage.

Sample	Phase	K/Ca Total	Total Fusion	Isochron analysis			Age spectrum			Lab ref	
			Age (Ma) ± 2σ	$^{40}Ar/^{39}Ar_i$ ± 2σ	Age (Ma) ± 2σ	*N*	MSWD	^{39}Ar (%)	Age (Ma) ± 2σ		
O'Higgins Guyot											
D10-2	GM	0.025	8.40 0.20	295.4 2.1	8.41 0.08	8 of 8	0.41	100	**8.41 0.07**	1	Lara et al., 2018
D10-7	GM	0.054	8.99 0.52	301.8 6.4	6.46 2.47	8 of 10	0.88	93.8	8.97 0.52		
		0.061	9.12 0.35	296.0 3.9	9.20 1.39	14 of 22	0.8	88.5	9.28 0.33		
			Weighted mean plateau and isochron ages:		8.50 1.20	22 of 32			**9.26 0.28**	2	This study
Alpha Guyot											
D11-03	GM	0.304	4.54 0.11	292.6 4.3	4.63 0.11	8 of 8	0.82	100	**4.58 0.06**	1	This study
D11-04	GM	0.191	4.64 0.07	294.4 15.9	4.64 0.14	8 of 8	0.23	100,0	**4.63 0.06**	2	This study
Robinson Crusoe Island											
MP270112-4	GM	0.218	3.64 0.07	281.1 18.7	3.82 0.20	6 of 10	0.81	94.5	3.67 0.06		
		0.222	3.72 0.10	319.3 36.1	3.52 0.36	7 of 9	1.24	91.7	3.75 0.1		
			Weighted mean plateau and isochron ages:		3.75 0.17	13 of 19			**3.70 0.05**	2	This study
JR220112-2	GM	0.175	3.78 0.04	294.4 3.9	3.82 0.05	7 of 9	0.71	91.7	**3.81 0.04**	2	This study
LL240711-1	GM	0.002	3.80 0.06	296.0 3.0	3.79 0.04	7 of 7	1.17	100,0	3.79 0.04		
		0.012	3.82 0.06	294.0 2.0	3.85 0.04	7 of 7	1.17	100,0	3.85 0.03		
			Weighted mean plateau and isochron ages:		**3.83 0.03**	14 of 14	1.17	100,0	3.83 0.03	1	Reyes et al., 2017
LL230112-1	GM	0.152	3.47 0.28	292.9 2.4	4.07 0.33	10 of 13	1.05	89,0	3.79 0.22		
		0.147	3.67 0.38	293.8 2.1	4.08 0.29	8 of 8	0.69	100,0	3.91 0.21		
			Weighted mean plateau and isochron ages:		4.08 0.22	18 of 21			**3.85 0.15**	2	This study
MP260112-1	GM	0.123	3.85 0.06	293.2 3.5	3.90 0.06	11 of 11	0.92	100,0	**3.87 0.05**	2	This study
LL250711-8	WR	0.025	3.85 0.06	294.0 6.0	3.89 0.06	7 of 7	1.45	100,0	3.89 0.03		
	WR		3.87 0.10	297.0 3.0	3.85 0.08	7 of 7	0.07	100,0	3.86 0.06		
			Weighted mean plateau and isochron ages:		**3.88 0.04**	14 of 14	0.81	100,0	3.87 0.04	1	This study
LL260711-2	WR	0.023	3.94 0.07	296.0 2.0	3.94 0.02	7 of 7	0.48	100,0	3.94 0.02		
	WR	0.015	3.98 0.09	296.0 3.0	3.97 0.03	7 of 7	0.76	100,0	3.97 0.02		
			Weighted mean plateau and isochron ages:		**3.95 0.02**	14 of 14	0.95	100,0	3.96 0.02	1	This study
JR220112-1	Plag	0.045	3.7 0.5	296.6 54.5	3.41 0.59	7 of 7	0.69	100	**3.40 0.30**	1	This study
LL250711-5	GM	0.094	3.73 0.15	307.9 31.9	3.69 0.31	8 of 9	0.61	96.7	3.8 0.12		
		0.096	3.72 0.12	286,0 20.0	3.89 0.23	6 of 8	1.08	95.9	3.79 0.11		
			Weighted mean plateau and isochron ages:		3.82 0.19	14 of 17			**3.80 0.08**	2	This study
LL270711-5	GM	0.752	4.12 0.11	295.6 2.2	4.09 0.15	10 of 12	0.77	95.8	**4.10 0.09**	2	This study
Alejandro Selkirk Island											
LL270112-2	GM	0.22	0.98 0.07	301.6 34.0	0.89 0.23	9 of 11	0.47	90,0	**0.94 0.07**	2	This study
JR170913-16	GM	0.173	0.84 0.13	295.3 1.8	0.83 0.04	8 of 8	0.21	100	**0.83 0.03**	1	This study
LL260112-4	GM	0.185	1,00 0.10	266.4 51.1	1.11 0.19	8 of 9	0.93	99.5	1.01 0.08		
		0.191	0.90 0.02	291.1 20.4	0.94 0.07	6 of 8	1.15	97,0	0.92 0.02		
			Weighted mean plateau and isochron ages:		0.96 0.07	14 of 17			**0.93 0.02**	2	This study
JR180913-1	GM	0.104	0.87 0.02	243.3 5.0	0.88 0.02	7 of 7	0.63	100,0	**0.88 0.01**	1	This study
JR170913-7	WR	8407,000	0.93 0.06	294.1 3.6	0.93 0.02	7 of 7	0.3	100,0	**0.93 0.02**	1	This study
Friday											
FRIDAY	GM	0.143	0.59 0.13	296.3 3.6	0.97 0.91	16 of 16	1.08	100,0	**0.62 0.13**	2	This study

(1): SERNAGEOMIN Geochronology Laboratory, www.sernageomin.cl. (2): University of Wisconsin–Madison, WiscAr Laboratory, https://geochronology.geoscience.wisc.edu. GM, groundmass; WR, whole rock; Plag, plagioclase. MSWD is the mean standard weight deviation. Values in bold are preferred ages.

values as reported from the laboratories and a column with the recalculated values. Subsequent figures use corrected values.

Geological Mapping, Bathymetry and Sampling

Most dated samples come from the islands, and for them exist stratigraphic constraints on relative ages based on 1:25,000 scale geological mapping. Some others were dredged during cruises since 1995. Global low resolution bathymetry (e.g., Global Multi Resolution Topography at www.GeoMapApp.org) was used for first-order geomorphological analysis, complemented with multibeam surveys in the area, for example the Hydrosweep mapping of SO101 CONDOR cruise in 1995 (von Huene et al., 1997) and multibeam bathymetry of SO161 SPOC campaign in 2000 (Flueh et al., 2002; Reichert and Schreckenberger, 2002). Higher resolution bathymetric charts were produced with multibeam echosounders Kongsberg EM122 (12 kHz) and EM710 (70–100 kHz) on board of the AGS 61 Cabo de Hornos research vessel during the FIPA (Fondo de Investigación Pesquera y de Acuicultura) cruise in July 2014, mostly for Duke, Cinque Ports and Dresden seamounts (as named by Rodrigo and Lara, 2014). MB-System software (Caress and Chayes, 2017) was used for post-processing and GMT software (Wessel and Smith, 1995) served to prepare interpolation grids with 30 m of horizontal resolution for the whole depth range and with 6 m at seamounts summits (depth range from 300 to 1000 m). From the available bathymetry, seamount volumes were estimated from sections in which we identified basal planes as those where curvature change is maximum, and after assuming simple geometries for calculation purposes. We assign a nominal uncertainty of *ca*. 20% as a very conservative value for volume estimations, which also takes into account uncertainty related to erosion and total growth above sea level.

Geochemistry

In this article we briefly discuss the main geochemical signatures of the JFR rocks extensively described in Reyes et al. (2017), Reyes (2018, unpublished), and Lara et al. (2018), where methods and procedures for whole rock and mineral geochemistry are described in detail. We focus here on the shield stage because it is the main building stage with a long-term plumbing system (Reyes et al., 2017) and thus could provide clues about the nature of the underlying mantle source. There is evidence of a rejuvenated stage at O'Higgins Guyot (Lara et al., 2018) and Robinson Crusoe Island (Reyes et al., 2017) but we do not further discuss about its origin or driving factors. A discussion of the contrasting patterns of ascent and magmatic evolution between shield and rejuvenated stage lavas in JFR can be found in Reyes et al. (2017). Ongoing research about the mantle source of JFR magmas includes Sr-Nd-Pb isotope ratios and systematic modeling of the melting process. Whole rock major and trace elements here discussed were analyzed at AcmeLabs, Vancouver, BC, Canada[2]. Rock chips crushed from field hand samples were fused with lithium metaborate/tetraborate followed by a dilute nitric acid digestion prior to major element analysis by ICP-ES and trace elements by ICP-MS. In addition, a separate split was digested in Aqua Regia and analyzed by ICP-MS to report the precious and base metals content. Loss on ignition (LOI) is determined by weight difference after ignition at 1000°C. Precision and accuracy (2σ) is between 3–8% for all elements (in ICP-ES and ICP-MS).

[2]www.acmelab.com

JUAN FERNÁNDEZ RIDGE

Seamounts and Islands Along the JFR

The JFR is composed of more than 20 seamounts, a number of knolls and two main islands (Rodrigo and Lara, 2014 and references therein) emplaced on the Nazca Plate. JFR converges against the South American Plate at ∼33.4°S (**Figure 1**). An already subducted portion of this ridge was identified by magnetic anomalies (von Huene et al., 1997; Yáñez et al., 2001), the most prominent depicting the Papudo Seamount (von Huene et al., 1997), which has a volume of *ca*. 380 km^3, comparable to the O'Higgins Seamount further west (**Table 1**). On the overriding plate a tectonic fabric develops in response to the JFR subduction, the ENE-trending Punta Salinas Ridge being one of the more clear expressions (von Huene et al., 1997). Normal and thrust faults are widespread and subsidence of the Valparaiso basin is interpreted as a consequence of the collision (Laursen et al., 2002). Structural highs are controlled by a complex pattern of contractional structures possibly underlain by subducted seamounts, such as the Topocalma knoll well above San Antonio Seamount (Laursen and Normark, 2002). This oblique structural fabric is partially aligned with that of the O'Higgins seamounts cluster in the outer-rise region on the Nazca Plate (**Figure 1**).

The JFR comprises two volcanic segments separated by a ∼400 km wide gap with a common base at *ca*. 3900 m depth. The Easter group is located 120 km west of the trench and is composed by the O'Higgins seamounts (**Figure 2**): O'Higgins Guyot, O'Higgins Seamount, O'Higgins Ridge and a number of knolls. Although they seem to be part of the roughly EW trend of the western JFR segment, they actually form a ENE-trending (N70°E) alignment subparallel to the fault pattern of the incoming plate observed in this region (**Figure 2**; Laursen et al., 2002; Ranero et al., 2006). This structural feature, orthogonal to the magnetic fabric, is notably marked by the O'Higgins fault (Kopp et al., 2004), a deep scarp south of the O'Higgins Guyot but also by the elongation of the O'Higgins Ridge. The eastward projection of the O'Higgins group, however, still follows a more EW trend with the subducted Papudo Seamount (Yáñez et al., 2001) and maybe others inferred from the bulges in the marine forearc sequences. Laursen and Normark (2002) interpreted the structural high south of the Valparaiso basin as a consequence of the accretion of the San Antonio Seamount. O'Higgins Ridge is a ∼45 km long elongated feature composed by a number of juxtaposed seamounts, flanked by extremely deep fractures (von Huene et al., 1997; Ranero et al., 2006). The O'Higgins Guyot is a volcanic edifice *ca*. 3450 m high with a flat top at *ca*. 500 mbsl on average, which is overlain by a rejuvenated lava flow (Lara et al., 2018). A total eroded volume of *ca*. 1300 km^3 was inferred for the O'Higgins Guyot (Lara et al., 2018). Maximum volume estimated using the formulas by Vogt and Smoot (1984) and

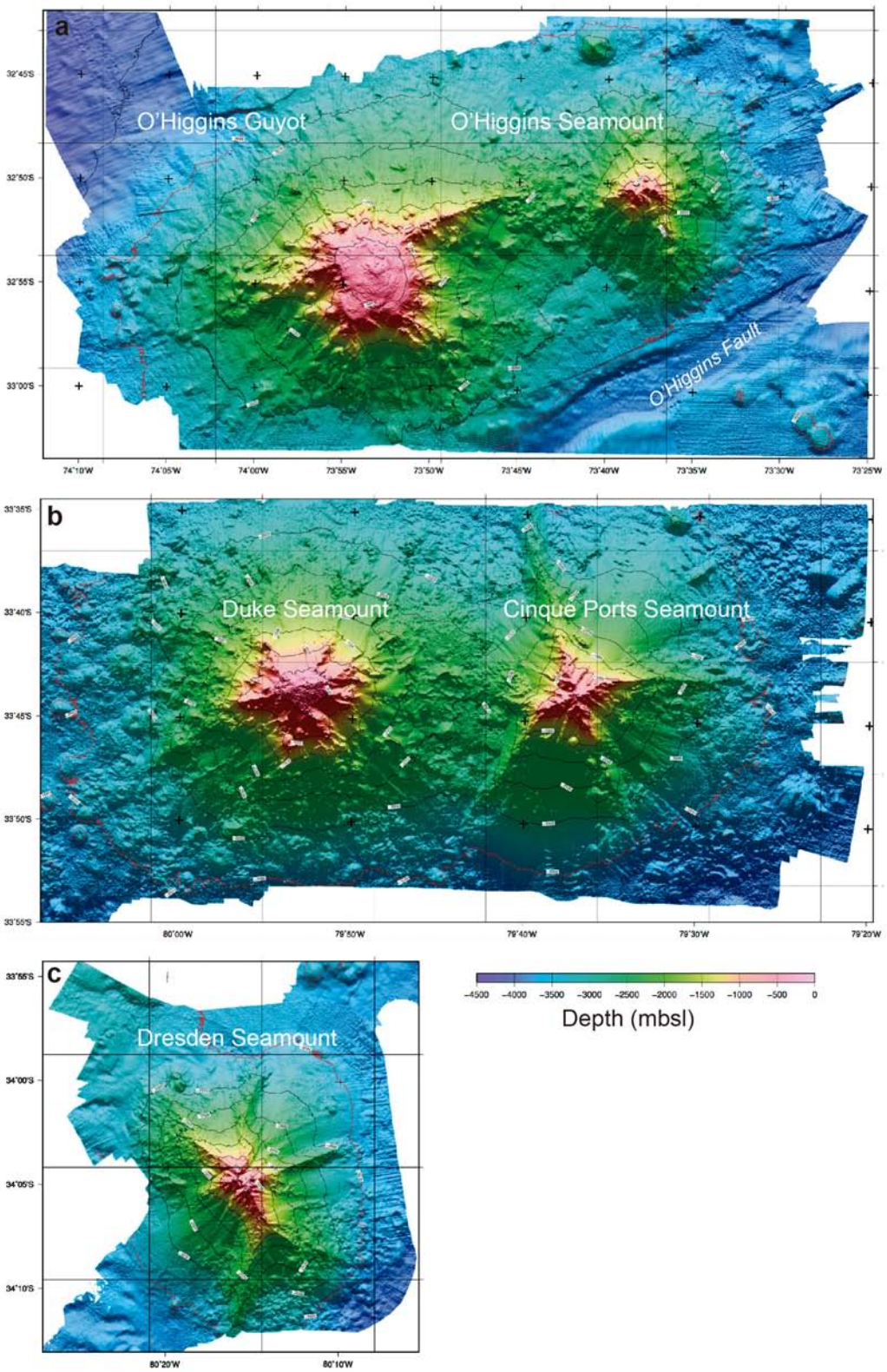

FIGURE 2 | Close up view for seamounts labeled in **Figure 1**. Contrasting morphologies (interpreted as different erosion degree) suggest a more complex evolution, despite the highly correlated linear trend described by geochronological data (see text for discussion). **(a)** O'Higgins cluster with O'Higgins Guyot and O'Higgins Seamount; **(b)** Duke, and Cinque Ports seamounts; **(c)** Dresden Seamount.

Mitchell (2001) is higher, within the range of uncertainty. The shelf break is partially obscured by the rejuvenated features. The summit cone is a compound structure *ca*. 2 km in diameter with a nested crater 930 m wide. From thickness estimated in bathymetric profiles a maximum volume of *ca*. 1.7 km^3 of rejuvenated basanites was deduced. The O'Higgins Seamount is a compound structure formed by two coalescent edifices with summits separated by 25 km with a saddle at *ca*. 2000 mbsl. Two ^{40}Ar/^{39}Ar groundmass ages of 9.26 ± 0.28 and 8.41 ± 0.07 were obtained by Lara et al. (2018), which are similar within uncertainty to the 8.5 ± 0.4 Ma total fusion age reported by von Huene et al. (1997). Above the summit plateau, a fresh and chemically distinctive rejuvenated lava flow was reported by Lara et al. (2018), with a groundmass age of *ca*. 8.2 Ma. The partially stellate edifice O'Higgins Seamount is *ca*. 3280 m high, has the summit at 720 mbsl and a present volume of *ca*. 380 km^3. About 45 km south of the O'Higgins Guyot, Hirano et al. (2013) reported two so-called "petit spots" (small seamounts sourced in the upper mantle and related to plate flexure, as defined in Hirano et al., 2006) dated at *ca*. 7–10 Ma.

The western segment is a nearly continuous ridge (N85°E) from Gamma to Domingo and includes 22 seamounts partially overlapping, 15 of them taller than 1000 m above seafloor. Gamma Seamount is a compound structure marking the resumption of volcanism after a ∼300 km gap. It is NE-elongated and has two summits, the shallowest at *ca*. 547 mbsl. A saddle at 3700 mbsl separates Gamma from the Beta seamounts cluster. Beta 2 is an apparently nested structure with a central cone at 700 mbsl and a total height of 2870 m. Beta 3 is a small perfect cone 1900 m high with a summit at 2020 mbsl, connected with Beta and Beta 2 through a saddle at 3000 mbsl. Beta is a prominent guyot with its flat surface only 250 mbsl and a total volume of *ca*. 3000 km^3. Beta and Beta 2 form a corridor joined by an unresolved bathymetric high, maybe representing another seamount. Omega Seamount, a perfect cone 2200 m high, is the bridge between Beta cluster and the large Alpha volcanic complex. The latter is a guyot with its flat surface gently dipping to the north, at 260–450 mbsl. A volume of *ca*. 4300 km^3 is inferred for this structure, which partially overlaps with the pedestal of Robinson Crusoe Island.

Robinson Crusoe Island (915 masl) and the nearby Santa Clara (375 masl) are part of the same edifice. Their advanced erosion exposes a continuous sequence of shiled stage lavas (Baker et al., 1987; Farley et al., 1993; Reyes et al., 2017; Truong et al., 2018). Submerged marine abrasion terraces (at ∼ 200 and ∼ 500 mbsl; Astudillo, 2014) and sedimentary layers of marine origin now uplifted at 70 masl indicate a complex history of vertical displacement (Sepúlveda et al., 2015). K-Ar ages of *ca*. 3.5–3.8 Ma (Booker et al., 1967; Stuessy et al., 1984) were later refined with a ^{40}Ar/^{39}Ar age of 3.83 ± 0.03 Ma by Reyes et al. (2017) for a tholeiitic basalt from the Puerto Inglés shield sequence. Rejuvenated volcanism is also present in Robinson Crusoe complex as pyroclastic cones, dykes and associated lavas. A sharp erosion unconformity separates the shield stage sequence from the younger rejuvenated stage (**Figure 3**). A basanite lava flow from the Bahía del Padre rejuvenated sequence was dated by Reyes et al. (2017) in *ca*. 0.9 Ma.

A saddle at *ca*. 3500 mbsl separates Robinson Crusoe Island from the paired Cinque Ports and Duke seamounts 70 km west (**Figure 2**; Rodrigo and Lara, 2014). Duke Seamount has a stellate form with a summit at *ca*. 500 mbsl and a height of *ca*. 3500 m (**Figure 2**). Four radial rift zones are recognized in the flanks, which appear also dotted by small flank vents. The western slope of Duke Seamount overlaps with the Cinque Ports Guyot, whose summit is 25 km west. Rough topography on the lower flanks could be interpreted as mass wasting deposits from sector-collapses. Cinque Ports is a guyot with its summit plateau at *ca*. 440 mbsl, with a height of 3660 m. Notably, a number of small cones are present at the base of the western flank, some of them with resolved craters. They are small 100–300 m high cones with diameters of 2–3 km. Five kilometers further west, Delta Seamount is an isolated small cone with summit at 1954 mbsl and base at 3565 mbsl. About 30 km south of the main alignment, Dresden Seamount appears as a stellate cone with a summit 380 mbsl and a height of 3620 m. It is elongated in the NW-SE direction and presents three prominent rift zones, one of them sigmoidal. North of Dresden Seamount, in the main alignment, is Epsilon Seamount, which is a dome-shaped edifice with a summit at *ca*. 1960 mbsl and a base at *ca*. 3570 mbsl.

Separated from Epsilon by a short saddle, Alejandro Selkirk Island is the other emergent volcanic edifice, ∼180 km W of Robinson Crusoe, with a summit 1320 masl and *ca*. 3800 m of submerged section. The sequence is exposed inland as a homoclinal sequence dissected by straight valleys downward to the east and high cliffs on the west coast. For Alejandro Selkirk the published K-Ar ages range between 2.44 and 0.85 Ma, with most of them *ca*. 1.0–1.3 Ma (Booker et al., 1967; Stuessy et al., 1984).

In the saddle that separates Alejandro Selkirk platform from the Domingo Seamount and Friday complex emerges the isolated Xi Seamount, a small perfect cone *ca*. 1000 m high. Further west, Friday (Farley et al., 1993) and Domingo (Devey et al., 2000) seamounts form a cluster with unresolved additional centers included. Friday complex has a multiple summit area at *ca*. 2900 mbsl with the base in the abyssal plain at *ca*. 3800 mbsl. Domingo is volumetrically smaller with a height of *ca*. 636 m. West of Domingo and Friday cluster there is a flat area at *ca*. 3200 mbsl rising *ca*. 500 m above the seafloor, which roughly coincides with the inferred position of the present hotspot.

The Challenger Fracture Zone, which is clear ∼100 km south of the Alejandro Selkirk cluster, converges to the JFR and crosses in a diffuse zone somewhere between Alpha and Beta guyots, and also disturbs the magnetic anomalies of the seafloor fabric even west of Alejandro Selkirk Island (**Figure 1**). A magnetic fabric associated with this fracture zone is oblique to the JFR and defines an intrusive/extrusive domain that disrupts the regular fabric of the sea floor (Rodrigo and Lara, 2014). This feature resumes as a ∼N60-65°E linear bathymetric feature north of the JFR, where it offsets the magnetic anomalies of the seafloor in a left-lateral sense.

Geochemical Features

Juan Fernández Ridge samples are from the upper section of seamounts and islands (i.e., not including basal parts of the

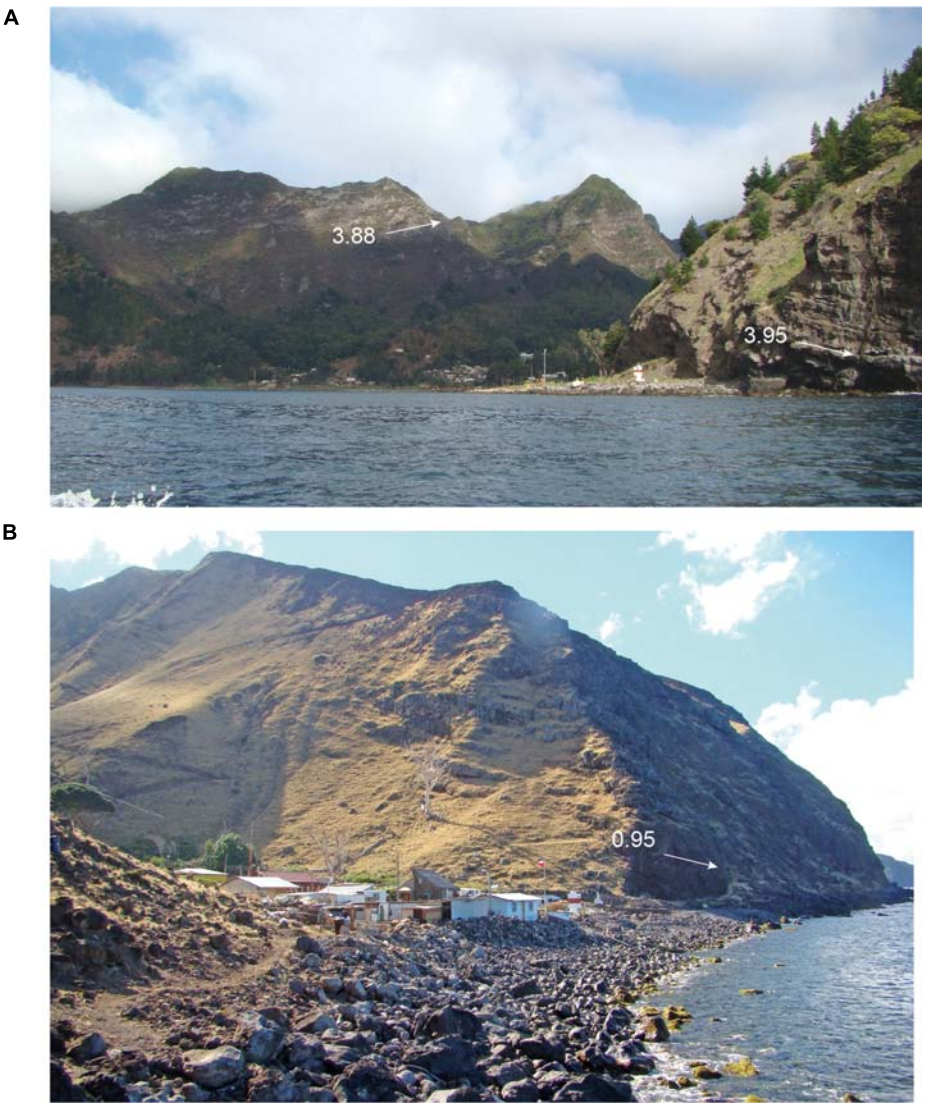

FIGURE 3 | Photographs representing the typical shield stage sequences of dominant tholeiitic basalts at Robinson Crusoe and Alejandro Selkirk islands. **(A)** Panoramic view of Cumberland Bay and San Juan Bautista village, Robinson Crusoe Island, with the exposed *ca*. 900 m thick, NE gently dipping sequence. **(B)** View of 'Quebrada de las Casas' village in Alejandro Selkirk Island and the exposed E dipping sequence. Numbers are $^{40}Ar/^{39}Ar$ ages (see **Table 2** for analytical details) in their stratigraphic position (white arrows).

major edifices) and rock types are mostly tholeiitic basalts and scarce alkaline basalts and basanites, representing both the shield and rejuvenated stages (**Figure 4**). As described from other hotspot volcanoes (e.g., Konter and Jackson, 2012; Garcia et al., 2016), basanites are typical of the rejuvenated stage, and they have been recovered from Robinson Crusoe Island (Reyes et al., 2017) and O'Higgins Guyot (Lara et al., 2018). We here focus on the shield stage, and because samples come from the upper slope of seamounts and from the subaerial sections of Alejandro Selkirk and Robinson Crusoe islands, they most likely represent the late shield stage. Summarizing the main geochemical features of the shield stage based on recent results (Reyes et al., 2017; Truong et al., 2018) and our ongoing research, JFR is formed by basic lavas highly enriched in incompatible elements (LIL and HFSE) compared to MORB, probably due to a more enriched mantle source and smaller degrees of melting. This geochemical enrichment is more marked in Robinson Crusoe Island and Alpha Guyot, and extends to higher La/Sm and Nb/Zr ratios compared to O'Higgins Guyot and Alejandro Selkirk Island (**Figure 4**). These features could be explained by differences in the partial melting degree and mantle potential temperature, although subtle changes in the composition of the source over time could also be playing a role. Basanites are also present at Friday Seamount and lavas from Domingo carry some signatures that mimic those recognized in lavas from the rejuvenated stage in O'Higgins Guyot and Robinson Crusoe Island (Reyes et al., 2017; Lara et al., 2018). Devey et al. (2000) interpreted these

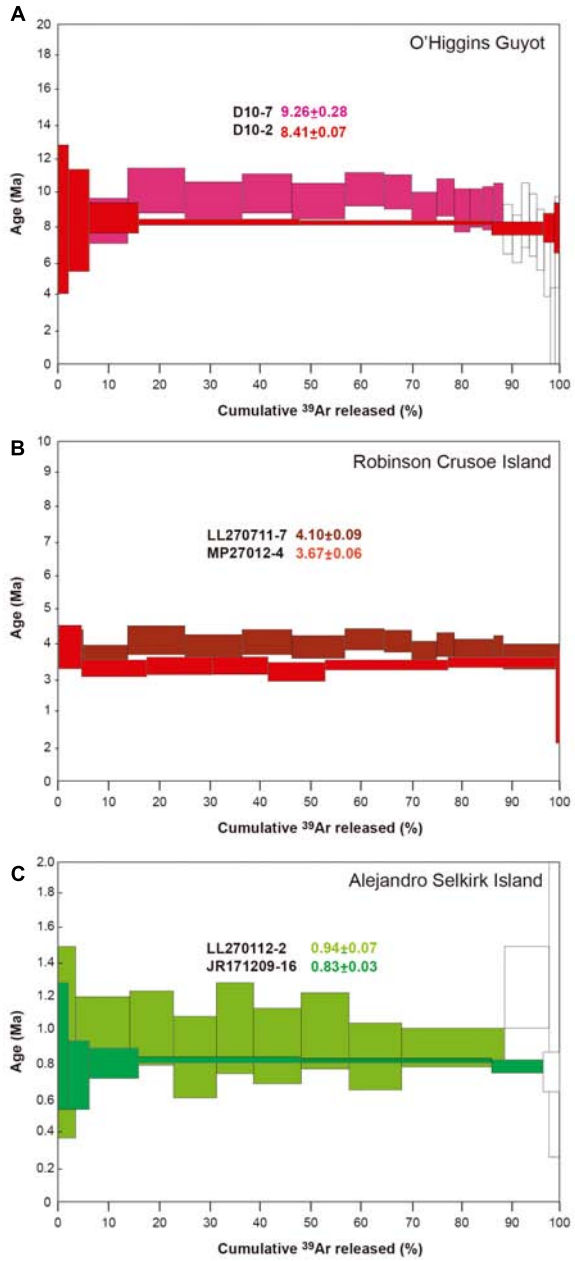

FIGURE 4 | Step heating diagrams for selected samples (analytical data in **Table 2**). **(A)** Stacked plateaux for shield stage lavas from O'Higgins Guyot (samples D10-2 and D10-7; Lara et al., 2018); **(B)** Robinson Crusoe Island; and **(C)** Alejandro Selkirk Island. Plateau ages are shown before recalculation reported in **Table 2**.

features as the effect of source metasomatism at early stages of extrusion.

Published Sr-Nd-Pb isotopic ratios suggest source enrichment with respect to depleted mantle source of MORB (Farley et al., 1993; Truong et al., 2018), including those from the East Pacific Rise and North Chile Ridge and excluding the extensive participation of the lithospheric mantle. Local differences cannot be explained only by changes in the degree of partial melting and thus subtle variations in the enriched source are needed. These mantle heterogeneities could also explain the low values of $^{3}He/^{4}He$ in Alejandro Selkirk compared to the higher values reported for Robinson Crusoe (Farley et al., 1993; Truong et al., 2018), the latter usually interpreted as evidence of an origin in the deep mantle (Hahm et al., 2009) and one of the most compelling probes of a mantle plume involvement in JFR. Despite the internal variation, the narrow field of isotopic values implies a relatively stable source beneath JFR, which is in contrast to the large variation observed in coeval chains on the Nazca Plate like the Easter Seamount Chain (Ray et al., 2012), where a mixture of enriched and depleted sources has been proposed (e.g., Kingsley and Schilling, 1998; Simons et al., 2002). Data from San Félix and San Ambrosio islands also reflect mantle heterogeneities beneath the Nazca Plate in the SE Pacific (Gerlach et al., 1986).

RESULTS

Ages and Age Progression

Seventeen new $^{40}Ar/^{39}Ar$ ages, and 3 recently published (Reyes et al., 2017; Lara et al., 2018) were determined from experiments that yield well defined plateaux following Sharp and Renne (2005), all comprising > 60% of the ^{39}Ar released, with probability of fits of at least 0.05, and having no resolvable slopes (**Figure 5** and **Table 2**). Isochron regressions (York, 1969) indicate that $^{40}Ar/^{36}Ar$ intercepts are indistinguishable from the atmospheric value of 295.5 (Steiger and Jagger, 1977). Thus, we consider the plateau ages as the best estimate of the time elapsed since eruption or cooling below closure temperature and we used these data to calculate the age progression and cumulative eruptive volumes. In two cases we preferred the isochrones because of the lower uncertainty at 2σ.

Radioisotopic ages form a linear array when plotted against great circle distance to Domingo Seamount (thought to be near the present hotspot) and thus a clear age progression. We obtain thus a velocity of 81.30 ± 1.70 mm/year (R^2 = 0.96) using all the samples, which is slightly better when only latest shield stage samples are considered (80.65 ± 1.70 mm/year with R^2 = 0.99) (**Figure 6**). There are no significant outliers, even taking into account the poorly constrained stratigraphic position for submarine samples. For example, Domingo and the more mature Friday Seamount are probably in the early stage of shield volcanism and thus only comparable with the unsampled, older section of the others. We included Friday Seamount age in the regression despite its signature comparable with that of the rejuvenated stage, basically because of the short time span represented by these lavas. In fact, when the age of Friday Seamount is excluded, the trendline does not change significantly. On the other hand, the regression line predicts younger ages for Robinson Crusoe Island, which is expected since all the samples are from the exposed stratigraphic section with an eroded section of yet unknown thickness inferred. From the reported ages in consecutive seamounts along the JFR, the duration of the shield stage would have been *ca.* 1 My. From

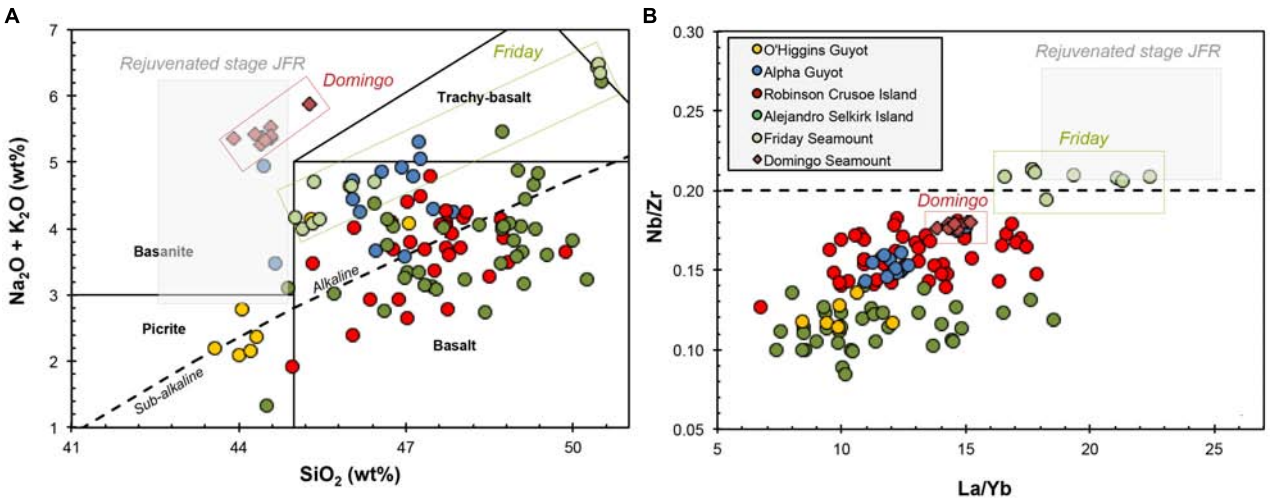

FIGURE 5 | Major and incompatible trace elements ratios for JFR samples. **(A)** $N_2O + K_2O$ vs. SiO_2 plot with data from Reyes (2018, unpublished), Lara et al. (2018), and Reyes et al. (2017) for O'Higgins and Alpha guyots, and Robinson Crusoe and Alejandro Selkirk islands. Data for Domingo and Friday seamounts are from Devey et al. (2000). The field for the rejuvenated stage recognized at O'Higgins Guyot (Lara et al., 2018) and Robinson Crusoe Island (Reyes et al., 2017) is shown in light gray box. Note that Domingo Seamount is close to the rejuvenated field. **(B)** Nb/Zr vs. La/Yb ratios. La/Yb increases with the differentiation and Nb/Zr is higher at lower degrees of partial melting (see text for details).

the regression line, the intercept at $y = 0$ implies that the hotspot is presently *ca*. 20 km west of the Domingo Seamount (33°55.5′S/82°2.9′W).

Volumes and Eruptive Rates

We use radiometric ages obtained for shield units and independently estimated volumes from bathymetry to document changes in the eruptive volumes over time (**Figure 7**). We found that the 400 km gap between O'Higgins seamounts and the western JFR segment marks a temporal gap of *ca*. 4 Ma without eruptive record. The onset of a period with the highest eruptive rate occurred at 5.5 Ma and lasted for *ca*. 2 My (from Gamma to Robinson Crusoe). A more moderate growth period extended from *ca*. 3–1.5 Ma (Duke to Alejandro Selkirk) and the more recent episode occurred at an even lower eruption rate. The earlier low volumetric growth period coincides with a decreasing difference between the age of the oceanic crust and the age of volcanism (Δ_{age} in **Figure 7**); the rapid growth period occurs with a nearly constant Δ_{age} and the change to a lower growth rate is accompanied by a slight increase in Δ_{age}, which also corresponds to the intersection of the Challenger Fracture Zone (**Figure 7**). On the other hand, geochemical tracers only show minor changes along the chain (related to variations in partial melting degree and subtle mantle source changes) and thus volumes, eruptive rates and continuity of the alignment seems to be independent of the nature of the source.

DISCUSSION

Velocity of the Nazca Plate

Age progressions along hotspot trails are useful to test absolute plate tectonic models. The early idea of a possible age progression along JFR was based on very few imprecise K-Ar dates for Robinson Crusoe and Alejandro Selkirk islands and a single total fusion $^{40}Ar/^{39}Ar$ date for the O'Higgins Guyot. Despite the high uncertainty of these values, the velocity inferred for the Nazca Plate is not significantly different from our result, which is based on more precise radiometric dating. The velocity here obtained is close to the value deduced at Domingo Seamount with the NUVEL 1A model (DeMets et al., 1994) and slightly higher than that obtained with MORVEL (DeMets et al., 2010). However, these models are in a no-net-rotation frame, and when converted to fixed-hotspot frames, inferred velocities are much lower. When absolute plate models with moving hotspots are considered (e.g., T25M by Wang et al., 2018; 57.04 mm/year at Domingo Seamount), the difference is less and could be reconciled with a *ca*. 20 mm/year westward drift of the mantle plume. In addition, if the convergence rate between the Nazca and South-American plates is higher than the inferred absolute motion of the Nazca Plate, then South America is advancing toward the trench. In fact, Schepers et al. (2017) showed that South-American Plate advance has been accompanied by > 200 km of trench retreat since ∼12 Ma.

On the other hand, our estimated velocity for the Nazca Plate is lower than the value published by Ray et al. (2012) based on the age progression along the coeval Easter Seamount Chain (110 mm/year for the range 0–20 Ma). In order to perform a more robust comparison, we scrutinized the dates obtained by Ray et al. (2012) removing values possibly related to rejuvenated stages (those with Nb/Zr > 0.2 and La/Yb > 15 being also clear age outliers) and those without clear plateau ages. For this subset we obtained a slightly lower velocity of 106.38 mm/year ($R^2 = 0.96$) when all the < 20 Ma samples are taken into account. A closer inspection in this range allow us to identify a break at *ca*. 10 Ma from which we obtain a velocity of 89.29 mm/year ($R^2 = 0.99$)

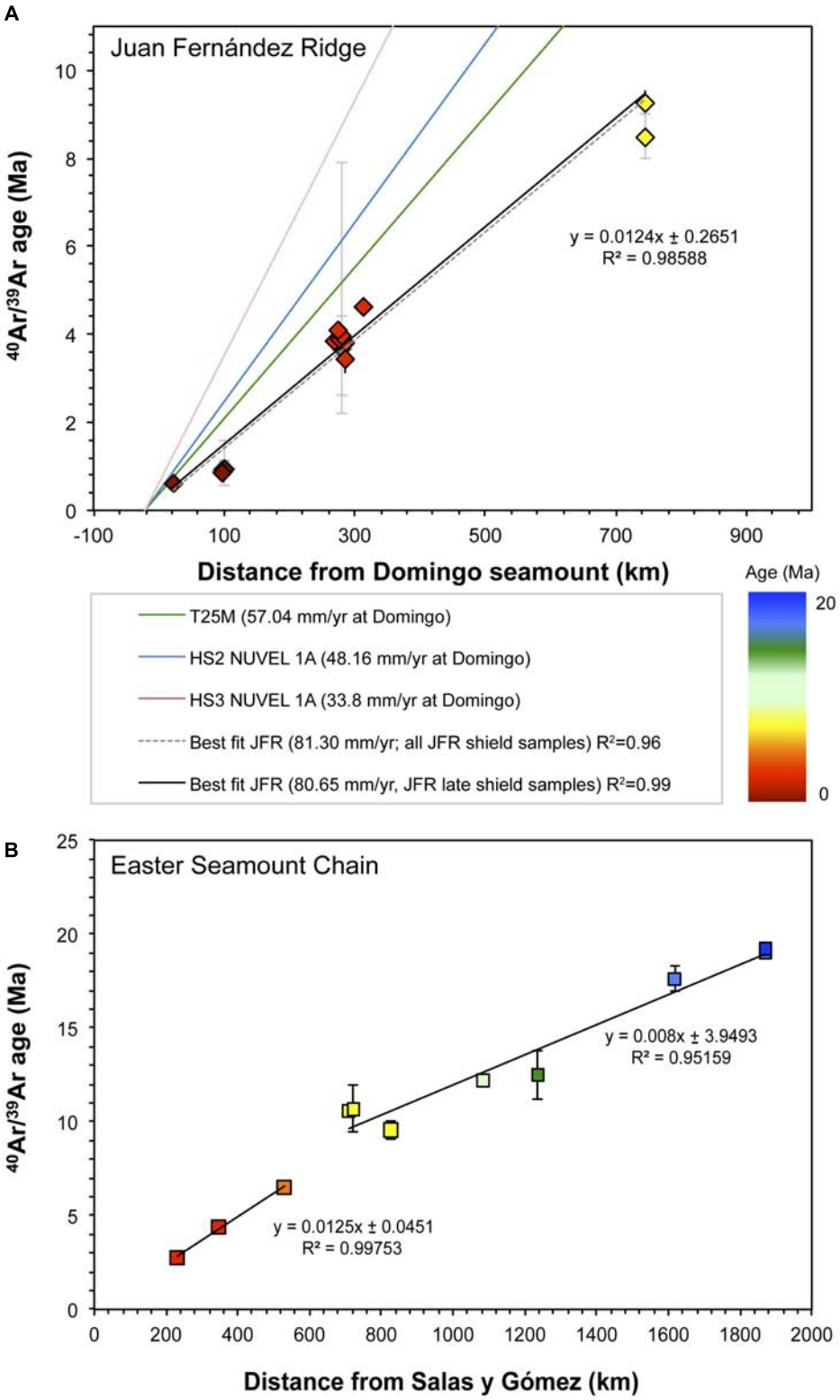

FIGURE 6 | $^{40}Ar/^{39}Ar$ groundmass age vs. great circle distance from Domingo Seamount **(A)**. A linear regression line is shown with corresponding equation and coefficient of determination R^2. Lower panel in **(B)** shows the correlation for Easter Seamount Chain (data modified from Ray et al., 2012 only removing the outliers in the range 0–10 Ma). Velocity from the T25M model taking into account moving hotspots (Wang et al., 2018) is shown for comparison, together with other fixed hotspots plate tectonic models as NUVEL 1A (DeMets et al., 1994) and MORVEL56 (DeMets et al., 2010) computed at Domingo Seamount.

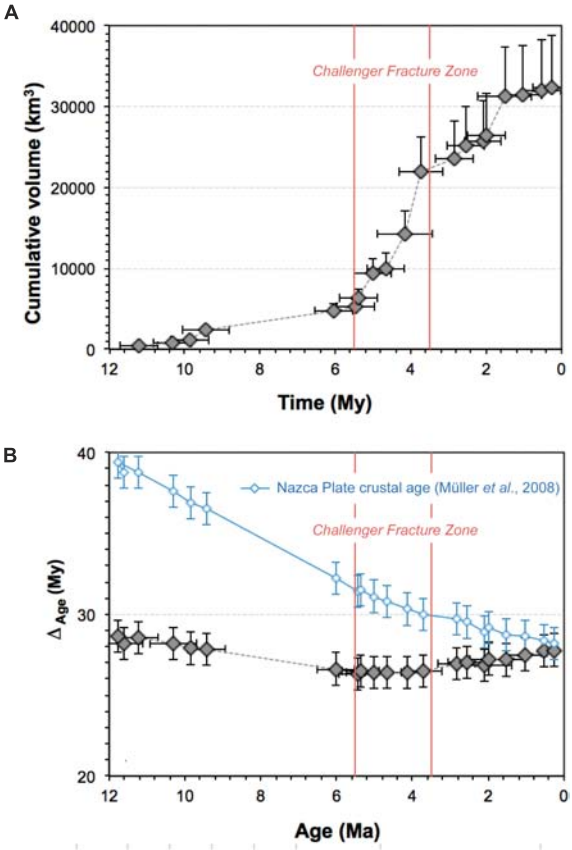

FIGURE 7 | Evolution of JFR as constrained by volumetric eruption rate and Δ_{age} (see text for details). **(A)** Cumulative volume; **(B)** Δ_{age} and crust age from Müller et al. (2008) (**Table 1**).

for samples < 10 Ma (**Figure 7**). Despite the uncertainty of radiometric dating, this value is closer to the velocity deduced from the JFR and thus both seems to unravel coherent drift of mantle plumes beneath the Nazca Plate.

A Weak Primary Mantle Plume Beneath JFR?

Preliminary geochemical evidence suggests the possible involvement of pyroxenite in the source of JFR magmas. Our modeling effort (e.g., Reyes, 2018, unpublished) shows in fact a spatially heterogeneous mantle plume beneath JFR with a minor but relevant pyroxenite fraction (5–12%) and a relatively low potential temperature (T_p, *ca*. 1330°C). This model T_p is low, in general, compared to some other OIB (e.g., Herzberg et al., 2007; Putirka, 2008; Kimura and Kawabata, 2015), but similar or slightly higher than some estimates for the ambient mantle temperature, e.g., ∼1396°C (Putirka, 2008), ∼1280–1400°C (Herzberg et al., 2007) or ∼1300–1310°C (Kimura and Kawabata, 2015), the latter calculated with the same method. A low temperature in a pyroxenite-bearing plume could be explained by its disposition to cool because of the low ascent velocity imparted by its density, high viscosity (Adam et al., 2017) and its possible volatile content (e.g., Devey et al., 2000). Thus, although a more precise appraisal of the nature of the mantle plume beneath JFR is beyond the scope of this article, we speculate that discontinuities along the JFR, and the variations of the eruptive rates, could be a result of the weakness of the feeding mantle plume with temporal changes in T_p implying different partial melting degree over time.

In addition, gaps and changes in volumetric magma production could be also related to the dynamic nature of the oceanic plate. Orellana-Rovirosa and Richards (2017) proposed a dimensionless parameter (R) as a proxy for rough or smooth topography along seamount chains, with $R < 1.5$ for rough, discontinuous ridges and $R > 3$ for those with a smooth topography. R is approximated by the equation $R = (Q/V)^{-2}/T_e$ as function of buoyancy flux Q (m^3/s), plate velocity V (m/s) and elastic thickness of the lithosphere T_e (m). When computing R for JFR with appropriate values (buoyancy flux = 0.19 m^3/s from the review by King and Adam, 2014; T_e = 5–15 km from Manríquez et al., 2013) we obtain 1.3 ± 0.5, which is consistent with a mostly rough topography. From that reasoning we speculate that a low buoyancy flux combined with an old oceanic lithosphere (*ca*. 26 Ma at the time of volcanism) are the main controlling factors for the observed discontinuity. A low buoyancy flux is also consistent with a low volumetric eruption rate (**Figure 7**), and also with an independently estimated low T_p in the pyroxenite-bearing source. Recent global seismic tomography (French and Romanowicz, 2015) beneath JFR shows a partially resolved anomaly of low shear-wave velocities that is consistent with this interpretation.

A Reappraisal of the JFR Collision Against the Continental Margin Over Time

The apparent age progression along JFR was used by a number of authors to assess the possible geological effects of the collision of this ridge against the continental margin (e.g., Martinod et al., 2010 and references therein). Some of them proposed a fast migration velocity of the collision point (Yáñez et al., 2001) based on an extremely sharp ridge bending at *ca*. 25–26 Ma (from ENE to NNE). However, close inspection of the intraslab seismicity reported by Kirby et al. (1996), and the updated picture by Clouard et al. (2007) from the NEIC catalog (1993–2003), shows a clear pattern of earthquakes clustering in an ENE trend (N78°E), which coincides with the convergence vector, and the absence of any major bending of the seismicity at depth that shed light on the older JFR segment. In addition, the geometry of the Easter Seamount Chain shows a more complex pattern instead of a simple bending when it continues on the Nazca Ridge at *ca*. 25 Ma. The latter is a NE-trending structure and could be a closer analog of the subducted portion of the JFR older than 25 Ma. Thus, we consider NE rather than NNE as a more plausible trend for the older Oligocene segment and hence a lower migration velocity of the collision point would be implied. A recent study of the ridge-trench collision along the Andean margin by Bello-González et al. (2018) reaches the same conclusion based on a reconstruction of the Nazca Plate hotspot trails.

On the other hand, and more directly related to the younger segment of the JFR, we interpret the morphology and alignment of the O'Higgins seamounts as indicating a more recent and gradual change in the strike of the JFR that would produce a gentle concavity to the north (∼15–20°). This hypothesis was also considered by von Huene et al. (1997), but discarded because of apparent inconsistency with other temporal and physical indicators. One objection came from the apparent absence of an equivalent geometry in the coeval segment of the Easter Seamount Chain. Interestingly, and despite the rough morphological continuity, the Easter Seamount Chain does show a jump in the age progression just at *ca*. 9–10 Ma after removal of the anomalous values reported by Ray et al. (2012) (**Figure 6**). There is not a clear reason for such a subtle bending because the Nazca Plate has been stable after the last major reorganization at 26 Ma (Tebbens and Cande, 1997), although changes in the Nazca-South America convergence velocity have been reported (e.g., *ca*. 5% reduction of convergence velocity at 10 Ma and 20% at 5 Ma; Somoza and Ghidella, 2012). Most importantly, Tebbens et al. (1997) found an increase of the half spreading rate at the Chile Ridge at ∼9.58 Ma (from 37.8 to 45.6 mm/year), which could be enough to drive some change in the plate movement considering that the south portion of the Nazca Plate is being created at the Chile Ridge. Thus, we suggest that the JFR trace has a primary curvature with an inflection point at O'Higgins seamounts, now accentuated by the NE-trending structural fabric acquired in the outer-rise region.

Taking advantage of refined plate tectonic models (e.g., Seton et al., 2012) and tools in GPlates 2.0 (Cannon et al., 2014), we used the rectified JFR trace to reconstruct the migration of the collision point over time (with South-American Plate fixed and JFR parallel to the convergence velocity). Our preliminary result yields a velocity of *ca*. 90 (± 20) mm/year southward from 15 to 10 Ma, which is lower than the value of *ca*. 200 mm/year obtained by Yáñez et al. (2001) and comparable with the value reported by Bello-González et al. (2018). For this reconstruction we partially modified the subducted segment older than 25 Ma to be parallel to the Nazca Ridge, a reasonable assumption before the major plate reorganization at *ca*. 26 Ma. If a restored continental margin is considered as in Arriagada et al. (2008, 2013) and Martinod et al. (2010), an even lower value would be obtained. Despite the significant uncertainty, the latter imply that JFR arrived at 27–28°S (northern limit of the Pampean flat slab segment) at *ca*. 15 Ma, and reached 31°S at *ca*. 10 Ma migrating since then at a lower velocity (*ca*. 25 mm/year). This slower migration velocity seems to be more consistent with the gradual initiation of the flat slab at this latitude (e.g., Kay et al., 1991), where the arc front started to decline in the Upper Miocene but persisted until Late Pliocene (Bissig et al., 2002), and the evidence of protracted uplift at coastal areas (e.g., Le Roux et al., 2005).

CONCLUSION

Juan Fernández Ridge is a *ca*. 800 km long and partially discontinuous chain of seamounts and islands in the Nazca Plate. 17 new and 3 recently published $^{40}Ar/^{39}Ar$ ages indicate a clear age progression with a mean velocity of *ca*. 81 mm/year. This is consistent with an origin of the JFR above a hotspot rooted in a mantle plume. The inferred velocity is much higher than obtained from models based on stationary hotspots, and still higher than those absolute plate motion models that consider moving mantle plumes. A westward drift of the mantle plume beneath JFR is thus implied. Morphological discontinuity along the ridge and along chain variations of the eruptive rates could be either related to changes in the petrological signature of the source and/or the dynamic nature of the overriding plate. Preliminary geochemical evidence suggests the possible involvement of a pyroxenite-bearing source from which low temperatures and low ascent velocities could be inferred. Such a nature of the source and the overlying lithosphere could explain both the diffuse geophysical signature of the plume and its intermittent upwelling. Both the age progression along the JFR based on new geocronological data and a detailed inspection of the morphology at O'Higgins seamounts cluster, allow a reappraisal of the subducted segment and hence a review of some of the postulated effects of the collision against the continental margin, at least during the last 15 Ma.

AUTHOR CONTRIBUTIONS

LL conceived and leaded the project, wrote the manuscript and prepared relevant figures and complements. JR organized de petrological section. JD-N produced the bathymetric data. BJ reduced the geochronological data. All discussed preliminary and final version.

FUNDING

This research was funded by Fondecyt grants 1141303 and 1110966 (LL). Sampling on board of the Cabo de Hornos vessel in 2015 was funded by project AUB150007 (LL). High resolution multibeam bathymetry was provided by FIPA 2014-04-1 project (JD-N), obtained during a cruise of Cabo de Hornos vessel in 2014. Claudia González carefully processed the multibeam dataset and Valentina Astudillo acted as an outstanding research assistant. Mirella Piña-Gauthier and Gabriel Orozco were tireless partners during fieldwork at Robinson Crusoe Island. Luna Pérez was a key research assistant during the manuscript preparation. Dedicated work by staff at both the WiscAr Lab at the University of Wisconsin–Madison and SERNAGEOMIN is greatly appreciated. CONAF (Corporación Nacional Forestal) granted access to protected lands in Robinson Crusoe and Alejandro Selkirk islands. DIFROL (Ministry of Foreign Affairs) was also supportive to reach remote insular areas.

ACKNOWLEDGMENTS

We greatly acknowledge the constructive comments by Bernhard Steinberger, the editor Adriano Pimentel and two reviewers.

REFERENCES

Adam, C., Caddick, M. J., and King, S. D. (2017). Pyroxenite causes fat plumes and stagnant slabs. *Geophys. Res. Lett.* 44, 4730–4737. doi: 10.1002/2017GL072943

Amante, C., and Eakins, B. W. (2009). *ETOPO1 1 Arc-Minute Global Relief Model: Procedures, Data Sources and Analysis. NOAA Technical Memorandum NESDIS NGDC*-24. Silver Spring, MD: NOAA, doi: 10.7289/V5C8276M

Anderson, D. (2005). "Scoring hotspots: the plume and plate paradigms," in *Plates, Plumes, and Paradigms: Geological Society of America Special Paper 388*, eds G. R. Foulger, J. H. Natland, D. C. Presnall, and D. L. Anderson (Boulder, CO: Geological Society of America), 31–54. doi: 10.1130/0-8137-2388-4.31

Argus, D. F., Gordon, R. G., Heflin, M. B., Ma, C., Eanes, R. J., Willis, P., et al. (2010). The angular velocities of the plates and the velocity of Earth's centre from space geodesy. *Geophys. J. Int.* 180, 913–960. doi: 10.1111/j.1365-246X.2009.04463.x

Arriagada, C., Ferrando, R., Córdova, L., Morata, D., and Roperch, P. (2013). The Maipo Orocline: a first scale structural feature in the Miocene to Recent geodynamic evolution in the central Chilean Andes. *Andean Geol.* 40, 419–437. doi: 10.5027/andgeoV40n3-a02

Arriagada, C., Roperch, P., Mpodozis, C., and Cobbold, P. R. (2008). Paleogene building of the Bolivian Orocline: tectonic restoration of the Central Andes in 2-D map view. *Tectonics* 27:TC6014. doi: 10.1029/2008TC002269

Astudillo, V. (2014). *Geomorfología y Evolución Geológica de la isla Robinson Crusoe, Archipiélago Juan Fernández*. Ph.D. thesis Santiago, Universidad de Chile, 154.

Baker, P. E., Gledhill, A., Harvey, P. K., and Hawkesworth, C. J. (1987). Geochemical evolution of the Juan Fernández Islands, SE Pacific. *J. Geol. Soc. Lond.* 144, 933–944. doi: 10.1144/gsjgs.144.6.0933

Ballmer, M. D., van Hunen, J., Ito, G., Tackley, P. J., and Bianco, T. (2007). Non-hotspot volcano chains originating from small-scale sublithospheric convection. *Geophys. Res. Lett.* 34:L23310. doi: 10.1029/2007GL031636

Bello-González, J. P., Contreras-Reyes, E., and Arriagada, C. (2018). Predicted path for hotspot tracks off South America since Paleocene times: tectonic implications of ridge-trench collision along the Andean margin. *Gondwana Res.* 64, 216–234. doi: 10.1016/j.gr.2018.07.008

Bissig, T., Clark, A. H., and Lee, J. K. (2002). Cerro de Vidrio rhyolitic dome: evidence for Late Pliocene volcanism in the central Andean flat-slab region, Lama-Veladero district, 29° 20' S, San Juan Province, Argentina. *J. South Am. Earth Sci.* 15, 571–576. doi: 10.1016/S0895-9811(02)00077-9

Bonatti, E., Harrison, C. G. A., Fisher, D. E., Honnorez, J., Schilling, J. G., Stipp, J. J., et al. (1977). Easter volcanic chain (Southeast Pacific): a mantle hot line. *J. Geophys. Res.* 82, 2457–2478. doi: 10.1029/JB082i017p02457

Booker, J., Bullard, E. C., and Grasty, R. L. (1967). Palaeomagnetism and age of rocks from easter island and juan fernández. *Geophys. J. Int.* 12, 469–471. doi: 10.1111/j.1365-246X.1967.tb03127.x

Cande, S. C., and Haxby, W. F. (1991). Eocene propagating rifts in the southwest Pacific and their conjugate features on the Nazca Plate. *J. Geophys. Res.* 96, 148–227. doi: 10.1029/91JB01991

Cannon, J., Lau, E., and Müller, R. D. (2014). Plate tectonic raster reconstruction in GPlates. *Solid Earth Dis.* 5, 741–755. doi: 10.5194/se-5-741-2014

Caress, D. W., and Chayes, D. N. (2017). *MB-System: Mapping the Seafloor*. Available at: https://www.mbari.org/products/research-software/mb-system

Clouard, V., and Bonneville, A. (2001). How many Pacific hotspots are fed by deep-mantle plumes? *Geology* 29, 695–698. doi: 10.1130/0091-7613(2001)029<0695:HMPHAF>2.0.CO;2

Clouard, V., Campos, J., Lemoine, A., Perez, A., and Kausel, E. (2007). Outer rise stress changes related to the subduction of the Juan Fernández Ridge, central Chile. *J. Geophys. Res.* 112:B05305. doi: 10.1029/2005JB003999

DeMets, C., Gordon, R. G., and Argus, D. F. (2010). Geologically current plate motions. *Geophys. J. Int.* 181, 1–80. doi: 10.1111/j.1365-246X.2009.04491.x

DeMets, C., Gordon, R. G., Argus, D. F., and Stein, S. (1994). Effect of recent revisions to the geomagnetic reversal time scale on estimates of current plate motions. *Geophys. Res. Lett.* 21, 2191–2194. doi: 10.1029/94GL02118

Devey, C. W., Hémond, C., and Stoffers, P. (2000). Metasomatic reactions between carbonated plume melts and mantle harzburgite: the evidence from Friday and Domingo Seamounts (Juan Fernández chain, SE Pacific). *Contrib. Mineral. Petrol.* 139, 68–84. doi: 10.1007/s004100050574

Farley, K. A., Basu, A. R., and Craig, H. (1993). He, Sr and Nd isotopic variations in lavas from the Juan Fernández archipelago, SE pacific. *Contrib. Mineral. Petrol.* 115, 75–87. doi: 10.1007/BF00712980

Fleck, R. J., Sutter, J. F., and Elliot, D. H. (1977). Interpretation of discordant 40Ar/39Ar age-spectra of Mesozoic tholeiites from Antarctica. *Geochim. Cosmochim. Acta* 41, 15–32. doi: 10.1016/0016-7037(77)90184-3

Flueh, E. R., Kopp, H., and Schreckenberger, B. (2002). *SPOC (SONNE Cruise SO-161 Leg 1 and 4), Subduction Processes off Chile, Geomar Rep. 102*. Kiel: Geomar.

French, S. W., and Romanowicz, B. (2015). Broad plumes rooted at the base of the Earth's mantle beneath major hotspots. *Nature* 525, 95–99. doi: 10.1038/nature14876

Garcia, M. O., Weis, D., Jicha, B. R., Ito, G., and Hanano, D. (2016). Petrology and geochronology of lavas from Ka'ula Volcano: implications for rejuvenated volcanism of the Hawaiian mantle plume. *Geochim. Cosmochim. Acta* 185, 278–301. doi: 10.1016/j.gca.2016.03.025

Gerlach, D. C., Hart, S. R., Morales, V. W. J., and Palacios, C. (1986). Mantle heterogeneity beneath the Nazca plate: san Felix and Juan Fernández islands. *Nature* 322, 165–169. doi: 10.1038/322165a0

Hahm, D., Castillo, P., and Hilton, D. (2009). A deep mantle source for high 3He/4He ocean island basalts (OIB) inferred from Pacific near-ridge seamount lavas. *Geophys. Res. Lett.* 36:L20316. doi: 10.1029/2009GL040560

Herzberg, C., Asimow, P. D., Arndt, N., Niu, Y., Lesher, C. M., Fitton, J. G., et al. (2007). Temperatures in ambient mantle and plumes: constraints from basalts, picrites, and komatiites. *Geochem. Geophys. Geosyst.* 8, 1–34. doi: 10.1029/2006GC001390

Hirano, N., Machida, S., Abe, N., Morishita, T., Tamura, A., and Arai, S. (2013). Petit-spot lava fields off the central Chile trench induced by plate flexure. *Geochem. J.* 47, 249–257. doi: 10.2343/geochemj.2.0227

Hirano, N., Takahashi, E., Yamamoto, J., Abe, N., Ingle, S. P., Kaneoka, I., et al. (2006). Volcanism in response to plate flexure. *Science* 313, 1426–1428. doi: 10.1126/science.1128235

Jackson, M. G., Konter, J. G., and Becker, T. W. (2017). Primordial helium entrained by the hottest mantle plumes. *Nature* 542, 340–343. doi: 10.1038/nature21023

Jicha, B. R., and Brown, F. H. (2014). An age for the Korath Range, Ethiopia and the viability of 40Ar/39Ar dating of kaersutite in Late Pleistocene volcanics. *Quat. Geochronol.* 21, 53–57. doi: 10.1016/j.quageo.2013.03.007

Jicha, B. R., Singer, B. S., and Sobol, P. (2016). Re-evaluation of the ages of 40Ar/39Ar sanidine standards and supereruptions in the western US using a Noblesse multi-collector mass spectrometer. *Chem. Geol.* 431, 54–66. doi: 10.1016/j.chemgeo.2016.03.024

Kay, S. M., Mpodozis, C., Ramos, V. A., and Munizaga, F. (1991). Magma source variations for mid-late Tertiary magmatic rocks associated with a shallowing subduction zone and the thickening crust in the central Andes (28-33°S). *Spec. Pap. Geol. Soc. Am.* 265, 113–137. doi: 10.1130/SPE265-p113

Kimura, J. I., and Kawabata, H. (2015). Ocean Basalt Simulator version 1 (OBS1): trace element mass balance in adiabatic melting of a pyroxenite-bearing peridotite. *Geochem. Geophys. Geosyst.* 16, 267–300. doi: 10.1002/2014GC005606

King, S. D., and Adam, C. (2014). Hotspot swells revisited. *Phys. Earth Planet. Inter.* 235, 66–83. doi: 10.1016/j.pepi.2014.07.006

Kingsley, R. H., and Schilling, J. G. (1998). Plume-ridge interaction in the Easter-Salas y Gomez seamount chain-Easter Microplate system: Pb isotope evidence. *J. Geophys. Res. Solid Earth* 103, 24159–24177. doi: 10.1029/98JB01496

Kirby, S., Engdahl, R. E., and Denlinger, R. (1996). Intermediate-depth intraslab earthquakes and arc volcanism as physical expressions of crustal and uppermost mantle metamorphism in subducting slabs. *Geophys. Monogr. Ser.* 96, 195–214. doi: 10.1029/GM096p0195

Konter, J. G., and Jackson, M. G. (2012). Large volumes of rejuvenated volcanism in Samoa: evidence supporting a tectonic influence on late-stage volcanism. *Geochem. Geophys. Geosyst.* 13:Q0AM04. doi: 10.1029/2011GC003974

Kopp, H., Flueh, E. R., Papenberg, C., and Klaeschen, D. (2004). Seismic investigations of the O'Higgins Seamount Group and Juan Fernández Ridge: aseismic ridge emplacement and lithosphere hydration. *Tectonics* 23:TC2009. doi: 10.1029/2003TC001590

Kuiper, K. F., Deino, A., Hilgen, F. J., Krijgsman, W., Renne, P. R., and Wijbrans, J. R. (2008). Synchronizing rock clocks of earth history. *Science* 320, 500–504. doi: 10.1126/science.1154339

Lara, L. E., Díaz-Naveas, J., Reyes, J., Jicha, B., Orozco, G., and Kay, S. M. (2018). Unraveling short-lived rejuvenated volcanism and a rapid transition from shield stage at O'Higgins Guyot, Juan Fernández Ridge, Pacific SE. *Deep Sea Res. Part I Oceanogr. Res. Pap.* 141, 33–42. doi: 10.1016/j.dsr.2018.08.012

Lara, L. E., Moreno, H., Naranjo, J. A., Matthews, S., and Pérez de Arce, C. (2006). Magmatic evolution of the Puyehue-Cordón Caulle Volcanic Complex (40°S), Southern Andean Volcanic Zone: from shield to unusual rhyolitic fissure volcanism. *J. Volcanol. Geotherm. Res.* 157, 343–366. doi: 10.1016/j.jvolgeores.2006.04.010

Laursen, J., and Normark, W. R. (2002). Late Quaternary evolution of the San Antonio Submarine Canyon in the central Chile forearc (33°S). *Mar. Geol.* 188, 365–390. doi: 10.1016/S0025-3227(02)00421-8

Laursen, J., Scholl, D. W., and von Huene, R. (2002). Neotectonic deformation of the central Chile margin: deepwater forearc basin formation in response to hot spot ridge and seamount subduction. *Tectonics* 21, 2-1–2-27. doi: 10.1029/2001TC901023

Le Roux, J. P., Gómez, C. A., Olivares, D. M., and Middleton, H. (2005). Determining the Neogene behavior of the Nazca plate by geohistory analysis. *Geology* 33, 165–168. doi: 10.1130/G21101.1

Manríquez, P., Contreras-Reyes, E., and Osses, A. (2013). Lithospheric 3-D flexure modelling of the oceanic plate seaward of the trench using variable elastic thickness. *Geophys. J. Int.* 196, 681–693. doi: 10.1093/gji/ggt464

Martinod, J., Husson, L., Roperch, P., Guillaume, B., and Espurt, N. (2010). Horizontal subduction zones, convergence velocity and the building of the Andes. *Earth Planet. Sci. Lett.* 300, 299–309. doi: 10.1016/j.epsl.2010.09.010

McDougall, I. (1964). Potassium-argon ages from lavas of the Hawaiian Islands. *Geol. Soc. Am. Bull.* 75, 107–128. doi: 10.1130/0016-7606(1964)75[107:PAFLOT]2.0.CO;2

McDougall, I. (1971). Volcanic island chains and sea floor spreading. *Nature* 231, 141–144. doi: 10.1038/physci231141a0

Mercer, C. M., and Hodges, K. V. (2016). ArAR-A software tool to promote the robust comparison of K-Ar and 40Ar/39Ar dates published using different decay, isotopic, and monitor-age parameters. *Chem. Geol.* 440, 148–163. doi: 10.1016/j.chemgeo.2016.06.020

Min, K., Mundil, R., Renne, P. R., and Ludwig, K. R. (2000). A test for systematic errors in 40Ar/39Ar geochronology through comparison with U/Pb analysis of a 1.1-Ga rhyolite. *Geochim. Cosmochim. Acta* 64, 73–98. doi: 10.1016/S0016-7037(99)00204-5

Mitchell, N. C. (2001). Transition from circular to stellate forms of submarine volcanoes. *J. Geophys. Res. Solid Earth* 106, 1987–2003. doi: 10.1029/2000JB900263

Morgan, W. J. (1971). Convection plumes in the lower mantle. *Nature* 230, 42–43. doi: 10.1038/230042a0

Morgan, W. J. (1972). Deep mantle convection plumes and plate motions. *Am. Assoc. Pet. Geol. Bull.* 56, 203–213. doi: 10.1038/nature17422

Müller, R. D., Sdrolias, M., Gaina, C., and Roest, W. R. (2008). Age, spreading rates, and spreading asymmetry of the world's ocean crust. *Geochem. Geophys. Geosyst.* 9:Q04006. doi: 10.1029/2007GC001743

Orellana-Rovirosa, F., and Richards, M. (2017). Rough versus smooth topography along oceanic hotspot tracks: observations and scaling analysis. *Geophys. Res. Lett.* 44, 4074–4081. doi: 10.1002/2016GL072008

Putirka, K. (2008). Excess temperatures at ocean islands: implications for mantle layering and convection. *Geology* 36, 283–286. doi: 10.1130/G24615A.1

Ramos, V., Cristallini, E. O., and Pérez, D. J. (2002). The Pampean flat-slab of the Central Andes. *J. South Am. Earth Sci.* 15, 59–78. doi: 10.1016/S0895-9811(02)00006-8

Ramos, V., and Folguera, A. (2009). Andean flat-slab subduction through time. *Geol. Soc. Lond. Spec. Publ.* 327, 31–54. doi: 10.1144/SP327.3

Ranero, C. R., von Huene, R., Weinrebe, W., and Reichert, C. (2006). "Tectonic processes along the Chile convergent margin," in *The Andes-Active Subduction Orogeny*, eds O. Oncken, G. Chong, G. Franz, P. Giese, H.-J. Götze, V. Ramos, et al. (Berlin: Springer), 91–121. doi: 10.1007/978-3-540-48684-8_5

Ray, J. S., Mahoney, J. J., Duncan, R. A., Ray, J., Wessel, P., and Naar, D. F. (2012). Chronology and geochemistry of lavas from the Nazca Ridge and Easter Seamount Chain: a 30 Myr hotspot record. *J. Petrol.* 53, 1417–1448. doi: 10.1093/petrology/egs021

Reich, M., Parada, M. A., Palacios, C., Dietrich, A., Schultz, F., and Lehmann, B. (2003). Adakite-like signature of Late Miocene intrusions at the Los Pelambres giant porphyry copper deposit in the Andes of central Chile: metallogenic implications. *Miner. Depos* 38, 876–885. doi: 10.1007/s00126-003-0369-9

Reichert, C., and Schreckenberger, B. (2002). Cruise Report SO161, leg 2&3, SPOC, subduction processes off Chile. *BGR Int. Rep.* 1–154.

Renne, P. R., Deino, A. L., Walter, R. C., Turrin, B. D., Swisher, C. C., Becker, T. A., et al. (1994). Intercalibration of astronomical and radioisotopic time. *Geology* 22, 783–786. doi: 10.1130/0091-7613(1994)022<0783:IOAART>2.3.CO;2

Reyes, J., Lara, L. E., and Morata, D. (2017). Contrasting P-T paths of shield and rejuvenated volcanism at Robinson Crusoe Island, Juan Fernández Ridge, SE Pacific. *J. Volcanol. Geotherm. Res.* 341, 242–254. doi: 10.1016/j.jvolgeores.2017.05.035

Rodrigo, C., and Lara, L. E. (2014). Plate tectonics and the origin of the Juan Fernández Ridge: analysis of bathymetry and magnetic patterns. *Lat. Am. J. Aquat. Res.* 42, 907–917. doi: 10.3856/vol42-issue4-fulltext-15

Rosenbaum, G., and Mo, W. (2011). Tectonic and magmatic responses to the subduction of high bathymetric relief. *Gondwana Res.* 19, 571–582. doi: 10.1016/j.gr.2010.10.007

Sandwell, D., and Fialko, Y. (2004). Warping and cracking of the Pacific plate by thermal contraction. *J. Geophys. Res.* 109:B10411. doi: 10.1029/2004JB003091

Schepers, G., Van Hinsbergen, D. J., Spakman, W., Kosters, M. E., Boschman, L. M., and McQuarrie, N. (2017). South-American plate advance and forced Andean trench retreat as drivers for transient flat subduction episodes. *Nat. Commun.* 8:15249. doi: 10.1038/ncomms15249

Sepúlveda, P., Le Roux, J. P., Lara, L. E., Orozco, G., and Astudillo, V. (2015). Biostratigraphic evidence for dramatic Holocene uplift of Robinson Crusoe Island, Juan Fernández Ridge, SE Pacific Ocean. *Biogeosciences* 12, 1993–2001. doi: 10.5194/bg-12-1993-2015

Seton, M., Müller, R. D., Zahirovic, S., Gaina, C., Torsvik, T., Shephard, G., et al. (2012). Global continental and ocean basin reconstructions since 200 Ma. *Earth Sci. Rev.* 113, 212–270. doi: 10.1016/j.earscirev.2012.03.002

Sharp, W. D., and Renne, P. R. (2005). The 40Ar/39Ar dating of core recovered by the Hawaii Scientific Drilling Project (phase 2), Hilo, Hawaii. *Geochem. Geophys. Geosyst.* 6:18. doi: 10.1029/2004GC000846

Simons, K., Dixon, J., Schilling, J.-G., Kingsley, R., and Poreda, R. (2002). Volatiles in basaltic glasses from the Easter-Salas y Gomez Seamount Chain and Easter Microplate: implications for geochemical cycling of volatile elements. *Geochem. Geophys. Geosyst.* 3, 1–29. doi: 10.1029/2001GC000173

Somoza, R., and Ghidella, M. E. (2012). Late Cretaceous to recent plate motions in western South America revisited. *Earth Planet. Sci. Lett.* 331, 152–163. doi: 10.1016/j.epsl.2012.03.003

Steiger, R. H., and Jagger, E. (1977). Subcommission on geochronology: convention on the use of decay constants in geo- and cosmochronology. *Earth Planet. Sci. Lett.* 36, 359–362. doi: 10.1016/0012-821X(77)90060-7

Steinberger, B., and Torsvik, T. H. (2012). A geodynamic model of plumes from the margins of Large Low Shear Velocity Provinces. *Geochem. Geophys. Geosyst.* 13:Q01W09. doi: 10.1029/2011GC003808

Stuessy, T. F., Foland, K. A., Sutter, J. F., Sanders, R. W., and Silva, M. (1984). Botanical and geological significance of potassium-argon dates from the Juan Fernández Islands. *Science* 225, 49–51. doi: 10.1126/science.225.4657.49

Tassara, A., Götze, H. J., Schmidt, S., and Hackney, R. (2006). Three-dimensional density model of the Nazca plate and the Andean continental margin. *J. Geophys. Res. Solid Earth* 111:B09404. doi: 10.1029/2005JB003976

Tebbens, S. F., and Cande, S. C. (1997). Southeast Pacific tectonic evolution from early Oligocene to present. *J. Geophys. Res. Solid Earth* 102, 12061–12084. doi: 10.1029/96JB02582

Tebbens, S. F., Cande, S. C., Kovacs, L., Parra, J. C., LaBrecque, J. L., and Vergara, H. (1997). The Chile ridge: a tectonic framework. *J. Geophys. Res. Solid Earth* 102, 12035–12059. doi: 10.1029/96JB02581

Truong, T. B., Castillo, P. R., Hilton, D. R., and Day, J. M. D. (2018). The trace element and Sr-Nd-Pb isotope geochemistry of Juan Fernández lavas reveal variable contributions from a high- 3He/4He mantle plume. *Chem. Geol.* 476, 280–291. doi: 10.1016/j.chemgeo.2017.11.024

Vogt, P. R., and Smoot, N. C. (1984). The Geisha Guyots: multibeam bathymetry and morphometric interpretation. *J. Geophys. Res. Solid Earth* 89, 11085–11107. doi: 10.1029/JB089iB13p11085

von Huene, R., Corvalán, J., Flueh, E. R., Hinz, K., Korstgard, J., Ranero, C. R., et al. (1997). Tectonic control of the subducting Juan Fernández Ridge on the Andean margin near Valparaiso, Chile. *Tectonics* 16, 474–488. doi: 10.1029/96TC03703

Wang, S., Yu, H., Zhang, Q., and Zhao, Y. (2018). Absolute plate motions relative to deep mantle plumes. *Earth Planet. Sci. Lett.* 490, 88–99. doi: 10.1016/j.epsl.2018.03.021

Weatherall, P., Marks, K. M., Jakobsson, M., Schmitt, T., Tani, S., Arndt, J. E., et al. (2015). A new digital bathymetric model of the world's oceans. *Earth Space Sci.* 2, 331–345. doi: 10.1002/2015EA000107

Wessel, P., and Smith, W. H. F. (1995). New version of the Generic Mapping Tools released. *EOS Trans. Am. Geophys. Union* 76:329. doi: 10.1029/95EO00198

Wilson, J. (1963). A possible origin of the Hawaiian islands. *Can. J. Phys.* 41, 863–870. doi: 10.1139/p63-094

Yáñez, G., Cembrano, J., Pardo, M., Ranero, C., and Selles, D. (2002). The Challenger–Juan Fernández–Maipo major tectonic transition of the Nazca–Andean subduction system at 33-34 S: geodynamic evidence and implications. *J. South Am. Earth Sci.* 15, 23–38. doi: 10.1016/S0895-9811(02)00004-4

Yáñez, G. A., Ranero, C. R., Huene, R., and Díaz, J. (2001). Magnetic anomaly interpretation across the southern central Andes (32-34 S): the role of the Juan Fernández Ridge in the late Tertiary evolution of the margin. *J. Geophys. Res.* 106, 6325–6345. doi: 10.1029/2000JB900337

York, D. (1969). Least-squares fitting of a straight line. *Can. J. Phys.* 44, 1079–1086. doi: 10.1139/p66-090

Conflict of Interest Statement: The authors declare that the research was conducted in the absence of any commercial or financial relationships that could be construed as a potential conflict of interest.

Copyright © 2018 Lara, Reyes, Jicha and Díaz-Naveas. This is an open-access article distributed under the terms of the Creative Commons Attribution License (CC BY). The use, distribution or reproduction in other forums is permitted, provided the original author(s) and the copyright owner(s) are credited and that the original publication in this journal is cited, in accordance with accepted academic practice. No use, distribution or reproduction is permitted which does not comply with these terms.

frontiers in Earth Science

ORIGINAL RESEARCH
published: 07 September 2018
doi: 10.3389/feart.2018.00119

The Effect of Ocean Loading on the Growth of Basaltic Ocean Island Volcanoes and Their Magmatic Plumbing System

Nicolas Le Corvec[1]* *and Patrick J. McGovern*[2]

[1] Laboratoire Magmas et Volcans, Université Clermont Auvergne–CNRS–IRD, OPGC, Aubière, France, [2] Lunar and Planetary Institute, Universities Space Research Association, Houston, TX, United States

OPEN ACCESS

Edited by:
Laura Becerril Carretero,
Instituto de Ciencias de la Tierra Jaume Almera (ICTJA), Spain

Reviewed by:
Alessandro Tibaldi,
Università degli studi di Milano Bicocca, Italy
Marco Neri,
Istituto Nazionale di Geofisica e Vulcanologia (INGV), Italy

***Correspondence:**
Nicolas Le Corvec
nicolas.le_corvec@uca.fr

Specialty section:
This article was submitted to Volcanology, a section of the journal Frontiers in Earth Science

Received: 26 January 2018
Accepted: 30 July 2018
Published: 07 September 2018

Citation:
Le Corvec N and McGovern PJ (2018) The Effect of Ocean Loading on the Growth of Basaltic Ocean Island Volcanoes and Their Magmatic Plumbing System. Front. Earth Sci. 6:119. doi: 10.3389/feart.2018.00119

Basaltic shield volcanoes most commonly form as intraplate volcanic ocean islands that arise from the ocean floor and continue to grow above the sea water level to form gigantic volcanic edifices. The volcanic edifice evolution and the internal stress distribution may be influenced by the water load of the surrounding ocean. We therefore investigate how the presence of an ocean affects the internal stress of a volcanic edifice and thus magma propagation by means of axisymmetric elastic models of a volcanic edifice overlying an elastic lithosphere. We designed a volcanic edifice featuring a height of ∼6,000 m and a radius of ∼ 60 km which was build up either instantaneously or incrementally, i.e., by emplacing new layers of equal volumes on top of each other. The latter was done in a way that the resulting stress and edifice geometry from one step served as the initial condition of the subsequent step. Thus, each new deposit was emplaced on an already deformed and stressed model layer. The ocean load was simulated using a boundary condition at the surface of the model. For the instantaneous volcano growth scenario, different water levels were investigated, while for the incrementally growing volcano the water level was fixed to 4,000 m. We employed both half-space and flexural models and compared the deformation of the volcanic edifice, as well as its internal stress orientation and magnitude with and without applying an ocean load. Our results show major differences in the resulting state of stress between an instantaneous and an incrementally built volcanic edifice. Further, our results imply that stress orientations and types of potential magma intrusions within the volcano as well are influenced by the loading effect of an ocean. Ocean loading reduces the effective load magnitude of an edifice via a buoyancy effect, reducing edifice stress magnitudes and substrate subsidence. Ocean loading also adds vertical compression to edifices; in half-space models, this addition reinforces the existing principal stress orientations and increases the differential stress, whereas in flexural models, ocean loading reduces the differential stress

and favors re-orientation of principal stresses within the edifices. Our results therefore provide new insights into the state of stress and deformation within the edifices of basaltic ocean island volcanoes with significant implications for magma ascent and eruption and edifice construction.

Keywords: basaltic ocean island volcano, magmatic system, finite element models, flexure, numerical modeling, volcano deformation

INTRODUCTION

Basaltic ocean island shield volcanoes are the largest volcanic edifices on Earth. While these islands develop over millions of years as a result of continuous volcanic hot spot activity [e.g., La Réunion: ∼5 Ma (Gillot et al., 1994), Galapagos Islands ∼4 Ma (Bailey, 1976), Hawaiian Islands: ∼5.1 Ma (Clague and Dalrymple, 1987)], individual volcanic centers that build those islands have a shorter lifespan [e.g., Piton de la Fournaise at La Réunion: ∼530 ka (Gillot et al., 1994), and Mauna Kea at Hawaii: ∼700 ka (Frey et al., 1990)]. Growth mechanisms include both magmatic intrusions that generate dike and sill complexes (Walker, 1993, 1999) and volcanic eruptions characterized by lava flow emplacement and pyroclastic or volcanoclastic material deposition (Walker, 1973, 2000). The contribution of magmatic intrusions to the growth and therefore overall volume of a volcanic edifice can be significant: for instance, at Ko'olau Volcano (O'ahu Island, HI, USA) sill complexes may be responsible for at least half of the height of the edifice (Annen et al., 2001). As a basaltic volcano grows, the increasing gravitational load causes a flexure of the underlying lithosphere (McNutt and Menard, 1978; McGovern, 2007), generating horizontal compressional stresses within the volcanic edifice and clamping the propagation of magmas toward the surface and promoting the formation of sills (McGovern and Solomon, 1998; Pinel and Jaupart, 2004; McGovern, 2007; Menand et al., 2010; Galgana et al., 2011). The accumulation of magma within the volcanic edifice leads to the formation of magmatic reservoirs (Annen, 2011; Menand et al., 2011), wherein pressure can then build up to generate eruptions at the surface (Tait et al., 1989; McLeod and Tait, 1999; Pinel et al., 2010; Becerril et al., 2013). These eruptions are the result of magma propagation through the volcanic edifice, which is largely controlled by the internal state of stress in response to structural controls (Fiske and Jackson, 1972; Carracedo, 1994; Rubin, 1995; Acocella and Neri, 2009; Bagnardi et al., 2013; Chestler and Grosfils, 2013; Tibaldi, 2015), the mechanical layering (Gudmundsson, 2005; Kavanagh et al., 2006; Maccaferri et al., 2011), and pre-existing fractures (Gaffney et al., 2007; Le Corvec et al., 2013).

Volcanic edifices are often modeled as instantaneous volume (referred subsequently as instantaneous volcano; van Wyk de Vries and Matela, 1998; Pinel and Jaupart, 2003; Casagli et al., 2009; Galgana et al., 2011), while in fact they grow incrementally over time (referred subsequently as incremental volcano; McGovern and Solomon, 1993, 1998; Apuani et al., 2005; Musiol et al., 2016). Stresses within instantaneously-formed and incrementally-grown volcanoes are significantly different. While instantaneously-formed edifices show high differential stresses in the upper parts of the volcano and low differential stresses in the lower parts, incrementally-grown edifices show low differential stresses in in upper and lower parts of the volcano, separated by a zone of high differential stresses (McGovern and Solomon, 1993). Over the course of their life, basaltic ocean island volcanoes rose from the bottom of the ocean and emerged to form the islands that we observe today. Previous research has shown that ocean loading alters the state of stress within the lithosphere at near-shore plate boundaries (Luttrell and Sandwell, 2010) and influences volcanic eruptive activity (McNutt, 1999), and that glacial cycles can cause pressure changes in the mantle that yet affect the melt production at mid-oceanic ridges (Crowley et al., 2015). Here, we investigate the role of ocean loading on the growth of basaltic ocean island volcanoes and suggest that edifice internal stresses and magma propagation pathways may in fact be biased by ocean loads.

In the following, we present finite element models of both instantaneously- and incrementally grown volcanic edifices and show the effect of the presence or absence of ocean load on their internal stresses. Furthermore, we illustrate scenarios incorporating or ignoring lithospheric flexure. We provide the amount of displacement and the favored type of magmatic intrusion (dyke or sill) within the edifice as calculated from the edifice internal state of stress and we discuss the implications of our models for tackling edifice internal stresses and magma propagation at basaltic ocean island volcanoes.

METHODOLOGY

In this study, we use finite element models (FEMs) to investigate the effect of ocean load on the vertical deformation and the state of stress within a basaltic ocean island volcano. We develop axisymmetric elastic models of a volcanic edifice overlying an elastic lithosphere following the work of Galgana et al. (2011) and using the COMSOL Multiphysics software. All our models have similar physical parameters (**Table 1**) and are loaded gravitationally with body forces and initial lithostatic stresses (**Table 2**, no ocean load). The boundary condition applied at the base of the lithosphere balance the loading of the lithostatically-prestressed lithosphere ($-g.\rho_{lith}.T_l$) and simulates buoyant restoring forces ($g.\ \rho_{asth}.w$) in response to the lithosphere subsidence within a denser asthenosphere (**Table 2**; Watts, 2001). In our models, we adopt the convention that extension is positive while compression is negative.

By developing and testing different model scenarios, we investigate or account for: 1- a half-space configuration vs. the flexure of the lithosphere below the edifice, 2- instantaneous

TABLE 1 | Constant physical model parameters.

	Name	Expression
Constants	Lithosphere density (ρ_{lith})	2,800 kg/m^3
	Asthenosphere density (ρ_{asth})	3,300 kg/m^3
	Volcano density (ρ_{volc})	2,800 kg/m^3
	Radius Lithosphere (R_{lith})	1,000 km
	Young's Modulus (E_c)	1.10^{11} Pa
	Poisson's ratio (ν)	0.25
	Earth gravitational acceleration (g)	−9.81 m/s^2

TABLE 2 | Boundary conditions of the initial finite element models (FEM), where *w* is the vertical displacement, *g* is the Earth's gravitational acceleration; ρ_{lith}, ρ_{asth} and ρ_{water} are the lithosphere, asthenosphere and water densities, respectively, H_{water} is the water height, T_L is the thickness of the lithosphere, *Z* represents the depth of any point of the initial geometry (negative downward).

	No ocean load		Ocean load	
	Lithosphere	Volcano	Lithosphere	Volcano
Body load	$g^*\rho_{lith}$	$g^*\rho_{volc}$	$g^*\rho_{lith}$	$g^*\rho_{volc}$
Initial stress	$-g^*\rho_{lith}{}^*Z$	/	$-g^*(\rho_{lith}{}^*Z-\rho_{water}{}^*H_{water})$	/
Bottom equilibrium	$-g^*(\rho_{lith}{}^*T_L-\rho_{asth}{}^*w)$		$-g^*(\rho_{water}{}^*H_{water}+\rho_{lith}{}^*T_L-\rho_{asth}{}^*w)$	
Ocean load	/		$(\rho_{water}{}^*g^*(H_{water}-Z))^*(Z<H_{water})$	

volcano existence vs. incremental volcano evolution, and 3- the presence (or absence) of ocean load.

Half-Space vs. Flexural Models

In order to understand the role of flexure on edifice internal stresses, two sets of models were developed (1) half-space models, where the domain underlying the volcanic edifice is considered as infinite ($T_L = 1{,}000$ km), and (2) flexural models where the thickness of the domain ($T_L = 30$ km) represents an average elastic thickness of the oceanic lithosphere (**Figure 1**; Watts and ten Brink, 1989; Wessel, 1993).

Instantaneous Edifice Existence vs. Incremental Edifice Growth

Following the work of McGovern and Solomon (1993, 1998), we reconstruct the volcanic edifice (a) as if it was existing instantaneously, and (b) as if it was building up incrementally, assuming a constant magma supply rate over time. For the latter case, we start with an initial edifice of height $V_h = 3{,}000$ m and radius $V_r = 30{,}000$ m (**Figure 1**) and then we subsequently emplace seven new layers, each of them featuring the same volume as the initial edifice (representing a constant magma flux rate). The lithospheric and edifice internal stresses, as well as the deformed geometry that result from one step, serve as the initial conditions before the emplacement of the subsequent layer. For each new layer, we apply two bottom boundary conditions (**Table 3**); the first one in order to compensate for the imported geometry and the second one in order to act as the buoyant response of the asthenosphere to the load of the new layer. To be computationally efficient and keep run-times less than 1 day long, a maximum of seven increments were performed for any incrementally-grown edifice. The instantaneously-formed volcanoes were built to match the final volumes of their counterpart incrementally-grown volcano model (bold values in **Tables S1**,**S2**).

Ocean Load

In order to understand the effect of the ocean on a growing volcanic edifice, two kinds of models were developed and tested in combination with the half-space and flexural models (section Half-Space vs. Flexural Models) and the two distinct edifice growth scenarios (section Instantaneous Edifice Existence vs. Incremental Edifice Growth). For the scenario of instantaneously-formed volcanoes, we tested eight different ocean levels (from 0 to 7km) in order to study the effect of different amounts of oceanic load on a volcano of constant height. For the scenario of incrementally-grown volcanoes, the ocean level was set to either 0 or 4,000 m [similar to the mean depth of the ocean floor worldwide (Sverdrup et al., 1942; Vezzi et al., 2005)] in order to study the rise and emergence of a basaltic ocean island volcano. The ocean load was simulated as a boundary load at the surface of the model, and taken into account in buoyant restoring forces (Bottom equilibrium in **Tables 2**, **3**).

Limitations

In order to focus our interest on the mechanical response of a volcanic edifice to the presence of an ocean load, we made a series of simplifications. First, the growth of volcanic islands is also affected by the process of gravitational spreading, usually facilitated by basal sediments units (Borgia et al., 1992; Le Corvec and Walter, 2009; McGovern and Morgan, 2009; Byrne et al., 2013; McGovern et al., 2015; Musiol et al., 2016). However, not all volcanic edifices are subject to decollement-based gravitational spreading [e.g., the volcanoes of the Canary Islands (Carracedo, 1994; Mitchell et al., 2002)]; therefore in order to focus on the flexural response and the ocean load effect, we neglect the effect of gravitational spreading in our models. Second, the development of magma reservoirs is known to influence the surrounding state of stress and the type of magma intrusions (Chestler and Grosfils, 2013; Le Corvec et al., 2015); however the influence of the magma reservoirs is localized compared to the scale of an edifice as modeled in this study. Finally, we limit our models to the elastic rheology, the viscoelastic response of the asthenosphere (McGovern and Solomon, 1993, 1998; Musiol et al., 2016) and the hot cumulates within the volcanic edifice (Clague and Denlinger, 1994) are neglected. These behaviors will be integrated in future work. As we show in the following section, although our models are simplified, important information can be extracted that helps in understanding real volcano behavior.

RESULTS

In the following, we first present the vertical displacements observed at the surface of the models (**Figure 2**). For our incrementally-grown volcano models, the final vertical displacement corresponds to the cumulative vertical displacements of all successive steps. Then we describe the

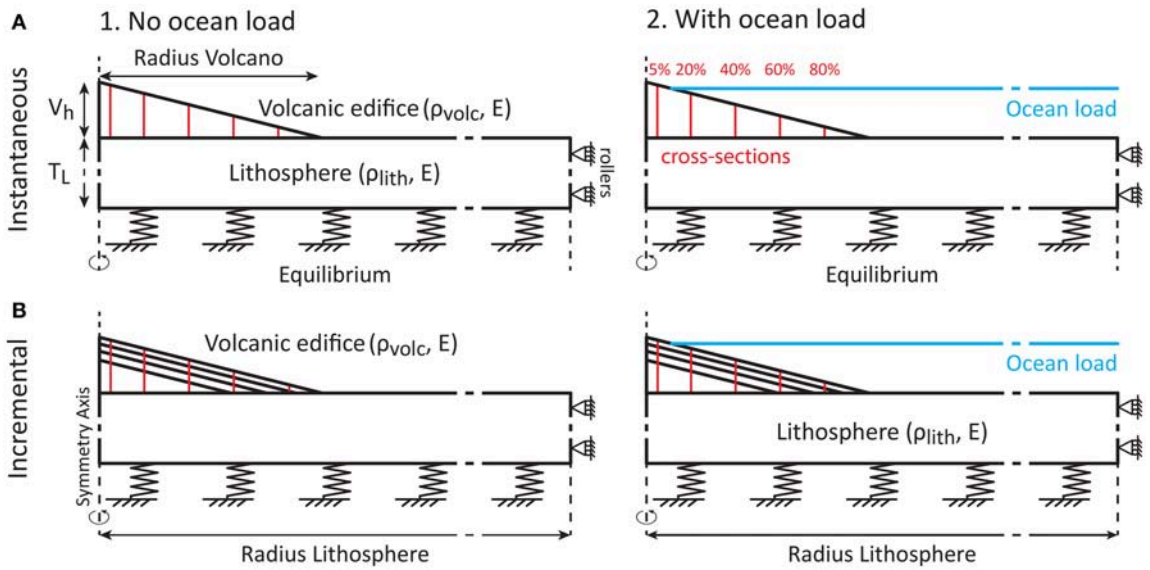

FIGURE 1 | Boundary conditions for the different axisymmetric finite element models (FEMs) used in this study. Initially, models are composed of an elastic lithosphere and an elastic volcanic edifice with or without an ocean load, with buoyant restoring forces applied at the base of the model and rollers applied to the right margin to constrain horizontal movements. Models are tested for a half-space geometry where T_L = 1,000 km, and a flexure geometry where T_L = 30 km. We studied two types of edifice growth: **(A)** an instantaneously-formed volcanic edifice, and **(B)** an incrementally-grown volcanic edifice consisting of layers of equal volumes as the initial edifice. In the models taking into account an ocean load, the ocean level varies from 1,000 to 7,000 m in instantaneously-formed volcano models (A2), while it stays constant at 4,000 m in incrementally-grown volcano models (B2). Cross-sections were created at 5, 20, 40, 60, and 80% of the resulting length of the volcanic edifice away from the symmetry axis (**Table S3**). These cross-sections are used to plot the differential stress and the type of magmatic intrusions within the edifice (cf. **Figures 3**, **5**, **7**).

TABLE 3 | Boundary conditions of the subsequent FEMs, where w_n is the vertical displacement in the nth model.

	No ocean load		Ocean load	
	Imported geometry	**New volcanic layer**	**Imported geometry**	**New volcanic layer**
Body load	$g^*\rho_{lith}$	$g^*\rho_{volc}$	$g^*\rho_{lith}$	$g^*\rho_{volc}$
Initial stress	Transferred	/	Transferred	/
Bottom equilibrium 1	$-g^*(\rho_{lith}{}^* T_L - \rho_{asth}{}^*(Z + T_L))$		$-g^*((\rho_{water}{}^* H_{water} + \rho_{lith}{}^* T_L) - \rho_{asth}{}^*(Z + T_L))$	
Bottom equilibrium 2	$-g^*(-\rho_{asth}{}^* w_n)$		$-g^*(-\rho_{asth}{}^* w_n)$	
Ocean load	/		$(\rho_{water}{}^* g^*(H_{water} - Z))^*(Z < H_{water})$	

Legend as in ***Table 2.***

state of stress within the volcanic edifice along cross sections by means of the differential stress ($\Delta\sigma = \sigma_1 - \sigma_3$). The cross sections were created at 5, 20, 40, 60, and 80% of the length of the volcanic edifice away from the symmetry axis (red lines in **Figure 1**). The initial 5% cross-section was chosen to avoid the stress orientation degeneracy at the symmetric axis (i.e., r = 0 km). Pathways of magmatic intrusions are defined by the orientation of the minimum compressional stress (σ_3; Rubin, 1995). Sills, angular dikes and circumferential dikes are formed when σ_3 is in the r-z plane (with r being the radial (horizontal) distance from the symmetry axis, z corresponds to the vertical coordinates); sills are sub-horizontal intrusions, and are defined for angles $\leq 20^\circ$ between σ_3 and the z-axis (cf. dark blue color in **Figures 3–8**), angular dikes are defined for angles $>20^\circ$ and $<70^\circ$ (cf. light blue in **Figures 3–8**), finally circumferential dikes are sub vertical intrusions, and are defined for angles of $\geq 70^\circ$ (cf. green color in **Figures 3–8**). Radial dikes are formed when σ_3 is the "out of plane" stress, perpendicular to the r-z plane (cf. red color in **Figures 3–8**).

Vertical Displacements

Instantaneous Volcano

For an instantaneous volcano, the vertical displacements we observe differ significantly between half-space and flexural models. We compare the ratio between the vertical displacements and the final height of the volcanic edifice (**Figure 2** and **Tables S1**,**S2**). Without an ocean load, the displacement ratio in the half-space model reaches $\sim 0.15 \times 10^{-3}$ (blue color at 0 m sea level in **Figure 2A**), while in the flexural model the displacement ratio is about two orders of magnitude higher and reaches $\sim 123 \times 10^{-3}$ (blue color at 0 m sea level in **Figure 2B**). In the presence of an ocean load, we observe decreasing vertical displacements with increasing sea levels (blue dotted lines in **Figures 2A,B**).

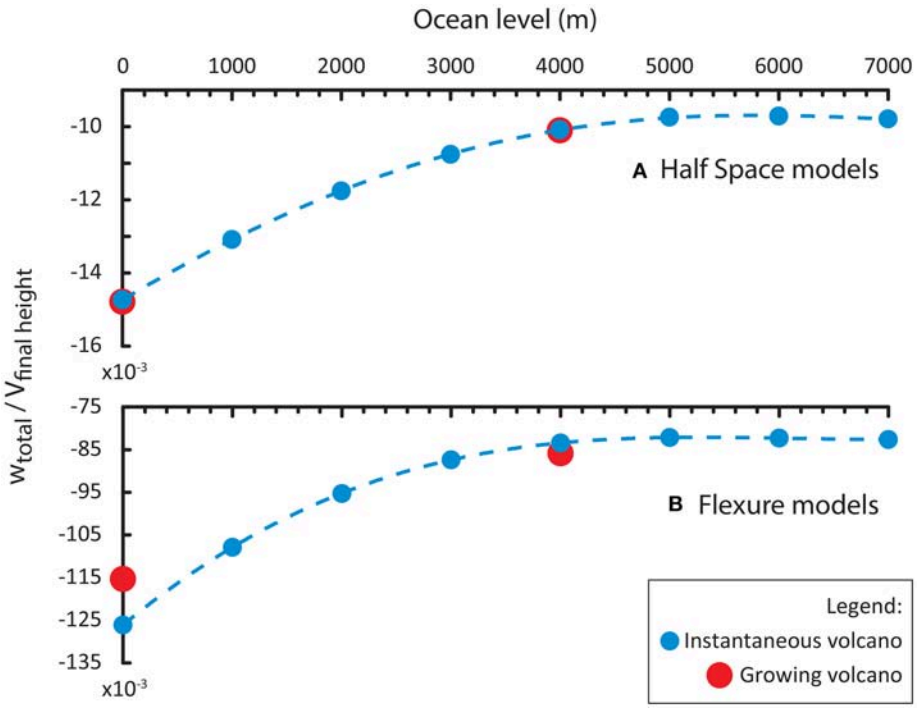

FIGURE 2 | Ratios between the vertical displacements at summit of the volcanic edifice (w) and its the final height (Vh) for instantaneously-formed (blue) and incrementally-grown (red) volcano models. Different sea levels are displayed for instantaneously-formed volcano models (0, 3,000, 5,000, and 7,000 m), and for incrementally-grown volcano models (0 or 4,000 m). Results for half-space models are shown in the upper panel **(A)** while results for flexural models are shown in the lower panel **(B)**.

This tendency is valid until a certain water level threshold is reached at ∼5,500 m after which the vertical displacements slowly increase again.

Incremental Volcano

We obtain quasi-identical vertical displacements for incrementally-grown volcanoes and the equivalent instantaneously-formed volcano simulations when applying half-space models without the effect of ocean loading and also for incrementally-grown volcanoes and the analogous instantaneous volcano modeled in half-space with an oceanic load (red dots at 0 and 4,000 m ocean level in **Figures 2A**, and **Tables S1**,**S2**). For flexural models, we observe slightly lower vertical displacements for the incrementally-grown volcano without an ocean load as compared to the analogous instantaneous volcano, but slightly more displacements from models with the presence of an ocean load (red dots at 0 and 4,000 m seal level in **Figures 2B**, and **Tables S1**,**S2**).

State of Stress and Magmatic Intrusions

Instantaneous Volcano

Instantaneous volcano half-space models

A volcanic edifice that is instantaneously-formed in a half-space model and is not affected by an ocean load shows a curved state of stress, i.e., high $\Delta\sigma$ in the upper and lower parts of the edifice, separated by a zone of low $\Delta\sigma$ in most part of the edifice (cf. dotted lines from 5 to 60% in **Figures 3A**, **4A** and **Figure S1.1**). At the tip of the edifice (cf. dotted line at 80% in **Figure 3A**), the $\Delta\sigma$ decreases from top to bottom. Below the summit (i.e., at 5% distance from the symmetry axis), the state of stress promotes circumferential dike intrusions and sill emplacement at the lower and upper parts of the edifice, respectively, separated by an intermediate zone of angular dike intrusion. Such state of stress becomes more prominent with increasing distance from the symmetry axis, replacing the deep zones prone to circumferential dikes and decreasing the vertical extent of sill emplacements (cf. cross-sections at 20–80% in **Figure 3A**).

We find that rising ocean levels decrease the amount of $\Delta\sigma$ within the upper part of the volcanic edifice while at deeper levels of the edifice $\Delta\sigma$ increases with increasing oceanic load (cf. solid lines in **Figures 3A**, **4B** and **Figures S1.2–4**). In addition, the zone of low $\Delta\sigma$ shifts upward within the edifice, which ultimately changes the curved state of stress into a linear one (e.g., the cross-section at 40% distance from the symmetry axis with an ocean level of 7 km in **Figure 3A**). At the highest water level (+7,000 m), we also observe that the magnitude of $\Delta\sigma$ becomes larger at the surface of the lower flanks than the models with lower ocean load (cf., cross-sections 60 and 80% in **Figures 3A**, **4B** and **Figures S1.2–4**). Furthermore, our results show that the type of magmatic intrusions is also affected when applying oceanic loading. We find that increasing

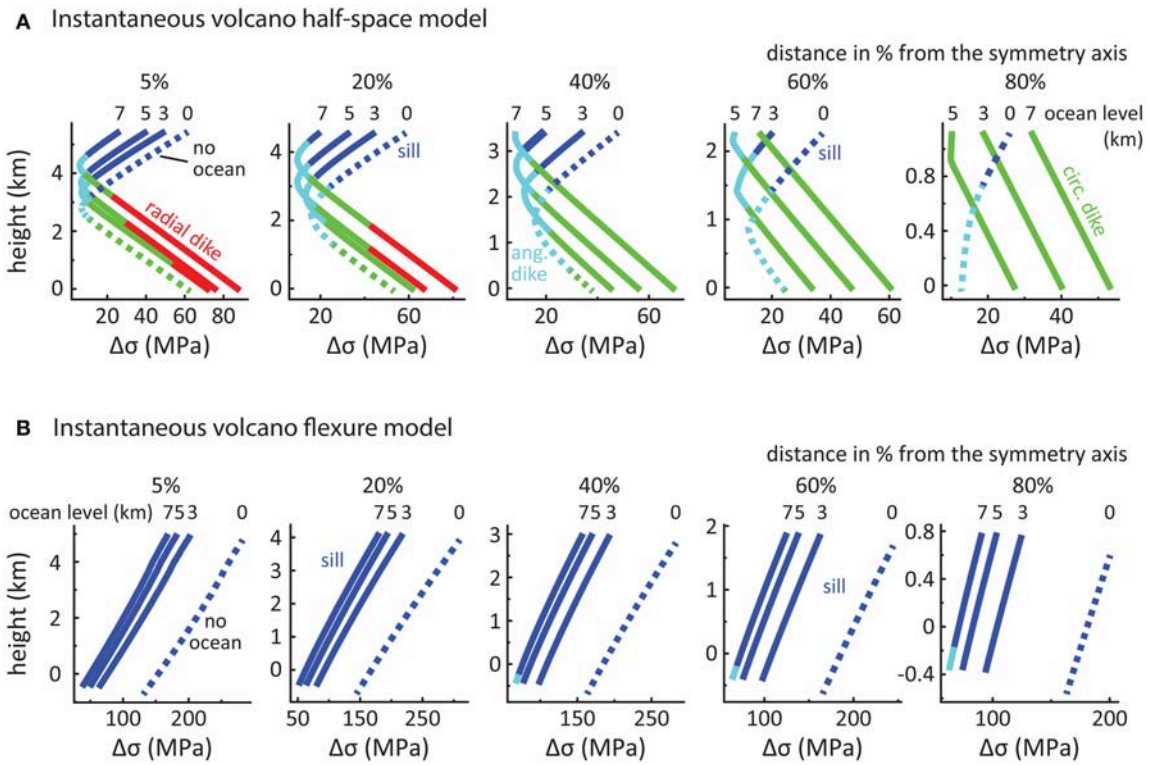

FIGURE 3 | Differential stress magnitudes, and magmatic intrusion types predicted from principal stress orientations along the internal cross-sections for instantaneously-formed volcanoes in **(A)** half-space and **(B)** flexure models. Dashed lines represent the model without an ocean load. Solid lines represent models taking into account different ocean loads (with the sea levels in km given above each line). Dark blue color represents sill intrusion ([0°-20°] between σ_3 and the z-axis), light blue color represents angular dike intrusion [(20°-70°) between σ_3 and the z-axis], green color represents circumferential dike intrusion ([70°-90°] between σ_3 and the z-axis), and red color represents radial dike intrusion.

the ocean load increases the fraction of the edifice that is subject to stress states favoring circumferential dike development. Furthermore, we find stress states that facilitate radial diking at the base of the volcanic flank near the summit and that the vertical extent of such conditions increases with increasing ocean levels (cf., e.g., the cross-sections at 5 and 20% distance from the symmetry axis with ocean levels of 3, 5, and 7 km in **Figure 3A**).

Instantaneous volcano flexure models

When ignoring oceanic load, a volcanic edifice instantaneously-formed on an elastic 30 km thick lithosphere shows increasing differential stresses $\Delta\sigma$ from deeper to shallower levels within the volcanic edifice (dotted lines in **Figures 3B**, **4C** and **Figure S2.1**). The state of stress promotes sill intrusions throughout the entire edifice (**Figures 3B**, **4C**).

Increasing the ocean load causes the magnitude of $\Delta\sigma$ to decrease without substantially changing the slope or shape of the $\Delta\sigma$ (solid lines in **Figures 3B**, **4D** and **Figures S2.2–4**). While $\Delta\sigma$ decreases in magnitude, the stress orientations are not affected and continue to favor the formation of sills throughout the entire edifice, with the exception of small zones favoring angular dikes at the base of the outer flanks for an ocean level of 7,000 m (**Figure 3B**).

Incremental Volcano

Incremental volcano half-space models

When neglecting the loading effect of the ocean (dashed lines in **Figures 5**, **6A,B**, and **Figure S3**), the initial volcanic edifice that is emplaced on a half-space shows essentially the same curved stress distribution as the corresponding instantaneous volcano model (dashed lines in **Figure 3A** in comparison with the dotted lines in step 1 of **Figure 5**). In the subsequent layers, the differential stress $\Delta\sigma$ at the center of the edifice (i.e., at 5% distance from the symmetry axis) increases almost linearly with depth (first row of steps 3 to 7 in **Figure 5**), a pattern that becomes more curved toward the flanks (e.g., cross-section at 60% in step 3 in **Figure 5**). However, this curved differential stress gradient becomes more linear upon the emplacement of new layers [e.g., the curved dashed line at 60% distance from the symmetry axis (18 km) in step 1 of **Figure 5** becomes the linear dashed line at a similar distance (40%) from the summit (∼17.4 km) at deep levels within the edifice (0–1 km) in step 3 of **Figure 5** upon the emplacement of two new layers (during step 2 and 3). The predominant type of magmatic intrusions (dikes or sills) that are likely to form within the edifice also changes in response to the emplacement of new layers. In the first stage, only angular, circumferential dikes (light blue and green) and sills (dark blue) can be formed (colored dashed lines in step 1 in **Figure 5**). Their occurrence decreases

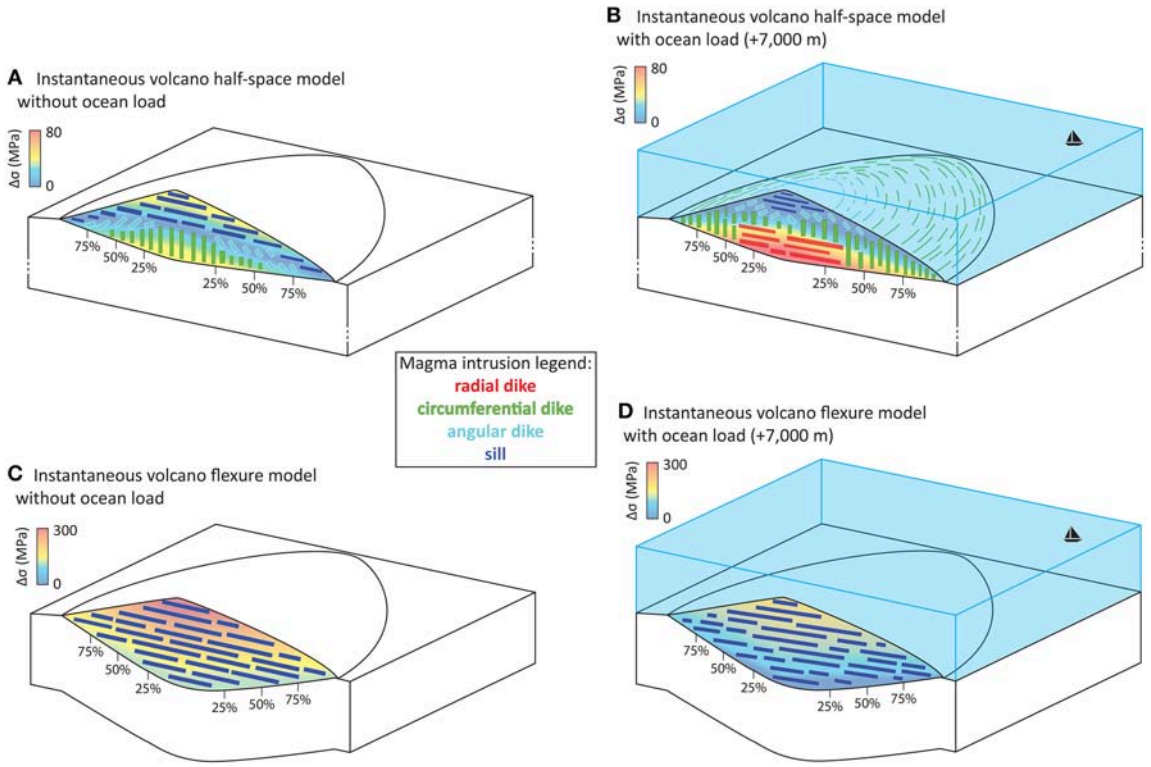

FIGURE 4 | Sketch illustrating the state of stress and the type of magmatic intrusions within instantaneously-formed volcanoes in **(A,B)** half-space and **(C,D)** flexure models without an ocean load **(A,C)** and **(B,D)** with an ocean load (+7,000 m). Sill intrusions are presented by dark blue-colored bars, while angular, circumferential and radial dikes presented by light blue, green and red-colored bars (in cross-section) and lines (at the surface of the edifice). Background colors represent the amount of differential stress ($\Delta\sigma$; similar $\Delta\sigma$ scales are applied for **A,B**; and for **C,D**).

simultaneously with the increase of radial dikes in consequence of additional layer emplacement (red dashed lines in steps 2–7 in **Figures 5**, **6**). The emplacement of angular and circumferential dikes is favored below the summit and in the deeper parts below the flanks (light blue and green dotted lines in steps 2–6 from 5 to 80% in **Figures 5**, **6**) while radial dikes become predominant with edifice growth within the edifice (red dotted lines in steps 4–7 from 5 to 80% in **Figure 5**). While sill formation can be observed at the surface of the entire edifice, sills are more prominent near the surface of the outer parts of the edifice (dark blue dashed lines in steps 2–7 from 40 to 80% in **Figures 5**, **6**).

When taking the effect of ocean loading into account (solid lines in **Figures 5**, **6C,D**, and **Figures S4**), the initial volcanic edifice that is emplaced on a half-space (first row of **Figure 5**) again gives a similar edifice internal stress distribution to that obtained for the corresponding instantaneous volcano model (**Figure 3B**). In comparison to our simulations ignoring the oceanic loading, we observe lower differential stresses at the shallower parts of the edifice, and higher $\Delta\sigma$ magnitudes at deeper levels of the edifice (solid lines from 5 to 60% in Step 1 in **Figures 5**, **6C,D**, and **Figures S4**). However, we observe that at the tip of the flank the $\Delta\sigma$ displays higher values along the entire cross-section than the model without an ocean load (solid line at 80% in Step 1 in **Figure 5**). As the volcano grows, we observe that the loading effect of an ocean results in a homogeneous linear increase of the differential stress ($\Delta\sigma$) within each layer from top to bottom and overall in the entire edifice (solid lines in **Figure 5**), and we observe that the magnitudes of $\Delta\sigma$ are slightly higher near the summit than the models without an ocean (from 5 to 40% in **Figure 5**), while further within the flank the magnitudes of $\Delta\sigma$ are much larger than for the model without an ocean load (solid lines at 60 and 80% in (**Figure 5**).

Magmatic intrusions are only slightly influenced by the growth of the edifice from the initial step promoting mostly circumferential and radial dikes (green and red solid lines in step 1 in **Figure 5**). Angular dikes and sills (light and dark blue) are restricted to the upper part of the flank near the summit of the volcano (from 5 to 40% in step 1 in **Figure 5**). As the volcano grows radial dikes (red) are favored throughout the entire volcanic edifice near the summit (at 5% from the symmetrical axis during steps 2–7 in **Figure 5**) and near the surface of the flanks in the first steps (red solid lines in steps 2–4 from 20 to 60% in **Figure 5**). In the subsequent steps, radial dikes are formed mostly within the edifice flanks (red solid lines in steps 4–7 from 20 to 60% in **Figure 5**). Finally, we observe that more circumferential dikes are dictated by the state of stress within the edifice's flanks when compared to the non-ocean load model as the volcano grows larger (green solid lines in steps 1–7 from 40 to 80% in **Figures 5**, **6**).

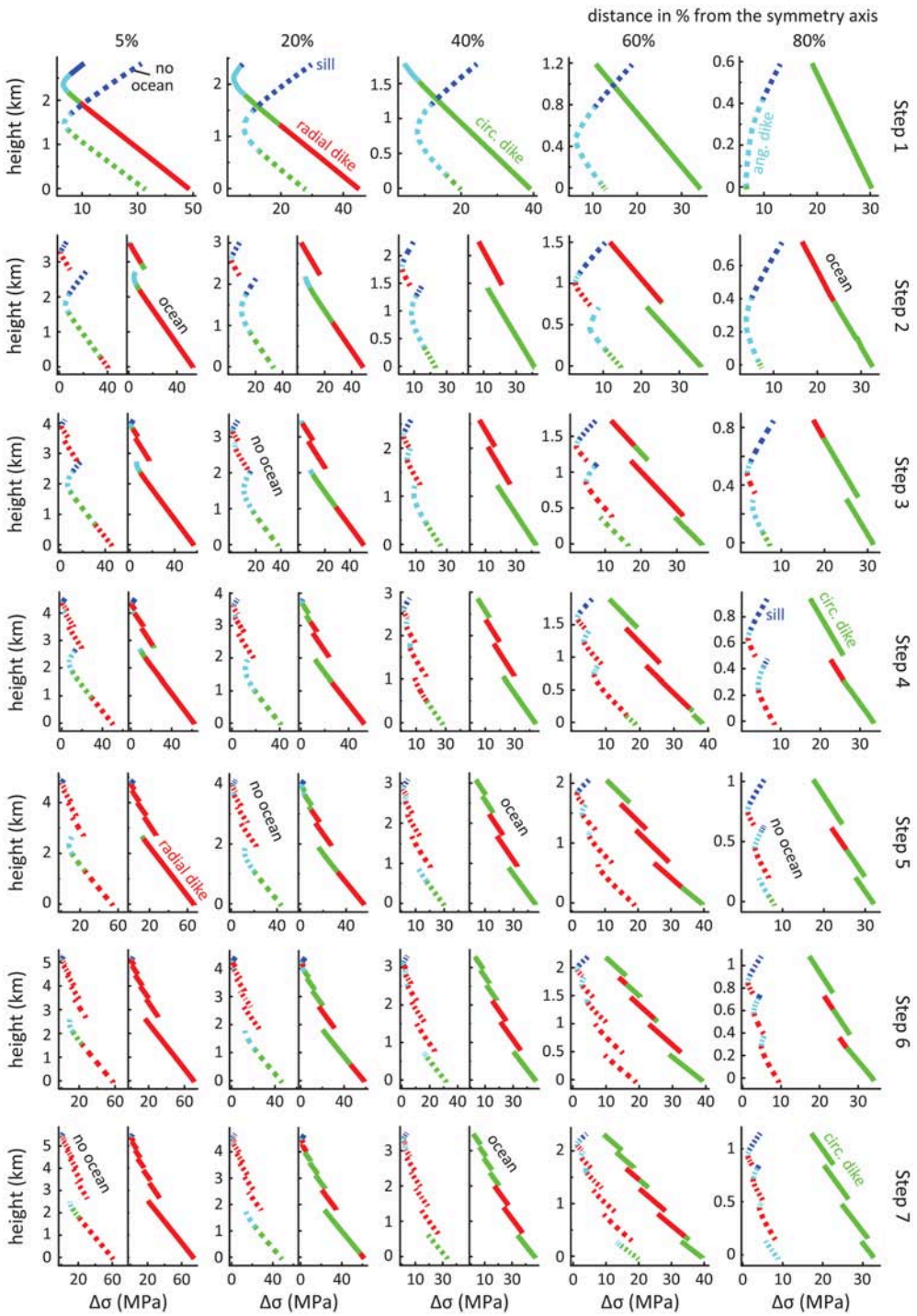

FIGURE 5 | Differential stress magnitudes, and magmatic intrusion types predicted from principal stress orientations along the internal cross-sections for incrementally-grown volcanoes in half-space models with and without an ocean load (solid and dashed lines, respectively). Legend as in **Figure 3**.

Incremental volcano flexure models

We study the effect of an incrementally growing volcanic edifice on an elastic lithosphere by allowing lithospheric flexure (**Figures 7**, **8** and **Figures S5–S6**). When neglecting the effect of an ocean, the initial step is again similar to the instantaneously-formed volcano model (**Figure 3B**) with the magnitude of $\Delta\sigma$ increasing from the base to the surface of the edifice (dotted lines in step 1 in **Figures 7**, **8** and **Figure S5.1**). As the edifice

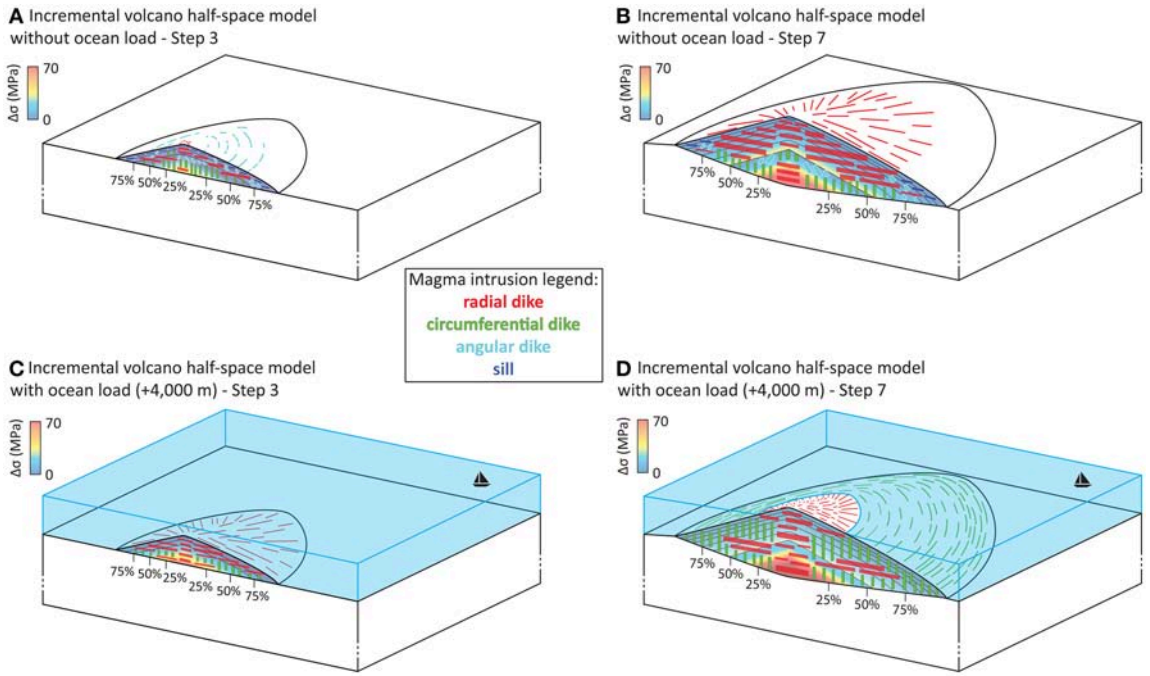

FIGURE 6 | Sketch illustrating the state of stress and the type of magmatic intrusions within incrementally-grown volcanoes for half-space models. Steps 3 **(A)** and 7 **(B)** of the model without an ocean load. Steps 3 **(C)** and 7 **(D)** of the model with an ocean load (+4,000 m). Legend as in **Figure 4**.

grows, we find that overall the magnitude of $\Delta\sigma$ within each load increment increases with increasing edifice height, i.e., with the emplacement of subsequent layers, e.g., $\Delta\sigma$max in step 1 equals ∼70 MPa while $\Delta\sigma$max in step 7 equals ∼200 MPa (in **Figures 7**, **8** and **Figure S5**). However and more specifically, the magnitude of $\Delta\sigma$ in each successive increment decreases compared to that of the previous layer, such that the lowest differential stresses are observed at shallow levels within the edifice, i.e., within the youngest, uppermost increment. The combination of these effects produces a characteristic "zig-zag" pattern of $\Delta\sigma$ within the edifice [see also (McGovern et al., 2001)] at all distances from the symmetry axis (**Figure 7**). The characteristics described above occur regardless of the presence or absence of a water load as the volcano grows. We observe however that the ocean load influences the state of stress within the initial edifice (solid lines in step 1 in **Figure 7**), which produced a curved state of stress within the edifice (solid lines in step 1 from 5 to 40% in **Figure 7**). As in the instantaneously-formed volcano models (**Figure 3B**), the presence of an ocean results in a significant decrease of the differential stress $\Delta\sigma$, e.g., $\Delta\sigma$max in step 1 equals ∼40 MPa vs. ∼80 MPa for the model without an ocean load, while $\Delta\sigma$max in step 7 equals ∼150 MPa vs. ∼210 MPa (solid lines in **Figure 7**, **8** and **Figure S6**).

Magmatic intrusions formed within a growing edifice without the presence of an ocean will only be sills (dark blue dashed lines in **Figures 7**, **8**). When considering the ocean load, we observe that the proportion of the edifice with internal stresses promoting angular and circumferential dike intrusions increases (cf. light blue and green portions of solid lines in **Figure 7**). Circumferential dikes are favored in the base of the initial edifice below the summit (cf. green portions in step 1 from 5 to 20% in **Figure 7**), while the proportion of angular dike within the edifice increase away from the summit (cf. light blue portions of solid lines in steps 1–3 from 5 to 80% in **Figures 7**, **8**). As the edifice grows, sill intrusions are favored closer to the summit (cf. cross-sections at 5 and 20% in steps 3–7 in **Figure 7**) while the proportion of angular dike decreases and becomes restricted at the extremities of the edifice (c.f. light blue solid lines in steps 1–7 at 80% in **Figures 7**, **8**) with limited opportunities for circumferential dikes (e.g., green solid lines in steps 2–7 at 80% in **Figure 7**).

DISCUSSION

Vertical Displacement

In our experiments, we observed that the increase of an ocean load decreases the subsidence of the volcanic edifice until the ocean depth level becomes greater than the original height of the edifice load (**Figure 2**). The decrease in subsidence is due to the buoyancy imparted to the volcanic rock by the pre-existing ocean water (Wessel and Keating, 1994; Kim and Wessel, 2010). For segments of the edifice deeper than the ocean level, volcanic rock replaces water, and therefore the net change in load felt by the lithosphere is proportional to the difference of rock and water densities. This reduction of load magnitude relative to the oceanless case reduces the vertical displacement and the magnitude of $\Delta\sigma$ as seen in **Figure 2** until the ocean greater than the total edifice height.

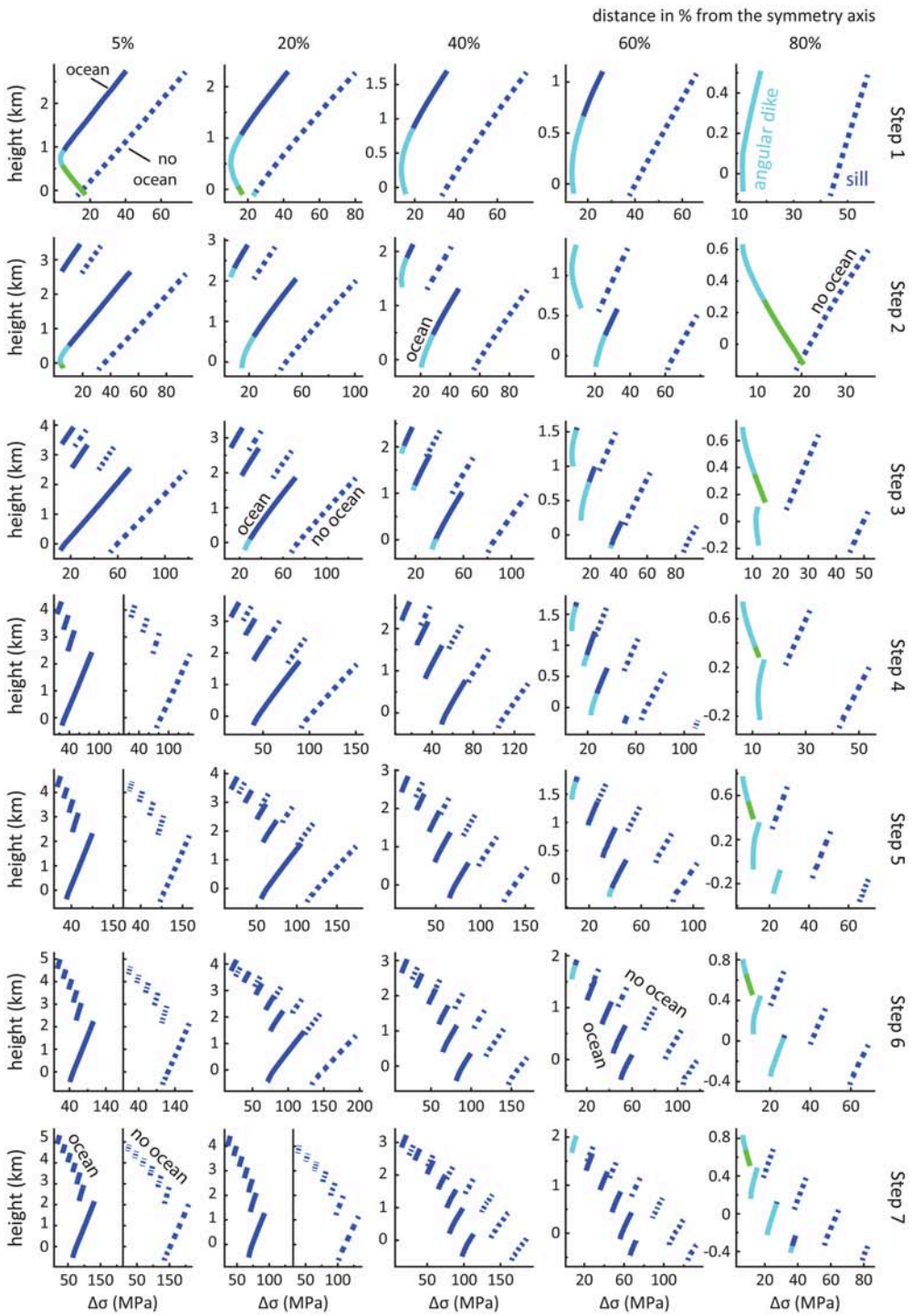

FIGURE 7 | Differential stress magnitudes, and magmatic intrusion types predicted from principal stress orientations along the internal cross-sections for incrementally-grown volcanoes in flexure models with and without an ocean load (solid and dashed lines, respectively). Legend as in **Figure 3**.

No significant differences of the edifice vertical deformation are observed between instantaneously-formed and incrementally-grown volcanoes in a half-space model (blue and red circles, respectively in **Figure 2A**), nor in the oceanless flexure model (**Figure 2B**). However, we observe that in the flexural model subjected to an ocean load the vertical displacement is larger for the incrementally-grown volcanoes. This result likely stems from a reduced contribution of the growing edifice to local

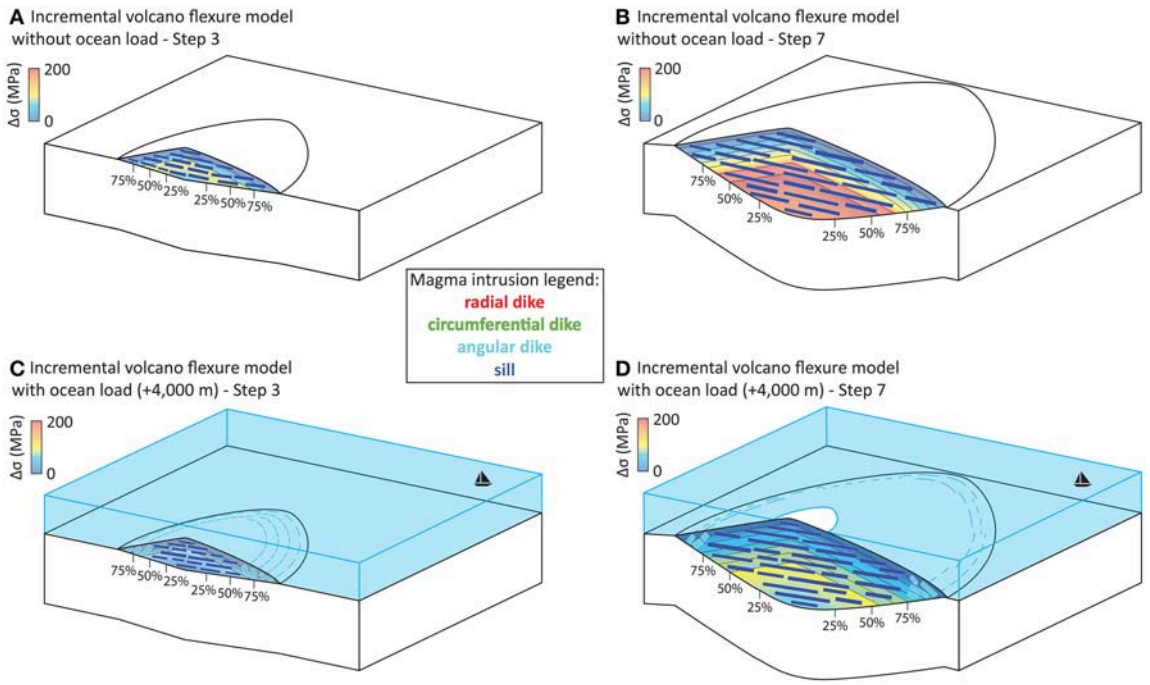

FIGURE 8 | Sketch illustrating the state of stress and the type of magmatic intrusions within incrementally-grown volcanoes for flexure models. Steps 3 **(A)** and 7 **(B)** of the model without an ocean load. Steps 3 **(C)** and 7 **(D)** of the model with an ocean load (+4,000 m). Legend as in **Figure 4**.

thickening (effective stiffening) of the lithosphere (see Figures 14 and Figure 19A of McGovern and Solomon, 1993) vs. that of the instantaneous edifice. The full height of the instantaneous edifice is present throughout the flexural response, whereas the growing edifice is shorter during early increments, and thus the response to those is not affected by as much effective stiffening, resulting in greater final displacements at the end of loading.

Volcanic Growth and Magma Intrusions

An important difference in the effects of ocean loads on half-space loads vs. flexural loads can be explained in terms of the stress tensor. For the half-space incremental loads (**Figure 5**, steps 2–7), the effect of the ocean load is to generally increase $\Delta\sigma$, while in contrast, for the flexural incremental loads (**Figure 7**, steps 2–7) the ocean load generally decreases $\Delta\sigma$. This phenomenon can be understood in terms of the orientation of the stress tensors in these edifices. For the half-space cases shown in **Figure 5**, σ_1, the most compressive principal stress, is vertical. Thus, adding another component of vertical compressive load from an overlying ocean will reinforce this stress state, thereby driving $\Delta\sigma$ higher. Conversely, the flexural loading case without an ocean is generally characterized by horizontal principal compression and vertical principal extension (σ_1 horizontal and σ_3 vertical, the "sill" stress state; see the dark blue dashed lines in **Figure 7**). Thus, the imposed vertical compression from the ocean will add to σ_3, thereby reducing $\Delta\sigma$ and in some cases reorienting the stress tensor such that σ_3 is horizontal (the light blue and green solid lines in **Figure 7**).

The loads acting on the volcanic edifice and on the orientation of the state of stress will therefore influence volcanic edifices growth as a result of magmatic intrusions and/or eruptions (Annen et al., 2001; Pinel et al., 2010; Roman and Jaupart, 2014), where buoyant magma is propagating through the lithosphere, and finally through the volcanic edifice via self-induced fractures that form perpendicular to σ_3 (Nakamura, 1977; Rubin, 1995). The flexural response of the lithosphere to the increasing gravitational load is dependent on the viscous flow of the underlying asthenosphere (Watts and Zhong, 2000). Therefore our models can be seen as temporal growth end-members such that instantaneously-formed volcanoes could represent the fastest growth rate of a volcanic edifice (**Figures 3**, **4**), while incrementally-grown volcanoes the slowest growth rate (**Figures 5**–**8**). The behavior of the lithosphere depends on the geodynamic environment and is represented in our simulations using flexural models describing the simplest mechanical response of a lithosphere to a load (**Figures 3B**, **7**), and the half-space models that enable us to take into account (1) the delayed mechanical response of the lithosphere due to a fast volcanic growth, and (2) the counteracting load of a plume, magmatic underplating and/or crustal accumulation (**Figures 3A**, **5**; Wolfe et al., 1994; Michon et al., 2007; Klügel et al., 2015; Ramalho et al., 2017).

We show that the magmatic systems within volcanic edifices subject or not to flexural subsidence are highly different (**Figures 3**–**8**). In fact, the lithospheric flexure inhibits the vertical propagation of magmas as it generates horizontal compressive stresses within the edifice (McGovern and Solomon, 1993, 1998; Galgana et al., 2011). This will ultimately favor endogenous growth through sill-like magmatic intrusions (Francis et al., 1993). On the other hand, when volcanic edifices are not

subjected to flexure, magmas are more able to propagate vertically and eventually erupt (Grosfils et al., 2013), favoring exogenous edifice growth through subaerial emplacement (Annen et al., 2001; Garcia and Davis, 2001).

The ocean load significantly increases the proportion of a volcanic edifice that is favorable to the development of radial dikes (c.f. red lines in **Figures 5**, **6**). This especially applies to the early increments of the half-space, incremental case (**Figure 5**, Steps 1–3). However, as the edifice grows (**Figure 5**, Steps 4–7), the prominence of radial dike-favoring zones becomes less pronounced. In fact, the difference between models taking into account or ignoring the ocean load becomes negligible or might even turn into the opposite effect of predominant radial dike development as a result of lacking ocean load. This trend suggests that oceanic load can facilitate early-stage radial diking in incrementally-grown volcanic edifices. However, if the magma supply rate is low with respect to the relaxation time of the lithosphere, allowing for flexure to occur (**Figures 7**, **8**), the presence of radial dikes is not predicted anywhere in the edifice regardless of the presence or absence of an ocean. This can be understood in terms of the substantial horizontal compression induced in edifices welded to a flexing lithosphere (e.g., McGovern and Solomon, 1993, 1998; McGovern et al., 2001). The compression results in stress states consistent with sill intrusions for most of the edifice (c.f. dark blue lines in **Figure 7**), although small portions at the lower parts of the flanks exhibit stress states that allow for angular diking and few occurrences of circumferential dikes (c.f. light blue and green lines in **Figure 7**). This horizontal compressional stresses increase will promote the formation of magmatic reservoirs by trapping intrusions within the edifice (Klügel et al., 2015; McGovern et al., 2015). The resulting oblate reservoirs or sill complexes can lead to the lateral migration of magmas into the edifice's flank; these magmas can ultimately reach zones favoring vertical propagation (Chestler and Grosfils, 2013) and ultimately promote lateral migration of volcanic activity (Maccaferri et al., 2017). Furthermore, the reduction in $\Delta\sigma$ and increase in vertical compression experienced by a sub-ocean volcanic edifice subject to flexure (**Figures 7**, **8**) will increase the likelihood that a stress perturbation of given magnitude (such as magma chamber inflation Chestler and Grosfils, 2013, regional stress fields, or local edifice deformation) can re-orient the principal stresses to achieve a state of horizontal principal extension consistent with magma ascent.

APPLICABILITY TO NATURAL VOLCANIC SYSTEMS

Our models represent theoretical end-members that do not imitate the full reality of natural volcanic systems, which are known to be far more complex. Nonetheless, we will discuss similarities and differences between our results and several natural examples worldwide.

More common on continental basaltic volcanoes (Poland et al., 2008; Roman and Jaupart, 2014), the formation of radial dike systems on basaltic ocean island volcanoes, as observed on Fernandina (Galapagos; Chadwick and Howard, 1991), Fogo (Day et al., 1999) or Piton de la Fournaise (Michon et al., 2016) is explained by some authors by the behavior of the magmatic system and/or with its interaction with the volcanic edifice (Chestler and Grosfils, 2013; Corbi et al., 2015). However, the state of stress within an edifice subjected to flexural deformation inhibits radial intrusions to develop (**Figures 3B**, **4C,D**, **7**, **8**). Here, we show that growing edifices lacking flexural deformation will tend to promote the formation of radial dike systems (**Figures 3A**, **4B**, **5**, **6**) which can be applied at Piton de la Fournaise (Lénat, 2016) where the plume positive buoyancy contribute to the dynamic support of the load of La Réunion. Flexure can also be counteracted by magmatic intrusions at crustal levels that can lead to uplift deformation of the basaltic ocean island volcano allowing potential stress state rotation and the formation of radial dike intrusions in the upper part of the edifice (e.g., Fogo, Cape Verde; Klügel et al., 2015; Ramalho et al., 2017).

Hawaiian volcanoes are the typical example of volcanic edifice subjected to flexural deformation (Thurber and Gripp, 1988; Watts and ten Brink, 1989; Wessel, 1993; Pritchard et al., 2007). Geophysical data have provided information on the growth and contemporary magmatic processes occurring at these volcanoes (Hill and Zucca, 1987) and their structural interpretation defines the Hawaiian flanks to be composed of basaltic dikes overlaid by pillow lavas and subaerial flows and clastic deposits (Hill and Zucca, 1987). While recent formation of pillow lavas is linked to the subaerially erupted material traveling through lava tubes (Garcia and Davis, 2001), the formation of dikes in the flanks of a growing underwater edifice and their accompanying pillow lavas could correlate with the stress orientation favoring angular and circumferential dike formation in the flanks of the growing flexural model subjected to an ocean load (**Figure 8C**). As the volcanic edifice grows and the flexural response increases, compressional stresses will inhibit vertical magma propagation favoring sill intrusion and the development of accumulation zones or reservoir within the edifice (**Figures 8D**; Staudigel and Schmincke, 1984; Ryan, 1988; Pietruszka et al., 2015).

Our results also have implications for the outer flank submarine structure of basaltic ocean island volcanoes. Bathymetry data for Fernandina volcano (Galápagos Islands) reveal three focused offshore rift zones emanating from the southwest, west, and northwest submerged flanks (Geist et al., 2006). These workers attribute the rift zones to a rift-normal orientation of the least compressive stress σ_3, arguing for a transition in stress states between low differential stress in and beneath the subaerial edifice (producing diffuse radial rift zones) and high differential stress in the outer flanks (producing strongly defined radial rift zones). Our results suggest an alternative scenario: incrementally grown ocean loaded edifices in a half-space configuration predict outer flank stress states with high $\Delta\sigma$ and principal stress orientations consistent with radial diking (red solid lines in **Figure 5**), an effect that is particularly enhanced relative to oceanless models for early stages of growth (steps 2–4, with edifice dimensions comparable to those of Fernandina) and for the 60% flank position. Thus, radial dikes within the edifice, predicted by the stress states of **Figure 5**, could

transport magmas from centrally located magma bodies to the locations of the rift zones, as inferred on petrological grounds by Geist et al. (2006). We note that such a scenario is not consistent with the stress states found for the flexural models (**Figures 7**, **8**), suggesting that expected downward flexure at Fernandina is being counteracted by some mechanism. The inference of substantial crustal underplating at the western Galápagos based on analysis of bathymetry and gravity data provides such a mechanism (Mittelstaedt et al., 2014).

The presence of thick and dense fluid layers at other planetary bodies in the solar systems provides a final application for our analysis. The ∼9 MPa surface atmospheric pressure on Venus can provide a stress-altering effect comparable to an ocean depth of about 1 km on Earth, helping to counteract the magma ascent-inhibiting effects of the large magnitude horizontal compressive stresses predicted for the very broad basaltic volcanic edifices on Venus (e.g., McGovern and Solomon, 1998). Further, worlds with substantial water oceans that envelop silicate cores, such as Jupiter's moon Europa, may exhibit silicate edifice-building volcanism at the surfaces of the cores. In the case of Europa, the total thickness of outer ice shell plus ocean may be as high as 100 km (Nimmo and Pappalardo, 2016), providing an immense vertical load on an edifice that could re-orient the principal stresses to enhance horizontal extension (and thus magma ascent) at a magnitude at least comparable to, and likely greater than, the effects shown in **Figures 3**–**7**. Thus, the mechanical effects of an icy planet ocean may facilitate eruption and edifice construction at the top of a silicate core, in turn enhancing delivery of heat and chemical energy to the subsurface ocean, with important implications for surface ice shell structure and astrobiological potential.

CONCLUSION

The growth of basaltic ocean island volcanoes is linked to their growth rate, the flexural response of their underlying lithosphere and the presence of an ocean. Specifically, these factors significantly influence a volcano's internal stress distribution and preferred pathways of magma propagation.

In this work, we show that vertical propagation of magmas is favored for a limited flexural response of the lithosphere, which can be caused by a balance between edifice growth (i.e., loading) and (a) mantle plume rise, magmatic underplating and/or crustal accumulation (pushing against the load), or (b) the presence of an ocean (pushing on the flanks). We translate predominant types of magmatic intrusions at volcanic ocean islands into edifice growth mechanisms: extrusive/exogenous growth is more like to occur within incrementally-grown edifices that are affected or not by the load of a water body, but where the stress signatures of lithospheric flexure are reduced (for the above described reasons). In addition, the transfer from extrusive/exogenous to intrusive/endogenous growth mechanisms at basaltic ocean island volcanoes is largely governed by the growth rate of the edifice (fast/instantaneous vs. slow/incremental). The application of these results to natural examples (e.g., Hawai'i, La Réunion, Galapagos) show that growing mechanisms can provide new explanation in understanding the formation of radial diking as well as potential submarine rift zone formations on the outer flanks of these edifices. Although we focus on ocean island volcanoes, our methods and findings can be applied to study active seamounts [e.g., Nishinoshima Volcano (Maeno et al., 2016)] or other volcanic phenomena in various environments, including extra-terrestrial volcanism. Future investigations should address and take into account the viscoelastic rheology of the mantle and its temporal response to flexural deformation, as well as edifice internal inelastic processes, such as the inelastic material response to magmatic intrusions (e.g., fracturing).

AUTHOR CONTRIBUTIONS

NLC contributed to the conception and conduction of the modeling, and the writing of the manuscript. PJM contributed to the initial project idea, aspects of the modeling, and writing of the manuscript.

FUNDING

This work is produced as part of NASA Planetary Geology and Geophysics grant NX12AO49G, with additional support graciously provided by the Lunar and Planetary Institute/USRA and le LaboratoireMagmas et Volcans, Université Clermont Auvergne - CNRS - IRD, OPGC.

ACKNOWLEDGMENTS

We would like to thank Nicole Richter for her help in improving the content of the manuscript. We are grateful for the insightful critiques provided by Marco Neri, Alessandro Tibaldi, associate editor Laura Becerril Carretero and chief editor Valerio Acocella. Data supporting this manuscript are available through the main author. This is LPI contribution 2111. This work represents LMV/ClerVolc contribution #291.

SUPPLEMENTARY MATERIAL

The Supplementary Material for this article can be found online at: https://www.frontiersin.org/articles/10.3389/feart.2018.00119/full#supplementary-material

REFERENCES

Acocella, V., and Neri, M. (2009). Dike propagation in volcanic edifices: overview and possible developments. *Tectonophysics*. 471, 67–77. doi: 10.1016/j.tecto.2008.10.002

Annen, C. (2011). Implications of incremental emplacement of magma bodies for magma differentiation, thermal aureole dimensions and plutonism–volcanism relationships. *Tectonophysics*. 500, 3–10. doi: 10.1016/j.tecto.2009.04.010

Annen, C., Lénat, J. F., and Provost, A. (2001). The long-term growth of volcanic edifices: numerical modelling of the role of dyke intrusion

and lava-flow emplacement. *J. Volcanol. Geother. Res.* 105, 263–289. doi: 10.1016/S0377-0273(00)00257-2

Apuani, T., Corazzato, C., Cancelli, A., and Tibaldi, A. (2005). Stability of a collapsing volcano (Stromboli, Italy): Limit equilibrium analysis and numerical modelling. *J. Volcanol. Geother. Res.* 144, 191–210. doi: 10.1016/j.jvolgeores.2004.11.028

Bagnardi, M., Amelung, F., and Poland, M. P. (2013). A new model for the growth of basaltic shields based on deformation of Fernandina volcano, Galápagos Islands. *Earth Planet. Sci. Lett.* 377–378, 358–366. doi: 10.1016/j.epsl.2013.07.016

Bailey, K. (1976). Potassium-argon ages from the Galápagos Islands. *Science* 192, 465–467. doi: 10.1126/science.192.4238.465

Becerril, L., Galindo, I., Gudmundsson, A., and Morales, J. M. (2013). Depth of origin of magma in eruptions. *Sci. Rep.* 3:2762. doi: 10.1038/srep02762

Borgia, A., Ferrari, L., and Pasquare, G. (1992). Importance of gravitational spreading in the tectonic and volcanic evolution of Mount Etna. *Nature* 357, 231–235. doi: 10.1038/357231a0

Byrne, P. K., Holohan, E. P., Kervyn, M. B., van Wyk de Vries, Troll, V. R., and Murray, J. B. (2013). A sagging-spreading continuum of large volcano structure. *Geology* 41, 339–342. doi: 10.1130/G33990.1

Carracedo, J. C. (1994). The Canary Islands: an example of structural control on the growth of large oceanic-island volcanoes. *J. Volcanol. Geother. Res.* 60, 225–241. doi: 10.1016/0377-0273(94)90053-1

Casagli, N., Tibaldi, A., Merri, A., Del Ventisette, C., Apuani, T., Guerri, L., et al. (2009). Deformation of Stromboli Volcano (Italy) during the 2007 eruption revealed by radar interferometry, numerical modelling and structural geological field data. *J. Volcanol. Geother. Res.* 182, 182–200. doi: 10.1016/j.jvolgeores.2009.01.002

Chadwick, W. W., and Howard, K. A. (1991). The pattern of circumferential and radial eruptive fissures on the volcanoes of Fernandina and Isabela islands, Galapagos. *Bull. Volcanology* 53, 259–275. doi: 10.1007/BF00414523

Chestler, S. R., and Grosfils, E. B. (2013). Using numerical modeling to explore the origin of intrusion patterns on Fernandina volcano, Galapagos Islands. Ecuador. *Geophys. Res. Lett.* 40, 4565–4569. doi: 10.1002/grl.50833

Clague, D. A., and Dalrymple, G. B. (1987). The Hawaiian-Emperor volcanic chain, Part 1: geologic evolution. *USGS. Prof.* Pap. 1350, 5–54.

Clague, D. A., and Denlinger, R. P. (1994). Role of olivine cumulates in destabilizing the flanks of Hawaiian volcanoes. *Bull. Volcanol.* 56, 425–434. doi: 10.1007/BF00302824

Corbi, F., Rivalta, E., Pinel, V., Maccaferri, F., Bagnardi, M., and Acocella, V. (2015). How caldera collapse shapes the shallow emplacement and transfer of magma in active volcanoes. *Earth Planetary Sci. Lett.* 431, 287–293. doi: 10.1016/j.epsl.2015.09.028

Crowley, J. W., Katz, R. F., Huybers, P., Langmuir, C. H., and, Park, S. H. (2015). Glacial cycles drive variations in the production of oceanic crust. *Science* 347, 1237–1240. doi: 10.1126/science.1261508

Day, S. J., Heleno da Silva, S. I. N., and Fonseca, J. F. (1999). A past giant lateral collapse and present-day flank instability of Fogo, Cape Verde Islands. *J. Volcanol. Geother. Res.* 94, 191–218. doi: 10.1016/S0377-0273(99)00103-1

Fiske, R. S., and Jackson, E. D. (1972). Orientation and growth of hawaiian volcanic rifts: the effect of regional structure and gravitational stresses. *Proc. R. Soc. Lond. Math. A. Phys. Sci.* 329, 299–326.

Francis, P., Oppenheimer, C., and Stevenson, D. (1993). Endogenous growth of persistently active volcanoes. *Nature* 366:554. doi: 10.1038/366554a0

Frey, F. A., Wise, W. S., Garcia, M. O., West, H., Kwon, S. T., and Kennedy, A. (1990). Evolution of Mauna Kea Volcano, Hawaii: Petrologic and geochemical constraints on postshield volcanism. *J. Geophys. Res.* 95, 1271–1300. doi: 10.1029/JB095iB02p01271

Gaffney, E. S., Damjanac, B., and Valentine, G. A. (2007). Localization of volcanic activity: 2. Effects of pre-existing structure. *Earth Planetary Sci. Lett.* 263, 323–338. doi: 10.1016/j.epsl.2007.09.002

Galgana, G. A., McGovern, P. J., and Grosfils, E. B. (2011). Evolution of large Venusian volcanoes: insights from coupled models of lithospheric flexure and magma reservoir pressurization. *J. Geophys. Res.* 116:E03009. doi: 10.1029/2010JE003654

Garcia, M. O., and Davis, M. G. (2001). Submarine growth and internal structure of ocean island volcanoes based on submarine observations of Mauna Loa volcano, Hawaii. *Geology* 29, 163–166. doi: 10.1130/0091-7613(2001)029<0163:SGAISO>2.0.CO;2

Geist, D. J., Fornari, D. J., Kurz, M. D., Harpp, K. S., Soule, S. A., Koleszar, A. M., et al. (2006). Submarine Fernandina: Magmatism at the leading edge of the Galápagos hot spot. *Geochem. Geophys. Geosyst.* 7:Q12007. doi: 10.1029/2006GC001290

Gillot, P. Y., Lefèvre, C. J., and, Nativel, P. E. (1994). Model for the structural evolution of the volcanoes of Réunion Island. *Earth Planetary Sci. Lett.* 122, 291–302. doi: 10.1016/0012-821X(94)90003-5

Grosfils, E. B., McGovern, P. J., Gregg, P. M., Galgana, G. A., Hurwitz, D., M., Chestler, S. R., et al. (2013). Elastic models of magma reservoir mechanics: a key tool for investigating planetary volcanism, *Geol. Soc. Lond. Spec.* 401, 239–267. doi: 10.1144/SP401.2

Gudmundsson, A. (2005). The effects of layering and local stresses in composite volcanoes on dyke emplacement and volcanic hazards. *Compt. Rendus Geosci.* 337, 1216–1222. doi: 10.1016/j.crte.2005.07.001

Hill, D. P., and Zucca, J. J. (1987). Geophysical constraints on the structure of Kilauea and Mauna Loa Volcanoes and some implications for seismomagmatic processes, U.S. *Geol. Surv. Prof. Pap.* 1350, 903–917.

Kavanagh, J. L., Menand, T., and Sparks, R. S. J. (2006). An experimental investigation of sill formation and propagation in layered elastic media. *Earth Planetary Sci. Lett.* 245, 799–813. doi: 10.1016/j.epsl.2006.03.025

Kim, S. S., and Wessel, P. (2010). Flexure modelling at seamounts with dense cores. *Geophys. J. Int.* 182, 583–598. doi: 10.1111/j.1365-246X.2010.04653.x

Klügel, A., Longpré, M. A., García-Cañada, L., and Stix, J. (2015). Deep intrusions, lateral magma transport and related uplift at ocean island volcanoes. *Earth Planetary Sci. Lett.* 431, 140–149. doi: 10.1016/j.epsl.2015.09.031

Le Corvec, N., McGovern, P. J., Grosfils, E. B., and Galgana, G. (2015). Effects of crustal-scale mechanical layering on magma chamber failure and magma propagation within the Venusian lithosphere. *J. Geophys. Res.* 120: 1279–1297. doi: 10.1002/2015JE004814

Le Corvec, N., Menand, T., and Lindsay, J. (2013). Interaction of ascending magma with pre-existing crustal fractures in monogenetic basaltic volcanism: an experimental approach. *J. Geophys. Res.* 118, 968–984. doi: 10.1002/jgrb.50142

Le Corvec, N., and Walter, T. R. (2009). Volcano spreading and fault interaction influenced by rift zone intrusions: insights from analogue experiments analyzed with digital image correlation technique. *J. Volcanol. Geothermal Res.* 183, 170–182. doi: 10.1016/j.jvolgeores.2009.02.006

Lénat, J.-F. (2016). "Construction of La Réunion," in *Active Volcanoes of the Southwest Indian Ocean: Piton de la Fournaise and Karthala*, eds P. Bachelery, J. F. Lenat, A. Di Muro, and L. Michon. (Berlin; Heidelberg: Springer Berlin Heidelberg), 31–44.

Luttrell, K., and Sandwell, D. (2010). Ocean loading effects on stress at near shore plate boundary fault systems. *J. Geophys. Res.* 115:B08411. doi: 10.1029/2009JB006541

Maccaferri, F., Bonafede, M., and Rivalta, E. (2011). A quantitative study of the mechanisms governing dike propagation, dike arrest and sill formation. *J. Volcanol. Geother. Res.* 208, 39–50. doi: 10.1016/j.jvolgeores.2011.09.001

Maccaferri, F., Richter, N., and Walter, T. R. (2017). The effect of giant lateral collapses on magma pathways and the location of volcanism. *Nature Commun.* 8:1097. doi: 10.1038/s41467-017-01256-2

Maeno, F., Nakada, S., and Kaneko, T. (2016). Morphological evolution of a new volcanic islet sustained by compound lava flows. *Geology* 44, 259–262. doi: 10.1130/G37461.1

McGovern, P. J. (2007). Flexural stresses beneath Hawaii: Implications for the October 15, 2006, earthquakes and magma ascent. *Geophys. Res. Lett.* 34:*L*23305. doi: 10.1029/2007GL031305

McGovern, P. J., Grosfils, E. B., Galgana, G. A., Morgan, J. K., Rumpf, M. E., Zimbelman, J. R., et al. (2015). Lithospheric flexure and volcano basal boundary conditions: keys to the structural evolution of large volcanic edifices on the terrestrial planets. *Geol. Soc. Lond. Spec. Pub.* 401, 219–237. doi: 10.1144/SP401.7

McGovern, P. J., and Morgan, J. K. (2009). Volcanic spreading and lateral variations in the structure of Olympus Mons, Mars. *Geology*. 37, 139–142. doi: 10.1130/G25180A.1

McGovern, P. J., and Solomon, S. C. (1993). State of stress, faulting, and eruption characteristics of large volcanoes on Mars. *J. Geophys. Res.* 98, 23553–23579. doi: 10.1029/93JE03093

McGovern, P. J., and Solomon, S. C. (1998). Growth of large volcanoes on Venus: Mechanical models and implications for structural evolution, *J. Geophys. Res.* 103, 11071–11101. doi: 10.1029/98JE01046

McGovern, P. J., Solomon, S. C., Head, J. W., Smith, D. E., Zuber, M. T., and Neumann, G. A. (2001). Extension and uplift at Alba Patera, Mars: Insights from MOLA observations and loading models, *J. Geophys. Res.* 106. 23769–23809. doi: 10.1029/2000JE001314

McLeod, P., and Tait, S. (1999). The growth of dykes from magma chambers. *J. Volcanol. Geother. Res.* 92, 231–245. doi: 10.1016/S0377-0273(99)00053-0

McNutt, M., and Menard, H. W. (1978). Lithospheric flexure and uplifted atolls, *J. Geophys. Res.* 83, 1206–1212. doi: 10.1029/JB083iB03p01206

McNutt, S. R. (1999). "Eruptions of pavlof volcano, alaska, and their possible modulation by ocean load and tectonic stresses: re-evaluation of the hypothesis based on new data from 1984-1998," in *Seismicity Patterns, their Statistical Significance and Physical Meaning*, eds M. Wyss, K. Shimazaki, and A. Ito (Basel; Boston, MA; Berlin: Birkhäuser), 701–712.

Menand, T., Daniels, K. A., and Benghiat, P. (2010). Dyke propagation and sill formation in a compressive tectonic environment. *J. Geophys. Res.* 115:B08201. doi: 10.1029/2009JB006791

Menand, T., M., de Saint-Blanquat, and Annen, C. (2011). Emplacement of magma pulses and growth of magma bodies. *Tectonophysics* 500, 1–2. doi: 10.1016/j.tecto.2010.05.014

Michon, L., Ferrazzini, V., and Di Muro, A. (2016). "Magma Paths at Piton de la Fournaise Volcano," in *Active Volcanoes of the Southwest Indian Ocean: Piton de la Fournaise and Karthala*, eds P. Bachelery, J. F. Lenat, A. Di Muro, L. and Michon (Berlin; Heidelberg: Springer Berlin Heidelberg), 91–106.

Michon, L., Saint-Ange, F., Bachelery, P., Villeneuve, N., and Staudacher, T. (2007). Role of the structural inheritance of the oceanic lithosphere in the magmato-tectonic evolution of Piton de la Fournaise volcano (La Réunion Island). *J. Geophys. Res.* 112: B04205. doi: 10.1029/2006JB004598

Mitchell, N. C., Masson, D. G., Watts, A. B., Gee, M. J. R., and Urgeles, R. (2002). The morphology of the submarine flanks of volcanic ocean islands: a comparative study of the Canary and Hawaiian hotspot islands. *J. Volcanol. Geothermal Res.* 115, 83–107. doi: 10.1016/S0377-0273(01)00310-9

Mittelstaedt, E., Soule, A. S., Harpp, K. S., and Fornari, D. (2014). "Variations in crustal thickness, plate rigidity, and volcanic processes throughout the northern galápagos volcanic province," in *The Galápagos: A Natural Laboratory for the Earth Sciences,* eds K. S. Harpp, E. Mittelstaedt, N. D. W. d'Ozouville and Graham (Hoboken, NJ: American Geophysical Union, Geophysical Monograph 204), 263–284.

Musiol, S., Holohan, E. P., Cailleau, B., Platz, T., Dumke, A., van Gasselt, S., et al. (2016). Lithospheric flexure and gravity spreading of Olympus Mons volcano, Mars. *J. Geophys. Res.* 121, 255–272. doi: 10.1002/2015JE004896

Nakamura, K. (1977). Volcanoes as possible indicators of tectonic stress orientation - principle and proposal. *J. Volcanol. Geother. Res.* 2, 1–16. doi: 10.1016/0377-0273(77)90012-9

Nimmo, F., and Pappalardo, R. T. (2016). Ocean worlds in the outer solar system. *J. Geophys. Res.* 121, 1378–1399. doi: 10.1002/2016JE005081

Pietruszka, A. J., Heaton, D. E., Marske, J. P., and Garcia, M. O. (2015). Two magma bodies beneath the summit of Kilauea Volcano unveiled by isotopically distinct melt deliveries from the mantle. *Earth Planetary Sci. Lett.* 413, 90–100. doi: 10.1016/j.epsl.2014.12.040

Pinel, V., and Jaupart, C. (2003). Magma chamber behavior beneath a volcanic edifice. *J. Geophys. Res.* 108:2072. doi: 10.1029/2002JB001751

Pinel, V., and Jaupart, C. (2004). Magma storage and horizontal dyke injection beneath a volcanic edifice. *Earth Planetary Sci. Lett.* 221, 245–262. doi: 10.1016/S0012-821X(04)00076-7

Pinel, V., Jaupart, C., and Albino, F. (2010). On the relationship between cycles of eruptive activity and growth of a volcanic edifice. *J. Volcanol. Geother. Res.* 194, 150–164. doi: 10.1016/j.jvolgeores.2010.05.006

Poland, M., Moats, W., and Fink, J. (2008). A model for radial dike emplacement in composite cones based on observations from Summer Coon volcano, Colorado, U. *S.* A. *Bull. Volcanol.* 70, 861–875. doi: 10.1007/s00445-007-0175-9

Pritchard, M. E., Rubin, A. M., and Wolfe, C. J. (2007). Do flexural stresses explain the mantle fault zone beneath Kilauea volcano? *Geophys. J. Int.* 168, 419–430. doi: 10.1111/j.1365-246X.2006.03169.x

Ramalho, R. S., Helffrich, G., Madeira, J., Cosca, M., Thomas, C., Quartau, R., et al. J., and Ávila, S. P. (2017). Emergence and evolution of Santa Maria Island (Azores)—The conundrum of uplifted islands revisited. *GSA Bull.* 129, 372–390. doi: 10.1130/B31538.1

Roman, A., and Jaupart, C. (2014). The impact of a volcanic edifice on intrusive and eruptive activity. *Earth Planetary Sci. Lett.* 408, 1–8. doi: 10.1016/j.epsl.2014.09.016

Rubin, A. M. (1995). Propagation of magma-filled cracks. *Ann. Rev. Earth Planet. Sci.* 23, 287–336. doi: 10.1146/annurev.ea.23.050195.001443

Ryan, M. P. (1988). The mechanics and three-dimensional internal structure of active magmatic systems: Kilauea Volcano, Hawaii. *J. Geophys. Res.* 93, 4213–4248. doi: 10.1029/JB093iB05p04213

Staudigel, H., and Schmincke, H. U. (1984). The Pliocene seamount series of La Palma/Canary Islands. *J. Geophys. Res.* 89, 11195–11215. doi: 10.1029/JB089iB13p11195

Sverdrup, H. U., Johnson, M. W., and Fleming, R. H. (1942). *The Oceans: Their Physics, Chemistry, and General Biology*. New York, NY: Prentice-Hall.

Tait, S., Jaupart, C., and Vergniolle, S. (1989). Pressure, gas content and eruption periodicity of a shallow, crystallising magma chamber. *Earth Planetary Sci. Lett.* 92, 107–123. doi: 10.1016/0012-821X(89)90025-3

Thurber, C. H., and Gripp, A. E. (1988). Flexure and seismicity beneath the south flank of Kilauea Volcano and tectonic implications. *J. Geophys. Res.* 93, 4271–4278. doi: 10.1029/JB093iB05p04271

Tibaldi, A. (2015). Structure of volcano plumbing systems: a review of multi-parametric effects. *J. Volcanol. Geother. Res.* 298, 85–135. doi: 10.1016/j.jvolgeores.2015.03.023

van Wyk de Vries, B., and Matela, R. (1998). Styles of volcano-induced deformation: numerical models of substratum flexure, spreading and extrusion. *J. Volcanol. Geother. Res.* 81, 1–18. doi: 10.1016/S0377-0273(97)00076-0

Vezzi, A., Campanaro, S. M., D'angelo, Simonato, F., Vitulo, N., Lauro, F., et al. (2005). Life at depth: Photobacterium profundum genome sequence and expression analysis. *Science* 307, 1459–1461. doi: 10.1126/science.1103341

Walker, G. P. L. (1973). Lengths of lava flows. *Philos. Trans. R. Soc. Lond.* 274, 107–118. doi: 10.1098/rsta.1973.0030

Walker, G. P. L. (1993). Basaltic-volcano systems. *Geological Society, London, Special Publications*, 76, 3–38. doi: 10.1144/GSL.SP.1993.076.01.01

Walker, G. P. L. (1999). Volcanic rift zones and their intrusion swarms, *Journal of Volcanology and Geothermal Research*, 94, 21–34. doi: 10.1016/S0377-0273(99)00096-7

Walker, G. P. L. (2000). "Basaltic volcanoes and volcanic systems," in *Encyclopedia of Volcanoes*. eds H. Sigurdsson, B. F. Houghton, S. R. McNutt, H. Rymer, J. Stix (San Diego, CA: Academic Press), 283–289.

Watts, A. B. (2001). *Isostasy and Flexure of the Lithosphere.* Cambridge, UK: Cambridge Univercity Press.

Watts, A. B., and ten Brink, U. S. (1989). Crustal structure, flexure, and subsidence history of the Hawaiian Islands. *J. Geophys. Res.* 94, 10473–10500. doi: 10.1029/JB094iB08p10473

Watts, A. B., and Zhong, S. (2000). Observations of flexure and the rheology of oceanic lithosphere. *Geophys. J. Int.* 142, 855–875. doi: 10.1046/j.1365-246x.2000.00189.x

Wessel, P. (1993). A reexamination of the flexural deformation beneath the Hawaiian Islands. *J. Geophys. Res.* 98, 12177–12190. doi: 10.1029/93JB00523

Wessel, P., and Keating, B. H. (1994). Temporal variations of flexural deformation in Hawaii. *J. Geophys. Res.* 99, 2747–2756. doi: 10.1029/93JB02876

Wolfe, C. J., McNutt, M. K., and Detrick, R. S. (1994). The Marquesas archipelagic apron: Seismic stratigraphy and implications for volcano growth, mass wasting, and crustal underplating. *J. Geophys. Res.* 99, 13591–13608. doi: 10.1029/94JB00686

Conflict of Interest Statement: The authors declare that the research was conducted in the absence of any commercial or financial relationships that could be construed as a potential conflict of interest.

Copyright © 2018 Le Corvec and McGovern. This is an open-access article distributed under the terms of the Creative Commons Attribution License (CC BY). The use, distribution or reproduction in other forums is permitted, provided the original author(s) and the copyright owner(s) are credited and that the original publication in this journal is cited, in accordance with accepted academic practice. No use, distribution or reproduction is permitted which does not comply with these terms.

frontiers in Earth Science

ORIGINAL RESEARCH
published: 13 June 2018
doi: 10.3389/feart.2018.00078

Correlated Changes Between Volcanic Structures and Magma Composition in the Faial Volcanic System, Azores

René H. W. Romer[1], Christoph Beier[1], Karsten M. Haase[1] and Christian Hübscher[2]*

[1] GeoZentrum Nordbayern, Friedrich-Alexander-Universität Erlangen-Nürnberg, Erlangen, Germany, [2] Center for Earth System Research and Sustainability, Institut für Geophysik, Universität Hamburg, Hamburg, Germany

OPEN ACCESS

Edited by:
Adriano Pimentel, Centro de Informação e Vigilância Sismovulcânica dos Açores (CIVISA), Portugal

Reviewed by:
David A. Neave, Leibniz Universität Hannover, Germany
Valerio Acocella, Università degli Studi Roma Tre, Italy
Ralf Gertisser, Keele University, United Kingdom

***Correspondence:**
René H. W. Romer
rene.romer@fau.de

Specialty section:
This article was submitted to Volcanology, a section of the journal Frontiers in Earth Science

Received: *26 January 2018*
Accepted: *25 May 2018*
Published: *13 June 2018*

Citation:
Romer RHW, Beier C, Haase KM and Hübscher C (2018) Correlated Changes Between Volcanic Structures and Magma Composition in the Faial Volcanic System, Azores. Front. Earth Sci. 6:78. doi: 10.3389/feart.2018.00078

The interaction between magmatic and tectonic processes in ocean intraplate volcanism yields insights into the ascent and transport of magmas. Many oceanic intraplate studies lack a temporal component and do not consider changes in tectonic regime and/or magmatic processes during the evolution of magmatic systems. The eastern part of the Azores archipelago formed under the influence of both an intraplate melting anomaly and a system of ultraslow spreading rift axes. The majority of recent submarine and subaerial eruptions in the Azores occur along volcanic rift zones and thus melt transport and volcanic processes are largely controlled by tectonic processes, and are therefore ideally suited to study volcano-tectonic interactions. Here, we investigate how variable the magmatic and tectonic processes are in space and time and how they interact. We present new bathymetric, geophysical, geochemical, and Sr-Nd-Pb isotope data from Faial Island and the surrounding seafloor, providing insights into the interaction between the asthenospheric melting anomaly and extensional lithospheric stresses. The bathymetry reveals large submarine volcanic rift zones on the western flank of Faial, including that of the 1957–1958 Capelinhos eruption. Based on absolute ages and seismic imagery, we develop a relative chronology of the magmatic evolution of the submarine rift zones. Their preferred WNW-ESE orientation implies that the stress field has not changed within the last ∼1 Ma. We can however show that melt productivity progressively decreased with time. Compositionally different magma batches fed distinct volcanic rift zones and edifices, suggesting that changes in the melting regime occur on a small spatial scale and that the distribution of compositionally similar lavas is tectonically controlled. As melt supply decreases, the tectonic influence on volcanism increases with a stronger localisation of melts along tectonically controlled lineaments. The youngest mafic and intermediate melts (<10 ka) on Faial are exclusively erupted along single rift zones and cover a smaller area, whereas the older volcanism was more widespread.

Keywords: oceanic intraplate volcanism, tectonic stress, lithospheric extension, rift zones, melt transport, dyking

INTRODUCTION

Volcanoes situated close to plate boundaries form by the interaction between magmatic intraplate processes and those associated with the tectonic stress field. Tectonic and magmatic processes both affect melt formation, ascent, movement in the shallow crust, and finally eruption. For example, volcanoes at oceanic spreading axes are commonly elongated reflecting the intrusion of kilometer long dikes above which lavas erupt and build up volcanic ridges (Morgan, 1987). Studies of oceanic island volcanoes, e.g., Hawaii, Iceland, and the Canary Islands, have shown that extensional forces on different local and regional scales generate lithospheric pathways for the ascending melts (Garcia et al., 1996; Klügel et al., 2005a; Gudmundsson et al., 2014). However, little is known on how structural features or compositions of magmas change if an extensional component is present as a response to either changes in melting or tectonic regime. If volcanism is predominantly concentrated along rift zones, melting rates and pathways of magma transport are strongly controlled by lithospheric extension (Galipp et al., 2006). Shorttle et al. (2013) show that magmas appear to be related to each other on length scales similar to those of individual, rift-parallel volcanic systems, implying that extension may impart some control on the development of segmentation.

The eruption of melts in intraplate environments generally produces alkaline basalts that display enriched trace element and isotope signatures (White et al., 1976; Zindler and Hart, 1986; Hofmann, 1997) and may be ideally suited to investigate the extent of mantle heterogeneity (Hofmann, 2003; Stracke, 2012). The formation of melts in intraplate environments has generally been attributed to either increased temperatures (Morgan, 1971; Schilling, 1975; White et al., 1976; Cannat et al., 1999) or increased volatile contents (Schilling et al., 1980; Bonatti, 1990) or a combination of these. Contrarily, melt formation at oceanic spreading axes frequently results from adiabatic decompression melting by the upwelling depleted upper mantle (McKenzie and Bickle, 1988). Melts that have formed in an intraplate environment from melting of an enriched mantle rising beneath an extensional regime, e.g., in the Azores, may provide a means to disentangle the processes influencing the final melt composition and those that influence the tectonic stress field and the structure of related volcanic bodies. Studies on ocean islands generally either deal with the volcanic evolution of the islands (e.g., in the Azores; Larrea et al., 2014) or the tectonic evolution of a particular system or area (e.g., Hildenbrand et al., 2014; Miranda et al., 2018), or a combination of both (e.g., on Faial, Trippanera et al., 2014). Yet, most of these studies do not consider the temporal and spatial evolution within a single magmatic system. In many intraoceanic systems these processes are however linked, i.e., tectonic stresses may affect volcanic processes. The variability in the temporal evolution of a single volcanic system and how and whether changes in either tectonic regime or melting conditions are reflected in the respective structural and compositional features remains however unknown.

Our main aim is to investigate how magma compositions and eruption patterns evolve at ocean volcanoes in space and time. The Azores submarine volcanic systems and islands are strongly influenced by extension of the lithosphere above a mantle melting anomaly (Gente et al., 2003; Vogt and Jung, 2004; Beier et al., 2008) making them an ideal target location for studying volcano-tectonic interactions. The boundary between the Eurasian, African and American lithospheric plates has experienced significant tectonic changes in the past 10 Ma (Miranda et al., 2018; Vogt and Jung, 2018). During this period the magmatism and the tectonic stress are probably an omnipresent feature in the Azores allowing to determine the impact of the structural regime on intraplate melting.

Here, we combine new bathymetric data with geochemical and petrological data from a series of subaerial and submarine mafic to intermediate igneous rock samples from Faial and the north- and southwestern submarine ridges extending from the island. We expand existing chemical and structural studies of the island toward the submarine volcanic edifices in order to reconstruct the volcanic evolution of Faial and the surrounding submarine structures. We show that much of the temporal evolution of melts on timescales >1 Ma are controlled by mantle melting processes, in which changes in degree of partial melting and enrichment result in geochemically distinct lavas. The tectonic control on the volcanism becomes more significant as mantle processes, i.e., the degree of partial melting and the mantle source, progressively change. Our observations may also be applicable to other smaller volcanic rift systems and indicate that mantle heterogeneity and extensional movements can impact on the composition and ascent of melts on different temporal and spatial length scales.

GEOLOGICAL SETTING

The Azores Plateau in the Central Northern Atlantic is separated by the Mid-Atlantic Ridge (MAR) into an eastern and western part (**Figure 1**). Six of the seven islands in the eastern part of the archipelago are influenced by the NW-SE striking Terceira Rift or its predecessors, only Santa Maria displays no substantial rift component. The Terceira Rift is an ultraslow oblique spreading axis that formed about 1 Ma ago (Vogt and Jung, 2004). The Terceira Rift and the MAR form the ridge-ridge-ridge triple junction located either west of Faial and/or Graciosa (Grimison and Chen, 1988). The easternmost island Santa Maria and the eastern part of São Miguel are related to the W-E striking East Azores Fracture Zone (EAFZ) which is the former boundary between the African and Eurasian plate (Luis et al., 1994). Three of the seven volcanic islands and an active seamount in the eastern plateau (São Miguel, Terceira, Graciosa, and João de Castro seamount) are located along the recently active Terceira Rift, divided by deep non-volcanic basins (Beier et al., 2008). Three islands south of the Terceira Rift (e.g., Faial, Pico, São Jorge) may also be related to a previous rifting movement (Vogt and Jung, 2004), forming parallel lineaments relative to the nowadays position of the Terceira Rift (Beier et al., 2015). They thus represent former extinct stages of the Terceira Rift reflecting its northwards shift with time (Krause and Watkins, 1970; Vogt and Jung, 2004). Recent earthquake orientations also imply that some of this extension is still active causing numerous and

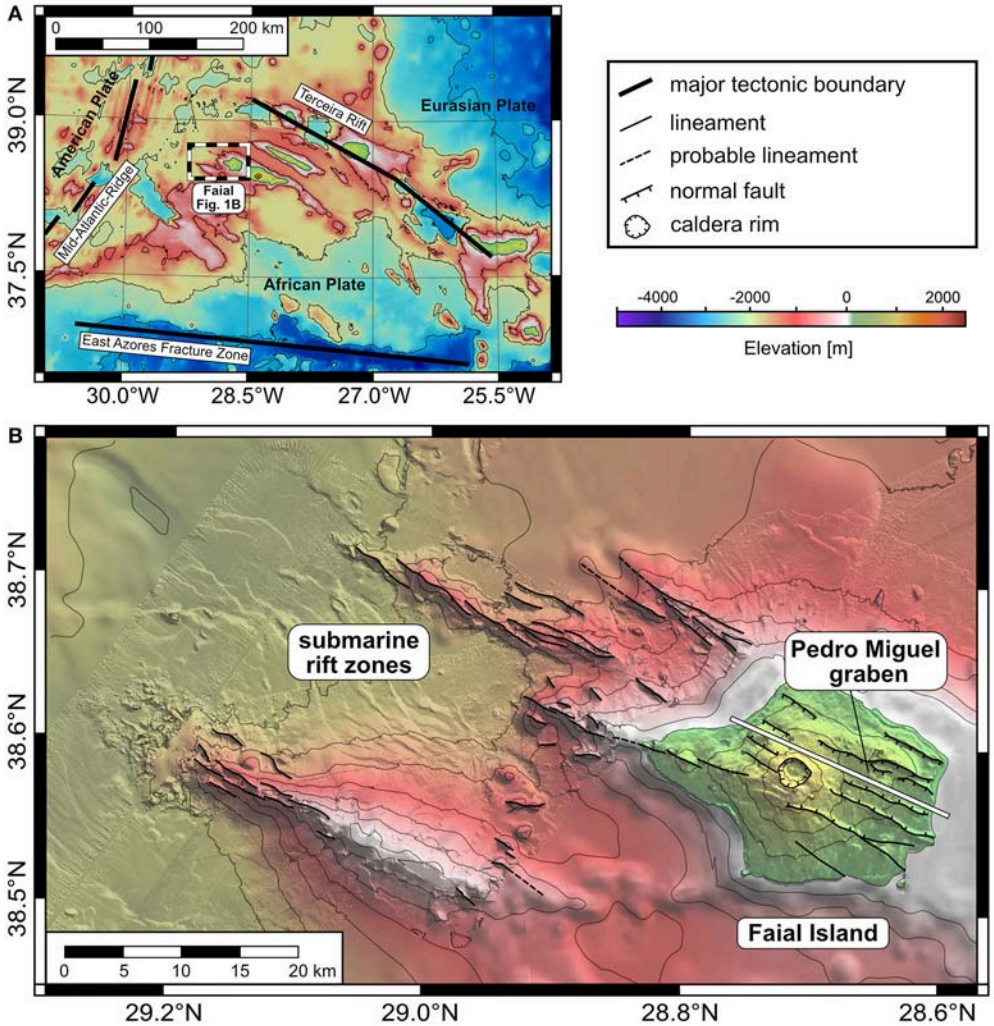

FIGURE 1 | Bathymetric maps and digital elevation models (DEM) of **(A)** the eastern Azores Plateau with major tectonic boundaries (contours are 1000 m elevation) and; **(B)** Faial Island with western adjoining submarine rift zones and major structural features (contours are 250 m elevation). Lineaments and faults on the island modified from Hildenbrand et al. (2012); Tempera et al. (2013); and Trippanera et al. (2014). Thick white line marks the position of the Pedro Miguel graben axis (Trippanera et al., 2014).

destructive earthquakes (e.g., in 1998; Matias et al., 2007), i.e., extension is still taking place in the vicinity of Faial (see also Fontiela et al., 2018).

The Azores Plateau as a whole likely formed from a melting anomaly in the mantle, either due to a small thermal plume head (Schilling, 1975; White et al., 1976; Cannat et al., 1999) or to an anomalous volatile-enriched mantle (Schilling et al., 1980; Bonatti, 1990; Beier et al., 2012; O'Neill and Sigloch, 2018). Noble gas isotopes and melting models suggest that a deep mantle plume may be located beneath Terceira (Moreira et al., 1999, 2018; Bourdon et al., 2005).

Faial Island is located on a subparallel lineament some 50 km SW of the recently active Terceira Rift. Structural features on the island, e.g., the Pedro Miguel graben (Trippanera et al., 2014; Pimentel et al., 2015) and the rift zones show that structures and lineaments on Faial are influenced by the general WNW-ESE striking extensional stress regime prevailing in the eastern Azores Plateau (**Figure 1**), perpendicular to the extensional movement of the African and Eurasian plates (Luis et al., 1998; Weiß et al., 2015a). The subparallel lineaments have previously been interpreted to be extinct rift axes related to the movement of the recently active Terceira Rift. Rift-related structural features on Faial imply that rifting has played a role in the past (Luis et al., 1994; Miranda et al., 1998; Gente et al., 2003) and recent observations of earthquake epicenters suggest that tectonic movements still occur (Fernandes et al., 2002; Dias et al., 2007; Matias et al., 2007; Marques et al., 2013). The extension combined with volcanic activity during the past 1 Ma (Madeira et al., 1995; Hildenbrand et al., 2012; Beier et al., 2015) and the most recent Capelinhos eruption in 1957–1958 provides an opportunity to investigate the interaction between magmatic and tectonic processes in time and space.

Faial can be divided into several volcanic units (Chovelon, 1982; Madeira, 1998; Pacheco, 2001) similar to other volcanic

islands in the Azores. The island is dominated by a central volcano with a caldera. Several adjoining rift zones extend in a north-westerly direction from the Caldeira Volcano into a submarine basin forming the submarine volcanic ridges (**Figure 1**). Similar features are observed along the western flanks of São Miguel (Weiß et al., 2015b). The oldest exposed lavas on the island belong to the Ribeirinha Volcano and were dated at 850–800 ka in the southern part and at 400–350 ka in the north of the volcano. (Hildenbrand et al., 2012; **Figure 2**). Although the younger ages for the northern part of the Ribeirinha Volcano are not supported by computed magnetisations, the gap in radiometric ages indicates a prolonged hiatus between the south and the north (Hildenbrand et al., 2012). However, based on insular shelf data from Quartau and Mitchell (2013) it can be excluded that the Ribeirinha Volcano consists of two central volcanoes. The system rather represents one central volcano with episodic activity, where the older lavas outcrop in the south and the younger eruptives outcrop in the north. A major part of the island consists of the central Caldeira Volcano with lavas dated between ∼120 and ∼40 ka (Hildenbrand et al., 2012), covering most of the older volcanic units. Further younger explosive volcanism through a central vent at the Caldeira Volcano occurred in the last 16 ka, erupting mostly trachytic pyroclastic material (Pimentel et al., 2015). Several studies (e.g., Madeira, 1998; Pacheco, 2001), have proposed that the volcanic activity at the Caldeira Volcano could be as old as 470 ka, based on a single K-Ar age from Demande et al. (1982). However, as discussed in detail in Hildenbrand et al. (2012), this radiometric age may be abnormally old, due to high amounts of pyroxene and olivine phenocrysts in the analyzed whole rock sample. Each volcanic eruption is associated with a distinct developing phase of the eastern and central Pedro Miguel graben (Hildenbrand et al., 2012).

Mafic and intermediate volcanism at the Horta Fissure Zone in the south-eastern part of Faial is exclusively younger than 40 ka (Hildenbrand et al., 2012). At the Capelo Fissure Zone in the western part volcanism is probably younger than 10 ka (Madeira et al., 1995; Madeira, 1998; Di Chiara et al., 2014). Historic eruptions at Capelo Fissure Zone occurred in 1672–1673 at Cabeço do Fogo, and in 1957–1958 at Capelinhos forming a complex tuff cone (Cole et al., 2001).

Generally, volcanism on Faial Island is characterized by short periods of volcanic activity, lasting less than 30 ka, with prolonged hiatuses of up to 500 ka between these periods (Hildenbrand et al., 2012). Hildenbrand et al. (2012) suggest that the volcanic pulses were coeval with tectonic movements and the faulting may be caused partly by deflation of shallow magma reservoirs and partly by extension of the lithosphere. Thus, Faial exhibits similar periodic volcanic activity compared to other islands from the eastern Azores Plateau (e.g., São Jorge, Graciosa; Feraud et al., 1980; Hildenbrand et al., 2008; Larrea et al., 2014; Sibrant et al., 2014).

SAMPLING AND METHODS

Bathymetry and Sampling of the Volcanic Structures

The submarine samples from the rift zones and new bathymetric data were obtained during R/V *Meteor* cruises M113 (Hübscher et al., 2016) and M128 (Beier et al., 2017a; see **Figure 2** for sampling localities). The high resolution bathymetric data were obtained using the hull mounted EM122 and EM710 multi-beam systems with signal frequencies of 12 and 70–100 kHz, respectively. In our working area, most rock samples were taken with a TV-guided grab. Samples from Condor rift (previously also referred to as Condor de Terra, Condor seamount, Condor

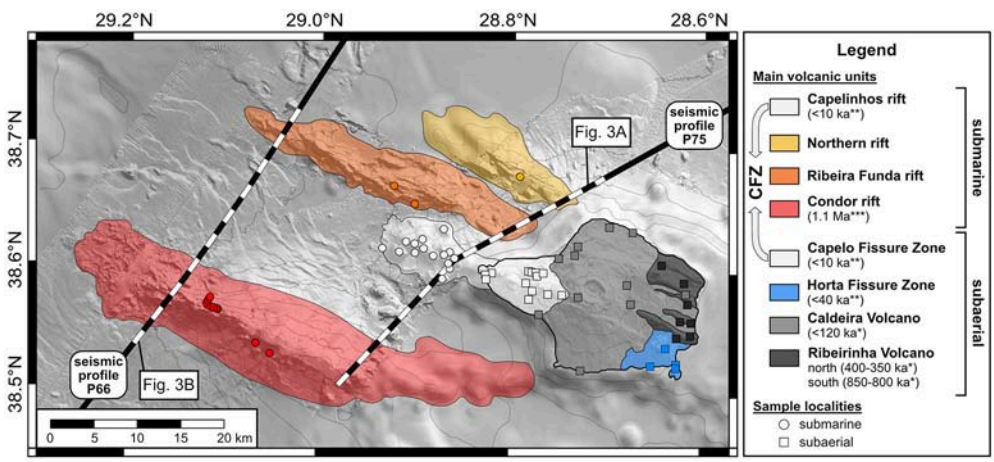

FIGURE 2 | Bathymetric map and DEM of Faial with its neighboring submarine rift zones (same as **Figure 1B**). Superimposed areas marked on the island are different volcanic units with distinct periods of volcanic activity based on K-Ar and radiocarbon ages and models from Hildenbrand et al. (2012) (*) and Madeira et al. (1995) (**). The age for Condor rift is based on Ar-Ar dating from Beier et al. (2015) (***). Black lines mark seismic profiles P66 an P75 from cruise M113, highlighted sections are shown in detail in **Figure 3**. Symbols mark the locations of lava samples, circles refer to submarine and squares to subaerial samples, respectively. The colors are the same as used in the following diagrams and refer to different volcanic units and their respective ages. (CFZ, Central Fissure Zone; comprising the submarine Capelinhos rift and the subaerial Capelo Fissure Zone).

bank, or Condor ridge in the literature, hereafter simply referred to as Condor rift for clarity), taken via Remotely Operated Vehicle (ROV MARUM Quest 4000), were obtained stratigraphically along a vertical profile and along the NW-SE oriented axis. The island of Faial was sampled during several field trips between 2001 and 2003. Samples from cruises Pos232, Pos286 with R/V *Poseidon* and the subaerial samples are the same used in Beier et al. (2012) and Beier et al. (2015).

The subaerial samples from Faial are divided into different volcanic units based on ^{14}C ages and models from Madeira et al. (1995) and K-Ar ages and models from Hildenbrand et al. (2012) according to the sampling localities (**Figure 2**). In this work, we treat the young volcanism at Capelo Fissure Zone and submarine lavas from Capelinhos rift as one geological unit, summarized as the Central Fissure Zone in agreement with a strong structural connection between the subaerial and submarine parts (**Figure 1**, Quartau et al., 2012). Samples from other submarine rift zones are treated as distinct volcanic units for the purpose of our work (**Figure 2**).

Geophysical Methods

The seismic data for this work were obtained during cruise M113 (Hübscher et al., 2016). Seismic signals were generated using an array of three GI-Guns and one Mini-Gun in a water depth of about 2.5 m. The streamer used was a digital 144-channel streamer of 600 m active length. Data processing included frequency filtering (15–350 Hz), gain, velocity analysis (every 50 CMPs), NMO-correction, coherency filtering, stacking, time-migration, bandpass, white noise removal, dip filtering, fx-deconvolution. For a detailed overview of the method see Hübscher and Gohl (2014).

Geochemical Methods

The major element analysis for whole rocks from cruises M113 and M128 were carried out using a Spectro XEPOS He—XRF spectrometer at the GeoZentrum Nordbayern, Friedrich-Alexander Universität Erlangen-Nürnberg using methods described in Woelki et al. (2018). Exactly 1.000 g of dried sample powder was mixed with 4.83 g of lithium tetraborate and 230 mg of di-iodpentoxide, fused to homogenous glass beads using an OXIFLUX burner. The loss on ignition was calculated by the difference between the weighted sample powders to 1 ± 0.0015 g and the same sample powders after 12 h at 1050°C. Using fused glass beads precision and accuracy are better than 0.8% (2σ) and 1% (2σ), respectively, based on repeated measurements of the international rock standard BE-N, BR, and BHVO-1.

The major element analyses of glasses were performed on a JEOL JXA-8200 Superprobe at the GeoZentrum Nordbayern, Universität Erlangen-Nürnberg using methods and standards described in Beier et al. (2017b). An acceleration voltage of 15 kV, a beam current of 15 nA, and a defocused beam (10 μm) were used. Counting times were set to 20 s for peaks and 10 s for backgrounds. Natural volcanic glass standards (basaltic glass standard VG-A99 and rhyolitic glass standard VG-568), together with mineral standards scapolite R-6600 (Smithsonian Institution), apatite, chalcopyrite, fluorite, and rhodonite (P and H Developments) were used for calibration. Glass standards VG-2, VG-A99, and VG-568 were analyzed periodically as unknowns in order to monitor the accuracy of the microprobe result (Brandl et al., 2012).

Trace element analyses for some samples were performed on an Agilent 7500c/s Quadrupole Inductively Coupled Plasma Mass Spectrometer (ICP-MS) at the Institut für Geowissenschaften, Universität zu Kiel. The samples were prepared as described in Beier et al. (2008) and Beier et al. (2012) with a standard deviation of the precision and accuracy of <5% (2σ) and <8% (2σ), respectively, based on repeated standard measurements. Further trace element analyses for submarine and selected subaerial samples from Faial were carried out using a Thermo Fisher Scientific X-Series 2 Quadrupole Inductively Coupled Plasma Mass Spectrometer (ICP-MS) connected to an Aridus 2 membrane desolvating sample introduction system at the GeoZentrum Nordbayern, Friedrich-Alexander Universität Erlangen-Nürnberg. For the dissolution of sample powder and rock standards (BHVO-2) we used the method as described in detail in Freund et al. (2013) following standard techniques using a 3:1 mixture of HF and HNO_3. The dissolved sample solution is diluted accordingly in order to get a dilution factor of about 4000. We use an internal standard containing elements not present in the sample solutions in order to correct the data for machine drifts during the duration of the measurements. Precision and accuracy are better than 1.1% (2σ) and 1.1% (2σ), respectively, based on repeated measurements of the international rock standard BHVO-2.

New Sr-Nd-Pb isotope data from submarine and subaerial samples from Faial were analyzed at the GeoZentrum Nordbayern, Friedrich-Alexander Universität Erlangen-Nürnberg. For Sr-Nd-Pb isotopes ∼150–200 mg dried sample powder were leached in hot 6M HCl for at least 2 h then dissolved (for Sr-Nd-Pb) and separated in ion-exchange columns (for Sr-Nd) using the method described in Haase et al. (2017). Strontium and Nd isotopes were analyzed using a Thermo-Fischer Triton thermal ionization multicollector mass spectrometer in static mode. Strontium isotope measurements were corrected for mass fractionation using $^{88}Sr/^{86}Sr = 0.1194$, and mass 85 monitored to correct for possible contribution of ^{87}Rb to mass 87. Neodymium isotope data were corrected for mass fractionation using a $^{146}Nd/^{144}Nd$ ratio of 0.7219. Samarium interference on masses 144, 148, 150 were corrected for by measuring ^{147}Sm, although the correction was negligible for all samples presented here. During the analysis, SRM987 standard yielded $^{87}Sr/^{86}Sr = 0.710256 \pm 0.000005$, and the Erlangen Nd standard gave $^{143}Nd/^{144}Nd = 0.511543 \pm 0.000003$ (corresponding to a value of 0.511850 for the La Jolla Nd isotope standard). The data were not normalized to the measured standards.

For the digestions and Pb column chemistry only double-distilled acids were used with dropper bottles to keep the blanks as low as possible. For the separation of Pb the dissolved samples were loaded on 100 μl Sr-Spec resin columns and washed with 1M HCl. The Pb was collected using 6M HCl. Lead isotope measurements were carried out on a Thermo-Fisher Neptune MC-ICP-MS using a $^{207}Pb/^{204}Pb$ double spike to correct

for instrumental mass fractionation. The double spike, with a $^{207}Pb/^{204}Pb$ ratio of 0.8135, was calibrated against a solution of the NBS982 equal atom Pb standard. Samples were diluted with 2% HNO_3 to a concentration of ∼20 ppb, and an aliquot of this solution spiked in order to obtain a $^{208}Pb/^{204}Pb$ ratio of about 1. Spiked and unspiked sample solutions were introduced into the plasma via a Cetac Aridus desolvating nebuliser and measured in static mode. Interference of ^{204}Hg on mass 204 was corrected by monitoring ^{202}Hg. An exponential mass fractionation correction was applied offline using the iterative method of Compston and Oversby (1969), the correction was typically 4.5 permil per amu. Twenty measurements of the NBS981 Pb isotope standard (measured as an unknown) over the course of this study gave $^{206}Pb/^{204}Pb$, $^{207}Pb/^{204}Pb$, $^{208}Pb/^{204}Pb$ ratios of 16.9410 ± 0.0020, 15.4993 ± 0.0019, and 36.7244 ± 0.0046 respectively. The Pb blanks are generally below 30 pg. The results for all samples can be found in Supplementary Tables 1 and 2.

RESULTS

Bathymetry

Our bathymetric data west of Faial Island display four WNW-ESE oriented volcanic ridges rising up to 1700 m above the surrounding seafloor (**Figure 1**). These ridges are structurally connected to the island with their south-eastern ends directly joining the western and south-western coast of Faial. Their elevation relative to the sea level decreases with increasing distance from the island. The central Capelinhos rift forms the western submarine extension of the subaerial Capelo Fissure Zone, where the most recent subaerial volcanic activity occurred. South and north of the Capelinhos rift, three rift zones can be distinguished. The Condor rift is located south of Capelinhos rift, the Ribeira Funda, and Northern rifts are located north of the Capelinhos rift (**Figure 2**). Amongst the rift zones north of Capelinhos, the southern rift (Ribeira Funda rift) is along the continuation of a large WNW-ESE subaerial normal fault near the village Ribeira Funda (NW sector of Faial) and the axis of the Pedro Miguel graben (Trippanera et al., 2014) and the northernmost rift zone is situated along the continuation of the northern coast of Faial (Northern rift; **Figure 2**). The length of these submarine rift zones varies between ∼8 km (Capelinhos rift) and ∼50 km (Condor rift), compared to ∼27 km for the SE-NW extent of the island of Faial. Apparently, much of the volcanic activity related to the vicinity of Faial formed only submarine volcanic ridges that did not reach subaerial levels. The WNW-ESE along-rift orientation of the submarine volcanic ridges (∼300°) is similar to the general orientation of faults related to the formation of the Pedro Miguel graben, the alignment and elongation of vents and the orientation of the majority of dikes on the island (Trippanera et al., 2014) and at Condor rift (Tempera et al., 2013). The morphology of the rift zones is dominated by isolated cones or groups of elongated cones and several kilometer-long ridges. In contrast to the Capelinhos rift, the Ribeira Funda, and Northern rifts show evidence for normal faulting in addition to structures related to volcanic activity. Similar features are observed on the island, where the flanks of the Caldeira Volcano and, in particular, the Ribeirinha Volcano are affected by normal faulting, whereas the morphology at the Horta and Capelo Fissure Zones is dominated by dikes and alignments of cones (Trippanera et al., 2014). On a smaller scale the orientation of lineaments within the rift zones does not entirely correspond to their general WNW-ESE orientation. Whereas most rift zones display almost exclusively subparallel oriented lineaments and elongation of cones, several elongated cones along the Capelinhos rift display orientations trending more SW and NW than the dominating orientation of lineaments, forming a fan-shaped system of lineaments (**Figure 1**).

Age Constraints

For the purpose of our work we use both absolute, radiometric, and relative ages from direct observations during ROV dives, geodynamic modeling and seismic profiles. Absolute, radiometric K-Ar and ^{14}C ages from Faial were published in Feraud et al. (1980), Hildenbrand et al. (2012), and Madeira et al. (1995), respectively. They range from 0.848 to 0.03 Ma and 10.25 to 0.32 ka with maximum errors of 0.012 Ma and 1.77 ka, respectively. Last eruptions on the Capelo Fissure Zone occurred in 1672–1673 and recently in 1957–1958 (Capelinhos eruption; Cole et al., 2001). The Capelinhos eruption initially started ∼1.2 km from the old coastline along the Capelinhos rift and rapidly migrated toward the island. The largest uncertainty in the ages used here lies in the submarine samples. Condor rift has been sampled by dredging during R/V *Poseidon* cruise POS 286. A single Ar-Ar age of a submarine lava displays 1.10 ± 0.80 Ma presented in Beier et al. (2015). We note however, that these are minimum ages. Dredging during POS 286 was performed at water depths from 356 to 470 m below sea level, while the ROV profiles during R/V *Meteor* cruise M128 range from 588 to 918 m below sea level. Hence, we treat the age by Beier et al. (2015) as minimum age. We also note that the Ar-Ar age determination on variably altered (Beier et al., 2015, 2017a) mafic submarine volcanic rocks may be challenging. However, geodynamic estimates (Cannat et al., 1999; Gente et al., 2003; Miranda et al., 2018) reveal that much of the igneous basement of Princessa Alice bank, to which Condor's basement may belong, formed at 8–10 Ma. Thus, within the uncertainties of the current ages, we treat Condor rift as the oldest exposed unit in the vicinity of Faial considering that older igneous strata may still be exposed at greater depth but covered by younger lavas. Older ages of formation of Condor rift would significantly strengthen our model presented below.

Seismic Profiles

Relative ages of the different submarine volcanic rift zones west of Faial can be obtained from two seismic profiles each with a length of ∼30 km (**Figure 3**). The two profiles are both SW-NE oriented, perpendicular to the orientation of the rift zones. Profile P75 is located proximal and profile P66 distal relative to Faial (**Figure 2**). P75 comprises all rift zones west of Faial, whereas P66 comprises only the Condor and Ribeira Funda rifts, because these two ridges extend further westwards than the Capelinhos and Northern rifts. In seismic profile P75 all rift zones are significantly elevated against the surrounding seafloor

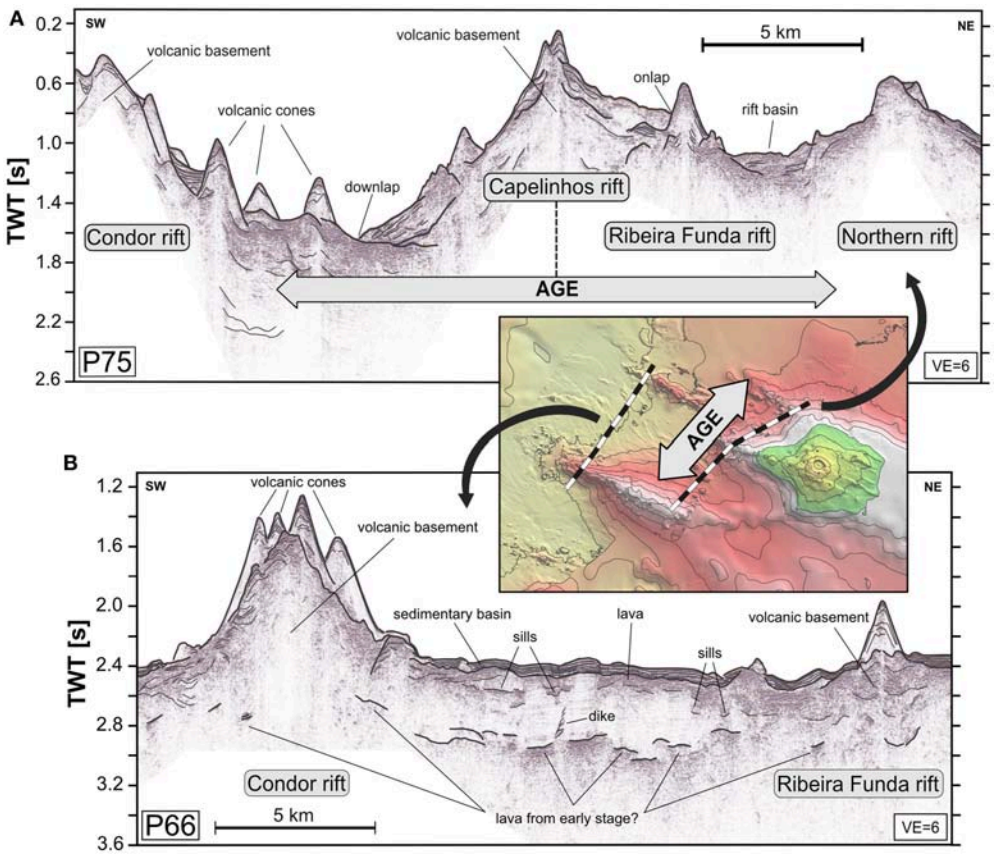

FIGURE 3 | Interpreted SW-NE seismic profiles across the rift zones with **(A)** proximal, and **(B)** distal relative to Faial. Inset map highlights the relative ages derived from seismic imagery, lines mark seismic profiles. Main seismic reflectors are marked with thick black lines. Note that the ages of the rift zones in **(B)** are increasing from Capelinhos rift toward Condor (SW) and Ribeira Funda rifts (NE) as illustrated by the double arrow in **(A)** and the inset map.

(**Figure 3**). The strong reflecting acoustic basement represents the volcanic basement of each rift zone overlain by several less strong reflecting cones. Weak reflecting horizons together with stratified basin fills are associated with marine sediments and debris flows extending from the volcanic bodies toward north-east and south-west (**Figure 3**). Onlap and downlap structures of such debris flows from the Capelinhos rift onto the volcanic basement and debris flows from Condor and Ribeira Funda rifts imply that the Capelinhos rift is younger than the rifts to the north and south. Symmetric and planar layered sediment-filled basins between the Ribeira Funda and Northern rifts suggest that they formed synchronously. The relative age relation between Condor and Ribeira Funda rifts given in profile P66 is less precise compared to the age constraints inferred from P75, because the distance between the rift zones is larger. However, the strong seismic reflection of the volcanic basement of Condor rift is comparable to that observed at Ribeira Funda rift, which may indicate a contemporaneous formation.

Geochemistry and Isotopes

The most abundant rock types from Faial Island and the adjoining rift zones are alkali basalts to trachybasalts, except for some lavas from Condor rift that are classified as tholeiites based on the Total Alkali vs. SiO_2 (TAS) classification of Le Maitre et al. (1989) (Supplementary Figure 1).

Lavas from Faial and associated submarine rift zones from this work range from mafic to evolved rocks covering a MgO content from ∼9 to 1 wt. % (**Figure 4**). Subaerial lavas from the Caldeira and Ribeirinha Volcanoes, ranging from ∼6 to 1 wt. % MgO, equivalent to SiO_2 contents between 45 and 65 wt. %, are generally more evolved than most submarine lavas. Many of the intermediate lavas from the Caldeira Volcano have SiO_2 contents ranging from 53 to 57 wt. %, contrasting observations from other large volcanoes in the Azores, e.g., Santa Barbara Volcano on Terceira (Daly et al., 2012) and the central volcano on Graciosa (Larrea et al., 2018). A larger volume of highly evolved (trachytic) pyroclastic rocks (up to ∼64 wt. % SiO_2 equivalent to MgO contents <1 wt. %) derive from explosive eruptions through a central vent from the Caldeira Volcano. They mainly erupted within the last 16 ka, in part associated with the formation of the caldera (Pimentel et al., 2015). For the purpose of this work, we focus on rock samples covering a range from mafic to intermediate composition (basaltic to trachy-andesitic) to disentangle deep magmatic processes and their interactions with

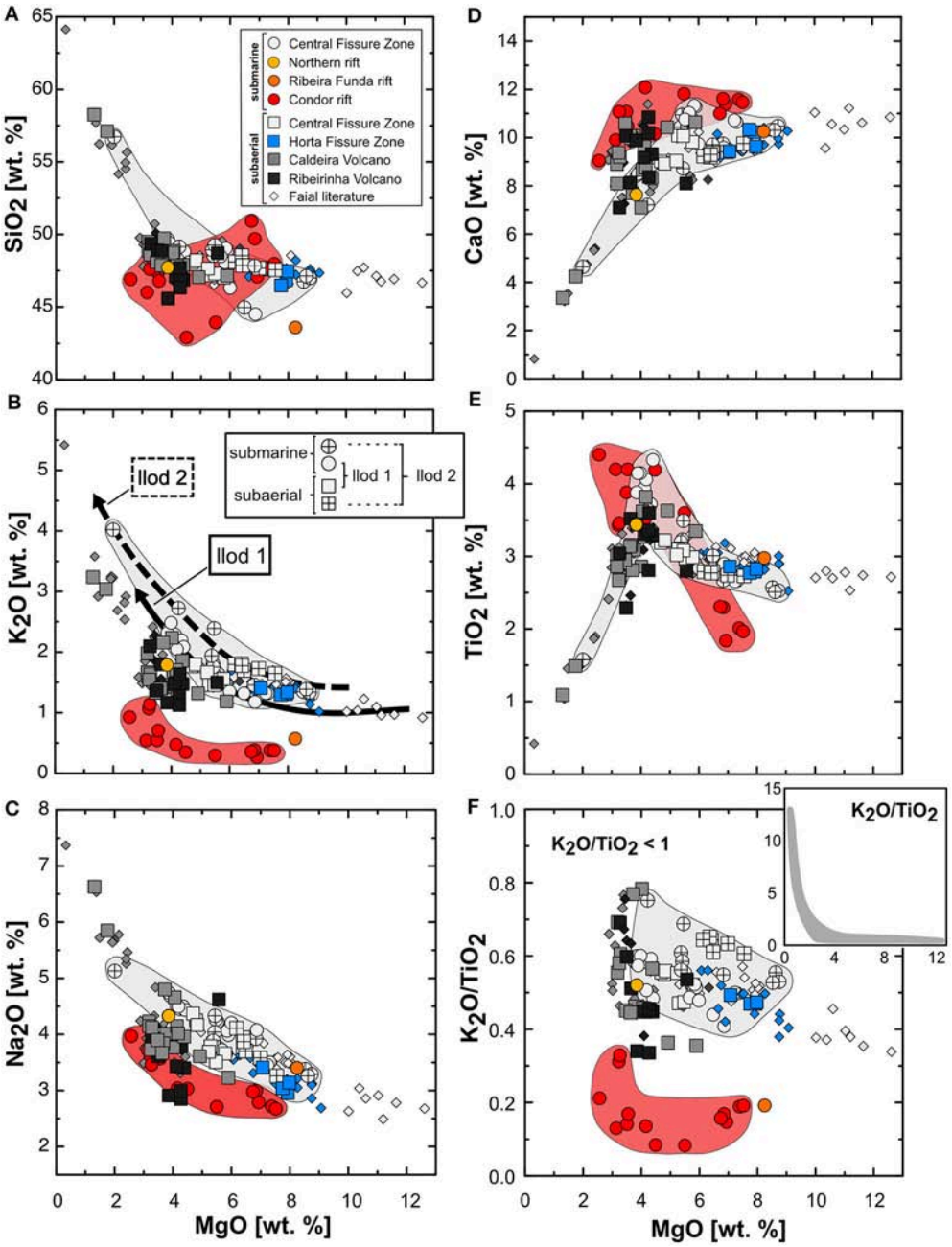

FIGURE 4 | (A-E) Major element contents and **(F)** K_2O/TiO_2 ratios vs. MgO [wt. %]. Symbols are the same as in **Figure 2**. Red and white areas highlight our samples from Condor rift and the Central Fissure Zone, respectively. Two liquid lines of descent with lower (llod 1) and higher (llod 2) K_2O contents are distinguished [**(B)**, see also **Figure 6**]. Arrows in **(B)** schematically highlight llod1 (solid line) and llod2 (dashed line). Diamonds are subaerial samples from Zanon et al. (2013) and Hildenbrand et al. (2014). The colors are the same as used for our samples and refer to the respective volcanic units distinguished in **Figure 2**. Inset in **(F)** highlights the range in K_2O/TiO_2 for all Faial lavas. Note that published samples largely overlap those from this study.

tectonic stresses. Thus, we exclude literature data dealing with the silicic (trachytic) eruptions from the Caldeira Volcano <16 ka, i.e., those from Pimentel et al. (2015), because they may rather reflect shallow magmatic processes.

The submarine lavas from the Central Fissure Zone are more evolved than their subaerial equivalents and cover almost the entire range in MgO for lavas from Faial from ∼9 to 2 wt. %, compared to ∼8 to 5 wt. % for the subaerial Central Fissure Zone lavas. The Na_2O, K_2O, and TiO_2 contents at a given MgO content from the Central Fissure Zone are significantly higher compared to both subaerial lavas from the Caldeira and Ribeirinha Volcanoes and submarine lavas from Condor and

Ribeira Funda rifts, however, they are also more variable. At a MgO content of 7 wt. % lavas from the Central Fissure Zone range from 1.2 to 1.7 wt. % K_2O and 3.4 to 4.1 wt. % Na_2O, compared to 0.3 to 0.4 wt. % and 2.8 to 3.0 wt. %, respectively, for lavas from Condor rift (**Figure 4**). Lavas from the Caldeira and Ribeirinha Volcanoes overlap in their K_2O contents. The Na_2O contents of lavas from the Ribeirinha Volcano are lower than those from the Caldeira Volcano ranging from 2.9 to 3.8 wt. % Na_2O compared to 3.8 to 4.7 wt. % Na_2O, respectively. Instead, lavas from Ribeirinha Volcano resemble those from Condor rift.

The incompatible element compositions of lavas from Faial and the rift zones display distinct signatures for the different volcanic units. Lavas from the Central and Horta Fissure Zones have higher La/Yb and Ba/Nb and lower Sm/Nd ratios compared to all other submarine rift zones, except for a single sample (IGSN: IEAZO1169) from the Northern rift (**Figure 5**). An additional Rare-Earth Element diagram is provided in the supplemental material (Supplementary Figure 2). On a larger scale lavas from the Central and Horta Fissure Zones are very similar in their compositions, however on a smaller scale they show subtle differences (Zanon et al., 2013) with lavas from the Central Fissure Zone being slightly more enriched in some incompatible trace element ratios. We use incompatible ratios for lavas between 3 and 5 wt. % MgO, because lavas from the Caldeira and Ribeirinha Volcanoes are mostly covering a comparable range in fractionation indices. We have tested for the influence of fractionation and conclude that most trace element ratios used here are only influenced by fractional crystallization at less than 3 wt. % MgO (**Figure 4**). Subaerial lavas from the Caldeira and Ribeirinha Volcanoes overlap and both lie between those lavas from Condor rift and the Central Fissure Zone with the notable exception of La/Yb ratios. Lavas from the Ribeirinha Volcano have La/Yb of 10 to 13 significantly lower than those from the Caldeira Volcano, ranging from 13 to 21, overlapping with lavas from the Central Fissure Zone (**Figure 5**).

The subaerial and submarine lavas from Faial also display distinct isotope signatures. The overall range is between 0.70343 and 0.70413 for $^{87}Sr/^{86}Sr$ and 0.51303 and 0.51283 for $^{143}Nd/^{144}Nd$, which is within the array of North Atlantic MORB from Dosso et al. (1999) (ranging from 0.70252 to 0.70414 for $^{87}Sr/^{86}Sr$ and 0.51267 to 0.51325 for $^{143}Nd/^{144}Nd$) but shifted toward higher $^{87}Sr/^{86}Sr$ ratios (**Figure 7**). The only exception

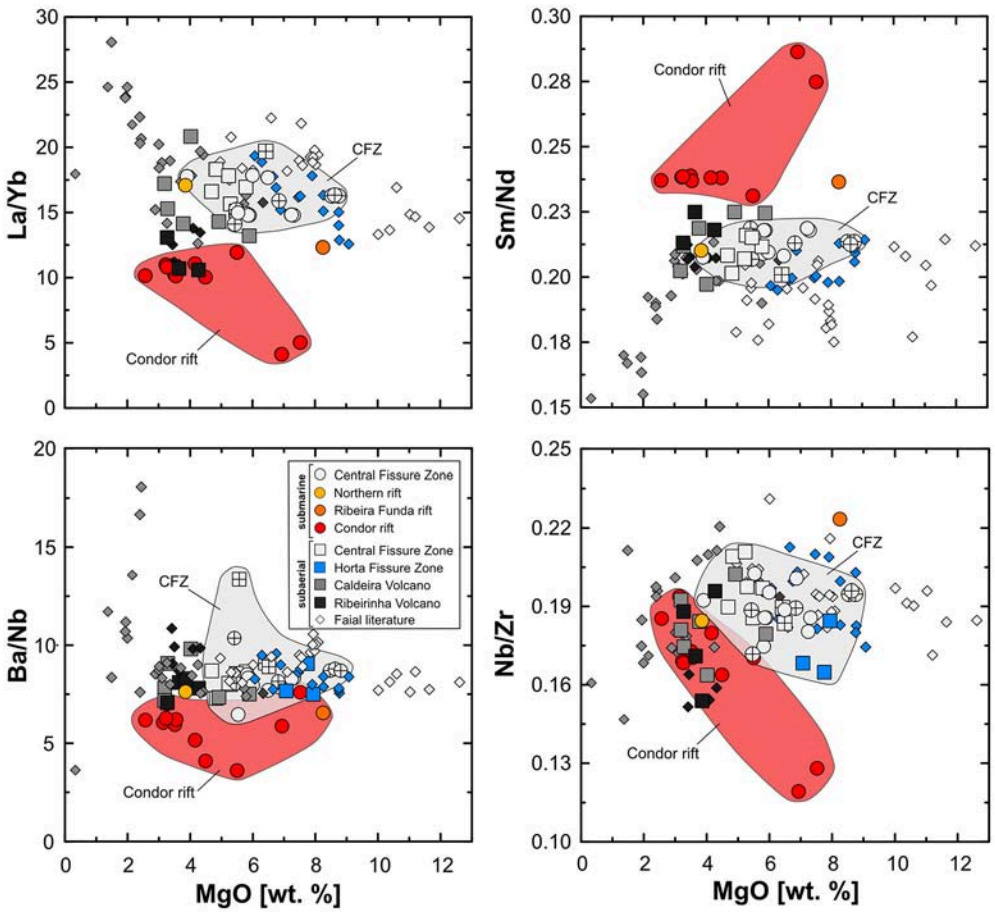

FIGURE 5 | Incompatible trace element variations of submarine and subaerial lavas from Faial. Data sources are the same as in **Figure 4**. (CFZ = Central Fissure Zone).

are the two lowermost samples from the stratigraphic profile at Condor rift (IGSN: IEAZO1135, IEAZO1136) which have notably lower $^{143}Nd/^{144}Nd$ of 0.51274 and 0.51285 compared to other lavas from this section and most other subaerial and submarine lavas. Other samples from Condor and Ribeira Funda rifts display the highest Nd and lowest Sr isotopes, whereas lavas from the Central Fissure Zone have the lowest $^{143}Nd/^{144}Nd$ and highest $^{87}Sr/^{86}Sr$ ratios, except for one sample from the Caldeira Volcano (IGSN: IEAZO0028) which has an elevated Sr isotope composition. Lavas from the Caldeira Volcano cover a large range in Sr-Nd isotope space overlapping with those from the Central Fissure Zone. Lavas from the Ribeirinha Volcano have homogenous Sr-Nd isotope compositions with slightly higher $^{143}Nd/^{144}Nd$ ratios compared to lavas from the Central Fissure Zone and the Caldeira Volcano. The overall range in Pb isotopes for Faial lavas is between 19.187 and 19.623 for $^{206}Pb/^{204}Pb$, 15.540 and 15.652 for $^{207}Pb/^{204}Pb$ and 38.671 and 39.393 for $^{208}Pb/^{204}Pb$. Lavas with the highest $^{87}Sr/^{86}Sr$ and lowest $^{143}Nd/^{144}Nd$ also have the lowest $^{206}Pb/^{204}Pb$ (**Figure 7**). Lavas from Faial lie on a linear array toward more radiogenic $^{207}Pb/^{204}Pb$ and $^{208}Pb/^{204}Pb$ at a given $^{206}Pb/^{204}Pb$ for lavas from the Central Fissure Zone and the Caldeira Volcano compared to lavas from Ribeirinha Volcano and Condor rift (**Figure 7**). Our Sr-Nd-Pb isotope data are in good agreement with those published previously by Hildenbrand et al. (2014) from respective volcanic units. Generally, lavas from Faial have slightly lower $^{206}Pb/^{204}Pb$ at similar $^{207}Pb/^{204}Pb$ and $^{208}Pb/^{204}Pb$ ratios compared to other islands from the Central Azores Plateau, i.e., Pico and São Jorge ($^{206}Pb/^{204}Pb = 19.347$ to 20.092; $^{207}Pb/^{204}Pb = 15.540$ to 15.650; $^{208}Pb/^{204}Pb = 38.744$ to 39.510; **Figure 7**). In Sr-Nd space, however, lavas from Faial cover a larger range in $^{87}Sr/^{86}Sr$ and a slightly elevated $^{143}Nd/^{144}Nd$ compared to samples from both Pico and São Jorge (ranging from 0.70338 to 0.70406 for $^{87}Sr/^{86}Sr$ and 0.51281 to 0.51300 for $^{143}Nd/^{144}Nd$; **Figure 7**).

In summary, lavas from different volcanic units on Faial and submarine rift zones generally have distinct major and trace element and Sr-Nd-Pb isotope signatures. The two most extreme compositions are observed in lavas from the Central Fissure Zone with the highest K_2O contents (at a given MgO content) and most radiogenic Sr and Pb isotope ratios compared to other subaerial and submarine units. Lavas from Condor rift display the lowest K_2O contents and least radiogenic Sr-Pb isotope ratios. Lavas from other volcanic units show major element, trace element and isotope pattern between these two groups. Comprehensive selected major and trace elements, and Sr-Nd-Pb isotopes from all volcanic units on Faial and submarine volcanic rift zones are provided in **Table 1**.

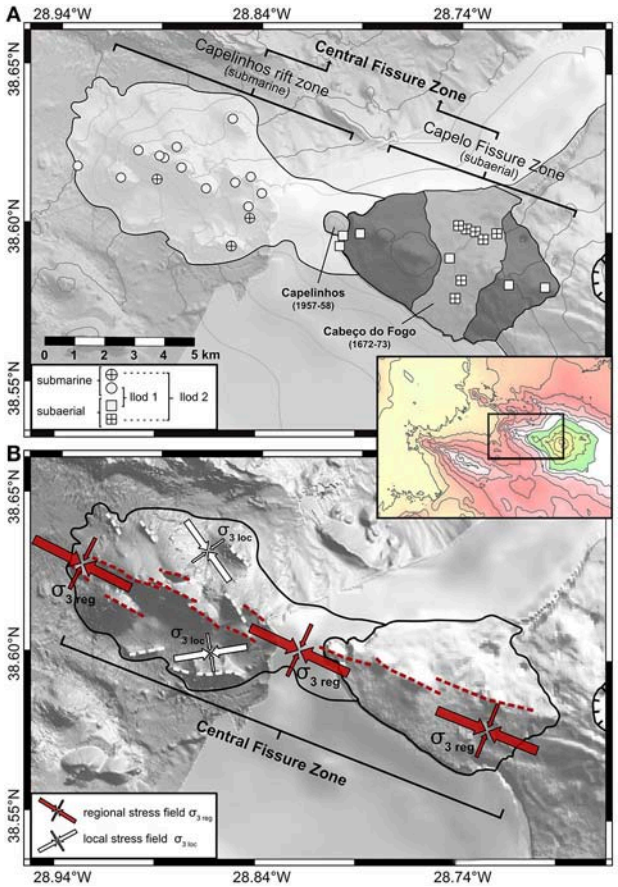

FIGURE 6 | Bathymetric map and DEM of the Central Fissure Zone comprising of a submarine part (Capelinhos rift) and a subaerial part (Capelo Fissure Zone). In **(A)** different smaller volcanic units are shown and refer to historic eruptions along the Central Fissure Zone. Numbers in brackets are year of eruption (A.D.). Symbols are the same as in **Figure 4** and refer to two liquid lines of descent with lower (llod 1) and higher (llod 2) K_2O contents. **(B)** Schematic model of the local and regional stress fields during the formation of the Central Fissure Zone. Red dashed lines and arrows display the orientation of lineaments reflecting the regional stress field (σ_{3reg} perpendicular to the WNW-ESE lineaments); white dashed lines and arrows display the orientation of the local stress field (σ_{3loc} perpendicular to NW-SE and WSW-ENE lineaments). Inset map for orientation.

DISCUSSION

The Formation of the Volcanic Rift Zones

The morphological, structural and geochemical features on Faial have been subject of several detailed studies in the last two decades (Madeira, 1998; Pacheco, 2001; Matias et al., 2007; Hildenbrand et al., 2012; Zanon and Frezzotti, 2013; Zanon et al., 2013; Di Chiara et al., 2014; Marques et al., 2014; Trippanera et al., 2014; Pimentel et al., 2015). Lithospheric extension is a major feature influencing both the morphology and structure of volcanic units forming the island. Bathymetric data from the seafloor west of Faial reveal that much of the volcanic activity is situated below sea level along WNW-ESE oriented rift zones, covering roughly the same areal extent compared to the subaerial volcanic units forming the island (**Figure 1**). In contrast to the central volcanic edifices, i.e., the Ribeirinha Volcano and Caldeira Volcano, which comprise a major volume of the island, the submarine volcanism occurs along narrow rift zones extending from the island over tens of kilometers into the basin. The submarine volcanism is structurally comparable to that occurring subaerially at the Capelo and Horta Fissure Zones, consisting mostly of fissure eruptions, isolated cones and alignments of

TABLE 1 | Comprehensive selected major and trace elements, and Sr-Nd-Pb isotopes from Faial Island and submarine volcanic rift zones.

Sample	**AZF-03-11**	**AZF-03-12**	**AZF-03-02**	**AZF-03-17**	**AZF-03-28**
IGSN	IEAZO0011	IEAZO0012	IEAZO0002	IEAZO0017	IEAZO0028
Location	Capelo FZ	Capelo FZ	Caldeira Volc.	Ribeirinha Volc.	Ribeirinha Volc.
Latitude (N)	38.596	38.592	38.519	38.547	38.583
Longitude (W)	28.826	28.827	28.725	28.626	28.614
Elevation (m)	62	8	10	78	155
(wt. %)					
SiO_2	*47.29*	*48.22*	*49.49*	*49.34*	*48.73*
TiO_2	*3.08*	*3.22*	*2.86*	*3.04*	*2.86*
Al_2O_3	*16.87*	*16.97*	*17.87*	*16.72*	*17.61*
FeO^T	*9.70*	*9.90*	*8.93*	*10.60*	*9.69*
MnO	*0.16*	*0.16*	*0.16*	*0.20*	*0.17*
MgO	*5.47*	*4.83*	*3.18*	*3.27*	*4.02*
CaO	*10.07*	*8.92*	*8.09*	*7.10*	*7.10*
Na_2O	*3.51*	*4.17*	*4.23*	*3.95*	*3.77*
K_2O	*1.46*	*1.80*	*1.98*	*2.10*	*2.24*
P_2O_5	*0.56*	*0.64*	*0.70*	*0.61*	*0.73*
SO_3	–	–	–	–	–
Cl	–	–	–	–	–
LOI	*0.060*	–	*0.710*	*1.31*	*1.26*
Total	*99.31*	*99.93*	*99.19*	*99.42*	*99.26*
(ppm)					
Rb	*31.7*	*41.9*	*42.6*	*43.4*	*47.9*
Sr	*747*	*749*	*749*	*565*	*791*
Y	*28.5*	*35.7*	*40.1*	*47.5*	*36.3*
Zr	*251*	*303*	*347*	*380*	*405*
Nb	*46.5*	*63.3*	*66.8*	*71.4*	*66.2*
Cs	*0.306*	*0.284*	*0.268*	*0.085*	*0.211*
Ba	*398*	*462*	*522*	*505*	*650*
La	*37.7*	*44.8*	*48.9*	*46.8*	*66.1*
Ce	*82.2*	*85.5*	*107*	*90.3*	*131*
Pr	*9.99*	*10.2*	*12.8*	*11.0*	*15.7*
Nd	*40.5*	*41.2*	*49.9*	*45.1*	*60.1*
Sm	*8.71*	*8.30*	*10.1*	*9.62*	*11.9*
Eu	*2.75*	*2.64*	*3.06*	*3.06*	*3.50*
Gd	*7.92*	*7.61*	*9.19*	*9.18*	*10.3*
Tb	*1.15*	*1.12*	*1.31*	*1.41*	*1.48*
Dy	*6.42*	*6.02*	*7.10*	*7.85*	*8.04*
Ho	*1.16*	*1.13*	*1.30*	*1.52*	*1.45*
Er	*2.98*	*2.88*	*3.36*	*3.93*	*3.76*
Tm	*0.396*	*0.398*	*0.450*	*0.564*	*0.507*
Yb	*2.49*	*2.45*	*2.84*	*3.57*	*3.17*
Lu	*0.347*	*0.353*	*0.401*	*0.530*	*0.442*
Hf	*6.05*	*5.91*	*7.74*	*7.11*	*9.42*
Ta	*3.02*	*3.11*	*3.52*	*3.35*	*4.18*
Pb	*2.75*	*3.12*	*3.12*	*2.77*	*4.41*
Th	*3.46*	*4.54*	*4.81*	*5.53*	*6.38*
U	*1.06*	*1.34*	*1.58*	*1.03*	*1.61*
$^{87}Sr/^{86}Sr$	*0.703840*	*0.703861*	*0.703888*	*0.703769*	*0.704129*
$^{143}Nd/^{144}Nd$	*0.512881*	*0.512858*	*0.512881*	*0.512916*	*0.512834*
$^{206}Pb/^{204}Pb$	*19.618*	19.567	19.563	19.314	19.437
$^{207}Pb/^{204}Pb$	*15.647*	15.641	15.639	15.553	15.624
$^{208}Pb/^{204}Pb$	*39.331*	39.286	39.238	38.819	39.140

(Continued)

TABLE 1 | Continued

Sample	814TVG-01	820TVG-01	817ROV-01	817ROV-07	817ROV-13
IGSN	IEAZO1131	IEAZO1151	IEAZO1135	IEAZO1141	IEAZO1147
Location	Capelinhos rift	Capelinhos rift	Condor rift	Condor rift	Condor rift
Latitude (N)	38.623	38.618	38.573	38.569	38.566
Longitude (W)	28.909	28.892	29.114	29.116	29.107
Elevation (m)	–663	–427	–918	–734	–588
(wt. %)					
SiO_2	46.32	49.42	46.91	43.94	47.18
TiO_2	2.84	4.15	4.40	3.60	3.52
Al_2O_3	17.94	15.30	18.54	17.56	18.49
FeO^T	9.33	11.07	10.29	10.85	8.63
MnO	0.16	0.20	0.13	0.13	0.12
MgO	6.00	3.90	2.57	5.50	4.16
CaO	9.74	8.50	9.05	11.82	12.08
Na_2O	4.21	4.69	3.97	2.71	3.04
K_2O	1.35	2.37	0.93	0.30	0.48
P_2O_5	0.62	0.97	0.53	0.59	0.32
SO_3	–	0.12	–	–	–
Cl	–	0.10	–	–	–
LOI	0.17	–	1.27	1.51	0.77
Total	99.71	100.76	99.73	99.73	99.75
(ppm)					
Rb	26.4	31.2	5.28	1.57	2.62
Sr	750	771	381	475	459
Y	28.7	31.9	36.6	22.7	27.5
Zr	248	296	218	165	185
Nb	48.5	56.9	40.4	28.1	33.3
Cs	–	–	–	–	–
Ba	386	444	250	101	172
La	36.8	42.0	29.8	21.0	23.3
Ce	70.7	82.9	58.5	42.2	47.6
Pr	8.76	10.3	7.57	5.30	6.16
Nd	36.1	42.6	33.0	22.6	26.7
Sm	7.57	8.84	7.82	5.22	6.35
Eu	2.33	2.71	2.43	1.63	2.05
Gd	6.89	7.98	7.97	5.16	6.29
Tb	0.981	1.14	1.20	0.770	0.936
Dy	5.54	6.43	7.09	4.43	5.43
Ho	0.994	1.15	1.33	0.814	0.995
Er	2.59	2.98	3.58	2.17	2.62
Tm	0.340	0.394	0.485	0.290	0.347
Yb	2.06	2.36	2.93	1.76	2.11
Lu	0.299	0.344	0.439	0.262	0.308
Hf	5.67	6.60	6.15	3.94	4.80
Ta	2.96	3.41	2.59	1.81	2.13
Pb	2.71	3.03	2.75	1.63	1.61
Th	3.37	3.88	2.91	2.09	2.23
U	0.971	1.13	2.92	1.58	1.00
$^{87}Sr/^{86}Sr$	0.703873	0.703812	0.703718	0.703686	0.703775
$^{143}Nd/^{144}Nd$	0.512870	0.512865	0.512737	0.512930	0.512925
$^{206}Pb/^{204}Pb$	19.528	19.468	19.187	19.502	19.439
$^{207}Pb/^{204}Pb$	15.643	15.642	15.624	15.608	15.571
$^{208}Pb/^{204}Pb$	39.272	39.241	38.946	38.924	38.884

Italic data were analyzed and published as described in Beier et al. (2012).

elongated cones, and dikes (Zanon et al., 2013; Trippanera et al., 2014). This is in contrast to eruptions forming the Caldeira Volcano and probably the Ribeirinha Volcano, which are large central volcanoes.

Generally, there are two different directions of lineations influencing the volcanic units on the island. Most structures, including those showing fissural and monogenetic volcanism along the Capelo and Horta Fissure Zones, are oriented

WNW-ESE with extension taking place in a mean 045° direction (Trippanera et al., 2014, **Figures 1**, **6**). Central volcanic edifices, e.g., the Caldeira Volcano, however, additionally show less dominant structures with a NNE-SSW orientation, which may be the result of far-field effects of activity along the MAR (Trippanera et al., 2014) or may be due to local stresses during magma emplacement. The orientation of the submarine rift zones (∼300°), parallel to the dominating WNW-ESE orientation of most lineaments on the island of Faial, indicate that they are also influenced by the general regional tectonic stress field prevailing at Faial (**Figures 1**, **6**). Studies on, e.g., Iceland have shown that melts can be transported along dikes up to tens of kilometers causing fissure eruptions and alignments of monogenetic cones, like the 2014 dike emplacements near Bardarbunga Volcano (Gudmundsson et al., 2014, 2016; Sigmundsson et al., 2014). Dikes are usually oriented rift-parallel and perpendicular to the least principal compressive stress σ_3 and, therefore, reflect the regional stress field (Schwarz et al., 2005). The occurrence and orientation of dikes in a mean 311° ± 15° direction on Faial (Trippanera et al., 2014) corresponds to the orientation of the submarine rift zones. Thus, we suggest that the lateral transport of melts via dikes into the basin is the major process during the formation of the rift zones. The direction of dikes on Faial is indeed slightly rotated against the general direction of lineaments (mean of 298° ± 16°(Trippanera et al., 2014), however, this is rather an effect of shallow en-echelon dyking, comparable to that observed at Desertas Islands in the Madeira archipelago (Klügel et al., 2005b; Trippanera et al., 2014).

Lineaments at the Capelinhos rift, differing from the otherwise consistent WNW-ESE orientation, reflect local rather than regional changes in the stress field. These lineaments are located at the north-eastern and south-western flanks of the Capelinhos rift in ∼265° and ∼320° directions, respectively (**Figure 6**). A recent study by Tibaldi et al. (2014) has shown that eruptions at the flanks of elongated volcanic edifices may result in locally rotated stress fields which are related to gravity forces and controlled by the topography forming a diverging volcanic rift system. We conclude that the fan-like arrangement of lineaments at Capelinhos rift is the result of a combination of dike emplacement at the flanks of existing volcanic edifices, the shallow rotation of σ_3 and, subsequently, a local change in the orientation of lineaments from the predominant WNW-ESE to a more E-W and NW-SE direction (**Figure 6**).

Lavas from the western tip of Faial (Capelo Fissure Zone) have erupted within the last ∼10 ka and represent the youngest volcanic unit on Faial (Madeira et al., 1995; Hildenbrand et al., 2012; Di Chiara et al., 2014). Samples taken along the western adjoining submarine Capelinhos rift using visual sampling techniques during R/V *Meteor* cruise M128 reveal that these are fresh, glassy lavas with scarce biological coatings (Beier et al., 2017a). We conclude that lavas along the entire Capelinhos rift are as young as those erupted subaerially along the Capelo Fissure Zone (<10 ka) forming a single volcanic unit. Lavas taken along the rift zones north and south of Capelinhos rift are strongly altered with biological overgrowths and are covered by carbonate sand and debris. Representative images of rock samples and the ocean seafloor west of Faial are provided in the supplements (Supplementary Figure 3) and in Beier et al. (2017a).

For the submarine rift zones north and south of Capelinhos rift, we combine absolute ages from geochronology with seismic data providing relative age constraints between individual larger units (**Figure 3**). In agreement with Ar-Ar ages and direct observations using visual sampling techniques, the seismic profiles show that the age of the rift zones increases with increasing distance from Capelinhos rift systematically to the south (Condor rift) and north (Ribeira Funda and Northern rifts; **Figure 3**). They are covering an age range from 1.1 Ma until recently, based on Ar-Ar ages from Beier et al. (2015). Hence, we have grouped our samples into subaerial and submarine lavas consistent with their approximate ages (**Figure 2**).

The seismic data allow to constrain the relative ages between the Ribeira Funda and Capelinhos rifts, but it is much more difficult to determine the age of Ribeira Funda rift relative to units on the island or Condor rift. In this case, structural features, however, can be used for a rough estimate of the relative age of the volcanic activity along Ribeira Funda. The Ribeira Funda rift has the same orientation and is located in the extension of the Pedro Miguel graben axis (**Figure 1**), which was active at 400 ka (Hildenbrand et al., 2012). We suggest that this strong structural connection could be explained by a contemporaneous formation. The internal structure of Ribeira Funda rift evidences normal faulting, in contrast to the Central Fissure Zone (**Figure 3**). This implies that Ribeira Funda rift was formed when tectonic activity along the Pedro Miguel graben began and was already formed while the displacement at the graben was still active, with the result that the existing ridge was rifted. Assuming that the orientation of the rift zones mirrors the tectonic stress field, it has not changed significantly during their evolution. Note that the submarine rift zones probably cover the entire age interval of subaerial volcanic activity on Faial (∼1 Ma until recently). This contrasts observations from São Miguel and to some extent Santa Maria, which experienced distinct major stress fields during their formation due to the reconfiguration of the Africa-Eurasia plate boundary (Sibrant et al., 2015, 2016; Ramalho et al., 2017).

Geochemical Relationship Between the Rift Zone Lavas

Models dealing with the formation of volcanic rift zones and dike emplacement suggest a central accumulation zone of melts feeding a central volcano, from which sills and dikes intrude along rift zones depending on the local and regional stress fields (e.g., Gudmundsson, 1995; Garcia et al., 1996; Paquet et al., 2007; Gudmundsson et al., 2014). These models have in common that melts feeding both the central volcanoes and the associated rift zones form from the same shallow crustal reservoir. The magmatic system of Faial consists of both large central volcanoes and distinct, individual rift zones with lavas derived from fissure eruptions and dyking deviating in age on the order of several 100 ka. This allows to test whether melts erupted from different volcanic structures (i.e., central volcanoes or rift zones) systematically deviate in source and composition and to determine what

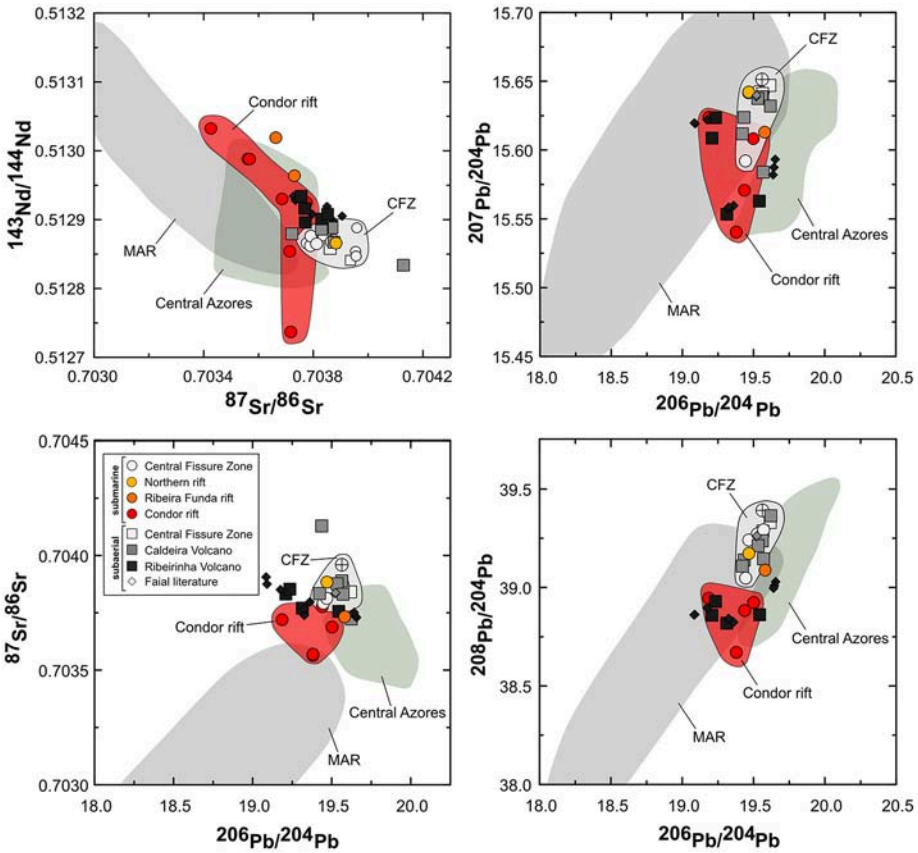

FIGURE 7 | Strontium-Nd-Pb isotope ratios of submarine and subaerial lavas from Faial. Green highlighted areas are samples from the Central Azores Plateau (São Jorge and Pico) from Hildenbrand et al. (2008), Beier et al. (2012), and Hildenbrand et al. (2014). Gray field are samples from the Mid-Atlantic-Ridge (MAR) from Dosso et al. (1999). CFZ, Central Fissure Zone.

the spatial and temporal parameters are that influence the melts.

All lavas from Faial and from the submarine rift zones display evidence for fractional crystallization during magma ascent. Most major elements (CaO, K_2O, Na_2O, FeO^T, and Al_2O_3) are correlated with fractionation indices, e.g., MgO (**Figure 4**) and SiO_2. The most primitive lava from Faial in this work has a MgO content of 8.62 wt. % (IGSN: IEAZO0651) and, thus is significantly more evolved than primitive lavas from the islands along the Terceira Rift with about 10–12.5 wt. % MgO (Beier et al., 2006, 2008). Zanon et al. (2013) showed that some Faial lavas have MgO contents up 12.5 wt. % (**Figure 4**) but their lavas with >10 wt. % MgO are highly porphyritic ankaramites and are thus considered to be the result of accumulation of olivine and clinopyroxene crystals. We conclude that the most primitive submarine and subaerial rocks from Faial have about 9 to 10 wt. % MgO in equilibrium with forsterite contents of Fo_{79} in olivines (Roeder and Emslie, 1970) analyzed in these lavas (Beier et al., 2012). Generally, lavas from the Caldeira and Ribeirinha Volcanoes are more evolved compared to other samples from the island and rift zones (**Figure 4**). We suggest that extensive fractional crystallization is dominant in these large volcanic edifices compared to lavas from the submarine rift zones and subaerial fissure zones. This is in agreement with thermobarometric calculations from Zanon et al. (2013) and Zanon and Frezzotti (2013), which have shown that rocks derived from fissure eruptions at the Capelo and Horta Fissure Zones have not stagnated significantly during their ascent from the mantle, whereas melts at the Caldeira Volcano have undergone polybaric fractional crystallization and stagnation at shallower crustal levels, leading to the formation of trachytes (Pimentel et al., 2015). The variability of most major elements, in particular K_2O, and incompatible trace element ratios, (e.g., La/Yb, Nb/Zr) at a given MgO content (**Figures 4**, **5**) however, cannot be explained by simple fractional crystallization and may rather be related to changes in mantle source composition or degree of partial melting, respectively (see below). We conclude that lavas from different subaerial and submarine units cannot be related to crystallization along a single liquid line of descent but may have experienced similar degrees of fractionation.

We also observe variable major element contents in single volcanic units. Using samples from the Central Fissure Zone as the best sampled unit, some major elements, in particular K_2O, imply that there are two slightly distinct liquid lines of descent

even within a volcanic unit (**Figures 4**, **6**). As a result, we divide the Central Fissure Zone lavas into two groups each representing liquid lines of descent with lower and higher K_2O contents, respectively. Small-scale compositional variations within a single volcanic system are also well-known from other oceanic volcanic systems (e.g., the 1783 Laki eruption; Neave et al., 2013) where multiple lines of evidence contradict the evolution of the erupted magma along a single liquid line of descent. Samples from recent eruptions along the Central Fissure Zone, including those from the 1957–58 Capelinhos eruption, form a lower K_2O liquid line of descent (llod1). Whereas most lavas from the historic 1672–73 Cabeço do Fogo eruption and a few submarine lavas from the Capelinhos rift lie on a liquid line with higher K_2O contents (llod2). Combining our data with those from Zanon et al. (2013), there is no clear correlation with historic eruption centers. Several other eruptions occurred within the last 10 ka along the Central Fissure Zone on a small spatial area which may be the result of overlapping eruptions. More importantly, lavas from both liquid lines of descent occur subaerially and along the entire submarine rift axis (**Figure 6**). We thus conclude that there are several magmatic phases in which melts are efficiently transported laterally within relatively short timescales over several kilometers (>12 km) along the rift zones prior to eruption, probably via sills and dikes.

This implies that melts erupted at length scales of <12 km, i.e., the length of Central Fissure Zone rift, provide information on the geochemical variability within relatively short timescales. Comparison of the northern and southern rift zones relative to submarine and subaerial lavas from Faial may, on the other hand, provide information on the temporal evolution of the melts over <1 Ma during which these rift zones have been active. The high K_2O and Na_2O contents of lavas from the Central Fissure Zone compared to the other lavas from the island and the rift zones (**Figure 4**) indicate that there are several magmatic series erupting along the rift zones and the central volcanoes. The distinct major element compositions not related to fractional crystallization thus may result from systematic changes in either the conditions and/or sources of melting and/or the tectonic regime influencing the magmatic system beneath Faial.

Melting Regime

Source of Melting

Incompatible trace element ratios can be used to distinguish between mantle sources (e.g., Sun and McDonough, 1989; Hofmann, 2003; and references therein). The variable K_2O contents and K_2O/TiO_2 ratios (**Figure 4**) of lavas from Faial combined with variable incompatible trace element ratios, e.g., Nb/Zr, Ba/Nb, Sm/Nd (**Figure 5**) and their Sr-Nd-Pb isotope compositions (**Figure 7**) indicate that subaerial and submarine lavas can indeed be distinguished based on their mantle source signatures. Lavas from Condor and Ribeira Funda rifts have lower Ba/Nb and higher Sm/Nd at a given MgO content and lower $^{87}Sr/^{86}Sr$ and higher $^{143}Nd/^{144}Nd$ isotope ratios, respectively, compared to lavas from the Central Fissure Zone. We suggest that lavas from Condor and Ribeira Funda rifts may have originated from a more depleted mantle source compared to Central Fissure Zone melts. The two stratigraphically lowermost lavas from the Condor section with lower $^{143}Nd/^{144}Nd$ are likely to reflect a more enriched mantle source compared to other lavas from this rift zone. Considering their relative stratigraphic position, we suggest that they are the oldest samples from Condor rift and might reflect a former more enriched mantle source which has progressively changed in composition toward the younger volcanism along this ridge. In agreement, the $^{206}Pb/^{204}Pb$ ratios are lower for lavas from Condor rift compared to those from the Central Fissure Zone. Lavas from Ribeira Funda rift tend to slightly more radiogenic $^{207}Pb/^{204}Pb$ and $^{208}Pb/^{204}Pb$ ratios compared to Condor rift at a given $^{206}Pb/^{204}Pb$ (**Figure 7**). Thus, melts feeding the volcanism on Faial and submarine rift zones originate from a variably heterogeneous mantle similar to that observed in other Azores islands (Hawkesworth et al., 1979; Turner et al., 1997; Widom et al., 1997; Haase and Beier, 2003; Beier et al., 2007, 2008; Elliott et al., 2007; Madureira et al., 2011).

The difference between the Condor rift and the Central Fissure Zone lavas indicates that the mantle source compositions became more radiogenic in Sr and Pb isotope compositions with decreasing age. The mantle source signatures for lavas from the Caldeira and Ribeirinha Volcanoes lie between those from the Central Fissure Zone and Condor and Ribeira Funda rifts, based on their K_2O contents and most incompatible element ratios (**Figures 4**, **5**) at a given MgO content. The Sr-Nd isotope ratios of the Ribeirinha Volcano suggest a slightly more depleted source than those from the Central Fissure Zone, whereas lavas from the Caldeira Volcano overlap those of the young lavas forming the Central Fissure Zone (**Figure 7**). Samples associated with the Ribeirinha Volcano deviate in Pb isotopes toward less radiogenic $^{207}Pb/^{204}Pb$ and $^{208}Pb/^{204}Pb$ ratios compared to the Caldeira Volcano consistent with small variations in major and trace elements. If Faial is treated as a single magmatic system, the trace element and isotope variability between distinct lava suites implies continuous trends in which some lavas form a compositional transition between the two most extreme compositions. We thus suggest that these lavas originate from a comparatively enriched but heterogeneous mantle. Combining these observations with the ages of the distinct lava suites implies that Faial lavas have experienced a progressive enrichment of the mantle source with time (**Figures 7**, **8**, **10**). Thus, as the chemical signatures of the Ribeira Funda rift lavas are comparable to lavas from Condor rift and the Ribeirinha Volcano, we suggest that Ribeira Funda rift is probably older than the Caldeira Volcano (**Figure 10**).

The progressive evolution of the mantle source composition is accompanied by changes in the spatial distribution of the volcanism. Older lavas with a more depleted mantle source composition cover a large spatial area, whereas the youngest and most enriched lavas erupted along a single rift zone, indicating that the composition of melts and their spatial distribution may be linked, the significance of which we will discuss below.

Conditions of Melting

The degree of partial melting can be estimated using moderately incompatible elements, e.g., Na_2O (Klein and Langmuir, 1987; Prytulak and Elliott, 2007) and incompatible trace element

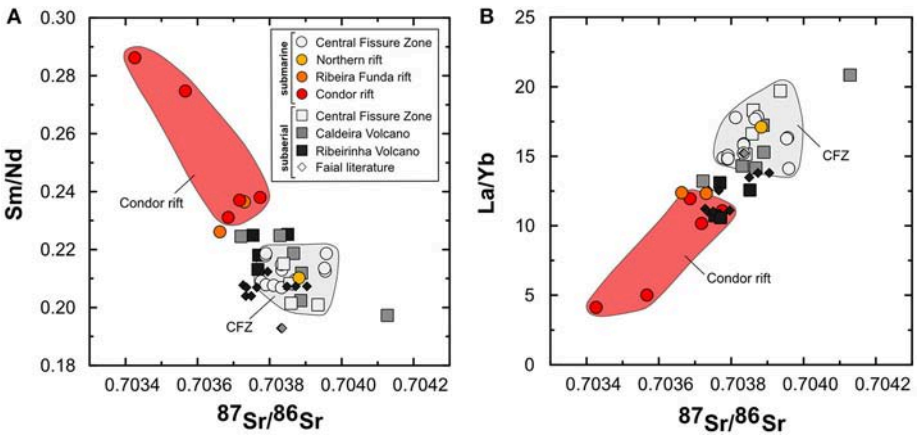

FIGURE 8 | Variations of **(A)** source sensitive trace element ratio Sm/Nd and **(B)** melting sensitive trace element ratios La/Yb vs. $^{87}Sr/^{86}Sr$. Data sources are the same as in **Figure 4**.

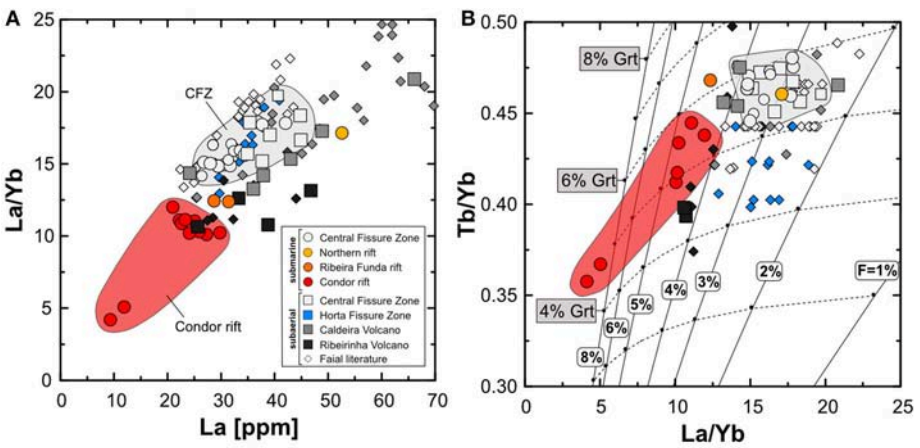

FIGURE 9 | La/Yb vs. **(A)** elemental concentration of La [ppm] and; **(B)** Fractional melting model modified from Bourdon et al. (2005) and Beier et al. (2013) for Faial lavas using a Tb/Yb vs. La/Yb space and a primitive mantle source from Sun and McDonough (1989) comprised of 55% olivine, 25% orthopyroxene and variable ratios of clinopyroxene and garnet as shown by gray boxes and dashed lines, respectively. White boxes and solid lines mark the degree of partial melting. Partition coefficients for olivine, orthopyroxene, and clinopyroxene were taken from those compiled in Halliday et al. (1995) and references therein, Adam and Green (2006) and Villemant et al. (1981), for garnet from Green et al. (2000). The distribution coefficients used for this model can be found in Supplementary Table 3. Data sources are the same as in **Figure 4**.

ratios, e.g., La/Yb. These values represent mean degrees of melting, given that most oceanic basalts probably represent the accumulated products of a continuous melting process that generates instantaneous melts at a range of melt fractions. Two groups can be distinguished based on their distinct La/Yb ratios (**Figure 9**). The consistently higher Na_2O contents and La/Yb ratios from the Central Fissure Zone imply slightly smaller degrees of partial melting compared to most of the surrounding volcanoes and rift zones (**Figures 4**, **5**). Both submarine lavas from Condor and Ribeira Funda rifts and subaerial lavas from the Ribeirinha Volcano indicate higher degrees of partial melting (based on lower La/Yb ratios), relative to lavas from the Central Fissure Zone and the Caldeira Volcano. These groups are similar to those observed with respect to their mantle source compositions, except for Ribeirinha Volcano which has a similar degree of partial melting compared to Condor rift but a more enriched source composition. Incompatible trace elements sensitive to either mantle source signatures (e.g., Sm/Nd) and the degree of partial melting (e.g., La/Yb) correlate with Sr-Nd isotope compositions (**Figure 8**) implying a heterogeneous mantle source. Hence, we conclude that the two distinct groups not only reflect changes in mantle source composition but may also reflect changes in degree of partial melting.

Using a fractional melting model modified from Bourdon et al. (2005) and Beier et al. (2013) we show that lavas from Condor and Ribeira Funda rifts, and the Ribeirinha Volcano are melting at higher degrees of partial melting between 4 and 8%, compared to 2–4% degree of partial melting at the Central

Fissure Zone and the Caldeira Volcano (**Figure 9**). In agreement with Na_2O, lavas from the Caldeira Volcano display slightly higher degrees of partial melting compared to the Central Fissure Zone (based on lower La/Yb; **Figure 9**). The island of Faial and its submarine ridges, however, are built on a lithosphere with approximately the same thickness of about 30 km, calculated using the 1300°C isotherm of Stein and Stein (1992) and a lithosphere age of about 10 Ma (Cande and Kent, 1995; Luis and Miranda, 2008). Robinson and Wood (1998) have shown that the fractionation of middle Rare Earth Elements (MREE) relative to heavy Rare Earth Elements (HREE) in the melt fraction depends on the amount of residual garnet in the mantle that may be increasing with increasing lithosphere thickness in the oceanic environment. Generally, lavas from Faial contain similar amounts of residual garnet between 4 and 6%. This is in agreement with the fact that the amount of garnet in the residual mantle should not differ significantly within the island and the neighboring rift zones if correlated to lithospheric thickness. Thus, we suggest that the small but notable variability in MREE/HREE ratios reflects variations in their mantle source composition rather than different melting depths, i.e., the lowest Tb/Yb ratios are limited to Condor rift and the Ribeirinha Volcano. We conclude that older lavas from Faial, lavas from Condor and Ribeira Funda rifts and the Ribeirinha Volcano formed at a higher degree of partial melting compared to the younger lavas.

The Origin of Chemical and Isotopic Variations

Changes in source composition may also be accompanied or influenced by changes in the degree of melting, i.e., variably more enriched sources may melt deeper and hence to a larger extent (Phipps Morgan, 2000; Niu et al., 2002; Shorttle et al., 2014). In other volcanic systems (e.g., on Iceland; Maclennan, 2008; Shorttle et al., 2014) neighboring volcanoes which have originated from a single mantle column have distinct correlated trace element and isotope patterns. These differences are probably related to mantle source heterogeneity showing that the source composition and the melting depth are closely linked. Comparatively, a study from the Galapagos Rise (Haase et al., 2011) has shown that differences in major and trace elements and isotopes are the result of different degrees of partial melting of a heterogeneous mantle source. The progressive decrease in degrees of partial melting with time occurred as the rifting of the Galapagos Rise slowed down and finally stopped. As a result incompatible element-enriched mantle lithologies can generate a systematic enrichment in incompatible elements with increasing alkalinity of the melt as they preferentially contribute to melts generated at smaller degrees of partial melting (Haase et al., 2011).

Similar to the Galapagos Rise case, lavas from Faial and adjoining submarine rift zones reflect progressive changes in both their mantle source compositions and degrees of partial melting since ∼1 Ma (from Condor rift to the Central Fissure Zone; **Figure 9**). We suggest that the similarity of both cases, changes in mantle source compositions and the conditions of melting in the Faial lavas result from a process that is linked. The youngest lavas from the Central Fissure Zone (<10 ka) have the most enriched mantle source composition, melting with a lower degree of partial melting compared to the older lavas. Hence, we conclude that the consequence of the progressive decrease in the degree of melting at Faial results in a larger contribution of trace element-enriched mantle lithologies from a heterogenous mantle source characteristic to the Azores melting anomaly (Beier et al., 2018).

Spatial and Temporal Evolution

The large compositional and age differences of the Faial lavas imply that they probably do not derive from one large reservoir beneath the Caldeira Volcano. Although volcanic units with comparable ages tend to be similarly enriched or depleted, they did not evolve along a single fractionation path. The differences in K_2O contents and K_2O/TiO_2 ratios between the Central Fissure Zone and the Caldeira Volcano (**Figures 4B,F**), for example, are too large to be explained by similar liquid lines of descent. Some volcanic systems on Hawaii, i.e., the Kilauea Volcano and the associated Pu'u O'o rift zone (Greene et al., 2013) are geochemically variable and probably derive from one plumbing system. However, the time scales of eruptions with lavas of distinct composition are much shorter (years to decades) compared to Faial. The nature of the periodicity of eruptions on Faial, with short periods of volcanic activity followed by hiatuses of up to several 100 ka (Hildenbrand et al., 2012) rather implies that the compositional differences between distinct volcanic units result from distinct primary magmas and plumbing systems. The younger volcanic units on the island, in particular the Caldeira Volcano, likely cover older units, and in the absence of samples one might speculate that these may form compositional equivalents to the lavas erupted along the submarine rift zones. Thus, we suggest that a model like on Iceland (Gudmundsson, 1995) or Hawaii (Garcia et al., 1996) with a summit reservoir feeding both a central volcano and the rift zones is not applicable for Faial. Instead, the volcanic structures may be comparable to those observed on La Palma where the central volcano and the rift zone formed above distinct plumbing systems (Galipp et al., 2006). Melts feeding the rift zones, e.g., the Central Fissure Zone, ascend from the mantle either directly beneath their locus of eruption or beneath a central volcano, i.e., the Caldeira Volcano. In the latter case, ascending melts would likely stagnate in the uppermost crust, where the base of volcanic edifices and their sedimentary covers have a lower density (Klügel et al., 2005a) and then get laterally transported as sills and dikes into the rift zone. Despite the fact that most samples from the Central Fissure Zone have mafic to intermediate compositions, stagnation and probably further cooling and fractionation beneath the Caldeira Volcano could explain why some samples from the Central Fissure Zone are relatively evolved. However, Zanon and Frezzotti (2013) showed that melts from the subaerial fissure zones have not stagnated significantly during their ascent. In both cases, the effective lateral transport of melts and eruption along fissures are a major process for the development of the rift zones. Elongated rift zones and large volcanic edifices imply that they are internally homogeneous but the distinct geochemical variability between the different rift zones and

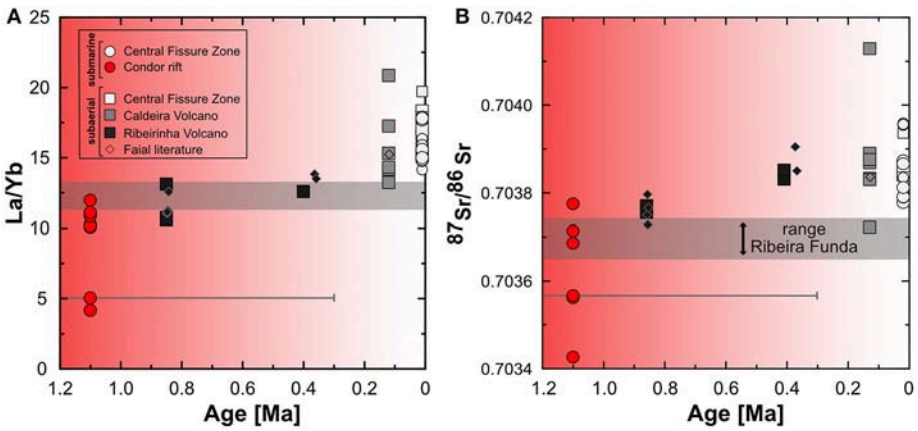

FIGURE 10 | (A) La/Yb and **(B)** $^{87}Sr/^{86}Sr$ vs. absolute (Madeira et al., 1995; Hildenbrand et al., 2012; Beier et al., 2015) and relative ages from seismic profiles of Faial lavas and respective rift zones. La/Yb and $^{87}Sr/^{86}Sr$ ratios display both a progressive decrease in the degree of partial melting and a progressive enrichment of the mantle source compositions. Color gradient schematically illustrates the progressive change in the melting regime from a more depleted mantle source and high degree of partial melting (red) to a more enriched mantle source and a lower degree of partial melting (white) (see also **Figure 11**). Gray area marks the range La/Yb and $^{87}Sr/^{86}Sr$ ratios of the Ribeira Funda rift lavas. Error bars display the analytical variation in Ar-Ar age form the submarine Condor rift. The analytical errors of the other absolute, radiometric ages are smaller than the respective symbols. Note that the lower La/Yb and $^{87}Sr/^{86}Sr$ for those lavas compared to the Caldeira Volcano may indicate that this rift zone is older. Literature data are from Hildenbrand et al. (2014) for La/Yb and $^{87}Sr/^{86}Sr$. The respective ages derive from K-Ar age dating from Hildenbrand et al. (2012) on the same rock specimen like on which the trace element and isotope analysis were carried out. Symbols are maximum radiometric ages from the respective volcanic units.

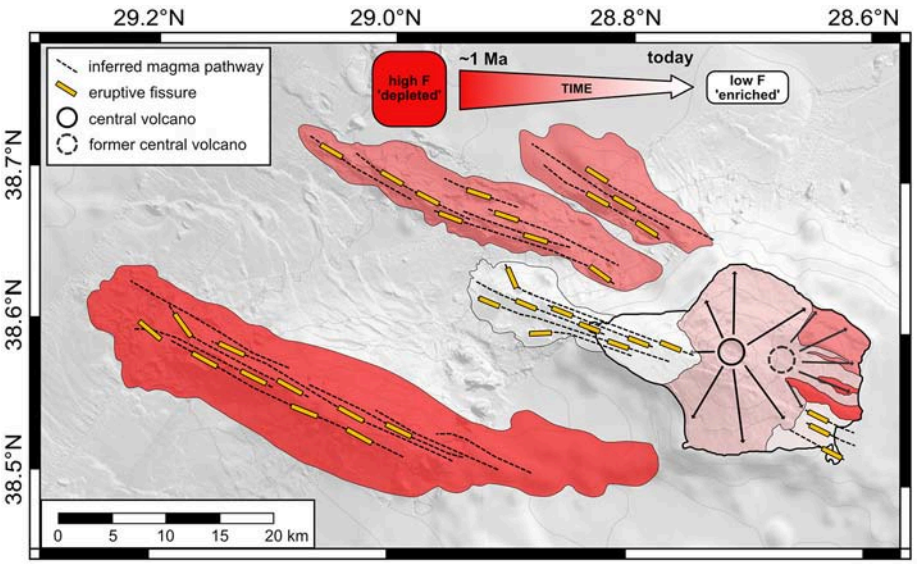

FIGURE 11 | Schematic illustration of the progressive spatial evolution of the conditions of melting and structural features. Note that older lavas with less enriched mantle source compositions at higher degrees of partial melting (F) (dark red colors, large box) occur more widespread than the younger lavas, having more enriched mantle source compositions at lower melting degrees (bright red to white colors, small box). The recent mafic and intermediate volcanic activity on Faial occurs exclusively along narrow rift zones, whereas the older volcanic activity is characterized by both volcanic rift zones and central volcanic edifices. Not to scale.

central volcanoes implies that these systems only show limited interaction.

Combining our chemical observations with the spatial distribution of eruption ages at Faial also provides the possibility to better constrain the temporal evolution of the sources and melting signatures (**Figure 10**). In contrast to the Ribeirinha Volcano forming the oldest volcanism on the island and to some extent the Caldeira Volcano, the youngest mafic and intermediate volcanic activity (<10 ka) on Faial exclusively occurs very localized along rift structures. This may be a result of melt focussing into the rift zones, because the structural features indicate that the tectonic control on youngest

volcanic units becomes stronger, i.e., a preferential formation of volcanic rift zones as opposed to central volcanic edifices. The distribution of lava ages suggests that the youngest mafic and intermediate volcanism occurs on a small area along the Central Fissure Zone and Horta Fissure Zone, whereas the older lavas form both submarine rift zones and large central volcanic edifices and cover large areas (**Figure 11**). The differences in spatial distribution of the volcanic activity correspond to the compositional differences of the groups reflecting different mantle source compositions and degrees of partial melting. This may indicate that the processes leading to compositional variation and eruption style are linked. Hence, the volcanism on Faial appears to become increasingly localized along tectonically controlled lineaments as changes in the melting regime occur.

The similarity of both source and melting signatures in the Faial lavas suggests that this magmatic system is significantly influenced by changes in the melting regime, particularly in the degree of partial melting. A decrease of melting productivity in the upper mantle beneath Faial may be due to a waning of the Azores melting anomaly (O'Neill and Sigloch, 2018). Variability in magmatic productivity is well-documented in other ocean island locations, classically in the alkaline pre-shield, tholeiitic shield and alkaline post-shield phases of Hawaiian volcanism (Clague and Dalrymple, 1987). However, a tholeiitic shield phase is not present in Faial. On Iceland changes in the plume temperature may be responsible for changes in lava compositions (Poore et al., 2011), indicating that geochemical variations in the produced melts are largely driven by changes in the melting regime. However, rift jumps and mantle plume migration may also be responsible for the alkaline volcanic activity of the Snaefellsnes Rift on Iceland (Hardarson et al., 1997), indicating that changes in both tectonic and magmatic processes may variably contribute to changes in the lava compositions. In the eastern Azores Plateau the successive jumps of the Terceira Rift (Gente et al., 2003; Vogt and Jung, 2004) to its present position may additionally support the decreasing degrees of partial melting beneath Faial. However, the position of the triple junction in the Azores remains unclear and may be treated as a diffuse plate boundary situated in the vicinity of the area west of Faial and/or Graciosa (Miranda et al., 2014). Noble gas isotopes and melting models suggest that a deep mantle plume may be located beneath Terceira (Moreira et al., 1999; Bourdon et al., 2005), some 150 km north-east of Faial, whereas geophysical models suggest the plume beneath Faial (Yang et al., 2006). However, our data suggest that the melt supply beneath Faial decreases toward the youngest volcanism. We conclude that the progressive changes in the melting regime, the composition of melts and their spatial distribution reflect changes in the plate tectonic regime and mantle plume upwelling. Even though the Azores case with an extensional tectonic regime above a (wet) melting anomaly may be treated as a rather unique case, these observations may also be applicable to other (intraplate) settings where both significant tectonic stresses and magmatism are present, e.g., in the Canary Islands or on Iceland. We note however, that the Canary Islands may contain less of a plate tectonic component whereas the Iceland volcanic systems combined a much stronger plume signal with a true spreading movement.

SUMMARY AND CONCLUSIONS

The island of Faial and the western adjoining submarine rift zones have undergone a complex volcano-tectonic evolution. We use new geophysical, high resolution bathymetric, geochemical, and Sr-Nd-Pb isotope data combined with published ages to expand existing models covering the volcanic and tectonic evolution of the island and its submarine rift zones in the Azores. Much of the volcanism related to Faial occurs below sea level, covering a similar spatial extent compared to the subaerial volcanism. The formation of four WNW-ESE oriented narrow submarine structural and magmatic features since ∼1 Ma together with the formation of the Pedro Miguel graben some 400 ka ago both likely resulting from extensional stresses, show that lithospheric extension is an important process during the evolution of the subaerial and submarine volcanic structures. We suggest that dikes efficiently transport melts along the volcanic rift zones at Faial over length scales of >12 km while plumbing systems parallel to the rift axes are distinct over a similar length scale, e.g., the distance between Capelinhos and Condor rifts. The fact that the orientation of the rift zones and other structural features related to tectonic stresses on Faial have generally not changed since their formation ∼1 Ma shows that the regional tectonic stress field has not changed significantly during the evolution of the island. Lavas from Faial and its respective submarine rift zones, however, display a regular spatial distribution in both compositional signatures (mantle source compositions and degree of partial melting) and ages of eruption (**Figures 10**, **11**). The older lavas from 1.1 Ma to ∼400 ka formed by higher degrees of partial melting from a more depleted mantle source and cover a larger area. The younger volcanic activity forms by smaller degrees of partial melting from a more enriched source. We suggest that the degree of partial melting decreases progressively toward the youngest volcanism resulting in increasingly enriched magmas, largely sampling the enriched mantle sources as they preferentially contribute to small degree melts. As melt supply decreases, volcanism appears to become increasingly localized along tectonically controlled (active and non-active) lineaments in the last 10 ka exclusively erupting along fissures, alignments of elongated cones and dikes. Hence, mafic and intermediate melts erupted during the youngest volcanic activity on Faial focus along single rift zones, whereas the old volcanism occurs more widespread. The compositional and age differences between the central volcanic edifices and the rift zones suggest that lavas feeding these systems do not derive from one shallow magma reservoir and rather derived from different plumbing systems. Our study demonstrates the importance of detailed geochemical investigations of ocean islands that are strongly influenced by tectonic stresses and their potential to disentangle how changes in the melting regime may be reflected in the structural features of volcanic bodies and their spatial distribution. A continuous change in divergent

plate movements may affect the melt formation and supply from the mantle.

AUTHOR CONTRIBUTIONS

All authors were involved in the data acquisition. CB was chief scientist on cruise M128 and was responsible for sampling of volcanic rocks during cruise M113 and on Faial. CH was chief scientist on cruise M113 and responsible for the seismic data acquisition, selection of sampling localities and their interpretation. RR prepared and analyzed the rock samples, wrote the manuscript and designed the manuscript. All authors discussed and contributed to the final manuscript.

ACKNOWLEDGEMENTS

We acknowledge help and support from captains M. Schneider and J. F. Schubert, crews and scientists during M113 and M128 for their invaluable, friendly support during the—at times difficult—operations. A special thanks to M. Regelous for support in the Erlangen clean laboratories. We acknowledge the constructive and helpful reviews by D. A. Neave, V. Acocella and R. Gertisser, and constructive and helpful annotations and editorial handling by A. Pimentel. We thank K. Knevels for providing help with the geophysical data. We thank V.H. Forjaz, Peter and Basalto for their support during the field work on the islands. RR thanks M.V. Schoenhofen, A. Eberts, C. Kraft, and B. Held for inspiration and support during this study. This study was funded by the Deutsche Forschungsgemeinschaft (DFG grant BE4459/9-1).

SUPPLEMENTARY MATERIAL

The Supplementary Material for this article can be found online at: https://www.frontiersin.org/articles/10.3389/feart.2018.00078/full#supplementary-material

REFERENCES

Adam, J., and Green, T. (2006). Trace element partitioning between mica- and amphibole-bearing garnet lherzolite and hydrous basanitic melt: 1. experimental results and the investigation of controls on partitioning behaviour. *Contrib.Mineral. Petrol.* 152, 1–17. doi: 10.1007/s00410-006-0085-4

Beier, C., Bach, W., Blum, M., Cerqueira, T. S., da Costa, I. R., Ferreira, P. J., et al. (2017a). *Azores Plateau - Cruise No. M128 - July 02, 2016 - July 27, 2016 - Ponta Delgada (Portugal) - Ponta Delgada (Portugal). METEOR-Berichte. DFG-Senatskommission für Ozeanographie*, 41

Beier, C., Haase, K. M., and Abouchami, W. (2015). Geochemical and geochronological constraints on the evolution of the Azores Plateau. *Geol. Soc. Am.Spec. Pap.* 511, 27–55. doi: 10.1130/2015.2511(02)

Beier, C., Haase, K. M., Abouchami, W., Krienitz, M. S., and Hauff, F. (2008). Magma genesis by rifting of oceanic lithosphere above anomalous mantle: Terceira Rift, Azores. *Geochem. Geophys. Geosyst.* 9:Q12013. doi: 10.1029/2008GC002112

Beier, C., Haase, K. M., and Brandl, P. A. (2018). "Melting and mantle sources in the Azores," in *Volcanoes of the Azores: Revealing the Geological Secrets of the Central Northern Atlantic Islands,* eds U. Kueppers and C. Beier (Heidelberg: Springer), 251–280.

Beier, C., Haase, K. M., Brandl, P. A., and Krumm, S. H. (2017b). Primitive andesites from the Taupo Volcanic Zone formed by magma mixing. *Contrib. Miner. Petrol.* 172:33. doi: 10.1007/s00410-017-1354-0

Beier, C., Haase, K. M., and Hansteen, T. H. (2006). Magma evolution of the Sete Cidades volcano, São Miguel, Azores. *J. Petrol.* 47, 1375–1411. doi: 10.1093/petrology/egl014

Beier, C., Haase, K. M., and Turner, S. P. (2012). Conditions of melting beneath the Azores. *Lithos* 144, 1–11. doi: 10.1016/j.lithos.2012.02.019

Beier, C., Mata, J., Stöckhert, F., Mattielli, N., Brandl, P. A., Madureira, P., et al. (2013). Geochemical evidence for melting of carbonated peridotite on Santa Maria Island, Azores. *Contrib. Mineral. Petrol.* 165, 823–841. doi: 10.1007/s00410-012-0837-2

Beier, C., Stracke, A., and Haase, K. M. (2007). The peculiar geochemical signatures of São Miguel (Azores) lavas: metasomatised or recycled mantle sources? *Earth Planet. Sci. Lett.* 259, 186–199.doi: 10.1016/j.epsl.2007.04.038

Bonatti, E. (1990). Not so hot "hot spots" in the oceanic mantle. *Science* 250, 107–111. doi: 10.1126/science.250.4977.107

Bourdon, B., Turner, S. P., and Ribe, N. M. (2005). Partial melting and upwelling rates beneath the Azores from a U-series isotope perspective. *Earth Planet. Sci. Lett.* 239, 42–56. doi: 10.1016/j.epsl.2005.08.008

Brandl, P. A., Beier, C., Regelous, M., Abouchami, W., Haase, K. M., Garbe-Schönberg, D., et al. (2012). Volcanism on the flanks of the east pacific rise: quantitative constraints on mantle heterogeneity and melting processes. *Chem. Geol.* 298, 41–56. doi: 10.1016/j.chemgeo.2011.12.015

Cande, S. C., and Kent, D. V. (1995). Revised calibration of the geomagnetic polarity timescale for the Late Cretaceous and Cenozoic. *J. Geophys. Res. Solid Earth* 100, 6093–6095. doi: 10.1029/94JB03098

Cannat, M., Briais, A., Deplus, C., Escartin, J., Georgen, J., Lin, J. et al. (1999). Mid-Atlantic Ridge–Azores hotspot interactions: along-axis migration of a hotspot-derived event of enhanced magmatism 10 to 4 Ma ago. *Earth Planet. Sci. Lett.* 173, 257–269. doi: 10.1016/S0012-821X(99)00234-4

Chovelon, P. (1982). *Évolution Volcanotectonique des Iles de Faial et de Pico*. Thesis Univ., Paris-Sud, Orsay, 186.

Clague, D. A., and Dalrymple, G. B. (1987). The Hawaiian-Emperor volcanic chain. part I. Geologic evolution. *Volcanism Hawaii* 1, 5–54.

Cole, P. D., Guest, J. E., Duncan, A. M., and Pacheco, J.-M. (2001). Capelinhos 1957–1958, Faial, Azores: deposits formed by an emergent surtseyan eruption. *Bull. Volcanol.* 63:204. doi: 10.1007/s004450100136

Compston, W., and Oversby, V. M. (1969). Lead isotopic analysis using a double spike. *J. Geophys. Res.* 74, 4338–4348.

Daly, G. E., Widom, E., and Franca, Z. (2012). Evolution of silicic magmas and the origin of the Daly Gap at Santa Barbara volcano, Terceira, Azores. *Miner. Mag.* 76, 1613–1674.

Demande, J., Fabriol, R., Gérard, A., and Iundt, F. (1982). *Prospection Géothermique des Iles de Faial et Pico (Açores). 82SGN003GTH.* Bureau de recherches géologiques et minières, Orléans.

Dias, N. A., Matias, L., Lourenço, N., Madeira, J., Carrilho, F., and Gaspar, J. L. (2007). Crustal seismic velocity structure near Faial and Pico Islands (AZORES), from local earthquake tomography. *Tectonophysics* 445, 301–317. doi: 10.1016/j.tecto.2007.09.001

Di Chiara, A., Speranza, F., Porreca, M., Pimentel, A., D'Ajello Caracciolo, F., and Pacheco, J. (2014). Constraining chronology and time-space evolution of Holocene volcanic activity on the Capelo Peninsula (Faial Island, Azores): the paleomagnetic contribution. *Bulletin* 126, 1164–1180. doi: 10.1130/B30933.1

Dosso, L., Bougault, H., Langmuir, C., Bollinger, C., Bonnier, O., and Etoubleau, J. (1999). The age and distribution of mantle heterogeneity along the Mid-Atlantic Ridge (31–41 N). *Earth Planet. Sci. Lett.* 170, 269–286. doi: 10.1016/S0012-821X(99)00109-0

Elliott, T., Blichert-Toft, J., Heumann, A., Koetsier, G., and Forjaz, V. (2007). The origin of enriched mantle beneath Sao Miguel, Azores. *Geochim. Cosmochim. Acta* 71, 219–240. doi: 10.1016/j.gca.2006.07.043

Feraud, G., Kaneoka, I., and Allègre, C. J. (1980). K/Ar ages and stress pattern in the Azores: geodynamic implications. *Earth Planet. Sci. Lett.* 46, 275–286. doi: 10.1016/0012-821X(80)90013-8

Fernandes, R. M. S., Miranda, J. M., Catalão, J., Luis, J. F., Bastos, L., and Ambrosius, B. A. C. (2002). Coseismic displacements of the MW = 6.1, July 9, 1998, Faial earthquake (Azores, North Atlantic). *Geophys. Res. Lett.* 29, 21.1–21.4. doi: 10.1029/2001GL014415

Fontiela, J., Oliveira, C. S., and Rosset, P. (2018). "Characterisation of seismicity of the azores archipelago: an overview of historical events and a detailed analysis for the period 2000–2012," in *Volcanoes of the Azores: Revealing the Geological Secrets of the Central Northern Atlantic Islands*, eds U. Kueppers and C. Beier (Heidelberg: Springer), 127–153

Freund, S., Beier, C., Krumm, S., and Haase, K. M. (2013). Oxygen isotope evidence for the formation of andesitic–dacitic magmas from the fast-spreading Pacific–Antarctic Rise by assimilation–fractional crystallisation. *Chem. Geol.* 347, 271–283. doi: 10.1016/j.chemgeo.2013.04.013

Galipp, K., Klügel, A., and Hansteen, T. H. (2006). Changing depths of magma fractionation and stagnation during the evolution of an oceanic island volcano: La Palma (Canary Islands). *J. Volcanol. Geotherm. Res.* 155, 285–306. doi: 10.1016/j.jvolgeores.2006.04.002

Garcia, M. O., Rhodes, J. M., Trusdell, F. A., and Pietruszka, A. J. (1996). Petrology of lavas from the Puu Oo eruption of Kilauea Volcano: III. The Kupaianaha episode (1986–1992). *Bull. Volcanol.* 58, 359–379. doi: 10.1007/s004450050145

Gente, P., Dyment, J., Maia, M., and Goslin, J. (2003). Interaction between the Mid-Atlantic Ridge and the Azores hot spot during the last 85 Myr: Emplacement and rifting of the hot spot-derived plateaus. *Geochem. Geophys. Geosyst.* 4:8514. doi: 10.1029/2003GC000527

Green, T. H., Blundy, J. D., Adam, J., and Yaxley, G. M. (2000). SIMS determination of trace element partition coefficients between garnet, clinopyroxene and hydrous basaltic liquids at 2–7.5 GPa and 1080–1200°C. *Lithos* 53, 165–187. doi: 10.1016/S0024-4937(00)00023-2

Greene, A. R., Garcia, M. O., Pietruszka, A. J., Weis, D., Marske, J. P., Vollinger, M. J., et al. (2013). Temporal geochemical variations in lavas from Kilauea's Pu 'u 'O 'o eruption (1983–2010): cyclic variations from melting of source heterogeneities. *Geochem. Geophys. Geosyst.* 14, 4849–4873. doi: 10.1002/ggge.20285

Grimison, N., and Chen, W.-P. (1988). Source mechanisms of four recent earthquakes along the Azores-Gibraltar plate boundary. *Geophys. J.* 92, 391–401.

Gudmundsson, A. (1995). Infrastructure and mechanics of volcanic systems in Iceland. *J. Volcanol. Geotherm. Res.* 64, 1–2. doi: 10.1016/0377-0273(95)92782-Q

Gudmundsson, A., Lecoeur, N., Mohajeri, N., and Thordarson, T. (2014). Dike emplacement at Bardarbunga, Iceland, induces unusual stress changes, caldera deformation, and earthquakes. *Bull. Volcanol.* 76:869. doi: 10.1007/s00445-014-0869-8

Gudmundsson, M. T., Jónsdóttir, K., Hooper, A., Holohan, E. P., Halldórsson, S. A., Ófeigsson, B. G., et al. (2016). Gradual caldera collapse at Bárdarbunga volcano, Iceland, regulated by lateral magma outflow. *Science* 353:aaf8988. doi: 10.1126/science.aaf8988

Haase, K. M., and Beier, C. (2003). Tectonic control of ocean island basalt sources on São Miguel, Azores? *Geophys. Res. Lett.* 30. doi: 10.1029/2003GL017500

Haase, K. M., Beier, C., Regelous, M., Rapprich, V., and Renno, A. (2017). Spatial variability of source composition and petrogenesis in rift and rift flank alkaline lavas from the Eger Rift, Central Europe. *Chem. Geol.* 455, 304–314. doi: 10.1016/j.chemgeo.2016.11.003

Haase, K. M., Regelous, M., Duncan, R. A., Brandl, P. A., Stroncik, N., and Grevemeyer, I. (2011). Insights into mantle composition and mantle melting beneath mid-ocean ridges from postspreading volcanism on the fossil Galapagos Rise. *Geochem. Geophys. Geosyst.* 12:Q0AC11. doi: 10.1029/2010GC003482

Halliday, A. N., Lee, D.-C., Tommasini, S., Davies, G. R., Paslick, C. R., Fitton, J. G., et al. (1995). Incompatible trace elements in OIB and MORB and source enrichment in the sub-oceanic mantle. *Earth Planet. Sci. Lett.* 133, 379–395.

Hardarson, B. S., Fitton, J. G., Ellam, R. M., and Pringle, M. S. (1997). Rift relocation — A geochemical and geochronological investigation of a palaeo-rift in northwest Iceland. *Earth Planet. Sci. Lett.* 153, 181–196.

Hawkesworth, C., Norry, M., Roddick, J., and Vollmer, R. (1979). $^{143}Nd/^{144}Nd$ and $^{87}Sr/^{86}Sr$ ratios from the Azores and their significance in LIL-element enriched mantle. *Nature* 280, 28–31.

Hildenbrand, A., Madureira, P., Marques, F. O., Cruz, I., Henry, B., and Silva, P. (2008). Multi-stage evolution of a sub-aerial volcanic ridge over the last 1.3 Myr: S. Jorge Island, Azores Triple Junction. *Earth Planet. Sci. Lett.* 273, 289–298. doi: 10.1016/j.epsl.2008.06.041

Hildenbrand, A., Marques, F. O., Costa, A. C. G., Sibrant, A. L. R., Silva, P. F., Henry, B., et al. (2012). Reconstructing the architectural evolution of volcanic islands from combined K/Ar, morphologic, tectonic, and magnetic data: the Faial Island example (Azores). *J. Volcanol. Geotherm. Res.* 241, 39–48. doi: 10.1016/j.jvolgeores.2012.06.019

Hildenbrand, A., Weis, D., Madureira, P., and Marques, F. O. (2014). Recent plate re-organization at the Azores Triple Junction: evidence from combined geochemical and geochronological data on Faial, S. Jorge and Terceira volcanic islands. *Lithos* 210, 27–39. doi: 10.1016/j.lithos.2014.09.009

Hofmann, A. (1997). Mantle geochemistry: the message from oceanic volcanism. *Nature* 385, 219–229.

Hofmann, A. (2003). Sampling mantle heterogeneity through oceanic basalts: isotopes and trace elements. *Treatise Geochem.* 2:568. doi: 10.1016/B0-08-043751-6/02123-X

Hübscher, C., Beier, C., Al-Hseinat, M., Batista, L., Blum, M., Bobsin, M., et al. (2016). *Azores Plateau - Cruise No. M113/1 - December 29, 2014 - January 22, 2015 - Ponta Delgada (Portugal) - Ponta Delgada (Portugal)*. METEOR-Berichte 31.

Hübscher, C., and Gohl, K. (2014). *Reflection/Refraction Seismology*. Encyclopedia of Marine Geosciences. New York, NY: Springer.

Klein, E. M., and Langmuir, C. H. (1987). Global correlations of ocean ridge basalt chemistry with axial depth and crustal thickness. *J. Geophys. Res. Solid Earth* 92, 8089–8115.

Klügel, A., Hansteen, T. H., and Galipp, K. (2005a). Magma storage and underplating beneath Cumbre Vieja volcano, La Palma (Canary Islands). *Earth Planet. Sci. Lett.* 236, 211–226. doi: 10.1016/j.epsl.2005.04.006

Klügel, A., Walter, T. R., Schwarz, S., and Geldmacher, J. (2005b). Gravitational spreading causes en-echelon diking along a rift zone of Madeira Archipelago: an experimental approach and implications for magma transport. *Bull. Volcanol.* 68, 37–46. doi: 10.1007/s00445-005-0418-6

Krause, D. C., and Watkins, N. D. (1970). North Atlantic Crustal Genesis in the Vicinity of the Azores. *Geophys. J. R. Astron. Soc.* 19, 261–283.

Larrea, P., França, Z., Widom, E., and Lago, M. (2018). "Petrology of the Azores Islands," in *Volcanoes of the Azores: Revealing the Geological Secrets of the Central Northern Atlantic Islands*,eds U. Kueppers and C. Beier (Heidelberg: Springer), 197–249.

Larrea, P., Wijbrans, J. R., Galé, C., Ubide, T., Lago, M., França, Z., et al. (2014). 40Ar/39Ar constraints on the temporal evolution of Graciosa Island, Azores (Portugal). *Bull. Volcanol.* 76:796. doi: 10.1007/s00445-014-0796-8

Le Maitre, R. W., Bateman, P., Dudek, A., Keller, J., LeBas, M. J., Sabine, P.A., et al. (1989). *A Classification of Igneous Rocks and Glossary of Terms*. Oxford: Blackwell.

Luis, J. F., and Miranda, J. M. (2008). Reevaluation of magnetic chrons in the North Atlantic between 35 degrees N and 47 degrees N: implications for the formation of the Azores Triple Junction and associated plateau. *J. Geophys. Res. Solid Earth* 113:B10105. doi: 10.1029/2007JB005573

Luis, J. F., Miranda, J. M., Galdeano, A., Patriat, P., Rossignol, J. C., and Victor, L. A. M. (1994). The Azores triple junction evolution since 10 Ma from an aeromagnetic survey of the Mid-Atlantic Ridge. *Earth Planet. Sci. Lett.* 125, 439–459.

Luis, J., Miranda, J., Galdeano, A., and Patriat, P. (1998). Constraints on the structure of the Azores spreading center from gravity data. *Mar. Geophys. Res.* 20, 157–170.

Maclennan, J. (2008). Lead isotope variability in olivine-hosted melt inclusions from Iceland. *Geochim. Cosmochim. Acta* 72, 4159–4176. doi: 10.1016/j.gca.2008.05.034

Madeira, J. (1998). *Estudos de Neotectónica nas Ilhas do Faial, Pico e S. Jorge: Uma Contribuição para o Conhecimento Geodinâmico da Junção Tripla dos Açores*. Ph.D. thesis, Lisbon University, Lisbon.

Madeira, J., Soares, A. M., Da Silveira, A. B., and Serralheiro, A. (1995). Radiocarbon dating recent volcanic activity on Faial Island (Azores). *Radiocarbon* 37, 139–147.

Madureira, P., Mata, J., Mattielli, N., Queiroz, G., and Silva, P. (2011). Mantle source heterogeneity, magma generation and magmatic evolution at Terceira

Island (Azores archipelago): constraints from elemental and isotopic (Sr, Nd, Hf, and Pb) data. *Lithos* 126, 402–418. doi: 10.1016/j.lithos.2011.07.002

Marques, F., Catalão, J., Hildenbrand, A., Costa, A., and Dias, N. (2014). The 1998 Faial earthquake, Azores: evidence for a transform fault associated with the Nubia–Eurasia plate boundary? *Tectonophysics* 633, 115–125. doi: 10.1016/j.tecto.2014.06.024

Marques, F. O., Catalão, J. C., DeMets, C., Costa, A. C. G., and Hildenbrand, A. (2013). GPS and tectonic evidence for a diffuse plate boundary at the Azores Triple Junction. *Earth Planet. Sci. Lett.* 381, 177–187. doi: 10.1016/j.epsl.2013.08.051

Matias, L., Dias, N. A., Morais, I., Vales, D., Carrilho, F., Madeira, J., et al. (2007). The 9th of July 1998 Faial Island (Azores, North Atlantic) seismic sequence. *J. Seismol.* 11, 275–298. doi: 10.1007/s10950-007-9052-4

McDonough, W. F., and Sun, S.-S. (1995). The composition of the Earth. *Chem. Geol.* 120, 223–253.

McKenzie, D., and Bickle, M. J. (1988). The volume and composition of melt generated by extension of the lithosphere. *J. Petrol.* 29, 625–679.

Miranda, J., Luis, J., Lourenço, N., and Goslin, J. (2014). Distributed deformation close to the Azores Triple "Point". *Mar. Geol.* 355, 27–35. doi: 10.1016/j.margeo.2014.05.006

Miranda, J. M., Luis, J. F., and Lourenço, N. (2018). "The tectonic evolution of the Azores based on magnetic data," in *Volcanoes of the Azores: Revealing the Geological Secrets of the Central Northern Atlantic Islands,* eds U. Kueppers and C. Beier (Heidelberg: Springer), 89–100

Miranda, J. M., Victor, L. A. M., Simões, J. Z., Luis, J. F., Matias, L., Shimamura, H., et al. (1998). Tectonic setting of the Azores Plateau deduced from a OBS survey. *Mar. Geophys. Res.* 20, 171–182.

Moreira, M. A., Madureira, P., and Mata, J. (2018). "Noble gas constraints on the origin of the Azores hotspot," in *Volcanoes of the Azores: Revealing the Geological Secrets of the Central Northern Atlantic Islands*, eds U. Kueppers and C. Beier (Heidelberg: Springer), 281–299.

Moreira, M., Doucelance, R., Kurz, M. D., Dupré, B., and Allègre, C. J. (1999). Helium and lead isotope geochemistry of the Azores Archipelago. *Earth Planet. Sci. Lett.* 169, 189–205.

Morgan, J. P. (1987). Melt migration beneath mid-ocean spreading centers. *Geophys. Res. Lett.* 14, 1238–1241.

Morgan, W. J. (1971). Convection plumes in the lower mantle. *Nature* 230, 42–43.

Neave, D. A., Passmore, E., Maclennan, J., Fitton, G., and Thordarson, T. (2013). Crystal–melt relationships and the record of deep mixing and crystallization in the ad 1783 laki eruption, Iceland. *J. Petrol.* 54, 1661–1690. doi: 10.1093/petrology/egt027

Niu, Y., Regelous, M., Wendt, I. J., Batiza, R., and O'Hara, M. J. (2002). Geochemistry of near-EPR seamounts: importance of source vs. process and the origin of enriched mantle component. *Earth Planet. Sci. Lett.* 199, 327–345. doi: 10.1016/S0012-821X(02)00591-5

O'Neill, C., and Sigloch, K. (2018). "Crust and mantle structure beneath the Azores Hotspot—Evidence from geophysics," in *Volcanoes of the Azores: Revealing the Geological Secrets of the Central Northern Atlantic Islands*, eds U. Kueppers and C. Beier (Heidelberg: Springer), 71–87.

Pacheco, J. (2001). *Processos Associados ao Desenvolvimento de Erupções Vulcânicas Hidromagmáticas na Ilha do Faial e sua Interpretação Numa Perspectiva de Avaliação do Hazard e Minimização do Risco.* Ph.D. Thesis, University of the Azores.

Paquet, F., Dauteuil, O., Hallot, E., and Moreau, F. (2007). Tectonics and magma dynamics coupling in a dyke swarm of Iceland. *J. Struct. Geol.* 29, 1477–1493. doi: 10.1016/j.jsg.2007.06.001

Phipps Morgan, J. (2000). Isotope topology of individual hotspot basalt arrays: mixing curves or melt extraction trajectories? *Geochem. Geophys. Geosyst.* 1:1003. doi: 10.1029/1999GC000004

Pimentel, A., Pacheco, J., and Self, S. (2015). The ∼1000-years BP explosive eruption of Caldeira Volcano (Faial, Azores): the first stage of incremental caldera formation. *Bull. Volcanol.* 77:42. doi: 10.1007/s00445-015-0930-2

Poore, H., White, N., and Maclennan, J. (2011). Ocean circulation and mantle melting controlled by radial flow of hot pulses in the Iceland plume. *Nat. Geosci.* 4:558. doi: 10.1038/NGEO1161

Prytulak, J., and Elliott, T. (2007). TiO2 enrichment in ocean island basalts. *Earth Planet. Sci. Lett.* 263, 388–403. doi: 10.1016/j.epsl.2007.09.015

Quartau, R., and Mitchell, N. C. (2013). Comment on "Reconstructing the architectural evolution of volcanic islands from combined K/Ar, morphologic, tectonic, and magnetic data: The Faial Island example (Azores)" by Hildenbrand et al. (2012) [J. Volcanol. Geotherm. Res. 241–242 (2012) 39–48]. *J. Volcanol. Geotherm. Res.* 255, 124–126. doi: 10.1016/j.jvolgeores.2012.12.020

Quartau, R., Tempera, F., Mitchell, N. C., Pinheiro, L. M., Duarte, H., Brito, P. O., et al. (2012). Morphology of the Faial Island shelf (Azores): the interplay between volcanic, erosional, depositional, tectonic and mass-wasting processes. *Geochem. Geophys. Geosyst.* 13:Q04012. doi: 10.1029/2011GC003987

Ramalho, R. S., Helffrich, G., Madeira, J., Cosca, M., Thomas, C., Quartau, R., et al. (2017). Emergence and evolution of Santa Maria Island (Azores)—The conundrum of uplifted islands revisited. *Bulletin* 129, 372–390. doi: 10.1130/B31538.1

Robinson, J. A. C., and Wood, B. J. (1998). The depth of the spinel to garnet transition at the peridotite solidus. *Earth Planet. Sci. Lett.* 164, 277–284.

Roeder, P., and Emslie, R. (1970). Olivine-liquid equilibrium. *Contrib. Mineral. Petrol.* 29, 275–289.

Schilling, J.-G. (1975). Azores mantle blob: rare-earth evidence. *Earth Planet. Sci. Lett.* 25, 103–115.

Schilling, J.-G., Bergeron, M., Evans, R., and Smith, J. (1980). Halogens in the mantle beneath the north atlantic [and discussion]. *Philos. Trans. R. Soc. Lond. A Math. Phys. Eng. Sci.* 297, 147–178.

Schwarz, S., Klugel, A., van den Bogaard, P., and Geldmacher, J. (2005). Internal structure and evolution of a volcanic rift system in the eastern North Atlantic: the Desertas rift zone, Madeira archipelago. *J. Volcanol. Geotherm. Res.* 141, 123–155. doi: 10.1016/j.jvolgeores.2004.10.002

Shorttle, O., Maclennan, J., and Lambart, S. (2014). Quantifying lithological variability in the mantle. *Earth Planet. Sci. Lett.* 395, 24–40. doi: 10.1016/j.epsl.2014.03.040

Shorttle, O., Maclennan, J., and Piotrowski, A. M. (2013). Geochemical provincialism in the Iceland plume. *Geochim. Cosmochim. Acta* 122, 363–397. doi: 10.1016/j.gca.2013.08.032

Sibrant, A. L. R., Hildenbrand, A., Marques, F. O., and Costa, A. C. G. (2015). Volcano-tectonic evolution of the Santa Maria Island (Azores): implications for paleostress evolution at the western Eurasia–Nubia plate boundary. *J. Volcanol. Geotherm. Res.* 291, 49–62. doi: 10.1016/j.jvolgeores.2014.12.017

Sibrant, A. L. R., Marques, F. O., Hildenbrand, A., Boulesteix, T., Costa, A. C. G., and Catalão, J. (2016). Deformation in a hyperslow oceanic rift: insights from the tectonics of the São Miguel Island (Terceira Rift, Azores). *Tectonics* 35, 425–446. doi: 10.1002/2015TC003886

Sibrant, A., Marques, F., and Hildenbrand, A. (2014). Construction and destruction of a volcanic island developed inside an oceanic rift: Graciosa Island, Terceira Rift, Azores. *J. Volcanol. Geotherm. Res.* 284, 32–45. doi: 10.1016/j.jvolgeores.2014.07.014

Sigmundsson, F., Hooper, A., Hreinsdóttir, S., Vogfjörd, K. S., Ófeigsson, B. G., and Heimisson, E.R. (2014). Segmented lateral dyke growth in a rifting event at Bárð*arbunga volcanic system, Iceland. *Nature* 517, 191–195. doi: 10.1038/nature14111

Stein, C. A., and Stein, S. (1992). A model for the global variation in oceanic depth and heat flow with lithospheric age. *Nature* 359, 123–129.

Stracke, A. (2012). Earth's heterogeneous mantle: a product of convection-driven interaction between crust and mantle. *Chem. Geol.* 330–331, 274–299. doi: 10.1016/j.chemgeo.2012.08.007

Sun, S.-S., and McDonough, W.-S. (1989). Chemical and isotopic systematics of oceanic basalts: implications for mantle composition and processes. *Geol. Soc. Lond. Spec. Publ.* 42, 113–345.

Tempera, F., Hipólito, A., Madeira, J., Vieira, S., Campos, A. S., and Mitchell, N. C. (2013). Condor seamount (Azores, NE Atlantic): a morpho-tectonic interpretation. *Deep Sea Res. Part II Top. Stud. Oceanogr.* 98, 7–23. doi: 10.1016/j.dsr2.2013.09.016

Tibaldi, A., Bonali, F. L., and Corazzato, C. (2014). The diverging volcanic rift system. *Tectonophysics* 611, 94–113. doi: 10.1016/j.tecto.2013.11.023

Trippanera, D., Porreca, M., Ruch, J., Pimentel, A., Acocella, V., Pacheco, J., et al. (2014). Relationships between tectonics and magmatism in a transtensive/transform setting: an example from Faial Island (Azores, Portugal). *GSA Bull.* 126, 164–181. doi: 10.1130/B30758.1

Turner, S., Hawkesworth, C., Rogers, N., and King, P. (1997). U-Th isotope disequilibria and ocean island basalt generation in the Azores. *Chem. Geol.* 139, 145–164.

Villemant, B., Jaffrezic, H., Joron, J.-L., and Treuil, M. (1981). Distribution coefficients of major and trace elements; fractional crystallization in the alkali basalt series of Chaine des Puys (Massif Central, France). *Geochim. Cosmochim. Acta* 45, 1997–2016.

Vogt, P., and Jung, W. (2004). The Terceira Rift as hyper-slow, hotspot-dominated oblique spreading axis: a comparison with other slow-spreading plate boundaries. *Earth Planet. Sci. Lett.* 218, 77–90. doi: 10.1016/S0012-821X(03)00627-7

Vogt, P. R., and Jung, W.-Y. (2018). "The "Azores Geosyndrome" and plate tectonics: research history, synthesis, and unsolved puzzles," in *Volcanoes of the Azores: Revealing the Geological Secrets of the Central Northern Atlantic Islands*, eds U. Kueppers and C. Beier (Heidelberg: Springer), 27–56.

Weiß, B. J., Hübscher, C., and Lüdmann, T. (2015a). The tectonic evolution of the southeastern Terceira Rift/São Miguel region (Azores). *Tectonophysics* 654, 75–95. doi: 10.1016/j.tecto.2015.04.018

Weiß, B. J., Hübscher, C., Wolf, D., and Lüdmann, T. (2015b). Submarine explosive volcanism in the southeastern Terceira Rift/São Miguel region (Azores). *J. Volcanol. Geotherm. Res.* 303, 79–91. doi: 10.1016/j.jvolgeores.2015.07.028

White, W. M., Schilling, J. G., and Hart, S. R. (1976). Evidence for Azores mantle plume from strontium isotope geochemistry of Central North-Atlantic. *Nature* 263, 659–663.

Widom, E., Carlson, R., Gill, J., and Schmincke, H.-U. (1997). Th–Sr–Nd–Pb isotope and trace element evidence for the origin of the Sao Miguel, Azores, enriched mantle source. *Chem. Geol.* 140, 49–68.

Woelki, D., Haase, K. M., Schoenhofen, M. V., Beier, C., Regelous, M., Krumm, S. H., et al. (2018). Evidence for melting of subducting carbonate-rich sediments in the western Aegean Arc. *Chem. Geol.* 483, 463–473. doi: 10.1016/j.chemgeo.2018.03.014

Yang, T., Shen, Y., van der Lee, S., Solomon, S. C., and Hung, S.-H. (2006). Upper mantle structure beneath the Azores hotspot from finite-frequency seismic tomography. *Earth Planet. Sci. Lett.* 250, 11–26. doi: 10.1016/j.epsl.2006.07.031

Zanon, V., and Frezzotti, M. L. (2013). Magma storage and ascent conditions beneath Pico and Faial islands (Azores archipelago): a study on fluid inclusions. *Geochem. Geophys. Geosyst.* 14, 3494–3514. doi: 10.1002/ggge.20221

Zanon, V., Kueppers, U., Pacheco, J. M., and Cruz, I. (2013). Volcanism from fissure zones and the Caldeira central volcano of Faial Island, Azores archipelago: geochemical processes in multiple feeding systems. *Geol. Mag.* 150, 536–555. doi: 10.1017/S0016756812000702

Zindler, A., and Hart, S. (1986). Chemical geodynamics. *Annu. Rev. Earth Planet. Sci.* 14, 493–571.

Conflict of Interest Statement: The authors declare that the research was conducted in the absence of any commercial or financial relationships that could be construed as a potential conflict of interest.

Copyright © 2018 Romer, Beier, Haase and Hübscher. This is an open-access article distributed under the terms of the Creative Commons Attribution License (CC BY). The use, distribution or reproduction in other forums is permitted, provided the original author(s) and the copyright owner are credited and that the original publication in this journal is cited, in accordance with accepted academic practice. No use, distribution or reproduction is permitted which does not comply with these terms.

frontiers in Earth Science

REVIEW
published: 20 November 2018
doi: 10.3389/feart.2018.00145

Peralkaline Felsic Magmatism of the Atlantic Islands

*Adam J. Jeffery and Ralf Gertisser**

School of Geography, Geology and the Environment, Keele University, Staffordshire, United Kingdom

The oceanic-island magmatic systems of the Atlantic Ocean exhibit significant diversity in their respective sizes, ages, and the compositional ranges of their eruptive products. Nevertheless, almost all of the Atlantic islands and island groups have produced peralkaline felsic magmas, implying that similar petrogenetic regimes may be operating throughout the Atlantic Ocean, and arguably elsewhere. The origins of peralkaline magmas are frequently linked to low-degree partial melting of enriched mantle, followed by protracted differentiation in the shallow crust. However, additional petrogenetic processes such as magma mixing, crustal melting, and contamination have been identified at numerous peralkaline centers. The onset of peralkalinity leads to magma viscosities lower than those typical for metaluminous felsic magmas, which has profound implications for processes such as crystal settling. This study represents a compilation of published and original data which demonstrates trends that suggest that the peralkaline magmas of the Atlantic Ocean islands are generated primarily via extended (up to ∼ 95%), open system fractional crystallization of mantle-derived mafic magmas. Crustal assimilation is likely to become more significant as the system matures and fusible material accumulates in the crust. Magma mixing may occur between various compositional end-members and may be recognized via hybridized intermediate magmas. The peralkaline magmas are hydrous, and frequently zoned in composition, temperature, and/or water content. They are typically stored in shallow crustal magma reservoirs (∼ 2–5 km), maintained by mafic replenishment. Low melt viscosities ($1 \times 10^{1.77}$ to $1 \times 10^{4.77}$ Pa s) facilitate two-phase flow, promoting the formation of alkali-feldspar crystal mush. This mush may then contribute melt to an overlying melt lens via filter pressing or partial melting. We utilize a three-stage model to account for the establishment, development, and termination of peralkaline magmatism in the ocean island magmatic systems of the Atlantic. We suggest that the overall control on peralkaline magmatism in the Atlantic is magma flux rate, which controls the stability of upper crustal magma reservoirs. The abundance of peralkaline magmas in the Atlantic suggests that their development must be a common, but not inevitable, stage in the evolution of ocean islands.

Keywords: peralkaline, ocean island, crystal mush, crystal settling, fractional crystallization

OPEN ACCESS

Edited by:
Patricia Larrea, Universidad Nacional Autónoma de México, Mexico

Reviewed by:
Felix Genske, University of Münster, Germany
Jakub Sliwinski, ETH Zürich, Switzerland
Teresa Ubide, The University of Queensland, Australia

***Correspondence:**
Ralf Gertisser
r.gertisser@keele.ac.uk

Specialty section:
This article was submitted to Volcanology, a section of the journal Frontiers in Earth Science

Received: *28 February 2018*
Accepted: *13 September 2018*
Published: *20 November 2018*

Citation:
Jeffery AJ and Gertisser R (2018) Peralkaline Felsic Magmatism of the Atlantic Islands. Front. Earth Sci. 6:145. doi: 10.3389/feart.2018.00145

INTRODUCTION

Oceanic island volcanic centers have been instrumental in the understanding of fundamental petrological features and processes, including mantle heterogeneity, melt generation, and magma evolution in oceanic intraplate settings (e.g., Hofmann, 2003; Fitton, 2007; White, 2010). Ocean island basalts (OIBs) can be related more directly to the underlying mantle source(s) than

continental basalts, undergoing less contamination on ascent and therefore serving as a fingerprint of mantle heterogeneity. In addition to OIBs, many oceanic island volcanic centers also exhibit a variety of magma compositions that are more felsic, extending to rhyolitic and phonolitic, with various intermediate compositions which are typically subordinate to the mafic and felsic compositions (e.g., Daly, 1925). In many cases, the felsic magmas are variably peralkaline (i.e., Peralkalinity index (PI) = molar ($Na_2O + K_2O$) / Al_2O_3) is greater than 1), making them particularly unusual not only due to their sometimes extreme enrichment in halogens, rare earth elements (REEs), high field strength elements (HFSEs), and large ion lithophile elements (LILEs), but also due to the occurrence of key minerals which are common in peralkaline rocks (e.g., Na-clinopyroxene, Na-amphibole, and aenigmatite), and their unusually fluid rheological behavior (e.g., Carmichael, 1962; Nicholls and Carmichael, 1969; Macdonald, 1974a; Sutherland, 1974; Kogarko, 1980; Sørensen, 1992; Dingwell et al., 1998; Bailey et al., 2001; Di Genova et al., 2013; Marks and Markl, 2017). These peralkaline rocks may be divided broadly into three groups: (1) the SiO_2-undersaturated group which evolves toward foid-bearing phonolites and foidites, (2) the SiO_2-saturated group which evolves toward trachytic compositions, and (3) the SiO_2-oversaturated group which evolves toward comenditic and pantelleritic trachytes and rhyolites, all three groups having their own intrusive equivalents (Le Maitre, 2003; Frost and Frost, 2008). Regardless of silica saturation, the peralkaline rocks may also be defined based upon mineralogy; if the HFSEs are hosted in zircon and titanite the rock is termed miaskitic, whereas the occurrence of rare zirconosilicate minerals, (e.g., eudialyte-group minerals; Johnsen et al., 2003, and/or wöhlerite- or rinkite-group minerals; Merlino and Perchiazzi, 1988; Sokolova and Cámara, 2017) defines the agpaitic rocks (Sørensen, 1960, 1997; Khomyakov, 1995; Marks and Markl, 2017). When compared with their metaluminous counterparts, peralkaline magmas are rare and less significant volumetrically. Despite this, they have attracted considerable attention from the academic community, with studies being devoted to magma genesis and evolution (e.g., Nicholls and Carmichael, 1969; Macdonald, 1974a, 2012; Baker and Henage, 1977; Larsen, 1979; Mahood and Hildreth, 1986; Macdonald et al., 1995, 2008, 2011, 2012; Bohrson and Reid, 1997; Sørensen, 1997; Markl, 2001; Scaillet and Macdonald, 2001; Avanzinelli et al., 2004; White et al., 2005; Macdonald and Scaillet, 2006; Pfaff et al., 2008; Markl et al., 2010; Marks et al., 2011; Rooney et al., 2012; Marks and Markl, 2015; Sliwinski et al., 2015; Wolff, 2017), eruptive behavior and degassing (e.g., Schmincke, 1974; Lowenstern, 1994; Barclay et al., 1996), and economic potential (e.g., Haffty and Noble, 1972; Pollard, 1995; Salvi and Williams-Jones, 2006; Goodenough et al., 2016).

The majority of reported peralkaline rocks are limited to locations such as the East African Rift, the Gardar Igneous Province (Macdonald, 1974b), Pantelleria Island (the type locality for pantellerite, a variety of strongly peralkaline rhyolite), and other localities such as the peralkaline granites of northern Corsica (e.g., Quin, 1962; Bonin et al., 1978), various peralkaline intrusive lithologies found within the alkaline province of central Europe and France (e.g., Brousse and Varet, 1966; Wimmenauer, 1974; Bernth et al., 2002), the peralkaline granitic dykes of the Oslofjord province (e.g., Nystuen, 1975; Rasmussen et al., 1988; Neumann et al., 1992), and British Tertiary Igneous Province (e.g., Sabine, 1960; Thompson, 1969; Macdonald, 1974b; Ferguson, 1978). However, peralkaline rocks have also been reported in many oceanic island settings, including Iceland, Socorro, the Canary Islands, the Azores, Kerguelen and Easter Island (e.g., Schmincke, 1973; Baker, 1974; White et al., 1979; Bohrson et al., 1996). The comparable peralkaline character of these systems may imply that similar petrogenetic frameworks may be operating in all of these systems, regardless of their contrasting geodynamic settings (i.e., continental vs. oceanic).

In this study, we review the occurrence of peralkaline felsic magmatism in the Atlantic Ocean, utilizing published geochemical, thermobarometric, and geochronological datasets. Where possible, we provide new data by building upon existing datasets with original thermohygrometric and rheological calculations. The study aims to identify the primary controls on the formation of peralkaline felsic magmas in oceanic island magmatic systems and to evaluate the architecture of the magmatic systems from which they are derived. We consider peralkaline rocks from all large Atlantic Ocean volcanic centers, from Iceland in the north to Bouvet Island in the South, aiming to: (1) summarize the key petrological features of Atlantic peralkaline oceanic island magmatism, including magma genesis and storage conditions, (2) discuss recent progress in the scientific understanding of how such magmatic systems originate and evolve through time, and (3) produce an original petrogenetic model which can account for the observed petrological features. Due to the considerable interest in the OIBs of these ocean island volcanic centers, the corresponding evolved compositions (where present) are in some cases somewhat under-studied in comparison. As such, the available datasets for peralkaline felsic rocks exhibit significant diversity in their respective sizes, ranging inevitably from detailed (e.g., Canary Islands) to sparse (e.g., Bouvet Island). Nevertheless, the available data do allow comparison between each of the eruptive centers of the study, facilitating a broad review of the peralkaline magmatism of the Atlantic Ocean as a whole.

PERALKALINE ROCKS OF THE ATLANTIC OCEAN ISLANDS

For the purpose of this study, we utilize thirteen examples of oceanic island magmatism from the Atlantic Ocean (**Figure 1**), where the described rocks are peralkaline *sensu stricto*, or have a peralkaline affinity, a term we apply qualitatively here for rocks (typically trachytes, phonolites, and rhyolites) which approach peralkalinity, typically with a peralkalinity index between 0.9 and 1.0. We consider the latter to be of importance as they may represent felsic magmas which act as progenitors to the peralkaline felsic compositions, either by representing a single step on an evolutionary trend from mafic to felsic compositions, or as a directly derived composition that may then evolve further (e.g., crustal melting followed by fractional crystallization; Bohrson and Reid, 1997;

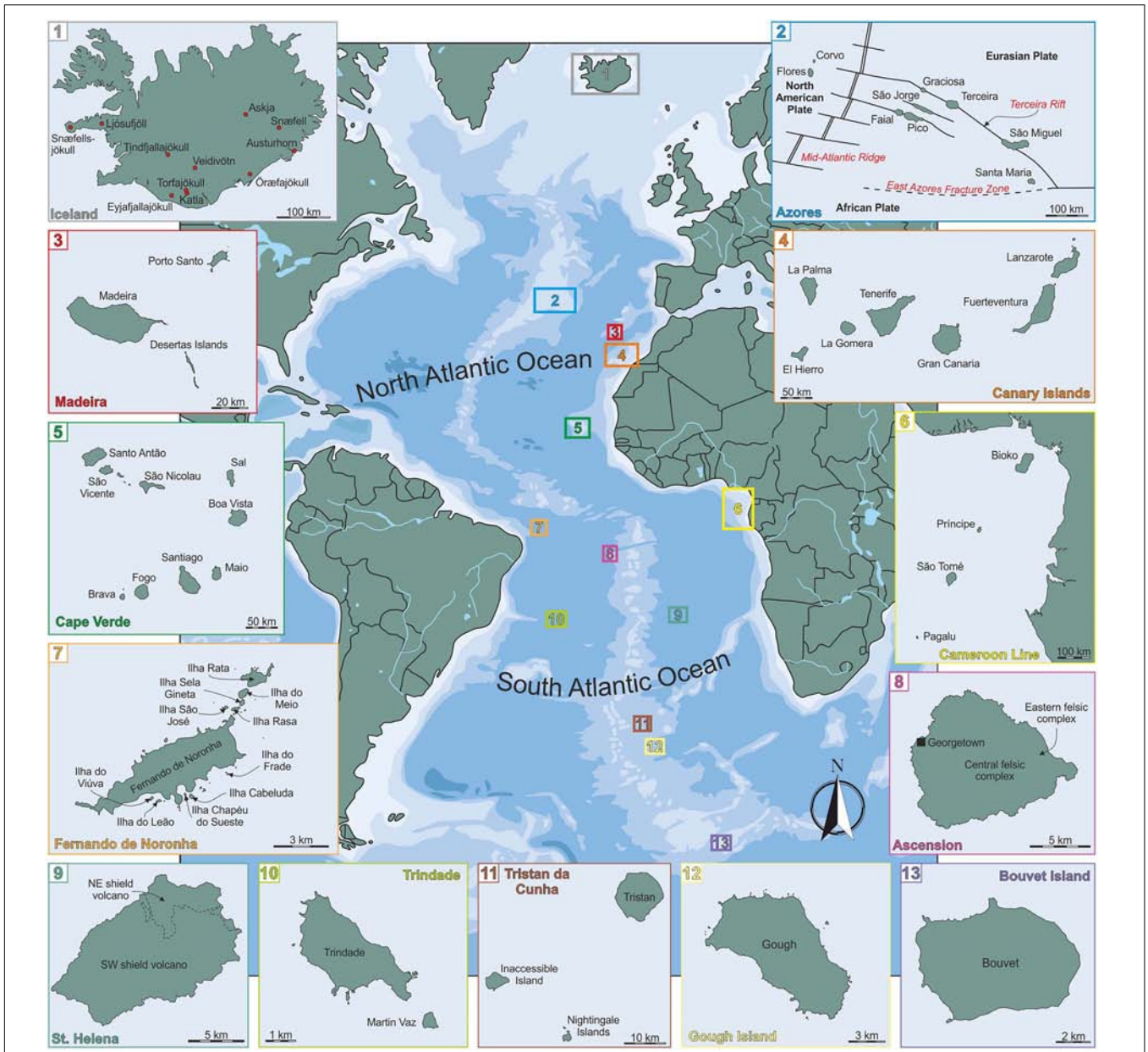

FIGURE 1 | Summary geographical maps showing each of the Atlantic Ocean island magmatic systems used as case studies in this contribution: (1) Iceland (with locations of reported peralkaline magmatism marked), (2) the Azores archipelago, (3) the Maediera archipelago, (4) the Canary Islands, (5) the Cape Verde archipelago, (6) the oceanic sector of the Cameroon Line, (7) Fernando de Noronha, (8) Ascension Island, (9) St. Helena, (10) Trindade, (11) Tristan da Cunha, (12) Gough Island, and (13) Bouvet Island. Map after Ericson et al. (2017).

Trua et al., 1999; Avanzinelli et al., 2004). As such, magmatic systems that have produced rocks with peralkaline affinity might reasonably be expected to produce peralkaline rocks in the future. All literature data were collected from the GEOROC database[1]. Where possible, data quality was evaluated using major element totals; totals below 96% or above 102% were not considered further. Below, we provide a brief account of the geodynamic setting and overall geochemical trends of each of our selected case studies, presented in order from north to south. A summary of the total combined dataset (e.g., published data supplemented with data from this study) is given in **Table 1**.

Iceland

Iceland is the largest of the Atlantic oceanic islands, comprising a submarine plateau that covers $\sim 3.5 \times 10^5$ km^2 and rises more than 3000 m above the surrounding sea floor (Gudmundsson, 2000 and references therein). Of this area, $\sim 1.3 \times 10^5$ km^2 is exposed subaerially. Magmatism in the

[1]http://georoc.mpch-mainz.gwdg.de/georoc/

TABLE 1 | Summary of the combined geochemical, rheological, and thermobarometric dataset used in this study.

Island group	Island	PI		Differentiation trend	Age (Ma)	Melt viscosity (Pa s)		T	H_2O (wt. %)	P (MPa)	fO_2	Present stage
		Average	Maximum			Low PI	High PI					
Iceland	Iceland	0.41	1.36	SiO_2-oversaturated	~ 16	$1 \times 10^{4.18}$	$1 \times 10^{3.96}$	720–990	<4–5	<100–200	FMQ to FMQ +1	2
Azores	Corvo	0.45	0.95	Transitional	~ 0.3	$1 \times 10^{4.46}$	$1 \times 10^{3.45}$					1
	Faial	0.53	0.93		0.85			923–1040	3.3–5.5		NNO	1
	Flores	0.51	0.92		2.15							1
	Graciosa	0.44	1.10		1.05							2
	Pico	0.45	0.76		~ 0.28							1
	Santa Maria	0.42	0.64		7.1							3
	São Jorge	0.44	0.65		~ 0.75							1
	São Miguel	0.74	1.17		~ 0.9			695–977	2.1–6.6	122–156	MH −1 to FMQ −2	2
	Terceira	0.94	2.37		~ 0.5			773–936	2.5–6.0	80–170	NNO −2.4 to NNO −1.8	2
Madeira group	Madeira	0.44	0.88	Both	5.6							1–2
	Porto Santo	0.56	0.91		14.3							1–2
	Desertas Islands	0.38	0.58		5.6							1
Canary Islands	El Hierro	0.61	1.49	Both	~ 1.12	$1 \times 10^{4.77}$	$1 \times 10^{3.55}$					2
	Fuertaventura	0.58	1.19		~ 25							1
	Gran Canaria	0.70	2.00		14.5			724–830	1.5–7.53	130–270	FMQ +1	1
	La Gomera	0.84	1.26		12			873–1004	2.2–6.4		~ FMQ	3
	La Palma	0.58	1.08		1.77							2
	Lanzarote	0.49	0.70		15.5							1
	Tenerife	0.78	1.34		11.6			798–1062	0.5–5.1	100–300	FMQ to FMQ +1	2
Cape Verde	Boa Vista	0.60	1.25	SiO_2-undersaturated	25?	$1 \times 10^{2.79}$	$1 \times 10^{1.77}$					3
	Brava	1.23	1.96		6							2
	Fogo	0.71	1.30		6							2
	Maio	0.53	0.82		23							1
	Sal	0.59	1.08		29							2
	Santiago	0.44	0.91		11							1
	Santo Antao	0.91	1.12		7			770–895	5.0–9.1	200–400		2
	São Nicolao	0.48	1.10		10							3–1
	São Vicente	0.47	1.04		7							3–1
Cameroon Line	Bioko	0.52	0.74	SiO_2-undersaturated	<1.33	$1 \times 10^{3.69}$	$1 \times 10^{3.52}$					
	Pagalu	0.56	0.95		18.4							2
	Principe	0.79	1.21		31							2
	São Tomé	0.71	1.05		15.7			727–827		100	FMQ −1.2 to FMQ −2.0	2

(Continued)

TABLE 1 | Continued

Island group	Island	PI		Differentiation trend	Age (Ma)	Melt viscosity (Pa s)		T	H_2O (wt. %)	P (MPa)	fO_2	Present stage
		Average	Maximum			Low PI	High PI					
Fernando de Noronha	Fernando de Noronha	0.71	1.14	SiO_2-undersaturated	12.5	$1 \times 10^{3.23}$	$1 \times 10^{3.06}$					1
Ascension	Ascension	0.82	1.77	SiO_2-oversaturated	1.09	$1 \times 10^{3.24}$	$1 \times 10^{3.13}$	841–902	0.5–6.4	216–250	NNO −2.42 to NNO −1.83	2
St. Helena Island	St Helena	0.58	1.12	SiO_2-undersaturated	14.3	$1 \times 10^{3.21}$	$1 \times 10^{3.08}$					2
Trindade	Trindade	0.78	1.32	SiO_2-undersaturated	3.22	$1 \times 10^{3.17}$	$1 \times 10^{2.34}$	767–803	5.65–7.77	<400	FMQ +1.5 to FMQ +2	1
	Martin Vaz	0.86	1.13		3.22							1
Tristan da Cunha group	Tristan	1	0.98	SiO_2-undersaturated	0.2	$1 \times 10^{2.82}$						2
	Inaccessible	0.58	1.03		3							3
	Nightingale group	0.75	0.97		>18							3
Gough Island	Gough	0.62	1.01	SiO_2-undersaturated	2.55	$1 \times 10^{2.76}$		918–965	2.4–4.6			2
Bouvet Island	Bouvet	0.65	1.17	SiO_2-oversaturated	<1.4	$1 \times 10^{3.46}$	$1 \times 10^{3.43}$	862–865	5.6–6.1			2

PI, Peralkalinity index. 'Present stage' column refers to the model described in the discussion. Melt viscosities were calculated using the model of Giordano et al. (2006), for the highest PI coupled with the lowest temperature, and the lowest PI coupled with the highest temperature. All rheological and pre-eruptive intensive parameter data are applicable to peralkaline compositions (and peralkaline affinity) only. Geochronological data sourced from: Iceland: Gale et al. (1966), McGarvie et al. (2006), Flude et al. (2008); Azores: Abdel-Monem et al. (1975), Self (1976), Feraud et al. (1981), Gandino et al. (1985), Serralheiro et al. (1989), Johnson et al. (1998), Nunes (1999, Unpublished), Calvert et al. (2006), Hildenbrand et al. (2008); Madeira: Watkins and Abdel-Monem (1971), Feraud et al. (1981), Ferreira et al. (1988), Geldmacher et al. (2000); Canary Islands: Abdel-Monem et al. (1971), Abdel-Monem et al. (1972), McDougall and Schmincke (1976), Carracedo (1979), Feraud et al. (1981), Ancochea et al. (1990), Guillou et al. (1996), Carracedo et al. (1997, 1998, 2002), Balogh et al. (1999), Muñoz et al. (2005), Paris et al. (2005), Becerril et al. (2016); Cape Verde: Faugeres et al. (1989), Torres et al. (2002), Plesner et al. (2003), Holm et al. (2008), Dyhr and Holm (2010), Madeira et al. (2010), Ramalho (2011) and references therein; Cameroon Line: Hedberg (1969), Aka et al. (2004), Chauvel et al. (2005), Déruelle et al. (2007) and references therein; Fernando de Noronha: Almeida (1955), Cordani (1970), Weaver (1990), Perlingeiro et al. (2013); Ascension: Harris et al. (1982), Nielson and Sibbett (1996), Kar et al. (1998), Jicha et al. (2013), Preece et al. (2016, 2018); St. Helena: Baker et al. (1967), Baker (1969), Chaffey et al. (1989); Trindade: Cordani (1970), Pires and Bongiolo (2016), Pires et al. (2016); Tristan da Cunha: Gass (1967), McDougall and Ollier (1982), Hicks et al. (2012); Gough: Maund et al. (1988); Bouvet: Verwoerd (1972), Prestvik et al. (1999); Pre-eruptive intensive parameter data sourced from: Iceland: Furman et al. (1992a), Furman et al. (1992b), Jónasson et al. (1992), Gunnarsson et al. (1998); Azores: Wolff and Storey (1983), Wolff et al. (1990), Renzulli and Santi (2000), Beier et al. (2006), Zanon et al. (2013), Pimentel et al. (2015), Jeffery et al. (2016b, 2017), D'Oriano et al. (2017); Canary Islands: Crisp and Spera (1987), Ablay et al. (1998), Troll and Schmincke (2002), Rodriguez-Losada and Martinez-Frias (2004), Klügel et al. (2005), Bryan (2006), Dávila-Harris et al. (2013), Sliwinski et al. (2015); this study; Cape Verde: Eisele et al. (2016); Cameroon Line: Mbowou et al. (2013); Ascension: Chamberlain et al. (2016); this study; Trindade: Ryabchikov and Kogarko (1994); Marques et al. (1999); this study; Gough Island: this study; Bouvet Island: this study.

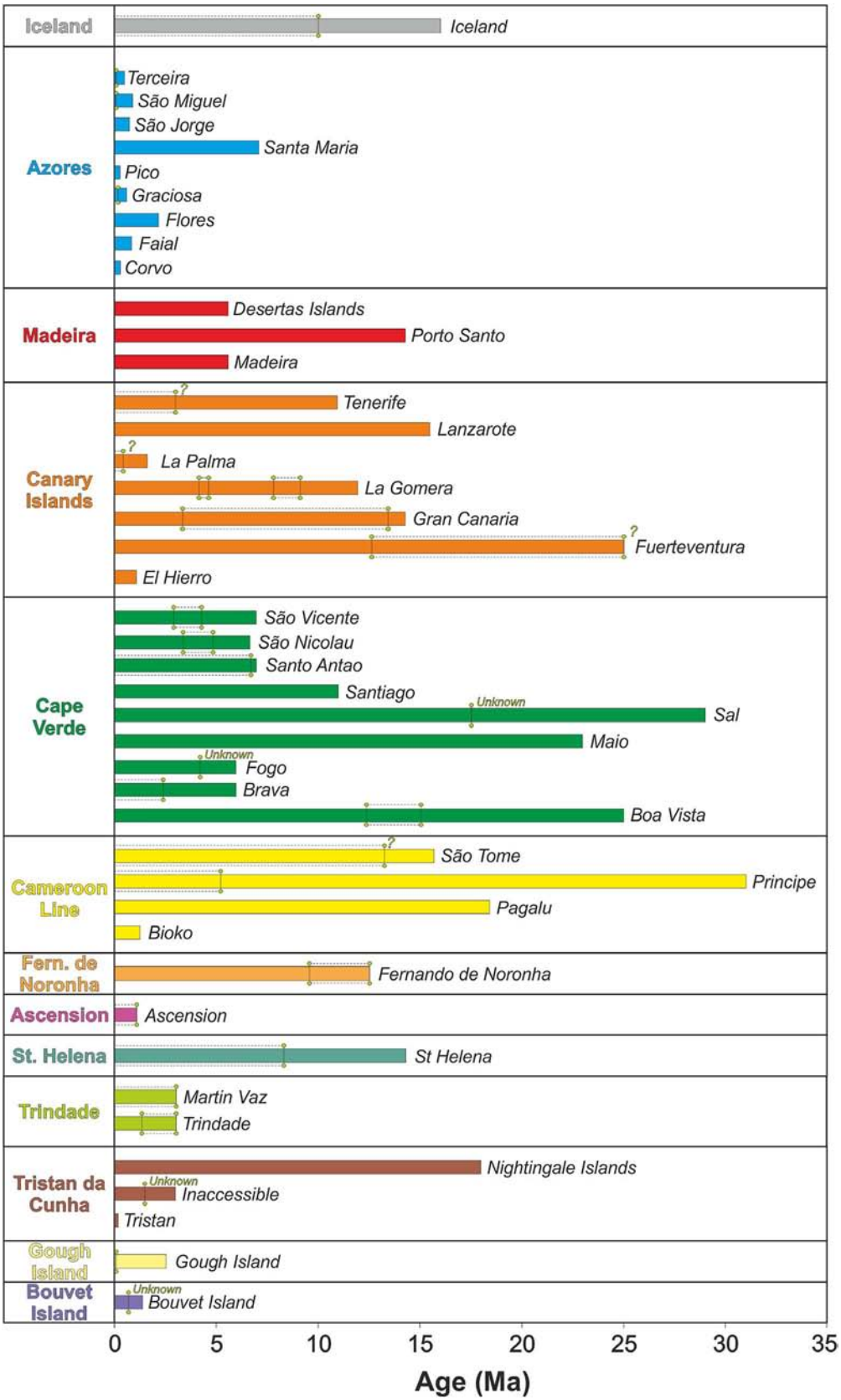

FIGURE 2 | Continued

FIGURE 2 | Summary figure showing the various subaerial ages of each of the individual volcanic islands of the Atlantic Ocean. The earliest known eruption of felsic magmas is marked for each island with a green, double-ended pin mark, highlighting the first known opportunity for peralkaline magmatism to occur. Where possible, the total temporal range of felsic magmatism is shown with dashed lines which delineate a field. Data sources are as follows: Iceland: Gale et al. (1966), McGarvie et al. (2006), Flude et al. (2008); Azores: Abdel-Monem et al. (1975), Self (1976), Feraud et al. (1981), Gandino et al. (1985), Serralheiro et al. (1989), Johnson et al. (1998), Nunes (1999, Unpublished), Calvert et al. (2006), Hildenbrand et al. (2008); Madeira: Watkins and Abdel-Monem (1971), Feraud et al. (1981), Ferreira et al. (1988), Geldmacher et al. (2000); Canary Islands: Abdel-Monem et al. (1971), Abdel-Monem et al. (1972), McDougall and Schmincke (1976), Carracedo (1979), Feraud et al. (1981), Ancochea et al. (1990), Guillou et al. (1996), Carracedo et al. (1998), Carracedo et al. (2002), Balogh et al. (1999), Muñoz et al. (2005), Paris et al. (2005), Becerril et al. (2016), Cape Verde: Faugeres et al. (1989), Torres et al. (2002), Plesner et al. (2003), Holm et al. (2008), Dyhr and Holm, 2010, Madeira et al. (2010), Ramalho (2011) and references therein; Cameroon Line: Hedberg (1969), Aka et al. (2004), Chauvel et al. (2005), Déruelle et al. (2007) and references therein; Fernando de Noronha: Almeida (1955), Cordani (1970), Weaver (1990), Perlingeiro et al. (2013); Ascension: Harris et al. (1982), Nielson and Sibbett (1996), Kar et al. (1998), Jicha et al. (2013), Preece et al. (2016, 2018); St. Helena: Baker et al. (1967), Baker (1969), Chaffey et al. (1989); Trindade: Cordani (1970), Pires and Bongiolo (2016), Pires et al. (2016); Tristan da Cunha: Gass (1967), McDougall and Ollier (1982), Hicks et al. (2012); Gough: Maund et al. (1988); Bouvet: Verwoerd (1972), Prestvik et al. (1999).

area reflects interaction between the Mid-Atlantic Ridge and a mantle plume (e.g., Schilling, 1973; Vink, 1984; White et al., 1995; Bjarnason et al., 1996; Wolfe et al., 1997; Allen et al., 1999; Parnell-Turner et al., 2014), and began around 24 Ma (Sæmundsson, 1978, 1979; Jóhannesson, 1980; Kristjánsson, 1982; Óskarsson et al., 1985), although the oldest dated subaerial rocks are up to 16 Ma (Moorbath et al., 1968; Watkins and Walker, 1977; McDougall et al., 1984; **Figure 2**). Volcanism is focussed in the neovolcanic zones, which represent the surface expression of this plume-ridge interaction (Sæmundsson, 1979; Vink, 1984; Óskarsson et al., 1985; Hardarson et al., 1997). The most prominent of these is the axial volcanic zone, which represents the boundary between the North American and Eurasian plates, and thus marks the focus of active spreading. In addition to the axial rift zone, two off-rift volcanic belts exist; the Öræfi Volcanic Belt in the east, which may reflect an embryonic rift (Thordarson and Hoskuldsson, 2002), and the Snæfellsnes Volcanic Belt in the west, which is an old, reactivated rift zone (Gudmundsson, 2000). Volcanism across Iceland includes polygenetic central volcanoes (e.g., Snæfellsjökull, Krafla, Askja, Torfajökull), as well as monogenetic vents including fissures, maars, and scoria cones (Thorarinsson and Sæmundsson, 1979; Thorarinsson, 1981; Thordarson and Larsen, 2007).

The magmatism of Iceland ranges from basalt to rhyolite and, unlike the other Atlantic Ocean islands, generally adheres to a subalkaline tholeiitic trend (**Figure 3A**), particularly in the NE portion of the axial rift zone. Magmatism becomes mildly alkaline toward the SW of the axial rift, and also in the two off-rift volcanic belts (the Öræfi Volcanic Belt and the Snæfellsnes Volcanic Belt; Jakobsson, 1979; Sæmundsson, 1979; Gudmundsson, 1995). Mafic eruptive products are volumetrically dominant, with a lesser contribution of intermediate and felsic products (Walker, 1959, 1963, 1966; Carmichael, 1964; Baker, 1974). The most recent (since $\sim$ 900 A.D.) eruptive products of Iceland as a whole, together comprising some 122 km^3 in volume, were estimated to include $\sim$ 79 vol. % mafic magma, with intermediate compositions accounting for $\sim$ 16 vol. %, and felsic magmas making up the remaining 5 vol. % (Thorarinsson and Sæmundsson, 1979; Thordarson and Larsen, 2007). Peralkaline felsic magmatism (typically comendites but also some reported pantellerites; e.g., McGarvie et al., 2006) is restricted to polygenetic volcanic centers (Jónasson, 2007), such as Askja (Hartley et al., 2016), Katla (Larsen et al., 2001; Lacasse et al., 2007), Ljósufjöll (Flude et al., 2008), and Torfajökull (McGarvie, 1984; Macdonald et al., 1990; McGarvie et al., 1990, 2006).

Azores

The Azores archipelago comprises nine islands located in the central North Atlantic Ocean (São Miguel, Santa Maria, Terceira, Pico, Graciosa, Faial, São Jorge, Corvo, and Flores). The islands themselves represent the subaerial expression of the Azores Plateau, a bathymetric and gravity anomaly denoting a morphologically complex area ($\sim 5.8 \times 10^6$ km^2) of thickened oceanic crust that formed between 20 and 7 Ma (e.g., Kaula, 1970; Krause and Watkins, 1970; Luis et al., 1994; Gente et al., 2003). The plateau is broadly triangular in shape, bounded by three major tectonic features; the Mid-Atlantic Ridge in the west, the East Azores Fracture Zone to the south and the Terceira Rift to the north-east (Krause and Watkins, 1970). Together these structures mark a triple junction between the North-American, Eurasian and Nubian plates (e.g., Vogt and Jung, 2004; Marques et al., 2013; Hildenbrand et al., 2014; Fernandes et al., 2018). The islands are relatively young amongst those of the Atlantic Ocean (**Figure 2**), and typically exhibit relatively youthful forms, with well-defined volcanic edifices. The notably older and heavily eroded island of Santa Maria (7.1 Ma; Abdel-Monem et al., 1975) stands in exception to this (e.g., Ramalho et al., 2017).

Magmatism in the Azores has been the subject of numerous scientific studies, particularly in recent years (e.g.; White et al., 1979; Madureira et al., 2011; Beier et al., 2013; Métrich et al., 2014; Larrea et al., 2014a, 2018; Zanon, 2015). The majority of the subaerially erupted magmas of the Azores archipelago have been mafic in composition, ranging from basalt/alkali basalt to hawaiite, which typically form lava flows, cinder cones, and spatter ramparts (e.g., Booth et al., 1978; Zanon et al., 2013). Felsic magmas have been erupted primarily via Plinian or sub-Plinian activity from the central vents of the various volcanic complexes (e.g., Self, 1976; Guest et al., 1999; Gertisser et al., 2010; Pimentel, 2015; Pimentel et al., 2015). Felsic magmas have also been erupted effusively, forming lava domes and coulées (e.g., Self, 1974, 1976; Booth et al., 1978; Pimentel, 2006).

When considered as a whole, the Azorean suite ranges from 40 to $\sim$ 68 wt. % SiO_2, forming an alkaline magma series from basalt or alkali basalt to trachyte, with some basanites

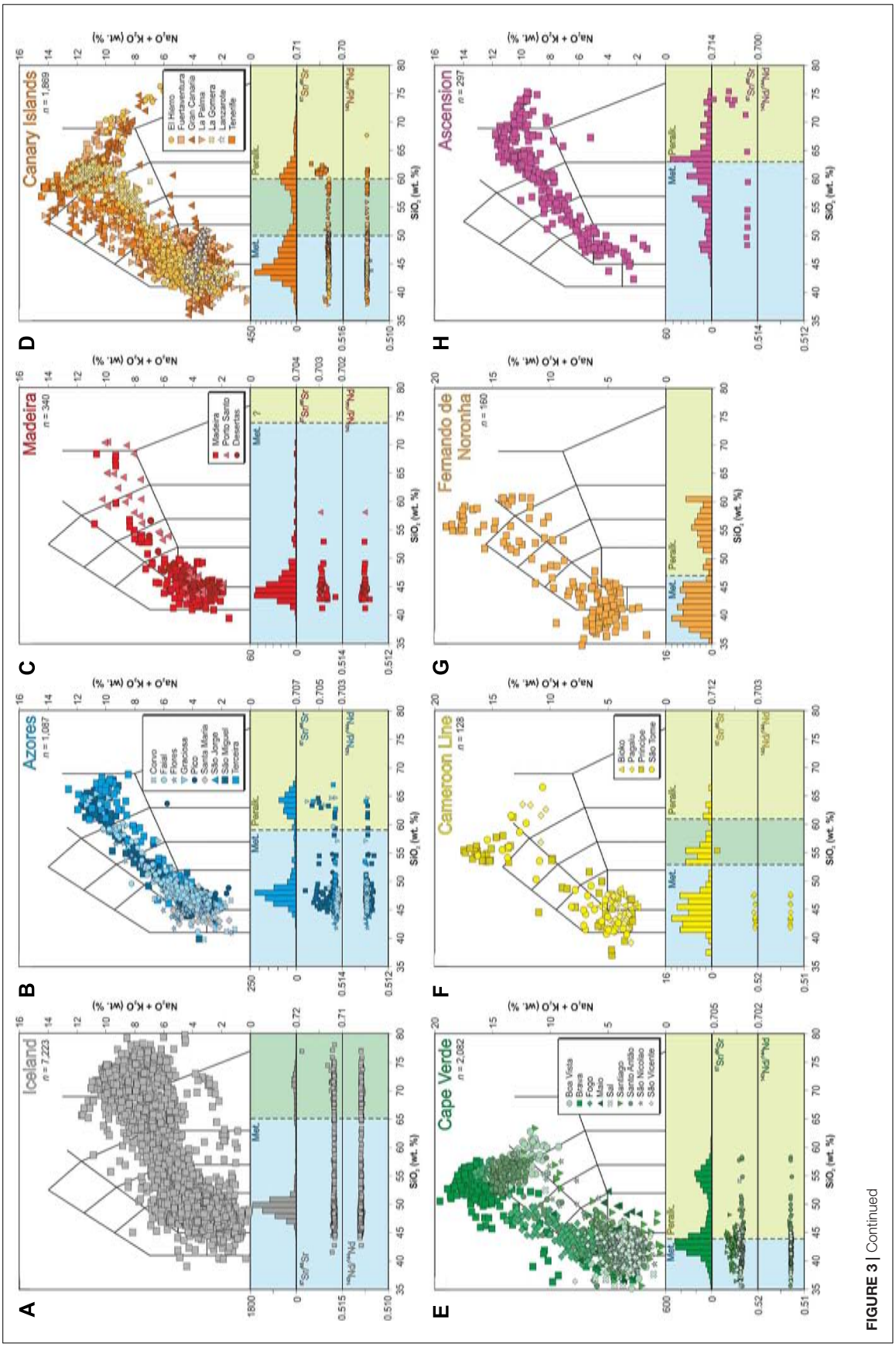

FIGURE 3 | Continued

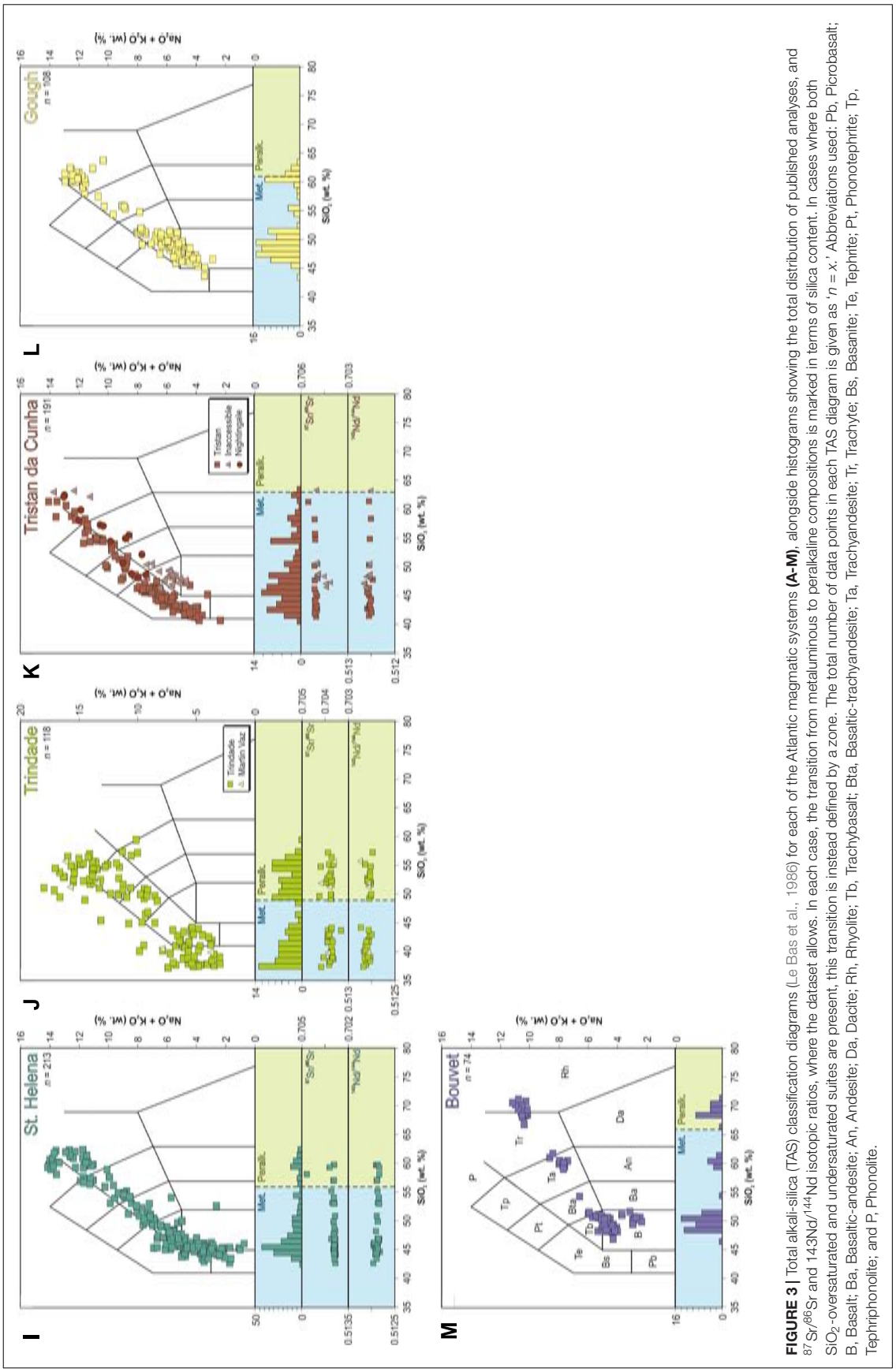

FIGURE 3 | Total alkali-silica (TAS) classification diagrams (Le Bas et al., 1986) for each of the Atlantic magmatic systems **(A-M)**, alongside histograms showing the total distribution of published analyses, and $^{87}Sr/^{86}Sr$ and $143Nd/^{144}Nd$ isotopic ratios, where the dataset allows. In each case, the transition from metaluminous to peralkaline compositions is marked in terms of silica content. In cases where both SiO_2-oversaturated and undersaturated suites are present, this transition is instead defined by a zone. The total number of data points in each TAS diagram is given as '*n = x*.' Abbreviations used: Pb, Picrobasalt; B, Basalt; Ba, Basaltic-andesite; An, Andesite; Da, Dacite; Rh, Rhyolite; Tb, Trachybasalt; Bta, Basaltic-trachyandesite; Ta, Trachyandesite; Tr, Trachyte; Bs, Basanite; Te, Tephrite; Pt, Phonotephrite; Tp, Tephriphonolite; and P, Phonolite.

on Santa Maria. Total alkali contents lie between 1.7 and 13.5 wt. % (**Figure 3B**), and Na/K ratios exceed unity. White et al. (1979) highlight the presence of a 'Daly gap,' describing bimodal eruptive products with a relative lack of intermediate. Mafic products have been generally erupted from fissural zones, and range from sub-aphyric to highly porphyritic with abundant olivine and clinopyroxene phenocrysts and xenocrysts, as well as glomerocrysts of varying composition (e.g., Genske et al., 2012; Larrea et al., 2013; Zanon and Frezzotti, 2013; Zanon et al., 2013; Zanon, 2015). Intermediate magmas are infrequent in occurrence, but have been described in some detail on São Miguel (Beier et al., 2006), Faial (Zanon et al., 2013), Corvo (Larrea et al., 2013), Graciosa (Zanon, 2015), Flores (Genske et al., 2012), and Terceira (Mungall, 1993). Mugearitic compositions are often highly porphyritic (∼ 30 vol. %), but benmoreitic compositions are frequently close to aphyric. In contrast to the mafic magmas, the trachytic magmas are generally sub-aphyric to aphyric, with phase assemblages which are invariably dominated by alkali feldspar. Variably peralkaline syenitic autoliths are also described in both mafic and felsic lithologies (e.g., Self, 1976; Booth et al., 1978; Mungall, 1993; Gertisser et al., 2010; Jeffery et al., 2016a).

The Madeira Archipelago

The Madeira archipelago comprises five islands (Madeira, Porto Santo, and the three Desertas Islands), located in the eastern North Atlantic Ocean, ∼ 700 km west of the African coastline. The islands sit upon 140 Ma old oceanic crust (Pitman and Talwani, 1972), rise ∼ 4 km from the sea floor, and mark the south-western end of a northeast-southwest trending alignment of seamounts and islands which extends for ∼ 700 km, with a width of ∼ 200 km (Geldmacher et al., 2005). The chain extends from mainland Portugal to the Madeira archipelago, and exhibits a crude age progression of ∼ 72 Ma (the Serra de Monchique igneous complex) to the present day (Madeira), which is typically interpreted as evidence for an underlying mantle plume (Morgan, 1981).

Together, Madeira and the Desertas islands are often considered to represent a single volcanic system (although geobarometric studies may provide evidence for two separate systems; Schwarz et al., 2004), dated at up to 5.6 Ma (e.g., Watkins and Abdel-Monem, 1971; Feraud et al., 1981; Ferreira et al., 1988; **Figure 2**), and comprising two rift arms: the Desertas Rift which trends NNW-SSE, and the E-W trending Madeira Rift (Geldmacher and Hoernle, 2000). The temporal evolution of this volcanic center was divided by Geldmacher et al. (2000) into two key portions: (1) the shield stage (>4.6 to 0.7 Ma), which accounts for 99.5% of the subaerial volume, and (2) the post-erosional phase (<0.7 Ma). The majority of volcanism on Madeira took place from 3.9 to 4.6 Ma, and 0.7 to 3 Ma, during the Early and Late Madeira rift phases, respectively. The formation of the Desertas islands occurred primarily between 3 and 4 Ma, during which time the Madeira Rift was inactive. The rocks of both islands adhere to the SiO_2-oversaturated trend, and are dominated by mildly alkaline picrites and basanites, with comparatively rare intermediate or felsic rocks including mugearite, benmoreite, and trachyte (Schwarz et al., 2004; **Figure 3C**). The mafic lithologies typically contain phenocrystic olivine and clinopyroxene, with plagioclase being present only in the basalts and hawaiites.

The stratigraphy of Madeira Island is divided into seven unconformity-bounded units, which are themselves grouped into the Lower, Middle, and Upper Volcanic Complexes (Brum da Silveira et al., 2010a,b,c). Within these formations, basaltic compositions are dominant. The Lower Volcanic Complex includes strongly altered hydrovolcanic rocks and marine sediments, and may represent the seamount-building stage of Madeira. The Middle Volcanic Complex (representative of the shield-building phase) comprises various lava flow successions and tephra layers which gradually became more intermediate in composition over time. The Upper Volcanic Complex is made up of topography-filling volcanic lava flows and scoria cones, representative of the erosional phase of the island (Czajkowski, 2002; Ramalho et al., 2015).

The island of Porto Santo lies 45 km to the northeast of Madeira, and reflects a distinct, older (11.1–14.3 Ma; Geldmacher et al., 2000; **Figure 2**) volcanic edifice. Unlike Madeira and the Desertas Islands, the compositional range of the rocks of Porto Santo extends from basalts to metaluminous trachytes. The northeast of the island comprises a predominantly submarine cone, with various trachytic and basaltic intrusions. By contrast, the lavas originating from the southwestern center are primarily mafic to intermediate (Czajkowski, 2002).

The Canary Islands

The Canary Island archipelago comprises seven volcanic islands (La Palma, El Hierro, Gomera, Tenerife, Gran Canaria, Fuerteventura, and Lanzarote), as well as a number of sea mounts, trending roughly WSW-ENE between 100 and 500 km from the coast of NW Africa, in an ∼ 800 km long, ∼ 400 km wide volcanic belt (Hoernle and Carracedo, 2009). The archipelago has received considerable attention from the scientific community, and has been the subject of numerous tectonic, petrological, volcanological, and geochronological studies (e.g., McDougall and Schmincke, 1976; Schmincke, 1976; Ancochea et al., 1990; Martí et al., 1994; Carracedo et al., 1998, 2002, 2007, 2011; Bryan et al., 2000; Thirlwall et al., 2000; Brown et al., 2003; Brown and Branney, 2004; Triebold et al., 2006; Edgar et al., 2007; Meletlidis et al., 2012; Longpré et al., 2014; Barker et al., 2015; Cooper et al., 2015; Troll and Carracedo, 2016). The easternmost islands of Fuertaventura and Lanzarote are underlain by transitional oceanic-continental crust, whereas the remaining islands overly oceanic crust (Robertson and Stillman, 1979; Ye et al., 1999), constrained in age to the Jurassic by magnetic anomalies S1 (175 Ma, located between the easternmost islands and the African coastline) and M25 (155 Ma, located between La Palma and El Hierro) (Klitgord and Schouten, 1986). A substantial radiometric dataset indicates that magmatism in the area began more than 20 m.y. ago, forming the eastern islands of Lanzarote and Fuerteventura (e.g., Abdel-Monem et al., 1971; Schmincke, 1976; Ancochea et al., 1999 and references therein; Geldmacher et al., 2005). Overall, the islands become younger toward the west, with the oldest subaerial volcanism for Fuerteventura,

Lanzarote, and Gran Canaria being constrained to 20.6, 15.5, and 13.7 Ma, respectively, compared with 2.0 and 1.12 Ma for La Palma and El Hierro, respectively (McDougall and Schmincke, 1976; Carracedo et al., 1998; **Figure 2**). Due to their age and morphologies, the eastern islands (Gran Canaria, Fuerteventura, and Lanzarote) are considered to be in a post-erosional stage, with a net decrease in the size of the island. By contrast, the western islands of El Hierro, La Palma, and Tenerife are each regarded as being in a constructive (shield) stage (e.g., Ancochea et al., 1990), with net growth of the edifice. La Gomera is intermediate between the two stages, due to an identified post-shield gap in volcanic activity (Carracedo et al., 1998) and an age of 9.4 Ma (Paris et al., 2005).

Chemically, the Canary Islands are arguably the most diverse of the Atlantic volcanic centers, with rock types including basanites, basalts (both alkali and tholeiitic), tephrites, nephelinites, melilitites, trachyandesites, rhyolites, trachytes, phonolites, comendites, pantellerites, and carbonatites (**Figure 3D**). Together, these lithologies define multiple evolutionary trends ranging from SiO_2-undersaturated (e.g., basanite to phonolite) to SiO_2-oversaturated (basalt to rhyolite) (e.g., Carracedo et al., 2002). Furthermore, a tholeiitic trend similar to that of Hawaii is recognized on a number of islands, where it has been linked to greater fusion rates, and assimilation of silicic crustal sediments (Carracedo et al., 2002; Aparicio et al., 2006, 2010; Troll et al., 2012; Troll and Carracedo, 2016). There is considerable variation in the geochemistry of eruptive deposits between the islands (Carracedo et al., 2002). For example, Gran Canaria exhibits the full range of compositions, including highly alkaline, mildly alkaline, and tholeiitic varieties. In contrast, the other islands exhibit more simplistic trends (**Figure 3D**). El Hierro, La Gomera, Lanzarote, and Fuertaventura display only mildly alkaline trends, compared with Tenerife and La Palma, which become more alkaline in nature. The abundance of felsic rocks is also variable, being greatest on Gran Canaria and Tenerife, and smallest on Lanzarote.

Cape Verde

The Cape Verde archipelago comprises nine islands (Santo Antão, São Vicente, São Nicolau, Sal, Boa Vista, Maio, Santiago, Fogo, and Brava) and eight minor islets, situated in the central Atlantic, approximately 450 km from the western coast of Africa. The islands sit on oceanic crust that ranges in age from 120 to 140 Ma (Müller et al., 2008), and represent the subaerial portion of the Cape Verde rise, a dome-shaped swell which is elevated by 2.2–2.4 km relative to the surrounding seafloor, and which occupies more than 300,000 km^2 (Crough, 1982; McNutt, 1988). Although traditionally divided based upon geographical position (the Windward Group and the Leeward Group), regional bathymetry indicates that two submarine chains exist: the northern chain which runs NW to SE and includes Santo Antão, São Vicente, Santa Luzia, and São Nicolau, and the curved southern chain, which runs broadly ENE to WSW before curving northward, and is composed of the islands of Sal, Boa Vista, Maio, Santiago, Fogo, and Brava (Ramalho, 2011).

The eastern islands generally exhibit flattened, eroded forms, suggesting that they are in a post-erosional stage. Moving westward, the islands become progressively youthful in appearance, with greater topographical relief and higher elevations. This is in accordance with available ages for each island (Ramalho, 2011 and references therein), which indicate that Sal, Maio, and potentially Boa Vista are the oldest islands, with a maximum age of ∼ 26 Ma (Torres et al., 2002; **Figure 2**). This age also coincides with the formation of the Cape Verde Rise (Faugeres et al., 1989). Around 8–10 Ma, volcanism was initiated further westward, leading to the development of Santiago and São Nicolau, and later (∼ 4 to 6 Ma), the broadly synchronous formation of the remaining islands (Holm et al., 2008; Ramalho, 2011). Modern day volcanic activity within the archipelago is limited to Fogo, where the primary eruptive center (Pico do Fogo) has erupted every 20 years, on average, since the island was settled, with the most recent eruption having occurred in 2014–2015 (e.g., Torres et al., 1997; Hildner et al., 2011; González et al., 2015).

The rocks of the Cape Verde archipelago are almost exclusively strongly silica-undersaturated, and range from picrites to peralkaline phonolites and trachytes (Ramalho, 2011; **Figure 3E**). Two magmatic series are identified; (1) a high alkali series comprising picrites, foidites, and phonolites, and (2) a moderately alkaline series comprising picrobasalts, basanites, tephrites, tephrophonolites, phonotephrites, phonolites, and trachytes (Kogarko, 2008). The plutonic cores of heavily eroded volcanic edifices are similar in composition, ranging from gabbro to syenite (Serralheiro, 1976). Not all of the islands exhibit the entire compositional range of the archipelago; for example, São Vicente is limited to mafic rocks, whereas Brava is dominated by peralkaline phonolites. Cape Verde also exhibits carbonatitic rocks, which are found in both the basement complexes and the mature stages of at least 5 of the 10 islands (Jørgensen and Holm, 2002; Mourão et al., 2010, 2012; Weidenorfer et al., 2016; Mata et al., 2017).

Cameroon Line

The Cameroon Line comprises a 1,600 km long, Y-shaped chain of intraplate volcanic centers with a broadly NE-SW alignment. This feature extends across both continental and oceanic crust, with both portions being believed to have formed simultaneously, beginning at around 52 Ma (Moundi et al., 2007; Yokoyama et al., 2007). Unlike other alignments of oceanic islands, there is no evidence for age progression along the Cameroon Line (Lee et al., 1994; Marzoli et al., 2000). The chain includes two sectors: the continental sector, which comprises a number of large massifs, including the currently active Mt. Cameroon (Suh et al., 2003), and the oceanic sector, which includes four volcanic islands (Pagalú, São Tomé, Principe, and Bioko) and two seamounts (Déruelle et al., 1991; Lee et al., 1994; Burke, 2001). Overall, the rocks of the Cameroon Line range from mafic compositions, including alkali basalts, picrites, hawaiites, through to felsic compositions such as phonolites, trachytes, and rhyolites, with comparatively less common intermediate compositions (mugearites, benmoreites) (Déruelle et al., 2007; **Figure 3F**). Unlike the mafic rocks, the felsic rocks exhibit clear spatial variation between the two sectors. The felsic rocks of the Oceanic Sector are primarily phonolites and trachytes, with

no rhyolitic compositions reported (Lee et al., 1994; Déruelle et al., 2007). By contrast, the continental sector includes primarily rhyolites and trachytes, leading some authors to invoke the role of varying degrees of crustal assimilation during fractional crystallization (e.g., Fitton, 1987). The proportion of felsic rocks relative to mafic rocks is generally recognized to increase to the SW and the NW of the boundary between the two sectors (e.g., in the vicinity of Bioko island). In this study, only the Oceanic Sector is considered.

Amongst the four islands of the Oceanic Sector, Bioko stands apart due to its young age (<1.33 Ma; Hedberg, 1969; Aka et al., 2004; Chauvel et al., 2005), youthful morphology, and exclusively mafic composition. By contrast, the three islands of Principe, São Tomé, and Pagalú are significantly older, reaching ages of 31, 16, and 20 Ma, respectively (Déruelle et al., 2007 and references therein; **Figure 2**). These three islands also exhibit more variation in the compositions of their eruptive lavas, ranging from basalt to trachyte and phonolite. The occurrence of peralkaline magmatism is limited to Principe and São Tomé, where mildly peralkaline phonolites are reported, although trachytes with a peralkaline affinity are also recognized on Pagalú.

Fernando de Noronha

The Fernando de Noronha archipelago is located ∼ 350 km ENE from the coast of Brazil, and comprises 21 individual islands and islets that have a cumulative surface area of 18.4 km^2 and rise ∼ 4.2 km from the ocean floor (Bryan et al., 1972). The archipelago lies at the eastern end of a linear chain of seamounts, named the Fernando de Noronha Ridge, which extends eastward from the Brazilian mainland. Magmatism situated at the westernmost end of this ridge is dated at 40 Ma, and is believed to represent the earliest activity of a mantle plume (the Fernando de Noronha plume) which later led to the formation of the archipelago of the same name (Fodor et al., 1998; Almeida, 2012; Lopes and Ulbrich, 2015).

The stratigraphy of the islands is divided into three distinct formations. The Remédios Formation comprises abundant, highly altered trachytic/phonolitic pyroclastic material, intruded by several dyke systems (lamprophyre, tephrite, basanite, trachyte, and trachyandesite), and various plugs and subvolcanic domes (phonolite, trachyte, basalt) (Almeida, 1955; Weaver, 1990; Ulbrich, 1993). Available $^{40}Ar/^{39}Ar$ ages indicate a range of 12.5–9.4 Ma for the Remédios Formation (Perlingeiro et al., 2013; *cf.* 12.3–8 Ma (^{40}K-^{40}Ar); Cordani, 1970). Above the Remédios Formation, and separated from it by a significant period of erosion, is the Quixaba Formation, which comprises extensive nepheline-basalt flows which formed between 6.2 and 1.3 Ma, with minor nephelinite dykes, tuffs, and breccias (Almeida, 1955; Weaver, 1990; Perlingeiro et al., 2013). The third formation is the São José Formation, which comprises a series of basanitic lava flows exposed exclusively on the islet of São José, NE of the main island. Almeida (1955) identified this formation as distinct on the basis of often abundant mantle xenoliths, and it has subsequently been suggested to represent the youngest portion of the Quixaba Formation (Ulbrich, 1993; Lopes, 2002). However, recent $^{40}Ar/^{39}Ar$ ages indicate an age of 9.2–9.0 Ma, suggesting that they are in fact coeval with the Remédios Formation (Perlingeiro et al., 2013; **Figure 2**).

The geochemical evolution of the Fernando de Noronha archipelago is complex, and is summarized by Lopes et al. (2014) and Lopes and Ulbrich (2015) (**Figure 3G**). The Remédios Formation includes two suites of rocks, each derived from a discrete parental magma, and each exhibiting continuous geochemical trends from their least to their most evolved compositions; (1) the sodic series (basanite-tephrite-phonotephrite-phonolite), and (2) the moderately potassic series (alkali basalt-basaltic trachyandesite-trachyandesite-trachyte). Evidence for open system evolution, such as xenocrysts and autolithic fragments, is common throughout the formation. Lamprophyric dykes are distinct in that they bear no clear relationship to any of the other rock types. The overlying Quixaba and São José Formations are much more restricted in composition, comprising almost exclusively nephelinites and basanites, which correlate geochemically and appear to form a single suite, despite belonging to two distinct stages in the evolution of islands.

Ascension

Ascension Island lies approximately 90 km west of the Mid-Atlantic Ridge, in the Southern Atlantic Ocean. The ∼ 3,800 km^3 volcanic edifice rises ∼ 4 km from the sea floor, with only 1% of its total volume exposed subaerially (Harris, 1983; Klingelhöfer et al., 2001). Submarine volcanism is believed to have begun at ∼ 6 to 7 Ma, with the edifice becoming subaerial at ∼ 1.09 Ma (Jicha et al., 2013; Preece et al., 2016, 2018; **Figure 2**). The geology of the island is well described (e.g., Daly, 1925; Darwin, 1845; Atkins et al., 1964; Nielson and Sibbett, 1996; Weaver et al., 1996; Kar et al., 1998). Approximately 57% of the island comprises effusive eruptive products (flows and domes), with the rest being pyroclastic lithologies (Harris, 1983). Mafic volcanic rocks are found across the island, whereas felsic eruptive products are found in two main areas; the Central Felsic Complex which forms the high ground in the island's center, and the Eastern Felsic Complex. There has been no historical volcanic activity on the island, although the youngest lava flows have recently been reliably dated at < 1 ka (Preece et al., 2018).

The subaerial rocks of Ascension form a transitional to sub-alkaline series, ranging from basalt to rhyolite (Jicha et al., 2013; **Figure 3H**). A general lack of intermediate compositions in the eruptive products of the island (a Daly Gap) has been observed, specifically within the compositional range of 58–63 wt. % SiO_2 (Daly, 1910, 1925). The mafic and intermediate lithologies are generally aphyric or sparsely phyric with phenocrystic plagioclase and olivine, with lesser clinopyroxene and Fe-Ti oxides, and rare amphibole in the intermediate rocks only (Weaver et al., 1996). Based upon Zr/Nb ratios, there are four distinct varieties of mafic rocks on Ascension, which are considered to reflect variation in the source characteristics beneath Ascension, despite erupting contemporaneously (Weaver et al., 1996; Kar et al., 1998). The felsic rocks, which account for ∼ 14% of the surface area of the island, are also generally aphyric or sparsely phyric, with alkali

feldspar representing the most abundant phase (Weaver et al., 1996; Kar et al., 1998).

St. Helena

The island of St. Helena lies ∼ 750 km east of the Mid-Atlantic Ridge, and ∼ 1,900 km west of Africa. The island sits upon oceanic crust dated at 39 Ma, rises ∼ 4 km from the ocean floor, and reaches 823 m above sea level, with a surface area of ∼ 122 km^2 (Baker, 1969). Together with the Bonaparte seamount, it forms a volcanic chain attributed to traditional hot-spot theory (Chaffey et al., 1989). Geochemically, the island comprises a single alkaline suite which extends from highly porphyritic alkali basalts to mildly peralkaline trachytes and phonolites (**Figure 3I**). This suite is biased volumetrically toward its mafic end, with basalts constituting 70–80 vol. % of the subaerial portion of the island, whilst trachybasalts represent 15–25 vol. %, trachyandesites 4 vol. %, and evolved felsic rocks only 1 vol. % (Baker, 1968, 1969). The alkali basalts contain primarily phenocrysts of clinopyroxene and olivine, with plagioclase becoming more significant in the trachybasalts and trachyandesites. The trachytes contain olivine and Ti-magnetite phenocrysts, with alkali feldspar, plagioclase, Ti-magnetite, and aegirine-augite in the groundmass, whereas the phonolites and phonolitic trachytes contain alkali feldspar as the dominant phenocryst phase, and a combination of alkali feldspar, aegirine-augite, Ti-magnetite, nepheline, aegirine, and aenigmatite in the groundmass (Baker, 1969; Kawabata et al., 2011).

There are two volcanic centers: an older, volumetrically less significant shield volcano which forms the NE of the island, and a younger, more complex shield volcano which forms the SW of the island. Both comprise predominantly basaltic lava flows and scoria cones extruded from centralized fissural systems. The older volcanic center is dated (by whole-rock ^{40}K-^{40}Ar) at 14.3–11.4 Ma (Baker et al., 1967; Chaffey et al., 1989; **Figure 2**), and comprises a thick (up to ∼ 400 m) sequence of altered mafic breccias, presumed to be of submarine origin, overlain by ∼ 800 m of interbedded basaltic lavas and pyroclastic deposits (Baker, 1969). At around 11.4 Ma, volcanism shifted to the SW, generating a complex series of mafic lavas and pyroclastic deposits with three unconformities, over the course of ∼ 3 m.y. (11.3–8.4 Ma; Baker, 1969; Chaffey et al., 1989). This activity was recognized to be cyclic in nature by Baker (1969), with individual cycles comprising effusive, then explosive activity, followed by a period of erosion. At around 7.6 Ma, approximately 1 m.y. after the cessation of volcanism, the SW center was intruded by a number of dykes and parasitic masses, ranging in composition from phonolites and trachytes, to trachyandesites and trachybasalts (Baker, 1969).

Trindade

The island of Trindade is situated approximately 1,140 km east of the Brazilian coast, and rises some 5 km from the surrounding ocean floor. Together with the nearby islet group of Martin Vaz, Trindade lies at the end of the Vitória-Trindade ridge, an E-W trending alignment of seamounts believed to represent the volcanic trail of the underlying Trindade mantle plume (e.g., Crough et al., 1980; O'Connor and Duncan, 1990; Thompson et al., 1998). Trindade itself has a surface area of 6 km^2, and represents a deeply eroded remnant of a once larger volcanic edifice.

The stratigraphy of Trindade was established by Almeida (1961), who provided a geological map (Almeida, 1963) and identified five distinct volcanic episodes in the islands history, ^{40}K-^{40}Ar dated from 3.6 Ma to present by Cordani (1970; **Figure 2**). More recently, the stratigraphy and determined ages have been revised by Pires and Bongiolo (2016) and Pires et al. (2016), respectively. The Trindade Complex (3.22–2.78 Ma) comprises a 500 m thick succession of nephelinitic to phonolitic pyroclastic deposits, cross-cut by various sills and dykes of nephelinitic, basanitic, and lamprophyric compositions, as well as necks and associated radial dykes of phonolitic composition (**Figure 3J**). The Desejado Formation (2.6–1.5 Ma) overlies the Trindade Complex uncomformably, comprising an ∼ 300 m thick succession of effusive and pyroclastic phonolitic nephelinites, olivine-poor nephelinites, and phonolites. The remaining three formations (the Morro Vermelho Formation, the Valado Formation, and the Paredão Formation, in order of decreasing age) comprise pyroclastic and effusive sequences of exclusively nephelinitic composition and variable thicknesses (∼ 250, ∼ 60, and ∼ 250 m, respectively). An ^{40}Ar/^{39}Ar age of 254 ± 198 ka was produced for an olivine-rich nephelinitic lava from the Paredão Formation, marking the youngest volcanic activity on the island (Pires et al., 2016). The stratigraphy of Martin Vaz is essentially unknown, although compositions including biotite-bearing nephelinite (ankaratrite), basanite, and peralkaline phonolite have been reported (Mitchell-Thomé, 1970; Marques et al., 1999; Siebel et al., 2000), and a ^{40}K-^{40}Ar age of <0.7 Ma was produced by Cordani (1970).

In terms of the overall evolution of the island, the older Trindade Complex is considered to represent an old, eroded volcanic edifice with a bimodal character, which experienced four magmatic pulses following a pronounced period of erosion. The occurrence of evolved, peralkaline rocks appears to have been restricted to the older portion of the island's history (the Trindade Complex and the Desejado Formation; 3.22–1.5 Ma) (Marques et al., 1999). The younger eruptive products are exclusively ultramafic, although two end-members are identified on the basis of mineral and whole-rock compositions, with the rocks of the youngest formation (Paredão Formation) representing a mixture of the two (Marques et al., 1999). The phonolitic rocks of Trindade are characterized petrographically by phenocrystic alkali feldspar and feldspathoids, with lesser clinopyroxene. The various ultramafic and mafic rocks typically exhibit much more diverse mineral contents, including phenocrystic olivine, nepheline, leucite, perovskite, clinopyroxene, and biotite, although their respective proportions vary considerably (Marques et al., 1999).

Tristan da Cunha

The Tristan da Cunha island group comprises three separate islands (Tristan da Cunha, Inaccessible, and the Nightingale Group) and various islets, located in the South Atlantic Ocean, approximately 400 km east of the Mid-Atlantic Ridge (Baker

et al., 1964). All three of the islands represent the peaks of volcanic cones which rise abruptly from the sea floor, some 3.5 km below (Heezen and Tharp, 1961). Tristan da Cunha (referred to hereafter as Tristan) comprises a near-perfect cone, whereas both Inaccessible and Nightingale have substantial shallow water platforms, suggesting considerable erosion of once larger edifices (Gass, 1967). The island of Tristan rises to 2,062 m above sea level, with a surface area of ∼ 100 km^2 and a circular shape. A single primary vent is located at the center of the island, with more than 30 parasitic vents and numerous radial dykes located on the flanks (Le Roex et al., 1990). Based upon its youthful morphology and a number of available ^{40}K-^{40}Ar ages, the subaerial portion of the main shield-building phase of the island is considered to have occurred between 0.2 and 0.1 Ma, with continued activity until the present day (McDougall and Ollier, 1982; Hicks et al., 2012; **Figure 2**). The most recent eruptive activity occurred in 1961, and around 1700 AD (Le Roex et al., 1990). The majority of the exposed eruptive products are variably porphyritic, silica undersaturated basanites (∼ 80%) (**Figure 3K**). Intermediate compositions (phonotephrites) account for ∼ 15% of the exposed rocks, and are similarly variable in crystal content. The most evolved compositions (tephriphonolites), restricted to only ∼ 5% of the exposed stratigraphy, are described as aphyric to porphyritic, with phenocrysts of kaersutitic amphibole, Ti-magnetite, plagioclase, clinopyroxene, sphene, and apatite (Le Roex et al., 1990).

Inaccessible Island has a surface area of ∼ 14 km^2 and is surrounded by a shallow (∼ 200 m) submarine platform, suggesting that it represents the erosional remnant of a larger volcanic cone that was once ∼ 16 km in diameter, making it somewhat larger than Tristan's current edifice (Baker et al., 1964). A ^{40}K-^{40}Ar age provided by Gass (1967) suggests that subaerial volcanism began at around 3 Ma (**Figure 2**), with the island subsequently achieving its maximum size and then being subjected to 90–95 vol. % erosion to reach its current form. Available geochemical data for Inaccessible Island indicate a somewhat less alkaline trend than seen on Tristan, ranging from alkali basalts (found as thin lava flows and cinder cones) to trachytes and phonolites (Cliff et al., 1991).

The Nightingale Group comprises three separate islands (Nightingale, Middle, and Stoltenhoff), with a combined surface area of ∼ 3 km^2. As for Inaccessible Island, there is substantial evidence to suggest that the islands are the heavily-eroded remnant of a single large volcanic cone (Gass, 1967). Two prominent lithologies are described; yellow ashes and agglomerates which dominate the lower portions of the islands, and massive units of porphyritic trachytes which form the upper portions (Baker et al., 1964). The former rocks are named collectively the Older Pyroclastic Sequence (Baker et al., 1964), and were subsequently intruded, initially by trachybasalts, followed by trachytic plugs which also formed lava flows (Gass, 1967). These are overlain by a localized trachytic flow and an extensive yellow pyroclastic unit which bear no intrusive lithologies, named the Younger Pyroclastic Group (Baker et al., 1964). Gass (1967) provided ^{40}K-^{40}Ar dates which constrain the Older Pyroclastic Sequence to more than 18 Ma, suggesting that the Nightingale Group represents volcanism considerably older than either Inaccessible or Tristan (**Figure 2**). Compositionally, the rocks of the Nightingale Group have a more limited span than observed on the other two islands, ranging from trachybasalts to trachyte (Baker et al., 1964; Gass, 1967; Mitchell-Thomé, 1970). Basaltic compositions are notably absent from the stratigraphy.

Gough Island

Gough Island lies in the southernmost Atlantic Ocean, ∼ 550 km east of the Mid-Atlantic Ridge, and 400 km south east of the Tristan da Cunha archipelago. The 13 × 7 km-wide island has a surface area of ∼ 67 km^2 and rises from a depth of ∼ 3.5 km to ∼ 910 m above sea level, overlying ∼ 38-million-year old (magnetic anomaly 13) oceanic crust of the African plate (Maund et al., 1988). The island is rugged and deeply dissected in nature, implying that erosion outpaces volcanic activity (Campbell, 1914). The rocks of Gough Island form a single, continuous, silica-undersaturated series from picrite basalt to aegirine-augite trachyte (Zielinski and Frey, 1970; Le Roex, 1985; **Figure 3L**), and are described in considerable detail by Le Maitre (1962). The picritic rocks are highly porphyritic with large phenocrysts of olivine and often strongly zoned clinopyroxene. By contrast, the felsic rocks are often phenocryst-poor, and contain phenocrysts and glomerocrysts of both plagioclase and alkali feldspar, alongside lesser biotite, fayalitic olivine, Ti-magnetite, apatite, clinopyroxene, and rare sodalite (Le Roex, 1985). Overall, felsic rocks are dominant in volume, occurring as thick lava flows and domes, pyroclastic deposits, and intrusive lithologies (Maund et al., 1988).

The stratigraphy of the island was first studied in detail by Le Maitre (1962), and subsequently revised by Maund et al. (1988). The latter authors utilized a number of ^{40}K-^{40}Ar ages to define an 'Older Basalt Group' (2.55–0.5 Ma) (**Figure 2**), followed by an erosive period of ∼ 0.3 m.y., followed by the 'Trachyte Extrusives' (∼ 0.2 Ma) and the 'Edinburgh Peak Basalts' (∼ 0.1 Ma). A number of aegirine-augite trachyte plugs are also described, intruded into the youngest rocks of the Older Basalt Group. Although Le Maitre (1962) linked these intrusive lithologies with the Trachyte Extrusives, the ^{40}K-^{40}Ar ages of Maund et al. (1988) suggest that they instead represent a period of felsic magmatism that is temporally distinct, being separated from the Trachyte Extrusives by ∼ 0.3 m.y. Overall, the history of the island can be divided into four key phases: (1) a basalt shield-building phase comprising basaltic hyaloclastites, pillow lavas, and lava flows, most likely from a single central vent, (2) A minor phase of peralkaline trachyte intrusions into the basaltic lavas, followed by a period of erosion, (3) a substantial phase of trachytic activity, erupted from a variety of vents and exhibiting a range of eruptive behavior, and (4) a minor phase of renewed basaltic activity, leading to the generation of a cinder cone complex (Maund et al., 1988).

Bouvet Island (Bouvetøya)

Bouvet Island (or Bouvetøya) is found in the southernmost Atlantic Ocean, close to the triple junction on the South Atlantic Ridge. The island has an above-sea-level volume of ∼ 25 km^3, and a surface area of 55 km^2, and rests upon oceanic crust ∼ 6 Ma in age (Imsland et al., 1977). Magmatism in the

region has been linked to the presence of a mantle plume (the Bouvet mantle plume; Morgan, 1972; Le Roex et al., 1985). No detailed geological map has been made for Bouvet Island due a substantial ice cap, which covers 95% of the islands surface. Instead, current knowledge relating to the volcanic evolution of the island is based upon limited exposure found at the island's margins. The age of the subaerial portion of the island is believed to be <0.7 Ma (Verwoerd, 1972) or <1.4 Ma (Prestvik et al., 1999; **Figure 2**). The primary eruptive center is in the NW of the island, where active fumaroles occur and where an ∼ 4 km wide topographic depression is believed to be a caldera (Imsland et al., 1977). The most recent volcanic activity may have occurred between 1955 and 1957, when a small platform formed on the western coast (Baker and Tomblin, 1964; Lunde, 1965).

The rocks of Bouvet Island belong to a single, sodic, silica-oversaturated series, which includes alkali basalts, hawaiites, mugearites, benmoreites, and mildly peralkaline trachytes and rhyolites (Verwoerd et al., 1976; Prestvik, 1982; **Figure 3M**). The mafic rocks contain Ca-rich plagioclase megacrysts and glomerocrysts, alongside less common olivine and clinopyroxene. Similarly, the intermediate rocks contain megacrysts and glomerocrysts, though they are more diverse, including Na-rich plagioclase, clinopyroxene, olivine, Ti-magnetite, and apatite (Imsland et al., 1977). By contrast, the felsic rocks are dominated by alkali feldspar, which exists as phenocrysts, microphenocrysts, and groundmass crystals. Olivine, clinopyroxene (including aegirine-augite), and Na-amphibole are found in small quantities as microphenocrysts or as groundmass microlites. Quartz is also rarely found in the groundmass, where it occurs alongside Na-amphibole near to vesicles (Imsland et al., 1977).

CHARACTERIZING THE MAGMATIC SYSTEMS: PETROGENESIS AND PRE-ERUPTIVE CONDITIONS

In this section, we apply the combined dataset gathered by this study to key topics associated with the petrogenesis of peralkaline felsic magmas within the magmatic systems of the Atlantic Ocean islands. This includes primarily compiled published datasets, but also a lesser amount of original data derived from this study, specifically pre-eruptive temperature, H_2O_{melt}, and melt viscosity estimates. Using this combined dataset, we evaluate firstly the role of fractional crystallization, crustal assimilation, and magma mixing in the formation of peralkaline felsic magmas. Second, we investigate the pre-eruptive P-T-fO_2-H_2O_{melt} conditions of the erupted peralkaline felsic magmas, applying available estimates from published studies, as well as new data derived from the application of thermo-hygrometrical models. We then go on to construct an integrated model for the physical and chemical configuration of the magma reservoirs from which the peralkaline felsic magmas are derived, and to develop an original, large-scale, schematic model which can account for the development of peralkaline felsic magmas in ocean island magmatic systems.

Petrogenesis of Atlantic Ocean Island Peralkaline Magmas

Fractional Crystallization

The majority of the peralkaline magmatic systems of the Atlantic Ocean are controlled primarily by fractional crystallization of mantle-derived, mafic magmas, with a significant portion of the fractionation history frequently taking place under shallow crustal conditions (e.g., Beier et al., 2006; Andújar et al., 2010; Sliwinski et al., 2015). This process not only controls the generation of peralkaline felsic magmas from basaltic progenitors, but also controls evolutionary trends *within* peralkaline felsic magmas, forming felsic magmas with varying degrees of peralkalinity. There exists a wide range of published studies and quantitative models which reliably recreate the compositions observed in the magmatic systems of the Atlantic, including major element, least-squares mass balance models, thermodynamic models, and trace element models (e.g., Iceland: Carmichael, 1964; Macdonald et al., 1990; Furman et al., 1992a; Sigmarsson et al., 1992; Hards et al., 2000; Prestvik et al., 2001; Martin and Sigmarsson, 2007; Azores: Widom et al., 1992; Mungall and Martin, 1995; Renzulli and Santi, 2000; Beier et al., 2006; Larrea et al., 2013, 2014a; Zanon et al., 2013; Zanon, 2015; Jeffery et al., 2016b, 2017; Canary islands: Freundt and Schmincke, 1995; Ablay et al., 1998; Neumann et al., 1999; Sliwinski et al., 2015; Tornare et al., 2016; Cape Verde: Holm et al., 2006; Kogarko, 2008; Hildner et al., 2011; Cameroon Line: Marzoli et al., 2000; Ascension Island: Harris, 1983; Kar et al., 1998; Chamberlain et al., 2016; Bouvet Island: Le Roex and Erlank, 1982; Prestvik et al., 1999; Tristan da Cunha: Le Roex et al., 1990; Harris et al., 2000; Gough Island: Le Roex, 1985; Harris et al., 2000; St. Helena: Baker, 1969; Fernando de Noronha: Weaver, 1990; Lopes and Ulbrich, 2015; Trindade: Weaver, 1990; Bongiolo et al., 2015). These are frequently supported by geochemical indicators of extensive fractionation, such as the depletion of Sr, Ba, Ti, and P, the formation of negative Eu anomalies, and the enrichment of incompatible trace elements such as Zr, Nb, Rb, and the REE (**Figures 4–6**). These features are frequent, but not ubiquitous, amongst the peralkaline rocks of the Atlantic Ocean. For example, negative Eu anomalies are not seen in the peralkaline rocks of Cape Verde, Fernando de Noronha, Trindade, or Tristan da Cunha, and are most pronounced in the rocks of Iceland, the Azores, and Ascension (**Figure 5**). This may show some correlation with the degree of silica-saturation in the erupted magmas, with the Si-oversaturated suites exhibiting the most pronounced anomalies. However, the Si-undersaturated rocks of St. Helena appear to contradict this, exhibiting a weakly developed negative Eu-anomaly. Furthermore, the pronounced troughs observed in **Figure 6** for Ba, Sr, P, and Ti are markedly less clear, or altogether absent from the peralkaline rocks of Trindade, suggesting the potential for a more complex petrogenetic regime.

Where determined, the total degree of fractionation in each case is considerable, ranging from ∼ 60% from parental OIB for felsic compositions transitional between metaluminous and mildly peralkaline, and in excess of 90% for the most extreme peralkaline compositions. For example, the strongly peralkaline (PI = 1.92–4.95) interstitial glass found within syenitic ejecta

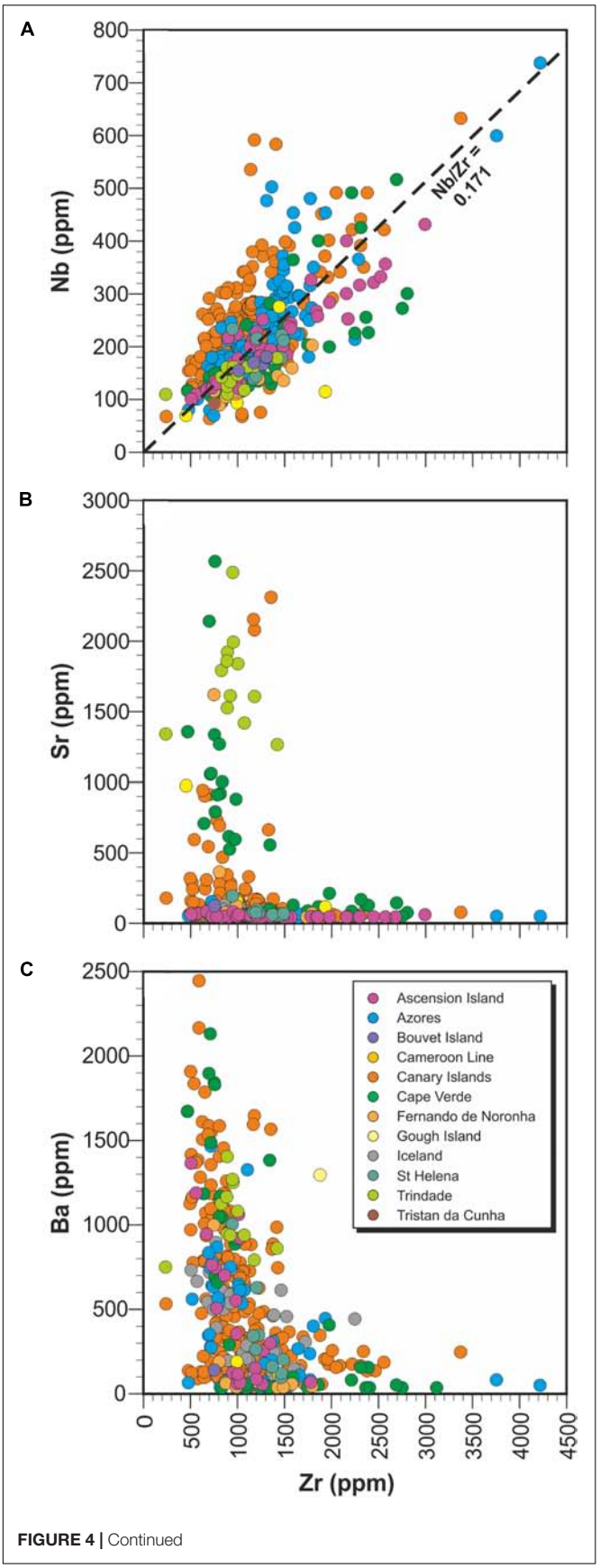

FIGURE 4 | Continued

FIGURE 4 | Bivariate plots showing published data for selected trace elements in peralkaline felsic rocks from across the Atlantic Ocean. In each plot, Zr is used as I fractionation index, with the highest Zr values assumed to reflect the most evolved compositions **(A)** Nb-Zr plot highlighting the general adherence of the data to the typical Nb/Zr ratio for OIB, which is shown as a dashed line (Sun and McDonough, 1989), **(B)** Sr-Zr plot highlighting 'enriched' Sr values at low Zr contents, and **(C)** Ba-Zr plot showing rapidly decreasing Ba trend with increasing Zr contents.

from Terceira, Azores is argued to represent the residual liquid from extreme fractionation, undoubtedly in excess of 95% from the original parental basalts (Mungall, 1993). The same author utilizes textural evidence to note that, in this instance, the glasses do not represent partial melting, as observed on Ascension (Harris and Bell, 1982). These high degrees of fractionation may effectively rule out single-stage evolutionary models due to the inherent difficulty in separating a 5% residual melt from an effectively 'locked' crystal mush (Dufek and Bachmann, 2010). As such, the volume of residual crystalline material which is contributed to the crust is debatable, and strongly influenced by the precise mechanisms of crystal-melt segregation during fractional crystallization, as well as the temporal extent of felsic peralkaline magmatism, and the potential for 'cannibalization' and recycling of such material (see below; e.g., Wiesmaier et al., 2013). Although it is logical that the volume of residual crystalline material increases with continued magmatism, the application of a more rheologically viable two-stage crystal mush extraction model may drastically reduce the volume of residual material for a given volume of fractionating magma, and therefore reduce the rate of accumulation of fusable crystal mush in the crust (*cf.* Sliwinski et al., 2015). For example, a single stage fractionation model applied to an erupted volume of 10 km^3 implies 90 km^3 of residual material has been added to the crust (assuming 90% total fractionation). By contrast, a two-stage fractionation model, with each stage assuming 60% fractionation, achieves a similar degree of fractionation in the erupted material but yields only 52.5 km^3 of residual material. As such, the volumetric ratio of residual to erupted material may be lower than implied by high degrees of fractionation, and the actual mechanisms of crystal-melt segregation may therefore impact significantly upon the viability of other magmatic processes, such as the partial melting of residual lithologies.

The results of various fractional crystallization models, as well as the predominance of alkali feldspar within the peralkaline rocks themselves, indicate that the final portion of the liquid line of descent, both in the Atlantic systems and globally, is characterized by alkali feldspar crystallization, which acts to drive the melt toward more peralkaline compositions (Bailey and Schairer, 1964; Thompson and MacKenzie, 1967; Nicholls and Carmichael, 1969). Additional phases which are common in small quantities and which play a secondary (and increasingly important as differentiation continues) role during the differentiation of peralkaline felsic melts include fayalitic olivine, clinopyroxene (which may be augitie or aegirine/aegirine-augite), Ti-magnetite, ilmenite, sodic plagioclase, kaersutite, apatite, biotite, feldspathoid group

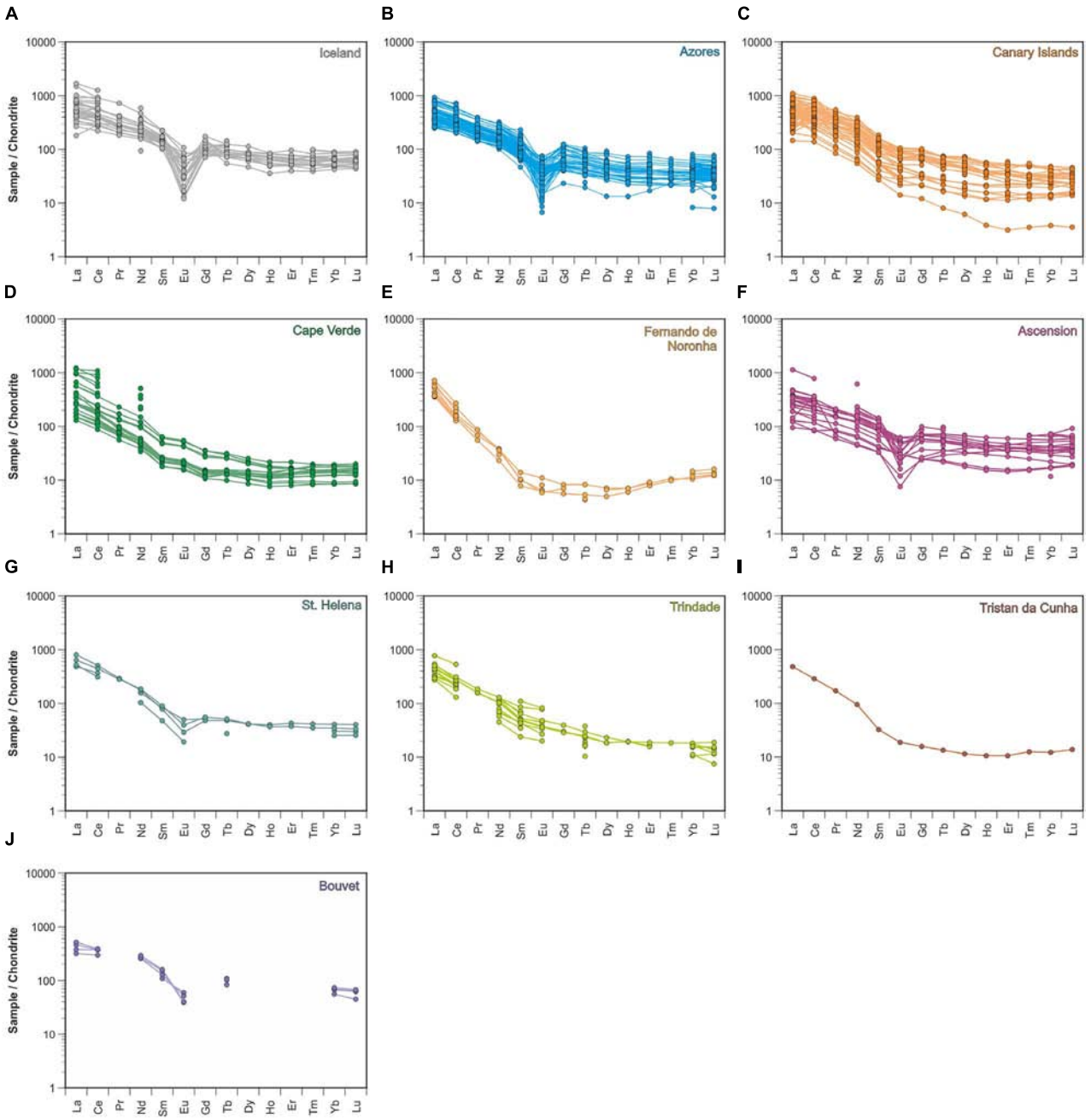

FIGURE 5 | Published chondrite-normalized (Sun and McDonough, 1989) REE profiles for **(A)** Iceland, **(B)** the Azores, **(C)** the Canary Islands, **(D)** Cape Verde, **(E)** Fernando de Noronha, **(F)** Ascension, **(G)** St. Helena, **(H)** Trindade, **(I)** Tristan da Cunha, and **(J)** Bouvet.

minerals, aenigmatite, and Na-amphiboles (e.g., Ablay et al., 1998; Kar et al., 1998; Scaillet and Macdonald, 2001; Kogarko, 2008; Macdonald et al., 2011; Zanon, 2015). The onset of peralkalinity may occur at highly variable melt SiO_2 contents (**Figure 3**), and is favored by low pressure conditions (Bailey, 1974). Thus, the development of a shallow crustal reservoir in which magmas can evolve via fractional crystallization is paramount to the development of peralkaline magmatism. In fact, the transfer of magmas from lower crustal or mantle depths into a shallow crustal reservoir, a process invoked at many Atlantic Ocean island systems (see below), may initiate plagioclase fractionation, acting as the trigger for the development of peralkaline magmas.

Crustal Assimilation and Partial Melting

Although seemingly of second order importance when compared to fractional crystallization, the role of crustal assimilation has also been recognized in various Atlantic magmatic systems (e.g.,

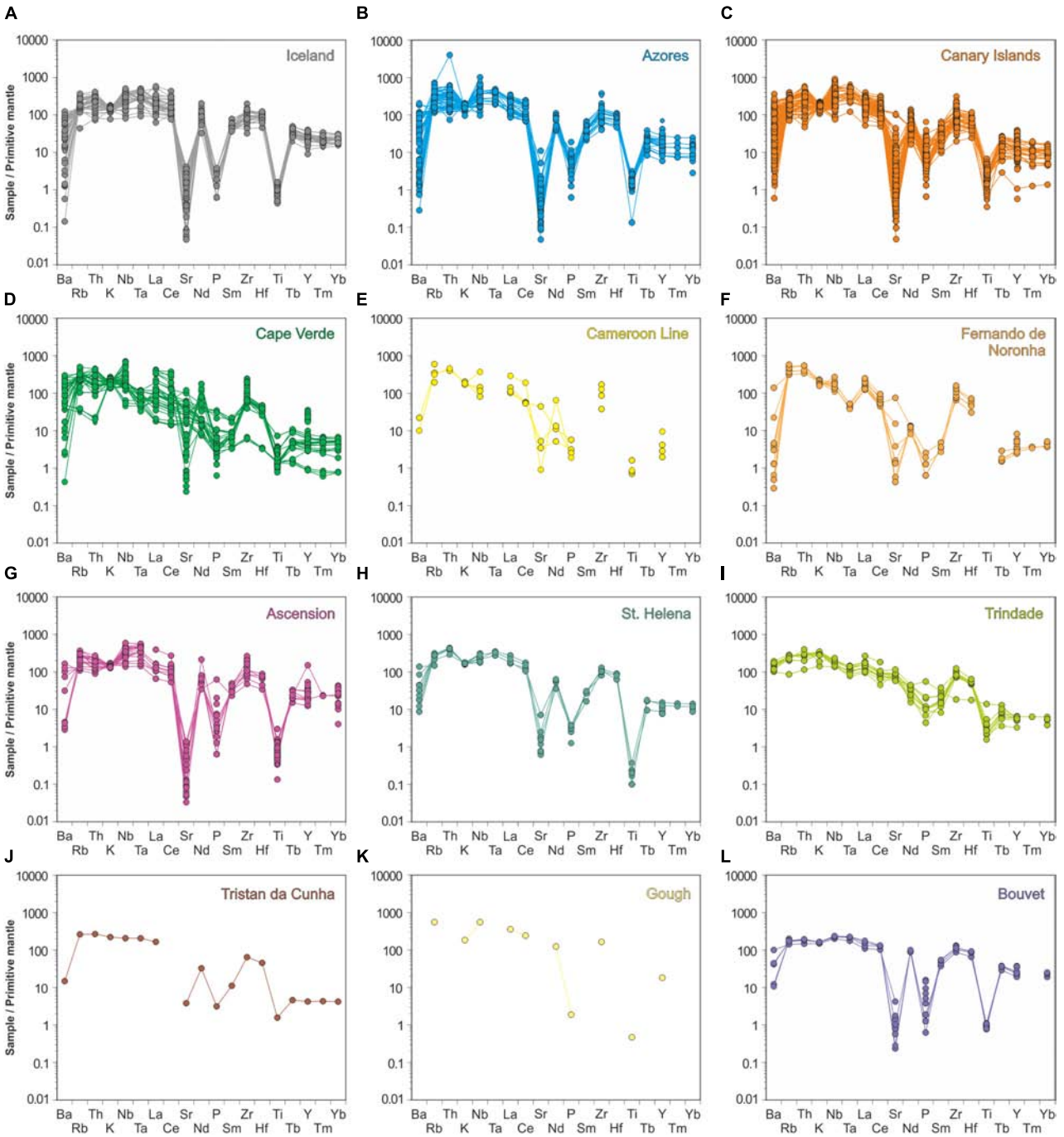

FIGURE 6 | Published primitive mantle-normalized (Sun and McDonough, 1989) multi-element profiles for **(A)** Iceland, **(B)** the Azores, **(C)** the Canary Islands, **(D)** Cape Verde, **(E)** the Cameroon Line, **(F)** Fernando de Noronha, **(G)** Ascension, **(H)** St. Helena, **(I)** Trindade, **(J)** Tristan da Cunha, **(K)** Gough, and **(L)** Bouvet.

Azores: Nielsen et al., 2007; Genske et al., 2013; Madeira: Widom et al., 1999; Canary Islands: Thirlwall et al., 1997; Widom et al., 1999; Troll and Schmincke, 2002; Hansteen and Troll, 2003; Cape Verde: Jørgensen and Holm, 2002; Doucelance et al., 2003; Ascension: Harris et al., 1982; Weis et al., 1987; Kar et al., 1998; Tristan da Cunha: Harris et al., 2000). Crustal assimilation may occur at any point within the system, and may therefore involve the assimilation of hydrothermally altered oceanic crust (e.g., Doucelance et al., 2003; Genske et al., 2013, marine sediments (e.g., Thirlwall et al., 1997; Widom et al., 1999), or previously intruded lithologies and crystal mush (e.g., Harris and Bell, 1982; Jørgensen and Holm, 2002). Nevertheless, there remain examples where crustal contamination has been essentially ruled out or merely inferred as a possibility (e.g.,

Canary Islands: Hoernle, 1998; Cameroon Line (Oceanic Sector): Déruelle et al., 2007; Bouvet Island: Imsland et al., 1977; Gough Island: Harris et al., 2000; Trindade: Siebel et al., 2000), although in some cases this may simply reflect the comparative lack of data for some of the Atlantic islands. Considering the inevitable accumulation of felsic crystalline residues in the upper crust during the establishment and development of a stable peralkaline magma reservoir, it follows that felsic lithologies must represent an increasingly viable and important contaminant during the peralkaline stage of magma evolution. These may take the form of accumulated crystal mush or solidified intrusive bodies of peralkaline felsic magma. Direct evidence for this process has been identified on Ascension, where glass-bearing syenitic inclusions in a trachyandesitic lava flow are interpreted to reflect partial melting of subvolcanic intrusive lithologies (Harris and Bell, 1982). Further evidence exists on São Miguel, Azores, where Snyder et al. (2004) identified the contamination of peralkaline trachytes with seawater-altered syenites, and in the Canary Islands, where recycling of subvolcanic differentiated rocks has been proposed on Tenerife (Ablay et al., 1998; Wolff et al., 2000; Sliwinski et al., 2015; Turner et al., 2017). This may be exemplified by the increase in $^{87}Sr/^{86}Sr$ values (and potential decoupling of Sr and Nd isotopic values) observed in the felsic rocks of the Azores, the Canary Islands, and Ascension, and possibly Iceland (**Figures 3**, **7**). In some cases, the melting of subvolcanic felsic rocks is sufficiently advanced that the generated melts can accumulate and be erupted (Wiesmaier et al., 2013), or accumulate into compositionally distinct layers within the magma reservoir (Wolff et al., 2015). Sliwinski et al. (2015) demonstrated that minor discrepancies in their efforts to model evolved melt compositions could be accounted for by recycling authigenic cumulates, effectively adding alkali feldspar back into the melt.

Despite the generally limited role of crustal assimilation in the generation of peralkaline silicic magmas in the Atlantic, Iceland represents a clear example where both fractional crystallization and bulk melting of the crust have led to the formation of peralkaline felsic magmas (Martin and Sigmarsson, 2007). The silicic magmas belonging to Iceland's central rift zone are somewhat unique in the Atlantic because the partial melting of hydrated metabasaltic crust has been invoked as the primary process responsible for their formation (e.g., Sigurdsson, 1977; Nicholson et al., 1991; Sigmarsson et al., 1991; Jónasson, 1994; Bindeman et al., 2012). By contrast, the peralkaline felsic magmas associated with central volcanoes peripheral to the rift are generally considered to be generated by fractional crystallization (e.g., Carmichael, 1964; Macdonald et al., 1990; Furman et al., 1992a; Prestvik et al., 2001; Martin and Sigmarsson, 2007), suggesting that this somewhat unusual occurrence of partial melt-derived peralkaline magmas is the result of variation in the local

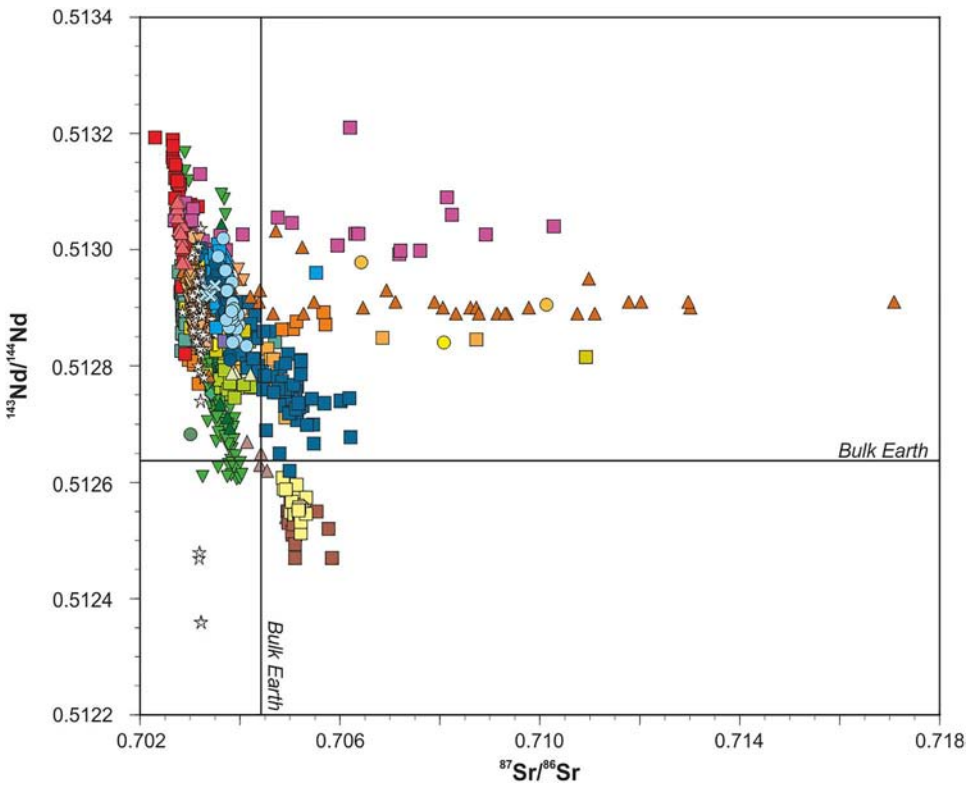

FIGURE 7 | Sr-Nd variation diagram for the magmatic systems of the Atlantic Ocean. All compositions are included, ranging from mafic to felsic. Symbols are as given in **Figure 3**. For clarity, a single outlier derived from the Fernando de Noronha archipelago is not shown ($^{87}Sr/^{86}Sr$ = 0.73499, $^{143}Nd/^{144}Nd$ = 0.51284; Gerlach et al., 1987).

geothermal gradient, which is strongly influenced by the rift and the underlying mantle plume (Martin and Sigmarsson, 2007, 2010). Nevertheless, this model is not without exception (e.g., Askja volcano; Sigurdsson and Sparks, 1981; Macdonald et al., 1987; Kuritani et al., 2011).

Magma Mixing/Mingling

Although they are not ubiquitous, the occurrence of pre-eruptive magma mixing/mingling processes is well documented for many of the Atlantic Ocean islands (e.g., Iceland: Sparks et al., 1977; McGarvie et al., 1990; Azores: Storey, 1981; Jeffery et al., 2016b, 2017; D'Oriano et al., 2017; Madeira: Klügel and Klein, 2006; Canary Islands: Wolff, 1985; Araña et al., 1994; Edgar et al., 2002; Cape Verde; Holm et al., 2006; Eisele et al., 2016; Ascension: Weaver et al., 1996; Gough Island: Le Roex, 1985; Bouvet Island: Prestvik et al., 1999). These mixing processes are diverse in their end-members, and include direct mixing between mafic and felsic magmas (e.g., Araña et al., 1994; Lopes and Ulbrich, 2015), mixing between felsic magmas (e.g., Troll and Schmincke, 2002; Bryan, 2006; Pimentel et al., 2015), mingling of melt and crystalline mush (i.e., mush remobilisation) (e.g., Weaver et al., 1996; Sliwinski et al., 2015; D'Oriano et al., 2017; Jeffery et al., 2017), and small-scale mixing of partially melted contaminants and volumetrically superior melt (e.g., Harris and Bell, 1982; Turner et al., 2017). In peralkaline magmatic systems other than those of the Atlantic Ocean, the mixing of mafic and felsic magmas is proposed as a process responsible for the formation of intermediate magmas, which are often scarce compared to mafic and felsic compositions (e.g., Pantelleria: Ferla and Meli, 2006; Gioncada and Landi, 2010). The paucity of intermediate magma compositions can be explained in a variety of ways, including the development of a silicic density barrier in the upper portions of a magma reservoir via sidewall crystallization (e.g., Turner and Campbell, 1986), or the high viscosity of crystal-rich intermediates (e.g., Mungall and Martin, 1995). Considering the common but not ubiquitous presence of bimodal magmatism throughout the Atlantic (Baker, 1974, **Figure 3**), and the recognition of hybridized magmas at a number of Atlantic volcanic centers (e.g., Iceland: Hards et al., 2000; Azores: Storey, 1981; Moore, 1990; Canary Islands: Wiesmaier et al., 2011), it seems likely that magma mixing plays some role in peralkaline magmatic systems throughout the Atlantic Ocean.

In some cases, mixing processes have been recognized on petrographic grounds, either through the identification of relict crystal populations which exhibit clear disequilibrium with their host magma, or through mineralogical evidence such as chemical zonation. This often takes the form of relict mafic phases such as Mg-rich olivine or clinopyroxene within felsic magmas, or relict felsic phases such as biotite in mafic or intermediate magmas (i.e., mafic-felsic mixing; e.g., Schmincke, 1969; Wolff, 1985; Storey et al., 1989; McGarvie et al., 1990; Neumann et al., 1999; Jeffery et al., 2017), or alternatively heavily resorbed feldspars within felsic magmas (i.e., felsic-felsic mixing; e.g., Troll and Schmincke, 2002). Additionally, partially resorbed and/or disaggregated glomerocrysts may be found, which are interpreted to represent portions of a remobilised crystal mush entrained within the erupted melt either during or prior to eruption (e.g., Sliwinski et al., 2015). Bulk rock data also provide evidence for mixing processes, and potentially the remobilisation of crystal mush. For example, the enrichment of elements such as Sr and Ba has been utilized to identify mixing between two variably evolved felsic magma (i.e., feldspar assimilation; e.g., Storey et al., 1989). This process may be responsible for the pronounced enrichments of these elements in the less evolved peralkaline magmas (demonstrated here by lower Zr contents; **Figures 4B,C**), which often exceed the maximum limits of fractional crystallization models (e.g., <1,000 ppm).

Pre-eruptive Conditions

In this section, we summarize available published estimates of pre-eruptive intensive variables representative of the felsic peralkaline magma systems of the Atlantic Ocean. We include magmas of peralkaline affinity within this dataset, as these represent a precursory evolutionary stage immediately prior to the onset of peralkalinity, which are considered to reflect the same conditions as their peralkaline equivalents. In some instances, this genetic link is emphasized by the gradual shift in peralkalinity index from peralkaline affinity to peralkaline within a single eruptive deposit. Where possible, these data are supplemented by newly determined estimates, derived from the application of the alkali feldspar-melt thermometer of Putirka (2008), and the alkali feldspar-melt hygrometer of Mollo et al. (2015) to previously published chemical data. In each case, the Kd_{Ab-Or} equilibrium test proposed by Mollo et al. (2015) was applied, allowing a single suitable liquid composition to be selected for each case. Input pressure values were set at 100 MPa, and it was observed that a variation of 0.1 GPa led to a change in temperature of only 0.1°C, suggesting that the thermometer is not significantly influenced by variations in pressure. The 1σ standard error of estimate (SEE) associated with the thermometer is ±23°C, whereas the SEE associated with the hygrometer is ± 0.75 wt. %. These models are particularly valuable in peralkaline systems due to the dominance of alkali feldspars during the later stages of fractionation, and were freshly applied in this study to existing chemical data for the following locations: the Azores (Storey, 1981; Renzulli and Santi, 2000), Canary Islands (Troll and Schmincke, 2002; Rodriguez-Losada and Martinez-Frias, 2004; Bryan, 2006; Jutzeler et al., 2010; Clay et al., 2011), Ascension (Chamberlain et al., 2016), Trindade (Siebel et al., 2000), Gough Island (Le Roex, 1985), and Bouvet Island (Imsland et al., 1977).

Temperature

Pre-eruptive temperatures for the combined dataset exhibit considerable range, extending from around 1,050°C for magmas with peralkaline affinity (e.g., the trachytes of Faial; Pimentel et al., 2015; the phonolites of the Granadilla eruption, Tenerife; Bryan, 2006), to ∼ 700°C for mildly to strongly peralkaline magmas (**Figure 8**). This range extends down to approximately 600°C if autolithic peralkaline syenite clasts, considered to

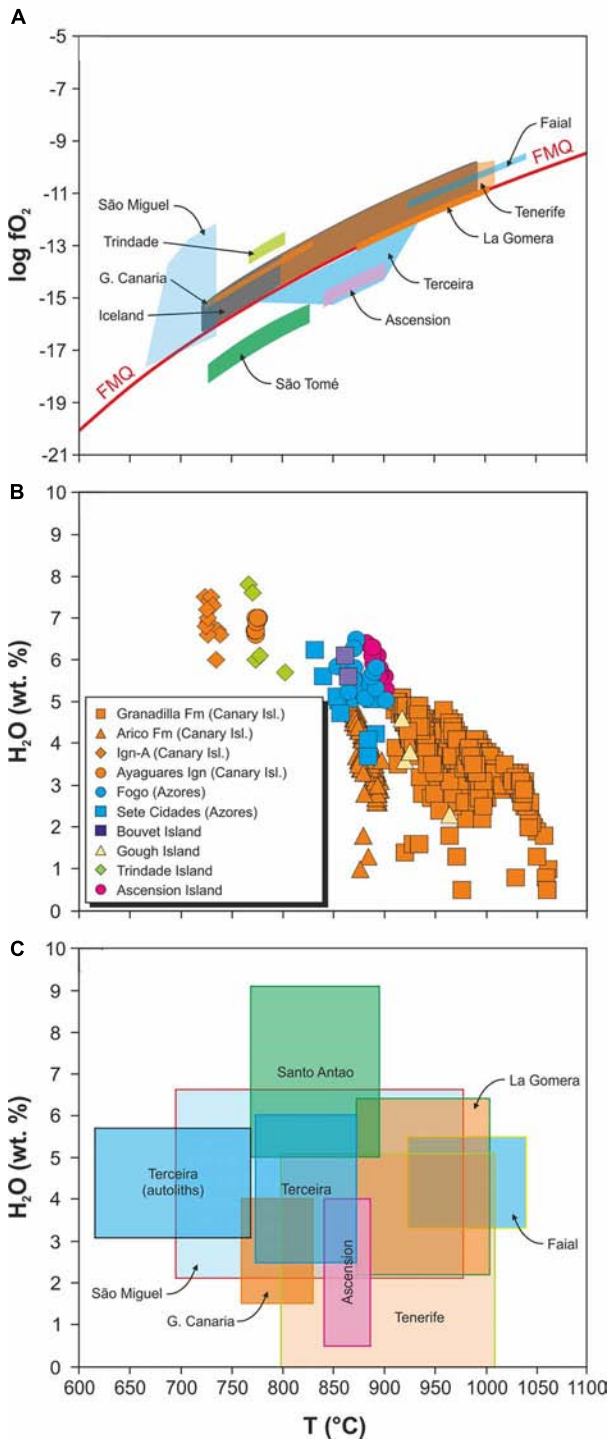

FIGURE 8 | Summarized temperature, fO_2, and H_2O_{melt} estimates for Atlantic Ocean peralkaline magmas (including those with peralkaline affinity). **(A)** Temperature–fO_2 estimates derived from published data. **(B)** Temperature-H_2Omelt contents derived via alkali feldspar-melt thermo hygrometry (Putirka, 2008; Mollo et al., 2015), calculated in this study using the data of Imsland et al. (1977), Storey (1981), Le Roex (1985), Renzulli and Santi (2000), Siebel et al. (2000), Troll and Schmincke (2002), Rodriguez-Losada and Martinez-Frias (2004), Clay et al. (2011). **(C)** Total ranges in temperature and *(Continued)*

FIGURE 8 | Continued
H_2O_{melt} based upon published estimates obtained via methods including two-oxide thermometry (Ablay et al., 1998; Troll and Schmincke, 2002; Rodriguez-Losada and Martinez-Frias, 2004; Bryan, 2006; Dávila-Harris et al., 2013; Zanon and Frezzotti, 2013; Pimentel et al., 2015; Chamberlain et al., 2016; Eisele et al., 2016; Jeffery et al., 2016b, 2017).

represent the near-complete solidification of peralkaline magmas, are included (e.g., Jeffery et al., 2017). There is a logical, broad correlation between temperature and peralkalinity, with the most peralkaline magmas recording the coolest temperatures. Temperature estimates derived from two-oxide and other models define considerable ranges for each volcanic island for which there are data. The data derived via alkali feldspar-melt models cluster within the broad range of 1,050–850°C, and include data from the Azores (Jeffery et al., 2016b, 2017, and calculated using the data of Storey, 1981; Renzulli and Santi, 2000), the Canary Islands (calculated in this study using the data of Troll and Schmincke, 2002; Rodriguez-Losada and Martinez-Frias, 2004; Bryan, 2006; Jutzeler et al., 2010; Clay et al., 2011), Bouvet Island (calculated in this study using the data of Imsland et al., 1977), Gough Island (calculated in this study using the data of Le Roex, 1985), and Trindade (calculated in this study using the data of Siebel et al., 2000). Specifically, the estimates from Gran Canaria (Canary Islands), Trindade, and a single ignimbrite formation from Terceira, Azores (GVI, Jeffery et al., 2017), lie at lower values of around 700–850°C. It is noteworthy that temperature estimates derived from alkali feldspar-melt models appear to record generally higher temperature values than the frequently applied two-oxide models, which likely reflects the comparatively earlier crystallization of alkali feldspar, as well as the rapid re-equilibration timescales of coexisting Fe-Ti oxides (e.g., Gardner et al., 1995; Venezky and Rutherford, 1999; Pimentel et al., 2015), meaning that the lower temperatures recorded by Fe-Ti oxide phases reflect the final pre-eruptive magma system and/or syn-eruptive conditions within the plumbing system.

Pressure

The results of numerous studies have indicated that peralkaline magmas from such classic peralkaline volcanic centers as the East African Rift System and Pantelleria originate from magma storage zones in the shallow crust (e.g., Mahood and Baker, 1986; Avanzinelli et al., 2004; Peccerillo et al., 2007; Macdonald, 2012). Available data for the Atlantic Ocean suggest that the Atlantic island peralkaline magmatic centers are similarly characterized by the presence of a shallow crustal magma storage zone. Pre-eruptive pressure estimates for peralkaline magmas from the islands of São Miguel and Terceira (Azores), derived from thermodynamic modeling and water solubility constraints, lie between 122 and 156 MPa, and 80 and 135 MPa, respectively (Beier et al., 2006; Jeffery et al., 2016b, 2017). These values correspond to depths of ∼ 3 km, placing them within the upper crust (crustal thickness = ∼ 15 km; Beier et al., 2006). The peralkaline magmas of Graciosa are also suggested, on the basis of MELTs modeling, to have formed under low pressure conditions (1–3 km; Larrea et al., 2014a). Peralkaline magmas from Gran

Canaria and Tenerife are estimated via geobarometry to have been stored at pressures between 130 and 270 MPa (Fe-Ti oxide – ferrosilite-based barometry; Crisp and Spera, 1987; amphibole-based barometry; Troll and Schmincke, 2002; clinopyroxene-melt barometry; Aulinas et al., 2010), and ∼ 150 MPa (water solubility constraints; Ablay et al., 1995; clinopyroxene-melt barometry and fluid inclusion barometry; Klügel et al., 2005; phase equilibrium experiments; Andújar et al., 2008, 2013), respectively. Scarce available pressure estimates derived from QUILF thermobarometry for peralkaline magmatism in the oceanic sector of the Cameroon Line may fall in line with these estimates (e.g., 100 MPa; Mbowou et al., 2013). Eisele et al. (2016) utilized clinopyroxene-melt barometry to report somewhat greater values of 200–400 MPa for the magma reservoirs which produced the partially peralkaline Cão Grande Formation on Santo Antão (Cape Verde), equating to depths of 7–16 km. Similarly, the pre-eruptive conditions of an eruption which produced a prominent fall deposit (with peralkaline affinity) on Ascension Island are estimated via melt inclusion barometry to have been between 216 and 250 MPa (Chamberlain et al., 2016), equating to the lower crust (∼ 8.5 km). In contrast to the evolved, peralkaline magmas, the mafic magmas from which they are most likely derived typically provide a wide range of pressure estimates, derived via clinopyroxene-melt barometry and fluid inclusion barometry, extending from shallow crustal values to the upper mantle, and often concentrated around the crust-mantle boundary (e.g., Azores: Zanon and Frezzotti, 2013; Zanon et al., 2013, Canary Islands: Hansteen et al., 1998; Klügel et al., 2005; Stroncik et al., 2009, Cape Verde: Hildner et al., 2011, 2012; Mata et al., 2017, Madeira: Schwarz et al., 2004; Klügel and Klein, 2006, Tristan da Cunha: Weit et al., 2017).

Overall, there is a general trend in which the more evolved the magmas become, the shallower their respective magma reservoirs are located. Magma reservoirs that produced peralkaline felsic magmas are generally located within at depths of around 2–4 km. The somewhat less-evolved magmas with peralkaline affinity tend to be stored at deeper depths; for example, the strongly zoned fall deposit on Ascension (PI = 0.55–1.00) was stored at lower crustal depths of approximately 8.5 km (Chamberlain et al., 2016). Similarly, a trachyandesitic lava flow erupted in 1961 on Tristan records depths of 6–10 km (Weit et al., 2017). The Cão Grande Formation of Santo Antão may represent an exception to this, in which two metaluminous to peralkaline magma bodies (PI = 0.70–1.12) apparently existed at lower crustal levels (7–16 km) (Eisele et al., 2015, 2016). However, these estimates were derived via clinopyroxene-melt barometry, which may record higher pressure values due to the potentially dominant crystallization of clinopyroxene in the lower crust, and its subsequent retention in upper crustal evolved magmas (*cf.* Klügel et al., 2005; Jeffery et al., 2016b). Furthermore, the errors associated with currently employed clinopyroxene-based barometers are often high (e.g., ±160 MPa, Putirka, 2008; ± 115 MPa, Masotta et al., 2013), limiting their resolution at shallow depths. The described trend is only applicable to the more evolved compositions of each system; mafic magmas are shown to occur at all depths.

Redox Conditions

The determination of redox conditions in peralkaline magmas is often complicated by the scarcity of rocks in which two coexisting oxide phases are present. Available estimates for Atlantic peralkaline rocks are highly variable, even within individual island systems. Peralkaline ignimbrites on Terceira evolved under relatively reducing conditions, ranging from 1 to 2 log units below the Fayalite-Magnetite-Quartz buffer (FMQ −1 to FMQ −2; Jeffery et al., 2017), whereas similarly peralkaline rocks from São Miguel yield redox conditions ranging from FMQ +4 to FMQ −2 (Wolff and Storey, 1983; Wolff et al., 1990; Renzulli and Santi, 2000; Jeffery et al., 2016b). The trachytes of Faial with peralkaline affinity record conditions close to FMQ +0.7 (Pimentel et al., 2015). The peralkaline rocks of the Canary Islands generally formed under more restricted conditions, ranging from FMQ +1 to FMQ (Gran Canaria: Troll and Schmincke, 2002, La Gomera: Rodriguez-Losada and Martinez-Frias, 2004, Tenerife: Ablay et al., 1998; Bryan, 2006; Dávila-Harris et al., 2013). Available estimates for São Tomé are similar to those of Terceira, ranging from FMQ −1 to FMQ −2 (Mbowou et al., 2013), whilst those of Ascension extend to slightly more reducing conditions of FMQ −1.8 to FMQ −2.4 (Chamberlain et al., 2016). Data from Ryabchikov and Kogarko (1994) and Marques et al. (1999) constrain the redox conditions of Trindade to FMQ +1.5 to FMQ +2, which may contribute to the lack of a negative Eu-anomaly described above (**Figure 5**). However, the comparatively reducing estimates for São Tomé, coupled with the similar absence of a negative Eu-anomaly, imply that redox conditions alone cannot account for this feature. The redox conditions of Madeira, Bouvet, Tristan da Cunha, Gough, St. Helena, and Fernando de Noronha are not well constrained.

Pre-eruptive Water Contents

The peralkaline magmas of the Atlantic Ocean are invariably hydrous, with a total range in predicted H_2O_{melt} values of 1.5–9.1 wt. % (e.g., Wolff and Storey, 1983; Wolff et al., 1990; Ablay et al., 1998; Troll and Schmincke, 2002; Pimentel et al., 2015; Eisele et al., 2016; Jeffery et al., 2016b, 2017; D'Oriano et al., 2017; this study; **Figures 8B,C**). The H_2O_{melt} values derived from alkali feldspar-melt hygrometry exhibit a similar range, reaching maximum values of ∼ 8 wt. %. The majority of estimates are concentrated within a smaller range of 2–6 wt. %, with values of up to 8 wt. % being limited to a small number of compositions specifically from Gran Canaria (Canary Islands), Trindade, and a single ignimbrite formation from Terceira, Azores (GVI, Jeffery et al., 2017). Overall, H_2O_{melt} values exhibit a negative correlation with temperature, with the most hydrous magmas also reporting the lowest temperatures. As observed with temperature estimates, H_2O_{melt} also correlates broadly with peralkalinity, with the most strongly peralkaline magmas recording the highest water contents (e.g., Ignimbrite A, Gran Canaria, Canary Islands; Troll and Schmincke, 2002), and the magmas of peralkaline affinity recording the lowest H_2O_{melt} values (e.g., the Granadilla eruption, Tenerife; Bryan, 2006). The observed increase in H_2O_{melt} values with decreasing temperature suggest that H_2O_{melt} concentration is controlled

by fractional crystallization, becoming enriched in the melt due to the crystallization of a largely anhydrous mineral assemblage.

TOWARD A MODEL FOR THE PERALKALINE MAGMATIC SYSTEMS OF THE ATLANTIC OCEAN

In the following section, we utilize the petrogenetic processes and pre-eruptive conditions defined above to construct two models which account for the features of Atlantic Ocean Island peralkaline systems. The first provides a general architecture for the magma reservoirs from which the peralkaline felsic magmas of the Atlantic Ocean islands are erupted, and is based upon published data and models, as well as original melt viscosity and crystal-settling calculations undertaken during this study. The second model utilizes a variety of published data and models, and takes a wider view, considering the crustal structure and temporal evolution of the magma plumbing systems which may or may not lead to the formation and eruption of peralkaline felsic magmas.

Zoned Magma Reservoirs

There is strong evidence to suggest that the upper crustal magma reservoirs in which ocean-island, peralkaline felsic magmas (and their metaluminous equivalents) are stored are compositionally zoned. This pre-eruptive zonation may be recognized by major and/or trace element bulk geochemistry, mineral chemistry, phenocryst content, or thermobarometry (*cf.* Macdonald, 2012), and may be gradational or sharply defined. For example, Ignimbrite 'A,' found on Gran Canaria (Canary Islands) exhibits a chemical transition from comendite at the base of the deposit, to comparatively phenocryst-rich trachyte at the top (Troll and Schmincke, 2002). Similar features are observed in other peralkaline deposits of the Canary Islands, such as Ignimbrite 'TL' (Gran Canaria, Sumner and Branney, 2002), the Ayagaures Ignimbrite (Gran Canaria, Jutzeler et al., 2010), and the deposits of Las Cañadas, Tenerife (Wolff and Storey, 1984; Wolff et al., 1990). A chemically zoned fall deposit on Ascension exhibits similar zonation, ranging from trachyte with peralkaline affinity at the base of the deposit, to basaltic trachyandesite at the top (Chamberlain et al., 2016). In the Azores, the peralkaline ignimbrites of Terceira exhibit more cryptic chemical zonation, with relatively uniform major element compositions, but often considerable variations in incompatible trace elements (e.g., 900–1,350 ppm Zr in the Caldeira-Castelinho Ignimbrite Formation, or 700–2,250 ppm Zr in the Vila Nova–Fanal Ignimbrite Formation; Gertisser et al., 2010). In this case, the zonation was suggested to result from between 15 and 50% fractionation within the peralkaline felsic compositions (Jeffery et al., 2017). This zonation is also observed in the results of thermometry and hygrometry, where individual eruptions can exhibit variation in temperature of $>50^{\circ}C$ and >2 wt. % H_2O_{melt} (Jeffery, 2016; D'Oriano et al., 2017). On São Miguel, the shallow magma reservoir of Furnas volcano is interpreted to have repeatedly developed a similarly cryptically zoned reservoir in response to at least 10 tapping events over a period of less than 5,000 years (Jeffery et al., 2016b). The Cão Grande Formation of Santo Antão (Cape Verde) also exhibits examples of pre-eruptive zonation, with minor variation in major elements, as well as upward (in the deposit) increases in phenocryst content and estimated temperature (up to 100°C difference) (Eisele et al., 2016). New hygrometric estimates for the Arico ignimbrite, using the data of Clay et al. (2011), indicate pronounced H_2O_{melt} zonation in the underlying magma reservoir, with a range of $\sim$ 4 wt. %.

Although the upward, gradational transition from more to less evolved deposits (representing the inverse within the original magma reservoir) appears to be the most common form of zonation, this is not always the case. For example, the Montaña Reventada lava flow on Tenerife (Canary Islands) exhibits a sharp interface between basanite and phonolite close to the transition to peralkalinity (Wiesmaier et al., 2011). However, in this instance these authors attribute this to the propagation of a basanitic dyke through an already-present phonolitic magma reservoir, citing the lack of obvious interaction between the two magmas as evidence for the short timescales between initial contact and eruption. Another example of potentially atypical zonation may be found in the Upper Furnas Group (Furnas volcano, São Miguel, Azores), where pronounced changes in trace element concentrations are observed between the early pumice falls and terminal lava domes of two sub-plinian eruptions of mildly peralkaline trachytes, suggesting that a sharp, compositional contact may have been present in the pre-eruptive reservoir (Jeffery et al., 2016b). The Granadilla eruption of Tenerife also exhibits complex, cryptic zonation, with a transition from reverse- to normal-zoning marked by trace element concentrations and phenocryst assemblages (Bryan, 2006). The same eruption also exhibits considerable variation in pre-eruptive temperature ($>100^{\circ}C$) and water content (>3 wt. %).

The development of zonation is a common feature of peralkaline magma systems, having been recognized not only in the studies described above, but also at many other peralkaline centers worldwide (e.g., Pantelleria**:** Mahood and Hildreth, 1986; Civetta et al., 1998; the East African Rift**:** Gibson, 1970; Leat, 1984; Macdonald et al., 1994; Peccerillo et al., 2003; Rogers et al., 2004; Marshall et al., 2009; the United States: Novak and Mahood, 1986; Parker and White, 2008). Macdonald (2012) noted that the degree of zonation in a number of individual deposits from Pantelleria, Gran Canaria, the United States, the East Africa Rift, and Mexico showed considerable variation and no clear correlation with eruptive volume, suggesting that magma reservoir geometry, temporal variation, or melt rheology could instead play a role. Ultimately, the mechanisms that are frequently considered to play a role in the formation of pre-eruptive zonation are as diverse as the varieties of zonation themselves, and include fractional crystallization, crystal settling, sidewall crystallization, and crystal mush extraction (see Wolff et al., 2015 and references therein for a detailed review). In particular, the same authors utilize the crystal mush extraction model to advocate the potential role of remelting of cumulates as a means of generating compositional zonation, whereby fusible cumulates are remelted during a replenishment

event, which contributes heat without matter transfer. This leads to the generation of felsic melt with very similar major element geochemistry to the overlying cupola, but with notably different trace element geochemistry and water content, in an essentially closed system process. In addition to reconciling the seemingly contrary evidence for both fractional crystallization and thermal rejuvenation, this model also accounts for the frequently identified Ba-rich magmas of peralkaline magmatic systems, which are traditionally ascribed to the development of a feldspar-rich layer at the interface between metaluminous and peralkaline magmas within a reservoir, due to the efficiency of crystal settling (e.g., Macdonald et al., 1994; Troll and Schmincke, 2002; Sumner and Wolff, 2003; Macdonald, 2012).

Magma Rheology

The rheological behavior of peralkaline felsic melts is recognized to be distinct relative to metaluminous and peraluminous melts, due primarily to the decrease in viscosity that results from the presence of excess alkalis (e.g., Bottinga and Weill, 1972; Shaw, 1972; Dingwell et al., 1998; Di Genova et al., 2013). This effect is enhanced by the abundance of volatiles in peralkaline magmas, primarily H_2O, but also F, which substitutes for bridging ions (e.g., Wyllie and Tuttle, 1961; Manning, 1981; Dingwell et al., 1985; Lange, 1994; Whittington et al., 2001; Giordano et al., 2004). This reduction in viscosity undoubtedly plays a role in the syn-eruptive behavior of peralkaline felsic magmas (e.g., Schmincke, 1974; Stevenson et al., 1993; Sumner and Branney, 2002), but also has significant implications for pre-eruptive processes. For example, fractional crystallization has been demonstrated to be the primary process of differentiation in Atlantic Ocean peralkaline magmatic systems (see above). This indicates that one or more processes of two-phase flow can operate efficiently throughout the system, allowing crystals and melt to be segregated. Classic models for two phase flow (e.g., crystal settling, Bowen, 1928) have been challenged in recent years, often due to the recognition of the difficulties of two-phase flow in voluminous, high viscosity, yet crystal-poor metaluminous felsic magmas, leading to the concept of the crystal mush extraction model (e.g., Bachmann and Bergantz, 2004; Hildreth, 2004). Although such models are highly attractive, due in no small part to their ability to account for many petrological features observed in felsic magmatic systems, their applicability is not universal. For example, Streck (2014) highlighted several case studies, including 'hot and dry' (or A-type) and calc-alkaline rhyolites and granites, in which geochemical compositions of inferred crystal mush and extracted melts were incompatible. Additionally, Macdonald (2012) noted that the application of such models to peralkaline felsic systems may be hindered by the lack of evidence for a crystal mush (i.e., erupted crystal-rich intermediate magmas or 'monotonous intermediates,' Hildreth, 1981, *cf.* Sliwinski et al., 2015). Macdonald et al. (1995, 2008) noted that the rarely erupted intermediate composition magmas of both Silali volcano and the Olkaria volcanic complex, Kenya, were similarly crystal poor to the erupted felsic magmas, suggesting that the presence of an intermediate crystal mush from which felsic magmas are extracted is unlikely (Macdonald, 2012).

To evaluate the efficiency of crystal settling in the low viscosity peralkaline magmas of the Atlantic Ocean, we applied the model of Giordano et al. (2006) to determine representative pre-eruptive melt viscosity values for each of the thirteen case studies described above. This model has been calibrated for a wide range of magma compositions and has been shown by experimental work to be able to reproduce melt viscosity to within <0.2 log units (Vona et al., 2011). For each center, two viscosity values were calculated on a crystal-free basis: one using a melt composition with the highest peralkalinity index, and one representative of melt compositions that have just crossed the boundary into peralkaline compositions (i.e., with a peralkalinity index in excess of, but as close as possible to, one). In each case, the most peralkaline composition was calculated using the highest available pre-eruptive H_2O_{melt} value and lowest suitable temperature value, and the least peralkaline composition was calculated with the lowest available value for water and the highest suitable temperature estimate. Where pre-eruptive H_2O_{melt} estimates were not available, the lowest and highest H_2O_{melt} values were set to 4 and 6 wt. %, respectively (e.g., Gough Island, Fernando de Noronha). Where temperature estimates were not available, a value of 900°C was selected for the lowest peralkalinity melt, and a value of 800°C was applied for the highest peralkalinity melt. For Tristan da Cunha, a single, mildly peralkaline magma composition was available, allowing the calculation of only a single viscosity value, assuming 6 wt. % H_2O_{melt} and a temperature of 900°C. The effects of additional volatile species such as F were not considered due to the lack of published data. The normalized major element data applied in each case are given in **Table 2**.

Overall, melt viscosity values range from $1 \times 10^{1.77}$ to $1 \times 10^{4.77}$ Pa s (**Table 1**), confirming that peralkaline felsic magmas of the Atlantic Ocean exhibit viscosities that are equal to or lower than their metaluminous equivalents ($\sim 10^{4.5}$ Pa s, Scaillet et al., 1998). Although all of the case studies yield low viscosities, the lowest reported values are generally restricted to the most strongly SiO_2-undersaturated compositions, most likely due to the abundance of alkalis compared with Si (e.g., Cape Verde, Trindade, Fernando de Noronha), suggesting that alkalinity plays the primary role in melt viscosity. Nevertheless, the role of peralkalinity remains, and is probably most significant in the Si-oversaturated magma evolutionary trend, where melt compositions remain mildly alkaline. These values were then used to estimate crystal settling rates via the calculation of Stokes' settling velocities for alkali feldspar crystals, supplemented by the hindered settling equation, which allows the estimation of settling rates in polydispersed suspensions (Bachmann and Bergantz, 2004):

$$U_{hs} = U_{Stokes} \times f(c) \quad (1)$$

where U_{hs} is the hindered settling velocity, U_{Stokes} is Stokes settling velocity, and (c) is a correction factor calculated as:

$$f(c) = \frac{(1-c)^2}{(1+c^{1/3})^{\left[\frac{5c}{3(1-c)}\right]}} \quad (2)$$

where c is equal to the crystal fraction. Crystal diameters were set to 2 mm and melt densities were set to 2250 kg/m^3 (*cf.*

TABLE 2 | Major element compositions (recalculated to 100 wt. %) used for viscosity calculations.

Island group	SiO_2	TiO_2	Al_2O_3	FeO^T	MnO	MgO	CaO	Na_2O	K_2O	P_2O_5	PI	Reference	Sample
Iceland	73.44	0.12	13.54	2.36	0.06	0.08	0.41	5.02	4.97		1.01	Larsen et al., 2001	SILK-A1
	73.25	0.24	10.34	5.83	0.23	0.00	0.12	5.70	4.29		1.36	Sigurdsson, 1971	331
Azores	63.89	0.80	17.40	3.17	0.20	0.66	1.20	7.15	5.37	0.15	1.01	Beier et al., 2006	SM220501-1
	67.66	0.54	10.69	8.22	0.34	0.08	0.52	7.40	4.51	0.04	1.59	Mungall and Martin, 1995	P16
Canary Islands	69.92	0.76	14.61	3.44	0.18	0.36	0.37	6.39	3.91	0.06	1.01	Cousens et al., 1990	V5
	69.41	1.10	9.02	6.95	0.45	0.26	0.13	7.94	4.62	0.12	2.00	Kobberger and Schmincke, 1999	KOG16
Cape Verde	53.83	0.49	23.38	2.77	0.14	0.23	2.52	9.91	6.73	0.01	1.01	Eisele et al., 2015	FO024-1
	54.88	0.92	15.27	5.48	0.29	0.83	1.76	13.72	6.79	0.06	1.96	Eisele et al., 2015	B012-32
Cameroon Line	55.26	0.49	22.65	2.84	0.11	0.43	2.00	9.94	6.19	0.09	1.02	Fitton and Hughes, 1977	P11
	57.08	0.21	21.81	1.83	0.01	0.00	0.95	12.26	5.77	0.08	1.21	Mitchell-Thomé, 1970	4
Fernando de Noronha	57.75	0.17	22.40	1.96	0.14	0.18	1.35	9.75	6.28	0.02	1.02	Lopes, 2002	97FN16
	57.52	0.20	21.87	1.88	0.12	0.05	1.15	11.36	5.82	0.03	1.14	Lopes, 2002	89FN88*
Ascension	67.48	0.32	15.68	4.17	0.18	0.12	0.70	6.56	4.73	0.06	1.01	Jicha et al., 2013	AI-63
	72.56	0.24	10.40	3.93	0.14	0.00	0.06	8.31	4.36	0.00	1.77	Webster and Rebbert, 2001	AI-213G
St. Helena	60.49	0.06	19.97	3.99	0.19	0.00	1.23	8.88	5.13	0.06	1.01	Kawabata et al., 2011	SH-85
	60.87	0.08	18.00	3.73	0.14	1.04	0.60	8.83	5.27	1.45	1.12	Asavin et al., 1997	CE6
Trindade	54.62	0.64	21.70	3.66	0.13	0.98	2.68	9.22	6.20	0.17	1.01	Marques et al., 1999	TR-21
	52.31	0.31	20.77	4.73	0.15	0.82	2.27	13.33	5.13	0.18	1.32	Mitchell-Thomé, 1970	2
Tristan da Cunha group	63.31	0.47	18.47	2.02	0.12	0.35	1.36	7.13	6.72	0.05	1.03	Reagan et al., 2008	2004TDC2
Gough Island	61.67	0.14	18.04	5.41	0.25	0.18	1.27	7.43	5.57	0.03	1.01	Le Roex, 1985	G19C
Bouvet Island	68.43	0.31	14.64	4.35	0.13	0.00	1.58	6.03	4.50	0.03	1.01	Prestvik et al., 1999	B16
	71.15	0.31	12.72	4.19	0.11	0.02	0.78	5.80	4.89	0.03	1.17	Bailey and Macdonald, 1970	B2

PI, Peralkalinity index. All values (excluding PI) are reported as wt. %.

Jeffery et al., 2017). Settling rates were calculated for the highest and lowest viscosities calculated above, although it must be acknowledged that the lowest viscosity value of $1 \times 10^{1.77}$ (Cape Verde) represents the most extreme end of the compositional spectrum present in the Atlantic Ocean magmatic systems (e.g., highly alkaline, high water content, strongly peralkaline). As such, the values calculated for these conditions may not be broadly applicable, but rather an end-member achievable under specific circumstances. On this basis, settling rates for the most peralkaline compositions range from 143 m yr^{-1} (hindered settling assuming 40% crystallinity) to 734 m yr^{-1} (unhindered settling). The least peralkaline compositions return settling rates of 0.43 m yr^{-1} (unhindered settling) to 0.08 m yr^{-1} (hindered settling assuming 40% crystallinity). These values indicate that, although crystal settling may be rendered largely ineffective over short timescales by high melt viscosity in metaluminous felsic magmas, it may continue to play a role during the differentiation of peralkaline felsic magmas, even during the latest stages of melt evolution, and particularly in the most Si-undersaturated melts (e.g., Pfaff et al., 2008; Neave et al., 2012; Lindhuber et al., 2015; Jeffery et al., 2016b, 2017).

A Note on the Applicability of Crystal Mush Extraction Models to Peralkaline Systems

The commonly crystal-poor felsic magmas of the Atlantic Ocean may be accounted for by low melt viscosity, which facilitates the gravitational settling of alkali feldspar crystals over short timescales. This may also appear to preclude the application of crystal mush extraction models in such systems; however, it is argued here that the two are not mutually exclusive, and such a model may still be useful in accounting for the petrological features of peralkaline systems. The primary arguments against a crystal mush model in peralkaline systems are efficient crystal settling (which, to some extent, removes the need for mush extraction as a two-phase flow mechanism) and the apparent absence of erupted crystal-rich magmas termed monotonous intermediates (which are typically interpreted to represent

erupted portions of a crystal mush; e.g., Hildreth, 1981, 2004; Bachmann and Bergantz, 2004). Macdonald (2012) noted the lack of clear monotonous intermediates in peralkaline systems, but also highlighted the frequent identification of a feldspar (and Ba) -rich layer (e.g., Leat, 1984; Macdonald et al., 1994; Troll and Schmincke, 2002; Sumner and Wolff, 2003), which may be somewhat comparable to true monotonous intermediates.

We suggest that the predominance of fractional crystallization within the magmatic systems of this study implies that, to generate even the relatively small volumes of erupted peralkaline magmas observed in the Atlantic Ocean magmatic systems, considerably larger volumes of crystalline material must be deposited within the upper crust (although the actual ratio of residual to erupted volumes may be highly variable; see above). Crystals forming within the felsic peralkaline magmas must settle rapidly, and either accumulate to form a mush zone, or be entirely assimilated and reincorporated chemically back into the melt. Although petrographical observations and concentrations of Ba have been used to identify the latter process (e.g., Macdonald et al., 1994, 2008; Sumner and Wolff, 2003; D'Oriano et al., 2017; Jeffery et al., 2017), its efficiency is not constrained, and must relate to the total temperature gradient present within an individual magma reservoir. We therefore suggest that a 'mushy' zone inevitably forms at the base of the lower crustal magma reservoirs, which may then contribute melts to an overlying cupola via filter pressing, as well as potentially via partial melting in response to replenishment events (Wolff et al., 2015).

The absence of monotonous intermediates may simply result from the difficulty of erupting such highly crystalline material. Furthermore, the eruption of such material may be achievable only by receiving an input of comparatively hot, rejuvenating magma, sufficient in scale to unlock the crystal mush, potentially homogenizing the pre-eruptive reservoir in the process (e.g., Southern Rocky Mountain volcanic field; Huber et al., 2012). The applicability of such a process in the low volume systems of the ocean islands is unconstrained; however, the flux rate of ocean island magmatic systems, such as those of the Atlantic, is undoubtedly lower than that of the Southern Rocky Mountain volcanic field, suggesting that a large-scale replenishment event which unlocks the mush and homogenizes the reservoir is improbable. Furthermore, the frequency of zoned eruptive deposits in peralkaline systems (and beyond) suggests that if mush rejuvenation occurs in these systems, it must occur over sufficiently short timescales to prevent reservoir homogenization. Crystalline, autolithic nodules, typically of syenitic composition, may seem like a potential candidate for the peralkaline form of monotonous intermediates; however, where these rocks are found as inclusions within erupted lithologies (within the Atlantic Ocean and elsewhere), they often exhibit mineral assemblages representative of more extreme compositions than those of the erupted magmas. They are therefore frequently interpreted as the result of near-complete, *in situ*, bulk solidification at the margins of a magma reservoir, making them effectively the plutonic equivalents of the erupted peralkaline magmas (e.g., Harris, 1983; Wolff, 1987; Turbeville, 1993; Widom et al., 1993; Ridolfi et al., 2003, 2006; Jeffery et al., 2016b, 2017). These rocks, alongside some examples of exposed shallow intrusions, appear to be the only truly agpaitic rocks available in oceanic island systems (Marks and Markl, 2017). We therefore suggest that the absence of erupted monotonous intermediates reflects two processes: (1) the overall difficulty in erupting intermediate crystal mush due to the significant density contrast between them and overlying, hydrous peralkaline magmas, and (2) the potential for intermediate magmas to be essentially absent due to the mixing of mafic magmas into an established felsic system, being instead incorporated directly into felsic magmas, or becoming trapped within a crystal mush, where they may provoke partial melting (see below).

In summary, crystal mush extraction models are compatible with the primary petrological features of the peralkaline magmatic systems of the Atlantic Ocean. In fact, the rheological properties of the melt may enhance the potential for the development of cumulate mush at the base of the magma reservoir, with a crystal poor, compositionally zoned cupola of magma overlying it (**Figure 9**).

Constructing a Unifying Conceptual Model for the Peralkaline Magmatic Systems of the Atlantic

Existing data and models for the peralkaline magmatic systems of the Atlantic Ocean provide evidence for open system processes, with fractional crystallization representing the primary petrogenetic process, alongside variable contributions from magma mixing processes during replenishment events, and contamination with various crustal lithologies. In published models, the formation of peralkaline felsic magmas is generally limited to the uppermost crust (<5 km), where the extended fractionation of primarily alkali feldspar drives metaluminous progenitor magmas (phonolites, trachytes, and rhyolites) toward peralkalinity, typically within an evolved cap in the uppermost portion of the reservoir (e.g., Wolff, 1985, 1987; Neumann et al., 1999). Other magma reservoir models invoke a stratified magma reservoir, potentially containing three or more distinct melt compositions, which may be mixing with one another to varying degrees (e.g., Widom et al., 1992; Freundt and Schmincke, 1995; Sumner and Branney, 2002; Troll and Schmincke, 2002; Sumner and Wolff, 2003; Snyder et al., 2007; Jeffery et al., 2016b). Such models may also be applicable to a cupola overlying a crystal mush, as well as models based around liquid magma reservoirs (e.g., Sliwinski et al., 2015). Progenitor magmas are themselves the end product of fractionation from a mafic parent, which may range from transitional basalt to basanite or foidite. Many eruptive centers exhibit evidence for a polybaric fractionation process in their underlying magmatic systems, with a significant mafic magma reservoir situated close to the crust-mantle boundary (e.g., Ablay et al., 1998; Hansteen et al., 1998; Schwarz et al., 2004; Klügel et al., 2005; Beier et al., 2006; Hildner et al., 2011, 2012; Zanon and Frezzotti, 2013; Jeffery et al., 2017; Weit et al., 2017). In some instances, only a small portion of the fractionation history of the erupted peralkaline magmas occurs at these lower crustal depths, with mafic compositions generally evolving toward broadly hawaiitic or tephritic compositions before ascending into the upper crust, where they may then

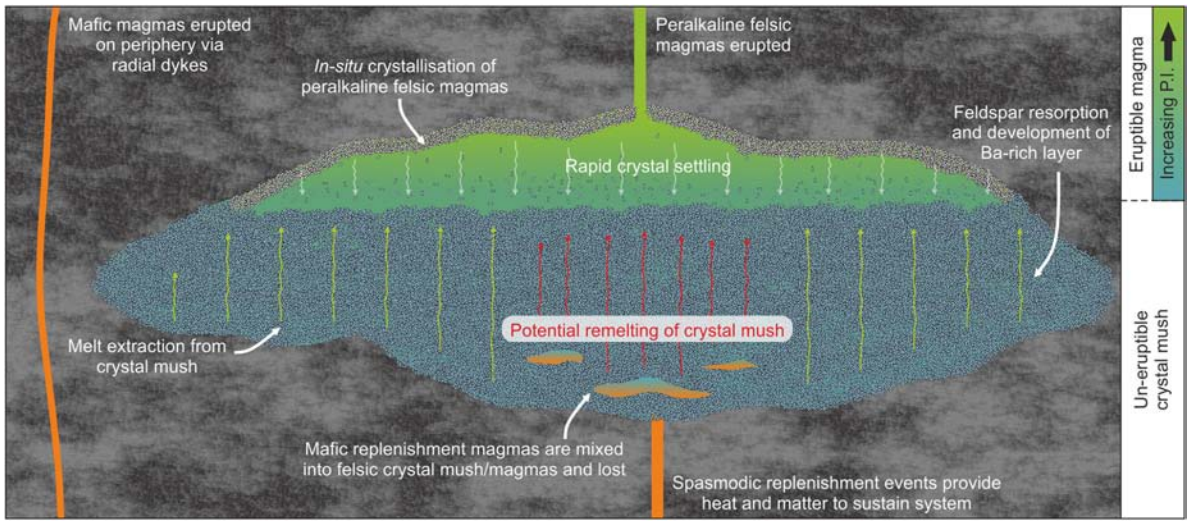

FIGURE 9 | Schematic model for an upper crustal magma reservoir containing peralkaline felsic magmas. The model aims to reconcile the crystal mush-extraction model with low viscosity peralkaline systems, and includes a number of features which are commonly recognized in such systems, including: (1) the development of compositional zoning within a crystal poor cupola, (2) the formation of a crystal- and Ba-rich lower layer in the cupola where settling alkali feldspars can be recycled chemically, (3) the potential for ascending mafic magmas to be lost via incorporation into the felsic reservoir, and the subsequent development of a shadow zone at the surface, (4) the accumulation of a substantial crystal mush pile, from which melt can be extracted via filter pressing, or which can itself be remelted by replenishment magmas, and (5) the near-complete solidification of peralkaline silicic magmas in the thermal boundary zone of the cupola, forming intrusive peralkaline lithologies which may be sampled during eruption.

continue to evolve toward felsic compositions in a shallow crustal magma reservoir, or travel directly to the surface. Direct transport of mafic magmas to the surface may only be possible by circumventing the shallow magma reservoirs, leading to the development of a 'shadow zone' at the surface, marked by central, polygenetic volcanoes which produce exclusively felsic magmas (e.g., Martí and Gudmundsson, 2000; Ebinger and Casey, 2001; Jónasson, 2007; Peccerillo et al., 2007; Acocella, 2014). For example, on São Miguel (Azores), moderately evolved mafic compositions are erupted only in fissure zones between the three central volcanoes (Booth et al., 1978). The development of such arrangements is likely to be dependent upon the stability of the upper crustal reservoir; in theory, the more established the felsic cap becomes (depending upon input via replenishment and output via eruption, or potentially solidification), the lower the chances of seeing evidence for a mafic component in the erupted magmas (Macdonald, 2012). Direct interaction between central and peripheral magmas has been observed on Tenerife (Canary Islands, Wiesmaier et al., 2011), where a sharp compositional interface within a single eruption marks the emplacement of a mafic sill into a colder, felsic magma reservoir, which initiated eruption. Overall, these concepts are broadly applicable to the magmatic centers of the Atlantic Ocean. However, two exceptions that should be noted are Ascension and Santo Antao, where peralkaline magmas may have been formed at unusually high pressures (∼ 250 to 400 MPa), which broadly equates to the lower crust. Furthermore, the peralkaline magmas of Ascension are suggested to have formed via closed system fractional crystallization (Chamberlain et al., 2016), a feature which makes them extremely unusual amongst the peralkaline magmas of the Atlantic. One possible contributing factor may be the greater depth of the magma reservoir, which places low temperature peralkaline magmas against comparatively high-solidus mafic country rock, inhibiting any form of crustal assimilation during the later stages of evolution.

We propose the following three stage model which incorporates the published data described above and accounts broadly for each of the peralkaline magmatic systems of the Atlantic Ocean (**Figure 10**). In stage 1, magmatism is initiated with mantle-derived mafic magmas ascending to generate a shield volcano at the surface, potentially stalling in the upper mantle and the crust-mantle boundary and differentiating via fractional crystallization to compositions such as hawaiite or tephrite/basanite. The transition to stage 2a is envisaged to occur when ascending mafic magmas are able to stall in the shallow crust and fractionate toward peralkaline felsic compositions. The factors controlling this are diverse but are likely to include both large scale and regional structural trends and processes. For example, peralkaline magmas in the Azores archipelago are concentrated on the islands of Graciosa, Terceira, and São Miguel, all three of which lie on a major extensional feature named the Terceira rift. The active extension in the crust may have facilitated formation of upper crustal magma reservoirs, effectively accelerating peralkaline magmatism. In order for this upper crustal reservoir, which may take the form of one or more discrete magma reservoirs, or potentially an intrusive complex of dykes and sills, to be maintained in the relatively cool upper crust, it must receive regular input from the deeper portion of the system, which provides thermal energy and matter. At this point, the liquid line of descent is greatly extended to

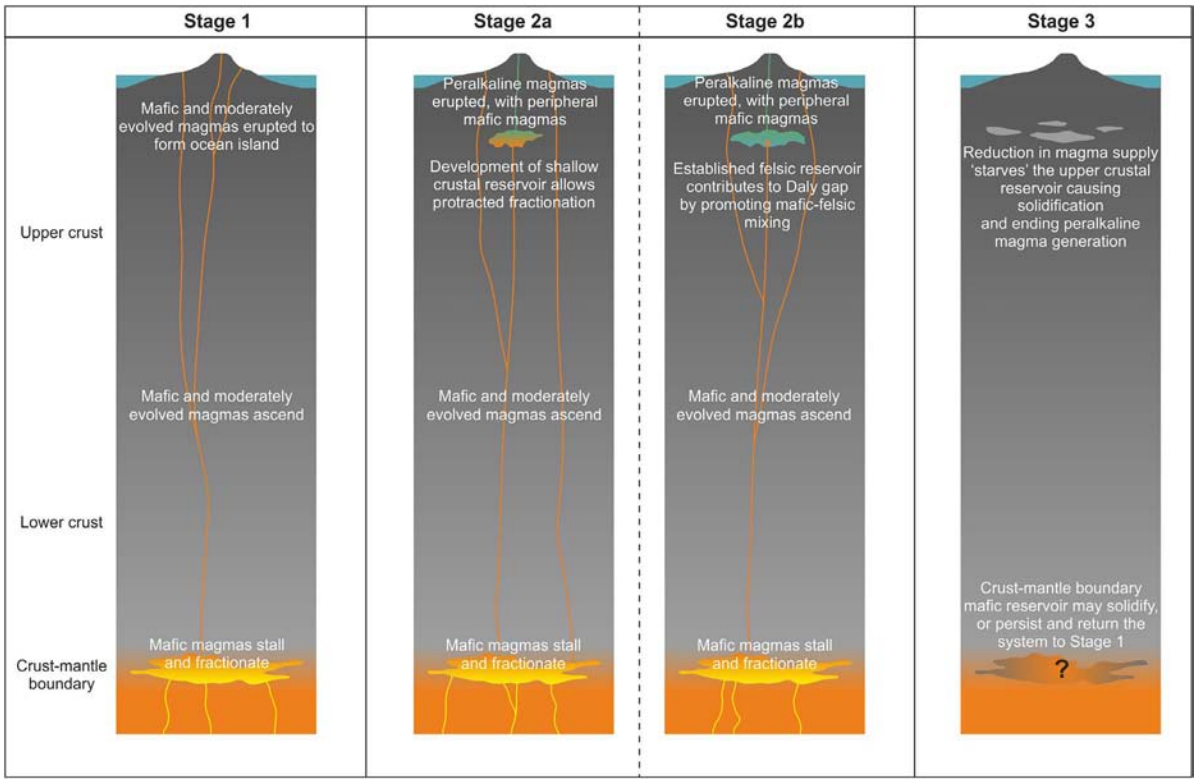

FIGURE 10 | Three-stage conceptual model for the origin, development, and subsequent cessation of peralkaline felsic magmatism beneath the Atlantic Ocean Islands. See text for discussion.

include more evolved products, and felsic crystal mush begins to accumulate in the shallow crust. True intermediate magmas must also exist in the shallow crustal reservoir, trapped beneath less dense, more volatile-rich felsic magmas. The shallow system may be tapped in response to fractional crystallization-induced magmatic overpressure, or potentially by the replenishment events themselves, whilst the deeper portions of the system may still be represented by magmas which ascend from the lower crust and do not interact with the shallow system, leading to eruptions of mafic magmas on the periphery of the central volcano. The establishment of a shallow crustal felsic magma reservoir is therefore envisaged to generate a shadow zone, where only felsic magmas are erupted at the surface, and ascending mafic magmas are only able to reach the surface via peripheral vents.

Stage 2b occurs if the upper crustal reservoir is maintained for long enough, in which case it is envisaged that magma mixing becomes more significant, with batches of ascending mafic magmas being mixed into comparatively large volumes of felsic magma and crystal mush. In effect, the liquid line of descent is cut into two segments (e.g., basalt to hawaiite, metaluminous trachyte to peralkaline trachyte). This may be manifested as a Daly gap, which is evident at many of the Atlantic Island magmatic systems (**Figure 3**). The felsic magmas in the upper crustal reservoir are maintained by replenishment events, effectively reversing the effects of fractional crystallization and generating hybrid intermediate magmas rather than 'true' intermediates derived via fractional crystallization of mafic progenitors (e.g., Storey et al., 1989; Ferla and Meli, 2006; Jeffery et al., 2017). The same replenishment events may also contribute to the felsic magma reservoir by partially melting previously deposited felsic cumulates, or even completely solidified felsic magma batches. Wiesmaier et al. (2013) demonstrated that the latter plays a distinct role in the formation of felsic magmas on Tenerife, and most likely becomes more important as such magmatic systems get older and the composition of the upper crust is made steadily more felsic. It might therefore be expected that this process is most significant in the Canary Islands, Cape Verde, and the Cameroon Line, where the magmatic systems are old enough to have added significant volumes of felsic material to the crust. By contrast, younger magmatic systems such as those of the Azores, Bouvet, Gough, Trindade, and Ascension, may be too young to have considerable reserves of low-solidus, felsic crust. The development of an established cap to the magma system, comprising low density, hydrous peralkaline magmas, is likely to strengthen the shadow zone by completely inhibiting the eruption of higher density magmas, whether they are highly phyric magmas derived from the felsic crystal mush, or dense, mafic magmas.

If the volume of replenishment decreases to levels below those required to maintain the upper crustal system, then the

system will enter stage 3. Without adequate heat and matter to sustain it, the upper crustal magma reservoir cools and solidifies, effectively shutting down the generation of peralkaline felsic magmas. Eruption of mafic magmas derived from the lower crustal magma reservoir may continue, but peralkaline felsic magmas cannot be generated until the upper crustal magma reservoir is re-established. If the overall magma flux of the system increases such that a shallow crustal reservoir can be re-established, then a resurgence in peralkaline magmatism may occur, following a period of mafic magmatism (e.g., La Gomera, Canary Islands).

The Onset of Peralkaline Magmatism Within the Life Cycle of Atlantic Ocean Islands

To further evaluate the development of peralkaline magmatism in the Atlantic Ocean, we now consider the onset of peralkaline magmatism relative to the respective ages of each Atlantic island. In **Figure 2**, the subaerial age of each of the Atlantic islands is plotted, and, where data permit, the earliest known occurrence of felsic magmatism, which we consider to represent the transition from stage 1 to stage 2. In many cases, there is a clear termination of felsic magmatism; for example, on Fernando de Noronha, where peralkaline felsic magmatism occurred between 12.5 and 9.4 Ma, followed by a period of ∼ 3 m.y. of quiescence, and then a resurgence in exclusively mafic magmatism. In this case, this represents the transition from stage 2 to stage 3, followed by a return to stage 1.

Beginning with the Azores, the islands of Graciosa, Terceira, and São Miguel appear to be in stages 2a to 2b (**Table 1**), with established peralkaline magma reservoirs. Additionally, the islands of Corvo, Flores, and Faial may also be in the early stages of Stage 2a, as they have begun to produce more evolved compositions (e.g., benmoreite, metaluminous trachyte). By contrast, the islands of Pico and São Jorge are still in stage 1, with almost exclusively mafic products. Santa Maria is considerably older than any other Azorean island, and although it has an exclusively mafic character, its heavily eroded form suggests that any prior felsic magmatism may have been lost. As such, it most likely lies between stages 3 and 1.

The Canary Islands are generally older than the Azorean islands, and it is perhaps not surprising that some appear to be in the more advanced stages of activity. For example, La Gomera, and Gran Canaria are all characterized by initial periods of mafic magmatism (stage 1), followed by one or more periods of felsic magmatism (stages 2), and, subsequent quiescence (stage 3). In the case of Gran Canaria, and also Fuerteventura, mafic activity began again following the termination of felsic magmatism, suggesting a return to stage 1. It is also noteworthy that La Gomera may have passed through the full cycle twice, with two distinct phases of peralkaline felsic magmatism separated by ∼ 2.5 Ma, and an eventual complete cessation of magmatism indicating stage 3. Despite its age, Lanzarote appears to be in stage 1, with no reported felsic magmas during its ∼ 15 m.y. lifespan. By contrast, Tenerife entered stage 2 after at least ∼ 5 m.y. in stage 1. Like Tenerife, the two youngest islands (La Palma and El Hierro) are in stage 2, despite their comparative youth.

The islands of the Cape Verde archipelago show similar diversity; Santo Antao, Fogo, and Brava are all in stage 2, with peralkaline felsic magmas being produced until the present day. Sal may have approached stage 2, with some peralkaline felsic magmas reported. Santiago and Maio, despite their considerable age, remain in stage 1, although magmatism on Maio appears to have already ceased without progressing beyond stage 1. The remaining islands of São Nicolau, São Vicente, and Boa Vista are all in stage 3, having previously produced peralkaline felsic magmas over periods of around 1–3 Ma. More recent mafic activity on São Nicolau and São Vicente may indicate the transition from stage 3 to stage 1.

The oceanic sector of the Cameroon Line includes some of the oldest islands in the Atlantic Ocean. The three older islands have clearly entered, or are approaching, stage 2, with peralkaline felsic rocks found on São Tomé, Principe, and metaluminous felsic rocks on Pagalu. Only the considerably younger island of Bioko remains in stage 1, with exclusively mafic compositions reported. Ascension Island remains in stage 2, having produced peralkaline felsic magmas during its entire subaerial lifespan of ∼ 1 Ma. In the Madeira archipelago, the predominance of mafic magmas and the absence of any reported peralkaline compositions suggests that all three islands are in stage 1, despite their age. In fact, the occurrence of comparatively rare metaluminous trachytes and rhyolites may indicate the onset of stage 2 on Madeira and Porto Santo. By contrast, the Desertas Islands most likely never progressed further than stage 1 before magmatic activity ceased. Bouvet Island is hard to evaluate due to the lack of data; however, the occurrence of peralkaline felsic magmas and its young age suggest that it is currently in stage 2.

In the Tristan da Cunha archipelago, the island of Tristan appears to be approaching stage 2. Despite the youth of the island (∼ 0.2 Ma), evolved compositions such as metaluminous phonolites and trachytes have been erupted, alongside volumetrically more abundant mafic compositions. Due to its highly eroded form, and the occurrence of peralkaline felsic eruptive products, Inaccessible Island should be considered to be in stage 3, having produced peralkaline magmas, and subsequently ceasing volcanism altogether. The situation is similar for the considerably older Nightingale Islands, and although there are no reported peralkaline compositions, metaluminous felsic rocks are present. Considering the islands' highly eroded form, many of the products of stage 2 may have been destroyed.

Gough Island is clearly at the onset of stage two, with an initially mafic history, and the very recent (∼ 0.2 Ma) development of peralkaline felsic magmatism. This period of approximately 0.1 m.y. ended with a phase of mafic magmatism, suggesting that Gough may in fact have progressed to stage 3, making its peralkaline phase particularly short compared to other examples in the Atlantic Ocean. The magmatism of St. Helena is characterized by a lengthy period of mafic magmatism (∼5 m. y.), followed by a longer period which included volumetrically inferior peralkaline felsic magmas, and lasted until the present day, suggesting that St. Helena is currently in stage 2. In this

instance, the lack of a well-developed Daly gap may indicate that the system remains in stage 2a.

As described above, Fernando de Noronha appears to be in Stage 1, having erupted peralkaline felsic magmas during its early subaerial lifespan, followed by a 3 m.y. period of quiescence, and subsequent renewed mafic magmatism. The island of Trindade (and nearby Martin Vaz) may be similar to Fernando de Noronha. Although the lack of available data makes any evaluation of Martin Vaz difficult, the peralkaline felsic magmatism of Trindade is limited exclusively to the first half of its subaerial life, followed by a period of $\sim$ 2 m.y. during which only mafic and ultramafic compositions were produced. Overall, it seems likely that a shallow crustal magma reservoir existed early in Trindade's lifespan, but was subsequently shut down, suggesting that it has re-entered stage 1.

We choose to consider Iceland separately when applying the model described above. In terms of its scale, geodynamic setting, reported magma compositions, and petrogenetic processes, Iceland stands apart from the remaining Atlantic islands. Nevertheless, Icelandic peralkaline magmatism is restricted to polygenetic volcanic centers, as seen elsewhere, and the general structure of those magma chambers which lie furthest from the rift, and which have therefore been linked to fractional crystallization (Carmichael, 1964; Macdonald et al., 1990; Furman et al., 1992a; Sigmarsson et al., 1992; Hards et al., 2000; Prestvik et al., 2001; Martin and Sigmarsson, 2007), may be very similar to those observed elsewhere. On this basis, it might be suggested that Iceland is currently in stage 2 of the presented model. We suggest that the abundance of peralkaline felsic magmatism that is derived from crustal melting is linked to the overall magma flux, which might be expected to be greater in the rift zones of Iceland than at any of the off-rift Atlantic hotspots (e.g., White, 2010, and references therein). It follows that the introduction of comparatively large volumes of mafic magma into the shallow crust could provide sufficient heat and time to melt the predominantly refractory oceanic crust, whereas the comparatively low volumes generated in locations such as St. Helena and Tristan da Cunha are unable to melt anything other than fusable crystal mush.

Overall, there is no clear correlation between the age of an Atlantic magmatic system and the development of peralkaline magmas. For example, Madeira Island may now be approaching a point at which peralkaline felsic magmas can be formed after $\sim$ 6 m.y. of subaerial activity. By contrast, Ascension, Bouvet, and Tristan have all developed peralkaline felsic magmas in 1 m.y. or less. Some of the Atlantic islands have been subaerial for more than 15 m.y. (e.g., Maio, Lanzarote) but have not produced peralkaline felsic magmas, and yet the young ($<$1 Ma) Azorean islands of Graciosa, Terceira, and São Miguel have all developed prominent peralkaline volcanic centers. Clearly, the conditions required to generate peralkaline felsic magmas occur sooner in some systems than in others. In many respects, this is unsurprising, as it seems likely that the primary control on the development of peralkaline felsic magmas is the overall flux of the magmatic system, which bears little relation to the subaerial exposure of the lava pile. We suggest that there must be a 'peralkalinity window' in the flux of the magmatic system in which the magma input rate into the shallow crust is sufficient to maintain active magma bodies over the timescales required to allow differentiation, and not so much that it accelerates the eruptive rate to the point at which magmas are not able to differentiate toward peralkaline compositions. As such, the generation of peralkaline felsic magmas is dependent upon the ability of the upper crustal magma reservoirs to remain active. The abundance of peralkaline magmas throughout the Atlantic Ocean islands implies that, in any individual magmatic system, these conditions are frequently, but not inevitably, met as part of the larger scale processes which drive magmatism in these regions. This is undoubtedly supplemented by secondary controls, such as tectonics. The Azores provide one example where the development of peralkaline felsic magmas appears to be concentrated on a large-scale extensional feature, which may accelerate the development of peralkaline felsic magmas by facilitating the formation of upper crustal magma reservoirs.

FUTURE RESEARCH DIRECTIONS

Recent advances in our understanding of magma reservoirs have fundamentally shifted the perception of how magmas are stored and evolve in the crust (e.g., Bachmann and Bergantz, 2004; Cashman and Sparks, 2013; Cashman and Giordano, 2014; Streck, 2014; Bachmann and Huber, 2016; Cashman et al., 2017). Similarly, considerable effort applied to the understanding of peralkaline magmatic systems in continental rifts has resulted in widely applicable models for the open system development of such systems in locations such as the East Africa Rift (e.g., Bailey and Macdonald, 1975; Black et al., 1997; Peccerillo et al., 2003, 2007; Macdonald and Scaillet, 2006; Ren et al., 2006; Macdonald et al., 2012). However, the applicability of these models and concepts of magma storage and evolution to the low volume, peralkaline magmatism of the Atlantic Ocean islands is often not well constrained. This is primarily due to the challenges associated with available data for the petrological reconstruction of subvolcanic magmatic systems. Although examples such as the Canary Islands are well studied (e.g., Freundt and Schmincke, 1995; Ablay et al., 1998; Neumann et al., 1999; Sliwinski et al., 2015), there remain examples where geochemical datasets for peralkaline felsic magmas in the Atlantic Ocean are small, incomplete, or essentially absent. Similarly, some settings such as Gough Island and Bouvet Island also lack sufficient geochronological data to develop a rigorous temporal framework of island evolution as a whole.

Overall, the felsic magmas of the Atlantic Ocean islands have received less attention than their mafic counterparts. As such, it is suggested here that the thorough testing of the models and concepts discussed in this contribution is dependent upon expanding the available dataset for Atlantic felsic peralkaline rocks, particularly in the less well-constrained locations such as Gough Island and Bouvet Island. We therefore suggest that further research should be aimed at constraining: (1) the precise P-T-fO_2-X conditions of the magma reservoirs which

produce and store peralkaline magmas in the oceanic crust, and (2) the overall timescales of magmatism. In the case of the former, the actual geometry of the underlying magma reservoirs is often poorly constrained, suggesting that further study into the pre-eruptive storage conditions of the erupted peralkaline magmas, particularly the relative depths of magma storage. Furthermore, the detailed study of individual, well-constrained eruptive units can yield valuable insights into the potentially zoned pre-eruptive reservoir. Similarly, where present, plutonic ejecta represent an opportunity to investigate processes such as *in situ* crystallization, melt extraction, mush remobilisation, and cannibalization. For the latter topic, we argue here that the generation of peralkaline felsic magmas in the oceanic magmatic systems of the Atlantic tends toward cyclicity, with individual magmatic systems having the potential to partially or completely pass through one or more cycles of magmatism, controlled largely by the overall magmatic flux of the system. The temporal model presented here for each of the Atlantic Islands could be improved via higher resolution dating, which may highlight higher-order variations in the production of peralkaline felsic magmas. Similarly, the determination of timescales for magmatic processes shows great promise in enhancing our understanding of how these relatively low volume magma chambers form, evolve, and eventually terminate (Bachmann and Huber, 2016). Although zircon is often not a fractionating phase in peralkaline rocks, U-series disequilibria of glass separates have been used to constrain the rates of evolution of peralkaline felsic magmas, providing timescales for pre-eruptive processes such as fractionation and the development of zonation (e.g., Widom et al., 1992; Snyder et al., 2007). Furthermore, diffusion modeling may provide a robust indication of timescales of processes such as mush reactivation and magma mixing (e.g., Martin et al., 2008; Matthews et al., 2012; Till et al., 2015). Finally, a key component in the continued investigation of the precise state of the described, upper crustal felsic magma reservoirs is the consideration of their thermal state. Numerical modeling of the thermal evolution of such systems will provide invaluable insights into the timescales over which a given magma reservoir can exist without entirely solidifying without the input of additional heat via replenishment events (Annen et al., 2008; Gelman et al., 2013), which may be of particular interest in the potentially low-volume magma reservoirs of ocean islands (*cf.* Bachmann and Huber, 2016 and references therein).

CONCLUSION

Peralkaline magmatism occurs frequently throughout the various magmatic systems of the Atlantic Ocean islands. The generation of such magmas is ultimately controlled by fractional crystallization of mantle-derived mafic magmas. Nevertheless, there is abundant evidence for open system evolution. Crustal assimilation may occur at any point in the system, with assimilants ranging from mafic lower crust to upper crustal felsic lithologies such as crystalline mush or previously intruded and solidified magmas. Older magmatic systems may be more susceptible to assimilation of the latter due to the continued accumulation of low-solidus felsic material in the upper crust. Magma mixing is also recognized in the majority of systems and includes mixing between mafic and felsic end-members, two variably felsic end-members, and the remobilisation of crystal mush. This process frequently leads to the formation of hybrid magmas which lie compositionally within the Daly gap, a feature which is recognized at many of the Atlantic islands volcanic centers. The peralkaline felsic magmas of the Atlantic are formed primarily in established shallow crustal reservoirs (generally between 2 and 5 km depth), which are fed by replenishment from mafic magma reservoirs at greater depth, typically around the crust-mantle boundary. The peralkaline felsic magmas of the upper crustal system are invariably hydrous, with H_2O_{melt} values that typically range from 2 to 6 wt. %, and are frequently compositionally zoned. Zonation may be observed in major element chemistry or crystal content, or may be more subtle, recognizable only in trace element geochemistry and/or pre-eruptive temperatures and H_2O_{melt} contents. The upper crustal magma reservoirs are likely to include a lower crystal mush which forms due to the considerable degree of fractionation which occurs. Crystal mush formation may be accelerated by the low viscosity of the peralkaline magmas, which allows crystal settling to remain a viable mechanism of two-phase flow even at temperatures below 800°C. This potential for the rapid accumulation of alkali feldspar-based crystal mush suggests that the extraction of melt from crystal mush, as well as remelting of crystal mush, may have a role to play in low volume peralkaline systems. Single-stage mush extraction models may not be rheologically compatible with high degrees of fractionation. Two-stage extraction models have the potential to greatly reduce the total volume of fusable crystal mush that is added to the crust, and which may then be cannibalized via remelting. The various magmatic systems of the Atlantic islands can be described using a three stage model, in which peralkaline felsic magmas are only able to form when a stable upper crustal magma reservoir is able to form. The onset of peralkaline magmatism is highly variable, with no clear link to the age of the respective magmatic system. Tectonic controls are also possible, with extension potentially facilitating the formation of upper crustal reservoirs in which magmas can stagnate and evolve, as may be the case in the Azores. Ultimately, the generation of peralkaline magmas is likely to be controlled by the magma flux rate of the magmatic system. If the flux is too low, an established magma reservoir in the cool, upper crust will cool and solidify. If the flux is too high, then the upper crustal reservoir will erupt before evolved magmas can form. Despite this, more than half of the Atlantic islands exhibit peralkaline rocks, suggesting that these conditions, although not inevitable, are common in the life cycle of the Atlantic Ocean island volcanoes.

AUTHOR CONTRIBUTIONS

The project was initially conceived by AJ and RG. The published data used by the study were collated by AJ. The manuscript,

figures, and tables were jointly produced and subsequently revised by AJ and RG.

FUNDING

This work was supported by Keele University.

ACKNOWLEDGMENTS

An earlier form of this manuscript was greatly improved by the constructive and detailed reviews of F. Genske, J. Sliwinski, and T. Ubide. We are also very grateful to P. Larrea and V. Acocella for their insightful comments and editorial handling.

REFERENCES

Abdel-Monem, A., Watkins, N., and Gast, P. (1971). Potassium-argon ages, volcanic stratigraphy, and geomagnetic polarity history of the Canary Islands; Lanzarote, Fuerteventura, Gran Canaria, and La Gomera. *Am. J. Sci.* 271, 490–521. doi: 10.2475/ajs.271.5.490

Abdel-Monem, A., Watkins, N., and Gast, P. (1972). Potassium-argon ages, volcanic stratigraphy and geomagnetic polarity history of the Canary Islands: Tenerife, La Palma and Hierro. *Am. J. Sci.* 272, 805–825. doi: 10.2475/ajs.272.9.805

Abdel-Monem, A. A., Fernandez, L. A., and Boone, G. M. (1975). K-Ar ages from the eastern Azores group (Santa Maria, São Miguel and the Formigas islands). *Lithos* 8, 247–254. doi: 10.1016/0024-4937(75)90008-0

Ablay, G. J., Carroll, M. R., Palmer, M. R., Martí, J., and Sparks, R. S. J. (1998). Basanite-phonolite lineages of the Teide-Pico Viejo volcanic complex, Tenerife, Canary Islands. *J. Petrol.* 39, 905–936. doi: 10.1093/petroj/39.5.905

Ablay, G. J., Ernst, G. G. J., Martí, J., and Sparks, R. S. J. (1995). The ∼2 ka subplinian eruption of Montaña Blanca, Tenerife. *Bull. Volcanol.* 57, 337–355.

Acocella, V. (2014). Structural control of magmatism along divergent and convergent plate boundaries: Overview, model, problems. *Earth Sci. Rev.* 136, 226–288. doi: 10.1016/j.earscirev.2014.05.006

Aka, F. T., Nagao, K., Kusakabe, M., Sumino, H., Tanyileke, G., Ateba, B., et al. (2004). Symmetrical helium isotope distribution on the Cameroon volcanic line, West Africa. *Chem. Geol.* 203, 205–223. doi: 10.1016/j.chemgeo.2003.10.003

Allen, R. M., Nolet, G., Morgan, W. J., Vogfjörd, K., Bergsson, B. H., Erlendsson, P., et al. (1999). The thin hot plume beneath Iceland. *Geophys. J. Int.* 137, 51–63. doi: 10.1046/j.1365-246x.1999.00753.x

Almeida, F. F. M. (1955). *Geologia e Petrologia do Arquipélago de Fernando de Noronha*. Rio de Janeiro: Servicão Grafico do Instituto Brasileiro de Geografia e Estatiìstica.

Almeida, F. F. M. (1961). *Geologia e Petrologica da Ilha da Trindade*. Rio de Janeiro: DNPM.

Almeida, F. F. M. (1963). *Mapa Geológico da Ilha da Trindade*. Rio de Janeiro: DNPM.

Almeida, F. F. M. (2012). "Ilhas ceânicas brasileiras," in *Geologia do Brasil*, eds Y. Hasui, C. D. R. Caqrneiro, F. F. M. Almeida, and A. Bartorelli (São Paulo: Beca), 658–662.

Ancochea, E., Fuster, J., Ibarrola, E., Cendrero, A., Coello, J., Hernan, F., et al. (1990). Volcanic evolution of the island of Tenerife (Canary Islands) in the light of new K-Ar data. *J. Volcanol. Geother. Res.* 44, 231–249. doi: 10.1016/0377-0273(90)90019-C

Ancochea, E., Huertas, M. J., Cantagrel, J. M., Coello, J., Fúster, J. M., Arnaud, N., et al. (1999). Evolution of the Cañadas edifice and its implications for the origin of the Cañadas Caldera (Tenerife, Canary Islands). *J. Volcanol. Geother. Res.* 88, 177–199. doi: 10.1016/S0377-0273(98)00106-1

Andújar, J., Costa, F., and Martí, J. (2010). Magma storage conditions of the last eruption of Teide volcano (Canary Islands, Spain). *Bull. Volcanol.* 72, 381–395. doi: 10.1007/s00445-009-0325-3

Andújar, J., Costa, F., Martí, J., Wolff, J. A., and Carroll, M. R. (2008). Experimental constraints on pre-eruptive conditions of phonolitic magma from the caldera-forming El Abrigo eruption, Tenerife (Canary Islands). *Chem. Geol.* 257, 173–191. doi: 10.1016/j.chemgeo.2008.08.012

Andújar, J., Costa, F., and Scaillet, B. (2013). Storage conditions and eruptive dynamics of central versus flank eruptions in volcanic islands: the case of Tenerife (Canary Islands, Spain). *J. Volcanol. Geother. Res.* 260, 62–79. doi: 10.1016/j.jvolgeores.2013.05.004

Annen, C., Pichavant, M., Bachmann, O., and Burgisser, A. (2008). Conditions for the growth of a long-lived shallow crustal magma chamber below Mount Pelee volcano (Martinique, Lesser Antilles Arc). *J. Geophys. Res. Solid Earth* 113:B7. doi: 10.1029/2007JB005049

Aparicio, A., Bustillo, M. A., Garcia, R., and Araña, V. (2006). Metasedimentary xenoliths in the lavas of the Timanfaya eruption. (1730–1736, Lanzarote, Canary Islands): metamorphism and contamination processes. *Geol. Mag.* 143, 181–193. doi: 10.1017/S0016756806001713

Aparicio, A., Tassinari, C. C., García, R., and Araña, V. (2010). Sr and Nd isotope composition of the metamorphic, sedimentary and ultramafic xenoliths of Lanzarote (Canary Islands): implications for magma sources. *J. Volcanol. Geother. Res.* 189, 143–150. doi: 10.1016/j.jvolgeores.2009.10.017

Araña, V., Marti, J., Aparicio, A., García-Cacho, L., and García- García, R. (1994). Magma mixing in alkaline magmas: an example from Tenerife, Canary Islands. *Lithos* 32, 1–19. doi: 10.1016/0024-4937(94)90018-3

Asavin, A. M., Kogarko, L. N., Kryuchkova, O. I., Tyurin, D. A., and Kolesov, G. M. (1997). Grand Canary, Saint Helena, and Tristan da Cunha Oceanic Islands: variations of trace element partition coefficients in pyroxene-melt equilibria during alkaline magma evolution. *Geochem. Int.* 35, 415–423.

Atkins, F. B., Baker, P. E., Bell, J. D., and Smith, D. G. W. (1964). Oxford expedition to Ascension Island. *Nature* 204, 722–724. doi: 10.1038/204722a0

Aulinas, M., Gimeno, D., Fernandez-Turiel, J. L., Perez-Torrado, F. J., Rodriguez-Gonzalez, A., and Gasperini, D. (2010). The Plio-Quaternary magmatic feeding system beneath Gran Canaria (Canary Islands, Spain): constraints from thermobarometric studies. *J. Geol. Soc. London* 167, 785–801. doi: 10.1144/0016-76492009-184

Avanzinelli, R., Bindi, L., Menchetti, S., and Conticelli, S. (2004). Crystallisation and genesis of peralkaline magmas from Pantelleria volcano, Italy: an integrated petrological and crystal-chemical study. *Lithos* 73, 41–69. doi: 10.1016/j.lithos.2003.10.007

Bachmann, O., and Bergantz, G. W. (2004). On the origin of crystal-poor rhyolites: extracted from batholithic crystal mushes. *J. Petrol.* 45, 1565–1582. doi: 10.1093/petrology/egh019

Bachmann, O., and Huber, C. (2016). Silicic magma reservoirs in the Earth's crust. *Am. Mineral.* 101, 2377–2404. doi: 10.1038/nature17401

Bailey, D. K. (1974). Experimental petrology relating to oversaturated peralkaline volcanics. A review. *Bull. Volcanol.* 38, 637–652. doi: 10.1007/BF02596901

Bailey, D. K., and Macdonald, R. (1970). Petrochemical variations among mildly peralkaline (comendite) obsidians from the oceans and continents. *Contrib. Mineral. Petrol.* 28, 340–351. doi: 10.1007/BF00388955

Bailey, D. K., and Macdonald, R. (1975). Fluorine and chlorine in peralkaline liquids and the need for magma generation in an open system. *Mineral. Mag.* 40, 405–414. doi: 10.1180/minmag.1975.040.312.10

Bailey, D. K., and Schairer, J. F. (1964). Feldspar-liquid equilibria in peralkaline liquids – the orthoclase effect. *Am. J. Sci.* 262, 1198–1206. doi: 10.2475/ajs.262.10.1198

Bailey, J. C., Gwozdz, R., Rose-Hansen, J., and Sørensen, H. (2001). Geochemical overview of te Ilimaussaq alkaline complex, South Greenland. *Geol. Greenland Surv. Bull.* 190, 35–53.

Baker, B. H., and Henage, L. F. (1977). Compositional changes during crystallization of some peralkaline silicic lavas of the Kenya rift valley. *J. Volcanol. Geother. Res.* 2, 17–28. doi: 10.1016/0377-0273(77)90013-0

Baker, I. (1968). Intermediate oceanic volcanic rocks and the 'Daly Gap'. *Earth Planet. Sci. Lett.* 4, 103–106. doi: 10.1016/0012-821X(68)90002-2

Baker, I. (1969). Petrology of the volcanic rocks of Saint Helena Island, South Atlantic. *Geol. Soc. Am. Bull.* 80, 1283–1310. doi: 10.1130/0016-7606(1969)80[1283:POTVRO]2.0.CO;2

Baker, I., Gale, N. H., and Simons, J. (1967). Geochronology of the St. Helena volcanoes. *Nature* 215, 1451–1454. doi: 10.1038/2151451a0

Baker, P. E. (1974). Peralkaline acid volcanic rocks of oceanic islands. *Bull. Volcanol.* 38, 737–754. doi: 10.1007/BF02596906

Baker, P. E., Gass, I. G., Harris, P. G., and Le Maitre, R. W. (1964). The volcanological report of the Royal Society expedition to Tristan da Cunha, 1962. *Philos. Trans. R. Soc. A* 256, 439–575. doi: 10.1098/rsta.1964.0011

Baker, P. E., and Tomblin, J. F. (1964). A recent volcanic eruption on Bouvetøya, South Atlantic Ocean. *Nature* 203, 1055–1056. doi: 10.1038/2031055a0

Balogh, K., Ahijado, A., Casillas, R., and Fernandez, C. (1999). Contributions to the chronology of the Basal Complex of Fuerteventura, Canary Islands. *J. Volcanol. Geother. Res.* 90, 81–101. doi: 10.1016/S0377-0273(99)00008-6

Barclay, J., Carroll, M. R., Houghton, B. F., and Wilson, C. J. N. (1996). Pre-eruptive volatile content and degassing history of an evolving peralkaline volcano. *J. Volcanol. Geother. Res.* 74, 5–87. doi: 10.1016/S0377-0273(96)00058-3

Barker, A. K., Troll, V. R., Carracedo, J. C., and Nicholls, P. A. (2015). The magma plumbing system for the 1971 Teneguía eruption on La Palma, Canary Islands. *Contrib. Mineral. Petrol.* 170:21. doi: 10.1007/s00410-015-1207-7

Becerril, L., Ubide, T., Sudo, M., Martí, J., Galindo, I., Galé, C., et al. (2016). Geochronological constraints on the evolution of El Hierro (Canary Islands). *J. Afr. Earth Sci.* 113, 88–94. doi: 10.1016/j.jafrearsci.2015.10.012

Beier, C., Haase, K. M., and Hansteen, T. H. (2006). Magma evolution of the Sete Cidades volcano, São Miguel, Azores. *J. Petrol.* 47, 1375–1411. doi: 10.1093/petrology/egl014

Beier, C., Mata, J., Stöckhert, F., Mattielli, N., Brandl, P. A., Madureira, P., et al. (2013). Geochemical evidence for melting of carbonated peridotite on Santa Maria Island, Azores. *Contrib. Mineral. Petrol.* 165, 823–841. doi: 10.1007/s00410-012-0837-2

Bernth, U., Brousse, R., Frei, R., and Sørensen, H. (2002). The origin of phonolites and trachytes from the Col de Guéry area, le Mont-Dore, Massif Central, France. *Matematisk Fysiske Medd.* 50:61.

Bindeman, I., Gurenko, A., Carley, T., Miller, C., Martin, E., and Sigmarsson, O. (2012). Silicic magma petrogenesis in Iceland by remelting of hydrothermally altered crust based on oxygen isotope diversity and disequilibria between zircon and magma with implications for MORB. *Terra Nova* 24, 227–232. doi: 10.1111/j.1365-3121.2012.01058.x

Bjarnason, I. T., Wolfe, C. J., Solomon, S. C., and Gudmundsson, G. (1996). Initial results from the ICEMELT experiment: body-wave delay times and shear-wave splitting across Iceland. *Geophys. Res. Lett.* 23, 459–462. doi: 10.1029/96GL00420

Black, S., Macdonald, R., and Kelly, M. R. (1997). Crustalorigin for peralkaline rhyolites from Kenya: evidence ffrom U-series disequilibria and Th-isotopes. *J. Petrol.* 38, 277–297. doi: 10.1093/petroj/38.2.277

Bohrson, W. A., and Reid, M. R. (1997). Genesis of silicic peralkaline volcanic rocks in an ocean island setting by crustal melting and open-system processes: socorro Island, Mexico. *J. Petrol.* 38, 1137–1166. doi: 10.1093/petroj/38.9.1137

Bohrson, W. A., Reid, M. R., Grunder, A. L., Heizler, M. T., Harrison, T. M., and Lee, J. (1996). Prolonged history of silicic peralkaline volcanism in the eastern Pacific Ocean. *J. Geophys. Res. Solid Earth* 101, 11457–11474. doi: 10.1029/96JB00329

Bongiolo, E. M., Pires, G. L. C., Geraldes, M. C., Santos, A. C., and Neumann, R. (2015). Geochemical modelling and Nd-Sr data links nephelinite-phonolite successions and xenoliths of Trindade Island (South Atlantic Ocean, Brazil). *J. Volcanol. Geother. Res.* 306, 58–73. doi: 10.1016/j.jvolgeores.2015.10.002

Bonin, B., Grelou-Orsini, C., and Vialette, Y. (1978). Age, origin and evolution of the anorogenic complex of Evisa (Corsica): a K-Li-Rb-Sr study. *Contrib. Mineral. Petrol.* 65, 425–432. doi: 10.1007/BF00372289

Booth, B., Croasdale, R., and Walker, G. P. L. (1978). A quantitative study of five thousand years of volcanism on São Miguel, Azores. *Philos. Trans. R. Soc. London A Math. Phys. Sci.* 288, 271–319.

Bottinga, Y., and Weill, D. (1972). The viscosity of magmatic silicate liquids: a model for calculation. *Am. J. Sci.* 272, 438–475. doi: 10.2475/ajs.272.5.438

Bowen, N. L. (1928). *The Evolution of Igneous Rocks*. New York, NY: Dover, 332.

Brousse, R., and Varet, J. (1966). Les trachytes du Mont-Dore et du Cantal septentrional et leurs enclaves. *Bull. Soc. Geol. France* 8, 246–262.

Brown, R. J., Barry, T. L., Branney, M. J., Pringle, M. S., and Bryan, S. E. (2003). The Quaternary pyroclastic succession of southeast Tenerife, Canary Islands: explosive eruptions, related caldera subsidence, and sector collapse. *Geol. Mag.* 140, 265–288. doi: 10.1017/S0016756802007252

Brown, R. J., and Branney, M. J. (2004). Event-stratigraphy of a caldera-forming ignimbrite eruption on Tenerife: the 273 ka Poris Formation. *Bull. Volcanol.* 66, 392–416. doi: 10.1007/s00445-003-0321-y

Brum da Silveira, A., Madeira, J., Ramalho, R., Fonseca, P., Rodrigues, C., and Prada, S. (2010a). *Carta Geológica da Ilha da Madeira na Escala de1:50000, Folha A, Technical Report*. Funchal: Secretaria Regional do Ambiente e Recursos Naturais.

Brum da Silveira, A., Madeira, J., Ramalho, R., Fonseca, P., Rodrigues, C., and Prada, S. (2010b). *Carta Geológica da Ilha da Madeira na Escala de1:50000, Folha B, Technical Report*. Funchal: Secretaria Regional do Ambiente e Recursos Naturais.

Brum da Silveira, A., Madeira, J., Ramalho, R., Fonseca, P., Rodrigues, C., and Prada, S. (2010c). *Notícia Explicativa da Carta Geológica da Ilha daMadeira na Escala de 1:50000, Technical Report*. Funchal: Secretaria Regional do Ambiente e Recursos Naturais.

Bryan, G. M., Kumar, N., and Castro, P. J. (1972). "The north Brazilian Ridge and the extension of equatorial fracture zones into the continent," in *Anais do XXVI Congresso Brasileiro de Geologia*, Belém, 133–144.

Bryan, S. E. (2006). Petrology and geochemistry of the Quaternary caldera-forming, phonolitic Granadilla eruption, Tenerife (Canary Islands). *J. Petrol.* 47, 1557–1589. doi: 10.1093/petrology/egl020

Bryan, S. E., Cas, R. A. F., and Martí, J. (2000). The 0.57 Ma plinian eruption of the Granadilla Member, Tenerife (Canary Islands): an example of complexity in eruption dynamics and evolution. *J. Volcanol. Geother. Res.* 103, 209–238. doi: 10.1016/S0377-0273(00)00225-0

Burke, K. (2001). Origin of the Cameroon Line of volcano-capped swells. *J. Geol.* 109, 349–362. doi: 10.1086/319977

Calvert, A. T., Moore, R. B., McGeehin, J. P., and Rodrigues da Silva, A. M. (2006). Volcanic history and $^{40}Ar/^{39}Ar$ and 14C geochronology of Terceira Island, Azores, Portugal. *J. Volcanol. Geother. Res.* 156, 103–115. doi: 10.1016/j.jvolgeores.2006.03.016

Campbell, R. (1914). Rocks from Gough Island, South Atlantic. *Trans. R. Soc. Edinb.* 50, 397–404. doi: 10.1017/S0080456800035997

Carmichael, I. S. E. (1962). Pantelleritic liquids and their phenocrysts. *Mineral. Mag.* 33, 86–113. doi: 10.1180/minmag.1962.033.257.03

Carmichael, I. S. E. (1964). The petrology of Thingmuli, a Tertiary volcano in eastern Iceland. *J. Petrol.* 5, 435–460. doi: 10.1093/petrology/5.3.435

Carracedo, J. C. (1979). *Paleomagnetismo e Historia Volcánica de Tenerife*. Santa Cruz de Tenerife: Aula de Cultura de Tenerife, 82.

Carracedo, J. C., Badiola, E. R., Guillou, H., Paterne, M., Scaillet, S., Torrado, F. P., et al. (2007). Eruptive and structural history of Teide Volcano and rift zones of Tenerife, Canary Islands. *Geol. Soc. Am. Bull.* 119, 1027–1051. doi: 10.1130/B26087.1

Carracedo, J. C., Day, S., Guillou, H., Rodríguez Badiola, E., Canas, J. A., and Pérez Torrado, J. F. (1997). "Geochronological, structural and morphological constraints in the genesis and evolution of the Canary Islands," in *Proceedings of the International Workshop on Immature Oceanic Islands*, La Palma, 45–48.

Carracedo, J. C., Day, S., Guillou, H., Rogríguez Badiola, E., Canas, J. A., and Pérez Torrado, F. J. (1998). Hotspot volcanism close to a passive continental margin: the Canary Islands. *Geol. Mag.* 135, 591–604. doi: 10.1017/S0016756898001447

Carracedo, J. C., Guillou, H., Nomade, S., Rodríguez-Badiola, E., Pérez-Torrado, F. J., Rodríguez-González, A., et al. (2011). Evolution of ocean-island rifts: the northeast rift zone of Tenerife, Canary Islands. *Bull. Geol. Soc. Am.* 123, 562–584. doi: 10.1130/B30119.1

Carracedo, J. C., Pérez, F. J., Ancochea, E., Meco, J., Hernán, F., Cubas, C. R., et al. (2002). "Cenozoic volcanism II: the Canary Islands," in *The Geology of Spain*, eds W. Gibbons and T. Moreno (London: The Geological Society of London), 439–472.

Cashman, K., and Sparks, R. S. J. (2013). How volcanoes work: a 25 year perspective. *Geol. Society of Am. Bull.* 125, 664–690. doi: 10.1130/B30720.1

Cashman, K. V., and Giordano, G. (2014). Calderas and magma reservoirs. *J. Volcanol. Geother. Res.* 288, 25–45. doi: 10.1016/j.jvolgeores.2014.09.007

Cashman, K. V., Sparks, R. S., and Blundy, J. D. (2017). Vertically extensive and unstable magmatic systems: a unified view of igneous processes. *Science* 355, 1–9. doi: 10.1126/science.aag3055

Chaffey, D. J., Cliff, R. A., and Wilson, B. M. (1989). "Characterisation of the St Helena magma source," in *Magmatism in the Ocean Basins*, Vol. 42, eds A. D. Saunders and M. J. Norry (London: Geological Society of London), 257–276.

Chamberlain, K. J., Barclay, J., Preece, K., Brown, R. J., Davidson, J. P., and Eimf. (2016). Origin and evolution of silicic magmas at ocean islands: perspectives from a zoned fall deposit on Ascension Island, South Atlantic. *J. Volcanol. Geother. Res.* 327, 349–360. doi: 10.1016/j.jvolgeores.2016.08.014

Chauvel, C., Dia, A. N., Bulourde, M., Chabaux, F., Durand, S., Ildefonse, P., et al. (2005). Do decades of tropical rainfall affect the chemical compositions of basaltic lava flows in Mt Cameroon? *J. Volcanol. Geother. Res.* 141, 195–223. doi: 10.1016/j.jvolgeores.2004.10.008

Civetta, L., Antonio, M., Orsi, G., and Tilton, G. R. (1998). The geochemistry of volcanic rocks from Pantelleria Island, Sicily Channel: petrogenesis and characteristics of the mantle source region. *J. Petrol.* 39, 1453–1491. doi: 10.1093/petroj/39.8.1453

Clay, P. L., Kelley, S. P., Sherlock, S. C., and Barry, T. L. (2011). Partitioning of excess argon between alkali feldspars and glass in a young volcanic system. *Chem. Geol.* 289, 12–30. doi: 10.1016/j.chemgeo.2011.07.005

Cliff, R. A., Baker, P. E., and Mateer, N. J. (1991). Geochemistry of inaccessible island volcanics. *Chem. Geol.* 92, 251–260. doi: 10.1016/0009-2541(91)90073-Z

Cooper, L. B., Bachmann, O., and Huber, C. (2015). Volatile budget of Tenerife phonolites inferred from textural zonation of S-rich haüyne. *Geology* 43, 423–426. doi: 10.1130/G36505.1

Cordani, U. G. (1970). Idade do vulcanismo no Atlântico Sul. *Boletim IGA* 1, 9–75. doi: 10.11606/issn.2316-9001.v1i0p09-75

Cousens, B. L., Spera, F. J., and Tilton, G. R. (1990). Isotopic patterns in silicic ignimbrites and lava flows of the Mogan and lower Fataga Formations, Gran Canaria, Canary Islands: temporal changes in mantle source composition. *Earth Planet. Sci. Lett.* 96, 319–335. doi: 10.1016/0012-821X(90)90010-U

Crisp, J. A., and Spera, F. J. (1987). Pyroclastic flows and lavas of the Mogan and Fataga formations, Tejeda volcano, Gran Canaria, Canary Islands: mineral chemistry, intensive parameters, and magma chamber evolution. *Contrib. Mineral. Petrol.* 96, 503–518. doi: 10.1007/BF01166695

Crough, S. T. (1982). Geoid anomalies over the Cape Verde Rise. *Mar. Geophys. Res.* 5, 263–271. doi: 10.1007/BF00305564

Crough, S. T., Morgan, W. J., and Hargraves, R. B. (1980). Kimberlites: their relation to mantle hot spots. *Earth Planet. Sci. Lett.* 50, 260–274. doi: 10.1016/0012-821X(80)90137-5

Czajkowski, M. (2002). Excursion guide 15: a geological tour of the islands of Madeira and Porto Santo. *Geol. Today* 18, 26–34. doi: 10.1046/j.1365-2451.2002.00009.x

Daly, R. A. (1910). Origin of alkaline rocks. *Geol. Soc. Am. Bull.* 21, 87–118. doi: 10.1130/GSAB-21-87

Daly, R. A. (1925). The geology of Ascension Island. *Proc. Am. Acad. Arts Sci.* 60, 1–80. doi: 10.2307/25130043

Darwin, C. (1845). *Journal of Researches into the Natural History and Geology of the Various Countries Visited during the Voyage of HMS Beagle Round the World*, 2nd Edn. London: John Murray, 324.

Dávila-Harris, P., Ellis, B. S., Branney, M. J., and Carrasco-Núñez, G. (2013). Lithostratigraphic analysis and geochemistry of a vitric spatter-bearing ignimbrite: the Quaternary Adeje Formation, Cañadas volcano, Tenerife. *Bull. Volcanol.* 75:722. doi: 10.1007/s00445-013-0722-5

Déruelle, B., Moreau, C., Nkoumbou, C., Kambou, R., Lisssom, J., Njonfang, E., et al. (1991). "The Cameroon Line: a review," in *Magmatism in Extensional Structural Settings. The Phanerozoic African Plate*, eds A. B. Kampunzu and R. Lubala (Berlin: Springer), 274–327. doi: 10.1007/978-3-642-73966-8_12

Déruelle, B., Ngounouno, I., and Demaiffe, D. (2007). The 'Cameroon Hot Line' (CHL): a unique example of active alkaline intraplate structure in both oceanic and continental lithospheres. *Comptes Rendus Geosci.* 339, 589–600. doi: 10.1016/j.crte.2007.07.007

Di Genova, D., Romano, C., Hess, K.-U., Vona, A., Poe, B. T., Giordano, D., et al. (2013). The rheology of peralkaline rhyolites from Pantelleria Island. *J. Volcanol. Geother. Res.* 249, 201–216. doi: 10.1016/j.jvolgeores.2012.10.017

Dingwell, D. B., Hess, K.-U., and Romano, C. (1998). Extremely fluid behaviour of hydrous peralkaline rhyolites. *Earth Planet. Sci. Lett.* 158, 31–38. doi: 10.1016/S0012-821X(98)00046-6

Dingwell, D. B., Scarfe, C. M., and Cronin, D. J. (1985). The effect of fluorine on viscosities in the system Na2O-Al2O3-SiO2: implications for phonolites, trachytes and rhyolites. *Am. Mineral.* 70, 80–87.

D'Oriano, C., Landi, P., Pimentel, A., and Zanon, V. (2017). Magmatic processes revealed by anorthoclase textures and trace element modelling: the case of the Lajes Ignimbrite eruption (Terceira Island, Azores). *J. Volcanol. Geother. Res.* 347, 44–63. doi: 10.1016/j.jvolgeores.2017.08.012

Doucelance, R., Escrig, S., Moreira, M., Gariépy, C., and Kurz, M. D. (2003). Pb-Sr-He isotope and trace element geochemistry of the Cape Verde archipelago. *Geochim. Cosmochim. Acta* 67, 3717–3733. doi: 10.1016/S0016-7037(03)00161-3

Dufek, J., and Bachmann, O. (2010). Quantum magmatism: magmatic compositional gaps generated by melt-crystal dynamics. *Geology* 38, 687–690. doi: 10.1130/G30831.1

Dyhr, C. T., and Holm, P. M. (2010). A volcanological and geochemical investigation of Boa Vista, Cape Verde Islands; 40 Ar/39 Ar geochronology and field constraints. *J. Volcanol. Geother. Res.* 189, 19–32. doi: 10.1016/j.jvolgeores.2009.10.010

Ebinger, C. J., and Casey, M. (2001). Continental breakup in magmatic provinces: an Ethiopian example. *Geology* 29, 527–530. doi: 10.1130/0091-7613(2001)029<0527:CBIMPA>2.0.CO;2

Edgar, C. J., Wolff, J. A., Nichols, H. J., Cas, R. A. F., and Martı, J. (2002). A complex Quaternary ignimbrite-forming phonolitic eruption: the Poris member of the Diego Hernández Formation (Tenerife, Canary Islands). *J. Volcanol. Geother. Res.* 118, 99–130. doi: 10.1016/S0377-0273(02)00252-4

Edgar, C. J., Wolff, J. A., Olin, P. H., Nichols, H. J., Pittari, A., Cas, R. A. F., et al. (2007). The late Quaternary Diego Hernandez Formation, Tenerife: volcanology of a complex cycle of voluminous explosive phonolitic eruptions. *J. Volcanol. Geother. Res.* 160, 59–85. doi: 10.1016/j.jvolgeores.2006.06.001

Eisele, S., Freundt, A., Kutterolf, S., Hansteen, T. H., Klügel, A., and Irion, I. M. (2016). Evolution of magma chambers generating the phonolitic Cão Grande Formation on Santo Antão, Cape Verde Archipelago. *J. Volcanol. Geother. Res.* 327, 436–448. doi: 10.1016/j.jvolgeores.2016.09.016

Eisele, S., Freundt, A., Kutterolf, S., Ramalho, R. S., Kwasnitschka, T., Wang, K.-L., et al. (2015). Stratigraphy of the Pleistocene, phonolitic Cão Grande Formation on Santo Antão, Cape Verde. *J. Volcanol. Geother. Res.* 301, 204–220. doi: 10.1016/j.jvolgeores.2015.03.012

Ericson, D. B., Fleming, R. H., LaMourie, M. J., Barnes, C. A., Namias, J., and Broadus, J. M. (2017). *Atlantic Ocean*. Chicago, IL: Encyclopaedia Britannica, inc.

Faugeres, J. C., Legigan, P., Maillet, N., and Latouche, C. (1989). Pelagic, turbiditic, and contouritic sequential deposits on the Cape Verde plateau (leg 108, site 659, Northwest Africa): sediment record during Neogene time. *Proc. Ocean Drill. Program Sci. Results* 108, 311–328. doi: 10.2973/odp.proc.sr.108.138.1989

Feraud, G. (1981). *Datations des Résaux de Dykes et de Roches Volcaniques Sous-Marines par les Methods K-Ar et 40Ar-39Ar. Utilisation des Dykes Comme Marqueurs de Paleocontraintes*. Ph.D. thesis, University of Nice Sophia Antipolis, Nice, 146.

Feraud, G., Gastaud, J., Schmincke, H., Pritchard, G., Lietz, J., and Bleil, U. (1981). New K-Ar ages, chemical analyses and magnetic data of rocks from the islands of Santa Maria (Azores), Porto Santo and Madeira (Madeira archipelago) and Gran Canaria (Canary Islands). *Bull. Volcanol.* 44, 359–375. doi: 10.1007/BF02600570

Ferguson, A. K. (1978). The crystallisation of pyroxenes and amphiboles in some alkaline rocks and the presence of a pyroxene compositional gap. *Contrib. Mineral. Petrol.* 67, 11–15. doi: 10.1007/BF00371628

Ferla, P., and Meli, C. (2006). Evidence of magma mixing in the 'Daly Gap' of alkaline suites: a case study from the enclaves of Pantelleria (Italy). *J. Petrol.* 47, 1467–1507. doi: 10.1093/petrology/egl015

Fernandes, R. M. S., Catalão, J., and Trota, A. N. (2018). "The contribution of space-geodetic techniques to the understanding of the present-day geodynamics of the Azores triple junction," in *Volcanoes of the Azores*, eds U. Kueppers and C. Beier (Berlin: Springer), 57–69. doi: 10.1007/978-3-642-32226-6_4

Ferreira, M., Macedo, C., and Ferreira, J. (1988). K-Ar geochronology in the Selvagens, Porto Santo and Madeira islands (Eastern Central Atlantic): a 30 m.y. spectrum of submarine and subaerial volcanism. *Lunar Planet. Sci. Conf.* 19:325.

Fitton, J. G. (1987). "The Cameroon line, West Africa: a comparison between oceanic and continental alkaline volcanism," in *Alkaline Igneous Rocks. Geological Society Special Publications*, Vol. 30, eds J. G. Fitton and B. G. J. Upton (London: The Geological Society of London), 273–291. doi: 10.1144/GSL.SP.1987.030.01.13

Fitton, J. G. (2007). "The OIB paradox," in *Plates, Plumes, and Planetary Processes. Geological Society of America Special Paper*, Vol. 430, eds G. R. Foulger and D. M. Jurdy (Boulder, CO: Geological Society of America), 387–412.

Fitton, J. G., and Hughes, D. J. (1977). Petrochemistry of the volcanic rocks of the Island of Principe, Gulf of Guinea. *Contrib. Mineral. Petrol.* 64, 257–272. doi: 10.1007/BF00371757

Flude, S., Burgess, R., and McGarvie, D. W. (2008). Silicic volcanism at Ljósufjöll, Iceland: insights into evolution and eruptive history from Ar–Ar dating. *J. Volcanol. Geother. Res.* 169, 154–175. doi: 10.1016/j.jvolgeores.2007.08.019

Fodor, R. V., Mukasa, S. B., and Sial, A. N. (1998). Isotopic and trace-element indications of lithospheric and asthenospheric components in Tertiary alkali basalts, northeastern Brazil. *Lithos* 43, 197–217. doi: 10.1016/S0024-4937(98)00012-7

Freundt, A., and Schmincke, H.-U. (1995). Petrogenesis of rhyolite-trachyte-basalt composite ignimbrite P1, Gran Canaria, Canary Islands. *J. Geophys. Res.* 100, 455–474. doi: 10.1029/94JB02478

Frost, B. R., and Frost, C. D. (2008). A geochemical classification for feldspathic igneous rocks. *J. Petrol.* 49, 1955–1969. doi: 10.1093/petrology/egn054

Furman, T., Frey, F. A., and Meyer, P. S. (1992a). Petrogenesis of evolved basalts and rhyolites at Austurhorn, southeastern Iceland: the role of fractional crystallization. *J. Petrol.* 33, 1405–1445. doi: 10.1093/petrology/33.6.1405

Furman, T., Meyer, P. S., and Frey, F. (1992b). Evolution of Icelandic central volcanoes: evidence from the Austerhorn intrusion, southeastern Iceland. *Bull. Volcanol.* 55, 45–62. doi: 10.1007/BF00301119

Gale, N. H., Moorbath, S., Simons, J., and Walker, G. P. L. (1966). K-Ar ages of acid intrusive rocks from Iceland. *Earth Planet. Sci. Lett.* 1, 284–288. doi: 10.1016/0012-821X(66)90008-2

Gandino, A., Guidi, M., Merlo, C., Mete, L., Rossi, R., and Zan, L. (1985). Preliminary model of the Ribeira Grande geothermal field (Azores Islands). *Geothermics* 14, 91–105. doi: 10.1016/0375-6505(85)90096-3

Gardner, J. E., Rutherford, M., Carey, S., and Sigurdsson, H. (1995). Experimental constraints on pre-eruptive water contents and changing magma storage prior to explosive eruptions of Mount St Helens volcano. *Bull. Volcanol.* 57, 1–17. doi: 10.1007/BF00298703

Gass, I. G. (1967). Geochronology of the Tristan da Cunha group of islands. *Geol. Mag.* 104, 160–170. doi: 10.1017/S0016756800040620

Geldmacher, J., and Hoernle, K. (2000). The 72 Ma geochemical evolution of the Madeira hotspot (eastern North Atlantic): recycling of Paleozoic (≤500 Ma) oceanic lithosphere. *Earth Planet. Sci. Lett.* 183, 73–92. doi: 10.1016/S0012-821X(00)00266-1

Geldmacher, J., Hoernle, K., van den Bogaard, P., Duggen, S., and Werner, R. (2005). New $^{40}Ar/^{39}Ar$ age and geochemical data from seamounts in the Canary and Madeira volcanic provinces: support for the mantle plume hypothesis. *Earth Planet. Sci. Lett.* 237, 85–101. doi: 10.1016/j.epsl.2005.04.037

Geldmacher, J., van den Bogaard, P., Hoernle, K., and Schmincke, H. U. (2000). The $^{40}Ar/^{39}Ar$ age dating of the Madeira Archipelago and the hotspot track (eastern North Atlantic). *Geochem. Geophys. Geosyst.* 1:1008. doi: 10.1029/1999GC000018

Gelman, S. E., Gutiérrez, F. J., and Bachmann, O. (2013). On the longevity of large upper crustal silicic magma reservoirs. *Geology* 41, 759–762. doi: 10.1130/G34241.1

Genske, F. S., Beier, C., Haase, K. M., Turner, S. P., Krumm, S., and Brandl, P. A. (2013). Oxygen isotopes in the Azores islands: crustal assimilation recorded in olivine. *Geology* 41, 491–494. doi: 10.1130/G33911.1

Genske, F. S., Turner, S. P., Beier, C., and Schaefer, B. F. (2012). The petrology and geochemistry of lavas from the western Azores islands of Flores and Corvo. *J. Petrol.* 53, 1673–1708. doi: 10.1093/petrology/egs029

Gente, P., Dyment, J., Maia, M., and Goslin, J. (2003). Interaction between the Mid-Atlantic Ridge and the Azores hot spot during the last 85 Myr: emplacement and rifting of the hotspot derived plateaus. *Geochem. Geophys. Geosyst.* 4:8514. doi: 10.1029/2003GC000527

Gerlach, D. C., Stormer, J. C. Jr., and Mueller, P. A. (1987). Isotopic geochemistry of Fernando de Noronha. *Earth Planet. Sci. Lett.* 85, 129–144. doi: 10.1016/0012-821X(87)90027-6

Gertisser, R., Self, S., Gaspar, J. L., Kelley, S. P., Pimentel, A., Eikenberg, J., et al. (2010). Ignimbrite stratigraphy and chronology on Terceira Island, Azores. *Geol. Soc. Am. Spec. Paper* 464, 133–154. doi: 10.1130/2010.2464(07)

Gibson, I. L. (1970). A pantelleritic welded ash-flow from the Ethiopian Rift Valley. *Contrib. Mineral. Petrol.* 28, 89–111. doi: 10.1007/BF00404992

Gioncada, A., and Landi, P. (2010). The pre-eruptive volatile contents of recent basaltic and pantelleritic magmas at Pantelleria (Italy). *J. Volcanol. Geother. Res.* 271, 123–201. doi: 10.1016/j.jvolgeores.2009.11.006

Giordano, D., Mangiacapra, A., Potuzak, M., Russell, J. K., Romano, C., Dingwell, D. B., et al. (2006). An expanded non-Arrhenian model for silicate melt viscosity: a treatment for metaluminous, peraluminous and peralkaline liquids. *Chem. Geol.* 229, 42–56. doi: 10.1016/j.chemgeo.2006.01.007

Giordano, D., Romano, C., Dingwell, D. B., Poe, B., and Behrens, H. (2004). The combined effects of water and fluorine on the viscosity of silicic magmas. *Geochim. Cosmochim. Acta* 68, 5159–5168. doi: 10.1016/j.gca.2004.08.012

González, P. J., Bagnardi, M., Hooper, A. J., Larsen, Y., Marinkovic, P., Samsonov, S. V., et al. (2015). The 2014–2015 eruption of Fogo volcano: Geodetic modelling of Sentinel-1 TOPS interferometry. *Geophys. Res. Lett.* 42, 9239–9246. doi: 10.1002/2015GL066003

Goodenough, K. M., Schilling, J., Jonsson, E., Kalvig, P., Charles, N., Tuduri, J., et al. (2016). Europe's rare earth element resource potential: an overview of REE metallogenetic provinces and their geodynamic setting. *Ore Geol. Rev.* 72, 838–856. doi: 10.1016/j.oregeorev.2015.09.019

Gudmundsson, A. (1995). Ocean-ridge discontinuities in Iceland. *J. Geol. Soc. London* 152, 1011–1015. doi: 10.1144/GSL.JGS.1995.152.01.22

Gudmundsson, A. (2000). Dynamics of volcanic systems in Iceland: example of tectonism and volcanism at juxtaposed hot spot and mid-ocean ridge systems. *Annu. Rev. Earth Planet. Sci.* 28, 107–140. doi: 10.1146/annurev.earth.28.1.107

Guest, J. E., Gaspar, J. L., Cole, P. D., Queiroz, G., Duncan, A. M., Wallenstein, N., et al. (1999). Volcanic geology of Furnas volcano, São Miguel, Azores. *J. Volcanol. Geother. Res.* 92, 1–29. doi: 10.1016/S0377-0273(99)00064-5

Guillou, H., Carracedo, J. C., Torrado, F. P., and Badiola, E. R. (1996). K-Ar ages and magnetic stratigraphy of a hotspot-induced, fast grown oceanic island: El Hierro, Canary Islands. *J. Volcanol. Geother. Res.* 73, 141–155. doi: 10.1016/0377-0273(96)00021-2

Gunnarsson, B., Marsh, B., and Taylor, H. P. Jr. (1998). Generation of Icelandic rhyolites: silicic lavas from the Torfajökull central volcano. *J. Volcanol. Geother. Res.* 83, 1–45. doi: 10.1016/S0377-0273(98)00017-1

Haffty, J., and Noble, D. C. (1972). Release and migration of molybdenum during the primary crystallization of peralkaline silicic volcanic rocks. *Econ. Geol.* 67, 768–775. doi: 10.2113/gsecongeo.67.6.768

Hansteen, T. H., Klügel, A., and Schmincke, H. U. (1998). Multi-stage magma ascent beneath the Canary Islands: evidence from fluid inclusions. *Contrib. Mineral. Petrol.* 132, 48–64. doi: 10.1007/s004100050404

Hansteen, T. H., and Troll, V. R. (2003). Oxygen isotope composition of xenoliths from the oceanic crust and volcanic edifice beneath Gran Canaria (Canary Islands): consequences for crustal contamination of ascending magmas. *Chem. Geol.* 193, 181–193. doi: 10.1016/S0009-2541(02)00325-X

Hardarson, B. S., Fitton, J. G., Ellam, R. M., and Pringle, M. S. (1997). Rift relocation—a geochemical and geochronological investigation of a palaeo-rift in Northwest Iceland. *Earth Planet. Sci. Lett.* 153, 181–196. doi: 10.1016/S0012-821X(97)00145-3

Hards, V. L., Kempton, P. D., Thompson, R. N., and Greenwood, P. B. (2000). The magmatic evolution of the Snæfell volcanic centre; an example of volcanism during incipient rifting in Iceland. *J. Volcanol. Geother. Res.* 99, 97–121. doi: 10.1016/S0377-0273(00)00160-8

Harris, C. (1983). The petrology of lavas and associated plutonic inclusions of Ascension Island. *J. Petrol.* 24, 424–470. doi: 10.1093/petrology/24.4.424

Harris, C., and Bell, J. D. (1982). Natural partial melting of syenite blocks from Ascension Island. *Contrib. Mineral. Petrol.* 79, 107–113. doi: 10.1007/BF01132880

Harris, C., Bell, J. D., and Atkins, F. B. (1982). Isotopic composition of lead and strontium in lavas and coarse-grained blocks from Ascension Island, South Atlantic. *Earth Planet. Sci. Lett.* 60, 79–85. doi: 10.1016/0012-821X(82)90022-X

Harris, C., Smith, H. S., and le Roex, A. P. (2000). Oxygen isotope composition of phenocrysts from Tristan da Cunha and Gough Island lavas: variation with fractional crystallisation and evidence for assimilation. *Contrib. Mineral. Petrol.* 138, 164–175. doi: 10.1007/s004100050015

Hartley, M. E., Thordarson, T., and de Joux, A. (2016). Postglacial eruptive history of the Askja region, North Iceland. *Bull. Volcanol.* 78:28. doi: 10.1007/s00445-016-1022-7

Hedberg, J. D. (1969). *A Geological Analysis of the Cameroon Trend*. Ph.D. thesis, Princeton University, Princeton, NJ, 188.

Heezen, B. C., and Tharp, M. (1961). *Physiographic Diagram of the South Atlantic Ocean*. Boulder: Geological Society of America.

Hicks, A., Barclay, J., Mark, D. F., and Loughlin, S. (2012). Tristan da Cunha: constraining eruptive behaviour using the $^{40}Ar/^{39}Ar$ dating technique. *Geology* 40, 723–726. doi: 10.1130/G33059.1

Hildenbrand, A., Madureira, P., Marques, F. O., Cruz, I., Henry, B., and Silva, P. (2008). Multi-stage evolution of a sub-aerial volcanic ridge over the last 1.3 Myr: S. Jorge Island Azores Triple Junction. *Earth Planet. Sci. Lett.* 273, 289–298. doi: 10.1016/j.epsl.2008.06.041

Hildenbrand, A., Weis, D., Madureira, P., and Marques, F. O. (2014). Recent plate re-organization at the Azores Triple Junction: evidence from combined geochemical and geochronological data on Faial, S. Jorge and Terceira volcanic Islands. *Lithos* 210, 27–39. doi: 10.1016/j.lithos.2014.09.009

Hildner, E., Klügel, A., and Hansteen, T. H. (2012). Barometry of lavas from the 1951 eruption of Fogo, Cape Verde Islands: implications for historic and prehistoric magma plumbing systems. *J. Volcanol. Geother. Res.* 21, 73–90. doi: 10.1016/j.jvolgeores.2011.12.014

Hildner, E., Klügel, A., and Hauff, F. (2011). Magma storage and ascent during the 1995 eruption of Fogo, Cape Verde archipelago. *Contrib. Mineral. Petrol.* 162, 751–772. doi: 10.1007/s00410-011-0623-6

Hildreth, W. (1981). Gradients in silicic magma chambers: implications for lithospheric magmatism. *J. Geophys. Res.* 86, 10153–10192. doi: 10.1029/JB086iB11p10153

Hildreth, W. (2004). Volcanological perspectives on Long Valley, Mammoth Mountain, and Mono Craters: several contiguous but discrete systems. *J. Volcanol. Geother. Res.* 136, 169–198. doi: 10.1016/j.jvolgeores.2004.05.019

Hoernle, K. (1998). Geochemistry of Jurassic oceanic crust beneath Gran Canaria (Canary Islands): implications for crustal recycling and assimilation. *J. Petrol.* 39, 859–880. doi: 10.1093/petroj/39.5.859

Hoernle, K., and Carracedo, J. C. (2009). "Canary Islands, geology," in *Encyclopedia of Islands*, eds R. G. Gillespie and D. A. Clague (Berkeley, CA: Press), 133–143.

Hofmann, A. W. (2003). Sampling mantle heterogeneity through oceanic basalts: isotopes and trace elements. *Treatise Geochem.* 2, 61–101.

Holm, P. M., Grandvuinet, T., Friis, J., Wilson, J. R., Barker, A. K., and Plesner, S. (2008). An ^{40}Ar-^{39}Ar study of the Cape Verde hot spot: temporal evolution in a semistationary plate environment. *J. Geophys. Res.* 113:B08201. doi: 10.1029/2007JB005339

Holm, P. M., Wilson, J. R., Christensen, B. P., Hansen, L., Hansen, S. L., Hein, K. M., et al. (2006). Sampling the Cape Verde mantle plume: evolution of melt compositions on Santo Antão, Cape Verde Islands. *J. Petrol.* 47, 145–189. doi: 10.1093/petrology/egi071

Huber, C., Bachmann, O., and Dufek, J. (2012). Crystal-poor versus crystal-rich ignimbrites: a competition between stirring and reactivation. *Geology* 40, 115–118. doi: 10.1130/G32425.1

Imsland, P., Larsen, J. G., Prestvik, T., and Sigmond, E. M. (1977). The geology and petrology of Bouvetøya, south Atlantic Ocean. *Lithos* 10, 213–234. doi: 10.1016/0024-4937(77)90049-4

Jakobsson, S. P. (1979). Petrology of recent basalts of the Eastern Volcanic Zone, Iceland. *Acta Naturalia Island.* 26, 1–103.

Jeffery, A. J. (2016). *Petrogenesis and Contrasting Eruption Styles of Peralkaline Silicic Magmas from Terceira and São Miguel, Azores*. Ph.D. thesis, Keele University, Newcastle, 746.

Jeffery, A. J., Gertisser, R., Jackson, R. A., O'Driscoll, B., and Kronz, A. (2016a). On the compositional variability of dalyite, K2ZrSi6O15: a new occurrence from Terceira, Azores. *Mineral. Mag.* 80, 547–565. doi: 10.1180/minmag.2016.080.018

Jeffery, A. J., Gertisser, R., O'Driscoll, B., Pacheco, J. M., Whitley, S., Pimentel, A., et al. (2016b). Temporal evolution of a post-caldera, mildly peralkaline magmatic system: Furnas volcano, São Miguel, Azores. *Contrib. Mineral. Petrol.* 171:42. doi: 10.1007/s00410-016-1235-y

Jeffery, A. J., Gertisser, R., Self, S., Pimentel, A., O'Driscoll, B., and Pacheco, J. M. (2017). Petrogenesis of the peralkaline ignimbrites of Terceira, Azores. *J. Petrol.* 58, 2365–2402. doi: 10.1093/petrology/egy012

Jicha, B. R., Singer, B. S., and Valentine, M. J. (2013). $^{40}Ar/^{39}Ar$ geochronology of subaerial Ascension Island and a re-evaluation of the temporal progression of basaltic to rhyolitic volcanism. *J. Petrol.* 54, 2581–2596. doi: 10.1093/petrology/egt058

Jóhannesson, H. (1980). Jardlagaskipan og þróun rekbelta á Vesturlandi (Stratigraphy and evolution of rift zones in West Iceland). *Náttúrufrædingurinn* 50, 13–31.

Johnsen, O., Ferraris, G., Gault, R. A., Grice, J., Kampf, A. R., and Pekov, I. V. (2003). The nomenclature of eudialyte-group minerals. *Can. Mineral.* 41, 785–794. doi: 10.2113/gscanmin.41.3.785

Johnson, C. L., Wijbrans, J. R., Constable, C. G., Gee, J., Staudigel, H., Tauxe, L., et al. (1998). $^{40}Ar/^{39}Ar$ ages and paleomagnetism of Sao Miguel lavas, Azores. *Earth Planet. Sci. Lett.* 160, 637–649. doi: 10.1016/S0012-821X(98)00117-4

Jónasson, K. (1994). Rhyolite volcanism in the Krafla central volcano, north-east Iceland. *Bull. Volcanol.* 56, 516–528. doi: 10.1007/BF00302832

Jónasson, K. (2007). Silicic volcanism in Iceland: composition and distribution within the active volcanic zones. *J. Geodyn.* 43, 101–117. doi: 10.1016/j.jog.2006.09.004

Jónasson, K., Holm, P. M., and Pedersen, A. K. (1992). Petrogenesis of silicic rocks from the Króksfjördur central volcano, NW Iceland. *J. Petrol.* 33, 1345–1369. doi: 10.1093/petrology/33.6.1345

Jørgensen, J., and Holm, P. (2002). Temporal variation and carbonatite contamination in primitive ocean island volcanics from São Vicente, Cape Verde Islands. *Chem. Geol.* 192, 249–267. doi: 10.1016/S0009-2541(02)00198-5

Jutzeler, M., Schmincke, H. U., and Sumita, M. (2010). The incrementally-zoned Miocene Ayaguares ignimbrite (Gran Canaria, Canary Islands). *J. Volcanol. Geother. Res.* 196, 1–19. doi: 10.1016/j.jvolgeores.2010.07.002

Kar, A., Weaver, B., Davidson, J., and Colucci, M. (1998). Origin of differentiated volcanic and plutonic rocks from Ascension Island, South Atlantic Ocean. *J. Petrol.* 39, 1009–1024. doi: 10.1093/petroj/39.5.1009

Kaula, W. M. (1970). Earth's gravity field: relation to global tectonics. *Science* 169, 982–985. doi: 10.1126/science.169.3949.982

Kawabata, H., Hanyu, T., Chang, Q., Kimura, J., Nichols, A. R. L., and Tatsumi, Y. (2011). The petrology and geochemistry of St. Helena alkali basalts: evaluation of the oceanic crust-recycling model for HIMU OIB. *J. Petrol.* 52, 791–838. doi: 10.1093/petrology/egr003

Khomyakov, A. (1995). *Mineralogy of Hyperagpaitic Alkaline Rocks*. Oxford: Clarendon Press, 222.

Klingelhöfer, F., Minshull, T. A., Blackman, D. K., Harben, P., and Childers, V. (2001). Crustal structure of Ascension Island from wide-angle seismic data: implications for the formation of near-ridge volcanic islands. *Earth Planet. Sci. Lett.* 190, 41–56. doi: 10.1016/S0012-821X(01)00362-4

Klitgord, K. D., and Schouten, H. (1986). "Plate kinematics of the Central Atlantic," in *The Geology of North America, The Western North Atlantic Region*, Vol. M, eds P. R. Vogt and B. E. Tucholke (Boulder, CO: Geological Society of America), 351–378.

Klügel, A., Hansteen, T. H., and Galipp, K. (2005). Magma storage and underplating beneath Cumbre Vieja volcano, La Palma (Canary Islands). *Earth Planet. Sci. Lett.* 236, 211–226. doi: 10.1016/j.epsl.2005.04.006

Klügel, A., and Klein, F. (2006). Complex magma storage and ascent at embryonic submarine volcanoes from the Madeira archipelago. *Geology* 34, 337–340. doi: 10.1130/G22077.1

Kobberger, G., and Schmincke, H.-U. (1999). Deposition of rheomorphic ignimbrite D (Mogán Formation), Gran Canaria, Canary Islands, Spain. *Bull. Volcanol.* 60, 465–485. doi: 10.1007/s004450050246

Kogarko, L. N. (1980). Ore-forming potential of alkaline magmas. *Lithos* 26, 167–175. doi: 10.1016/0024-4937(90)90046-4

Kogarko, L. N. (2008). Characteristics of alkali magma differentiation at the Cape Verde Islands. *Geochem. Int.* 46, 1071–1080. doi: 10.1134/S0016702908110013

Krause, D. C., and Watkins, N. D. (1970). North Atlantic crustal genesis in the vicinity of the Azores. *Geophys. J. R. Astron. Soc.* 19, 261–283. doi: 10.1111/j.1365-246X.1970.tb06046.x

Kristjánsson, L. (1982). Geomagnetic polarity mapping in Icelandic lavas. Comparison with ocean-floor magnetic lineations. *Earth Evol. Sci.* 2, 126–129.

Kuritani, T., Yokoyama, T., Kitagawa, H., Kobayashi, K., and Nakamura, E. (2011). Geochemical evolution of historical lavas from Askja Volcano, Iceland: implications for mechanisms and timescales of magmatic differentiation. *Geochim. Cosmochim. Acta* 75, 570–587. doi: 10.1016/j.gca.2010.10.009

Lacasse, C., Sigurdsson, H., Carey, S. N., Jóhannesson, H., Thomas, L. E., and Rogers, N. W. (2007). Bimodal volcanism at the Katla subglacial caldera, Iceland: insight into the geochemistry and petrogenesis of rhyolitic magmas. *Bull. Volcanol.* 69:373. doi: 10.1007/s00445-006-0082-5

Lange, R. A. (1994). "The effect of H_2O, CO_2 and F on the density and viscosity of silicate melts," in *Volatiles in Magmas*, Vol. 30, eds M. R. Carroll and J. R. Holloway (Chantilly, VA: Mineralogical Society of America), 331–365.

Larrea, P., França, Z., Lago, M., Widom, E., Galé, C., and Ubide, T. (2013). Magmatic processes and the role of antecrysts in the genesis of Corvo island (Azores archipelago), Portugal. *J. Petrol.* 54, 769–793. doi: 10.1093/petrology/egs084

Larrea, P., França, Z., Widom, E., and Lago, M. (2018). "Petrology of the Azores Islands," in *Volcanoes of the Azores*, eds U. Kueppers and C. Beier (Berlin: Springer), 197–249. doi: 10.1007/978-3-642-32226-6_10

Larrea, P., Galé, C., Ubide, T., Widom, E., Lago, M., and França, Z. (2014a). Magmatic evolution of Graciosa (Azores), Portugal. *J. Petrol.* 55, 2125–2154. doi: 10.1093/petrology/egu052

Larrea, P., Wijbrans, J. R., Galé, C., Ubide, T., Lago, M., França, Z., et al. (2014b). $^{40}Ar/^{39}Ar$ constraints on the temporal evolution of Graciosa Island, Azores (Portugal). *Bull. Volcanol.* 76:796. doi: 10.1007/s00445-014-0796-8

Larsen, G., Newton, A. J., Dugmore, A. J., and Vilmundardottir, E. G. (2001). Geochemistry, dispersal, volumes and chronology of Holocene silicic tephra layers from the Katla volcanic system, Iceland. *J. Quaternary Sci.* 16, 119–132. doi: 10.1002/jqs.587

Larsen, L. M. (1979). Distribution of REE and other trace elements between phenocrysts and peralkaline undersaturated magmas, exemplified by rocks from the Gardar igneous province, south Greenland. *Lithos* 12, 303–315. doi: 10.1016/0024-4937(79)90022-7

Le Bas, M. J., Le Maitre, R. W., Streckeisen, A., and Zanettin, B. (1986). A chemical classification of volcanic rocks based on the total alkali-silica diagram. *J. Petrol.* 27, 745–750. doi: 10.1093/petrology/27.3.745

Le Maitre, R. W. (1962). Petrology of volcanic rocks, Gough Island, South Atlantic. *Geol. Soc. Am. Bull.* 73, 1309–1340. doi: 10.1130/0016-7606(1962)73[1309:POVRGI]2.0.CO;2

Le Maitre, R. W. (2003). *International A Classification of Igneous Rocks and Glossary of Terms: Recommendations of the International Union of Geological Sciences Subcommission on the Systematics of Igneous Rocks*. Oxford: Blackwell Scientific Publications, 193.

Le Roex, A. P. (1985). Geochemistry, mineralogy, and magmatic evolution of the basaltic and trachytic lavas from Gough Island, South Atlantic. *J. Petrol.* 26, 149–186. doi: 10.1093/petrology/26.1.149

Le Roex, A. P., Cliff, R. A., and Adair, B. J. I. (1990). Tristan da Cunha, South Atlantic: geochemistry and petrogenesis of a basanite-phonolite lava series. *J. Petrol.* 31, 779–812. doi: 10.1093/petrology/31.4.779

Le Roex, A. P., Dick, H. J. B., Reid, A. M., Frey, F. A., Erlank, A. J., and Hart, S. R. (1985). Petrology and geochemistry of basalts from the American-Antarctic Ridge, Southern Ocean: implications for the westward influence of the Bouvet mantle plume. *Contrib. Mineral. Petrol.* 90, 367–380. doi: 10.1007/BF00384715

Le Roex, A. P., and Erlank, A. J. (1982). Quantitative evaluation of fractional crystallisation in Bouvet Island lavas. *J. Volcanol. Geother. Res.* 13, 309–338. doi: 10.1016/0377-0273(82)90055-5

Leat, P. T. (1984). Geological evolution of the trachytic caldera volcano Menengai, Kenya Rift Valley. *J. Geol. Soc. London* 141, 1057–1069. doi: 10.1144/gsjgs.141.6.1057

Lee, D. C., Halliday, A. N., Fitton, G. J., and Poli, G. (1994). Isotopic variations with distance and time in the volcanic islands of the Cameroon Line: evidence of the mantle plume origin. *Earth Planet. Sci. Lett.* 123, 119–138. doi: 10.1016/0012-821X(94)90262-3

Lindhuber, M. J., Marks, M. A., Bons, P. D., Wenzel, T., and Markl, G. (2015). Crystal mat-formation as an igneous layering-forming process: textural and geochemical evidence from the 'lower layered' nepheline syenite sequence of the Ilímaussaq complex, South Greenland. *Lithos* 224, 295–309. doi: 10.1016/j.lithos.2015.03.007

Longpré, M. A., Klügel, A., Diehl, A., and Stix, J. (2014). Mixing in mantle magma reservoirs prior to and during the 2011–2012 eruption at El Hierro, Canary Islands. *Geology* 42, 315–318. doi: 10.1130/G35165.1

Lopes, R. P. (2002). *O vulcanismo do Arquipélago de Fernando de Noronha, PE: Química Mineral e Geoquímica*. Ph.D. thesis, Universidade de São Paulo, São Paulo.

Lopes, R. P., and Ulbrich, M. N. C. (2015). Geochemistry of the alkaline volcanic-subvolcanic rocks of the Fernando de Noronha archipelago, southern Atlantic Ocean. *Braz. J. Geol.* 45, 307–333. doi: 10.1590/231748892015000020009

Lopes, R. P., Ulbrich, M. N. C., and Ulbrich, H. (2014). The subvolcanic rocks of the Fernando de Noronha archipelago, southern Atlantic Ocean: mineral chemistry. *Central Eur. J. Geosci.* 6, 422–456. doi: 10.2478/s13533-012-0195-7

Lowenstern, J. B. (1994). Chlorine, fluid immiscibility, and degassing in peralkaline magmas from Pantelleria, Italy. *Am. Mineral.* 79, 353–369.

Luis, J. F., Miranda, J. M., Galdeano, A., Patriat, P., Rossignol, J. C., and Mendes Victor, L. A. (1994). The Azores triple junction evolution since 10 Ma from an aeromagnetic survey of the Mid-Atlantic Ridge. *Earth Planet. Sci. Lett.* 125, 439–459. doi: 10.1016/0012-821X(94)90231-3

Lunde, T. (1965). Fra et besøk på Bouvetøya. *Norsk Polarinstitutt Årbok* 1963, 197–203.

Macdonald, R. (1974a). Nomenclature and petrochemistry of the peralkaline oversaturated extrusive rocks. *Bull. Volcanol.* 38, 495–505.

Macdonald, R. (1974b). Tectonic settings and magma associations. *Bull. Volcanol.* 38, 575–593. doi: 10.1007/BF02596899

Macdonald, R. (2012). Evolution of peralkaline silicic complexes: lessons from the extrusive rocks. *Lithos* 152, 11–22. doi: 10.1016/j.lithos.2012.01.014

Macdonald, R., Bagiński, B., Leat, P. T., White, J. C., and Dzierżanowski, P. (2011). Mineral stability in peralkaline silicic rocks: information from trachytes of the Menengai volcano, Kenya. *Lithos* 125, 553–568. doi: 10.1016/j.lithos.2011.03.011

Macdonald, R., Bagiński, B., Ronga, F., Dzierżanowski, P., Lustrini, M., Marzoli, A., et al. (2012). Evidence for extreme fractionation of peralkaline silicic magmas, the Boseti volcanic complex, Main Ethiopian Rift. *Mineral. Petrol.* 104, 163–175. doi: 10.1007/s00710-011-0184-4

Macdonald, R., Belkin, H. E., Fitton, J. G., Rogers, N. W., Nejbert, K., Tindle, A. G., et al. (2008). The roles of fractional crystallisation, magma mixing, crystal mush remobilisation, and volatile-melt interactions in the genesis of a young basalt-peralkaline rhyolite suite, the Greater Olkaria Volcanic Complex, Kenya Rift Valley. *J. Petrol.* 49, 1515–1547. doi: 10.1093/petrology/egn036

Macdonald, R., Davies, G. R., Upton, B. G. J., Dunkley, P. N., Smith, M., and Leat, P. T. (1995). Petrogenesis of Silali volcano, Gregory Rift, Kenya. *J. Geol. Soc. London* 152, 703–720. doi: 10.1144/gsjgs.152.4.0703

Macdonald, R., McGarvie, D. W., Pinkerton, H., Smith, R. L., and Palacz, A. (1990). Petrogenetic evolution of the Torfajökull Volcanic Complex, Iceland I. Relationship between the magma types. *J. Petrol.* 31, 429–459. doi: 10.1093/petrology/31.2.429

Macdonald, R., Navarro, J. M., Upton, B. G. J., and Davies, G. R. (1994). Strong compositional zonation in peralkaline magma: Menengai, Kenya Rift Valley. *J. Volcanol. Geother. Res.* 60, 301–325. doi: 10.1016/0377-0273(94)90057-4

Macdonald, R., and Scaillet, B. (2006). The central Kenya peralkaline province: insights into the evolution of peralkaline salic magmas. *Lithos* 91, 59–73. doi: 10.1016/j.lithos.2006.03.009

Macdonald, R., Sparks, R. S. J., and Sigurdsson, H. (1987). The 1875 eruption of Askja volcano, Iceland: combined fractional crystallization and selective contamination in the generation of rhyolitic magma. *Mineral. Mag.* 51, 183–202. doi: 10.1180/minmag.1987.051.360.01

Madeira, J., Mata, J., Mourão, C., da Silveira, A. B., Martins, S., Ramalho, R., et al. (2010). Volcano-stratigraphic and structural evolution of Brava Island (Cape Verde) based on $^{40}Ar/^{39}Ar$, U–Th and field constraints. *J. Volcanol. Geother. Res.* 196, 219–235. doi: 10.1016/j.jvolgeores.2010.07.010

Madureira, P., Mata, J., Mattielli, N., Queiroz, G., and Silva, P. (2011). Mantle source heterogeneity, magma generation and magmatic evolution at Terceira

Island (Azores archipelago): constraints from elemental and isotopic (Sr, Nd, Hf, and Pb) data. *Lithos* 126, 402–418. doi: 10.1016/j.lithos.2011.07.002

Mahood, G. A., and Baker, D. R. (1986). Experimental constraints on depths of fractionation of mildly alkali basalts and associated felsic rocks: Pantelleria, Strait of Sicily. *Contrib. Mineral. Petrol.* 93, 251–264. doi: 10.1007/BF00371327

Mahood, G. A., and Hildreth, W. (1986). Geology of the peralkaline volcano at Pantelleria, Strait of Sicily. *Bull. Volcanol.* 48, 143–172. doi: 10.1007/BF01046548

Manning, D. A. C. (1981). The effect of fluorine on liquidus phase relationships in the system Qz-Ab-Or with excess water. *Contrib. Mineral. Petrol.* 76, 206–215. doi: 10.1007/BF00371960

Markl, G. (2001). A new type of silicate liquid immiscibility in peralkaline nepheline syenites (lujavrites) of the Ilimaussaq complex, South Greenland. *Contrib. Mineral. Petrol.* 141, 458–472. doi: 10.1007/s004100100252

Markl, G., Marks, M. A., and Frost, B. R. (2010). On the controls of oxygen fugacity in the generation and crystallization of peralkaline melts. *J. Petrol.* 51, 1831–1847. doi: 10.1093/petrology/egq040

Marks, M. A. W., Hettmann, K., Schilling, J., Frost, B. R., and Markl, G. (2011). The mineralogical diversity of alkaline igneous rocks: critical factors for the transition from miaskitic to agpaitic phase assemblages. *J. Petrol.* 52, 439–455. doi: 10.1093/petrology/egq086

Marks, M. A. W., and Markl, G. (2015). "The ilímaussaq alkaline complex, South Greenland," in *Layered Intrusions*, eds B. Charlier, O. Namur, R. Latypov, and C. Tegner (Dordrecht: Springer), 649–691.

Marks, M. A. W., and Markl, G. (2017). A global review on agpaitic rocks. *Earth Sci. Rev.* 173, 229–258. doi: 10.1016/j.earscirev.2017.06.002

Marques, F. O., Catalão, J. C., DeMets, C., Costa, A. C. G., and Hildenbrand, A. (2013). GPS and tectonic evidence for a diffuse plate boundary at the Azores triple junction. *Earth Planet. Sci. Lett.* 281, 177–187. doi: 10.1016/j.epsl.2013.08.051

Marques, L. S., Ulbrich, M. N. C., Ruberti, E., and Tassinari, C. G. (1999). Petrology, geochemistry and Sr-Nd isotopes of the Trindade and Martin Vaz volcanic rocks (Southern Atlantic Ocean). *J. Volcanol. Geother. Res* 93, 191–216. doi: 10.1016/S0377-0273(99)00111-0

Marshall, A. S., Macdonald, R., Rogers, N. W., Fitton, J. G., Tindle, A. G., Nejbert, K., et al. (2009). Fractionation of peralkaline silicic magmas: the Greater Olkaria Volcanic Complex, Kenya Rift Valley. *J. Petrol.* 50, 323–359. doi: 10.1093/petrology/egp001

Martí, J., and Gudmundsson, A. (2000). The Las Cañadas caldera (Tenerife, Canary Islands): an overlapping collapse caldera generated by magma-chamber migration. *J. Volcanol. Geother. Res.* 103, 161–173. doi: 10.1016/S0377-0273(00)00221-3

Martí, J., Mitjavila, J., and Araña, V. (1994). Stratigraphy, structure and geochronology of the Las Cañadas caldera (Tenerife, Canary Islands). *Geol. Mag.* 131, 715–727. doi: 10.1017/S0016756800012838

Martin, E., and Sigmarsson, O. (2007). Crustal thermal state and origin of silicic magma in Iceland: the case of Torfajökull, Ljósufjöll and Snæfellsjökull volcanoes. *Contrib. Mineral. Petrol.* 153, 593–605. doi: 10.1007/s00410-006-0165-5

Martin, E., and Sigmarsson, O. (2010). Thirteen million years of silicic magma production in Iceland: links between petrogenesis and tectonic settings. *Lithos* 116, 129–144. doi: 10.1016/j.lithos.2010.01.005

Martin, V. M., Morgan, D. J., Jerram, D. A., Caddick, M. J., Prior, D. J., and Davidson, J. P. (2008). Bang! Month-scale eruption triggering at Santorini volcano. *Science* 321, 1178–1178. doi: 10.1126/science.1159584

Marzoli, A., Peccirillo, E. M., Renne, P. R., Bellieni, G., Iacumin, M., Nyobe, J. B., et al. (2000). The Cameroon Volcanic Line revisited: petrogenesis of continental basaltic magmas from lithospheric and asthenospheric mantle sources. *J. Petrol.* 41, 87–109. doi: 10.1093/petrology/41.1.87

Masotta, M., Mollo, S., Freda, C., Gaeta, M., and Moore, G. (2013). Clinopyroxene-liquid thermometers and barometers specific to alkaline differentiated systems. *Contrib. Mineral. Petrol.* 166, 1545–1561. doi: 10.1007/s00410-013-0927-9

Mata, J., Martins, S., Mattielli, N., Madeira, J., Faria, B., Ramalho, R. S., et al. (2017). The 2014-15 eruption and the short-term geochemical evolution of the Fogo volcano (Cape Verde): evidence for small scale mantle heterogeneity. *Lithos* 288-289, 91–107. doi: 10.1016/j.lithos.2017.07.001

Matthews, N. E., Pyle, D. M., Smith, V. C., Wilson, C. J. N., Huber, C., and Van Hinsberg, V. (2012). Quartz zoning and the pre-eruptive evolution of the∼ 340-ka Whakamaru magma systems, New Zealand. *Contrib. Mineral. Petrol.* 163, 87–107. doi: 10.1007/s00410-011-0660-1

Maund, J. G., Rex, D. C., Le Roex, A. P., and Reid, D. L. (1988). Volcanism on Gough Island: a revised stratigraphy. *Geol. Mag.* 125, 175–181. doi: 10.1017/S0016756800009572

Mbowou, I. B. G., Nguihdama, D., Yamgouot, F. N., Ntoumbe, M., and Ngounouno, I. (2013). Ti-bearing aenigmatite from Djinga Tadorgal (Adamawa plateau) and Sao Tomé (Cameroon Line) phonolites: geochemical implications and application of the QUILF thermobarometer for the crystallisation conditions. *Int. J. Biol. Chem. Sci.* 7, 2600–2610. doi: 10.4314/ijbcs.v7i6.34

McDougall, I., Kristjansson, L., and Saemundsson, K. (1984). Magnetostratigraphy and geochronology of NW-Iceland. *J. Geophys. Res.* 89, 7029–7060. doi: 10.1029/JB089iB08p07029

McDougall, I., and Ollier, C. D. (1982). Potassium-argon ages from Tristan da Cunha, South Atlantic. *Geol. Mag.* 119, 87–93. doi: 10.1017/S0016756800025681

McDougall, I., and Schmincke, H.-U. (1976). Geochronology of Gran Canaria, Canary Islands: age of shield building volcanism and other magmatic phases. *Bull. Volcanol.* 40, 57–77. doi: 10.1007/BF02599829

McGarvie, D. W. (1984). Torfajokull: a volcano dominated by magma mixing. *Geology* 12, 685–688. doi: 10.1130/0091-7613(1984)12<685:TAVDBM>2.0.CO;2

McGarvie, D. W., Burgess, R., Tindle, A. G., Tuffen, H., and Stevenson, J. A. (2006). Pleistocene rhyolitic volcanism at Torfajökull, Iceland: eruption ages, glaciovolcanism, and geochemical evolution. *Jökull* 56, 57–75.

McGarvie, D. W., Macdonald, R., Pinkerton, H., and Smith, R. L. (1990). Petrogenetic evolution of the Torfajökull volcanic complex, Iceland II. The role of magma mixing. *J. Petrol.* 31, 461–481. doi: 10.1093/petrology/31.2.461

McNutt, M. (1988). Thermal and mechanical properties of the Cape Verde Rise. *J. Geophys. Res. Solid Earth* 93, 2784–2794. doi: 10.1029/JB093iB04p02784

Meletlidis, S., Di Roberto, A., Pompilio, M., Bertagnini, A., Iribarren, I., Felpeto, A., et al. (2012). Xenopumices from the 2011–2012 submarine eruption of El Hierro (Canary Islands, Spain): constraints on the plumbing system and magma ascent. *Geophys. Res. Lett.* 39, L17302. doi: 10.1029/2012GL052675

Merlino, S., and Perchiazzi, N. (1988). Modular mineralogy in the cuspidine group of minerals. *Can. Mineral.* 26, 933–943.

Métrich, N., Zanon, V., Créon, L., Hildenbrand, A., Moreira, M., and Marques, F. O. (2014). Is the 'Azores hotspot'a wetspot? Insights from the geochemistry of fluid and melt inclusions in olivine of Pico basalts. *J. Petrol.* 55, 377–393. doi: 10.1093/petrology/egt071

Mitchell-Thomé, R. C. (1970). *Geology of the South Atlantic Islands*. Berlin: Bebruder Borntraeger.

Mollo, S., Masotta, M., Forni, F., Bachmann, O., De Astis, G., Moore, G., et al. (2015). A K-feldspar-liquid hygrometer specific to alkaline differentiated magmas. *Chem. Geol.* 392, 1–8. doi: 10.1016/j.chemgeo.2014.11.010

Moorbath, S., Sigurdson, H., and Goodwin, R. (1968). K-Ar ages of oldest exposed rocks in Iceland. *Earth Planet. Sci. Lett.* 4, 197–205. doi: 10.1016/0012-821X(68)90035-6

Moore, R. (1990). Volcanic geology and eruption frequency, São Miguel, Azores. . *Bull. Volcanol.* 52, 602–614. doi: 10.1007/BF00301211

Morgan, W. J. (1972). Deep mantle convection plumes and plate motions. *Bull. Am. Associat. Petrol. Geol.* 56, 203–213. doi: 10.1038/nature17422

Morgan, W. J. (1981). "Hotspot tracks and the opening of the Atlantic and Indian Oceans," in *The Sea: Oceanic Lithosphere*, Vol. 7, ed. C. Emiliani (New York, NY: John Wiley & Sons), 443–487.

Moundi, A., Wandji, P., Bardintzeff, J.-M., Ménard, J.-J., Atouba, L. C. O., Mouncherou, O. F., et al. (2007). Les basaltes éocènes à affinité transitionnelle du plateau Bamoun, témoins d'un réservoir mantellique enrichi sous la ligne volcanique du Cameroun. *Comptes Rendus Geosci.* 339, 396–406. doi: 10.1016/j.crte.2007.04.001

Mourão, C., Mata, J., Doucelance, J., Maderia, J., Brum da Silveira, A., Silva, L., et al. (2010). Quaternary extrusive calciocarbonatite volcanism on Brava Island, (Cape Verde). *J. Afr. Earth Sci.* 56, 59–74. doi: 10.1016/j.jafrearsci.2009.06.003

Mourão, C., Mata, J., Doucelance, R., Madeira, J., Millet, M. A., and Moreira, M. (2012). Geochemical temporal evolution of Brava Island magmatism: constraints on the variability of Cape Verde mantle sources and on carbonatite–silicate magma link. *Chem. Geol.* 334, 44–61. doi: 10.1016/j.chemgeo.2012.09.031

Müller, R. D., Sdrolias, M., and Roest, W. R. (2008). Age, spreading rates and spreading symmetry of the world's oceanic crust. *Geochem. Geophys. Geosyst.* 9, 1525–2027. doi: 10.1029/2007GC001743

Mungall, J. E. (1993). *Compositional effects of Magma Mixing and Diffusive Mass Transport on a Basalt-Pantellerite Suite, Terceira, Azores*. Ph.D. thesis, McGill University, Montreal, 385.

Mungall, J. E., and Martin, R. F. (1995). Petrogenesis of basalt-comendite and basalt-pantellerite suites, Terceira, Azores, and some implications for the origin of ocean-island rhyolites. *Contrib. Mineral. Petrol.* 119, 43–55. doi: 10.1007/BF00310716

Muñoz, M., Sagredo, J., de Ignacio, C., Fernández-Suárez, J., and Jeffries, T. E. (2005). New data (U–Pb, K–Ar) on the geochronology of the alkaline-carbonatitic association of Fuerteventura, Canary Islands, Spain. *Lithos* 85, 140–153. doi: 10.1016/j.lithos.2005.03.024

Neave, D. A., Fabbro, G., Herd, R. A., Petrone, C. M., and Edmonds, M. (2012). Melting, differentiation and degassing at the Pantelleria volcano, Italy. *J. Petrol.* 53, 637–663. doi: 10.1093/petrology/egr074

Neumann, E.-R., Olsen, K. H., Baldridge, W. S., and Sundvoll, B. (1992). The Oslo Rift: a review. *Tectonphysics* 208, 1–18. doi: 10.1016/0040-1951(92)90333-2

Neumann, E.-R., Wulff-Pedersen, E., Simonsen, S. L., Pearson, N. J., Martí, J., and Mitjavila, J. (1999). Evidence for fractional crystallisation of periodically refilled magma chambers in Tenerife, Canary Islands. *J. Petrol.* 40, 1089–1123. doi: 10.1093/petroj/40.7.1089

Nicholls, J., and Carmichael, J. S. E. (1969). Peralkaline acid liquids: a petrological study. *Contrib. Mineral. Petrol.* 20, 268–294. doi: 10.1007/BF00377480

Nicholson, H., Condomines, M., Fitton, J. G., Fallick, A. E., Grönvold, K., and Rogers, G. (1991). Geochemical and isotopic evidence for crustal assimilation beneath Krafla, Iceland. *J. Petrol.* 32, 1005–1020. doi: 10.1093/petrology/32.5.1005

Nielsen, S. G., Rehkämper, M., Brandon, A. D., Norman, M. D., Turner, S., and O'Reilly, S. Y. (2007). Thallium isotopes in Iceland and Azores lavas – implications for the role of altered crust and mantle geochemistry. *Earth Planet. Sci. Lett.* 264, 332–345. doi: 10.1016/j.epsl.2007.10.008

Nielson, D. L., and Sibbett, B. S. (1996). Geology of ascension Island, South Atlantic Ocean. *Geothermics* 25, 427–448. doi: 10.1016/0375-6505(96)00018-1

Novak, S. W., and Mahood, G. A. (1986). Rise and fall of a basalt–trachyte–rhyolite magma system at the Kane Springs Wash Caldera, Nevada. *Contrib. Mineral. Petrol.* 94, 352–373. doi: 10.1007/BF00371444

Nystuen, J. P. (1975). Plutonic and subvolcanic intrusions in the Hurdal area, Oslo region. *Norges Geol. Undersok. Bull.* 317, 1–21.

O'Connor, J. M., and Duncan, R. A. (1990). Evolution of the Walvis Ridge – Rio Grande Rise hot spot system: implications for African and South American plate motions over plumes. *J. Geophys. Res.* 95, 17475–17502. doi: 10.1029/JB095iB11p17475

Óskarsson, N., Steinþórsson, S., and Sigvaldason, G. E. (1985). Iceland Geochemical anomaly: origin, volcanotectonics, chemical fractionation and isotope evolution of the crust. *J. Geophys. Res.* 90, 10011–10025. doi: 10.1029/JB090iB12p10011

Paris, R., Guillou, H., Carracedo, J. C., and Perez Torrado, F. J. (2005). Volcanic and morphological evolution of La Gomera (Canary Islands), based on new K-Ar ages and magnetic stratigraphy: implications for ocean island evolution. *J. Geol. Soc. London* 162, 501–512. doi: 10.1144/0016-764904-055

Parker, D. F., and White, J. C. (2008). Large-scale silicic alkalic magmatism associated with the Buckhorn Caldera, Trans-Pecos Texas, USA: comparison with Pantelleria, Italy. *Bull. Volcanol.* 70, 403–415. doi: 10.1007/s00445-007-0145-2

Parnell-Turner, R., White, N., Henstock, T., Murton, B., Maclennan, J., and Jones, S. M. (2014). A continuous 55-million-year record of transient mantle plume activity beneath Iceland. *Nat. Geosci.* 7, 914–919. doi: 10.1038/ngeo2281

Peccerillo, A., Barberio, M. R., Yirgu, G., Ayalew, D., Barbieri, M., and Wu, T. W. (2003). Relationships between mafic and peralkaline silicic magmatism in continental rift settings: a petrological, geochemical and isotopic study of the Gedemsa volcano, central Ethiopian rift. *J. Petrol.* 44, 2003–2032. doi: 10.1093/petrology/egg068

Peccerillo, A., Donati, C., Santo, A. P., Orlando, A., Yirgu, G., and Ayalew, D. (2007). Petrogenesis of silicic peralkaline rocks in the Ethiopian rift: geochemical evidence and volcanological implications. *J. Afr. Sci.* 48, 161–173. doi: 10.1016/j.jafrearsci.2006.06.010

Perlingeiro, G., Vasconcelos, P. M., Knesel, K. M., Thiede, D. S., and Cordani, U. G. (2013). ^{40}Ar/^{39}Ar geochronology of the Fernando de Noronha Archipelago and implications for the origin of alkaline volcanism in the NE Brazil. *J. Volcanol. Geother. Res.* 249, 140–154. doi: 10.1016/j.jvolgeores.2012.08.017

Pfaff, K., Krumrei, T., Marks, M., Wenzel, T., Rudolf, T., and Markl, G. (2008). Chemical and physical evolution of the 'lower layered sequence' from the nepheline syenitic Ilímaussaq intrusion, South Greenland: Implications for the origin of magmatic layering in peralkaline felsic liquids. *Lithos* 106, 280–296. doi: 10.1016/j.lithos.2008.07.018

Pimentel, A. (2006). *Domos e Coulées da Ilha Terceira: Contribuição por o Estudo dos Mecanismos de Instalação*. M.Sc. thesis, Universidade dos Açores, Ponta Delgada.

Pimentel, A. (2015). *Pyroclastic Density Current-Forming Eruptions on Faial and Terceira islands, Azores*. Ph.D. thesis, Universidade dos Açores, Ponta Delgada.

Pimentel, A., Pacheco, J., and Self, S. (2015). The ∼1000-years BP explosive eruption of Caldeira Volcano (Faial, Azores): the first stage of incremental caldera formation. *Bull. Volcanol.* 77:42. doi: 10.1007/s00445-015-0930-2

Pires, G. L. C., and Bongiolo, E. M. (2016). The nephelinitic-phonolitic volcanism of the Trindade Island (South Atlantic Ocean): review of the stratigraphy, and inferences on the volcanic styles and sources of nephelinites. *J. South Am. Earth Sci.* 72, 49–62. doi: 10.1016/j.jsames.2016.07.008

Pires, G. L. C., Bongiolo, E. M., Geraldes, M. C., Renac, C., Santos, A. C., Jourdan, F., et al. (2016). New ^{40}Ar/^{39}Ar ages and revised ^{40}K/^{40}Ar data from nephelinitic-phonolitic volcanic successions of the Trindade Island (South Atlantic Ocean). *J. Volcanol. Geother. Res.* 327, 531–538. doi: 10.1016/j.jvolgeores.2016.09.020

Pitman, W., and Talwani, M. (1972). Sea floor spreading in the North Atlantic. *Geol. Soc. Am. Bull.* 83, 619–646. doi: 10.1130/0016-7606(1972)83[619:SSITNA]2.0.CO;2

Plesner, S., Holm, P. M., and Wilson, J. R. (2003). ^{40}Ar–^{39}Ar geochronology of Santo Antão, Cape Verde Islands. *J. Volcanol. Geother. Res.* 120, 103–121. doi: 10.1016/S0377-0273(02)00367-0

Pollard, P. J. (1995). A special issue dedicated to the geology of rare metal deposits: geology of rare metal deposits: an introduction an overview. *Econ. Geol.* 90, 489–494. doi: 10.2113/gsecongeo.90.3.489

Preece, K., Barclay, J., Brown, R., and Mark, D. F. (2016). A 1 million year eruption history of Ascension Island: Insights from stratigraphy and ^{40}Ar/^{39}Ar dating. *Goldschmidt Abstracts* 2017:3215.

Preece, K., Mark, D. F., Barclay, J., Cohen, B. E., Chamberlain, K. J., Jowitt, C., et al. (2018). Bridging the gap: ^{40}Ar/^{39}Ar dating of volcanic eruptions from the 'Age of Discovery'. Geology. doi: 10.1130/G45415.1

Prestvik, T. (1982). "Trace element geochemistry of volcanic rocks from Bouvetøya, South Atlantic," in *Antarctic Geoscience*, ed. C. Craddock (Madison, WI: The University of Wisconsin press), 771–774.

Prestvik, T., Goldberg, S., and Goles, G. (1999). Petrogenesis of the volcanic suite of Bouvetøya (Bouvet Island), South Atlantic. *Norsk Geologisk Tidsskrift* 79, 205–218. doi: 10.1080/002919699433663

Prestvik, T., Goldberg, S., Karlsson, H., and Grönvold, K. (2001). Anomalous strontium and lead isotope signatures in the off-rift Öræfajökull central volcano in south-east Iceland: Evidence for enriched endmember(s) of the Iceland mantle plume? *Earth Planet. Sci. Lett.* 190, 211–220. doi: 10.1016/S0012-821X(01)00390-9

Putirka, K. D. (2008). Thermometers and barometers for volcanic systems. *Rev. Mineral. Geochem.* 69, 61–120. doi: 10.2138/rmg.2008.69.3

Quin, J. P. (1962). La lindinosite (granite mesocrate à riebeckite) du massif d'Evisa. *Bull. Soc. Geol. France* 4, 380–383.

Ramalho, R. A. (2011). *Building the Cape Verde Islands*. Berlin: Springer Science and Business Media. doi: 10.1007/978-3-642-19103-9

Ramalho, R. S., Brum da Silveira, A., Fonseca, P. E., Madeira, J., Cosca, M., Cachão, M., et al. (2015). The emergence of volcanic islands on a slow-moving

plate: the example of Madeira Island, NE Atlantic. *Geochem. Geophys. Geosyst.* 16, 522–537. doi: 10.1002/2014GC005657

Ramalho, R. S., Helffrich, G., Madeira, J., Cosca, M., Thomas, C., Quartau, R., et al. (2017). Emergence and evolution of Santa Maria Island (Azores)—The conundrum of uplifted islands revisited. *Geol. Soc. Am. Bull.* 129, 372–390. doi: 10.1130/B31538.1

Rasmussen, E., Neumann, E.-R., Andersen, T., Sundvoll, B., Fjerdingstad, V., and Stabel, A. (1988). Petrogenetic processes associated with intermediate and silicic magmatism in the Oslo Rift, south-east Norway. *Mineral. Mag.* 52, 293–307. doi: 10.1180/minmag.1988.052.366.01

Reagan, M. K., Turner, S., Legg, M., Sims, K. W., and Hards, V. L. (2008). 238U- and 232Th-decay series constraints on the timescales of crystal fractionation to produce the phonolite erupted in 2004 near Tristan da Cunha, South Atlantic Ocean. *Geochim. Cosmochim. Acta* 72, 4367–4378. doi: 10.1016/j.gca.2008.06.002

Ren, M., Omenda, P. A., Anthony, E. Y., White, J. C., Macdonald, R., and Bailey, D. K. (2006). Application of the QUILF thermobarometer to the peralkaline trachytes and pantellerites of the Eburru volcanic complex, East African Rift, Kenya. *Lithos* 91, 109–124. doi: 10.1016/j.lithos.2006.03.011

Renzulli, A., and Santi, P. (2000). Two-stage fractionation history of the alkali basalt-trachyte series of Sete Cidades volcano (São Miguel, Azores). *Eur. J. Mineral.* 12, 469–494. doi: 10.1127/0935-1221/2000/0012-0469

Ridolfi, F., Renzulli, A., Macdonald, R., and Upton, B. G. J. (2006). Peralkaline syenite autoliths from Kilombe volcano, Kenya Rift Valley: evidence for subvolcanic interaction with carbonatitic fluids. *Lithos* 91, 373–392. doi: 10.1016/j.lithos.2006.03.026

Ridolfi, F., Santi, P., Renzulli, A., and Upton, B. G. J. (2003). Evolutionary stages of crystallisation of weakly peralkaline syenites: evidence from ejecta in the Plinian deposits of Agua de Pau volcano (São Miguel, Azores Islands). *Mineral. Mag.* 67, 749–767. doi: 10.1180/0026461036740131

Robertson, A. H. F., and Stillman, C. J. (1979). Late Mesozoic sedimentary rocks of Fuerteventura, Canary Islands: implications for West African continental margin evolution. *J. Geol. Soc.* 136, 47–60. doi: 10.1144/gsjgs.136.1.0047

Rodriguez-Losada, J. A., and Martinez-Frias, J. (2004). The felsic complex of Vallehermoso Caldera: interior of an ancient volcanic system (La Gomera, Canary Islands). *J. Volcanol. Geother. Res.* 137, 261–284. doi: 10.1016/j.jvolgeores.2004.05.021

Rogers, N. W., Evans, P. J., Blake, S., Scott, S. C., and Hawkesworth, C. J. (2004). Rates and timescales of fractional crystallization from 238U–230Th–226Ra disequilibria in trachyte lavas from Longonot volcano, Kenya. *J. Petrol.* 45, 1747–1776. doi: 10.1093/petrology/egh032

Rooney, T. O., Hart, W. K., Hall, C. M., Ayalew, D., Ghiorso, M. S., Hidalgo, P., et al. (2012). Peralkaline magma evolution and the tephra record in the Ethiopian Rift. *Contrib. Mineral. Petrol.* 164, 407–426. doi: 10.1007/s00410-012-0744-6

Ryabchikov, I. D., and Kogarko, L. N. (1994). Redox equilibria in alkaline lavas from Trindade Island, Brazil. *Int. Geol. Rev.* 36, 473–483. doi: 10.1080/00206819409465472

Sabine, P. A. (1960). The geology of Rockall, north Atlantic. *Bull. Geol. Surv. Great Britain* 16, 156–178.

Salvi, S., and Williams-Jones, A. E. (2006). Alteration, HFSE mineralisation and hydrocarbon formation in peralkaline igneous systems: insights from the Strange Lake Pluton, Canada. *Lithos* 91, 19–34. doi: 10.1016/j.lithos.2006.03.040

Scaillet, B., Holtz, F., and Pichavant, M. (1998). Phase equilibrium constraints on the viscosity of silicic magmas 1. Volcanic-plutonic comparison. *J. Geophys. Res.* 103, 27257–27266. doi: 10.1029/98JB02469

Scaillet, B., and Macdonald, R. (2001). Phase relations of peralkaline silicic magmas and petrogenetic implications. *J. Petrol.* 42, 825–845. doi: 10.1093/petrology/42.4.825

Schilling, J. G. (1973). Iceland mantle plume. *Nature* 246, 141–143. doi: 10.1038/246141a0

Schmincke, H.-U. (1969). Ignimbrite sequence on Gran Canaria. *Bull. Volcanol.* 33, 1199–1219. doi: 10.1007/BF02597716

Schmincke, H.-U. (1973). Magmatic evolution and tectonic regime in the Canary, Madeira, and Azores Island groups. *Geol. Soc. Am. Bull.* 84, 633–648. doi: 10.1130/0016-7606(1973)84<633:MEATRI>2.0.CO;2

Schmincke, H.-U. (1974). Volcanological aspects of peralkaline silicic welded ash-flow tuffs. *Bull. Volcanol.* 38, 594–636. doi: 10.1007/BF02596900

Schmincke, H.-U. (1976). "The geology of the Canary Islands," in *Biogeography and Ecology in the Canary Islands*, ed. G. Kunkel (Berlin: Springer), 67–184. doi: 10.1007/978-94-010-1566-0_4

Schwarz, S., Klügel, A., and Wohlgemuth-Ueberwasser, C. (2004). Melt extraction pathways and stagnation depths beneath the Madeira and Desertas rift zones (NE Atlantic) inferred from barometric studies. *Contrib. Mineral. Petrol.* 147, 228–240. doi: 10.1007/s00410-004-0556-4

Self, S. (1974). *Recent Volcanism on Terceira, Azores*. Ph.D. thesis, Imperial College London, London, 236.

Self, S. (1976). The recent volcanology of terceira, azores. *J. Geol. Soc. London* 132, 645–666. doi: 10.1144/gsjgs.132.6.0645

Serralheiro, A. (1976). A geologia da Ilha de Santiago (Cabo Verde). *Bol. Museu Lab. Mineral. Geol. Faculdade Ciênc.* 14, 157–369.

Serralheiro, A., Forjaz, V. H., Alves, C. A. M., and Rodrigues, B. (1989). *Carta vulcanológica dos Açores, ilha do Faial (1:15000) Sheets 1, 2, 3 & 4*. Ponta Delgada: Centro de Vulcanologia do INIC, Serviço Regional de Proteção Civil dos Açores e Universidade dos Açores.

Shaw, H. R. (1972). Viscosities of magmatic silicate liquids – empirical method of prediction. *Am. J. Sci.* 272, 870–893. doi: 10.2475/ajs.272.9.870

Siebel, W., Becchio, R., Volker, F., Hansen, M. A. F., Viramonte, J., Trumbull, R., et al. (2000). Trindade and Martin Vaz Islands, South Atlantic: isotopic (Sr, Nd, Pb) and trace element constraints on plume-related magmatism. *J. South Am. Earth Sci.* 13, 79–103. doi: 10.1016/S0895-9811(00)00015-8

Sigmarsson, O., Condomines, M., and Fourcade, S. (1992). A detailed Th, Sr and O isotope study of Hekla: differentiation processes in an Icelandic volcano. *Contrib. Mineral. Petrol.* 112, 20–34. doi: 10.1007/BF00310953

Sigmarsson, O., Hémond, C., Condomines, M., Fourcade, S., and Oskarsson, N. (1991). Origin of silicic magma in Iceland revealed by Th isotopes. *Geology* 19, 621–624. doi: 10.1130/0091-7613(1991)019<0621:OOSMII>2.3.CO;2

Sigurdsson, H. (1971). Feldspar relations in Icelandic alkalic rhyolites. *Mineral. Mag.* 38, 503–510. doi: 10.1180/minmag.1971.038.296.13

Sigurdsson, H. (1977). Generation of Icelandic rhyolites by melting of plagiogranites in the oceanic layer. *Nature* 269, 25–28. doi: 10.1038/269025a0

Sigurdsson, H., and Sparks, R. S. J. (1981). Petrology of rhyolitic and mixed magma ejecta from the 1875 eruption of Askja, Iceland. *J. Petrol.* 22, 41–84. doi: 10.1093/petrology/22.1.41

Sliwinski, J. T., Bachmann, O., Ellis, B. S., Dávila-Harris, P., Nelson, B. K., and Dufek, J. (2015). Eruption of shallow crystal cumulates during explosive phonolitic eruptions on Tenerife, Canary Islands. *J. Petrol.* 56, 2173–2194. doi: 10.1093/petrology/egv068

Snyder, D. C., Widom, E., Pietruszka, A. J., and Carlson, R. W. (2004). The role of open-system processes in the development of silicic magma chambers: a chemical and isotopic investigation of the Fogo A trachyte deposit, São Miguel, Azores. *J. Petrol.* 45, 723–738.

Snyder, D. C., Widom, E., Pietruszka, A. J., Carlson, R. W., and Schmincke, H. U. (2007). Time scales of formation of zoned magma chambers: U-series disequilibria in the Fogo A and 1563 AD trachyte deposits, Sao Miguel, Azores. *Chem. Geol.* 239, 138–155. doi: 10.1016/j.chemgeo.2007.01.002

Sokolova, E., and Cámara, F. (2017). The seidozerite supergroup of TS-block minerals: nomenclature and classification, with change of the following names: rinkite to rinkite-(Ce), mosandrite to mosandrite-(Ce), hainite to hainite-(Y) and innelite-1T to innelite-1A. *Mineral. Mag.* 81, 1457–1484. doi: 10.1180/minmag.2017.081.010

Sørensen, H. (1960). "On the agpaitic rocks," in *International Geological Congress, Report of the Twenty-First Session Norden, Part XIII, Proceedings of Section 13, Petrographic Provinces, Igneous and Metamorphic Rocks*, Norden, 319–327.

Sørensen, H. (1992). Agpaitic nepheline syenites: a potential source of rare elements. *Appl. Geochem.* 7, 417–427. doi: 10.1016/0883-2927(92)90003-L

Sørensen, H. (1997). The agpaitic rocks – an overview. *Mineral. Mag.* 61, 485–498. doi: 10.1180/minmag.1997.061.407.02

Sparks, R. S. J., Sigurdsson, H., and Wilson, L. (1977). Magma mixing: a mechanism for triggering acid explosive eruptions. *Nature* 267, 315–318. doi: 10.1038/267315a0

Stevenson, R. J., Briggs, R. M., and Hodder, A. P. W. (1993). Emplacement history of a low-viscosity, fountain-fed pantelleritic lava flow. *J. Volcanol. Geother. Res.* 57, 39–56. doi: 10.1016/0377-0273(93)90030-U

Storey, M. (1981). Trachytic pyroclastics from Agua de Pau volcano, São Miguel, Azores: evolution of a magma body over 4,000 years. *Contrib. Mineral. Petrol.* 78, 423–432. doi: 10.1007/BF00375204

Storey, M., Wolff, J. A., Norry, M. J., and Marriner, G. F. (1989). Origin of hybrid lavas from Agua de Pau volcano, São Miguel, Azores. *Geol. Soc. London Spec. Publications* 42, 161–180. doi: 10.1144/GSL.SP.1989.042.01.11

Streck, M. J. (2014). Evaluation of crystal mush extraction models to explain crystal-poor rhyolites. *J. Volcanol. Geother. Res.* 284, 79–94. doi: 10.1016/j.jvolgeores.2014.07.005

Stroncik, N. A., Klügel, A., and Hansteen, T. H. (2009). The magmatic plumbing system beneath El Hierro (Canary Islands): contrasts from phenocrysts and naturally quenched basaltic glasses in submarine rocks. *Contrib. Mineral. Petrol.* 157, 593–607. doi: 10.1007/s00410-008-0354-5

Suh, C. E., Sparks, R. S. J., Fitton, J. G., Ayonghe, S. N., Annen, C., Nana, R., et al. (2003). The 1999 and 2000 eruptions of Mount Cameroon: eruption behaviour and petrochemistry of lava. *Bull. Volcanol.* 65, 267–283. doi: 10.1007/s00445-002-0257-7

Sumner, J. M., and Branney, M. J. (2002). The emplacement history of a remarkable heterogeneous, chemically-zoned, rheomorphic and locally lava-like ignimbrite: 'TL' on Gran Canaria. *J. Volcanol. Geother. Res.* 115, 109–138. doi: 10.1016/S0377-0273(01)00311-0

Sumner, J. M., and Wolff, J. (2003). Petrogenesis of mixed-magma, high-grade, peralkaline ignimbrite 'TL' (Gran Canaria): diverse styles of mixing in a replenished, zoned magma chamber. *J. Volcanol. Geother. Res.* 126, 109–126. doi: 10.1016/S0377-0273(03)00121-5

Sun, S., and McDonough, W. F. (1989). "Chemical and isotopic systematics of ocean basins: implications for mantle composition and processes," in *Magmatism in the Ocean Basins*, Vol. 42, eds A. D. Saunders and M. J. Norry (London: Geological Society of London Special Publication), 313–346.

Sutherland, D. S. (1974). Petrography and mineralogy of the peralkaline silicic rocks. *Bull. Volcanol.* 38, 518–547. doi: 10.1007/BF02596897

Sæmundsson, K. (1978). Fissure swarms and central volcanoes of the neovolcanic zones of Iceland. *Geol. Soc. London Spec. Issue* 10, 415–432.

Sæmundsson, K. (1979). Outline of the geology of Iceland. *Jökull* 29, 7–28.

Thirlwall, M. F., Jenkins, C., Vroon, P. Z., and Mattey, D. P. (1997). Crustal interaction during construction of oceanic islands: Pb-Sr-Nd-O isotope geochemistry of the shield basalts of Gran Canaria, Canary Islands. *Chem. Geol.* 135, 233–262. doi: 10.1016/S0009-2541(96)00118-0

Thirlwall, M. F., Singer, B. S., and Marriner, G. F. (2000). 39Ar–40Ar ages and geochemistry of the basaltic shield stage of Tenerife, Canary Islands, Spain. *J. Volcanol. Geother. Res.* 103, 247–297. doi: 10.1016/S0377-0273(00)00227-4

Thompson, R. N. (1969). Tertiary granites and associated rocks of the Marsco area, Isle of Skye. *Quarterly J. Geol. Soc. London* 124, 349–385. doi: 10.1144/gsjgs.124.1.0349

Thompson, R. N., Gibson, S. A., Mitchell, J. G., Dickin, A. P., Leonardos, O. H., Brod, J. A., et al. (1998). Migrating Cretaceous-Eocene magmatism in the Serra do Mar Alkaline Province, SE Brazil: melts from the deflected Trindade mantle plume? *J. Petrol.* 39, 1493–1526. doi: 10.1093/petroj/39.8.1493

Thompson, R. N., and MacKenzie, W. S. (1967). Feldspar-liquid equilibria in peralkaline acid liquids: an experimental study. *Am. J. Sci.* 265, 714–734. doi: 10.2475/ajs.265.8.714

Thorarinsson, S. (1981). "Jardeldasvædi á nútíma (Volcanic areas of the Holocene)," in *Nattúra Íslands*, 2nd Edn, (Reykjavík: Almenna bókafélagid), 81–119.

Thorarinsson, S., and Sæmundsson, K. (1979). Volcanic activity in historical time. *Jökull* 29, 29–32.

Thordarson, T., and Hoskuldsson, A. (2002). *Iceland. Classic Geology in Europe* 3. Harpenden: Terra Publishing, 200.

Thordarson, T., and Larsen, G. (2007). Volcanism in Iceland in historical time: volcano types, eruption styles and eruptive history. *J. Geodyn.* 43, 118–152. doi: 10.1016/j.jog.2006.09.005

Till, C. B., Vazquez, J. A., and Boyce, J. W. (2015). Months between rejuvenation and volcanic eruption at Yellowstone caldera, Wyoming. *Geology* 43, 695–698. doi: 10.1130/G36862.1

Tornare, E., Pilet, S., and Bussy, F. (2016). Magma differentiation in vertical conduits reealed by the complementary study of plutonic and volcanic rocks from Fuertaventura (Canary Islands). *J. Petrol.* 57, 2221–2250. doi: 10.1093/petrology/egx004

Torres, P., Madeira, J., Silva, L., Brum da Silveira, A., Serralheiro, A., and Mota Gomes, A. (1997). "Carta Geológica das erupções históricas da Ilha do Fogo: revisão e actualização," in *A Erupção Vulcânica de 1995 na Ilha do Fogo, Cabo Verde. Ministério da Ciencia e da Tecnologia*, eds A. Réffega, M. Figueiredo, L. Silva, F. Costa, M. Mendes, P. Torres, et al. (Lisbon: Instituto de Investigação Científica Tropical), 119–132.

Torres, P. C., Silva, L. C., Serralheiro, A., Mendes, M. H., Macedo, J. R., and Gomes, M. (2002). *Geologia da Ilha do Sal*. Lisbon: Comunicações do Instituto de Investigação Científica Tropical.

Triebold, S., Kronz, A., and Wörner, G. (2006). Anorthite-calibrated backscattered electron profiles, trace elements, and growth textures in feldspars from the Teide–Pico Viejo volcanic complex (Tenerife). *J. Volcanol. Geother. Res.* 154, 117–130. doi: 10.1016/j.jvolgeores.2005.09.023

Troll, V. R., and Carracedo, J. C. (2016). *The geology of the Canary Islands*. Amsterdam: Elsevier, 636.

Troll, V. R., Klügel, A., Longpré, M. A., Burchardt, S., Deegan, F. M., Carracedo, J. C., et al. (2012). Floating stones off El Hierro, Canary Islands: xenoliths of pre-island sedimentary origin in the early products of the October 2011 eruption. *Solid Earth* 3, 97–110. doi: 10.5194/se-3-97-2012

Troll, V. R., and Schmincke, H.-U. (2002). Magma mixing and crustal recycling recorded in ternary feldspar from compositionally zoned peralkaline ignimbrite 'A', Gran Canaria, Canary Islands. *J. Petrol.* 43, 243–270. doi: 10.1093/petrology/43.2.243

Trua, T., Deniel, C., and Mazzuoli, R. (1999). Crustal control in the genesis of Plio-Quaternary bimodal magmatism of the Main Ethiopian Rift (MER): geochemical and isotopic (Sr, Nd, Pb) evidence. *Chem. Geol.* 155, 201–231. doi: 10.1016/S0009-2541(98)00174-0

Turbeville, B. N. (1993). Sidewall differentiation in an alkalic magma chamber: evidence from syenite xenoliths in tuffs of the Latera caldera, Italy. *Geol. Mag.* 130, 453–470. doi: 10.1017/S0016756800020537

Turner, J. S., and Campbell, I. H. (1986). Convection and mixing in magma chambers. *Earth Sci. Rev.* 23, 255–352. doi: 10.1016/0012-8252(86)90015-2

Turner, S., Kokfelt, T., Hoernle, K., Johansen, T. S., Hauff, F., Lundstrom, C., et al. (2017). Contrasting magmatic cannibalism forms evolved phonolitic magmas in the Canary Islands. *Geology* 45, 147–150. doi: 10.1130/G38566.1

Ulbrich, M. N. C. (1993). Petrography of alkaline volcanic-subvolcanic rocks from the Brazilian Fernando de Noronha archipelago, southern Atlantic Ocean. *Bull. Instit. Geosci. Univ. São Paulo* 24, 77–94.

Venezky, D. Y., and Rutherford, M. J. (1999). Petrology and Fe-Ti oxide reequilibration of the 1991 Mount Unzen mixed magma. *J. Volcanol. Geother. Res.* 89, 213–230. doi: 10.1016/S0377-0273(98)00133-4

Verwoerd, W. J. (1972). Islands on the mid-ocean ridge between Africa and Antarctica. *Trans. Am. Geophys. Union* 53, 168–170.

Verwoerd, W. J., Erlank, A. J., and Kable, E. J. D. (1976). "Geology and geochemistry of Bouvet Island," in *Andean and Antarctic Volcanology Problems*, ed. O. Gonzales Ferran (Naples: IAVCEI), 203–237.

Vink, G. E. (1984). A hotspot model for Iceland and the Voring Plateau. *J. Geophys. Res.* 89, 9949–9959. doi: 10.1029/JB089iB12p09949

Vogt, P. R., and Jung, W. Y. (2004). The Terceira Rift as hyper-slow, hotspot-dominated oblique speeding axis: a comparison with other slow-spreading plate boundaries. *Earth Planet. Sci. Lett.* 218, 77–90. doi: 10.1016/S0012-821X(03)00627-7

Vona, A., Romano, C., Dingwell, D. B., and Giordano, D. (2011). The rheology of crystal-bearing basaltic magmas from Stromboli and Etna. *Geochim. Cosmochim. Acta* 75, 3214–3236. doi: 10.1016/j.gca.2011.03.031

Walker, G. P. L. (1959). Geology of the Reydarfjördur area, eastern Iceland. *Quarterly J. Geol. Soc. London* 68, 515–528.

Walker, G. P. L. (1963). The Breiddalur central volcano, eastern Iceland. *Quarterly J. Geol. Soc. London* 119, 29–63. doi: 10.1144/gsjgs.119.1.0029

Walker, G. P. L. (1966). Acid volcanic rocks in Iceland. *Bull. Voclanol.* 29, 376–402. doi: 10.1007/BF02597164

Watkins, N. D., and Abdel-Monem, A. (1971). Detection of the Gilsa geomagnetic polarity event on the island of Madeira. *Geol. Soc. Am. Bull.* 82, 191–198. doi: 10.1130/0016-7606(1971)82[191:DOTGGP]2.0.CO;2

Watkins, N. D., and Walker, G. P. L. (1977). Magnetostratigraphy of Eastern-Iceland. *Am. J. Sci.* 277, 513–584. doi: 10.2475/ajs.277.5.513

Weaver, B., Kar, A., Davidson, J., and Collucci, M. (1996). Geochemical characteristics of volcanic rocks from Ascension Island, South Atlantic Ocean. *Geothermics* 25, 449–470. doi: 10.1016/0375-6505(96)00014-4

Weaver, B. L. (1990). Geochemistry of highly-undersaturated ocean island basalt suites from the Southern Atlantic Ocean: Fernando de Noronha and Trindade islands. *Contrib. Mineral. Petrol.* 105, 502–515. doi: 10.1007/BF00302491

Webster, J. D., and Rebbert, C. R. (2001). The geochemical signature of fluid-saturated magma determined from silicate melt inclusions in Ascension Island granite xenoliths. *Geochim. Cosmochim. Acta* 65, 123–136. doi: 10.1016/S0016-7037(00)00515-9

Weidenorfer, D., Schmidt, M. W., and Mattsson, H. B. (2016). Fractional crystallisation of Si-undersaturated alkaline magmas leading to unmixing of carbonatites on Brava Island (Cape Verde) and a general model of carbonatite genesis in alkaline magma suites. *Contrib. Mineral. Petrol.* 171:43. doi: 10.1007/s00410-016-1249-5

Weis, D., Demaiffe, D., Cauet, S., and Javoy, M. (1987). Sr, Nd, O and H isotopic ratios in Ascension Island lavas and plutonic inclusions; cogenetic origin. *Earth Planet. Sci. Lett.* 82, 255–268. doi: 10.1016/0012-821X(87)90200-7

Weit, A., Trumbull, R. B., Keiding, J. K., Geissler, W. H., Gibson, S. A., and Veksler, I. V. (2017). The magmatic system beneath the Tristan da Cunha Island: insights from thermobarometry, melting models and geophysics. *Tectonophysics* 716, 64–76. doi: 10.1016/j.tecto.2016.08.010

White, J. C., Ren, M., and Parker, D. F. (2005). Variation in mineralogy, temperature, and oxygen fugacity in a suite of strongly peralkaline lavas and tuffs, Pantelleria, Italy. *Can. Mineral.* 43, 1331–1347. doi: 10.2113/gscanmin.43.4.1331

White, R. S., Brown, J. W., and Smallwood, J. R. (1995). The temperature of the Iceland plume and origin of outward-propagating V-shaped ridges. *J. Geol. Soc. London* 152, 1039–1045. doi: 10.1144/GSL.JGS.1995.152.01.26

White, W. M. (2010). Oceanic island basalts and mantle plumes: the geochemical perspective. *Annu. Rev. Earth Planet. Sci.* 38, 133–160. doi: 10.1146/annurev-earth-040809-152450

White, W. M., Tapia, M. D. M., and Schilling, J.-G. (1979). The petrology and geochemistry of the Azores islands. *Contrib. Mineral. Petrol.* 69, 201–213. doi: 10.1007/BF00372322

Whittington, A. G., Richet, P., Linard, Y., and Holtz, F. (2001). The viscosity of hydrous phonolites and trachytes. *Chem. Geol.* 174, 209–223. doi: 10.1016/S0009-2541(00)00317-X

Widom, E., Gill, J. B., and Schmincke, H.-U. (1993). Syenite nodules as a long-term record of magmatic activity in Agua de Pau, São Miguel, Azores. *J. Petrol.* 34, 929–953. doi: 10.1093/petrology/34.5.929

Widom, E., Hoernle, K. A., Shirey, S. B., and Schmincke, H.-U. (1999). Os isotope systematics in the Canary Islands and Madeira: lithospheric contamination and mantle plume signatures. *J. Petrol.* 40, 279–296. doi: 10.1093/petroj/40.2.279

Widom, E., Schmincke, H.-U., and Gill, J. B. (1992). Processes and timescales in the evolution of a chemically zoned trachyte: Fogo A, São Miguel, Azores. *Contrib. Mineral. Petrol.* 111, 311–328. doi: 10.1007/BF00311194

Wiesmaier, S., Deegan, F. M., Troll, V. R., Carracedo, J. C., Chadwick, J. P., and Chew, D. M. (2011). Magma mixing in the 1100 AD Montaña Reventada composite lava flow, Tenerife, Canary Islands: interaction between rift zone and central volcano plumbing systems. *Contrib. Mineral. Petrol.* 162, 651–669. doi: 10.1007/s00410-010-0596-x

Wiesmaier, S., Troll, V. R., Wolff, J. A., and Carracedo, J. C. (2013). Open-system processes in the differentiation of mafic magma in the Teide-Pico Viejo succession, Tenerife. *J. Geol. Soc. London* 170, 557–570. doi: 10.1144/jgs2012-016

Wimmenauer, W. (1974). "Chapter 4.4: the alkaline province of central Europe and France," in *The Alkaline Rocks*, ed. H. Sørensen (London: Wiley and Sons), 238–271.

Wolfe, C. J., Bjarnason, I. T., Van Decar, J. C., and Soloman, S. C. (1997). Seismic structure of the Iceland mantle plume. *Nature* 385, 245–247. doi: 10.1038/385245a0

Wolff, J. A. (1985). Zonation, mixing and eruption of silica-undersaturated alkaline magma: a case study from Tenerife, Canary Islands. *Geol. Mag.* 122, 623–640. doi: 10.1017/S0016756800032039

Wolff, J. A. (1987). Crystallisation of nepheline syenite in a subvolcanic magma system: Tenerife, Canary Islands. . *Lithos* 20, 207–223. doi: 10.1016/0024-4937(87)90009-0

Wolff, J. A. (2017). On the syenite-trachyte problem. *Geology* 45, 1067–1070. doi: 10.1130/G39415.1

Wolff, J. A., Ellis, B. S., Ramos, F. C., Starkel, W. A., Boroughs, S., Olin, P. H., et al. (2015). Remelting of cumulates as a process for producing chemical zoning in silicic tuffs: a comparison of cool, wet and hot, dry rhyolitic magma systems. *Lithos* 23, 275–286. doi: 10.1016/j.lithos.2015.09.002

Wolff, J. A., Grandy, J. S., and Larson, P. B. (2000). Interaction of mantle-derived magma with island crust? Trace element and oxygen isotope data from the Diego Hernandez Formation, Las Cañadas, Tenerife. *J. Volcanol. Geother. Res.* 103, 343–366. doi: 10.1016/S0377-0273(00)00230-4

Wolff, J. A., and Storey, M. (1983). The volatile component of some pumice-forming alkaline magmas from the Azores and Canary Islands. *Contrib. Mineral. Petrol.* 82, 66–74. doi: 10.1007/BF00371176

Wolff, J. A., and Storey, M. (1984). Zoning in highly alkaline magma bodies. *Geol. Mag.* 121, 563–575. doi: 10.1017/S0016756800030715

Wolff, J. A., Wörner, G., and Blake, S. (1990). Gradients in physical parameters in zoned felsic magma bodies: implications for evolution and eruptive withdrawal. *J. Volcanol. Geother. Res.* 43, 37–55. doi: 10.1016/0377-0273(90)90043-F

Wyllie, P. J., and Tuttle, O. F. (1961). Experimental investigation of silicate systems containing two volatile components. Part II. The effects of NH3 and HF in addition to water on the melting temperatures of granite and albite. *Am. J. Sci.* 259, 128–143. doi: 10.2475/ajs.259.2.128

Ye, S., Canales, J. P., Rihm, R., Dañobeita, J. J., and Gallart, J. (1999). A crustal transect through the northern and northeastern part of the volcanic edifice of Gran Canaria, Canary Islands. *Geodynamics* 28, 3–26. doi: 10.1016/S0264-3707(98)00028-3

Yokoyama, T., Aka, F. T., Kusakabe, M., and Nakamura, E. (2007). Plume-lithosphere interaction beneath Mt. Cameroon volcano, West Africa: constraints from 238U–230Th–226Ra and Sr–Nd–Pb isotopes systematics. *Geochim. Cosmochim. Acta* 71, 1835–1854. doi: 10.1016/j.gca.2007.01.010

Zanon, V. (2015). "The magmatism of the Azores islands," in *Volcanic Geology of São Miguel Island (Azores Archipelago)*, Vol. 44, eds J. L. Gaspar, J. E. Guest, A. M. Duncan, F. J. A. S. Barriga, and D. K. Chester (London: Geological Society of London Memoirs), 51–64.

Zanon, V., and Frezzotti, M. L. (2013). Magma storage and ascent conditions beneath Pico and Faial islands (Azores archipelago): a study on fluid inclusions. *Geochem. Geophys. Geosyst.* 14, 3494–3514. doi: 10.1002/ggge.20221

Zanon, V., Kueppers, U., Pacheco, J. M., and Cruz, I. (2013). Volcanism from fissure zones and the Caldeira central volcano of Faial Island, Azores archipelago: geochemical processes in multiple feeding systems. *Geol. Mag.* 150, 536–555. doi: 10.1017/S0016756812000702

Zielinski, R. A., and Frey, F. A. (1970). Gough Island: evaluation of a fractional crystallisation model. *Contrib. Mineral. Petrol.* 29, 242–254. doi: 10.1007/BF00373308

Conflict of Interest Statement: The authors declare that the research was conducted in the absence of any commercial or financial relationships that could be construed as a potential conflict of interest.

Copyright © 2018 Jeffery and Gertisser. This is an open-access article distributed under the terms of the Creative Commons Attribution License (CC BY). The use, distribution or reproduction in other forums is permitted, provided the original author(s) and the copyright owner(s) are credited and that the original publication in this journal is cited, in accordance with accepted academic practice. No use, distribution or reproduction is permitted which does not comply with these terms.

frontiers in Earth Science

ORIGINAL RESEARCH
published: 28 May 2019
doi: 10.3389/feart.2019.00122

Biased Volcanic Hazard Assessment Due to Incomplete Eruption Records on Ocean Islands: An Example of Sete Cidades Volcano, Azores

Ulrich Kueppers[1], Adriano Pimentel[2,3], Ben Ellis[4], Francesca Forni[4], Julia Neukampf[4], José Pacheco[3], Diego Perugini[5] and Gabriela Queiroz[3]*

[1] Department für Geo- und Umweltwissenschaften, Ludwig-Maximilians-Universität, Munich, Germany, [2] Centro de Informação e Vigilância Sismovulcânica dos Açores, Ponta Delgada, Portugal, [3] Instituto de Investigação em Vulcanologia e Avaliação de Riscos (IVAR), Universidade dos Açores, Ponta Delgada, Portugal, [4] Institut für Geochemie und Petrologie, ETH Zürich, Zurich, Switzerland, [5] Department of Physics and Geology, University of Perugia, Perugia, Italy

OPEN ACCESS

Edited by:
Roberto Sulpizio, University of Bari Aldo Moro, Italy

Reviewed by:
Dario Pedrazzi, Instituto de Ciencias de la Tierra Jaume Almera (ICTJA), Spain
Federico Lucchi, University of Bologna, Italy

***Correspondence:**
Ulrich Kueppers
u.kueppers@lmu.de

Specialty section:
This article was submitted to Volcanology, a section of the journal Frontiers in Earth Science

Received: *20 November 2018*
Accepted: *07 May 2019*
Published: *28 May 2019*

Citation:
Kueppers U, Pimentel A, Ellis B, Forni F, Neukampf J, Pacheco J, Perugini D and Queiroz G (2019) Biased Volcanic Hazard Assessment Due to Incomplete Eruption Records on Ocean Islands: An Example of Sete Cidades Volcano, Azores. Front. Earth Sci. 7:122. doi: 10.3389/feart.2019.00122

It is well known that explosive volcanic eruptions pose serious hazards to local communities and may have worldwide impacts. However, the products of explosive eruptions on volcanic ocean islands are almost inevitably incompletely preserved as a significant portion of the erupted material is deposited into the ocean, thereby impeding our ability to accurately reconstruct past events, determine eruptive source parameters and ultimately assess the associated hazards. Sete Cidades is the westernmost central volcano of São Miguel Island, Azores. Although currently dormant, it has been the most active volcano on the island in the last 5 ky, with at least 17 trachytic explosive eruptions, some of which sub-Plinian, that took place inside the summit caldera. The last paroxysmal explosive eruption took place at ∼16 ka, enlarging the caldera to its present dimensions, and is recorded by the Santa Bárbara Formation. We here present evidence of a mid-distal deposit (>25 km from the vent) that can be correlated with the proximal (on Sete Cidades volcanic edifice) pumice fall deposit of the Santa Bárbara Formation based on deposit characteristics, textural features and geochemistry. This is the first evidence of a decimeter-thick deposit of Sete Cidades volcano in the central part of São Miguel Island, which allows to constrain eruptive source parameters and wind conditions. Given the predominant winds blowing from westerly directions, Sete Cidades is considered the most hazardous volcano for the entire island of São Miguel with its current population of >137,000 inhabitants. Most critically, the main harbor, only airport and hospital are located in the capital city of Ponta Delgada, ∼12 km SE from Sete Cidades caldera. In case of a future explosive eruption, under westerly blowing wind conditions, the impact on São Miguel could be catastrophic, with long-term economic consequences.

Keywords: ocean island volcano, incomplete eruption record, explosive eruption, tephra fallout, inverse problem, volcanic hazard, eruptive scenarios, São Miguel Island

INTRODUCTION

Explosive volcanic eruptions are recognized as one of the most violent natural events that pose a plethora of hazards to local communities, economic sectors, and infrastructure, but may also cause widespread disruption of air traffic (e.g., Mazzocchi et al., 2010; Wilson et al., 2012; Biass et al., 2014; Scaini et al., 2014). This threat is even greater for volcanic islands as the ocean is a strong impediment for the evacuation of large numbers of people. The reconstruction of past eruptions on volcanic ocean islands (including the determination of eruptive source parameters) and consequently the assessment of their impact is greatly conditioned by various factors, including, but not limited to: (1) number of outcrops (small subaerial area of deposition), (2) outcrop accessibility (e.g., vegetation cover) and (3) preservation of primary features of deposits (degree of erosion and weathering). Several studies have discussed the sensitivity of determining eruptive source parameters from deposits. This is true for older deposits with incomplete preservation (e.g., Heiken and McCoy, 1984; Costantini et al., 2009; Longchamp et al., 2011) but also holds for recent and well-monitored eruptions (e.g., Spanu et al., 2016).

São Miguel is the largest and most populated (>137,000 inhabitants) island of the Azores archipelago and comprises three trachytic central volcanoes that have been active during the Holocene: Sete Cidades, Fogo and Furnas. The summit of all three volcanoes is truncated by a caldera. Sete Cidades (hereafter 7C), in the western end of São Miguel, is the central volcano with the highest eruptive frequency on the island in the last 5 ky and most probably in the entire Azores archipelago (Cole et al., 2008; Queiroz et al., 2008, 2015). The caldera of 7C is located ∼12 km NW of Ponta Delgada city, the island's capital, where the main harbor, hospital, and only airport are located. Ponta Delgada is frequently downwind from 7C under the predominant westerly winds, posing serious concerns regarding the assessment of volcanic hazard (Pimentel et al., 2006; Cole et al., 2008; Gaspar et al., 2015).

The stratigraphy of 7C provides evidence for several large explosive eruptions in the past. Three paroxysmal explosive eruptions associated with different stages of evolution of the caldera have taken place between 36 and 16 ka (Queiroz, 1997; Queiroz et al., 2015). The last paroxysmal eruption was related to the caldera-enlarging event dated at ∼16 ka BP (Queiroz, 1997) and is recorded by the Santa Bárbara Formation (SBF) – the present case study. Its stratigraphy and emplacement mechanisms have been recently reanalyzed in detail by Porreca et al. (2018). In the last 5 ky, at least 17 explosive eruptions from within the summit caldera have been recognized in the stratigraphic record (Queiroz, 1997; Queiroz et al., 2008, 2015). All intra-caldera eruptions are of trachytic composition and the related deposits are dominated by ash and lapilli fall deposits. Although 7C volcano is currently dormant, with no historic eruption on land (i.e., since the 15th century), it is considered one of the most hazardous volcanoes in the Azores archipelago (Gaspar et al., 2015).

The reconstruction of the past eruptions of 7C volcano has been, in most cases, limited to proximal areas (i.e., on the edifice of 7C volcano) due to the short distance between the caldera rim and the coast (<2–5 km) and the overlying products from the adjacent basaltic fissure system (see Queiroz et al., 2008; Porreca et al., 2018). Based on isopach and isopleth maps, Cole et al. (2008) reconstructed eruptive source parameters of three recent (<5 ky) intra-caldera eruptions and modeled tephra dispersal to assess the associated hazard. They showed that there is a high probability that explosive eruptions will affect the entire western third of São Miguel as well as the central part of the island. However, apart from loosely constrained isopachs of recent deposits in the area of Ponta Delgada (Queiroz, 1997; Dinis, 2006; Gonçalves, 2006), there are no reports of a distal deposit of 7C in the central part of São Miguel Island that would allow for an accurate determination of the eruption source parameters.

Here, we present evidence for a mid-distal pumice lapilli fall deposit of 7C volcano on the north coast of Fogo volcano (>25 km from 7C caldera; **Figure 1**). We use the term "mid-distal" to describe any outcrop on São Miguel beyond the edifice of 7C volcano as the distribution of subaerial deposits adumbrates submarine deposits at even greater distance. The goals of this paper are to: (1) demonstrate the correlation of the mid-distal fall deposit with the SBF of 7C volcano by means of textural features and geochemistry, (2) constrain eruption source parameters with/without considering the mid-distal outcrop by best-fitting tephra fallout simulations and (3) assess the potential impact of a future sub-Plinian eruption under wind conditions blowing toward Ponta Delgada city. This study has strong implications for the realistic assessment of the volcanic hazard on São Miguel Island in a worst-case scenario (large sub-Plinian eruption) and on other ocean islands vulnerable to explosive volcanic eruptions.

GEOLOGICAL SETTING

The Azores archipelago corresponds to a set of nine volcanic islands in the North Atlantic Ocean. The island of São Miguel is located on the eastern section of the NW-SE-trending Terceira Rift, that extends eastward from the Mid-Atlantic Ridge and separates the Eurasian and Nubian lithospheric plates (inset of **Figure 1**). São Miguel Island has an area of 744 km^2 and is composed of three active trachytic central volcanoes with summit calderas, Sete Cidades (7C), Fogo (also known as Água de Pau) and Furnas (**Figure 1**), separated by two basaltic fissure systems, Picos and Congro. The eastern third of the island is comprised of Povoação and Nordeste volcanic systems, which are considered extinct (Gaspar et al., 2015).

The central volcano of 7C (maximum altitude of 845 m a.s.l.) forms the westernmost sector of São Miguel and its' caldera is located only 12 km NW of the city of Ponta Delgada. The volcanic edifice is strongly controlled by tectonic structures associated with the Terceira Rift (e.g., Queiroz, 1997; Carmo et al., 2015). Its summit caldera is approximately circular, 5 km wide and 250–350 m deep, and is today partially occupied by lakes. Several intra-caldera landforms prove the ongoing volcanic activity after the formation of the caldera. Their hemicircular alignment points to a ring fault with a diameter of ∼3.5 km (Kueppers et al., 2018). To the NW of the caldera, the structural control is expressed by the

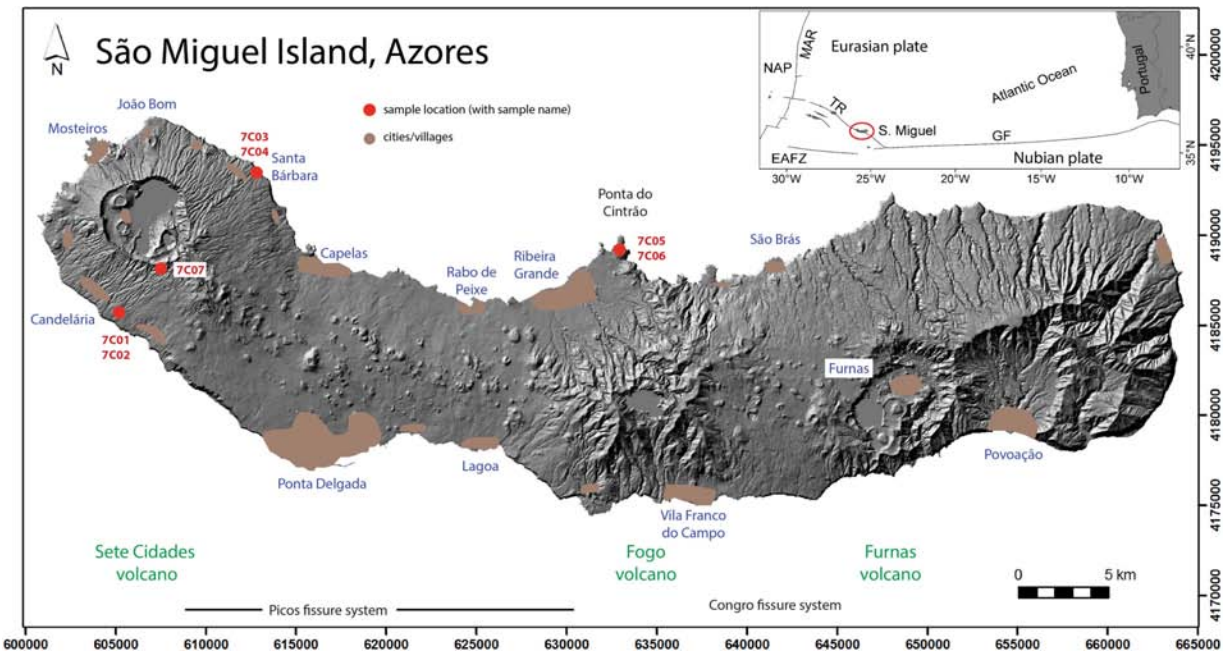

FIGURE 1 | Map of São Miguel Island showing the location of the three central volcanoes (Sete Cidades, Fogo, and Furnas), the main inhabited areas (cities and villages) and collected samples. Samples 7C01 and 7C02 collected near Candelária (outcrop A) on the southern slope of Sete Cidades volcano (7C), samples 7C03 and 7C04 near Santa Bárbara (outcrop B) on the NE slope, samples 7C05 and 7C06 at a distal location on the Ponta do Cintrão peninsula (outcrop C) and sample 7C07 collected close to 7C caldera rim (outcrop D). Inset illustrates the geographic position of São Miguel (Azores archipelago) in the Atlantic Ocean and the main structural features (NAP, North American plate; MAR, Mid-Atlantic Ridge; TR, Terceira Rift; EAFZ, East Azores Fracture Zone; GF, GLORIA Fault).

Mosteiros Graben (∼2.5 km wide). To the SE, a several kilometer-long rift system has repeatedly allowed for basaltic eruptions to form alignments of scoria cones (Pedrazzi et al., 2015).

The stratigraphy of 7C is divided into two lithostratigraphic groups (Queiroz, 1997; Queiroz et al., 2015): The *Inferior Group* includes the volcanic products dated from ∼210 ka (Moore, 1990) to ∼36 ka and is formed mainly by basaltic or trachytic lavas and to a lesser extent pyroclastic deposits (Queiroz, 1997; Beier et al., 2006; Queiroz et al., 2015). The *Superior Group* includes all products younger than ∼36 ka. It is composed of three major trachytic pyroclastic formations, namely Risco (36 ka), Bretanha (29 ka), and Santa Bárbara (16 ka) (Queiroz, 1997), related to three major phases of caldera formation, which are intercalated with deposits from subordinate eruptions. In the last 5 ky, at least 17 trachytic pumice and ash fall deposits (P1–P17) resulting from eruptions with vents inside the caldera and at least 12 flank basaltic lava flow and scoria deposits have been recognized (Booth et al., 1978; Queiroz, 1997; Queiroz et al., 2008, 2015).

According to the stratigraphic record, the eruptive history of 7C can be briefly summarized in three main stages (Queiroz, 1997; Beier et al., 2006; Queiroz et al., 2015): (1) the shield-building stage of the subaerial volcanic edifice lasting from > 210 ka to ∼36 ka and dominated by effusive volcanism (Inferior Group), (2) the caldera-forming stage, characterized by three paroxysmal explosive eruptions associated with the formation of the present day caldera, between ∼36 and ∼16 ka, and (3) the post-caldera stage, dominated by intra-caldera explosive eruptions and low-explosivity or effusive flank eruptions, from ∼16 ka to today (Superior Group). In particular, during the last 5 ky, the eruptive frequency increased and was marked predominantly by intra-caldera eruptions, some of which of sub-Plinian dimensions (Queiroz, 1997; Cole et al., 2008; Queiroz et al., 2008). The last explosive eruption occurred ∼700 years ago (Queiroz et al., 2008) and although 7C had no subaerial historic eruption (i.e., since Portuguese settlement in the first half of the 15th century), the high eruptive frequency makes it the most active and hazardous volcano of São Miguel Island (Gaspar et al., 2015).

Overview of the Santa Bárbara Formation

The Santa Bárbara Formation (SBF) results from the last major explosive eruption of 7C volcano and is related to the final phase of caldera-enlarging. Its deposits are mainly preserved along a narrow area between the caldera rim and the coastline (<5 km distance), while a large portion of the pyroclastic products were deposited into the ocean (Kueppers et al., 2009; Porreca et al., 2018).

This complex pyroclastic sequence (dated at 15,740 ± 200 uncalibrated ^{14}C years BP; Queiroz, 1997) is divided into three distinct members: Lower, Middle, and Upper. The *Lower Member* consists of a succession of ash beds alternating with fine-grained pumice lapilli beds, deposited mainly on the SW flank of the caldera, which is interpreted as ash fallout and

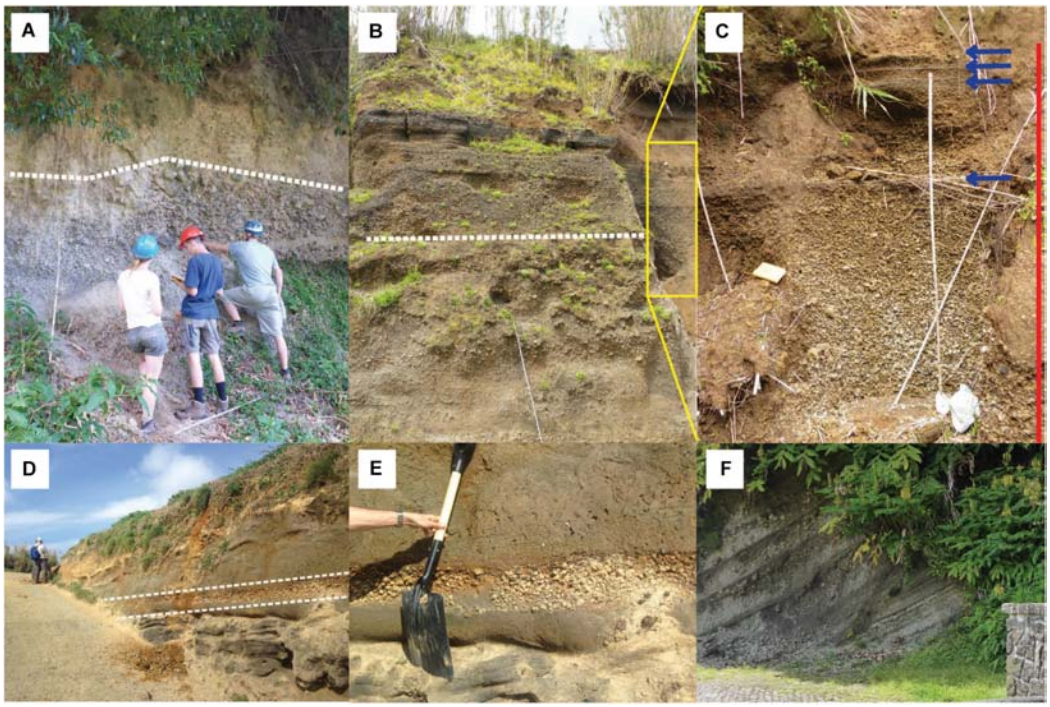

FIGURE 2 | General aspects of outcrops of the Santa Bárbara Formation (SBF). **(A)** Outcrop A, sampling location for samples 7C01 and 7C02 near Candelária (**Figure 1**). Two different PDC deposit lithofacies from the *Middle Member* showing massive lapilli tuffs with variable content of lithic clasts (white dashed line indicating the boundary). **(B)** Type locality (UK080, MP020) of the *Middle* and *Upper Members* near the village of Santa Bárbara; outcrop B for samples 7C03 and 7C04 (**Figure 1**), showing massive lapilli tuffs in the lower half (below dashed line), overlain by massive pumice fall deposits showing normal grading (height of outcrop 8 m). **(C)** Zoom into **Figure 2B**, see yellow box for stratigraphic location. General aspect of the two pumice lapilli beds of the *Upper Member* separated by a 12 cm ash layer (field book for scale). Red vertical line (approximately 3.5 m) shows the vertical extent. Blue arrows indicate the presence of thin ash layers. **(D)** In a road cut at Ponta do Cintrão (Outcrop C for samples 7C05 and 7C06), a pumice lapilli fall deposit in between two paleosol layers shows similar features to the proximal *Upper Member* of the SBF (between dashed lines). **(E)** Close-up of the pumice lapilli fall deposit of **Figure 2D**, sharing many characteristics and textures of the SBF proximal deposits. **(F)** General aspect of layered units from a recent (<5 ky) pumice fall deposit near the Vista do Rei viewpoint; outcrop D for sample 7C07 (spring catchment for scale). For details of **(A–C)** see Porreca et al. (2018).

dilute pyroclastic density current (PDC) deposits from short-lived unstable columns. The *Middle Member* corresponds to pumice and lithic-rich ash-lapilli tuffs, found on the SW and NE sectors, interpreted as deposited from high particle concentration PDCs (**Figure 2A**). The *Upper Member* is a pumice lapilli deposit with a narrow distribution along the NE flank, which records fallout from a sub-Plinian eruption column (**Figures 2B,C**, **3A**). Several intercalated ash-rich horizons indicate that the eruption column at times experienced unsteadiness. The detailed stratigraphy and eruption history of the SBF are described in Queiroz et al. (2015) and more recently in Porreca et al. (2018).

A distinctive feature of the SBF is the occurrence of black trachybasaltic inclusions, also known as magmatic mafic enclaves (MME; Kueppers et al., 2009), within white or banded trachytic pumice clasts (**Figures 3C,D**). These are found in the *Middle* and *Upper Members* and increase upward (in both frequency and size) throughout the pyroclastic sequence (Porreca et al., 2018). The MME have been interpreted to result from magma mingling following intrusion of trachybasaltic magma into a trachytic magma reservoir (Queiroz, 1997; Kueppers et al., 2009; Porreca et al., 2018). Upon contact, the trachybasalt was quenched and experienced brittle fragmentation. The resulting fragments (MME) served as favorable sites for bubble nucleation and growth. The combined effect of thermodynamic instability and volatile exsolution, leading to increase in the magmatic pressure of the reservoir, acted as the eruption trigger and subsequent enhancement of the explosivity (see Paredes-Mariño et al., 2017; Porreca et al., 2018; Laeger et al., 2019).

METHODOLOGY

Fieldwork

The proximal deposits of the SBF outcropping on the flanks of 7C edifice were first investigated by Queiroz (1997). Kueppers et al. (2007, 2009) and ultimately Porreca et al. (2018) reinvestigated the SBF combining field methods (geological mapping and stratigraphic analysis) with laboratory analyses (granulometry, componentry, and scanning electron microscope imaging) to reconstruct the eruption history in more detail. To that end, deposit characteristics (e.g., grain size and particle shape) were investigated to decipher

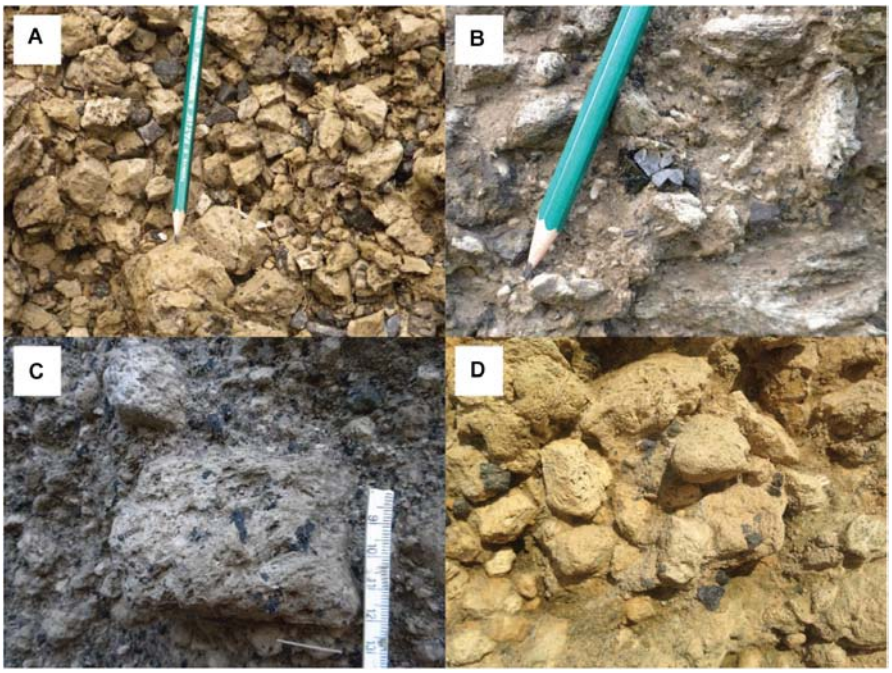

FIGURE 3 | (A) General aspect of the well-sorted fall deposit with angular pumice lapilli and subordinate lithic clasts (near Santa Bárbara village). **(B)** Obsidian fragments contained in the deposits of the Upper Member of the Santa Bárbara Formation (near Santa Bárbara village). **(C)** Large pumice lapilli with several MME (magmatic mafic enclaves) near Santa Bárbara village and **(D)** on the Ponta do Cintrão peninsula.

different lithofacies and ultimately constrain transport and deposition conditions. All outcrops on the 7C edifice are considered proximal. Given the prevailing winds from westerly directions (see Pimentel et al., 2006; Cole et al., 2008; Gaspar et al., 2015), a detailed field survey was extended along the north and south coasts of São Miguel Island to verify the presence of mid-distal deposits of 7C belonging to the SBF (**Figure 1**). This fieldwork was concentrated along coastal cliffs as outcrops inland are rare due to: (1) substantial urbanization, (2) widespread distribution of younger (<16 ky) basaltic tephra and lava flows from the Picos Fissure System, (3) widespread distribution of younger (<5 ky) trachytic fall deposits related to 7C and Fogo volcanoes and (4) luxuriant vegetation cover.

Seven separate samples of pumice clasts were collected at four locations (**Figure 1**): (1) outcrop A of PDC deposits from the SBF (*Middle Member)* on the south flank of 7C near the village of Candelária (samples 7C01 and 7C02; **Figure 2A**), (2) outcrop B of pumice fall deposit from the SBF (*Upper Member*) on the NE flank of 7C near Santa Bárbara village (7C03 and 7C04; **Figures 2B,C**), (3) outcrop C of a pumice fall bed at Ponta do Cintrão peninsula, containing pumice clasts that are texturally very similar to the ones of SBF (7C05 and 7C06; **Figures 2D,E**) and (4) outcrop D of a younger pumice fall deposit (P17) on the south flank of 7C caldera close to the viewpoint Vista do Rei (7C07; **FigurE 2F**). The sample from outcrop D was included in this study to check for geochemical variability of 7C products. All collected pumice clasts were in the size range of coarse lapilli. Pumice clasts from outcrops A, B, and C visually contain millimeter-sized MME (**Table 1**).

Textural and Geochemical Analyses

Several dozen pumice lapilli clasts were investigated macroscopically for their bubble and MME textures. Two instruments hosted at the *Department for Earth and Environmental Sciences, Ludwig-Maximilians-Universität (LMU) Munich, Germany* were used to investigate polished surfaces of selected pumice clasts from outcrops B and C (Cameca SX100 electron probe microanalyzer) as well as selected ash grains (scanning electron microscope HITACHI SU5000) operating at secondary electron mode with an acceleration voltage of 15 kV.

Major element compositions of glasses from pumice clasts were determined using a JEOL JXA 8200 Superprobe at the *Institut für Geochemie und Petrologie, ETH Zürich, Switzerland*. Operating conditions were as follows: 15 kV accelerating voltage, current of 10 nA, counting times of 20 s on peak and 10 s on background and a defocused beam of 20 μm to minimize alkali migration. The analyses were organized such that the most potentially mobile elements (Na, K) were measured first.

Trace element compositions of groundmass glass were measured by LA-ICPMS at *ETH Zürich* using a 193 nm ArF Excimer laser from *Resonetics* coupled to a Thermo Element XR ICPMS. Analyses involved a spot size of 29 μm with an output energy of the laser beam maintained at ∼3.5 J/cm^2. Raw counts per second were reduced using identical methods to Szymanowski et al. (2015) with the MATLAB-based SILLS software (Guillong et al., 2008). NIST-610 glass was used as

TABLE 1 | Overview of the samples used in this study.

Outcrop	Location	Samples	Main macroscopic features
A	Candelária village	7C01, 7C02	Rounded, whitish/yellowish pumice lapilli with magmatic mafic enclaves (MME), collected from PDC deposits (Middle Member of SBF)
B	Santa Bárbara village	7C03, 7C04	Angular, whitish/yellowish pumice lapilli with MME, collected from fall deposit (Upper Member of SBF)
C	Ponta do Cintrão peninsula	7C05, 7C06	Angular, whitish/yellowish pumice lapilli with MME, collected from fall deposit
D	Near Vista do Rei viewpoint	7C07	Angular, whitish pumice lapilli, no MME, collected from fall deposit (P17)

primary standard and GSD-1G as a secondary standard to monitor instrumental performance. Data were reduced using the appropriate SiO_2 content (from microprobe measurements) as internal standard. Long-term (>5 years) reproducibility of a range of homogeneous glass standards indicates precision typically better than 5% for elements with elemental abundances significantly (i.e., >2x) above detection limit. The full data are provided as online **Supplementary Materials**.

Tephra Fallout Simulations

In order to constrain the eruptive source parameters and wind conditions we used the tephra fallout model of the GIS-based *VORIS 2.0.1* tool (Felpeto et al., 2007) to reconstruct the dispersal and thickness of the pumice fall deposit of the *Upper Member* of the SBF. Tephra fallout simulations were performed with an advection-diffusion model that assumes that above the vent the mass is distributed along a vertical line following the approximation proposed in equation 3 by Armienti et al. (1988) to the model of Suzuki (1983). Away from the vent the model assumes that the transport of particles is controlled by: (1) advective effect of the wind, (2) diffusion due to atmospheric turbulence and (3) terminal settling velocity of the particles (see Folch and Felpeto, 2005; Felpeto et al., 2007).

Input parameters were obtained from published data and when unavailable through the solution of the inverse problem, i.e., by best-fitting simulation results with field data to reconstruct the pumice fall deposit (cf. Macedonio et al., 2008; Scollo et al., 2008; Bonasia et al., 2010, 2011; Moiseenko and Malik, 2019). Three tephra fallout scenarios were simulated to obtain the eruptive source parameters, wind conditions and produce volcanic hazard maps. All three scenarios assume a single-spot vent location in the center of today's 7C caldera, as the widespread cover by deposits related to post-caldera volcanism (<16 ky) does not allow to constrain the exact location of the vent(s) of the Santa Bárbara eruption.

Scenario 1 reconstructs the proximal pumice fall deposit of the *Upper* Member of the SBF on the NE flank of 7C volcano. To reproduce its narrow distribution a unidirectional wind profile (blowing from WSW) was assumed following the deposit dispersal. Wind intensity was obtained by best-fit with field data. Eruptive source parameters were tested in pre-defined intervals (erupted volume 0.1–0.4 km^3; column height 10,000–20,000 m) until the combination of values agreed with field data. Scenario 2 reconstructs the proximal and mid-distal distribution and thickness of the pumice fall deposit, including the pumice lapilli bed at Ponta do Cintrão peninsula. To reproduce the field observations a complex wind profile was used, with directions varying from SW-blowing wind at lower altitude to WNW-blowing wind at higher altitude. Wind intensity was obtained through best-fit. Eruptive source parameters were changed within the same pre-defined intervals as in scenario 1 until their combination fitted proximal and distal field data. Finally, scenario 3 simulates the potential impact of an explosive eruption with the same eruptive source parameters of scenario 2 under wind conditions blowing from NW, i.e., toward the city of Ponta Delgada. This aims to reproduce the worst-case scenario of a future sub-Plinian eruption of 7C volcano (Cole et al., 2008; Queiroz et al., 2008), with the highest impact on the island's key infrastructure and economy, giving the predominant westerly blowing winds (see details of wind statistical analyses in Pimentel et al., 2006; Cole et al., 2008; Gaspar et al., 2015). **Table 2** summarizes the main input parameters used in the simulation of the three scenarios.

RESULTS

Field Data

The deposits of the SBF outcrop discontinuously along the flanks of 7C volcano, except on the SE sector where they are probably covered by basaltic products from the Picos Fissure System (see Porreca et al., 2018). It is likely that the SBF products were deposited over the entire volcanic edifice. However, due to significant erosion, vegetation cover and younger overlying deposits, the general stratigraphy and sedimentary features have been deciphered by the analysis of isolated outcrops. Stratigraphic correlations were facilitated by the presence of MME in juvenile pumice clasts, which increase in frequency and size toward the top of the pyroclastic sequence (Queiroz et al., 2015; Porreca et al., 2018).

The SBF *Upper Member* is only found in an area of approximately 10 km^2 on the NE flank of 7C. It is a typical fall deposit (**Figures 2B,C**, **3A**) with clast-supported fabric of well-sorted ($\sigma\phi$ 1.2), coarse-grained (Mdϕ −3.5) angular pumice lapilli clasts that are generally light-colored, occasionally banded, and contain MME up to 15% of the volume. Larger pumice clasts occur occasionally (average maximum size of the three largest clasts up to 15 cm). Centimeter-sized angular lithic clasts (up to 10% of total volume; basaltic and trachytic lava fragments and hydrothermally altered clasts) and minor obsidian chips are also present (**Figure 3B**).

In some outcrops, this deposit can be subdivided into two pumice fall beds separated by an ash-rich layer (12 cm thick, **Figures 2B,C**). The basal bed is thicker (up to 1.4 m), coarse-grained (Mdϕ −3.5) and more widespread than the top bed. The basal pumice lapilli bed does not show significant grain size variation, which suggests stable eruptive conditions (for more details see Porreca et al., 2018). The thin ash-rich layer found between the two pumice beds is weakly stratified and is interpreted as recording unsteadiness of the eruption column, possibly related to a small partial column collapse and generation of dilute PDCs. The top pumice lapilli bed is generally less than 1 m thick, overall finer-grained (Mdϕ −1.3) and shows slight fining upward. In the upper part of the top bed we occasionally find several thin layers of coarse-ash to fine-grained lapilli clasts. While the fining-upward trend indicates waning of the eruption column, these thin layers indicate a repetitive pattern of localized partial erosion and/or reworking of by dilute PDCs or strong winds during the final stages of deposition of the *Upper Member*. The narrow area of distribution of the *Upper Member* of the SBF, the small number of outcrops and the rather homogeneous thickness and grain size do not allow for the reconstruction of reliable isopachs and isopleths.

In 2008, we found one additional depositional area at Ponta do Cintrão peninsula (altitude of 103 m a.s.l.), on the north coast of São Miguel Island (i.e., on the north flank of Fogo volcano) >25 km east of 7C caldera (Kueppers et al., 2009, **Figure 1**). Here a pumice lapilli bed (up to 30 cm thick, **Figures 2D,E**) shows visually identical features to those reported for the proximal pumice fall deposit of the *Upper Member* of the SBF. It is a clast-supported, well-sorted pumice fall bed, with yellowish, angular, lapilli-sized pumice clasts (average maximum clast size of the three largest clasts is 4 cm) distinctive for the striking presence of small black inclusions. Lithic clasts (primarily basaltic lava fragments) are subordinate and up to 2 cm size. All characteristics of this pumice lapilli bed point to a primary deposit. The upper and lower limits are well defined by paleosols (**Figure 3D**). The underlying paleosol is fine-grained, 10–15 cm thick and of beige color. The overlying paleosol is considerably thicker (>70 cm) and contains (sub-)rounded pumice lapilli.

Later, Ponte (2013) described several outcrops of a locally restricted pumice lapilli bed along the north flank of Fogo volcano with similar features to the pumice bed described in this study. The area covered extends for about 9 km between the Ponta do Cintrão peninsula and São Brás village, at altitudes between 54 and 233 m a.s.l. (see **Supplementary Figure S1**). It is described as a fall deposit (up to 15–25 cm thick) with yellowish lapilli-sized pumice clasts (maximum size of 4 cm with abundant black scoriaceous inclusions), dispersed lithics (1–2 cm across) and small obsidian fragments. Ponte (2013) stated that it was not possible to correlate this bed to the stratigraphy of Fogo volcano. The textural description matches our findings.

Textural Aspects

Pumice lapilli clasts from the proximal SBF outcrops (A and B; PDC and fall deposits, respectively) and the mid-distal bed at Ponta do Cintrão peninsula (outcrop C) share the same textural features (Kueppers et al., 2009; Fahrner, 2012; Ortenzi, 2014). The pumice clasts are light-colored (whitish or yellowish),

TABLE 2 | Input parameters used for the simulation of scenarios 1, 2, and 3 with VORIS 2.0.1.

Eruptive source parameters						
Scenario 1	Erupted volume (km^3)		0.19	Best-fit (this study)		
	Column height (m)		12,000	Best-fit (this study)		
Scenario 2	Erupted volume (km^3)		0.27	Best-fit (this study)		
	Column height (m)		17,000	Best-fit (this study)		
Scenario 3	Erupted volume (km^3)		0.27	Following scenario 2		
	Column height (m)		17,000	Following scenario 2		
Grain size	Mean diameter (Mdϕ)		−3.5	Porreca et al., 2018		
	Sorting (σϕ)		1.2	Porreca et al., 2018		
	Minimum (ϕ)		4	Porreca et al., 2018		
	Maximum (ϕ)		−4	Porreca et al., 2018		
Clast density (kg/m^3)	Large (ϕ < 1)		800	Wilson and Huang, 1979		
	Medium (1≤ ϕ ≤3)		1200	Wilson and Huang, 1979		
	Small (ϕ > 3)		2400	Pimentel et al., 2015		
Wind conditions						
Scenario 1	Altitude (m)	2,000	4,000	6,000	8,000	13,000
	Direction (°)	253	253	253	253	253
	Intensity (m/s)	4	9	13	21	32
Scenario 2	Altitude (m)	2,000	4,000	8,000	13,000	18,000
	Direction (°)	230	245	265	280	290
	Intensity (m/s)	2	4	10	21	32
Scenario 3	Altitude (m)	2,000	4,000	8,000	13,000	18,000
	Direction (°)	322	322	322	322	322
	Intensity (m/s)	2	4	10	21	32

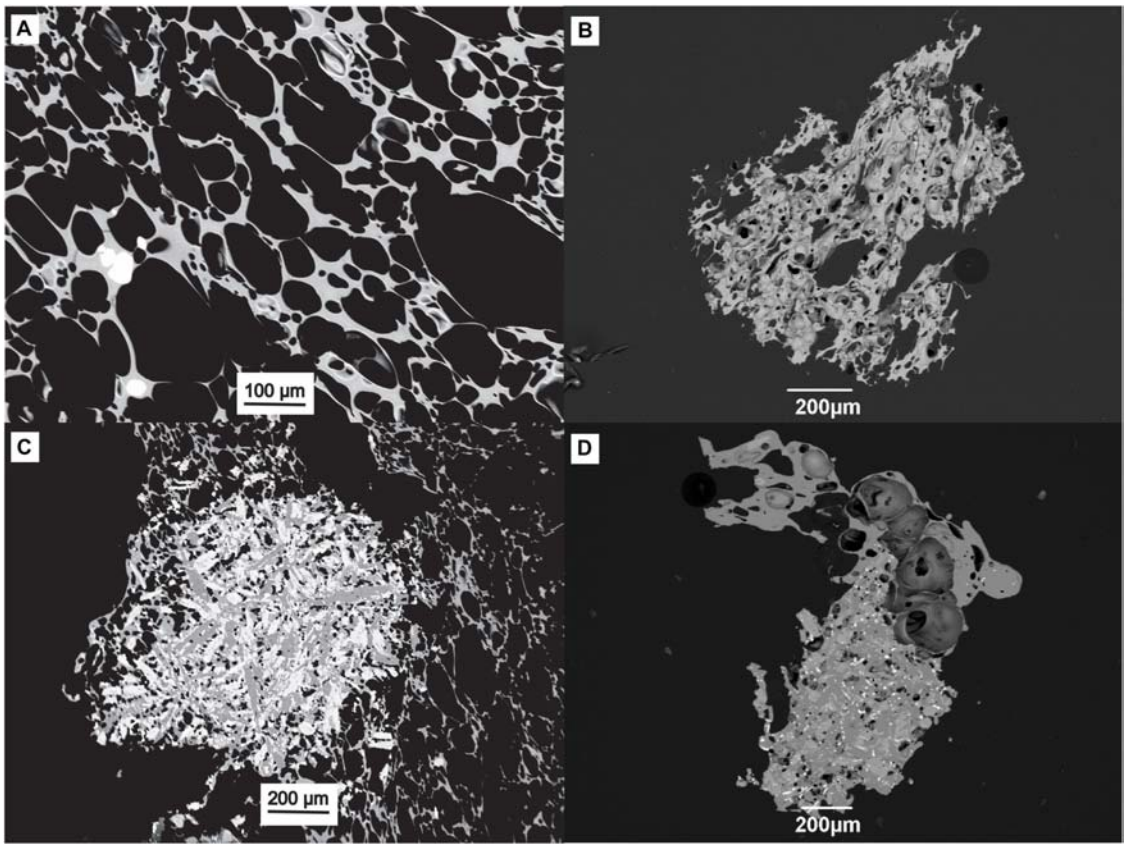

FIGURE 4 | Representative samples [lapilli **(A,C)** and ash **(B,D)**] from outcrops B and C, showing highly vesicular and almost aphyric trachytic pumice textures **(A,B)** and magmatic mafic enclaves (MME) of microcrystalline trachybasalt **(C,D)** in ash grains with low aspect ratio bubbles.

although banded clasts also occur. They are almost aphyric (up to 2 vol% phenocryst content) and highly vesicular (up to 80 vol% vesicularity, **Figure 4A**), exhibiting two populations of bubbles and high bubble connectivity (**Figures 4A,B**). While few large bubbles (up to 10 cm long, bubble aspect ratio 2:1) can be found in the largest clasts, the dominant bubble population is commonly < 150 µm long. Approximately 30% of the pumice clasts contain mafic magmatic enclaves (MME). They are variable in size and shape, ranging from single (sub-)millimeter-sized, scoriaceous fragments to MME-enriched areas up to 10 cm in large pumice clasts. The MME are microcrystalline and poorly vesicular, commonly showing diktytaxitic texture (**Figures 4C,D**) interpreted as evidence of quench crystallization (see Paredes-Mariño et al., 2017; Porreca et al., 2018; Laeger et al., 2019). In many pumice clasts the interior wall of large bubbles is dotted with angular MME. No MME are found within the small bubbles. By contrast, the pumice clasts from outcrop D of a recent pumice fall deposit (P17) are angular, whitish and almost aphyric but do not contain MME. The textural features of pumice clasts as well as of MME from outcrops A, B, and C are very similar, confirming that the Ponta do Cintrão pumice bed can be correlated with the *Upper Member* of the SBF, as already indicated by similar lithofacies. In order to further confirm this hypothesis, the geochemistry of pumice clasts from 4 different outcrops has been investigated.

Geochemistry

All normalized glass major elemental compositions from this study plot within the trachyte field of a classical total alkali vs. silica (TAS) diagram, similar to other compositions reported from 7C volcano (Beier et al., 2006; Queiroz et al., 2015; Johansson et al., 2017). Samples from SBF outcrops A and B, and Ponta do Cintrão outcrop C (7C01 to 7C06, see **Figure 1** for location) overlap in all major elements, while sample 7C07 from outcrop D is distinguished on the basis of a higher SiO_2 content and lower CaO, MgO, and TiO_2 (**Figure 5** and **Table 3**). Recently published glass major elements from pumices clasts (with and without flow bands) of the SBF (Laeger et al., 2019) overlap with our samples 7C01–7C06. The observed spread is due to the focus of Laeger et al. (2019) on the analysis of banded pumice clasts, which contain filaments of a less evolved composition, due to magma mixing/mingling. Glass geochemistry data from Fogo and Furnas volcanoes (Johansson et al., 2017) are also shown for comparison and clearly reveal different compositions (**Figure 5**).

In terms of trace elemental abundances, a similar behavior is observed with samples 7C01–06 showing identical compositions while sample 7C07 is compositionally distinct (**Figure 5**; the

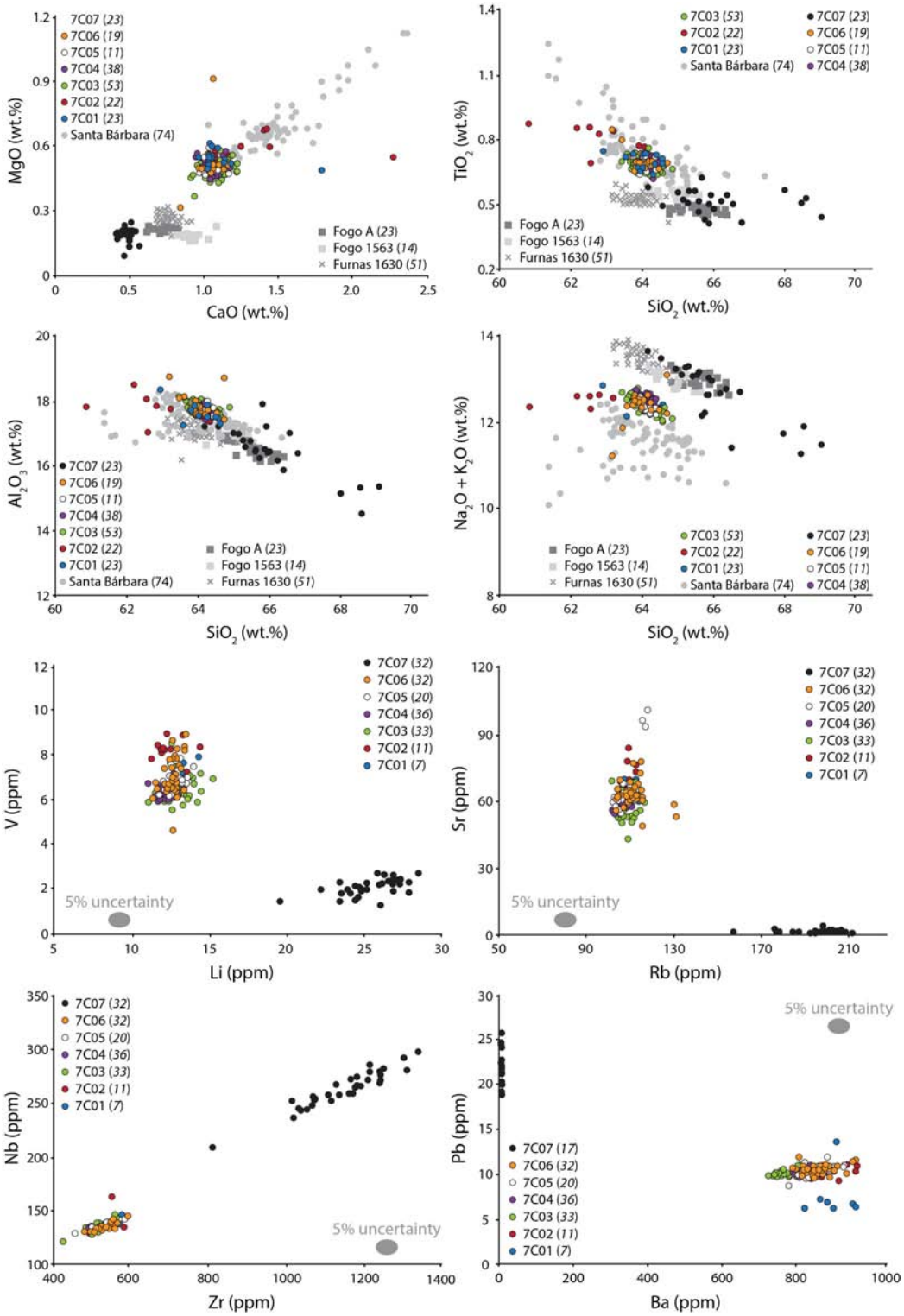

FIGURE 5 | Glass geochemistry results. Top 4 panels: major elements plotted vs. silica of glasses from Sete Cidades (7C), Fogo, and Furnas volcanoes. Samples 7C01 through 7C06 (macroscopically homogeneous pumices, colored circles) form clusters owing to the genetic relationship; sample 7C07 (black circles) is compositionally different. Gray circles (banded pumices of the SBF, Laeger et al., 2019) show larger spread owing to magma mixing/mingling. Comparative samples from Fogo (Fogo A and Fogo 1563) and Furnas (Furnas 1630) volcanoes (Johansson et al., 2017). All data are spot analysis obtained with EPMA. Lower 4 panels: Selected trace element plots supporting the genetic relationship of 7C01–04 to 7C05–06, evidencing a distal deposit of 7C on Ponta do Cintrão. All data were measured by LA-ICPMS. (Numbers in brackets indicate the number of measurements).

complete trace element dataset is given in **Supplementary Table S1**). The compositional difference between samples 7C01–06 and 7C07 is preserved across the range of geochemical affinities, being readily observed in compatible (e.g., Ba, Sr), incompatible (e.g., Zr, Hf, Nb) and moderately incompatible (e.g., Li) elements. The low Ba content in sample 7C07 is notable, with values approximating the analytical limits of detection (∼3 ppm Ba). While somewhat unusual, these extremely low Ba contents in sample 7C07 were measured in two different analytical sessions where trace elemental abundances of all samples showed good agreement between the two sessions. A final difference comes in the total abundances of the rare earth elements (REE) which are significantly higher (418–691, avg. 583 ppm) in sample 7C07 than in the six other samples (273–432, avg. 333 ppm).

Overall, the geochemical results (**Figure 5**) are strongly supportive of the correlation of the outcrop at Ponta do Cintrão peninsula with the proximal *Upper Member* deposit of the SBF, as assumed on the basis of textural features and field lithofacies data. The glass composition of sample 7C07 from a younger (<5 ka) pumice fall deposit shows that compositionally distinct magmas have been erupted from 7C volcano. This further underscores the significance of the identical geochemistry shown in samples 7C01–06.

Eruptive Source Parameters and Wind Conditions

Spatial distribution and thickness variation of the *Upper Member* pumice fall deposit of the SBF allowed us to constrain the eruptive source parameters and wind conditions during the final phase of this eruption. Three different fallout scenarios were simulated, always assuming a vent located in the center of the present summit caldera of 7C volcano (see Methodology section for details).

The tephra fall map of scenario 1 (**Figure 6**) takes into consideration the proximal outcrops of the *Upper Member* pumice fall deposit along the NE flank of 7C, assuming a unidirectional wind profile blowing from WSW (253°) and wind intensities increasing upward from 4 to 32 m/s. The solution of the inverse problem for the proximal deposits estimated an erupted volume of 0.19 km^3 and a column height of 12,000 m (**Table 2**). The simulation results are in good agreement with the observed distribution and thickness (up to 3 m) of the *Upper Member* outcrops (Porreca et al., 2018).

The tephra fall map resulting from scenario 2 (**Figure 7**) reconstructs a larger spatial distribution of the SBF *Upper* Member by including the proximal deposits and the mid-distal pumice lapilli bed recognized at Ponta do Cintrão. To reproduce the observed deposit distribution and thickness, a more complex wind profile (obtained through best-fit) was used in the simulation. Wind directions vary from SW (230°) at lower attitude (2,000 m a.s.l.) to WNW (290°) at higher altitude (18,000 m a.s.l.), while wind intensities range from 2 to 32 m/s (see **Table 2**). These wind directions are in good agreement with the prevailing westerly blowing winds (Pimentel et al., 2006; Cole et al., 2008; Gaspar et al., 2015). Eruptive source parameters obtained by solving the inverse problem yielded a tephra volume of 0.27 km^3 and column height of 17,000 m (**Table 2**) for the final phase of the eruption, related to the deposition of the *Upper Member*. The simulation adequately reproduces the distribution and thickness of the proximal pumice fall deposit, the measured thickness at Ponta do Cintrão outcrop (30 cm) and the rather homogenous thickness (25 to 15 cm, negatively correlated with increasing distance from 7C volcano) along the north flank of Fogo volcano described by Ponte (2013; see **Supplementary Figure S1**). Although not shown in the map, the simulation predicts that the entire north coast of São Miguel Island is affected by tephra fall (>5 cm thick).

Finally, the tephra fall map from scenario 3 (**Figure 8**) simulates the potential impact of a sub-Plinian eruption of 7C, under a unidirectional wind profile blowing from NW (322°), using the same wind intensities (2–32 m/s) and eruptive source parameters (erupted tephra volume 0.27 km^3; column height 17,000 m) obtained for scenario 2 (**Table 2**). Considering the predominant westerly wind directions, this is a highly plausible future scenario. The simulation predicts that the capital city of Ponta Delgada, located ∼12 km SE of 7C volcano, can be affected by 0.5–1 m of tephra fall.

DISCUSSION

The ∼16 ka eruption of 7C volcano, recorded by the SBF, was the last paroxysmal explosive event that enlarged the summit caldera to its present-day dimensions (Queiroz et al., 2015; Porreca et al., 2018). Although no continuous deposit is preserved along the flanks of the volcano, the distinctive presence of MME in juvenile pumice clasts allows for unambiguous correlation of the deposits of the SBF.

TABLE 3 | Overview of normalized values of major elements for the 7 different sample sets.

Major elements normalized	SiO_2	Na_2O	CaO	K_2O	FeO	MgO	Cl	TiO_2	MnO	Al_2O_3
7C01	64.08	6.91	1.09	5.53	3.04	0.54	0.16	0.69	0.17	17.66
7C02	63.64	6.95	1.27	5.53	3.12	0.56	0.15	0.74	0.16	17.69
7C03	64.11	6.76	1.07	5.62	3.03	0.50	0.14	0.68	0.19	17.81
7C04	64.17	6.89	1.04	5.56	3.07	0.51	0.13	0.68	0.18	17.67
7C05	64.13	6.81	1.05	5.53	3.08	0.52	0.15	0.68	0.18	17.80
7C06	64.02	6.76	1.05	5.60	3.03	0.54	0.18	0.68	0.17	17.89
7C07	66.17	7.19	0.48	5.43	3.00	0.19	0.34	0.51	0.23	16.44

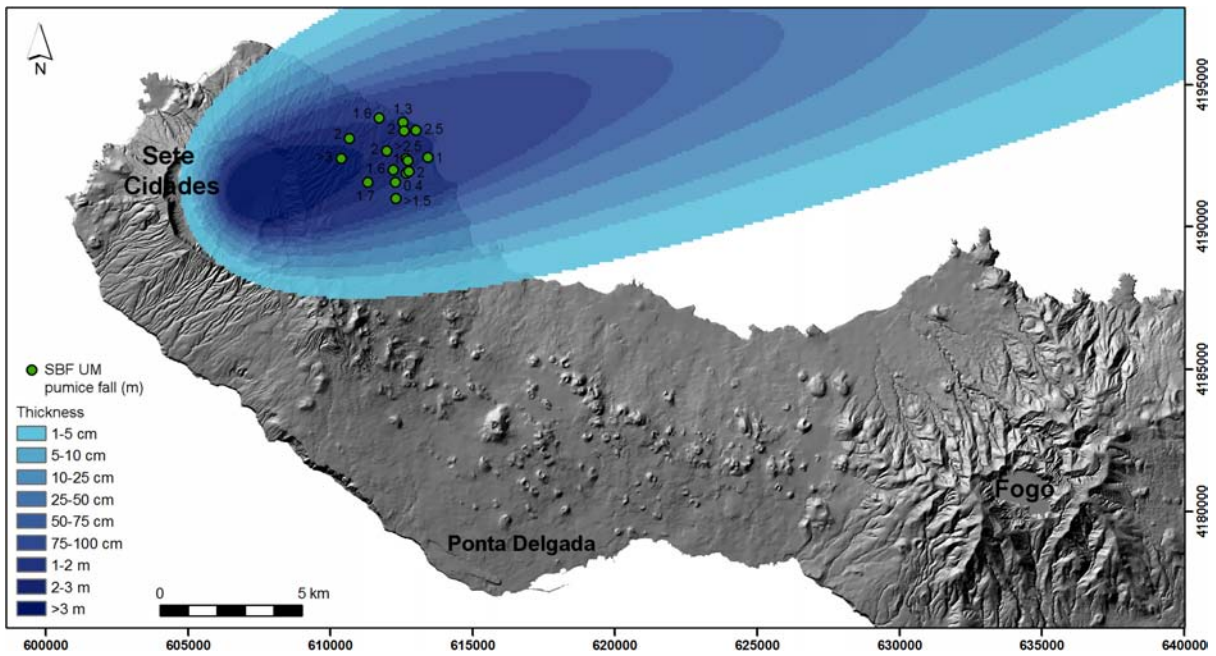

FIGURE 6 | Scenario 1 tephra fall map resulting from the simulations with VORIS 2.0.1, reconstructing the thickness of the proximal pumice fall deposit of the *Upper Member* of the SBF. Strong and unidirectional winds are interpreted to limit the dispersal and deposition to a narrow sector.

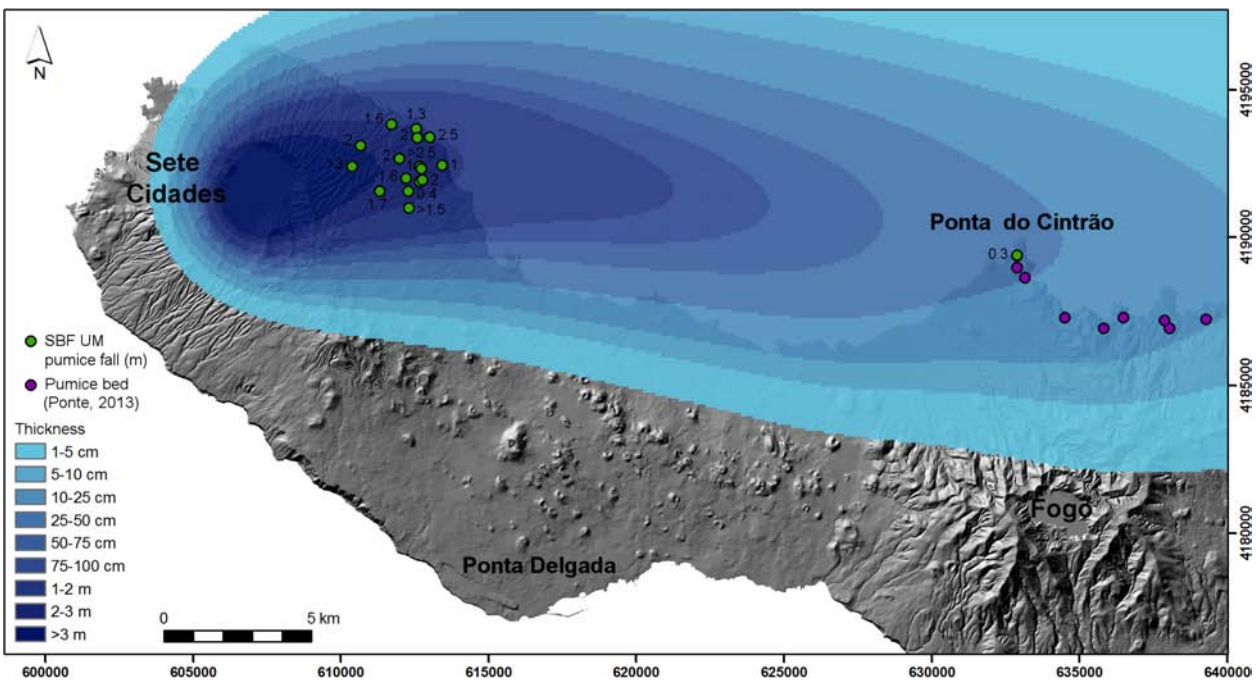

FIGURE 7 | Scenario 2 tephra fall map resulting from the simulations with VORIS 2.0.1, reconstructing the distribution of the proximal and mid-distal pumice fall deposit of the Upper Member of the SBF. Complex wind profile blowing from SW at lower altitude and from WNW at higher altitude are interpreted to be responsible for the deposition along the north coast of São Miguel.

The detailed analysis of > 150 proximal outcrops on the flanks of 7C allowed for reconstructing the stratigraphy and related eruption history of the SBF (Kueppers et al., 2007, 2009; Porreca et al., 2018). The extension of the study area further to the east revealed the existence of a mid-distal deposit on the north flank of Fogo volcano, on the Ponta do Cintrão

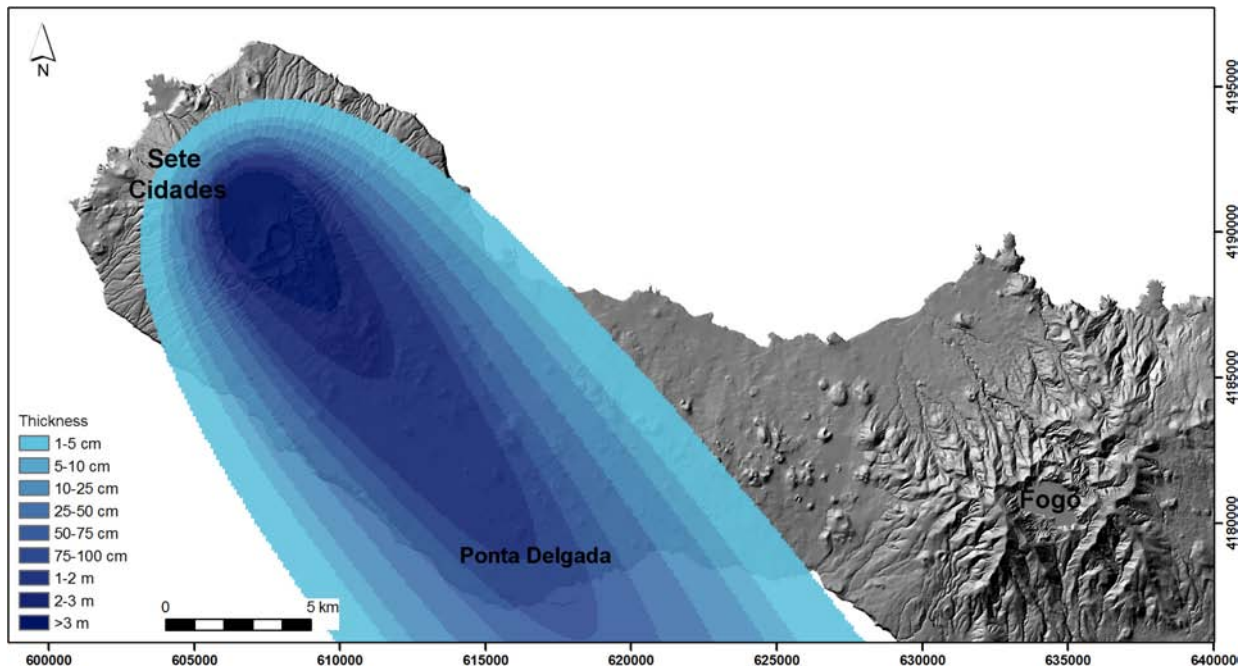

FIGURE 8 | Scenario 3 tephra fall map resulting from the simulations with VORIS 2.0.1, showing the potential impact of a future explosive eruption of Sete Cidades volcano, with the same eruptive source parameters obtained for scenario 2 and wind blowing from NW.

peninsula (∼100 m a.s.l.). Here, a 30 cm-thick, well-sorted, clast-supported bed composed of pumice clasts (average maximum size of 4 cm), dispersed lithic clasts (up to 2 cm across) and small obsidian fragments can be found. The pumice clasts are typically yellowish and contain abundant MME. The angular shape of the pumices and the clast-supported nature strongly suggest a primary fall deposit. This outcrop on the Ponta do Cintrão peninsula is the westernmost outcrop of pumice lapilli beds containing black inclusions described by Ponte (2013) on the north flank of Fogo volcano. Their textural similarity to the Ponta do Cintrão bed described here is striking and allows for extending its distribution to >9 km east of Ponta do Cintrão (**Supplementary Figure S1**). The presence of MME in trachytic pumice clasts from Fogo and Furnas volcanoes has never been described (N. Wallenstein personal communication; cf. Guest et al., 1999, 2015; Wallenstein, 1999; Wallenstein et al., 2015), making it a unique characteristic of the SBF deposits of 7C volcano.

A combination of textural and geochemical analyses, together with field characteristics, has shown that this pumice bed corresponds to the mid-distal part of the pumice fall deposit of the *Upper Member* of the SBF. At Ponta do Cintrão peninsula > 25 km distance from 7C caldera, the proximally observed separation into two pumice lapilli beds by a thin ash-rich layer is absent. We hypothesize that the interpreted unsteadiness of the eruption column was not recorded in the distal portion of the deposit.

The restricted dispersal of the proximal SBF *Upper Member* pumice fall deposit to a very narrow sector of the NE flank of 7C has been interpreted as the effect of deposition from an eruption column strongly controlled by SW-blowing wind. This local geographic restriction and the fairly homogeneous thickness and grain size do not allow the construction of isopach and isopleth maps, thereby limiting our ability to precisely determine eruptive source parameters and wind conditions. However, the finding of mid-distal deposits to the east of 7C volcano provides information for a quantitative analysis of fall dispersal and wind field conditions. The simulations performed in this study show the influence of different wind conditions on tephra fallout in the three considered scenarios. The effect of wind on the deposition of tephra has long been appreciated, manifested in deposits with:

- radial symmetry due to no wind or low wind intensity [e.g., Pululahua, Ecuador (Papale and Rosi, 1993) and Fogo A, Azores (Figure 2 in Walker and Croasdale, 1970)];
- bilateral symmetry due to simple wind conditions for 1 day [e.g., Eyjafjallajökull, Iceland (Figure 3 of Gudmundsson et al., 2012) and Shinmoe-dake, Japan (Figure 8A of Nakada et al., 2013)] or entire eruption sequences [e.g., Montagne Pelée, Martinique (Figures 5, 6 of Carazzo et al., 2012) and Fogo 1563, Azores (Walker and Croasdale, 1970)];
- curved dispersal axes due to complex wind conditions [Shinmoe-dake, Japan (Figures 8B,C of Nakada et al., 2013)]; or
- complex tephra deposition due to strong variability in wind direction [e.g., Cordon Caulle, Chile (Figure 7 and Table 2 of Pistolesi et al., 2015) and Laacher See, Germany (Figure 1 of Van den Boogard and Schmincke, 1985)].

Leder et al. (2017) used published eruptive source parameters for the Laacher See eruption, Germany, to model the tephra loading assuming a simple wind field in order to assess the possible loss in infrastructure by roof collapse. In the present case, the observed distribution of the SBF pumice fall deposit from proximal to mid-distal areas on São Miguel Island is interpreted as the result of complex wind conditions (variable direction and intensity with increasing altitude).

Given the short distance between the assumed vent location and the coastline, Porreca et al. (2018) estimated that only a minor fraction (<10%) of the total erupted volume of the SBF (0.3 km^3) was deposited on land. Here, we constrained eruption column height, erupted volume and wind conditions of the final sub-Plinian phase of the eruption (recorded in the Upper Member) by best-fitting the observed thickness of the pumice fall deposit in proximal and distal areas. This pumice fall deposit can be taken as a proxy to estimate the overall size of the eruption. Accordingly, the estimated eruption column height is 17,000 m, which should be considered as a lower estimate. Taking in account the observed field relations (Porreca et al., 2018), we conservatively estimate that the pumice fall deposit of the Upper Member (0.27 km^3) corresponds to about 25% of the SBF volume. This yields a total erupted volume for the SBF of at least 1.08 km^3, which is 3.6 times more than previously estimated by Porreca et al. (2018). In terms of DRE volume, this corresponds to about 0.25–0.54 km^3 of magma, assuming a deposit density between 550 and 1200 kg/m^3 and a trachytic magma density of 2400 kg/m^3 (Pimentel et al., 2015). This is in agreement with the general idea that single paroxysmal events in the Azores probably do not exceed 1 km^3 DRE (Gertisser et al., 2010; Pimentel et al., 2015), as consistent with the small size of the Azorean calderas (<6 km^3) and the evidence that they are enlarged incrementally through a series of major explosive eruptions (Walker, 1984; Pimentel et al., 2015).

Insights Into Hazard Assessment

There is no doubt that a future explosive eruption of 7C would severely impact the village of Sete Cidades located inside caldera, but also all villages along the volcano's flanks. However, the finding of a mid-distal portion of the *Upper Member* of the SBF deposits provides evidence that a future explosive eruption with similar characteristics has the potential to strongly impact most of the island. Importantly, all major infrastructure (main harbor, airport and hospital) are concentrated in the island's capital, the city of Ponta Delgada, only ∼12 km downwind from 7C caldera. The recent (<5 ky) eruptive history of 7C was marked by at least 17 trachytic intra-caldera explosive eruptions, some of which of sub-Plinian dimensions, and 12 basaltic flank eruptions (Booth et al., 1978; Queiroz, 1997; Cole et al., 2008; Queiroz et al., 2008, 2015). This high eruptive frequency makes 7C the most active volcano in the Azores in the recent geological past. The last intra-caldera explosive eruption (P17) occurred ∼700 years ago (Queiroz et al., 2008) and took place prior to the settlement of the Azores in the first half of the 15th century (Beier and Kramer, 2018). Based on available age constraints, the average eruption recurrence time of around 300 years has already been exceeded (Gaspar et al., 2015). Although 7C is closely monitored since 1998 by a network of seismic stations and episodic GPS/GNSS campaigns, seismic activity is low when compared with Fogo and Furnas volcanoes. The last seismic unrest occurred in 1998 inside the caldera and to the NW (Queiroz et al., 2015). Since then, 7C volcano has been relatively quiet.

Next, we discuss the impact of tephra fallout in proximal and mid-distal areas according to the three scenarios considered in the present work. All of them have a severe impact on São Miguel Island. In proximal areas (i.e., on the flanks of 7C), thick tephra fallout (but also PDCs, not simulated in this study) can have devastating consequences with similar impact assumed for the three scenarios. Buildings and infrastructure (roads, power lines, etc.) are expected to become damaged/destroyed by dynamic pressures (PDC) or load (tephra fall). Ground transportation and radio communication can be disrupted. Severe damage to vegetation, agricultural areas and water sources is also expected. Health hazards including respiratory problems due to ash and volcanic gasses can affect the local population (for a detailed review of the impacts of volcanic ash see Wilson et al., 2012, 2014). The different impacts on medial and distal areas, based on simulation results, are presented next.

Scenario 1 assumes a small sub-Plinian eruption with winds blowing from WSW (**Figure 6**) as reconstructed only from the distribution of the proximal pumice fall deposit of the *Upper Member* of the SBF. In this case, 0.19 km^3 of tephra are raining out from a 12,000 m high eruption column (**Table 2**) and cover the NE flank of 7C (between João Bom and Capelas villages) with up to 3 m thick deposits. Most of the material is going to be deposited into the ocean and form potentially thick and coherent pumice rafts. Depending on wind, wave and currents, pumice rafts may remain afloat for weeks to months (cf. Jutzeler et al., 2014) and will severely affect – if not halt – marine operations along the north coast of São Miguel and make important fishery ports (such as Rabo de Peixe) non-operational. Volcanic ash would shut down the international airport at Ponta Delgada as well as cause the partial closing of the airspace over the Azores, affecting inter-island traffic. At constant wind direction and intensity, the ash plume can reach Europe around NW Spain (∼1500 km distance) and affect flights between Central/SW Europe and Central/South America. As seen in the case of the 2010 Eyjafjallajökull eruption (Iceland) volcanic ash reached central Europe in less than 2 days (Gasteiger et al., 2011) and caused several days of airspace closure. In this scenario, the central and eastern part of São Miguel is not affected by tephra fallout and can likely serve as a retreat area in case of evacuation, similar to the case of Montserrat (West Indies) in 1995 when the population was evacuated to the northern part of the island (Kokelaar, 2002). Of the three considered scenarios, this is the one with the smallest impact on São Miguel and major infrastructure (hospital, port) are likely not affected.

Scenario 2 accounts for a larger sub-Plinian eruption with winds blowing from SW at lower altitude and from WNW at higher altitude (**Figure 7**) as reconstructed based on the proximal and mid-distal pumice fall deposit of the *Upper Member* of the SBF. Approximately 42% more tephra (0.27 km^3) is being erupted compared to scenario 1 from an eruption column up to 17,000 m high. The proximal deposits are expected to extend

further westwards to Mosteiros and cover most of the inhabited areas along the north coast of São Miguel (affecting > 50,000 persons in the villages of Capelas, Rabo de Peixe, Ribeira Grande, Porto Formoso, and Maia). These villages can be affected by 10–25 cm of tephra fall, which is enough to collapse ∼50% of the weakest types of roofs in São Miguel (Booth et al., 1983; Pomonis et al., 1999; Cole et al., 2008). As the area directly affected by tephra fall is substantially larger and comprises approximately half of São Miguel Island, human movement will be impaired by cutting off the main road along the north coast. The pumice deposit can likely have a severe impact on the two geothermal power plants located in the north slope of Fogo volcano. Marine operations would be affected to a comparable degree as in scenario 1. Volcanic ash would shut down the international airport at Ponta Delgada as well as cause the partial closing of the airspace over the Azores, affecting inter-island traffic. At constant wind direction and intensity, the ash plume can reach Europe near Portugal (∼1500 km distance) within 2 days and shut down flights between Europe and Central/South America as well as flights to the Canary Islands. In this scenario, the south part of São Miguel is not affected by tephra fallout and can serve as a retreat area in case of evacuation of the villages located on the north coast. The area of land that can still be used for human activities is significantly reduced, yet, the hospital and main harbor may continue to operate under emergency conditions.

Scenario 3 is based on a hypothetical future eruption with the same eruptive source parameters of scenario 2, under wind conditions blowing toward Ponta Delgada (**Figure 8**) The eruptive source parameters (erupted volume 0.27 km^3; column height 17,000 m) obtained from the reconstruction of the pumice fall deposit of the *Upper Member* of the SBF, through the solution of the inverse problem, are within the same range of values of the parameters of recent (<5 ky) intra-caldera eruptions of 7C (see Cole et al., 2008; Queiroz et al., 2008). This suggests that this pumice fall deposit can be used as a proxy for a future sub-Plinian eruption of 7C. Furthermore, in this case, more than 100,000 persons live in areas that can be affected by up to 1 m of tephra fall, including the capital Ponta Delgada (with Fajã de Cima, Fajã de Baixo, and São Roque in the direct periphery) and Lagoa, the third-largest city (15,000 inhabitants). This thickness of tephra is enough to cause the collapse of almost all buildings, including modern constructions reinforced with concrete (Spence et al., 2005; Cole et al., 2008). In this scenario the airport, the main harbor and critical infrastructure, such as the hospital are not operational, preventing immediate evacuation measures or arrival of first aid goods. At constant wind direction and intensity, the ash plume would reach the Madeira archipelago (∼1000 km distance) and the Canary Islands (∼1300 km) within 1 or 2 days and affect air traffic to these islands, in Northern Africa and between Europe and South America.

Although 7C volcano did not erupt in historic times, the 1563 eruption of Fogo volcano (Walker and Croasdale, 1970; Aguiar et al., 2018) and the 1630 eruption of Furnas volcano (Cole et al., 1995) provide evidence of the severe impact that sub-Plinian eruptions had on São Miguel in the past when the population density was much smaller. In the case of a future sub-Plinian eruption of 7C under the predominant westerly blowing winds, the local impact on the island itself will be catastrophic, likely leaving a long-term effect, with economic consequences for the entire Azores archipelago. As illustrated by scenario 3, the island of São Miguel with an estimated population of > 137,000 inhabitants, cannot be reached by major transportation devices, making evacuation or delivery of supplies very difficult. In the light of this and nonetheless the relatively low probability of such an event, this worst-case scenario should be part of hazard assessment strategies.

The volcanic hazard potential of 7C therefore should not be underestimated and the probability for future explosive eruptions should not be ignored. This work represents a first attempt to perform a realistic assessment of the impact of a major future explosive eruption of 7C on the island of São Miguel. The insights obtained here may be adopted as features of hazard assessment for other volcanic ocean islands prone to explosive eruptions. In general, this study has evidenced the importance of investigative prowess through synergetic studies of field work, textural/geochemical analyses and numerical simulations. A small number of additional, mid-distal to distal outcrops has proven to boost the precision of efforts to precisely constrain source parameters of past eruptions. In future, a supra-disciplinary approach involving scientists working on subaerial deposits, coring seafloor sediments and investigating ice cores should push our current limits of understanding of past eruptions on volcanic ocean islands or in remote positions.

CONCLUSION

Sete Cidades (7C) is the volcano with the highest eruptive frequency in the Azores archipelago in the past 5 ky. The last major explosive eruption (∼16 ka) enlarged the summit caldera to its present-day dimensions and produced a complex pyroclastic sequence known as the Santa Bárbara Formation (SBF). As on many other ocean island volcanoes, the eruption record is incomplete because of primary (large volume of tephra deposited on the ocean and widespread cover of younger deposits) and secondary (significant erosion) reasons that hinder the determination of eruptive source parameters.

New fieldwork, textural and geochemical data of a formerly uncorrelated pumice bed on the north flank of Fogo volcano allowed for its unequivocal correlation with the proximal pumice fall deposit of the *Upper Member* of the SBF. Numerical simulations reconstructed the proximal and distal dispersal of the pumice fall deposit and quantitatively constrained eruptive source parameters and wind conditions. Three different scenarios were considered to assess the impact of tephra fallout on São Miguel Island. Two scenarios (with and without accounting for the mid-distal part of the pumice fall deposit) have shown the strong influence of wind on tephra dispersal. The constrained eruptive source parameters were used to envisage a third scenario assuming wind blowing toward the island's capital. In this worst,

but plausible, scenario the city of Ponta Delgada (including main harbor, hospital and airport) and surrounding communities would be affected by up to 1 m of tephra.

Although 7C volcano has not erupted in historical times and is currently considered dormant, its potential to generated hazardous explosive eruptions should not be overlooked. Worst-case scenarios, such as the one considered in scenario 3, need to be included in holistic approaches of volcanic hazard assessment on active volcanic islands.

AUTHOR CONTRIBUTIONS

UK and AP carried out the fieldwork. UK found the distal outcrop at Ponta do Cintrão during the course of Project M1.1.2/I/009/2005/A, guided and designed by JP and GQ. AP preformed the numerical simulations. BE, FF, and JN performed the geochemical analyses. DP co-supervised two undergraduate thesis at LMU. UK, AP, and BE drafted the manuscript. All authors have read and commented on the manuscript.

FUNDING

UK acknowledges Project M1.1.2/I/009/2005/A (Fundação Gaspar Frutuoso). BE acknowledges funding from the Swiss National Science Foundation (200021_166281). This study was additionally supported by the European Union's Seventh Framework Program FP7 "FP7-PEOPLE-2013-ITN," under grant agreement number is 607905 – VERTIGO.

ACKNOWLEDGMENTS

UK thanks Catarina Goulart for her invaluable support with ArcGIS and Pedro Cerqueira, Roberto Hoge, and João Fontiela for logistical support during field work, Hilger Lohringer (LMU) for sample preparation for the theses of Dominik Fahrner and Gianluigi Ortenzi theses as well as Dirk Müller (LMU) for assistance with the microprobe. The authors thank the reviewers DP and FL as well as the editor RS and Valerio Acocella for their constructive comments.

SUPPLEMENTARY MATERIAL

The Supplementary Material for this article can be found online at: https://www.frontiersin.org/articles/10.3389/feart.2019.00122/full#supplementary-material

FIGURE S1 | Stratigraphic sections of nine outcrops along the north coast of São Miguel Island containing a pumice lapilli bed with black inclusions, highlighted in yellow (Ponte, 2013). In this study, this pumice fall bed is correlated to the *Upper Member* of the SBF.

TABLE S1 | Overview of values of trace elements for the 7 different sample sets.

REFERENCES

Aguiar, S., Pacheco, J., and Pimentel, A. (2018). Eruptive history of the 1563 eruption of fogo volcano (S. *Miguel, Azores*). *Geophys. Res. Abstr.* 20, EGU2018–EGU2776.

Armienti, P., Macedonio, G., and Pareschi, M. T. (1988). A numerical-model for simulation of tephra transport and deposition: applications to May 18, 1980, Mount St Helens eruption. *J. Geophys. Res.* 93, 6463–6476. doi: 10.1029/JB093iB06p06463

Beier, C., Haase, K. M., and Hansteen, T. H. (2006). magma evolution of the sete cidades volcano. são miguel, azores. *J. Petrol.* 47, 1375–1411. doi: 10.1093/petrology/egl014

Beier, R., and Kramer, J. (2018). "A portrait of the Azores: From natural forces to cultural identity," in *Volcanoes of the Azores, Active Volcanoes of the World*, eds U., Kueppers and C., Beier (Berlin: Springer), 3–26. doi: 10.1007/978-3-642-32226-6_2

Biass, S., Scaini, C., Bonadonna, C., Folch, A., Smith, K., and Höskuldsson, A. (2014). A multi-scale risk assessment for tephra fallout and airborne concentration from multiple Icelandic volcanoes - part 1: hazard assessment. *Nat. Hazards Earth Syst. Sci.* 14, 2265–2287. doi: 10.5194/nhess-14-2265-2014

Bonasia, R., Capra, L., Costa, A., Macedonio, G., and Saucedo, R. (2011). Tephra fallout hazard assessment for a Plinian eruption scenario at volcán de colima (Mexico). *J. Volcanol. Geotherm. Res.* 203, 12–22. doi: 10.1016/j.jvolgeores.2011.03.006

Bonasia, R., Macedonio, G., Costa, A., Mele, D., and Sulpizio, R. (2010). Numerical inversion and analysis of tephra fallout deposits from the 472 AD sub-plinian eruption at vesuvius (Italy) through a new best-fit procedure. *J. Volcanol. Geotherm. Res.* 189, 238–246. doi: 10.1016/j.jvolgeores.2009.11.009

Booth, B., Croasdale, R., and Walker, G. P. L. (1978). "A quantitative study of five thousand years of volcanism on São Miguel, Azores," in *Philosophical. Transactions of the Royal Society A*, eds H. Tazieff and J. C. Sabroux (Amsterdam: Elsevier), 99–109.

Booth, B., Croasdale, R., and Walker, G. P. L. (1983). "Volcanic hazard on São Miguel, Azores," in *Forecasting Volcanic Events. Developments in Volcanology, 1*, eds H. Tazieff and J. C. Sabroux (Amsterdam: Elsevier), 99–109.

Carazzo, G., Tait, S., Kaminski, E., and Gardner, J. E. (2012). The recent Plinian explosive activity of Mt. *Pelée volcano (Lesser Antilles): the P*1 AD 1300 eruption. *Bull. Volcanol.* 74, 2187–2203. doi: 10.1007/s00445-012-0655-4

Carmo, R., Madeira, J., Ferreira, T., Queiroz, G., and Hipólito, A. (2015). "Volcano-tectonic structures of São Miguel Island, Azores," in *Volcanic Geology of São Miguel Island (Azores Archipelago)*, eds J. L., Gaspar, J. E., Guest, A. M., Duncan, F. J. A. S., Barriga, and D. K., Chester (London: Geological Society London), 65–86. doi: 10.1144/M44.6

Cole, P. D., Pacheco, J. M., Gunasekera, R., Queiroz, G., Gonçalves, P., and Gaspar, J. L. (2008). Contrasting styles of explosive eruption at sete cidades, são miguel, azores, in the last 5000 years: hazard implications from modeling. *J. Volcanol. Geotherm. Res.* 178, 574–591. doi: 10.1016/j.volgeores.2008.01.008

Cole, P. D., Queiroz, G., Wallenstein, N., Gaspar, J. L., Duncan, A. M., and Guest, J. E. (1995). An historic subplinian to phreatomagmatic eruption: the 1630 eruption of furnas volcano, sao miguel, azores. *J. Volcanol. Geotherm. Res.* 69, 117–135. doi: 10.1016/0377-0273(95)00033-X

Costantini, L., Bonadonna, C., Houghton, B. F., and Wehrmann, H. (2009). new physical characterization of the fontana lapilli basaltic plinian eruption, nicaragua. *Bull. Volcanol.* 71, 337–355. doi: 10.1007/s00445-008-0227-9

Dinis, L. M. (2006). *Contribuição Para A Definição Da Escala Vulcanoestratigrafica Da Ilha De São Miguel (Açores)*. M.Sc. Thesis, Azores University, Portugal.

Fahrner, D. (2012). *Comparison Of Pumice Clasts From Proximal And Distal Fall Deposits Of Sete Cidades Volcano (São Miguel, Azores): Do They Belong To The Same Eruption?*. M.Sc. thesis, Ludwig-Maximilians-Universität Munich, Germany.

Felpeto, A., Martí, J., and Ortiz, R. (2007). Automatic GIS-based system for volcanic hazard assessment. *J. Volcanol. Geotherm. Res.* 166, 106–116. doi: 10.1016/j.jvolgeores.2007.07.008

Folch, A., and Felpeto, A. (2005). A coupled model for dispersal of tephra during sustained explosive eruptions. *J. Volcanol. Geotherm. Res.* 145, 337–349. doi: 10.1016/j.jvolgeores.2005.01.010

Gaspar, J. L., Guest, J. E., Queiroz, G., Pacheco, J., Pimentel, A., Gomes, A., et al. (2015). "Eruptive frequency and volcanic hazards zonation in São Miguel Island, Azores," in *Volcanic Geology of São Miguel Island (Azores Archipelago)*, eds J. L. Gaspar, J. E. Guest, A. M. Duncan, F. J. A. S. Barriga, and D. K. Chester (London: Geological Society London), 155–166. doi: 10.1144/M44.12

Gasteiger, J., Groß, S., Freudenthaler, V., and Wiegner, M. (2011). Volcanic ash from Iceland over Munich: mass concentration retrieved from ground-based remote sensing measurements. *Atmos. Chem. Phys.* 11, 2209–2223. doi: 10.5194/acp-11-2209-2011

Gertisser, R., Self, S., Gaspar, J. L., Kelley, S. P., Pimentel, A., Eikenberg, J., et al. (2010). "Ignimbrite stratigraphy and chronology on Terceira Island, Azores," in *Stratigraphy and geology of volcanic areas*, eds G. Groppelli and L. Viereck-Goette (London: Geological Society London), 133–154.

Gonçalves, P. (2006). *Caracterização do depósito sete-p11 (sete cidades, s. Miguel, açores): Implicações Para a História Eruptiva*. M.Sc. Thesis, Azores University, Portugal.

Gudmundsson, M. T., Thordarson, T., Höskuldsson, A., Larsen, G., Björnsson, H., Prata, F. J., et al. (2012). Ash generation and distribution from the April-May 2010 eruption of Eyjafjallajökull, Iceland. *Sci. Rep.* 2:572. doi: 10.1038/srep00572

Guest, J. E., Gaspar, J. L., Cole, P. D., Queiroz, G., Duncan, A. M., Wallenstein, N., et al. (1999). Volcanic geology of Furnas volcano. *São Miguel, Azores. J. Volcanol. Geotherm. Res.* 92, 1–29. doi: 10.1016/S0377-0273(99)00064-5

Guest, J. E., Pacheco, J. M., Cole, P. D., Duncan, A. M., Wallenstein, N., Queiroz, G., et al. (2015). "The volcanic history of Furnas Volcano, São Miguel, Azores," in *Volcanic Geology of São Miguel Island (Azores Archipelago)*, eds J. L. Gaspar, J. E. Guest, A. M. Duncan, F. J. A. S. Barriga, and D. K. Chester (London: Geological Society London), 125–134. doi: 10.1144/M44.9

Guillong, M., Meier, D., Allan, M., Heinrich, C., and Yardley, B. (2008). *Laser Ablation ICP–MS in the Earth Sciences: Current Practices and Outstanding Issues*. Canada: Mineralogical Association of Canada, 328–333.

Heiken, G., and McCoy, F. Jr. (1984). Caldera development during the minoan eruption, thira, cyclades, greece. *J. Geophys. Res.* 89, 8441–8462. doi: 10.1029/JB089iB10p08441

Johansson, H., Lind, E. M., and Wastegard, S. (2017). Compositions of glass in proximal tephras from eruptions in the azores archipelago and their links with distal sites in Ireland. *Quat. Geochronol.* 40, 120–128. doi: 10.1016/j.quageo.2016.07.006

Jutzeler, M., Marsh, R., Carey, R. J., White, J. D. L., Talling, P. J., and Karlstrom, L. (2014). On the fate of pumice rafts formed during the 2012 havre submarine eruption. *Nat. Commun* 5:3660. doi: 10.1038/ncomms4660

Kokelaar, B. P. (2002). "Setting, chronology and consequences of the eruption of Soufriere Hills Volcano, Montserrat (1995-1999)," in *The Eruption of Soufriere Hills Volcano, Montserrat, from 1995 to 1999*, eds T. H. Druitt and B. P. Kokelaar (London: Geological Society, London), 1–44. doi: 10.1144/GSL.MEM.2002.021.01.02

Kueppers, U., Beier, C., Genske, F. S., and Caetano, D. (2018). "Where to Go? A Selection and Short Description of Geological Highlights in the Azores," in *Volcanoes of the Azores, Active Volcanoes of the World*, eds U. Kueppers and C. Beier (Berlin: Springer), 331–355. doi: 10.1007/978-3-642-32226-6_14

Kueppers, U., Pimentel, A., and Pacheco, J. (2009). The 16 ka eruption of sete cidades volcano, são miguel island (Azores, Portugal): hazard assessment from mapping and simulation of tephra fall. *Geophys. Res. Abstr.* 11, EGU2009–EGU10816.

Kueppers, U., Queiroz, G., and Pacheco, J. (2007). *Eruptive and Transportation Processes During Caldera-Forming Eruptions of Sete Cidades Volcano, São Miguel, Azores*. AGU Fall Meeting 2007. San Francisco, CA

Laeger, K., Petrelli, M., Morgavi, D., Lustrino, M., Pimentel, A., Paredes-Mariño, J., et al. (2019). Pre-eruptive conditions and triggering mechanism of the ∼16 ka santa bárbara explosive eruption of sete cidades volcano (São Miguel. Azores). *Contrib. Mineral. Petrol.* 174:11. doi: 10.1007/s00410-019-1545-y

Leder, J., Wenzel, F., Daniell, J. E., and Gottschämmer, E. (2017). Loss of residential buildings in the event of a re-awakening of the laacher see volcano (Germany). *J. Volcanol. Geotherm. Res.* 337, 111–123. doi: 10.1016/j.jvolgeores.2017.02.019

Longchamp, C., Bonadonna, C., Bachmann, O., and Skopelitis, A. (2011). Characterization of tephra deposits with limited exposure: the example of the two largest explosive eruptions at Nisyros volcano (Greece). *Bull. Volcanol.* 73, 1337–1352. doi: 10.1007/s00445-011-0469-9

Macedonio, G., Costa, A., and Folch, A. (2008). Ash fallout scenarios at vesuvius: numerical simulations and implications for hazard assessment. *J. Volcanol. Geotherm. Res.* 178, 366–377. doi: 10.1016/j.jvolgeores.2008.08.014

Mazzocchi, M., Hansstein, F., and Ragona, M. (2010). The 2010 volcanic ash cloud and its financial impact on the European airline industry. *CESifo Forum* 11, 92–100.

Moiseenko, K., and Malik, N. (2019). Linear inverse problem for inferring eruption source parameters from sparse ash deposit data as viewed from an atmospheric dispersion modeling perspective. *Bull. Volcanol.* 81:19. doi: 10.1007/s00445-019-1281-1

Moore, R. (1990). Volcanic geology and eruption frequency. São Miguel, Azores. *Bull. Volcanol.* 52, 602–614. doi: 10.1007/BF00301211

Nakada, S., Nagai, M., Kaneko, T., Suzuki, Y., and Maeno, F. (2013). The outline of the 2011 eruption at Shinmoe-dake (Kirishima). Japan. *Earth Planets Space* 65:1. doi: 10.5047/eps.2013.03.016

Ortenzi, G. (2014). *Sete Cidades volcano (são miguel, azores) 16 kyr b.p. Explosive Eruption: 2d and 3d Analyses of Pumice Samples*. M.Sc. Thesis (Tesi di Laurea), Università di Perugia, Italy.

Papale, P., and Rosi, M. (1993). A case of no-wind plinian fallout at Pululagua caldera (Ecuador): implications for models of clast dispersal. *Bull. Volcanol.* 55:523. doi: 10.1007/BF00304594

Paredes-Mariño, J., Dobson, K. J., Ortenzi, G., Kueppers, U., Morgavi, D., Petrelli, M., et al. (2017). Enhancement of eruption explosivity by heterogeneous bubble nucleation triggered by magma mingling. *Sci. Rep.* 7, 1–10. doi: 10.1038/s41598-017-17098-3

Pedrazzi, D., Cappello, A., Zanon, V., and Del Negro, C. (2015). Impact of effusive eruptions from the eguas–carvão fissure system. são miguel island, azores archipelago (Portugal). *J. Volcanol. Geotherm. Res.* 291, 1–13. doi: 10.1016/j.jvolgeores.2014.12.012

Pimentel, A., Pacheco, J., and Self, S. (2015). The 1000-years BP explosive eruption of caldeira volcano (Faial. Azores): the first stage of incremental caldera formation. *Bull. Volcanol.* 77:42. doi: 10.1007/s00445-015-0930-2

Pimentel, A., Pacheco, J. M., and Felpeto, A. (2006). Influence of wind patterns on the dispersal of volcanic plumes in the Azores region: test study of the 1630 eruption of furnas volcano (S. *Miguel, Azores). Geophys. Res. Abstr.* 8, EGU06–A–04983.

Pistolesi, M., Cioni, R., Bonadonna, C., Elissondo, M., Baumann, V., Bertagnini, A., et al. (2015). Complex dynamics of small-moderate volcanic events: the example of the 2011 rhyolitic cordon caulle eruption. *Chile. Bull. Volcanol.* 77:1. doi: 10.1007/s00445-014-0898-3

Pomonis, A., Spence, R. J. S., and Baxter, P. J. (1999). Risk assessment of residential buildings for an eruption of furnas volcano. são miguel, the azores. *J. Volcanol. Geotherm. Res.* 92, 107–131. doi: 10.1016/S0377-0273(99)00071-2

Ponte, D. (2013). *Contribuição para o Conhecimento das Sequências Eruptivas dos Vulcões do Fogo e das Furnas, Entre Ribeirinha e Lomba da Maia, São Miguel (Açores)*. M.Sc. Thesis, Azores University, Portugal.

Porreca, M., Pimentel, A., Kueppers, U., Izquierdo, T., Pacheco, J., and Queiroz, G. (2018). Event stratigraphy and emplacement mechanisms of the last major caldera eruption on sete cidades volcano (são miguel, azores): the 16 ka santa bárbara formation. *Bull. Volcanol.* 80:76. doi: 10.1007/s00445-018-1250-0

Queiroz, G. (1997). *Vulcão das Sete Cidades (S. Miguel, Açores): História Eruptiva e Avaliação do Hazard*. Ph.D. Thesis, Azores University, Portugal.

Queiroz, G., Gaspar, J. L., Guest, J. E., Gomes, A., and Almeida, M. H. (2015). "Eruptive history and evolution of Sete Cidades Volcano, São Miguel Island, Azores," in *Volcanic Geology of São Miguel Island (Azores Archipelago)*, eds J. L. Gaspar, J. E. Guest, A. M. Duncan, F. J. A. S. Barriga, and D. K. Chester (London: Geological Society of London), 87–104. doi: 10.1144/M44.7

Queiroz, G., Pacheco, J. M., Gaspar, J. L., Aspinall, W. P., Guest, J. E., and Ferreira, T. (2008). The last 5000 years of activity at sete cidades volcano (são miguel island, azores): implications for hazard assessment. *J. Volcanol. Geotherm. Res* 178, 562–573. doi: 10.1016/j.jvolgeores.2008.03.001

Scaini, C., Biass, S., Galderisi, A., Bonadonna, C., Folch, A., Smith, K., et al. (2014). A multi-scale risk assessment for tephra fallout and airborne concentration

from multiple Icelandic volcanoes - part 2: vulnerability and impact. *Nat. Hazards Earth Syst. Sci.* 14, 2289–2312. doi: 10.5194/nhess-14-2289-2014

Scollo, S., Folch, A., and Costa, A. (2008). A parametric and comparative study of different tephra fallout models. *J. Volcanol. Geotherm. Res.* 176, 199–211. doi: 10.1016/j.jvolgeores.2008.04.002

Spanu, A., de' Michieli Vitturi, M., and Barsotti, S. (2016). Reconstructing eruptive source parameters from tephra deposit: a numerical study of medium-sized explosive eruptions at Etna volcano. *Bull. Volcanol.* 78:59. doi: 10.1007/s00445-016-1051-2

Spence, R. J. S., Kelman, I., Calogero, E., Toyos, G., Baxter, P. J., and Komorowski, J.-C. (2005). Modelling expected physical impacts and human casualties from explosive volcanic eruptions. *Nat. Hazards Earth Syst. Sci.* 5, 1003–1015. doi: 10.5194/nhess-5-1003-2005

Suzuki, T. (1983). "A theoretical model for dispersion of tephra," in *Arc volcanism: physics and tectonics*, eds D. Shimozuru and I. Yokoyama (Tokyo: Terra Scientific Publishing Company), 95–116.

Szymanowski, D., Ellis, B. S., Bachmann, O., Guillong, M., and Phillips, W. M. (2015). Bridging basalts and rhyolites in the yellowstone–snake river plain volcanic province: the elusive intermediate step. *Earth Planet. Sci. Lett.* 415, 80–89. doi: 10.1016/j.epsl.2015.01.041

Van den Boogard, P., and Schmincke, H. U. (1985). laacher see tephra: a widespread isochronous late quaternary tephra layer in central and northern Europe. *Geol. Soc. Am. Bull.* 96, 1554–1571.

Walker, G. P. L. (1984). Downsag calderas, ring faults, caldera sizes, and incremental caldera growth. *J. Geophys. Res.* 89, 8407–8416. doi: 10.1029/JB089iB10p08407

Walker, G. P. L., and Croasdale, R. (1970). Two Plinian-type eruptions in the Azores. *J. Geol. Soc.* 27, 17–55. doi: 10.1144/gsjgs.127.1.0017

Wallenstein, N. (1999). *Estudo da História Recente e do Comportamento Eruptivo do Vulcão do fogo (s. Miguel, açores). Avaliação Preliminar do Hazard*. Ph.D. thesis, Azores University, Portugal.

Wallenstein, N., Duncan, A., Guest, J. E., and Almeida, M. H. (2015). "Eruptive history of Fogo Volcano, São Miguel, Azores," in *Volcanic Geology of São Miguel Island (Azores Archipelago)*, eds J. L. Gaspar, J. E. Guest, A. M. Duncan, F. J. A. S. Barriga, and D. K. Chester (London: Geological Society of London), 105–123. doi: 10.1144/M44.8

Wilson, G., Wilson, T. M., Deligne, N. I., and Cole, J. W. (2014). Volcanic hazard impacts to critical infrastructure: a review. *J. Volcanol. Geotherm. Res.* 286, 148–182. doi: 10.1016/j.jvolgeores.2014.08.030

Wilson, L., and Huang, T. C. (1979). The influence of shape on the atmospheric settling velocity of volcanic ash particles. *Earth Planet. Sci. Lett.* 44, 311–324. doi: 10.1016/0012-821X(79)90179-1

Wilson, T. M., Stewart, C., Sword-Daniels, V., Leonhard, G. S., Johnston, D. M., Cole, J. W., et al. (2012). Volcanic ash impacts on critical infrastructure. *Phys. Chem. Earth* 4, 5–23. doi: 10.1016/j.pce.2011.06.006

Conflict of Interest Statement: The authors declare that the research was conducted in the absence of any commercial or financial relationships that could be construed as a potential conflict of interest.

Copyright © 2019 Kueppers, Pimentel, Ellis, Forni, Neukampf, Pacheco, Perugini and Queiroz. This is an open-access article distributed under the terms of the Creative Commons Attribution License (CC BY). The use, distribution or reproduction in other forums is permitted, provided the original author(s) and the copyright owner(s) are credited and that the original publication in this journal is cited, in accordance with accepted academic practice. No use, distribution or reproduction is permitted which does not comply with these terms.

Advantages of publishing in Frontiers

OPEN ACCESS
Articles are free to read for greatest visibility and readership

FAST PUBLICATION
Around 90 days from submission to decision

HIGH QUALITY PEER-REVIEW
Rigorous, collaborative, and constructive peer-review

TRANSPARENT PEER-REVIEW
Editors and reviewers acknowledged by name on published articles

Frontiers
Avenue du Tribunal-Fédéral 34
1005 Lausanne | Switzerland

Visit us: www.frontiersin.org
Contact us: info@frontiersin.org | +41 21 510 17 00

REPRODUCIBILITY OF RESEARCH
Support open data and methods to enhance research reproducibility

DIGITAL PUBLISHING
Articles designed for optimal readership across devices

FOLLOW US
@frontiersin

IMPACT METRICS
Advanced article metrics track visibility across digital media

EXTENSIVE PROMOTION
Marketing and promotion of impactful research

LOOP RESEARCH NETWORK
Our network increases your article's readership